

ATMOSPHERE, IONOSPHERE, SAFETY



Kaliningrad
2020

UDK 550.51
BBK 552.44
A92

A92 **Atmosphere, ionosphere, safety** / edited by O.P. Borchevkina,
M.G. Golubkov and I. V. Karpov. — Kaliningrad, 2020. — 272 p.
ISBN 978-5-6042044-3-6

Proceedings of International Conference "Atmosphere, ionosphere, safety" (AIS-2020) include materials reports on: (1) — response analysis of the atmosphere — ionosphere to natural and manmade processes, various causes related geophysical phenomena and evaluate possible consequences of their effects on the human system and process; (2) — to study the possibility of monitoring and finding ways to reduce risk. Scientists from different countries and regions of Russia participated in the conference. Attention was given to questions interconnected with modern nanotechnology and environmental protection. Knowledge of the factors influencing the atmosphere and ionosphere can use them to monitor natural disasters and to establish the appropriate methods on this basis.

Content of the reports is of interest for research and students specializing in physics and chemistry of the atmosphere and ionosphere.

UDK 550.51
BBK 552.44

ISBN 978-5-6042044-3-6

ATMOSPHERIC-IONOSPHERIC RELATIONS

METHOD FOR DETERMINING NEUTRAL WIND VELOCITY FULL VECTOR BY USING IGWS PROPAGATING PARAMETER STATISTICS

Andrey V. Medvedev, Konstantin G. Ratovsky, Maxim V. Tolstikov, Roman V. Vasilyev, Maxim F. Artamonov, Alexey V. Oinats

Institute of Solar-Terrestrial Physics, Irkutsk, Russia

Introduction. Ionosonde DPS-4 and two beams of the Irkutsk Incoherent Scatter Radar (IISR) form a triangle with ~ 100 km side, convenient for investigating medium and large-scale traveling ionospheric disturbances (TIDs). Automatic method for determining TIDs space-time structure and propagation parameters have been developed. The technique is described in detail [1]. TIDs are believed to be ionospheric manifestations of internal gravity waves (IGWs). Using the obtained statistics of TIDs parameters, we tested the Boussinesq and Hines dispersion relations for IGWs. It was shown that the observational data are in good consistence with theoretical concepts on IGW propagation in the upper atmosphere [2]. In linear approximation, IGW interaction with horizontal wind is limited to the Doppler frequency shift:

$$\omega' = \omega_{obs} - \vec{k} \cdot \vec{U} \quad (1)$$

where ω' is the intrinsic wave frequency (a wave frequency in moving medium), ω_{obs} is the observed frequency, U is the wind velocity vector, and k is the wave vector. The IGW intrinsic frequency can be obtained from a dispersion relation. Using expression (1), one can obtain the wind velocity projection along the IGW propagation direction:

$$U_p = \frac{\omega_{obs} - \omega'}{|k|} \quad (2)$$

In single measurements, this approach is not of high significance since the calculated wind velocities are highly dispersive. If we have sufficient statistics of the wind velocity projections, it is possible to determine monthly averages of zonal and meridional winds by minimizing functional [2]. The comparison of the obtained monthly average diurnal variations of zonal and meridional neutral winds with the HWM2007 model prediction and independent meridional wind measurements at the IISR, showed satisfactory agreement of wind patterns obtained in various ways [2-3]. In this paper, we propose a new method for determining the neutral wind velocity vector, based on IGW group velocity measurements. In contrast to the previously developed method, it allows us to obtain not only a statistical pattern but also potentially instantaneous values of the neutral wind velocity. Another advantage of the new method is the ability to measure the vertical velocity of the neutral wind.

Method for determining neutral wind velocity full vector. Automatic method of TIDs detection is based on selecting the dominant harmonic from all spectrum of a wave disturbance. The data from all beams were reduced to one point of time in 15 min increments by interpolation. The spectral analysis was carried out for each beam and at each height in the running 12-hour window. To reduce the effect of sidelobes the 12 h Blackman window was used. The coincidence of local spectral maxima at three neighbor heights as a minimum for each tool (DPS-4, and two IISR beams) was a criterion for the presence of a wave-like disturbance. Phase differences observed at different spatial points can be used to calculate the full wave vector by solving line equations system[1]. The measurement time was assigned to the middle of the current 12-hour window. Prolonged disturbances occurring in several

neighbor windows are taken into account several times in the overall statistics. Using Hines dispersion relation, we can obtain the full vector of group velocity in a coordinate system moving with the neutral wind velocity.

$$\begin{aligned} G'_x &= \frac{\partial \omega'}{\partial k_x} = \frac{k_x \omega' C_0^2 (\omega'^2 - \Omega_B^2)}{(\omega'^4 - (k_x^2 + k_y^2) \Omega_B^2 C_0^2)} \\ G'_y &= \frac{\partial \omega'}{\partial k_y} = \frac{k_y \omega' C_0^2 (\omega'^2 - \Omega_B^2)}{(\omega'^4 - (k_x^2 + k_y^2) \Omega_B^2 C_0^2)} \\ G'_z &= \frac{\partial \omega'}{\partial k_z} = \frac{k_z C_0^2 \omega'^3}{(\omega'^4 - (k_x^2 + k_y^2) \Omega_B^2 C_0^2)} \end{aligned} \quad (3)$$

The intrinsic period (frequency) can be found from the Hines equation.

From experimental data we can detect the group velocity in a fixed coordinate system. From dispersion relation one can obtain the exact expression:

$$d\omega = \frac{\partial \omega}{\partial k_x} dk_x + \frac{\partial \omega}{\partial k_y} dk_y + \frac{\partial \omega}{\partial k_z} dk_z = G_x dk_x + G_y dk_y + G_z dk_z \quad (4)$$

or an approximate expression for finite differences:

$$\Delta\omega = G_x \Delta k_x + G_y \Delta k_y + G_z \Delta k_z \quad (5)$$

To determine the group velocity full vector, one needs three equations similar to (5). So, besides frequency ω corresponding to local spectral maximum we need another three frequencies. Let assume that the disturbance covers a certain frequency band. For spectral neighbors ($\omega - 3\Delta\omega$, $\omega - 2\Delta\omega$, $\omega - \Delta\omega$, $\omega + \Delta\omega$, $\omega + 2\Delta\omega$, $\omega + 3\Delta\omega$), we calculate full wave vectors by using phase differences. Further we select three frequencies with the minimum azimuthal difference of wave vectors (assume these frequencies belong to the same disturbance). Assuming that group velocity varies slightly, we obtain liner equations system:

$$\begin{cases} \Delta\omega_1 = G_x \Delta k_{x1} + G_y \Delta k_{y1} + G_z \Delta k_{z1} \\ \Delta\omega_2 = G_x \Delta k_{x2} + G_y \Delta k_{y2} + G_z \Delta k_{z2} \\ \Delta\omega_3 = G_x \Delta k_{x3} + G_y \Delta k_{y3} + G_z \Delta k_{z3} \end{cases} \quad (6)$$

Knowing group velocity in a coordinate system moving with the neutral wind velocity and in a fixed coordinate system, we can calculate the neutral wind velocity full vector.

$$\begin{cases} U_x = G_x - G'_x \\ U_y = G_y - G'_y \\ U_z = G_z - G'_z \end{cases} \quad (7)$$

It should be noted, that determining intrinsic period (frequency) from the Hines equation we also determine wind along the IGW propagation direction (2). Therefore, system (7) should be added with equation:

$$\frac{k_x}{|k|} U_x + \frac{k_y}{|k|} U_y + \frac{k_z}{|k|} U_z = \frac{\omega - \omega'}{|k|} \quad (8)$$

In addition, when calculating group velocity in a fixed coordinate system we assumed that the dispersion relation was valid at least at three more frequencies (we call those $\omega 1$, $\omega 2$, $\omega 3$), hence, system (7) should be added with three more equations similar to (8). Final system is excessive, we will solve it with the midsquare method. Method is described in detail [4]. We compare neutral wind obtained by using measurements of IGWs group and phase velocities with the HWM2007 model, results of our previously

developed method [2-3] and Fabry-Pérot interferometer data. Figure 1 shows the winter wind patterns obtained in various ways.

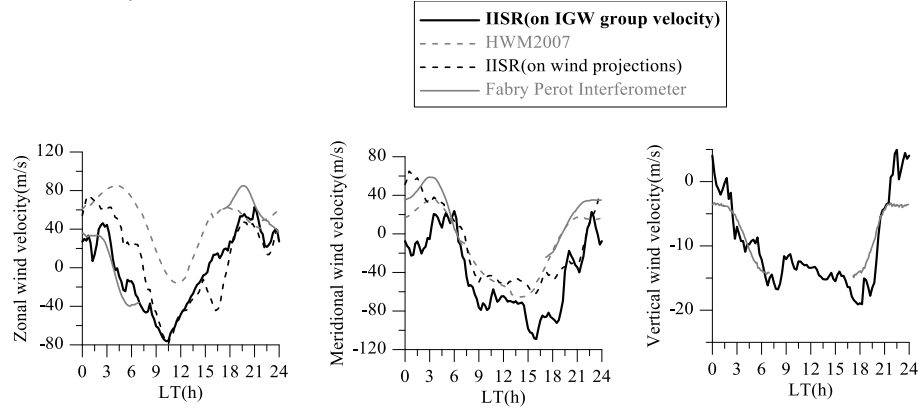


FIGURE 1. Wintertime diurnal variations in zonal (positive eastward, left panel), meridional (positive southward, central panel), and vertical (positive upward, right panel) winds obtained in various ways: new method based on IGW group velocity measurements (black), FPI (gray), HWM2007 (gray dotted), and previously developed method based on wind projection measurements (black dotted).

The horizontal wind diurnal variations obtained in various ways are in qualitative agreement. All the ways show eastward and southward winds in the nighttime, as well as westward and northward winds in the daytime. The zonal wind obtained by the new method agrees with the Fabry-Pérot interferometer. Insofar as FPI and new method give similar results we consider that in this case HWM2007 does not describe the wind accurately. Of particular interest is the vertical wind measurement. The presence of large vertical wind velocities in the upper thermosphere causes controversy in the scientific community. Neither empirical nor physical models predict the presence of large vertical wind velocities. Large vertical velocities obtained with Fabry-Pérot interferometer are sometimes interpreted as apparent vertical velocities due to horizontal wind and scattering in the upper troposphere. Figure 1 shows that both the new method and Fabry-Pérot demonstrate the same diurnal trend in the vertical wind. Thus, two absolutely independent methods give the presence of vertical wind velocities. Vertical winds can have a significant effect on the wind induced vertical drift of the ionospheric plasma. The effect may be comparable with the meridional wind effect. To clarify this issue, we calculated the contributions of the meridional VEFFX and vertical VEFFZ winds to the plasma drift velocity as well as the total contribution VEFF:

$$V_{EFFX} = U_x \cos I \sin I, V_{EFFZ} = U_z \sin^2 I, V_{EFF} = V_{EFFX} + V_{EFFZ} \quad (9)$$

where I is the magnetic field inclination ($\sim 72^\circ$). The calculated contributions were compared with the peak heights (hmF2) from the Irkutsk ionosonde averaged over the same period, and the correlation coefficients were calculated (Figure 2).

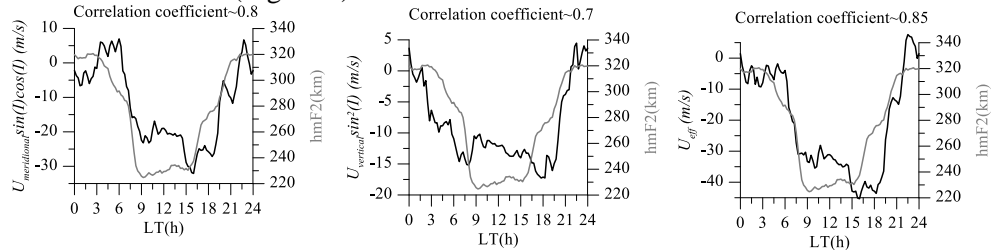


FIGURE 2. Comparison of meridional wind contribution (left, black), vertical wind contribution (central, black), and total contribution (right, black) to plasma drift velocity with peak height (gray) from the Irkutsk ionosonde.

Figure 2 demonstrates that the contributions of the meridional and vertical winds to the plasma drift velocity are really close to each other. The total contribution has the largest correlation coefficient with the height. These results clearly demonstrate the importance of vertical wind measurements and the need to take them into account in physical and empirical models of the ionosphere and thermosphere.

For the analysis, the methods obtained with budgetary funding of Basic Research program II.12 were used.

1. A.V. Medvedev, K.G. Ratovsky, M.V. Tolstikov, S.S. Alsatkin, A.A. Scherbakov, Studying of the spatial-temporal structure of wave like ionospheric disturbances on the base of Irkutsk incoherent scatter radar and Digisonde data, *Journal of Atmospheric and Solar-Terrestrial Physics*, 2013, 105–106, pp. 350–357, doi: 10.1016/j.jastp.2013.09.001.

2. A.V. Medvedev, K.G. Ratovsky, M.V. Tolstikov, S.S. Alsatkin, A.A. Scherbakov. A statistical study of internal gravity wave characteristics using the combined Irkutsk Incoherent Scatter Radar and Digisonde data, *Journal of Atmospheric and Solar-Terrestrial Physics*, 2015, 132, pp. 13–21, doi: 10.1016/j.jastp.2015.06.012.

3. A.V. Medvedev, K.G. Ratovsky, M.V. Tolstikov, A.V. Oinats, S.S. Alsatkin, G.A. Zhrebtsov, Relation of internal gravity wave anisotropy with neutral wind characteristics in the upper atmosphere, *J. Geophys. Res.*, 2017, 122(7), pp. 7567–7580, doi: 10.1002/2017JA024103.

4. A.V. Medvedev, K.G. Ratovsky, M.V. Tolstikov, R.V. Vasilyev, M.F. Artamonov, Method for Determining Neutral Wind Velocity Vectors Using Measurements of Internal Gravity Wave Group and Phase Velocities, *Atmosphere*, 2019, 10(9), pp. 546, doi: 10.3390/atmos10090546.

SATELLITE AND AIRCRAFT EVIDENCE OF STORM MASS TRANSPORT TO STRATOSPHERE

Pao K. Wang^{1,2}

¹Research Center for Environmental Changes, Academia Sinica, Taipei, Taiwan

²Department of Atmospheric and Oceanic Sciences, University of Wisconsin-Madison, , Madison, WI, USA

Introduction. At any instant around the globe, there are about 2000 thunderstorm cells occurring. They are known to cause severe damages to properties and pose serious threat to human lives, but at the same time, they play an important role in global atmospheric physical and chemical processes. Thunderstorm updrafts are the fastest vertical air speeds in the natural environment and we would expect that they serve as a very efficient transporter of various physical quantities from the boundary layer to the upper troposphere. It has been known for some time that thunderstorms transport energy and momentum to the upper atmosphere, but whether or not they can transport mass across the tropopause has not been settled completely. This is because the transport of energy of energy and momentum to the upper atmosphere is performed by waves (either electromagnetic or gravity waves), however, regular wave motions are an adiabatic process which cannot transport mass through an isentropic surface, and the tropopause is such an isentropic surface. Thus, wave motion may distort the shape of the tropopause, but may not be able to send mass through it.

Satellite Evidence. Setvak and Doswell [1] was the first one to point out that there exists a chimney plume-like cirrus cloud above the anvil of some severe storms and further evidence were reported by Levizzani and Setvak [2]. This phenomenon has now been called “above anvil cirrus plumes” (AACP). Figure 1 shows two more recent examples.

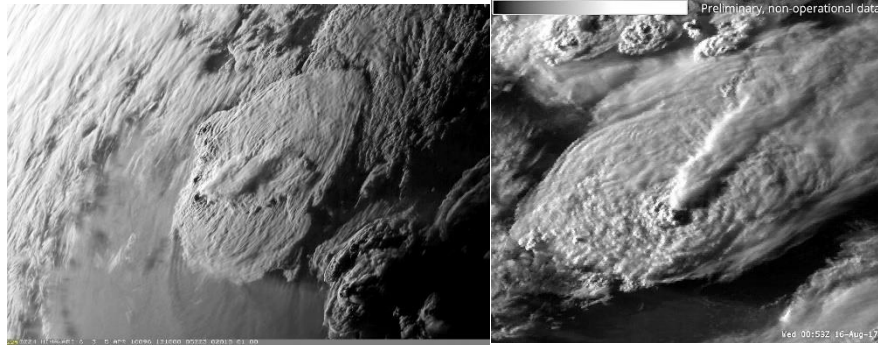


FIGURE 1. Satellite images of two examples of the above anvil cirrus plumes (AACP) that cast shadow on top of the anvil of severe thunderstorms. (left) Nepal case by Himawari-8 image (courtesy of Daniel Lindsey). (right) US case by GOES-16 (courtesy of Satellite Liaison Blog/NOAA).

Since the stratosphere is usually very dry with water vapor concentration of about 3-4 ppmv, it is not possible to form such extensive cloud plumes, indicating that the source of the water substance of AACP must come from other places.

Cloud Model Studies. Wang [3] performed a theoretical simulation of a severe storm case using a time-dependent 3-D cloud resolving model WISCDYMM with detailed cloud microphysics and showed that AACP can be produced by the breaking of internal gravity waves excited at the storm top by the strong updraft. Since wave breaking is a diabatic process, it is able to transport mass through an isentropic surface such as the tropopause. Wang [4] further shows that this wave breaking is exactly the mechanism that is responsible for producing the “jumping cirrus” observed by Fujita [5], and Wang [6] shows the more detailed storm top thermodynamic structure of the wave breaking process. Figure 2 shows the thermodynamic structure of the storm top wave breaking.

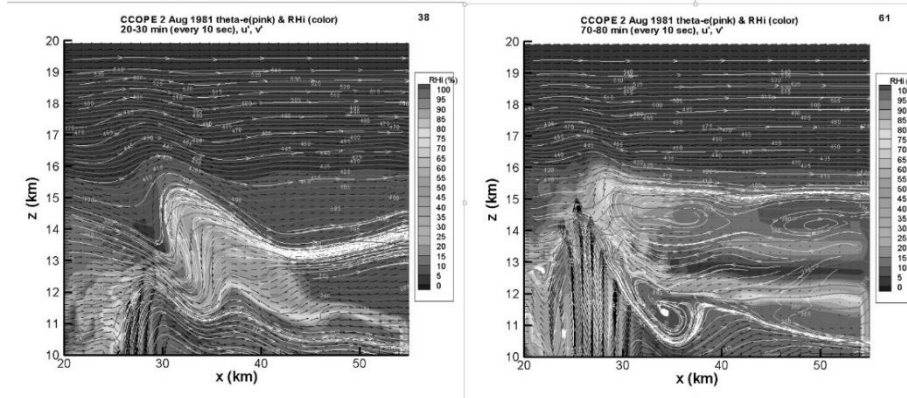


FIGURE 2. Two frames of WISCDYMM simulation of a supercell storm that show the internal wave breaking at the storm top. Shades are relative humidity with respect to ice, white contours with numbers are equivalent potential temperature isotherms and bright white contours are streamtraces showing the air flow.

Aircraft Evidence. Recently some direct aircraft observations of the AACP formation show that they match the theoretical predictions of the cloud model wave breaking features, giving further support of the wave breaking theory.

Acknowledgments. This research is partially supported by Taiwan Academia Sinica grant AS-TP-107-M10 and US NSF grant AGS-1633921,

1. M. Setvak and C. A. Doswell III, The AVHRR channel 3 cloud top reflectivity of convective storms, *Mon. Wea. Rev.*, 1991, 119, pp. 841-847.

2. V. Levizzani and M. Setvak, Multispectral, high resolution satellite observations of plumes on top of convective storms, *J. Atmos. Sci.*, 1996, 53, pp. 361-369.
3. P. K. Wang, Moisture Plumes above Thunderstorm Anvils and Their Contributions to Cross Tropopause Transport of Water Vapor in Midlatitudes, *J. Geophys. Res.*, 2003, 108(D6), pp. 4194, doi: 10.1029/2003JD002581.
4. P. K. Wang, A cloud model interpretation of jumping cirrus above storm top, *Geophys. Res. Lett.*, 2004, 31, pp. L18106, doi:10.1029/2004GL020787.
5. T. T. Fujita, Principle of stereographic height computations and their application to stratospheric cirrus over severe thunderstorms, *J. Meteor. Soc. Japan.*, 1982, 60, pp. 355-368.
6. P. K. Wang, The Thermodynamic Structure atop a Penetrating Convective Thunderstorm. *Atmos. Res.*, 2007, 83, pp. 254-262.

INVESTIGATION OF WAVE PROCESSES BY OBSERVING NOCTILUCENT CLOUDS

Semen V. Nikolashkin, Anastasia M. Ammosova, Igor I. Koltovskoi

Laboratory of Atmospheric Optics, Yu. G. Shafer Institute of Cosmophysical Research and Aeronomy of SB RAS, Yakutsk, Russia

Introduction. In summer, when the temperature of the mesopause region often falls below the freezing point of water vapor, ice crystals 10–100 nm in size are formed and so-called mesospheric (noctilucent) clouds arise at an altitude of 80–85 km, having a thickness of only a few kilometers. In this case, the condensation temperature at mesopause heights is approximately 140–150 K. It is considered that cosmic dust, cosmic rays, and the remains of meteor particles serve as crystallization centers. The total number of occurrences of noctilucent clouds during the season from year to year does not remain constant, but fluctuates, reaching occasionally 20-30 cases for one region. They are visible only at night from the second half of May until mid-August in the northern hemisphere. A characteristic feature of noctilucent clouds is that they are observed from the Earth only in the relatively narrow latitudinal zones of the northern and southern hemispheres. In the northern hemisphere, the distribution belt of noctilucent clouds is limited on average by latitudes (50-75 °). In the southern hemisphere, a similar belt is apparently located at lower latitudes (40-60 °). It is known that noctilucent clouds are only the part of the polar mesospheric clouds (PMCs) visible from the earth that capture the entire polar region of the summer mesosphere, studied using the SME and AIM satellites.

Investigation of the wave structure of temperature fields, wind, aerosol and clouds (including noctilucent clouds) in the form of internal gravity waves are important for understanding the processes of energy exchange in the average atmosphere and the formation of its dynamics. Nowadays, the role of atmospheric gravity waves in the formation and change in the dynamics of the average atmosphere, as well as the degree of influence of such waves on climate change in the region and on the planet as a whole remains much unexplored. There is also little information about tropospheric sources of atmospheric gravity waves and their propagation to the upper atmosphere. Noctilucent clouds are the best indicator of wave processes in the upper atmosphere. Nowadays noted that noctilucent clouds have begun to appear more often due to an increase in methane emissions into the atmosphere due to climate warming.

Instruments and research methods. In 2007 for the study of noctilucent clouds launched the American spacecraft AIM (Aeronomy of Ice in the Mesosphere), which is currently operating. Also, since 2004, in the Northern Hemisphere, an international network of automatic cameras for detecting noctilucent clouds (SAFSO) began to operate, which includes 7 observation posts located in Moscow, Novosibirsk, Petropavlovsk-Kamchatsky, Athabasca (Canada), Glasgow (Scotland), Silkeborg (Denmark) and Vilnius (Lithuania) [1].

The main method for observing noctilucent clouds is photographic observation using automatic cameras or their network. Noctilucent clouds have many complex spatial structures that reflect the dynamics of the summer mesosphere. For example, long parallel stripes [2] are caused by propagating atmospheric gravity waves. Another common feature of the structure of noctilucent clouds is that waves, defined as small-scale wave packets with a horizontal interval of 3–10 km, are considered as dynamic or convective instabilities that are created by strong localized areas of wind shear or by the destruction of gravity waves [3]. Optical measurements in the mesopause region through emission for studies of wave structures have already been performed [4], however, the emission layer has a thickness of 8–9 km, while the thickness of noctilucent clouds is 2–3 km, so the wave structures should be more clear and detailed in the images of noctilucent clouds. In addition, the study of wave processes through emission luminescence in the summer is complicated due to white nights at high latitudes; therefore, the method of studying internal gravity waves using images and video recording of noctilucent clouds is optimal [5].

Noctilucent clouds are an excellent indicator of wave processes in the upper atmosphere. Using modern methods of observation and data processing allows us to trace the evolution of noctilucent clouds and using these parameters to study the main dynamic characteristics of the upper atmosphere - wind speed and direction, atmospheric gravity waves and try to establish their sources. It is believed that the main sources of atmospheric gravity waves (including internal gravity waves) are disturbances in the troposphere - cyclones, atmospheric fronts and orographic features of the landscape.

Investigations of atmospheric gravity waves from observations of noctilucent clouds in 2018–2019. The shooting was carried out by the camera on the Samsung Galaxy S4 / mini phone using the free program Time Lapse Creator. Filming was carried out every 2 min with an exposure of 2 s, in the direction above the northern horizon. The determination of the main parameters of the internal

gravitational waves during such a video recording is difficult, since it is necessary to take into account the viewing angle of the camera in accordance with the received image. In order to simplify the assessment of the main parameters and to increase the accuracy to 90%, a special program was used according to the method of determining the projection of noctilucent clouds on the earth's surface by the



FIGURE 1. Two atmospheric gravity waves with different parameters and opposite in direction

photographic method [6]. The main parameters of the camera and the height of noctilucent clouds $h = 85$ km were set in the program. Figure 1 shows, as an example, two gravity waves of opposite direction, which were captured at 01:23 local time on the night of July 26, 2018 at the Institute.

To study small-scale wave processes in the mesosphere using noctilucent clouds, it is planned to create a network of automatic photography stations with a small base. At the same time, it is planned to create software for converting camera images into a geographical distribution, as well as measuring such parameters of gravity waves as the height of the wave layer, the speed and wavelength, the speed and direction of the neutral wind, as well as the lifetime of individual fragments. If possible, the problem of

the multilayered noctilucent clouds and the propagation of waves along them will be investigated. It is assumed that automatic photographing stations will be located in the following settlements: Yakutsk, Namtsy, the Maimaga optical station of SHICRA (Yu. G. Shafer Institute of Cosmophysical Research and Aeronomy), Oktemtsy (Yakutsk Extensive Air Shower Array SHICRA), Maya, Magarass located at a distance of 40-45 km from each other configuration "cross" with the center in Yakutsk.

To deploy a network of photo surveillance, automatic cameras with an angle of view of ~ 60 degrees with control from a minicomputer connected to a common network via the Internet will be purchased. After a night of observations, the data will be sent to the Institute server for further processing. It is assumed that surveys will be carried out every minute, with an exposure of 10 s, since with such an arrangement the field of view of the cameras will overlap and it is possible to conduct basic measurements of the heights and wave parameters in noctilucent clouds.

The work was partly supported by the Russian Foundation for Basic Research (Grants No. 18-45-140063, 18-45-140034) and by Program of State Academies of Science (Project II.16.1.7. 0375-2020-0004).

1. P. Dalin, N. Pertsev., A. Zadorozhny, M. Connors, I. Schofield, I. Shelton., M. Zalcik, T. McEwan, I. McEachran, S. Frandsen, O. Hansen, H. Andersen, V. Sukhodoev, V. Perminov and V. Romejko, Ground-based observations of noctilucent clouds with a northern hemisphere network of automatic digital cameras, *J. Atmos. Solar-Terr. Phys.*, 2009, 70, pp. 1460–1472, doi: 10.1016/j.jastp.2008.04.018.

2. M. J. Taylo, P.-D. Pautet, Y. Zhao, C. E. Randall, J. Lumpe, S. M. Bailey, J. Carstens K. Nielsen, J. M. Russell III and J. Stegman, High-latitude gravity wave measurements in noctilucent clouds and polar mesospheric clouds, in *Aeronomy of the Earth's Atmosphere and Ionosphere, IAGA Special Sopron Book Series*, 2011, 2(1), pp. 93–105, doi:10.1007/978-94-0070326-1_7.

3. J. Yue, B. Thurairajah, L. Hoffmann, M. J. Alexander, A. Chandran, M. J. Taylor, J. M. Russell III, C. E. Randall and S. M. Bailey, Concentric gravity waves in polar mesospheric clouds from the Cloud Imaging and Particle Size experiment, *J. Geophys. Res.*, 2014, 119, pp. 5115–5127, doi:10.1002/2013JD021385.

4. I.I. Koltovskoy, P.P. Ammosov, G.A. Gavriliev, A.M. Ammosova, S.G. Parnikov Short-period waves from images of cameras of the whole sky, *Vestnik NEFU*, 2018, 2 (64), pp. 70-76, doi 10.25587 / SVFU.2018.64.12154.

5. P.-D. Pautet, J. Stegman, C. Wrasse, K. Nielsen, H. Takahashi, M. Taylor, K. Hoppel and S. Eckermann, Analysis of gravity waves structures visible in noctilucent cloud images, *J. Atmos. Sol.-Terr. Phys.*, 2011, 73, pp. 2082–2090, doi:10.1016/j.jastp.2010.06.001.

6. M. I. Burov, Determination of the projection of silver clouds on the earth's surface by the photogrammetric method, *Proceedings of the meeting on silver clouds (III)*, 1962, pp. 90-104.

INFLUENCE OF SUDDEN STRATOSPHERIC WARMING ON POLAR MESOSPHERIC OZONE

Yuri Y. Kulikov¹, Alexander F. Andriyanov¹, Valery I. Demin², Valery M. Demkin³,
Andrei S. Kirillov², Vitaly G. Ryskin¹, Victor A. Shishaev²

¹Department of Atmospheric Physics, Institute Applied Physics, Nizhny Novgorod, Russia

²Laboratory for an Atmosphere of Arctic, Polar Geophysical Institute, Apatity, Russia

³Higher School of Economy, Nizhny Novgorod, Russia

Introduction. The results of ground-based microwave observations of the middle atmosphere ozone at Kola Peninsula in winters of 2017-2018 and 2018-2019 are presented. In each of these winters sudden stratospheric warming were marked. Measurements were carried out with the help of mobile ozonemeter (observation frequency 110.8 GHz), which was established at Polar Geophysical Institute in Apatity (67N, 33E). The parameters of the device allow to measure a spectrum of the ozone emission line for

time about 15 min a precision of $\sim 2\%$. The error of estimating the vertical distribution of ozone on the measured spectra by above described device does not exceed 10-15% [1]. On the measured spectra were appreciated of ozone vertical profiles in the layer of 22 – 60 km which were compared to satellite data MLS/Aura and with the data of ozonesonde at station Sodankyla (67N, 27E).

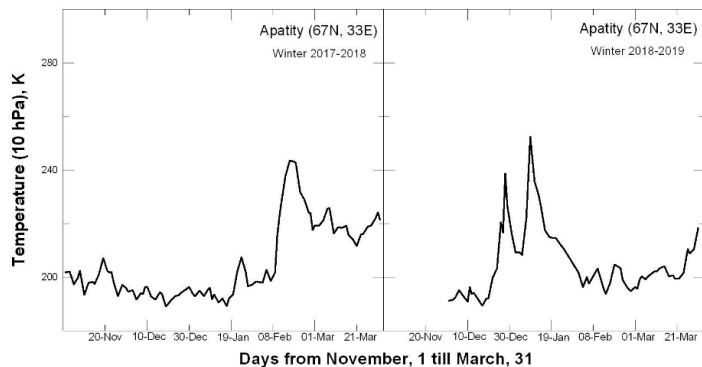


FIGURE 1. Temperature at level 10 hPa for two winters above Apatity (MLS/Aura data).

rose to 240 K on February, 16, which is higher on 50 K of the mid-temperature the January. In the winter 2018-2019 SSW began December, 27 both has terminated February, 1 and there was duration almost 40 days. The feature of warming was presence of two maxima of temperature at height about 30 km. The first maximum of temperature had value 239 K (28.12.2018), that has an increment concerning average temperature of the not indignant period in December till 24.12.2018 about 45 K. Second maximum of temperature has 252 K (09.01.2019) which had concerning average temperature for the period from 01.02.2019 up to 01.03.2019 value 54 K. Returning of temperature (level 10 hPa) has taken place in 2019 to mid-annual values at the end of March. Thus, development SSW for two winters had completely different character.

Let's consider changes of mesospheric ozone which were obtained from microwave measurements before and later SSW. In a Fig. 2 diurnal variations of ozone at 60 km which were received from continuous measurements December, 27-28 2017 before SSW near to a winter solstice are resulted.

The data given in a Fig. 2 show on a priority of dynamic processes above photochemical in polar mesosphere. Decreasing of ozone density in midday concerning midnight has made 25%. The values of the ozone density increase at night, mainly due to the absence of O_3 photodissociation and the changing $[O]/[O_3]$ ratio [4]. The attention a significant

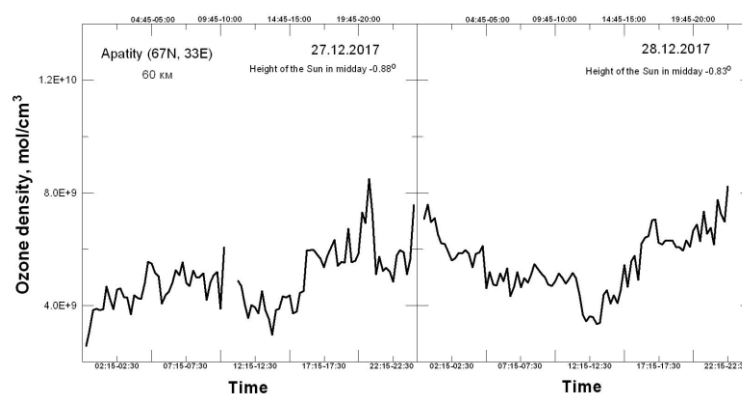


FIGURE 2. Diurnal variations of mesospheric ozone obtained by ground-based microwave radiometry in polar night above Apatity. Note the significant variations in the O_3 density, which apparently are not associated with sunrise and sunset. The amplitude of changes in ozone density reached 80%.

divergence (in 1.5-2 times) in ozone density at night for 27.12.2017 and 28.12.2017 pays to itself. Probably, it is caused by advective current of air in mesosphere.

In Fig. 3 the diurnal variations of the mesospheric ozone at 60 km for 14-15 March 2018 which was obtained in continuous microwave measurements later on SSW and near spring equinox is submitted. The average amplitude of diurnal changes of ozone was about 30%. It is important to note, that average of ozone density (60 km) for midday and midnight in March differed from similar values in December almost twice.

The numerical data of a diurnal variations of ozone density (60 km) are collected in the Table 1 near a winter solstice in December 2017 and 2018. The scale of diurnal cycle O_3 connected to photochemistry in different years in December has close values.

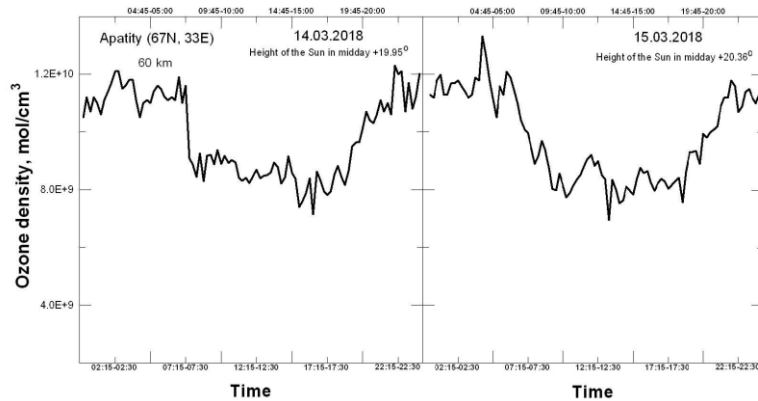


FIGURE 3. Diurnal cycle of ozone density at height 60 km in continuous series of microwave measurements in March 15-16, 2018. Time resolution of 15 min.

TABLE 1. Diurnal mesospheric ozone cycle in December 2017 and 2018

Date	Average mesospheric ozone density, mol/cm ³	
	Midday 10:00 – 14:00 msk	Midnight 22:00 – 02:00 msk
26.12.2017	$(4.32 \pm 0.15) \cdot 10^9$	$(4.25 \pm 0.23) \cdot 10^9$
27.12.2017	$(4.12 \pm 0.20) \cdot 10^9$	$(6.24 \pm 0.22) \cdot 10^9$
28.12.2017	$(4.28 \pm 0.16) \cdot 10^9$	
20.12.2018	$(4.35 \pm 0.12) \cdot 10^9$	$(5.30 \pm 0.13) \cdot 10^9$
21.12.2018	$(4.34 \pm 0.12) \cdot 10^9$	$(5.84 \pm 0.14) \cdot 10^9$
22.12.2018	$(4.77 \pm 0.15) \cdot 10^9$	$(5.76 \pm 0.19) \cdot 10^9$
23.12.2018	$(4.80 \pm 0.12) \cdot 10^9$	$(6.44 \pm 0.12) \cdot 10^9$
24.12.2018	$(4.95 \pm 0.18) \cdot 10^9$	

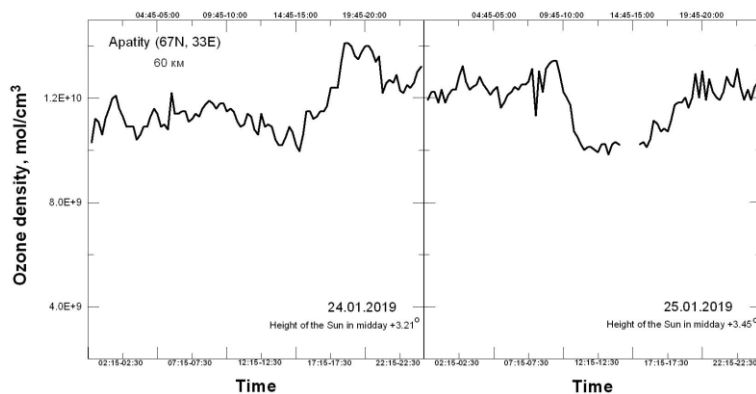


FIGURE 4. Diurnal cycle of ozone density at height 60 km in continuous series of microwave measurements in January 24-25, 2019. Time resolution of 15 min. The average height of the Sun above horizon in midday at the end of January had value +3.5°.

The Fig. 4 shows the behavior of ozone at height 60 km in January 24-25, 2019. A January series of measurements was carried out during a middle atmosphere disturbance caused by SSW in winter 2018-2019.

The Fig. 4 is confirmation of inconstancy of the diurnal ozone cycle, apparently under

influence of changes of atmospheric circulation on O₃ at heights of the mesosphere.

The analysis of the microwave data on behavior of polar mesospheric ozone in past winters shows, that SSW can cause significant and long influence on its diurnal variation which should be determined by photochemical processes. Thus is important, that microwave observations were carried out during a deep minimum of a solar cycle. It is established, that the ozone content in mesosphere considerable can differ from winter to winter. Apparently, dynamic processes through SSW influence transfer of ozone from low latitudes.

The work is supported by the RFBR grant No. 18-45-520009 (Kulikov Y.Y.)

1. Y.Y. Kulikov, A.A. Krasilnikov, V.G. Ryskin, et al., Ground-based microwave instrument to research of stratospheric ozone (some results of observations), *Proc. XXX Annual Seminar, Apatity*, 2007, pp. 218 – 221.

2. Y.Y. Kulikov, A.A. Krasilnikov, V.G. Ryskin, Microwave studies of the structure of the polar-latitude ozone layer during anomalous warming events in the stratosphere, *Izvestiya, Atmospheric and Oceanic Physics*, 2002, 38(2), pp. 182 – 191 (in Russian).

3. V.N. Marichev, G.G. Matvienko, A.A. Lisenko, et al., Microwave and optical observation of ozone and temperature of the middle atmosphere during stratospheric warming at Western Siberia, *Atmospheric and Oceanic Optics*, 2014, 27(1), pp. 46 – 52 (In Russian).

4. R. Rodrigo, J.J. Lopez-Moreno, M. Lopez-Puertas, et al., Neutral atmospheric composition between 60 and 220 km: a theoretical model for mid-latitudes, *Planet. Space Sci.*, 1986, 34(8), pp. 723 – 743.

NEW RESULTS OF THE RESEARCH OF THE EARTH'S LOWER IONOSPHERE BY THE METHOD OF CREATING OF ARTIFICIAL PERIODIC IRREGULARITIES

Nataliya V. Bakhmetieva

Radiophysical Research Institute Nizhny Novgorod State University, Nizhniy Novgorod, Russia

Introduction. The paper presents new results of the Earth's lower ionosphere studies in the altitude range 60–130 km, obtained by the method resonance scattering of radio waves on artificial periodic irregularities (APIs) of the ionospheric plasma. The method is based on the perturbation of the ionosphere by a powerful high-frequency radio emission and APIs creation in the field of a standing wave. It is formed by reflection from the ionosphere of a powerful radio wave with frequencies of 4.700 (4.785, 5.600) MHz emitted at the zenith by in-phase transmitters of the SURA heating facility (56.15 N; 46.13 E). The scattering of probe radio waves on these irregularities has resonant properties, that is, the API scattered signal has significant amplitude when frequencies and polarizations of the powerful and probe waves are identical. As a rule, a more intense scattered signal was observed when the ionosphere was disturbed by an extraordinary wave. The destruction or relaxation of irregularities after the end of the heating occurs under the ambipolar diffusion in the E-region and due to the temperature dependence of the electron detachment coefficient in the D-region [1]. A digital record of quadrature components of the scattered signal allows a detecting its fast fluctuations at interval of 15 seconds and a measuring of the amplitude and phase of the scattered signal. For scattered signal records a receiving part of partial reflections facility is used. The API creation in a quasi-continuous mode made it possible to diagnose the lower ionosphere during both the development of APIs and their relaxation conditions after the end of the heating interval [2].

API technique allows us to determine many characteristics of ionized and neutral components of the lower ionosphere with a great accuracy, including the electron density profile, the temperature and the density of the neutral atmosphere, the frequency of ion-molecular collisions, the velocity of regular vertical and turbulent plasma motions, and the turbopause level. The method based on the radio waves

scattering on APIs allows one to determine the parameters of internal gravity waves, to study the irregular structure of the lower ionosphere, to detect sporadic ionization layers and additional layers of the electron density from the lower part of the D-region to the height of the maximum of the F-layer. We present data on dynamics of the lower ionosphere and the neutral atmosphere on a base of experiments has been carried out during 2015–2019 using diagnostic tools located near the SURA heating facility. After the termination of the impact on the ionosphere, APIs disappear. The parameters of the ionosphere and the neutral atmosphere are measured at the API relaxation stage, i.e., for the unperturbed ionosphere.

Figure 1 shows API creation and diagnose scattered signals from the D to the F-regions.

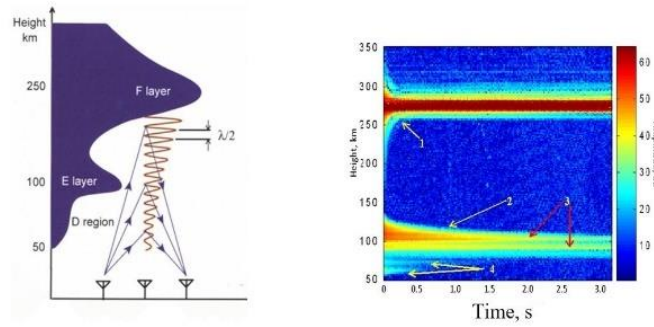


FIGURE 1. Scheme of the API creation and diagnose (left panel), scattered signals in the F-layer – 1, in the E-layer – 2, in the sporadic-E layer – 3, and in the two layered D-region – 4 (right panel) during the API relaxation.

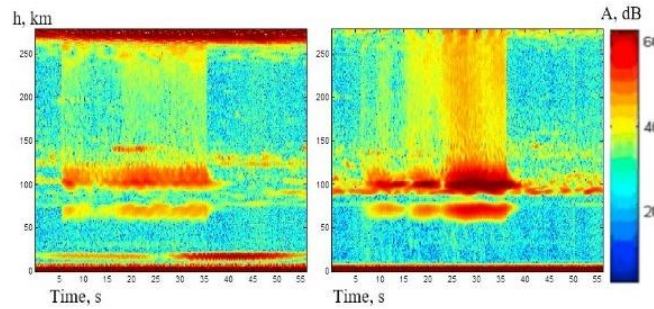


FIGURE 2. Amplitude-height-time-plot for API development and relaxation processes on September 13, 2019. The pumping frequency was of 4.700 MHz, X-mode.

API development and relaxation processes. At the SURA facility when exposed on the ionosphere, APIs are usually observed in the D-, E- and F-regions. The scattered signal in the D-region is greatly enhanced by the sporadic-E layer. Sometimes a stratification of the amplitude of the API scattered signal similar to the one shown in the Fig. 1 was observed in the D-region [1,2].

Figure 2 shows the height-time-amplitude plot of the API scattered signal formed by the SURA heating facility emission. There are scattered signals obtained in the API development and relaxation stages. It is new data in the API studies.

One can see API intense scattered signals in the D- and E-regions, and weaker signals occupying almost the entire altitude interval between E- and F-regions. On the right panel, at the height of 100 km, an intense sporadic-E layer with a critical frequency of about 4.5 MHz is seen; as a result, a significant part of the pumping wave power is reflected from it and the intense API signal in the D-region occurs. It can be seen that the amplitude of the API signals from the D- and E-regions gradually increases from 35 to 74 dB by the end of the SURA heating interval. Amplitudes of API scattered signals are

characterized by spatial and temporary variations. The processes of the development and relaxation of the API scattered signal during pumping of the ionosphere are shown in Fig. 3.

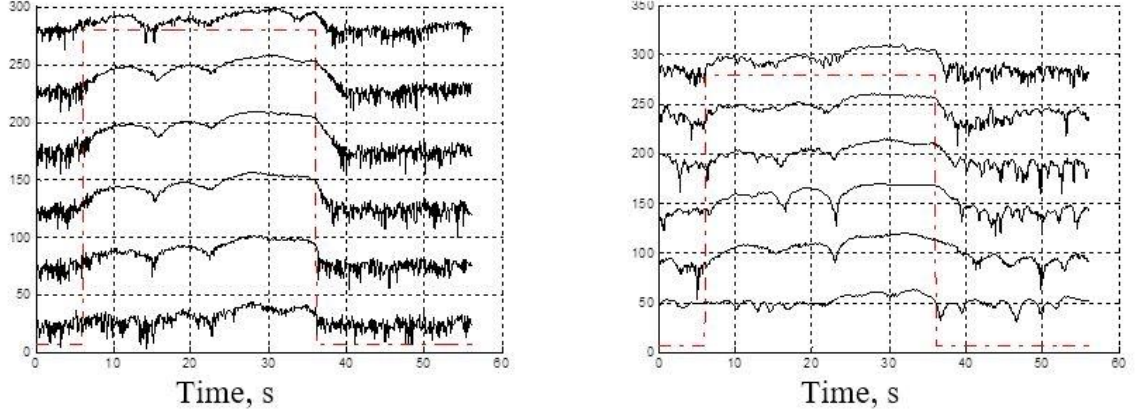


FIGURE 3. Amplitude of the API scattered signal on the six heights in the D-region from 57.4 km to 78.4 km (left panel) and in the E-region from 92.4 km to 113.4 km (right panel) with height step of 4.2 km. The dotted line shows the SURA facility work interval.

As a rule, the relaxation time of the API scattered signal is varying between 1–1.5 τ in the D-regions and equal to fractions of a second in the E-layer. Some times comparatively big values of the relaxation time are observed.

Velocity of vertical plasma movement. At altitudes, 50–120 km plasma is passive admixture; therefore, it moves with neutral gas. The plasma vertical movement velocity V is equal to the velocity of the neutral environment. The velocity V of the vertical movement of the plasma is determined by the change in time of the phase of the scattered signal. Figure 4 shows height (left) and temporal (right) variations of the vertical plasma velocity. Negative V values correspond to an upward movement.

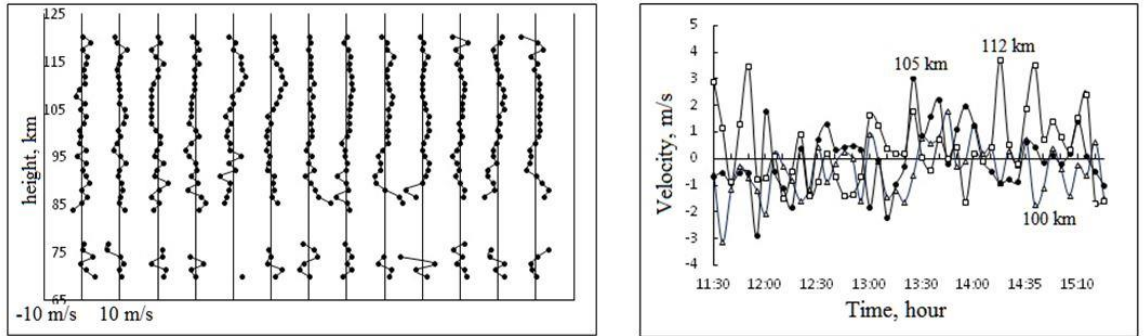


FIGURE 4. Height profiles of the vertical plasma velocity averaged on every 5 minutes for the hourly observation period from 13:00 to 14:00 (left panel) and temporal velocity dependences on 3 heights of the E-region (right panel) on September 28, 2018.

The average velocity varied usually from -6 to +6 m/s in the D-region and from -3 to +3.5 m/s in the E-layer. Wave-like variations of the velocity are seen with a change of direction and the period from 5 minutes to an hour in the D-region and up to 3 hours in the E-layer. It indicates the intensive dynamics of the studied height range. Obtained height profiles of the velocities of the vertical plasma motion have a scale of 5 km to 15 km usually.

Turbulent dynamics of the mesosphere and the lower thermosphere. The height-temporal dependences of the API relaxation time are used to determine a large number characteristics of the ionosphere and neutral atmosphere [1], including some turbulent parameters. Figure 5 shows some height profiles of the relaxation time and the amplitude of the API scattered signal (left panel). In this example the diffusion law of the relaxation corresponds to the altitude range of 100–125 km. The values of relaxation times are in good agreement with the diffusion dependence. Below 100 km, atmospheric turbulence begins to affect, and the relaxation time of the scattered signal decreases as compared with the diffusion time. On the right panel on Fig. 5 turbulent velocity V_t versus height is presented lower the turbopause level. This is the level at which turbulent mixing of atmosphere gases is replaced by their diffusion separation.

One can see on Fig. 5 turbulent velocity values can be of the same order as the vertical velocity V . We obtained in autumn seasons at mid-latitudes, the average level of turbopause was in the height range of 99–102 km with wave-like variations and with a tendency to decrease to 94 km in the evening hours.

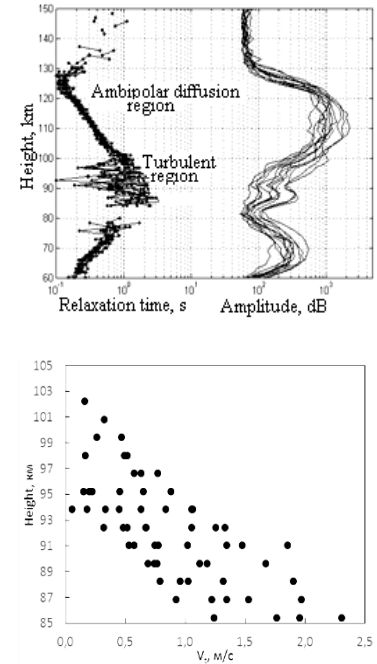


FIGURE 5. Height profiles of the amplitude and the relaxation time (left panel) and turbulent velocity V_t versus height on September 11, 2019.

The study was supported by the Russian Foundation for Basic Research, project 18-05-00293.

1. V.V. Belikov, E.A. Benediktov, A.V. Tolmacheva, N.V. Bakhmet'eva, *Ionospheric Research by Means of Artificial Periodic Irregularities – Copernicus GmbH*, 2002. Katlenburg-Lindau, Germany, 160 pp.

2. N.V. Bakhmetieva, S.M. Grach, E.N. Sergeev, A.V. Shindin, G.M. Milikh, C.L. Siefring, P.A. Bernhardt, and M. McCarrick, *Artificial periodic irregularities in the high-latitude ionosphere excited by the HAARP facility*, *Radio Science*, 2016, 51(7), pp. 999-1009, doi: 10.1002/2015RS005938.

COMPARISON OF PLANETARY WAVE ACTIVITY AT MAIMAGA AND TIKSI STATIONS

Vera I. Sivtseva¹, Petr P. Ammosov¹, Galina G. Gavril'yeva¹, Igor I. Koltovskoi¹, and Anastasia M. Ammosova¹

¹Laboratory of Atmospheric Optics, Yu. G. Shafer Institute of Cosmophysical Research and Aeronomy of SB RAS, Yakutsk, Russia

Introduction. Planetary waves or Rossby waves appear in the atmosphere due to the latitudinal gradient of Coriolis force and the inhomogeneity of the underlying surface. Rossby's waves originate in mid to high latitudes, although they can sometimes move to lower latitudes and even cross the equator. Planetary waves play an important role in the dynamics of the stratosphere. In particular, the wave

impulse they introduce leads to circulation between the poles. Another known phenomenon associated with planetary waves is sudden stratospheric warmings. The slowest planetary waves with horizontal wave number 1 or 2, which are tied to certain locations, are called "quasi-stationary" waves and are caused by inhomogeneity of the surface - the topography and surface temperature. According to the dispersion relation for Rossby waves, which includes the background zonal wind speed, quasi-stationary waves have higher chances of propagating into the upper atmosphere and transmitting their momentum and energy when dissipating [1]. Quasi-stationary planetary-scale waves are regularly observed in the winter mesosphere and lower thermosphere (MLT) [2, 3].

Instruments and research methods. Two identical spectrographs are installed at Maimaga station (63.04° N, 129.51° E) 150 km north of Yakutsk and at Tiksi station (71.58° N, 128.77° E). The device was installed at Maimaga station for permanent registration on January 17, 2013, and at high-latitude Tiksi station - on September 3, 2015. For mutual calibration of both instruments, simultaneous observations were made at the Maimaga station from 5 to 15 August 2015. The software we have developed allows the devices to operate in a fully autonomous mode.

Spectrographs record a band of hydroxyl OH (3, 1) in the close infrared region (about 1.5 μm), at an angle of immersion of the Sun >9°. Registration of the hydroxyl radiation band in close infrared region is advantageous because in this region of the spectrum the emission of polar lights is much smaller, and the contribution of parasitic light from the moon and stars is significantly reduced - 1/λ⁴ times [4]. The highest intensity of hydroxyl emission is also observed in this area. The working temperature of the spectrograph chamber cooling is set at -50°C to eliminate the temperature drift of dark current, the exposure time is 60 sec. Under these conditions spectrographs allow to measure mesopause temperature with accuracy ~2 K (error was calculated for each measurement separately).

The method for estimating the rotational temperature of molecular emissions is based on adjusting the model spectra built with the hardware function of the device for various predetermined temperatures to the actually measured spectrum [5, 6]. The OH band (3, 1) is sufficiently well thermallyized and the rotational temperature determined by it is close to the kinetic temperature of the surrounding neutral atmosphere at the height of its radiation. When estimating the rotational temperature on the hydroxyl band, the transition probabilities calculated in [7] were used.

The standard deviation of temperature from its mean value after deduction of the seasonal temperature variation – σ_{pw} is assumed as a characteristic of the planetary wave activity. To consider the seasonal temperature variation, harmonics corresponding to the annual, semi-annual and third annual components of the seasonal temperature variation were isolated from the night average temperature range.

$$f_{sv} = \overline{T_{year}} + A_1 \cos\left(\frac{2\pi}{365}(t - \varphi_1)\right) + A_2 \cos\left(\frac{2\pi}{183}(t - \varphi_2)\right) + A_3 \cos\left(\frac{2\pi}{122}(t - \varphi_3)\right) \quad (1)$$

Planetary wave activity. The result of subtracting the sum of harmonics of the seasonal variation from the night average temperature series corresponds to the contribution of planetary wave propagation to temperature (Figure 1).

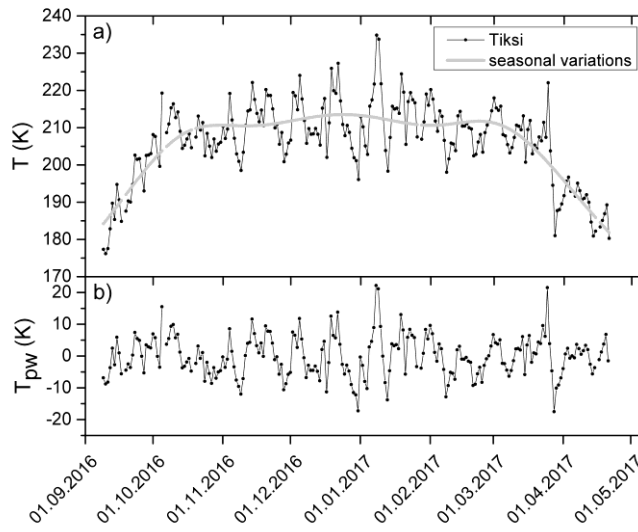


FIGURE 1. a) Night average temperature and seasonal variation of temperature during 2016-2017 at Tiksi station. b) Perturbations of temperature after subtracting the sum of harmonics of the seasonal variation

Simultaneous observations using Shamrock spectrographs at Tiksi and Maimaga stations were conducted for 3 full seasons from 2015 to 2018. Figure 2 shows the variations in average night temperature caused by planetary waves after deduction of the seasonal variation. There were selected days during which simultaneous observations were made at the stations. The coincidence of the planetary waves phases observed at the stations is monitored. The amplitudes of the planetary waves at the Tiksi station exceed the amplitudes at the Maimaga station.

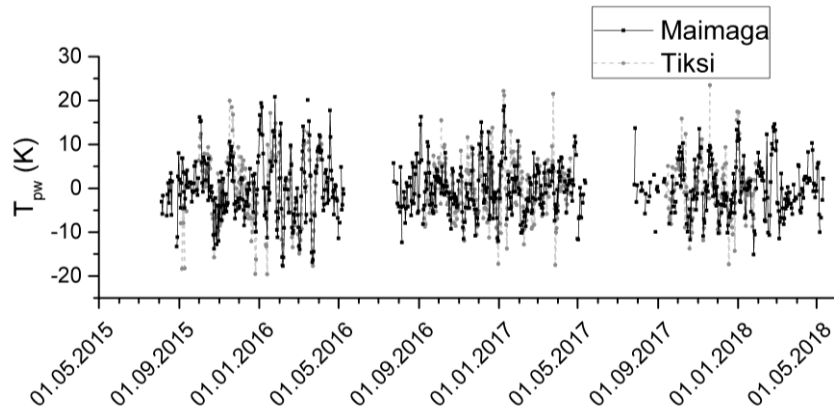


FIGURE 2. Average night temperature perturbations due to planetary waves

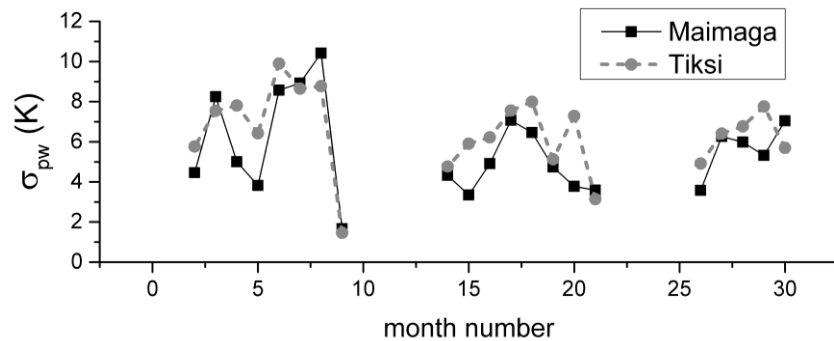


FIGURE 3. Standard temperature deviations due to planetary waves

In Figure 3 presents the activity of planetary waves by month numbers for the period of observations in 2015-2018. (first month - August 2015). The activity of the planetary waves at the station Tiksi slightly (1-2 K) exceeds the activity of waves at the station Maimaga.

The work was partly supported by the Russian Foundation for Basic Research (Grant No. 18-45-140063) and by Program of State Academies of Science (Project II.16.1.7. 0375-2020-0004).

1. E. Yiğit and A.S. Medvedev, Internal wave coupling processes in Earth's atmosphere. *Advances in Space Research*, 2015, 55(4), pp. 983–1003, doi:10.1016/j.asr.2014.11.020.
2. J.J. Barnett and K. Labitzke, Climatological distribution of planetary waves in the middle atmosphere. *Advances in Space Research*, 1990, 10(12), pp. 63–91, doi:10.1016/0273-1177(90)90387-F.
3. D.Y. Wang, W.E. Ward, G.G. Shepherd, and D.-L. Wu, Stationary Planetary Waves Inferred from WINDII Wind Data Taken within Altitudes 90–120 km during 1991–96. *Journal of The Atmospheric Sciences*, 2000, 57, pp. 13.
4. V.Yu. Khomich, A.I. Semenov, and N.N. Shefov, *Airglow as an Indicator of Upper Atmospheric Structure and Dynamics*. Berlin, Heidelberg: Springer Berlin Heidelberg, 2008.
5. P.P. Ammosov and G.A. Gavril'yeva, Infrared Digital Spectrograph for Hydroxyl Rotational Temperature Measurements. *Instruments and Experimental Techniques*, 2000, 43(6), pp. 792–797, doi:10.1023/A:1026680119998.
6. G.A. Gavril'yeva and P.P. Ammosov, Seasonal variations in the mesopause temperature over Yakutsk (63° N, 129.5° E). *Geomagnetism and Aeronomy*, 2002, 42(2), pp. 267–271.
7. F.H. Mies, Calculated vibrational transition probabilities of OH(X²Π). *Journal of Molecular Spectroscopy*, 1974, 53(2), pp. 150–188, doi:10.1016/0022-2852(74)90125-8.

RELATION BETWEEN VARIABILITY IN TOTAL ELECTRON CONTENT AND WINTER POLAR STRATOSPHERE

Anna S. Yasyukevich and Marina A. Chernigovskaya

Institute of Solar-terrestrial Physics, Irkutsk, Russia

Introduction. The ionosphere is an ionized layer of the Earth's atmosphere. The ionosphere is subject to both solar and magnetospheric effects, as well as the influence of the underlying neutral atmosphere. The determining factor for ionospheric thermodynamics is the helio-geomagnetic activity [1]. At the same time, ionospheric variations may be caused by internal atmospheric waves of various spatial and temporal scales (acoustic, internal gravitational (IGW), tidal and planetary) penetrating from the lower and middle atmosphere [2-3]. IGWs generated in the underlying neutral atmosphere make a significant contribution to dynamics and composition of the thermosphere (and as a consequence of the ionosphere) providing vertical coupling between atmospheric layers.

One of the sources for IGWs in the winter polar stratosphere and lower mesosphere is the circumpolar vortex (CPV) and the associated high-speed jet streams (JS) [4-6]. The vortex is a characteristic feature of the winter polar stratosphere. It was revealed that development and transformation of the winter circumpolar vortex can be a source for ionospheric disturbances in ionospheric electron density at the F2 layer height [5-7].

In this paper, we analyze the relation between changes in the level of short-period (up to several hours) variability in the total electron content (TEC) and variations in the stratosphere and lower mesosphere.

Data and Methods. For the study, we use the data from measurements of dual-frequency receivers of the Global Navigation Satellite Service (GNSS) International network (IGS) [8]. The receivers are located in the mid-latitude (Irkutsk, 52,22°N, 104,32°E; Novosibirsk 54,84°N, 83,23°E), subauroral

(Yakutsk, 62,03°N, 129,68°E) and high-latitude (Norilsk, 69,36°N, 88,36°E and Tiksi, 71,63°N, 128,87°E) regions. From the data, the absolute vertical TEC values I_V were calculated under the method described in [9]. As an indicator characterizing the level of ionospheric disturbance, we consider the coefficient of TEC variability $vrTEC$. The coefficient is the normalized dispersion of TEC within a defined local time interval which is 4 hours for the study. To analyze the seasonal dynamics in TEC variability, we averaged obtained $vrTEC$ coefficients for a local day. The calculated coefficient is proportional to the amplitude of TEC variations in the period range not exceeding the averaging period ($T \leq 4$ h). The source of ionospheric variations with periods of several hours is mainly traveling ionospheric disturbances (TID) associated with the gravity waves propagation. Thus, the $vrTEC$ coefficient is supposed to reflect the level of IGW-related short-period variability in the ionosphere.

Results. Figure 1 show the changes in $vrTEC$ index at the points considered (b-f) and dynamics in indices of solar ($F_{10.7}$) and geomagnetic (K_p) activity (a).

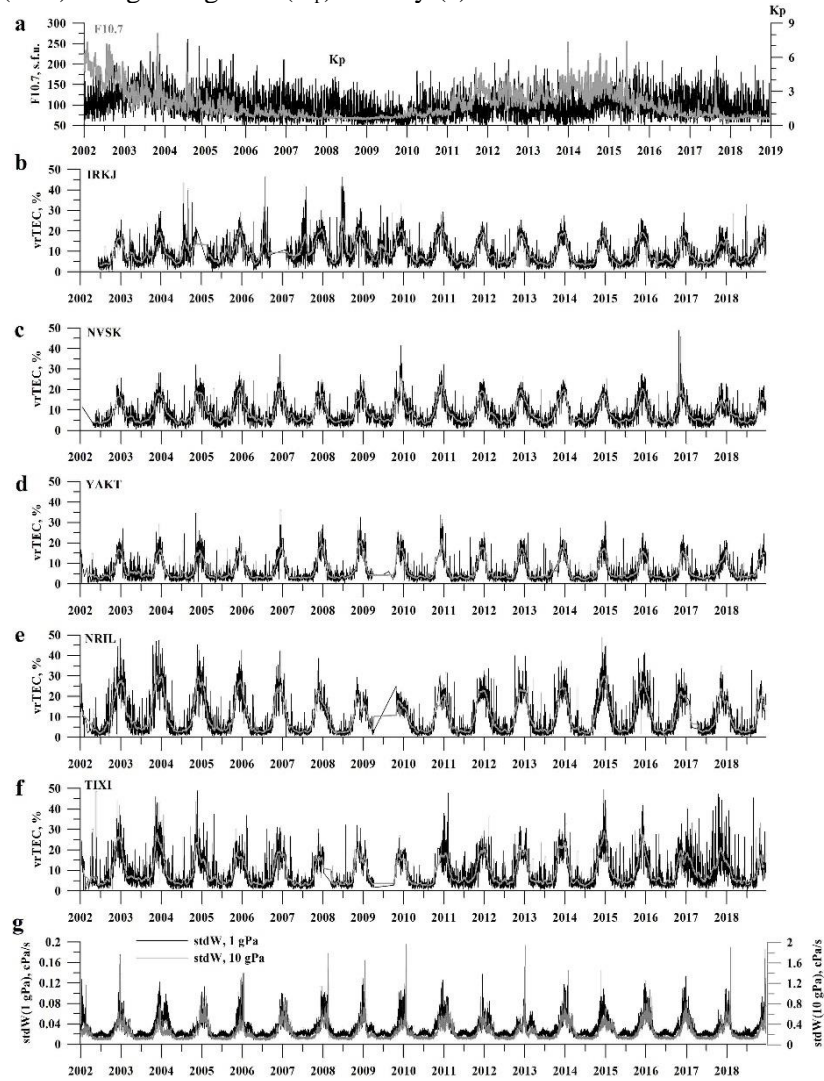


FIGURE 1. Changes in the helio-geomagnetic activity (a); dynamics of $vrTEC$ index in Irkutsk (b), Novosibirsk (c), Yakutsk (d), Norilsk (e) and Tiksi (f) for 2002-2018 (gray lines show 27-day moving average); (g) - variations in $stdW$ index at 60°N in the stratosphere (gray) and lower mesosphere (black).

The vrTEC coefficient is seen to experience significant regular seasonal variations. The lowest level is observed at all points in the summer months with vrTEC values of about 5-10%. The maximum values of vrTEC are recorded in winter periods and up to 5-6 times exceed the summer level. The coefficient maximum values in winter are greater at high-latitudes (~ 35-45%) comparing with those recorded at subauroral and mid-latitude points (~ 30%). Single bursts in the coefficient distributions reflect individual large geomagnetic events, or are associated with malfunctions in the TEC determination.

From Fig. 1 one also can see the dependence of the TEC variability level on solar activity in the winter seasons. There is a decrease in winter maximum vrTEC values by about 40% in solar activity minimum years. These changes are more pronounced at high latitude points Norilsk (e) and Tiksi (f). It is interesting to note that the level of variability in summer is independent on solar activity.

Regularly observed significant seasonal variations in TEC variability with a maximum in winter and a minimum in summer do not correlate with changes in helio-geomagnetic activity. The source of this variability may be in the underlying atmosphere (mesosphere, stratosphere). For example, a significant increase in wave activity at the altitudes of the stratosphere/lower mesosphere from November to February was revealed in [5, 7]. The source of this wave activity was associated with instabilities generated in a spatially non-uniform high-speed jet stream, connected with winter circumpolar vortex.

Using the data of ERA-Interim reanalysis meteorological archive (apps.ecmwf.int/datasets/data/), we propose the index to estimate the level of variability in the stratosphere and mesosphere, stdW. To obtain the index value, we calculate the standard deviation of the vertical gas velocity w from the zonal averaged value at a latitude of 60°N in the stratosphere (at 1 hPa level) and the lower mesosphere (at 1 hPa level).

The dynamics of the calculated indices is shown in Fig. 1 g. It can be seen that the indices experience similar regular seasonal variations with a maximum in the winter months. The difference between summer and winter values is 5-6 times. The correlation coefficients between the vrTEC and stdW indices (at 1 hPa level) is 0.42 for Irkutsk, 0.63 for Yakutsk and has a maximum of 0.68 at high latitude point Tiksi. Note that Yakutsk and Tiksi are located closer to the region in which the polar vortex exists.

We conclude, that such similarity in seasonal behavior of considered indexes indicates a relation between the variability in the ionosphere and the underlying neutral atmosphere during winter months.

The authors are grateful to IGS for GNSS data, as well as to ECMWF for the data of the ERA-5 meteorological archive. The study is supported by the Russian Science Foundation under the project No. 18-17-00042.

1. M. J. Buonsanto, Ionospheric Storms – A Review, *Space Sci. Rev.* 1999, 88(3/4), pp. 563-601, doi:10.1023/A:100510753263.
2. K. Hocke, K. Schlegel, A review of atmospheric gravity waves and travelling ionospheric disturbances 1982-1995, *Ann. Geophys.*, 1996, 14(5), pp. 917-940, doi:10.1007/s00585-996-0917-6.
3. J. Laštovička, Forcing of the ionosphere by waves from below, *J. Atmos. Sol. Terr. Phys.*, 2006, 68, pp. 479-497, doi:10.1016/j.jastp.2005.01.018.
4. D. L. Wu, J. W. Waters, Satellite observations of atmospheric variances: A possible indication of gravity waves, *Geophys. Res. Lett.*, 1996, 23(24), pp. 3631-3634, doi:10.1029/96GL02907.
5. B. G. Shpynev, S. M. Churilov, M. A. Chernigovskaya, Generation of waves by jet-stream instabilities in winter polar stratosphere/mesosphere, *J. Atmos. Sol. Terr. Phys.*, 2015, 136, pp. 201-215, doi:10.1016/j.jastp.2015.07.005.
6. N. A. Frissell, J. B. H. Baker, J. M. Ruohoniemi, et al., Sources and characteristics of medium-scale traveling ionospheric disturbances observed by high-frequency radars in the North American sector, *J. Geophys. Res. Space Phys.*, 2016, 121, pp. 3722-3739, doi:10.1002/2015JA022168.
7. M. A. Chernigovskaya, B. G. Shpynev, K. G. Ratovsky, Meteorological effects of ionospheric disturbances from vertical radio sounding data, *J. Atmos. Sol. Terr. Phys.*, 2015, 136, pp. 235-243, doi:10.1016/j.jastp.2015.07.006.

8. J. M. Dow, R. E. Neilan, C. Rizos, The International GNSS Service in a changing landscape of Global Navigation Satellite Systems, *J. Geod.*, 2009, 83, pp. 191-198, doi:10.1007/s00190-008-0300-3.

9. Yu. V. Yasyukevich, A. A. Mylnikova, A. S. Polyakova, Estimating the total electron content absolute value from the GPS/GLONASS data, *Results in Phys.* 2015, 5, pp. 32-33, doi:10.1016/j.rinp.2014.12.006.

VERTICAL REMOTE SENSING OF THE EARTH'S SURFACE USING GPS SIGNALS

Gennady V. Golubkov^{1,2}, Olga P. Borchevkina^{3,4}, Mikhail I. Manzhelii⁵, Sergey O. Adamson¹, Nikolay N. Bezuglov⁶, Alexey V. Dmitriev⁷, Yuri A. Dyakov³, Andrey N. Klyucharev⁶, Ivan V. Karpov^{3,4}, Alexey A. Lushnikov⁸, Lung C. Tsai⁷, Lev V. Eppelbaum⁹, Maxim G. Golubkov¹

¹Semenov Federal Research Center for Chemical Physics, Russian Academy of Sciences, Moscow, Russia

²National Research Center "Kurchatov Institute", Moscow, Russia

³Kaliningrad Department of Pushkov Institute of Terrestrial Magnetism, Ionosphere, and Radio Wave Propagation, Russian Academy of Sciences, Kaliningrad, Russia

⁴Immanuel Kant Baltic Federal University, Kaliningrad, Russia

⁵Center for Chemical Physics of Atmosphere, Moscow, Russia

⁶Saint-Petersburg State University, Saint-Petersburg, Russia

⁷National Central University, Taoyuan, Taiwan

⁸Geophysical Center, Russian Academy of Sciences, Moscow, Russia

⁹Tel Aviv University, Tel Aviv, Israel

Introduction. The use of GPS satellite grouping as a source of external radiation for remote sensing of the Earth's surface is very attractive at first glance, since it allows you to exclude radars and other satellite systems from consideration. This is especially useful for measuring of ocean surface level in order to detect the occurrence of a tsunami from space. The latter requires high accuracy and speed of measurement and should not include the time averaging function. These circumstances are the main difficulties of remote sensing, since they are related to the interaction of satellite signals with their propagation medium [1–3], as demonstrated in experiments [4]. Speaking about the accuracy of measurements, we should refer to the work of the Montenbruck group with employees to determine the water surface level of the mountain lake Walchen in Bavaria (Germany), which was carried out under the GORS (GPS Occultation, Reflectometry and Scatterometry) program [5–7]. This paper provides a detailed discussion of the results of their measurements based on the resonant quantum properties of the D and E layers of the ionosphere at altitudes of 60–110 km [8]. These properties are due to the settlement of orbitally degenerate states of Rydberg complexes in a non-equilibrium two-temperature plasma, the transitions between which include a decimeter range of wavelengths without changing the main quantum number $\Delta n=0$ [9]. These states lead to the spontaneous behavior of the signal-to-noise ratio at the specified altitudes [4] and are responsible for the delay of satellite signals [3].

Analysis of satellite measurement results. For certainty, we refer to the dependencies shown in fig. 1 for GPS signals L1 C/A (blue) and L2 C (magenta). It can be seen that these signals are almost in opposite phase, which is well explained in the framework of the theory [8–10] and convincingly demonstrated in fig. 2 for the power of the flow of incoherent UHF radiation from the ionosphere D and E layers coming to the Earth's surface. The dependences on the electron concentration n_e and temperature T_e at an altitude of 110 km are presented.

Note, that such unique properties of UHF radiation of the lower ionosphere were discovered independently starting from the first systematic studies on passive remote sensing of the Earth's surface and satellite correction [8]. The corresponding graph behavior in fig. 2 is called as "waist point". Note that the position of the "waist point" point on the frequency axis does not depend on the electron T_e

temperature. In this case, the power flux of radiation I_{tot} along the vertical axis increases as a quadratic function with increasing of the electron n_e concentration.

Note, that such unique properties of UHF radiation of the lower ionosphere were discovered independently starting from the first systematic studies on passive remote sensing of the Earth's surface and satellite correction [8]. The corresponding graph behavior in fig. 2 is called as "waist point". Note that the position of the "waist point" point on the frequency axis does not depend on the electron T_e temperature. In this case, the power flux of radiation I_{tot} along the vertical axis increases as a quadratic function with increasing of the electron n_e concentration.

Let us now give a qualitative explanation of the phenomena observed in the experiment [6]. It is known that at values of the non-adiabatic parameter $\lambda = B_a n^3 = 10^2$ in the orbitally degenerate complex $A^{**}M$ (where A^{**} is a Rydberg molecule, B_a is the average rotational constant of molecules M of the neutral medium), there is a significant violation of the adiabatic approximation by rotation, and the concept of the potential energy surface (PES) is fundamentally inapplicable [11]. In this case, the electronic subsystem determined by the presence of a weakly bound electron becomes slow compared to the nuclear subsystem, i.e., a physical situation occurs that is opposite to the adiabatic Born-Oppenheimer approximation. Taking into account a strong non-adiabatic coupling with the rotation of Rydberg molecular complexes leads to a stochastic quantum behavior of the electron motion, what has been actively studied in recent years [12].

The quantization of rotational motion of a quasimolecule A^+M in the intermediate region $\lambda = 1-10$ is possible due to the introduction of "rovibron" PES [11]. Under $\lambda = 1$ condition, a "quasi-adiabatic" approach is used to describe rotation. The classical description of rotational motion is fair provided under $\lambda \ll 1$ condition. Note that in the case of a diatomic nitrogen molecule the condition $\lambda = 10$ corresponds to $n \geq 30$ of the principal quantum number.

The effective population $m_n(T_e)$ of the orbital degenerate Rydberg states of $A^{**}M$ quasimolecule is located above of "neck of flow" in the two-temperature recombination plasma [8–10], is related to the concentration of free electrons $n_e(T_e)$ by the ratio [10]

$$m_n(T_e) = n_e^2(T_e) K_n(T_e), \quad (1)$$

$$K_n(T_e) = \frac{g_n}{2 \Sigma_i} P \left[\frac{2\pi}{T_e} \right]^{3/2} \exp(1/2 n^2 T_e)$$

where $g_n = 2n^2$ is the statistical weight of the Rydberg state, the P multiplier characterizes the degree of deviation from the equilibrium plasma and is determined by the electron flow. The total statistical sum of positive ions Σ_i is defined as

$$\Sigma_i \cong g_i \frac{T_a}{\langle B_i \rangle [1 - \exp(-\langle \omega_i \rangle / T_a)]}. \quad (2)$$

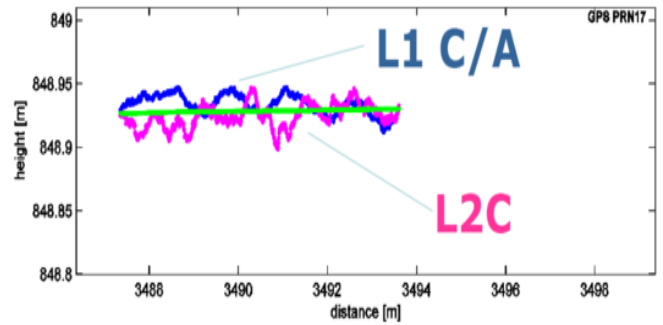


FIGURE 1. The surface profile of the lake Walchen calculated from the reflected signals of frequency L1 C/A (blue) and frequency L2 C (magenta) received from the GPS satellite PRN No. 17 [5]. Measurements were made on July 18, 2007 at 12: 54: 51 UTC. The water level in the lake is measured from the level of the world ocean.

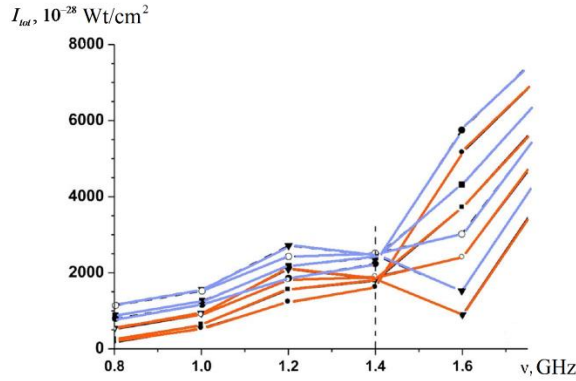


FIGURE 2. The dependence of the power flux of UHF radiation on frequency ν for different electron temperatures: black triangles – $T_e=1000^\circ\text{K}$; white circles – $T_e=1200^\circ\text{K}$; black squares – $T_e=1500^\circ\text{K}$; black circles – $T_e=2000^\circ\text{K}$. Orange lines correspond to electron concentration $n_e=10^4\text{ cm}^{-3}$; the blue lines correspond to $n_e=1.2\cdot 10^4\text{ cm}^{-3}$.

measurement errors) should increase according to (3). In the opposite case $\delta T_e > 0$, the populations $m_n(T_e)$ decrease, which leads to a decrease in these errors. As a result, such a sequential alternation of measurement errors should be most clearly manifested at the L2 frequency of the GPS signal. At the same time, at the incoherent microwave radiation frequency equal to the frequency L1, the region of the irregular stochastic spectrum in accordance with the data of [12] should make an insignificant contribution, therefore an increase in the population $m_n(T_e)$ here will follow after the change in the electron temperature T_e .

According to the calculations of the frequency dependences of the incoherent UHF radiation flux from D and E ionosphere layers obtained by “Rydberg” code for different electronic temperatures [8–10], the microwave powers for the base frequencies of GPS signals L1 and L2 at an average electron temperature of $\langle T_e \rangle = 1100\text{ K}$ are almost identical.

Let us discuss in more detail the experimental data shown in fig. 1. We divide the presented dependences into four intervals from left to right, where the quantities T_e and $\langle T_e \rangle$ are equal at the boundaries. The intervals 1 and 3 correspond to the case $T_e > \langle T_e \rangle$. According to the dependencies presented in Figure 2 measurement errors should increase for the curves obtained at the frequency L1 and decrease at the frequency L2, what coincides with the data shown in Figure 1. In the interval 2, where $T_e < \langle T_e \rangle$, there should be a slight decrease in errors at the frequency L1 and a noticeable increase at the frequency L2, which also corresponds to the behavior of the experimental curves shown in Figure 1. The exception is the last interval. Since it falls on the stage of the satellite’s exit from the observation zone, the results obtained do not agree with the predictions of the theory.

The presence of oscillations inside each of the first three intervals for the frequency L_2 is explained by the fact that the formation of incoherent UHF radiation of the D and E ionospheric layers is interference in nature and is associated with the random behavior of the coefficients in the total wave function of the complex $A^{**}M$, which takes into account the nonadiabatic rotation coupling. Moreover, the states corresponding to Rydberg series with rotational excitation of the ion core as in the case of l -mixing [11] are additionally included in the process. These states have lower values of the principal quantum number n .

In accordance with the frequency profiles of UHF radiation I_{tot} , presented in fig. 2 and converging at different temperatures at 1.4 GHz, variations in the curves at frequencies L_1 and L_2 are opposite in phase.

Here g_i is the statistical weight of molecular ion for a given total electron moment L and the AM^+ ion spin S , T_a is the temperature of the neutral medium equal to the ion temperature T_i in the plasma, $\langle \omega_i \rangle$ and $\langle B_i \rangle$ are the average values of the vibration frequencies and rotational constants. Then, according to (1) the variations in the populations of Rydberg states and temperature are related by a simple relation, i.e.

$$\delta m_n \cong - \frac{m_n}{(nT_e)^2} (3 + n^2 T_e) \delta T_e \quad (3)$$

It can be seen that at $n^2 T_e \sim 1$, when the stochastic regime is formed in the electronic spectrum [12], the population m_n variations are approximately 4 times larger than the electron temperature T_e variations. This means that for negative values $\delta T_e < 0$, the corresponding population $m_n(T_e)$ variations (as well as GPS

This means that an increase in the measurement error at one frequency simultaneously leads to a decrease in the error at the second. That was observed in the experiment of Montenbruck's group [5]. The presence of the same errors for the electron temperature $\langle T_e \rangle \cong 1100$ K can serve as a kind of standard in interpreting the results of satellite measurements. The foregoing is a direct confirmation of the validity of the theoretical approach based on the concept of resonant quantum properties of the propagation medium of GPS signals [8]. Moreover, with an increase in the electron temperature T_e associated with a change in D and E ionosphere layer plasma state, the errors in determining the effective water surface level increase for the frequency L_1 and decrease for the frequency L_2 respectively.

Conclusions. The problem of vertical sounding is extremely urgent at the present time. This is due to the need for observations of ocean level (tsunami formation) and snow depth (melting ice). It should be noted that in order to improve the experimental technique [5–7], it would be desirable to more accurately determine the points of geodetic reference. In addition, it follows from the proposed theory and experimental results [6] that the use of the “two microphones” method does not significantly increase the accuracy of the GPS altimeter. Apparently, an applying of the three-frequency method with the additional use of the unique properties of the “waist point” at a frequency of 1.4 GHz can lead to the desired result. However, the problem of determining the time-dependent electron concentration n_e in the lower ionosphere is still unresolved. Just to this circumstance the main efforts of researchers are to be directed.

Acknowledgements. This work was carried out in the framework of State Assignment of the Ministry of Science and Higher Education of the Russian Federation (project No. AAAA-A19-119010990034-5).

1. G.V. Golubkov, M. G. Golubkov, M.I. Manzhelii, “Microwave and IR Radiation of the Upper Atmosphere during Periods of Enhanced Solar Activity,” *Doklady Physics*, 2012, 57(2), pp. 461-464, doi: 10.1134/S102833581212004X.
2. G.V. Golubkov, M.I. Manzhelii, A.A. Berlin, et al., “Fundamentals of radio-chemical physics of the Earth's atmosphere,” *Russian Journal of Physical Chemistry B*, 10(1), 2016, p. 77-90, doi: 10.1134/S1990793116010024.
3. V.V. Kuverova, S.O. Adamson, A.A. Berlin, et al., “Chemical physics of D and E layers of the ionosphere,” *Advances in Space Research*, 64 (10), 2019, pp. 1876–1886, doi: 10.1016/j.asr.2019.05.041.
4. S.-Y. Su, L.-C. Tsai, C.H. Liu, et al., “Ionospheric Es layer scintillation characteristics studied with Hilbert-Huang transform,” *Advances in Space Research*, 64(10), 2019, pp. 2137–2144, doi: 10.1016/j.asr.2019.06.039.
5. A. Helm, O. Montenbruck, J. Ashjaee, et al., “GORS — A GNSS occultation, reflectometry and scatterometry space receiver,” *Proceedings of 20th International Technical Meeting of the Satellite Division of The Institute of Navigation (ION GNSS 2007)*, Fort Worth, 2007, pp. 2011–2021.
6. A. Helm, R. Stosius, O. Montenbruck, et al., “Utilizing ocean reflected GPS L_1 C/A and the new GPS L_2 C signals for tsunami detection from space: possible small satellite constellations and the GORS instrument,” *Proceedings of International Conference on Tsunami Warning (ICTW)*, Bali, 2008, pp. 1–8.
7. O. Montenbruck, P. Steigenberger, L. Prange, et al., “The Multi-GNSS Experiment (MGEX) of the International GNSS Service (IGS) – Achievements, prospects and challenges,” *Advances in Space Research*, 59(7), 2019, pp. 1671–1697, doi: 10.1016/j.asr.2017.01.011.
8. G.V. Golubkov, M.G. Golubkov, M.I. Manzhelii, “Rydberg states in the D layer of the atmosphere and the GPS positioning errors,” *Russian Journal of Physical Chemistry B*, 8(1), 2014, pp. 103–115, doi: 10.1134/S1990793114010126.
9. G.V. Golubkov, M.G. Golubkov, M.I. Manzhelii, I.V. Karpov, “Optical quantum properties of GPS signal propagation medium – D layer,” in: “The atmosphere and ionosphere: elementary processes, monitoring, and ball lightning,” eds. V.L. Bychkov, G.V. Golubkov, A.I. Nikitin, New York: Springer, 2014, pp. 1–68, doi: 10.1007/978-3-319-05239-7_1.

10. G.V. Golubkov, M.G. Golubkov, M.I. Manzhelii, "Microwave Radiation in the Upper Atmosphere of the Earth During Strong Geomagnetic Disturbances," *Russian Journal of Physical Chemistry B*, 6(1), 2012, pp. 112-127, doi: 10.1134/S1990793112010186.
11. G.V. Golubkov, M.G. Golubkov, G.K. Ivanov, "Rydberg States of Atoms and Molecules in a Field of Neutral Particles," in: "The Atmosphere and Ionosphere: Dynamics, Processes and Monitoring," eds. V.L. Bychkov, G.V. Golubkov, A.I. Nikitin, New York: Springer, 2010, p. 1-67, doi: 10.1007/978-90-481-3212-6_1.
12. N.N. Bezuglov, G.V. Golubkov, A.N. Klyucharev, "Rydberg Atoms: From Determinism to Chaos," *Russian Journal of Physical Chemistry B*, 11(6), 2017, pp. 912-927, doi: 10.1134/S1990793117050177.

EFFECTS OF THE JANUARY 2005 SOLAR PROTON EVENTS ON THE IONOSPHERE IN EAGLE MODEL

*Fedor S. Bessarab¹, Timofei V. Sukhodolov^{1,2}, Maxim V. Klimenko², Vladimir V Klimenko²,
Yurii N. Korenkov², Bernd Funke³, Eugene V. Rozanov^{1,2}*

¹*West Department of Pushkov Institute of Terrestrial Magnetism, Ionosphere and Radio Wave Propagation Russian Academy of Sciences, 236016, Kaliningrad, Russia*

²*Physikalisch-Meteorologisches Observatorium, World Radiation Center, Davos, Switzerland*

³*Instituto de Astrofísica de Andalucía, CSIC, Granada, Spain*

Introduction. The paper presents a study of the response of the parameters of the ionosphere and thermosphere to Solar Proton Events (ATP) in January 2005. Solar proton events (SPEs) correspond to the ejections of the solar coronal mass, during which a large number of protons and heavy ions are emitted. Solar protons entering into the Earth's magnetosphere precipitate in the regions of the polar caps. Protons can have very high energies up to several tens of MeV, which leads to the release of energy in the mesosphere and stratosphere. Thus, proton precipitations provide a direct connection between the Sun and the average atmosphere of the Earth.

In January 2005, two proton events took place: January 17 and 20, which differed from each other in the parameters of the energy spectrum and the magnitude of the fluxes. So, the main energy of the SPE on January 17 was accounted for by protons with the energy of more than 10 MeV, and on January 20 more than 100 MeV. The maxima of the ionization rate located at an altitude of about 60 km and 40 km in the first and second cases, respectively. The effect of high-energy proton fluxes on the Earth's atmosphere has been studied in many works (see, for example, [1]). Most of these studies examined the photochemical and dynamic effects of proton absorption at altitudes of the stratosphere and mesosphere, while ionospheric effects were not considered.

In our work, the investigation of the ionospheric effects of SPEs in January 2005 was carried out using the EAGLE model of the whole atmosphere, in which processes in the atmosphere and ionosphere are described in an interconnected manner.

Numerical simulations. The new Entire Atmosphere GLobal model (EAGLE) [2] combines the upper atmosphere model (GSM TIP) and the neutral atmosphere model (HAMMONIA).

Ionization from precipitating particles in the EAGLE model is calculated using the AIMOS module (Atmospheric Ionization Module Osnabruck). AIMOS models of ion pair production due to precipitating particles solar and magnetospheric origin. The AIMOS module consists of two parts: calculation of precipitating based on the processing of data from POES and GOES satellites and calculation of characteristic energies and fluxes using a procedure based on Monte Carlo simulation. To study ionospheric disturbances, we performed two model runs: the first is the basic one, in which proton events were not taken into account, and the second, in which amplification of proton precipitations occurred during SPEs. The perturbation of the electron concentration $\Delta Ne = Ne_d - Ne_{ref}$ in the E and F - regions

of the ionosphere is shown in Fig. 1. Note that the increase in the electron concentration on January 21 is caused by an increase of the electron precipitations that are not related to proton events.

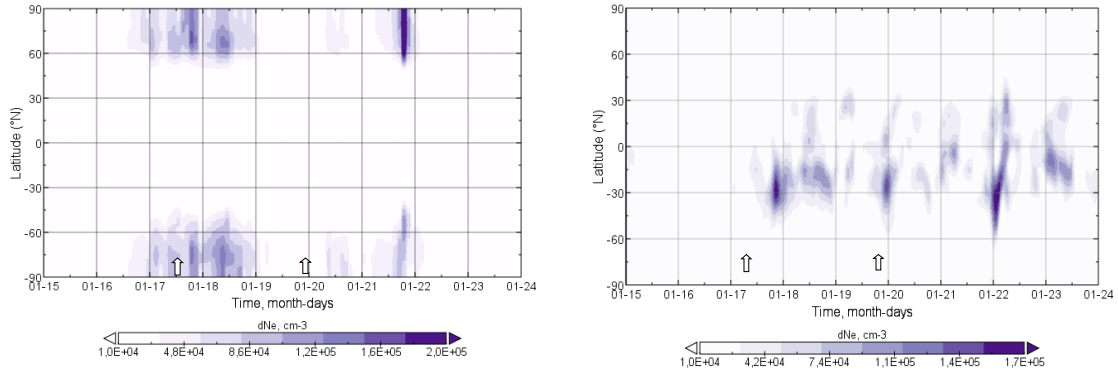


FIGURE 1. ΔNe , cm^{-3} at altitude 90 km (left) and 300 km (right). The arrows marked maximal phases of SPE on 17 and 20 of January.

Despite the relative transparency of the thermosphere for high-energy protons, the ionospheric response to SPE was obtained in numerical experiments. In the E-region of the ionosphere, additional ionization by the spectral “tails” of proton fluxes leads to an increase in the electron concentration above ± 60 latitudes of both hemispheres. At the height of the F2 region of the ionosphere, the near-equatorial region of positive perturbations of electron concentrations is distinguished. An additional analysis showed that this effect is due to indirect reasons, mainly, a change in the electric field and neutral composition generated by the absorption of electrons in the stratosphere and mesosphere.

Conclusion. It is known that the main part of the solar proton energy is absorbed in the ionosphere D region, therefore the direct effect by Solar Proton Events (SPE) on the E and F region ionospheric parameters is not strong. But besides the additional ionization that is observed in the E-region of the ionosphere, SPEs also generate chemical and thermodynamic processes in the mesosphere and stratosphere which can cause additional perturbations of the electric fields and thermospheric composition and as results perturbations in the ionospheric F2-region.

This work was supported by the grant of the Russian Science Foundation No. 17-17-01060.

1. I. A. Mironova, K. L. Aplin, F. Arnold, G. A. Bazilevskaya, R. G. Harrison, A. A. Krivolutsky, K. A. Nicoll, E. V. Rozanov, E. Turunen and I. Usoskin, Energetic Particle Influence on the Earth’s Atmosphere, *Space Science Reviews, Springer*, 2015, 194 (1-4), pp. 1-96, doi: 10.1007/s11214-015-0185-4.

2. M. V. Klimenko, V. V. Klimenko, F. S. Bessarab, T. V. Sukhodolov, P. A. Vasilev, I. V. Karpov, Yu. N. Korenkov, I. E. Zakharenkova, B. Funke and E. V. Rozanov, Identification of the mechanisms responsible for anomalies in the tropical lower thermosphere/ionosphere caused by the January 2009 sudden stratospheric warming, *J. Space Weather Space Clim.*, 2019, 9, pp. A39, doi: 10.1051/swsc/2019037.

INFLUENCE OF OSCILLATORY POLARIZING CURRENT UPON IONOSPHERIC DISTURBANCES DURING THE EISCAT HEATER OPERATION

Valery M. Krasnov¹, Yuri V. Kuleshov, Alexander A. Korystin¹, Yana V. Drobzheva²

¹Mozhaisky Military Space Academy, Saint Petersburg, Russia

²Russian State Hydrometeorological University, Saint Petersburg, Russia

The operation of heating stands in most cases leads to disturbances in the electron concentration and temperature. However, this does not always happen, and the reasons for this are not always clear. For example, when operating a stand in Tromsø on November 6, 2010 ($f = 4.544$ MHz) and 4.03. 2011 ($f = 4.04$ MHz): in the first case, heating led to a noticeable change in the temperature and electron concentration profile (Fig. 1), but in the second case it did not. Heating was carried out by an extraordinary wave with an average transmitter radiation power of ~ 80 kW.

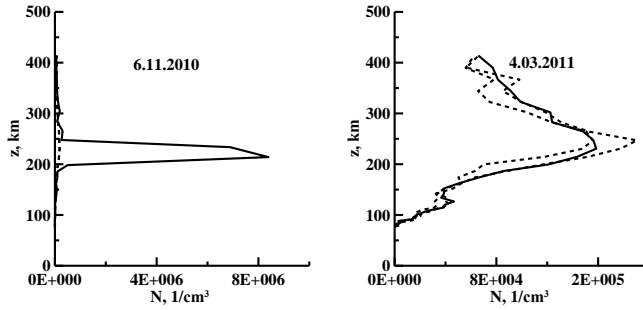


FIGURE 1. Electron concentration profiles according to the incoherent scattering radar: at the time of operation of the heating stand - solid lines, before and after operation of the stand with an interval of not more than ± 8 min - dashed lines.

The aim of this work is to consider the possibility of interpreting experiments based on the absorption of radio wave energy by an oscillating polarizing current.

It is known that when the ionosphere is exposed to alternating electric fields in the presence of a geomagnetic field, an oscillating polarization current occurs [1,2]. The solution of the equation of motion of charges

$$m \frac{d\vec{v}}{dt} = q[\vec{E} + (\vec{v} \times \vec{B}_0)], \quad (1)$$

is carried out in the approximation $\omega \ll$

Ω , where q is the particle's charge, \vec{v} is its velocity, \vec{B}_0 is the Earth's magnetic field, ω is the angular frequency of the radio wave, $\Omega = 2\pi f_H = qB_0/m$ is the electron gyrofrequency.

In [3], a solution to equation (1) was found not limited to this approximation

$$v_x = -\frac{\Omega}{B_0(\omega^2 - \Omega^2)}(\omega + \Omega \cos \alpha)E_1 \cos(\omega t - k_1 z) + \frac{\Omega}{B_0(\omega^2 - \Omega^2)}(\omega - \Omega \cos \alpha)E_2 \cos(\omega t - k_2 z), \quad (2)$$

$$v_y = \frac{\Omega}{B_0(\omega^2 - \Omega^2)}\left(\omega + \Omega \cos \alpha - \frac{\Omega^2}{\omega} \sin^2 \alpha\right)E_1 \sin(\omega t - k_1 z) + \frac{\Omega}{B_0(\omega^2 - \Omega^2)}\left(\omega - \Omega \cos \alpha - \frac{\Omega^2}{\omega} \sin^2 \alpha\right)E_2 \sin(\omega t - k_2 z), \quad (3)$$

$$v_z = -\frac{\Omega^2 \sin \alpha}{B_0(\omega^2 - \Omega^2)}\left(1 + \frac{\Omega}{\omega} \cos \alpha\right)E_1 \sin(\omega t - k_1 z) + \frac{\Omega^2 \sin \alpha}{B_0(\omega^2 - \Omega^2)}\left(1 - \frac{\Omega}{\omega} \cos \alpha\right)E_2 \sin(\omega t - k_2 z), \quad (4)$$

where E_1 , E_2 are the amplitudes of radio waves with electric vectors \vec{E}_1 and \vec{E}_2 , rotating in opposite directions in the xy plane; \vec{k}_1 and \vec{k}_2 are the wave vectors directed along the z axis.

Taking into account the expressions for the polarization - $\vec{P} = \sum_N e\vec{R} \left(\vec{v} = \frac{d\vec{R}}{dt} \right)$ and induction - $\vec{D} = \vec{E} + 4\pi\vec{P}$, it is easy to obtain using the Maxwell equation $rot\vec{B} = \frac{1}{c} \frac{\partial \vec{D}}{\partial t} + \frac{4\pi}{c} \vec{J}_{os}$ the expressions for conductivity of \vec{E}_1 and \vec{E}_2 :

$$\frac{4\pi\sigma_{z1}}{\omega} = \left| \frac{\omega_0^2 \Omega \sin \alpha}{\omega(\omega^2 - \Omega^2)} \left(1 + \frac{\Omega}{\omega} \cos \alpha \right) \right|, \quad \frac{4\pi\sigma_{z2}}{\omega} = \left| \frac{\omega_0^2 \Omega \sin \alpha}{\omega(\omega^2 - \Omega^2)} \left(1 - \frac{\Omega}{\omega} \cos \alpha \right) \right|. \quad (5)$$

In cases when the profiles of the dielectric permeability and conductivity of the ionosphere can be approximated by linear layers, the expression for the complex dielectric permeability has the form [4]

$$\varepsilon' = \varepsilon - i \frac{4\pi\sigma}{\omega} = \left(\varepsilon_0 \pm \frac{z - z_0}{z_r} \right) - i \left(\alpha_0 + \beta \frac{z - z_0}{z_r} \right) = a - b \frac{z - z_0}{z_r}. \quad (6)$$

The dependence of the amplitude of the incident wave on the height z is determined by the expression [5] $E(z) = E_0(R_0/R) \exp(R_0 \sin \eta_0) \exp(-R \sin \eta)$, where E_0 is the amplitude of the incident wave,

$$R = \frac{2\omega}{3c} \sqrt{\frac{\rho_1}{z_r}} \rho_3^{3/2}, \quad \eta = \varphi - 1.5 \arctg \frac{\alpha_0 + \beta \frac{z - z_0}{z_r}}{\varepsilon_0 \pm \frac{z - z_0}{z_r}}, \quad R_0 = R(z = z_0) = \frac{2\omega}{3c} \frac{z_r}{\rho_1} \rho_2^{3/2}, \quad \eta_0 = \varphi + 1.5\gamma,$$

$$\rho_1 = \sqrt{1 + \beta^2}, \quad \varphi = \pm \arctg \beta, \quad \rho_2 = \sqrt{\varepsilon_0^2 + \alpha_0^2}, \quad \gamma = -\arctg \frac{\alpha_0}{\varepsilon_0}, \quad \rho_3 = \sqrt{\left(\varepsilon_0 \pm \frac{z - z_0}{z_r} \right)^2 + \left(\alpha_0 + \beta \frac{z - z_0}{z_r} \right)^2} \frac{z_r}{\rho_1},$$

ε_0 - is the initial value of the dielectric permeability at the layer boundary $z = z_0$, $z_r = \left| \frac{1}{\frac{d\varepsilon}{dz}} \right|$ - the height interval in the linear layer, on which ε varies from unity to zero,

(in (6), when ε decreases with height, a minus sign is placed in front of the term $\frac{z - z_0}{z_r}$, and with the

growth of ε - plus); α_0 characterizes the constant component of conductivity at the beginning of the layer, and $\beta = z_r \frac{d\alpha}{dz}$ is the value of the conductivity gradient, c is the speed of light.

When the conductivity is zero (there is no absorption of radio waves), the formula takes the form

$$E_z = E_0 \left(\frac{\varepsilon_0}{\varepsilon_0 \pm \frac{z - z_0}{z_r}} \right)^{1/4}.$$

It can be seen that, at negative dielectric permittivity gradients, the wave field increases with height (the effect of “swelling” of the field, for example [4]).

6.11.2010 A_p - geomagnetic index equaled $A_p = 1$ and 4.03.2011 - $A_p = 13$, indicating quiet geomagnetic conditions. To carry out calculations of the parameters of the background geomagnetic field, the IGRF12 model was used. The results of calculations of the amplitude, declination,

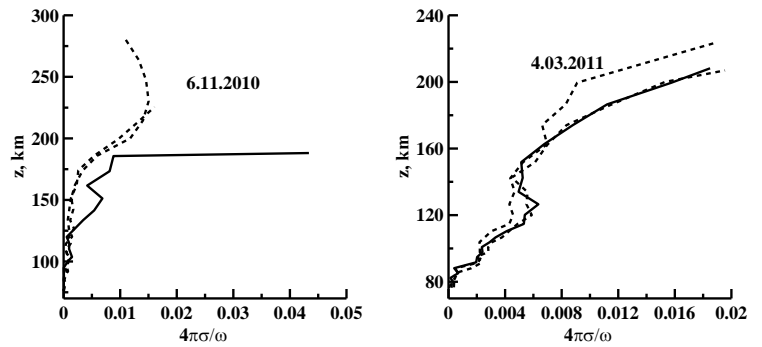


FIGURE. 2. Conductivity profiles: at the moment of operation of the heating stand - solid lines, before and after operation of the stand with an interval of no more than ± 8 min - dashed lines.

and inclination of the geomagnetic field for both days showed that they slightly differ from each other, and accordingly the profiles of the gyrofrequencies also differ little.

the ionospheric conductivity profile on November 6, 2010 (Fig. 2) changed significantly after heating: the conductivity increased sharply in the region of the reflection point at the altitude of ~ 188 km. In contrast, the conductivity profile of March 4, 2011, has not changed much since the start of the operation of the heating stand.

For both cases, Fig. 3 shows the results of calculating the attenuation of the amplitude of a plane radio wave with height. A comparison of the graphs shows that on 4.03.2011 the amplitude of the radio waves weakened sharply to altitude of 120 km, and it can be assumed that for this reason the heating stand did not have a noticeable effect on the electron concentration and their temperature at a reflection point height of ~ 200 km. A different picture is observed on 6.11.2010.

For 5 minutes before the heating the profiles of permeability and conductivity provided propagation radio waves without significant attenuation to the height of about 150 km. As a result the major energy absorption was in the height range of 150–180 km. Apparently, for this reason, when the heating stand was turned on, a maximum of electron concentration arose at altitudes of 200–250 km (Fig. 1a), and a sharp increase in temperature occurred at altitudes of 130–330 km.

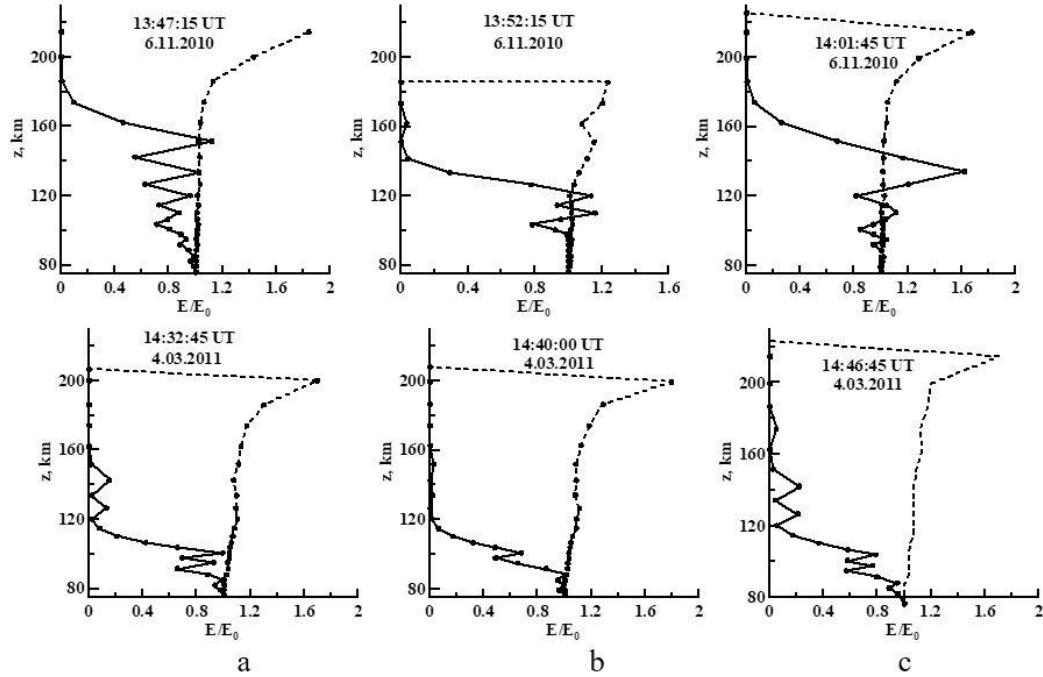


FIGURE 3. Altitude changes of the amplitude of the radio wave \vec{E}_2 for cases: a) the wave is emitted before the start of the heating stand, b) during and c) after - solid lines. Dashed lines - changes in the wave amplitude without taking into account conductivity.

Our gratitude to the EISCAT Scientific Association for the ionospheric data during operation of the heating stand.

1. F. Chen, Introduction to plasma physics, *Mir, Moscow*, 1987.
2. B.E. Brunelli, A.A. Namgaladze, Ionosphere Physics, *Science, Moscow*, 1988.
3. V.M. Krasnov, Propagation of radiowaves at frequencies below than electron gyrofrequency from the earth surface to the higher atmosphere, In a book “Solar Physics Research Trends”, *Nova Science Publishers, Washington*, 2008, pp. 381-399.

4. V.L. Ginzburg, Propagation of electromagnetic waves in plasma, *Fizmatgiz, Moscow*, 1960.
5. V.M. Krasnov, Influence of ionospheric conductivity on parameters of a radio wave at a reflection point, *Radio Sci.*, 2002, 37(6), pp. 11-1-11-5, doi: 10.1029/2002RS002690.

GLOBAL STRUCTURE OF ELECTRON DENSITY IN D AND E REGIONS SIMULATED WITH 3D PHOTOCHEMICAL MODEL CHARM-DE

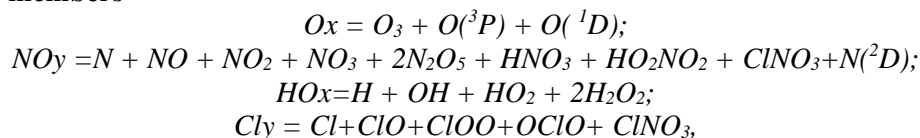
Alexei A. Krivolutsky, Lidiya A. Cherepanova, Tatyana Yu. Vyushkova, Maxim V. Banin,
Alexander I. Repnev

Laboratory for Atmospheric Chemistry and Dynamics, Roshydromet, Central Aerological Observatory, Dolgoprudny, Moscow Region, Russia

New version of 3D global photochemical model CHARM-DE (Chemical Atmospheric Research Model with D and E regions) was used to study global distribution of neutral chemical species, ions and electron density up to 130 km level. Model CHARM-DE is numerical model developed at the Laboratory for Atmospheric Chemistry and Dynamics of Central Aerological Observatory on the basis of the model CHARM-I [1]. Short description of the model and some results of simulations are presented in this paper.

Model description. Method of “chemical families” was used to calculate neutral species concentrations [2]. In order to calculate electrons and ions concentration neutrality condition were realized. List of neutral compounds looks like as follow:

“Families members”

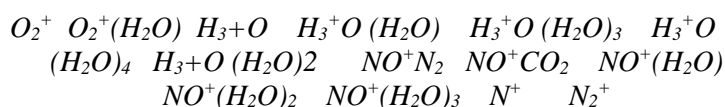


“Other species”: CH_3O_2 , CH_3O_2H , CH_3O , CHO , CO , $O_2(^1\Delta_g)$.

“Gas-sources”: CH_4 , CO_2 , N_2O , CF_2Cl_2 , $CFCl_3$, H_2 , Cl_4 , Cl_2 , CH_3Cl , CH_2Cl , O_2 , H_2O .

Corresponding list of ionized compounds looks like as follow:

“Positive ions”



“Negative ions and electrons”: $[e]$ O_2^- O_3^- O_4^- CO_4^- O^- OH^- HCO_3^- NO_3^- NO_2^-

Joint number of photochemical reaction including the reaction of ionization in the model equals 242. Ionization of NO is initiated by short UV (L- α). Corresponding well-known formula for its calculations is:

$$q_{Ly-\alpha}(z) = \sigma_{NO}^i n(NO) I_\infty (Ly - \alpha) \exp \left[-\sigma^a(O_2) \int_z^\infty n(O_2) dz \right] Ch(z, \chi),$$

Ionization of $O_2(^1\Delta_g)$ in range 102.7-111.8 nm is calculated by the following way:

$$\begin{aligned} q(z) = n(O_2(^1\Delta_g)) \{ 0,549 \cdot 10^{-9} \exp(-2,406 \cdot 10^{-20} N(O_2)) + \\ + 2,614 \cdot 10^{-9} \exp(-8,508 \cdot 10^{-20} N(O_2)) \} (sm^{-3}c^{-1}) \end{aligned}$$

where:

$$N(O_2) = \int_z^{\infty} n(O_2) dz Ch(z, \chi).$$

Ionization by Galactic Cosmic Rays is also taken into account (parameterization is used). Dissociation rates by UV are recalculated after each hour of integration in the model. The grid looks like as follow: vertical – 2 km; latitude - 50; longitude - 100. Time-step of integration is in range: 100-500 sec. To describe the global transport of chemical species Prather's scheme was used [3]. Global 3D of wind components and temperature fields has been calculated with Middle Atmosphere GCM ARM [4]. We present the results below, which illustrate global distribution of ozone (as the example of neutral species), electron density and vertical structure of several ions. We will show also the response of lower ionosphere to solar eleven-year forcing in UV radiation.

Results of simulations. Figures 1-4 shows global distributions of electron density at three different levels.

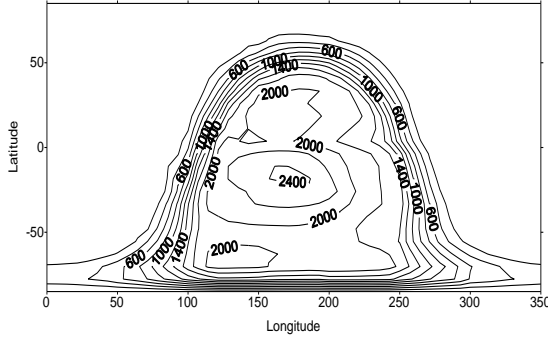


FIGURE 1. Global distribution of electron concentrations at 80 km in summer (00-00 UT) (simulation with CHARM-DE)

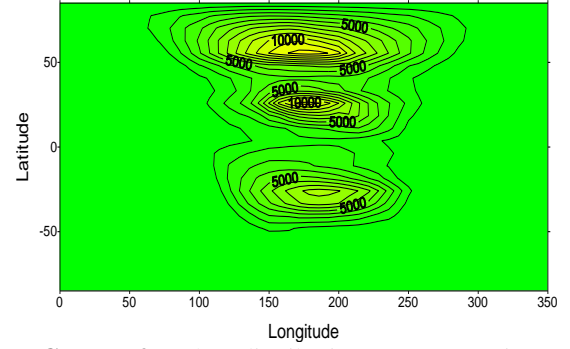


FIGURE 2. The distribution (concentration) of electrons simulated with CHARM-DE at 90 km.

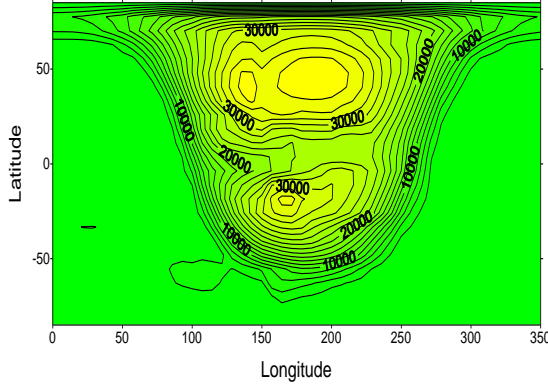


FIGURE 3. The distribution (concentration) of electrons simulated with CHARM-DE at 100 km.

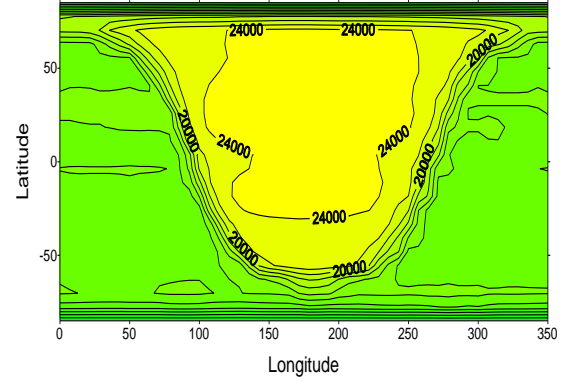


FIGURE 4. The distribution (concentration) of electrons simulated with CHARM-DE at 100 km.

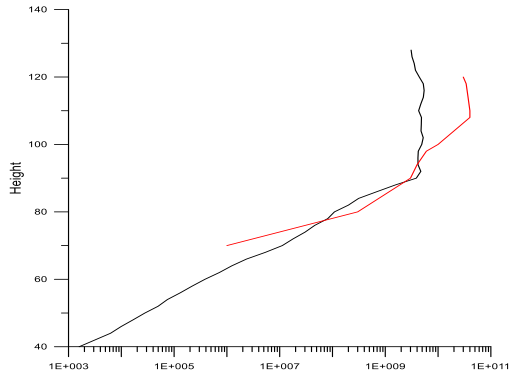


FIGURE 5. Model comparison with observations.

perspective instrument for solving different important problems solar influence on ionosphere, ions-neutral interaction, and of radio wave propagation.

Fig. 5 shows vertical profile of electron concentration calculated by the model in comparison with observations by rocket sounding.

Concluding remarks. So that, we can conclude that presented results based on a new version of global photochemical numerical model CHARM-DE, which describes the interaction between neutral and ionized chemical compounds in middle atmosphere and lower thermosphere up to 130 km level which includes D and E regions ionosphere, suggest the opportunity to have a new look on a problem of ionosphere behavior. It seems that this model is a

1. A.A. Krivolutsky, L.A. Cherepanova, T.Yu. Vyushkova, A.I. Repnev, The Three-Dimensional Numerical Model CHARM-I: The Incorporation of Processes in the Ionospheric D-region, *Geomagnetism and Aeronomy*, 2015, 55(4), pp. 468-487.
2. R.P. Turco, R.C. Whitten, A comparison of several computational techniques for solving some common aeronomic problems, *J. Geophys. Res.*, 1974, 79(22) pp. 317-319.
3. M. Prather, Numerical advection by conservation of second-order moments, *J. Geophys. Res.*, 1986, 91, pp. 6671-6681.
4. A.A. Krivolutsky, L.A. Cherepanova, T.Yu. Vyushkova, A.I. Repnev, A.V. Klyuchnikova, Global circulation of the Earth's atmosphere at altitudes from 0 to 135 km simulated with ARM model. Consideration of the solar activity contribution, *Geomagnetism and Aeronomy*, 2015, 55(6), pp. 468-487.

2-D MODEL OF THE GLOBAL IONOSPHERIC CONDUCTOR CONNECTED WITH THE MAGNETOSPHERIC CONDUCTORS

Valery V. Denisenko

Institute of Computational Modelling of the Siberian Branch of the Russian Academy of Sciences, Krasnoyarsk, Russia

The electric conductivity equation. The basic equations for the steady state electric field \mathbf{E} and current density \mathbf{j} are Faraday's law, the charge conservation law, and Ohm's law with conductivity tensor $\hat{\sigma}$. The electric potential V can be introduced so that $\mathbf{E} = -\text{grad} V$. Then the system of the equations is reduced to the electric conductivity equation

$$-\text{div}(\hat{\sigma} \text{grad} V) = q, \quad (1)$$

where q differs from zero if an external electric current exists.

2-D model of the ionospheric conductor. It is shown in [9] how to reduce a three-dimensional model to a two-dimensional one when the conductivity in the direction of the magnetic field σ_{\parallel} is much larger than Pedersen and Hall conductivities σ_p, σ_H . The subscripts \parallel, \perp denote the components parallel and normal to the magnetic field. It is possible to idealize this inequality as $\sigma_{\parallel} = \infty$. It means

that the electric current along a magnetic field line can be arbitrary, while the electric field component E_{\parallel} equals zero. Therefore the electric potential V is constant at each magnetic field line. Since the magnetic field lines are equipotentials, the ionospheric conductor may be represented by Pedersen and Hall conductances which are equal to integrals of the corresponding local conductivities σ_p, σ_H [9].

In such a model, a magnetic field line can obtain or lose charge by current \mathbf{j}_{\perp} and it does not matter for its total charge at what point at the magnetic field line \mathbf{j}_{\perp} exists. By summation of the inputs from all points of the magnetic field line, we obtain the conductance between magnetic field lines. The resulting 2-D Ohm's law can be written as $\mathbf{J}_{\perp} = \hat{\Sigma} \mathbf{E}_{\perp}$, where \mathbf{J}_{\perp} is the total current across magnetic field line. The components of the tensor $\hat{\Sigma}$ are Pedersen and Hall conductances Σ_p, Σ_H , if the segments of the magnetic field lines are parallel. They are obtained by integration σ_p, σ_H .

We calculate the space distributions of the local Pedersen and Hall conductivities σ_p, σ_H using the empirical models IRI, MSISE, IGRF [4]. The empirical model IRI does not present any auroral enhancement of electron concentration that is produced by high energy electron and proton precipitation from the magnetosphere. We use the model [10] of the enhancement of Σ_p, Σ_H in the auroral zones.

The equation (1) after integration along each magnetic field line is reduced to the 2-D charge conservation law. A flat domain is preferable for numerical solution. We use one of two methods of coordinate transformation presented in [1] and [7]. Then the equation at a plane with Cartesian coordinates x, y has shape

$$-\frac{\partial}{\partial x} \left(\Sigma_{xx} \frac{\partial V(x, y)}{\partial x} + \Sigma_{xy} \frac{\partial V(x, y)}{\partial y} \right) - \frac{\partial}{\partial y} \left(\Sigma_{yx} \frac{\partial V(x, y)}{\partial x} + \Sigma_{yy} \frac{\partial V(x, y)}{\partial y} \right) = Q. \quad (2)$$

It is proposed in [1] to use shown in Fig. 1a three flat domains Ω_N, Ω_S and Ω . This procedure includes tracing each magnetic field line to find the conjugate point in the Southern hemisphere and the point in Ω . It seems more adequate to transform the Northern and the Southern ionospheres to two flat planes as for the dipolar magnetic field can be done analytically with additional advantages of conformal transformations [7]. Then we unite the 2-D charge conservation equations from two conjugate points for the lines which can be regarded as ideally conducting ones. The last approximation is definitely correct in low and middle latitudes and we use it up to the auroral zones. In the rest polar parts of the ionosphere the 2-D charge conservation equations are independent. They are simplified as described in the next section due to magnetospheric conductors. In general case we have the boundary value problem in a non-schlicht domain that is mathematically studied in [3].

Conductance $0 < \Sigma_p < \infty$ in the domains of interest. For a physicist it means the natural property of positiveness of the Joule dissipation. From mathematical point of view it is an important property of the coefficients of the partial differential equation: symmetrical part of the conductivity tensor is a positive definite one. This property is not corrupted by the used coordinate transformation and symmetrical part of the tensor $\hat{\Sigma}$ in (2) also is a positive definite one. So the partial differential equation (2) has an elliptical type which means that one can use boundary conditions similar to ones for Poisson equation.

Magnetospheric conductor. A cross-section of the magnetosphere is schematically presented in Fig. 1a. The direction of the geomagnetic Northern pole is shown as \mathbf{N}_m vector as is in summer. The magnetosphere could be divided into 5 specific domains which are volumes of space. Their cross-sections are shown in Fig. 1a. The domain ω_1 consists of magnetic field lines in vicinity of the magnetopause which correspond to cusp. The domain ω_2 consists of magnetic field lines which

correspond to the plasma sheet. The domain ω_3 consists of closed magnetic field lines. The domains ω_4 and ω_5 consist of magnetic field lines which go to the distant tail from Northern and Southern polar caps respectively.

The conductivities σ_p , σ_H are small above 500 km in the ionosphere and in the whole magnetosphere with exclusion of the plasma sheet in the magnetospheric tail and vicinity of the magnetopause. Large conductivity in the last domains are equivalent to large conductivity in the auroral zones and cusps which are shown as the domains 1, 2 in Fig. 1b.

Boundary value problems. For the Northern polar cap we use the plane $z = z_N$ with z_N greater than the Earth's radius. The 3-D domain ω_4 crosses this plane in 2-D domain Ω_N which cross-section is plotted with bold line in Fig. 1a. Since the equipotential auroral zone is behind the boundary of Ω_N , the potential equals zero (or any constant) at the boundary. So we have Dirichlet boundary value problem. It has unique solution since the partial differential equation (2) is an elliptical one. We solve similar boundary value problem for the Southern polar cap.

For the main part of the ionosphere presented with 2-D domain Ω the same boundary condition can be used at its outer boundary. The interior boundary Γ_{eq} of Ω corresponds to the lowest magnetic field lines which are regarded as ionospheric ones and so as equipotential ones. The current to them from below must be given, and it equals zero if atmospheric currents are absent:

$$\mathbf{J}_\nu|_{\Gamma_{eq}} = 0,$$

where the subscript ν denotes the current component normal to the boundary.

This boundary condition defines the inclined derivative of $V(x, y)$. We obtain the boundary value problem of mixed type in the flat ring Ω . Such a problem also has the unique solution. Our method of numerical solution is described in [2].

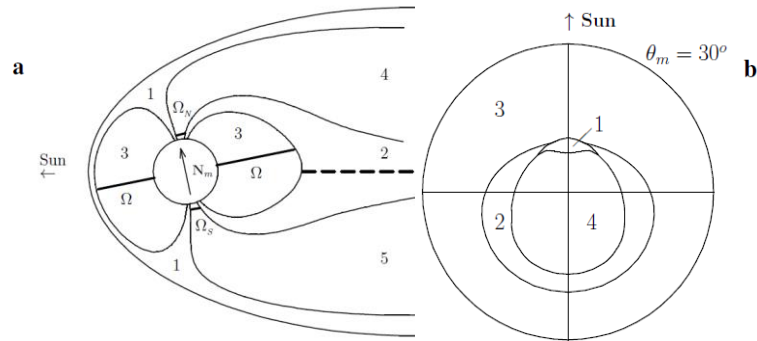


FIGURE 1. a - cross-section of the magnetosphere that contains the direction to the Northern magnetic pole \mathbf{N}_m and direction to the Sun. Magnetic field lines are plotted as the boundaries of 3-D domains described in the text. Bold segments are the cross-sections of flat 2-D domains Ω_N , Ω_S , Ω which are used for calculations. Dashed line - cross-section of the model thin plasma sheet. b - reproduced from [8] mapping of the plasma sheet (2) and magnetopause (1) to the ionosphere. (3) - closed magnetic field lines, (4) – Northern polar cup with open magnetic field lines.

Conclusions. A model of the ionospheric global conductor is constructed as the first approximation in the small parameter expansion of the solution of the three-dimensional problems of electrical conductivity. The small parameter is the ratio of Pedersen and field-aligned conductivities.

The cusps and the plasma layer make the auroral zones equipotential regions. So for the ionospheric electric fields, which generators are located in the ionosphere or in the atmosphere, the global problem of electrical conductivity is separated into three independent boundary value problems for two polar caps and the main domain which simulates the mid- and low-latitude parts of the ionosphere.

The presented model is described in details in the preprint [1]. It was used for mathematical simulation of the ionospheric part of the Global Electric Circuit. The results are presented in the paper [5] with corrections [6]. The model also can be used for calculation of the ionospheric dynamo electric field and as a fragment in more complex ionospheric and magnetospheric models. In the last case electric potential in the auroral zones can be taken from a magnetospheric model or field-aligned currents above the ionosphere can be presented with nonzero Q in (2).

The research is supported by Russian Foundation for Basic Research (project 18-05-00195).

1. V.V. Denisenko, 2-D model of the global ionospheric conductor connected with the magnetospheric conductors, *Cornell Univ. Library*, 2018, <http://arxiv.org/abs/1802.07955>.
2. V.V. Denisenko, Multigrid method for a global Hall conductor in the Earth's ionosphere, *Virtual Proceedings of the 10-th Anniversary Int. GAMM - Workshop on Multigrid Methods*, 1998, <http://www.mgnet.org/mgnet-parmgm98.html>.
3. V.V. Denissenko, A boundary value problem for an elliptic equations with asymmetric coefficients in a non-schlicht domain, *Siberian Mathematical Journal*, 2002, 43(6), pp. 1055-1068.
4. V.V. Denisenko, H.K. Biernat, A.V. Mezentsev, V.A. Shaidurov, S.S. Zama, Modification of conductivity due to acceleration of the ionospheric medium, *Ann. Geophys.*, 2008, 26, pp. 2111-2130.
5. V.V. Denisenko, M.J. Rycroft and R.G. Harrison, Mathematical Simulation of the Ionospheric Electric Field as a Part of the Global Electric Circuit, *Surveys in Geophysics*, 2019, 40(1), pp. 1-35, doi: 10.1007/s10712-018-9499-6.
6. V.V. Denisenko, M.J. Rycroft and R.G. Harrison, Correction to: Mathematical Simulation of the Ionospheric Electric Field as a Part of the Global Electric Circuit, *Surveys in Geophysics*, 2019, 40(1), pp. 37, doi: 10.1007/s10712-018-9505-z.
7. V.V. Denisenko and S.S. Zama, Electric field in the equatorial ionosphere, *Planetary and Space Science*, 1992, 40(7), pp. 941-952.
8. V.V. Denisenko, S.S. Zama and A.V. Kitaev, The effect of viscous friction between the Solar wind and plasma sheet on electric field generation in the magnetosphere, *Geomagnetism and Aeronomy*, 2003, 43(6), pp. 680-686.
9. J.K. Hargreaves, The upper atmosphere and Solar-Terrestrial relations, *Van Nostrand Reinold Co. Ltd*, NY, 1979.
10. D.R. Weimer, Substorm influence on the ionospheric electric potentials and currents, *J. Geophys. Res.*, 1999, 104(1), pp. 185-197.

EAGLE SIMULATION STUDY OF IONOSPHERIC ELECTRIC FIELD: IMPACT OF ATMOSPHERE-IONOSPHERE COUPLING AND GLOBAL ELECTRIC CIRCUIT

*Maxim V. Klimenko¹, Vladimir V. Klimenko¹, Fedor S. Bessarab¹, Timofej V. Sukhodolov^{1,2},
Valery V. Denisenko^{1,2}, Eugene V. Rozanov^{1,2}*

¹*West Department of Pushkov Institute of Terrestrial Magnetism, Ionosphere and Radio Wave Propagation RAS, Kaliningrad, Russia*

²*Physikalisch-Meteorologisches Observatorium, World Radiation Center, Davos, Switzerland*

³*Institute of Computational Modeling SB RAS, Krasnoyarsk, Russia*

Introduction. Ionospheric electric fields, in combination with the Earth's magnetic fields, cause different scale ionospheric irregularities. The electric field in the Earth's ionosphere is generated in the

magnetosphere and in a current-carrying layer of the ionosphere. A review of electric fields in the magnetosphere and ionosphere can be found in [1]. According to recent investigation results during quiet geomagnetic conditions, the spatial and temporal variation of the zonal and meridional electric field at low-latitudes are caused by the atmosphere-ionosphere coupling involving mesospheric tides and gravity waves [2]. Currently, the question about the influence of the global electric circuit on the variability of the ionospheric electric field is being actively discussed. The answer to this question requires research based on mathematical models. In this paper, we discuss the contribution of the atmosphere-ionosphere coupling processes and global electric circuit to the variability of the ionospheric electric field at low-latitudes.

Methods. For the simulations without taking into account low-atmosphere-ionosphere coupling processes we applied the Global Self-consistent Model of the Thermosphere, Ionosphere, and Protonosphere (GSM TIP) [3], which was developed in the WD IZMIRAN. In addition to the results of the GSM TIP model, we present the calculation results obtained using the new model EAGLE [4]. The EAGLE is a model that combined the GSM TIP model and the HAMMONIA (Hamburg Model of the Neutral and Ionized Atmosphere) climate model, which describes atmospheric processes in the altitude range from the Earth's surface to the heights of the thermosphere. Using the GSM TIP and EAGLE models, we calculated the parameters of the thermosphere-ionosphere system for quiet geomagnetic conditions ($K_p = 2$) on 15 January 2009 for a solar activity minimum ($F_{10.7} = 70$ s.f.u.). For the investigation of the ionospheric part of the Global Electric Circuit (GEC), we used GEC numerical model [5] and compared ionospheric electric potential obtained by EAGLE and GEC models to estimate the impact of GEC on the ionospheric electric field.

Results and Conclusion. The GSM TIP model without taking into account the mesospheric tides does not reproduce the evening pre-reversal enhancement of the eastward electric field and the four-peak structure of the longitudinal variation of the electric field at the equator and low-latitudes. On the contrary, the EAGLE model which includes the GSM TIP as an upper atmosphere module successfully reproduces the morphological features of the diurnal and longitudinal variation of the zonal electric field at the equator and low-latitudes. The results of the EAGLE model confirm that the four-peak longitudinal variation and the evening pre-reversal enhancement of the eastward electric field are caused by the atmosphere-ionosphere coupling involving mesospheric tides and gravity waves. The multipeak structure of the longitudinal variations of the equatorial electric field is formed due to the longitudinal variations of the horizontal wind and the Pedersen conductivity arising from the action of mesospheric tides. Based on the model results, we assumed that the longitudinal variation of the Pedersen conductivity is significantly affected by mesospheric tides, while the longitudinal variation of the Hall conductivity is mainly determined by the mismatch of geographic and geomagnetic poles. From comparison of the ionospheric potentials obtained using EAGLE and GEC model, we concluded that the global electric circuit (in such statement of the problem) has an insignificant impact on ionospheric electric field. Note that the two-dimensional GEC model uses IRI and MSIS empirical models for calculation of atmospheric and ionospheric conductivity. The combination of the entire atmospheric EAGLE model and the GEC model will make it possible to fundamentally refine the description of the ionospheric part of the GEC due to the transition from the strongly averaged parameters of the ionospheric medium, which are taken in GEC model from the empirical model IRI, to the values of these parameters calculated in the EAGLE model for specific time moments. Thus, in the future we will be able to estimate the effect of atmospheric and ionospheric conductivity variations on the ionospheric potential.

This work was performed with the financial support of the Russian Science Foundation grant (No. 17-17-01060).

1. M.C. Kelley, *The Earth's Ionosphere: Plasma Physics and Electrodynamics*, 2nd edition, Elsevier, London, 2009.
2. V.V. Klimenko, M.V. Klimenko, F.S. Bessarab et al., The dependence of four-peak longitudinal structure of the tropical electric field on the processes in the lower atmosphere and geomagnetic field configuration, *Adv. Space Res.*, 2019, 64(10), pp. 1854–1864. doi: 10.1016/j.asr.2019.06.029.
3. Yu.N. Korenkov, V.V. Klimenko, M. Forster et al., Calculated and observed ionospheric parameters for Magion-2 passage above EISCAT on July 31 1990, *Journal of Geophysical Research*, 1998, 103(A7), pp. 14697–14710, doi: 10.1029/98JA00210.
4. M. Klimenko, V. Klimenko, F. Bessarab et al., Identification of the mechanisms responsible for anomalies in the tropical lower thermosphere/ionosphere caused by the January 2009 sudden stratospheric warming, *J. Space Weather Space Clim.*, 2019, 9(A39), doi: 10.1051/swsc/2019037.
5. V.V. Denisenko, M.J. Rycroft, R.G. Harrison, Mathematical Simulation of the Ionospheric Electric Field as a Part of the Global Electric Circuit, *Surveys in Geophysics*, 2019, 40(1), pp. 1–35, doi: 10.1007/s10712-018-9499-6.

ANALYSIS OF GLOBAL ELECTRON CONTENT VARIATIONS DURING THE MAJOR SUDDEN STRATOSPHERIC WARMING EVENTS

Aleksandr V. Timchenko¹, Fedor S. Bessarab¹, Maxim V. Klimenko¹, Vladimir V. Klimenko¹, Olga P. Borchevkina¹, Timofei V. Sukhodolov^{1,2}, Yuriy N. Korenkov¹, Eugene V. Rozanov^{1,2}

¹*West Department of Pushkov Institute of Terrestrial Magnetism, Ionosphere and Radio Wave Propagation Russian Academy of Sciences, Kaliningrad, Russia*

²*Physikalisch-Meteorologisches Observatorium, World Radiation Center, Davos, Switzerland*

Introduction. It is known that the ionosphere is affected by a large number of processes associated with solar radiation, geomagnetic disturbance and meteorological disturbances. Recently, various aspects of the ionospheric response to Sudden Stratospheric Warming (SSW) events have been actively investigated. SSW events are characterized by a dramatically increase in temperature in the polar stratosphere in winter. There are two main types of SSW: minor events in which the stratospheric polar vortex is displaced from the pole and major events in which the vortex splits into two or more vortices.

In our study, we considered only major SSW events that occurred between 2000 and 2018, since major SSW events influence on the ionosphere are more pronounced. Also, we selected only those events that occurred during periods of minimal solar activity, when the effect of geomagnetic activity on the ionosphere is not large.

During stratospheric warming events, changes occur in the dynamic regime of all atmospheric layers, which lead to significant disturbances in the ionospheric dynamo electric field. In this paper, we analyze the Global Electron Content (GEC) variations during major SSW events. The Global Electron Content is the total number of electrons in near-Earth space to a GPS orbit of about 20,200 km. GEC is well suited for studying large-scale ionospheric disturbances [1]. The GEC calculation method and the corresponding software support were developed at the ISZF SB RAS, in Irkutsk.

Data and method. We selected major SSW events from the considered period 2000–2018 based on the papers [2]. To determine start and stop dates of SSW events we used reanalysis data NCEP/NCAR [3]. GEC data set were got from SIMuRG (System for the Ionosphere Monitoring and Researching from GNSS) of Institute of Solar-Terrestrial Physics SB RAS, Irkutsk.

Earlier, it was noted (see, for example, [4]) increasing of the semidiurnal tide amplitude in the parameters of the mesosphere and lower thermosphere, which lead to an increase in 12 hour variations of ionospheric parameters - foF2 and TEC. In [5], we used the continuous wavelet transform technique to determine the spectrum of the critical frequency of the F2 layer above the Kaliningrad and Irkutsk stations. The same analysis, but for variations of the Global Electron Content, we used in this work.

Wavelet transform coefficients are calculated by the formula:

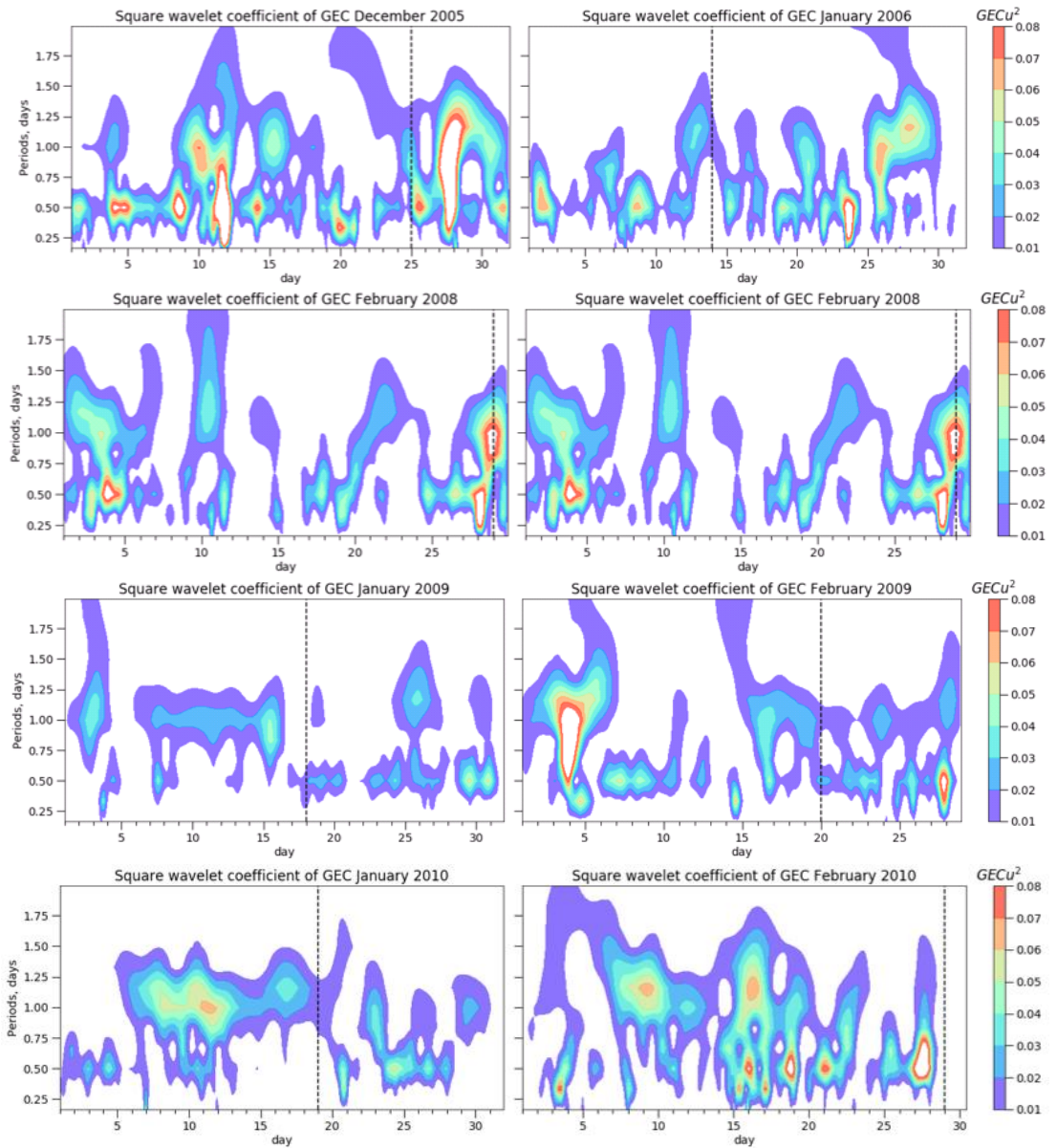
$$W(a,b) = \frac{1}{\sqrt{|a|}} \int_0^T f(t) \psi\left(\frac{t-b}{a}\right) dt,$$

where a — scale (analog of the oscillation period), b — time shift, $\psi(t) = e^{i\pi t} e^{(-t^2/\sigma^2)}$ — complex wavelet Morlet function.

For the convenience of analysis, we used the sum of the squares of the real and imaginary parts of the wavelet coefficients:

$$E(a,b) = \text{Re}(W(a,b))^2 + \text{Im}(W(a,b))^2$$

Result and discussions. Figure 1 shows the results of the wavelet analysis carried out for variations of GEC during the period of major SSWs, which took place in 2005 - 2018.



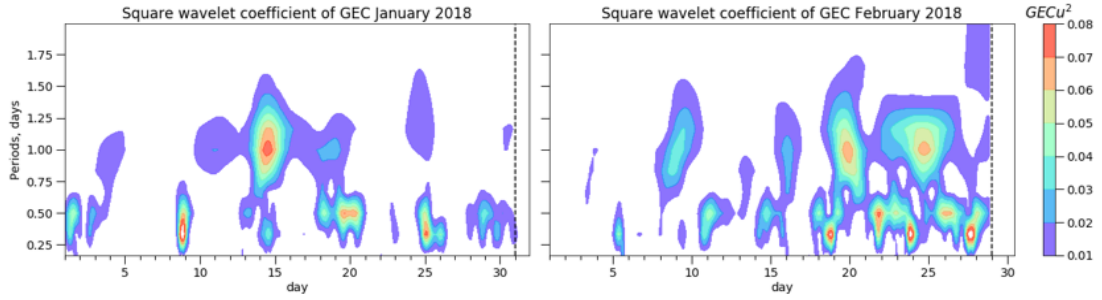


FIGURE 1. Square of wavelet coefficients ($GECu^2$), for GEC variations during SSW events 2005-2018. Dashed lines mark start and end of SSW events.

As can be seen, there is a tendency to increase the amplitude of semidiurnal waves and decrease the amplitude of diurnal oscillations of GEC during SSW event. This phenomenon is especially clear during the SSW event in 2009, which was an extremely quiet in terms of solar and geomagnetic activities. This trend is less pronounced in 2005 and 2010, and is practically absent in 2008 and 2018. We suppose the noted trends may be related to the changes in the mesosphere-thermosphere tides structure during SSW events. This phenomenon has been noted repeatedly both in observations and in numerical experiments on atmospheric models, but in the behavior of the mesosphere and thermosphere parameters.

In [6], the tides behavior during SSW-2009 was studied analyzing thermosphere parameters using EAGLE model. In this investigation we considered the spectrum of variations in global electron content obtained from the results of EAGLE calculations and observational data for January 2009 (Fig. 2).

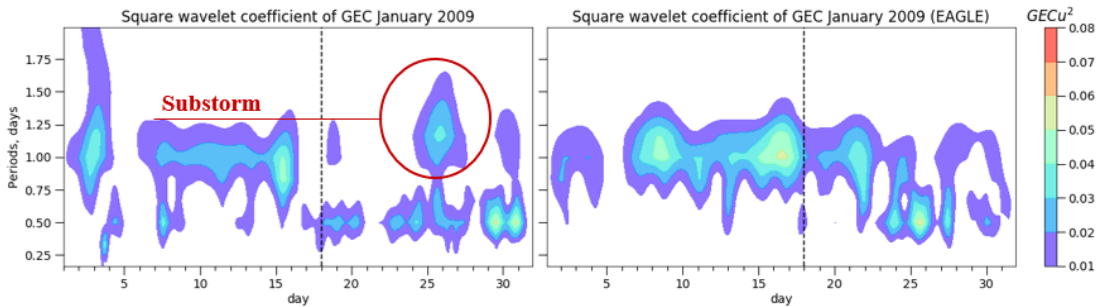


FIGURE 2. The square of wavelet coefficients for GEC calculated from observational data (left) and EAGLE model simulations (right) during stratospheric warming in 2009

As can be seen, model simulation results are in a good agreement with observations data. It is seen after the beginning of the warming; the weakening of diurnal fluctuations occurs simultaneously with an increase in semidiurnal variations for the case with observed GEC. The same thing happens with a model GEC, but with a delay of about 7 days. Also, in the spectrum according to the observational data, there is a small peak in the diurnal fluctuations on January 25th. This peak coincides in time with a small substorm. The peak is absent in the model data, since in our simulations was not taken into account changing in the geomagnetic condition during SSW event.

Conclusion. Analyzing the variations of the Global Electron Content during the major SSW events in 2005 - 2018, we found out tendency intensification of 12-h and weakening of 24-h oscillations the in most cases. An identical analysis of the EAGLE simulation data for the SSW-2009 event showed a similar behavior of the GEC spectrum. This tendency may be related to the changes in the mesosphere-thermosphere tides structure during SSW events.

This phenomenon has been noted repeatedly both in observations and in numerical experiments on atmospheric models, but in the mesosphere and thermosphere parameters variations.

This work was supported by the grant of the Russian Science Foundation No. 17-17-01060.

1. E. L. Afraimovich, E. I. Astafyeva, I. V. Zhivetiev. Solar activity and global electron content, *Doklady Earth Sciences*, 2006, 409A, N 6, pp. 921–924.
2. Y. Harada, K. Sato, T. Kinoshita, R. Yasui, T. Hirooka, H. Naoe. Diagnostics of a WN2-Type Major Sudden Stratospheric Warming Event in February 2018 Using a New Three-Dimensional Wave Activity Flux, *J. Geophys. Res(A)*, 2019, 124(12), pp. 6120–6142.
3. F. M. Palmeiro, D. Barriopedro, R. García-Herrera, N. Calvo, Comparing sudden stratospheric warming definitions in reanalysis data, *Journal of Climate*, 2015, 28(17), pp. 6823–6840, <https://doi.org/10.1175/JCLI-D-15-0004.1>
4. H. Jin, Y. Miyoshi, D. Pancheva, P. Mukhtarov, H. Fujiwara, H. Shinagawa, Response of migrating tides to the stratospheric sudden warming in 2009 and their effects on the ionosphere studied by a whole atmosphere-ionosphere model GAIA with COSMIC and TIMED/SABER observations, *Journal of Geophysical Research (Space Physics)*, 117, doi: 10.1029/2012JA017650.
5. A.V. Timchenko, F.S. Bessarab, Y. N. Korenkov, O. P. Borchevkina, K. G. Ratovskiy, Studying the ionospheric response to Sudden Stratospheric Warming (SSW), using data from mid-latitude stations, *BSFP-2019, Irkutsk*, 2019, pp. 219–222, (in Russian).
6. P.A. Vasiliev, F.S. Bessarab, I.V. Karpov, V.V. Klimenko, M.V. Klimenko, T.V. Sukhodolov, E.V. Rozanov Tidal and Planetary Waves in the Lower Thermosphere and Ionosphere Simulated with the EAGLE Model for the January 2009 Sudden Stratospheric Warming Conditions, *Izvestiya. Atmospheric and Oceanic Physics*, 2019, 55(2), pp. 178–187, doi:10.31857/S0002-351555241-50.

NEUTRAL WIND AZIMUTH ESTIMATING BY STATISTIC OF TIDS 2D PROPAGATION PARAMETERS

Maxim V. Tolstikov¹, Alexey V. Oinats¹, Irina V. Medvedeva¹, Nozomu Nishitani²

¹*Institute of Solar-Terrestrial Physics, Irkutsk, Russia*

²*Institute for Space-Earth Environmental Research, Nagoya University, Japan*

Introduction. Interaction of internal gravity waves (IGW) with a neutral wind has been studied for a long time. In [1] both the Irkutsk incoherent scattering radar and the EKB HF radar data were used to reveal significant anisotropy of TIDs occurrence and average horizontal velocities depending on the propagation direction. Observed effect is well explained by wind filtration. We have tested wind-filtering hypothesis by using representative TIDs statistics obtained by the Hokaido East SuperDARN radar during 2007–2014. Amplitudes of downwind propagating IGWs greatly decrease due to dissipation, and the amplitudes of upwind propagating IGWs increase. Therefore, if most TIDs are manifestation of IGWs, then maxima of TIDs distributions in times of day and azimuth should coincide with directions opposite to the strongest and most frequent wind propagation for a given season and diurnal time.

Figure 1 shows distribution of TIDs occurrence in time-azimuth plane (by color) and distributions of neutral wind projections (gray contours are the negative wind projections) for different seasons. Neutral wind was calculated using HWM2007 model. Hereinafter, the occurrence is a number of TIDs propagating in a given direction for a given time divided by a full number of TIDs observed for a given time. It should be noted that the radar operates at a frequency of ~11 MHz. This leads to the absence of ground backscatter registration during winter nighttime due to low background electron density. As can be seen from Figure 1, the vast majority of disturbances occur in the region of negative neutral wind

projections (black contours). Thus, we can assume that most of the observed TIDs are manifestations of IGWs. In [1-3] the average monthly diurnal neutral winds were obtained by using statistical data of TIDs 3-D propagation parameters and assuming that the Hines dispersion equation is satisfied. The Hokkaido East SuperDARN radar can obtain only TIDs 2-D propagation parameters (azimuth and apparent horizontal velocity). In this case using dispersion equation is impossible. The question arises whether it is possible to estimate the azimuth of neutral wind from representative statistics of TID 2-D propagation parameters?

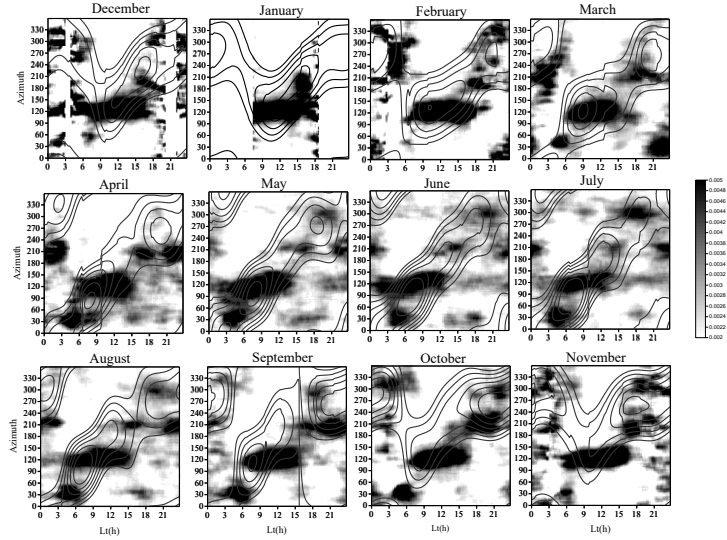
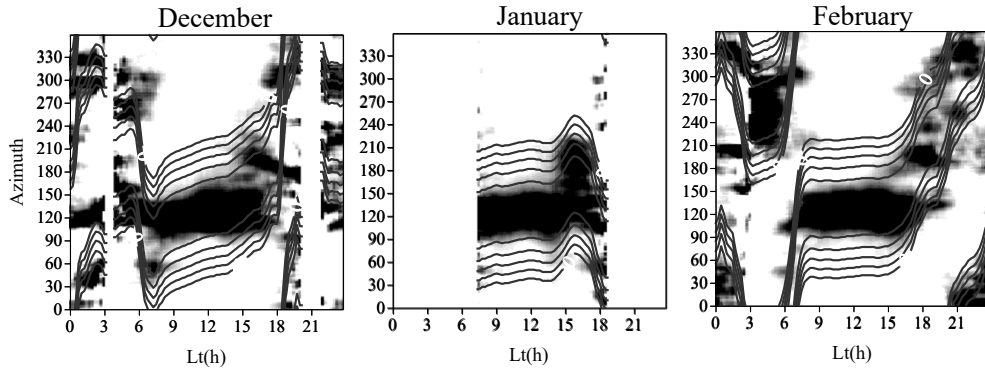


FIGURE 1. Distribution of TIDs occurrence in time- azimuth plane (by color) and distributions of neutral wind projections (by contours).

Method for Estimating Neutral Wind Azimuth. Let's try to solve the problem inverse to testing of wind-filtering hypothesis. For each time moment, for each possible wind azimuth ($0^\circ-359^\circ$) we will consider how many disturbances occur in the regions of negative wind projection, and how many disturbances occur in the regions of positive wind projection. The optimized function looks like this:

$$I(t, \alpha) = - \sum_{\varphi=0}^{\varphi=359} N(t, \varphi) \cos(\alpha\varphi) \rightarrow \max \quad (1)$$

In (1) N is number of TIDs propagating at time t with azimuth φ , $\alpha\varphi$ is angle between φ and α . The angle α providing the maximum of the function $I(t, \alpha)$ is considered as neutral wind azimuth at time t . Below are the calculations results.



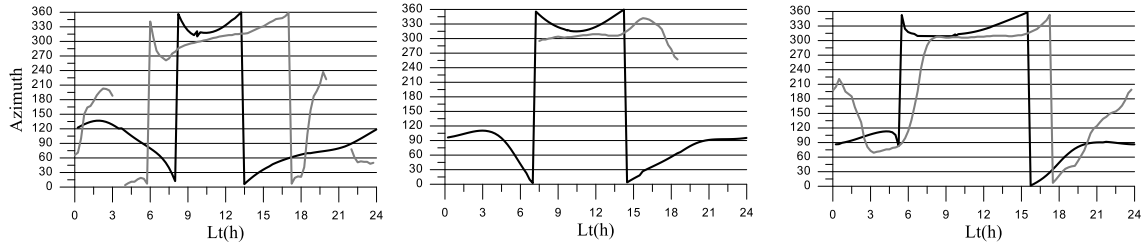


FIGURE 2. Winter season. The left side: TIDs distribution (color) and distributions of neutral wind (calculated azimuth) projections (gray contours are the negative wind projections). The right side: the black line is neutral wind azimuth (HWM2007), and gray line is calculated azimuth.

As can be seen from Figure 2, in the daytime the calculated azimuth and HWM2007 model are in good agreement. As noted earlier the nighttime echoes are almost absent during winter season. Nevertheless, in February the calculated azimuth fits the model well even at night.

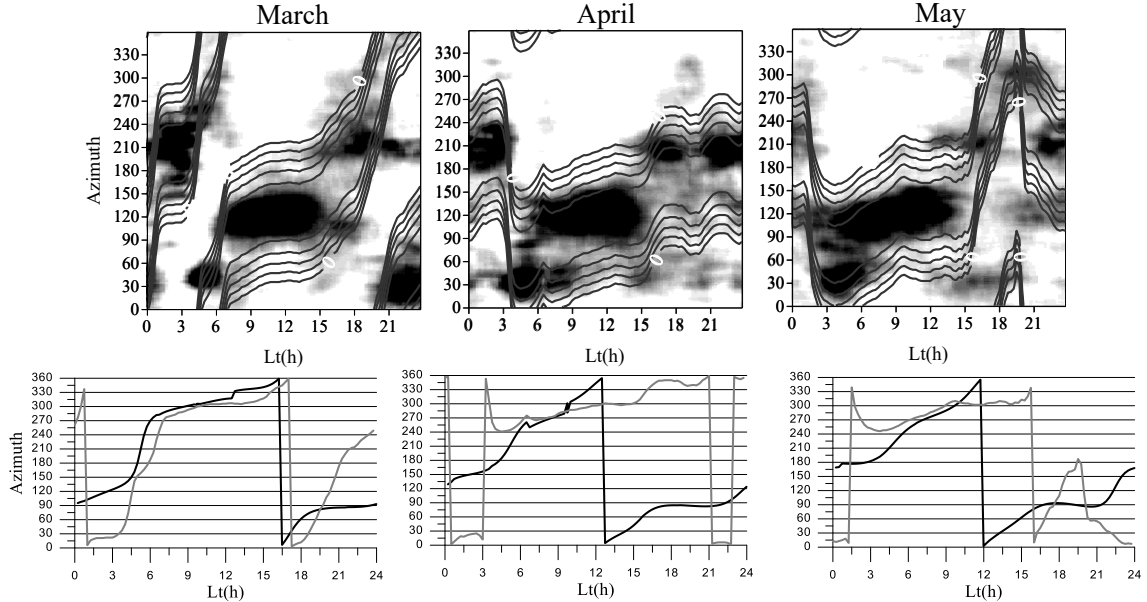


FIGURE 3. Spring season. The left side: TIDs distribution (color) and distributions of neutral wind (calculated azimuth) projections (gray contours are the negative wind projections). The right side: the black line is neutral wind azimuth (HWM2007), and gray line is calculated azimuth.

As can be seen from Figure 3, the calculated wind azimuth generally corresponds to the HWM2007 model (especially good in March), except for midnight hours. As can be seen from the TIDs distributions in time and azimuth, there are maxima about 210° in the midnight hours. This maxima leads to obtaining north azimuth instead of the south and east azimuths. Further we discuss the possible causes of such situations.

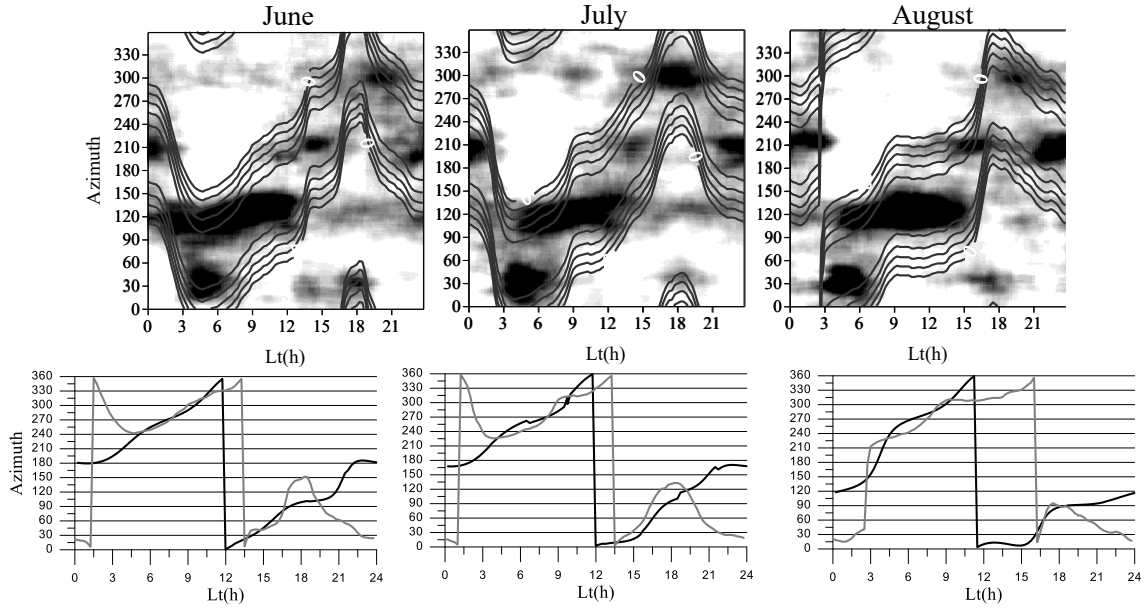


FIGURE 4. Summer season. The left side: TIDs distribution (color) and distributions of neutral wind (calculated azimuth) projections (gray contours are the negative wind projections). The right side: the black line is neutral wind azimuth(HWM2007), and gray line is calculated azimuth.

For summer season the calculated azimuth again fits well with the HWM2007 model, except for the midnight hours. As can be seen from Figure 4 there is stable maximum of about 210° around midnight hours for all months.

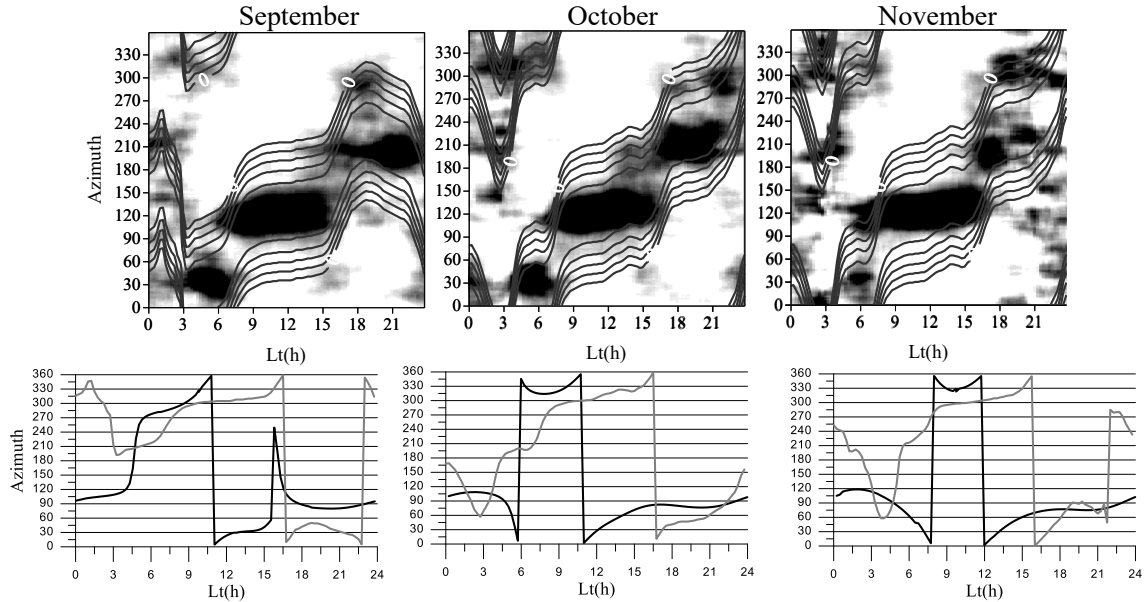


FIGURE 5. Autumn season. The left side: TIDs distribution (color) and distributions of neutral wind (calculated azimuth) projections (gray contours are the negative wind projections). The right side: the black line is neutral wind azimuth(HWM2007), and the gray line is calculated azimuth.

As can be seen from Figure 5, the calculated wind azimuth generally corresponds to the HWM2007 model. However, according to the HWM2007 model in October and November, the wind azimuth is

already being changed to the winter mode, whereas calculated wind azimuth is similar to the September azimuth. For the first time in October (with the exception of the winter season), we do not observe a maximum of about 210° at midnight and the calculated azimuth corresponds to HWM2007. There is a surprisingly stable maximum of about 210° in the TIDs distribution in time and azimuth for all months around midnight (except for October and the winter season). This maximum does not correspond to the wind pattern according to HWM2007. We can assume the following reasons for this phenomenon: some data processing artifact, presence of TIDs not corresponding to IGW (for example, various instabilities), or wind behavior features not described by HWM2007. We can exclude data processing artifact, because of other researches using other techniques also observed such TIDs at these hours. Shiokawa et al. [4] presented a statistical study of TIDs using mid-latitude 630-nm airglow images and reported that most of the observed TIDs propagate southwestward during all seasons. Similar results were obtained from GPS TEC maps [5,6]. The authors assume that these TIDs are not manifestations of IGWs.

The reported study was funded by RFBR, project number 19-05-00889 and project number 20-05-00212. For the analysis, the methods obtained with budgetary funding of Basic Research program II.12 were used.

1. A.V. Medvedev, K.G. Ratovsky, M.V. Tolstikov, A.V. Oinats, S.S. Alsatkin, G.A. Zhrebtsov, Relation of internal gravity wave anisotropy with neutral wind characteristics in the upper atmosphere, *J. Geophys. Res.*, 2017, 122(7), pp. 7567–7580, doi: 10.1002/2017JA024103.
2. A.V. Medvedev, K.G. Ratovsky, M.V. Tolstikov, S.S. Alsatkin, A.A. Scherbakov, A statistical study of internal gravity wave characteristics using the combined Irkutsk Incoherent Scatter Radar and Digisonde data, *Journal of Atmospheric and Solar-Terrestrial Physics*, 2015, 132, pp. 13–21, doi: 10.1016/j.jastp.2015.06.012.
3. A.V. Medvedev, K.G. Ratovsky, M.V. Tolstikov, R.V. Vasilyev, M.F. Artamonov, Method for Determining Neutral Wind Velocity Vectors Using Measurements of Internal Gravity Wave Group and Phase Velocities, *Atmosphere*, 2019, 10(9), pp. 546, doi: 10.3390/atmos10090546.
4. K. Shiokawa, C. Ihara, Y. Otsuka, T. Ogawa, Statistical study of nighttime medium-scale traveling ionospheric disturbances using midlatitude airglow images, *J Geophys Res*, 2003, 108(A1), pp. 1052. doi:10.1029/2002JA009491.
5. Y. Otsuka, N. Kotake, K. Shiokawa, T. Ogawa, T. Tsugawa, A. Saito, Statistical Study of Medium-Scale Traveling Ionospheric Disturbances Observed with a GPS Receiver Network in Japan, In: *Abdu M. Pancheva D, Bhattacharyya A (eds) Aeronomy of the Earth's Atmosphere and Ionosphere*, Springer Netherlands, Dordrecht, 2011.
6. N. Kotake, Y. Otsuka, T. Ogawa, T. Tsugawa, A. Saito, Statistical study of medium-scale traveling ionospheric disturbances observed with the GPS networks in Southern California, *Earth Planets Space*, 2007, 59, pp. 95–102.

IMPACT OF ATMOSPHERIC WAVES ON THE HIGH-LATITUDE IONOSPHERE DURING LAUNCHES FROM THE VOSTOCHNY COSMODROME

Natalia P. Perevalova¹, Geliy A. Zhrebtsov¹, Mikhail A. Serov², and Vladimir S. Zhizherin²

¹*Institute of Solar-Terrestrial Physics SB RAS, Irkutsk, Lermontov st., 126a, Russia*

²*Institute of Geology and Nature Management FEB RAS, Blagoveshchensk, Relochii st., 1, Russia*

On 28 April 2016, the first spacecraft launch was successfully performed from the Vostochny cosmodrome (<http://www.roscosmos.ru>). Vostochny is the new Russian spaceport located in the Far East. The first results of detecting ionospheric disturbances during the 28 April 2016 launch from Vostochny were obtained in [1]. The paper showed that despite the small number of GPS/GLONASS

stations located near Vostochny, these stations assure detection of the ionospheric responses to launches in any direction from the spaceport and allow for estimating the launch vehicle (LV) moving direction.

Five launches were performed from Vostochny in 2016-2019: 28 April 2016 at 02:01 UT (<https://www.roscosmos.ru/22116/>); 28 November 2017 at 05:41 UT (<https://www.roscosmos.ru/24383/>); 1 February 2018 at 02:07 UT (<https://www.roscosmos.ru/24526/>); 27 December 2018 at 02:07 UT (<https://www.roscosmos.ru/25863/>); 5 July 2019 at 05:41 UT (<https://www.roscosmos.ru/26335/>).

Using data of Global Navigation Satellite Systems (GNSS), namely GPS and GLOGNASS, we studied the disturbances generated by atmospheric waves in the ionosphere during these launches. We utilized data from GNSS receivers of the IGS International Network (<http://sopac.ucsd.edu>) as well as from GNSS receivers of the Institute of Geology and Nature Management FEB RAS (IGNM FEB RAS). IGNM FEB RAS receivers are located in close proximity to Vostochny and provide registration of the ionospheric disturbances at short distances from the launch pad. To study ionospheric disturbances, total electron content (TEC) variations were calculated based on GNSS carrier phase measurements at two frequencies.

Various types of waves (shock acoustic waves, acoustic gravity waves) are generated in the atmosphere by LV motion. A significant part of wave energy is concentrated in a shock acoustic wave (SAW). A SAW is caused by LV supersonic motion in the upper atmosphere, is observed first and, as a rule, is the most powerful in the spectrum of waves formed during the launch. Ionospheric responses to SAWs generated during launches from different spaceports, were observed repeatedly [1-8]. However, virtually all the results obtained so far refer to the launch impacts on the mid-latitude and equatorial ionosphere. This is due to the fact that the most spaceports are located at equatorial and middle latitudes. Vostochny is also located at middle latitudes. But trajectories of the first launches mostly passed through high latitudes. This allowed us to analyze the effects of atmospheric SAWs on the subauroral ionosphere and to compare spatio-temporal characteristics of wave TEC disturbances caused by launches in the subauroral and mid-latitude ionosphere. As a rule, at high-latitude GNSS stations, behavior of ionospheric TEC shows greater variability than at mid-latitude stations. Nevertheless, our study shows that the subauroral ionospheric response to atmospheric SAW is clearly detected in data from high-latitude GNSS stations.

During all launches, SAW-generated TEC disturbances were registered. TEC disturbances had the shape of a single pulse that corresponded to the SAW shape. The average period and average amplitude of TEC disturbances were 3-6 min and 0.1-0.18 TECU respectively. The proximity of ascent trajectories (all spacecraft were put into orbits with inclinations $i \sim 98^\circ$) during first launches from Vostochny determined the similarity of spatial distributions of SAW-generated TEC disturbances caused by these launches. Detection of SAW-generated TEC disturbances began 7-15 min after the liftoff, at the distances about 810-2000 km from the launch pad. The disturbances were observed mainly in the north-west direction from Vostochny along the $i \sim 98^\circ$ ascent trajectory [9]. Analysis of TEC disturbance spatio-temporal dynamics indicated that the disturbance wave propagated away from the LV trajectory.

It turned out that the shape, period and amplitude of SAW-generated TEC disturbances in the subauroral ionosphere during launches from Vostochny were close to parameters (amplitude 0.01-0.5 TECU, periods 2-20 min) of similar disturbances observed earlier in the mid-latitude and equatorial ionosphere during a large number of launches from different spaceports (Baikonur, Kennedy Space Center, Vandenberg, Jiuquan, Tongchangri, etc. [2-8]). In general, spatial-temporal distribution and propagation direction of SAW-generated TEC disturbances after launches from Vostochny also agree with the results obtained for other spaceports. According to [2-8], detection of SAW-generated TEC disturbances began 4-8 min after the liftoff at the distances about 200-1000 km from the launch pad. This corresponds to theoretical model: a SAW is formed during LV supersonic motion at the heights of 100-130 km and at the distance more than 200 km from the launch pad [2-8].

The authors thank the Scripps Orbit and Permanent Array Center (SOPAC, <http://sopac.ucsd.edu>) for providing data from the international network of GNSS receivers. This study was supported by the Grant of the Russian Science Foundation (Project No 18-17-00042). The data of GNSS receivers operated by IGM FEB RAS were obtained with the support of the FEB RAS comprehensive program for basic scientific research "Far East" (№18-5-024).

1. G. A. Zherebtsov, N. P. Perevalova, Ionospheric Response to a Rocket Launch from the Vostochny Cosmodrome, *Doklady Earth Sciences*, 2016, 471(2), pp. 1280-1283, doi:10.1134/S1028334X16120151.
2. E. Calais, J. B. Minster, GPS detection of ionospheric perturbations following a Space Shuttle ascent, *Geophys. Res. Lett.*, 23, 1996, pp. 1897-1900, doi:10.1029/96GL01256.
3. E. L. Afraimovich, E. A. Kosogorov, K. S. Palamartchouk, N. P. Perevalova, A. V. Plotnikov, The use of GPS arrays in detecting the ionospheric response during rocket launchings, *Earth, Planets, and Space*, 2000, 52(11), pp. 1061-1066, doi:10.1186/BF03352331.
4. Y. Kakinami, M. Yamamoto, C. H. Chen et al., Ionospheric disturbances induced by a missile launched from North Korea on 12 December 2012, *J. Geophys. Res. Space. Phys.*, 2013, 118, pp. 1-6, doi:10.1002/jgra.50508.
5. F. Ding, W. Wan, T. Mao et al., Ionospheric response to the shock and acoustic waves excited by the launch of the Shenzhou 10 spacecraft, *Geophys. Res. Lett.*, 2014, 41, pp. 3351-3358, doi:10.1002/2014GL060107.
6. C. H. Lin, J. T. Lin, C. H. Chen et al., Ionospheric shock waves triggered by rockets, *Ann. Geophys.*, 2014, 32, pp. 1145-1152, doi:10.5194/angeo-32-1145-2014.
7. C. H. Lin, M.-H. Shen, M.-Y. Chou et al., Concentric traveling ionospheric disturbances triggered by the launch of a SpaceX Falcon 9 rocket, *Geophys. Res. Lett.*, 2017, 44, pp. 7578-7586, doi:10.1002/2017GL074192.
8. M.-Y. Chou, M.-H. Shen, C. C. H. Lin et al., Gigantic circular shock acoustic waves in the ionosphere triggered by the launch of FORMOSAT-5 satellite, *Space Weather*, 2018, 16, pp. 172-184, doi:10.1002/2017SW001738.
9. I. A. Komarov, A. G. Milovanov, K. V. Chmarov, Vostochny launch site - the future of Russian spaceflight, *Space Engineering and Technology magazine*, 2015, 3(10), pp. 3-14. (in Russian).

ESTIMATION OF THE ION COMPOSITION OF THE OUTER IONOSPHERE FROM THE CHARACTERISTICS OF ELF-VLF WAVES

Alexander O. Ryabov

Lobachevsky State University of Nizhny Novgorod, Nizhny Novgorod, Russia

Introduction. Ionosphere heating by a powerful short-wavelength radiation of ground-based facilities is an efficient method allowing one to perform systematic studies of the near-Earth plasma with controllable action parameters. The action of a powerful short-wavelength radiation on the F-region of the ionosphere can produce considerable perturbations in both the reflection region of the pumping wave and the entire volume of the ionosphere. In [1], the results of observations of artificial plasma perturbations produced by the *Sura* heating facility were presented. The observations were performed using the onboard equipment of the *DEMETER* French microsatellite [2]. In particular, in a series of *Sura-DEMETER* full-scale experiments, generation of ELF-VLF radio waves in the perturbed region of the ionosphere was revealed. In this work, it is proposed to study specific features of the observed radio waves by means of the singular value decomposition (SVD) method. This method has an advantage of geometric visualization and can be conveniently used to solve various problems. In particular, it allows one to determine the propagation characteristics of electromagnetic waves excited by a powerful short-wavelength radiation. A method for estimating the ion composition at altitudes

corresponding to the outer ionosphere from the characteristics of the observed ELF–VLF radio waves is proposed.

Conditions and results of the experiments.

We use the results obtained with the onboard equipment of the *DEMETER*

French microsatellite with an orbital height of about 660 km. The *Sura* heating facility is located to the east of Nizhny Novgorod (56.15° N, 46.1° E). The effective radiation power of the facility monotonically increases with increasing frequency f_r : from 80 MW at $f_r = 4300$ kHz to 280 MW at $f_r = 9300$ kHz. The data obtained in the experiment carried out on August 27, 2009 in the evening were used. Planetary geomagnetic activity index was $Kp = 3$.

Figure 1 shows the spectrogram of wave perturbations of the magnetic field during the session of August 27, 2009. In this spectrogram, one can observe

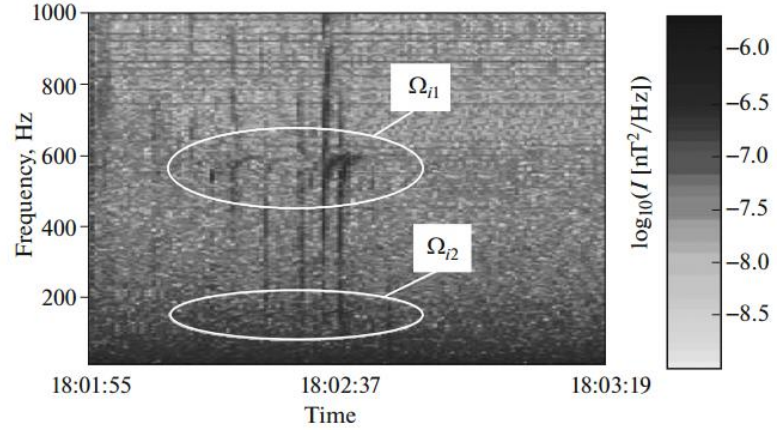


FIGURE 1. Spectrogram of wave perturbations of the magnetic field for the session of August 27, 2009. The spectral density I of magnetic field perturbations is shown by shades of gray.

typical curves having singularities in the form of bends at frequencies on the order of the proton gyrofrequency (600 Hz) and helium ion gyrofrequency (150 Hz).

Method for determining the ion composition. After a number of mathematical operations, which are described in the paper [3], we get the expressions:

$$\theta = \arctan(\sqrt{k_1^2 + k_2^2} / k_3),$$

$$\phi = \arctan(k_2 / k_1), \quad k_1 \geq 0,$$

$$\phi = \arctan(k_2 / k_1) - \pi, \quad k_1 < 0, \quad k_2 < 0,$$

$$\phi = \arctan(k_2 / k_1) + \pi, \quad k_1 < 0, \quad k_2 \geq 0,$$

where θ is the polar angle varying from 0° to 90° in the coordinate system associated with the geomagnetic field and ϕ is the azimuthal angle varying from -180° to 180°.

In the upper panel of Fig. 2, the vertical lines in the spectrograms correspond to almost constant values of the polar angle (deviations do not exceed 10°) and azimuthal angle (deviations do not exceed 20°). The bends of the spectral characteristics are accompanied by a change in the polar angle by 35° – 45° and an abrupt change in the azimuthal angle (up to 90°). Note that the bends themselves also have variations in angles (about 20°). The singularities (bends) of the dispersion curves indicate the possibility of energy exchange between the characteristic waves (fast magnetoacoustic wave and ion-cyclotron wave) at a certain frequency, called the crossover frequency. The onboard equipment of the *DEMETER* satellite did not provide a sufficient accuracy required to analyze similar spectral characteristics at frequencies close to the helium ion gyrofrequency (150 Hz). The results of the session of August 27, 2009 were corroborated by similar results from other sessions.

As follows from Fig. 2, the crossover frequency corresponds to the quasi-longitudinal propagation of waves along the geomagnetic field (about 9° between the wave vector and the direction of the geomagnetic field).

For wave normals close to the direction of the magnetic field, the polarization and refractive indices of two characteristic waves are almost the same in the region where and one propagating wave excites another one. It is necessary to take into account that there are several ion species with different masses in and, therefore, different gyrofrequencies in the ionospheric plasma.

The most abundant ion species in the ionospheric plasma are H^+ , He^+ and O^+ ions with densities n_1 , n_2 , n_3 and masses m_1 , m_2 , m_3 .

For these ions, the quasineutrality condition $n_1 + n_2 + n_3 = n_e$, where n_e is the electron density, should be satisfied.

Let us introduce the parameters:
$$X_1 = \frac{n_1 e^2}{\epsilon_0 m_1 \omega^2} = \frac{n_1}{n_e} \cdot \frac{m_e}{m_1} X_e = \frac{N_1}{M_1} X_e$$

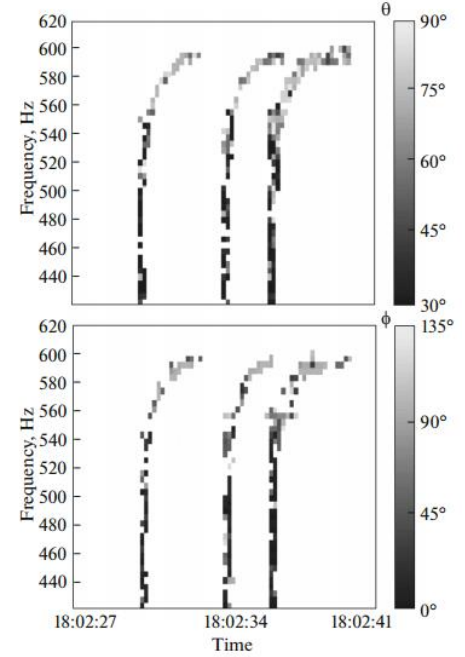


FIGURE 2. Characteristics of plasma wave perturbations in the ionosphere: frequency–time dependences of the polar (on top) and azimuthal (on bottom) angles.

for hydrogen ions, where $N_1 = \frac{n_1}{n_e}$, $M_1 = \frac{m_1}{m_e}$, and similar parameters for helium and oxygen ions. We

also introduce the notation $Y = \frac{\Omega}{\omega}$ according to which we have $Y_1 = Y_e / M_1$, $Y_2 = Y_e / M_2$, $Y_3 = Y_e / M_3$. After a number of mathematical operations, which are described in the paper [3], we get the expressions:

$$\begin{cases} \frac{N_1}{\alpha_1^2 - 1} + \frac{N_2}{\alpha_1^2 - 16} + \frac{N_3}{\alpha_1^2 - 256} = \frac{1}{\alpha_1^2}, \\ \frac{N_1}{16\alpha_2^2 - 1} + \frac{N_2}{16\alpha_2^2 - 16} + \frac{N_3}{16\alpha_2^2 - 256} = \frac{1}{16\alpha_2^2}, \\ N_1 + N_2 + N_3 = 1 \end{cases} \quad (1)$$

where $\alpha_1 = \frac{\Omega_{i1}}{\omega_{co1}}$, $\alpha_2 = \frac{\Omega_{i2}}{\omega_{co2}}$; Ω_{i1} , Ω_{i2} are the

hydrogen and helium ion gyrofrequencies, respectively; and ω_{co1} , ω_{co2} are the crossover frequencies. From system (1), knowing the gyrofrequencies and crossover frequencies, we can determine the ion composition of the medium. Using the data of the session of August 27, 2009 (Fig. 1), we find the ion gyrofrequencies and crossover frequencies.

The cutoff frequency for the upper bend corresponds to the gyrofrequency of hydrogen ions ($\Omega_{i1} = 600$ Hz). The frequency at which the vertical line begins to bend corresponds to the crossover frequency ($\omega_{co1} = 570$ Hz).

In a similar way, for the lower bend, we obtain $\Omega_{i2} = 150$ Hz and $\omega_{co2} = 138$ Hz. Substituting these values into system of equations (1), we obtain the relative contents of the ion species for three time instants: (1) $N_1 = 0.19$, $N_2 = 0.20$, and $N_3 = 0.61$ for 18:02:30; (2) $N_1 = 0.22$, $N_2 = 0.20$, and $N_3 = 0.58$ for 18:02:34; (3) $N_1 = 0.13$, $N_2 = 0.15$, and $N_3 = 0.72$ for 18:02:37. Figure 3 presents data on the concentrations of the main ion species obtained using the onboard equipment of the *DEMETER* satellite (vertical lines 1, 2 and 3 correspond to the times 18:02:30, 18:02:34, and 18:02:37).

The numerals show the absolute values of the ion densities in cm^{-3} . The results obtained by the above method agree well with experimental data (the discrepancy is about 7%). Thus, the described method allows one to sufficiently accurately determine the ion composition at altitudes of the Earth's outer ionosphere. Possible errors can be related to the inaccuracy of the input data, the choice of the three-component model (hydrogen, helium, and oxygen ions), and the use of the expression for the refractive index of quasilongitudinally propagating waves.

The work is supported by a grant from the Ministry of science and higher education of the Russian Federation, received in the framework of the Federal target program "Research and development on priority directions of development of the scientific and technological complex of Russia on 2014-2020". Unique identifier of the project RFMEFI62020X0003. Agreement number 075-15-2020-529.

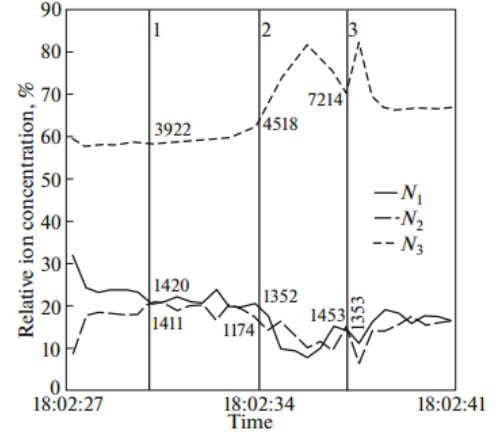


FIGURE 3. Time evolution of the relative concentrations of hydrogen (N_1), helium (N_2), and oxygen (N_3) ions.

1. V.O. Rapoport, V.L. Frolov, S.V. Polyakov, G.P. Komrakov, N.A. Ryzhov, G.A. Markov, A.S. Belov, M. Parrot, J.-L. Rauch, VLF electromagnetic field structures in ionosphere disturbed by Sura RF heating facility, *J. Geophys. Res.*, 2010, 115(A10), doi: 10.1029/2010JA015484.
2. M. Parrot, Special issue of Planetary and Space Science ‘DEMETER’, *Planet. Space Sci.*, 2006, 54(5), pp. 411–412, doi: 10.1016/j.pss.2005.10.012.
3. A.O. Ryabov, Determination of the Ion Composition of the Outer Ionosphere from the Characteristics of ELF–VLF Waves Detected during the Operation of the Sura Facility, *Plasma Physics Reports*, 2018, 44(12), pp. 1140–1145, doi: 10.1134/S1063780X1809012X.

SEARCHING OF IONOSPHERIC WAVEGUIDED PROPAGATION OF RADIO RAYS BY A DIRECT VARIATIONAL METHOD

Igor A. Nosikov¹, Maxim V. Klimenko¹, Daria S. Kotova¹ and Pavel F. Bessarab²

¹ West Department of Pushkov Institute of Terrestrial Magnetism, Ionosphere and Radio Wave Propagation of the Russian Academy of Sciences, Kaliningrad, Russia

² Science Institute of the University of Iceland, Reykjavik, Iceland

Introduction. As was shown in previous publications [1, 2], the direct variational method is an effective method for calculating ray paths when the endpoints are known and fixed. It was shown that direct optimization identifies the high and low rays, which correspond to the minima and first order saddle points consequently. At the same time, an important task is to expand the capabilities of the variational approach for determining the rays in the ionospheric waveguide that can form in a valley region between the E- and F- layers of the ionosphere.

Ionospheric Waveguide Radiowave Propagation. It is well known that the ray approximation is characterized by the presence of focal points and caustics. Our recent preliminary investigation shows that the number of caustic features is possibly related to the order of the saddle points. This situation is especially characteristic of multi-hop and waveguide propagation.

For the isotropic ionosphere, phase distance is given by the following line integral:

$$S = \int_A^B n(\vec{r}) dl, \quad (1)$$

Here, the integration is performed along the curve γ connecting the endpoints A and B , $n(\vec{r})$ is the refractive index at point \vec{r} , and dl is the length element along γ . A higher order saddle point can be determined by optimizing the phase path functional of the radio ray under the control of an artificial force $\tilde{\mathbf{F}}$:

$$\tilde{\mathbf{F}} = \begin{cases} \mathbf{F} - \sum_{j=0}^M 2(\mathbf{F} \cdot \mathbf{Q}_\lambda^j) \mathbf{Q}_\lambda^j, & \text{if } \lambda_M < 0 \\ - \sum_{j=0}^M 2(\mathbf{F} \cdot \mathbf{Q}_\lambda^j) \mathbf{Q}_\lambda^j, & \text{if } \lambda_M \geq 0 \end{cases} \quad (2)$$

Where

$$\mathbf{F} = -\nabla S.$$

Here S is functional of the ray path, λ_j is the negative eigenvalue of the Hessian and \mathbf{Q}_λ^j is the corresponding normalized eigenvector, M is the number of the negative eigenvalues.

Let us consider the example of waveguide propagation in the ionosphere with local inhomogeneity. The electron density of the two-layer ionospheric model is described by the analytic function [3]:

$$N(\vec{r}) = N_0 \left\{ \exp \frac{1}{2} \left[1 - \left(\frac{z - z_{01}}{z_{m1}} \right) - \exp \left(- \left(\frac{z - z_{01}}{z_{m1}} \right) \right) \right] + \beta \cdot \exp \left[- \left(\frac{z - z_{01}}{z_{m2}} \right)^2 \right] \right\}, \quad (3)$$

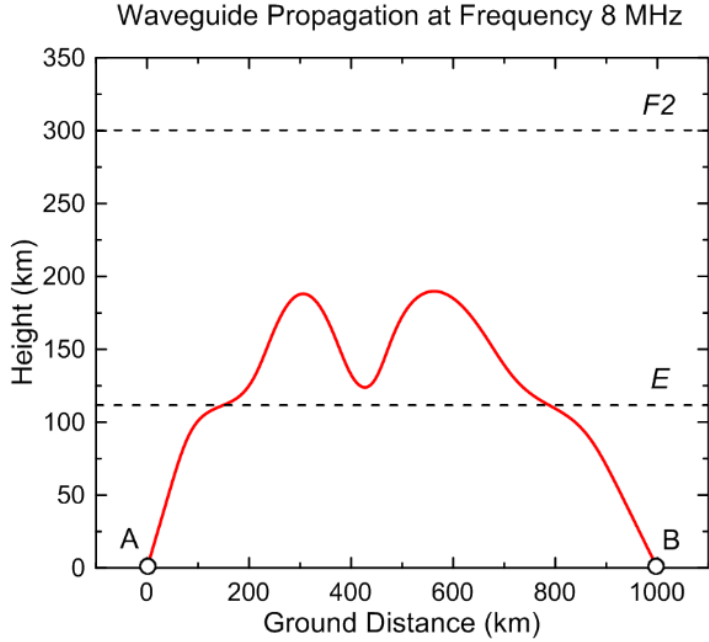


FIGURE 1. Simulation of the two-point ray tracing in the two-layer ionosphere with local inhomogeneity defined by (4). Operating frequency is 8 MHz. Red line shows the waveguide ray.

where N_0 is maximum of F2 layer electron density; z_{01} is F2 layer peak height; z_{m1} is half-thickness of the layer; β is coefficient of proportionality of F2 and E layers; z_{02} is E layer peak height; z_{m2} is half-thickness of the E layer. Simulation of two-layer ionosphere was given by setting the parameters: $N_0 = 1 \cdot 10^6 \text{ cm}^{-3}$, $z_{01} = 300 \text{ km}$, $z_{m1} = 150 \text{ km}$, $\beta = 0.6$, $z_{02} = 110 \text{ km}$, $z_{m2} = 30 \text{ km}$.

The resulting electron density distribution is given by the following formula:

$$\tilde{N}(\vec{r}) = N(\vec{r}) \left(1 - \exp \left(\frac{(\vec{r} - \vec{r}_d)^2}{\sigma^2} \right) \right), \quad (4)$$

where $\vec{r}_d = (500, 110) \text{ km}$ is the position center of the inhomogeneity and $\sigma = 100 \text{ km}$ is the parameter characterizing the size of the inhomogeneity.

The ray tracing was performed between the endpoints A and B fixed at $\vec{r}_A = (0, 0) \text{ km}$ and $\vec{r}_B = (1000, 0) \text{ km}$ and the radio wave frequency was chosen to be 8 MHz. In search of the waveguide ray, the initial path (straight line) was iteratively moved away from the convex region near the minimum to the region where more than one eigenvalues of the Hessian of functional are negative. Figure 1 illustrates the ray tracing using the higher order saddle point optimization. As a result, waveguide ray is found which corresponds to the third order saddle point.

Discussion. In this paper, we considered the problem of the identification of the waveguide ray. It can be accomplished by including additional negative modes in the optimization procedure that determine the higher-order saddle points. The proposed approach was applied to the search of waveguide radiowave propagation in a valley region between the E- and F- layers of the isotropic ionosphere.

Ray tracing simulation was performed (I. A. Nosikov, D. S. Kotova) with the financial support of the Grant of the President of Russian Federation for young scientists (MK- 2584.2019.5). Development of the variational approach for higher-order saddle point identification (M. V. Klimenko) was supported by the Russian Science Foundation (project №17-77-20009).

1. C. J. Coleman, Point-to-point Ionospheric Ray Tracing by a Direct Variational Method, *Radio Science*, 2011, 46(5), pp. RS5016, doi: 10.1029/2011RS004748.
2. Nosikov I.A., Klimenko M.V., Zhabankov G.A., Podlesnyi A.V., Ivanova V.A., Bessarab P.F., Generalized Force Approach to Point-to-Point Ionospheric Ray Tracing and Systematic Identification of High and Low Rays, *IEEE Trans. Antennas Propag.*, 2020, 68(1), pp. 455-467.

3. A. S. Kryukovskii, D. S. Lukin, and K. S. Kiryanova, Method of extended bicharacteristic system in simulating wave propagation in ionospheric plasma, *J. Commun. Technol. Electron.*, 2012, 57(9), pp. 1039–1045.

FABRY-PEROT INTERFEROMETER OBSERVATIONS OF MLT DURING SUDDEN STRATOSPHERIC WARMING'S FROM 2016 TO 2019 OVER SIBERIA

Olga S. Zorkaltseva^{1,2}, Roman V. Vasilyev^{1,2}

¹Department of Physic of Lower and Middle Atmosphere, Institute of Solar-Terrestrial Physics SB RAS, Irkutsk, Russia

²Department of Meteorology and Near-Earth Space Physics, Irkutsk State University, Irkutsk, Russia

Abstract. In this paper, we study the response of the MLT to sudden stratospheric warmings. We observe the variation of middle atmosphere by a unique Fabry-Perot interferometer (FPI), which has no analogues in Russia. FPI is located in the middle latitudes of Eastern Siberia in the geophysical observatory of the Institute of Solar-Terrestrial Physics SB RAS (Tory - 51.8N, 103.1E). Regular monitoring by interferometer starts in December 2016. We consider the FPI observations in the winter from 2016 to 2019 years; analyze the temporary variations in wind, temperature and tides before, during and after sudden stratospheric warmings. It turns out that sudden stratospheric warmings has a strong effect. Zonal winds reverse and amplitudetidesincrease in the middle atmosphere during major warmings in the stratosphere. Minor sudden stratospheric warmings have a similar (but much lower in intensity) effect in the MLT.

Introduction. The mesosphere-lower thermosphere (MLT) is defined as the region of the atmosphere between about 60 and 110 km in altitude. It constitutes the upper part of what is often referred to as the middle atmosphere (10 to 110 km) [1]. Long-term observations spanning few and more years of the MLT region are sparse, especially at Siberia region in the vicinity of the appearance and development sudden stratospheric warmings (SSW). Analysis of such observations is useful for understanding and predictive of global circulation and forecast middle and upper atmospheric models.

Earlier (1976–1996), in Eastern Siberia, the wind of MLT was monitored by method to receive signals from the separated radio reception of broadcasting stations in the long wavelength range [2]. According to study [2], over eastern Siberia, the wind at the heights of the MNT in calm conditions has western directions, during which it sharply weakens and changes direction to the east. It was shown that over site Badary (51 N, 105 E) during stratospheric warming, as a rule, the zonal wind at the heights of the MLT weakens or changes direction from west to east. There have been cases when changes in the amplitude and phase of the semidiurnal tide occurred in the south wind.

The monitoring of temperature regime in Siberia region provided by the hydroxyl emission spectral observations at geophysical station (Tory) Institute of Solar Terrestrial Physics [3,4]. It turned out, that the MLT heights a significant increase in the OH and O₂ emission intensities, a decrease in the atmosphere temperature, and an increase in wave activity were observed during SSW.

Data. The Fabry-Perot Interferometer (FPI) conducts regular spectrometric observations of the lines 557.7 nm, 630 nm and 843 nm, the natural glow of the night atmosphere. From the observations of the FPI, it is possible to restore the values of the total wind vector and temperature [5]. In our work, we used the line 557.7 nm, which corresponds to an altitude of about 90km. An FPI with a temporal resolution of about 10 minutes observes. The data were filtered for each 10 min UT mark using 13 day window by running average method over several months. The procedure allows filling the gaps in data and reducing amplitude of fast variations due to internal gravity waves and other short-time processes to focus on the variations continue several days and more.

We analyze the temperature of the stratosphere according to the data of modern climatic archive - ERA-interim [6].

Results. ERA-interim zonal mean temperature at 60N at 10 hPa were used to reveal the evolution of the SSW events. Figure 1 shows the evolution of the SSW event (solid line) and the FPI temperature, zonal and meridional wind (fill) from December 2016 to March 2017.

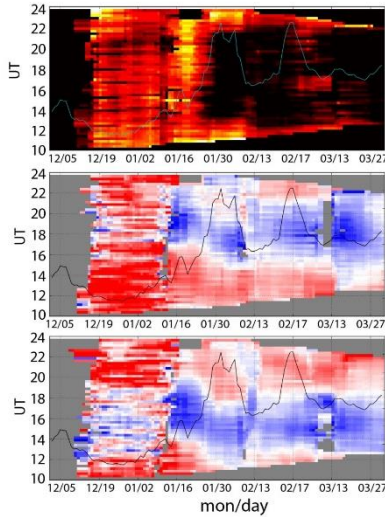


FIGURE 1. Top down: FPI temperature, zonal and meridional wind (fill). In each diagram, the solid line shows the ERA-interim zonal mean temperature at 60N at 10 from December 2016 to March 2017.

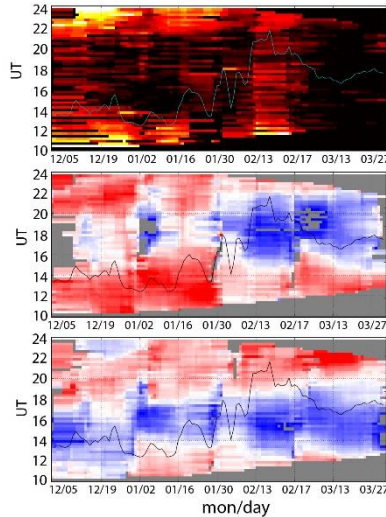


FIGURE 2. Same as figure1, but from November 2017 to March 2018.

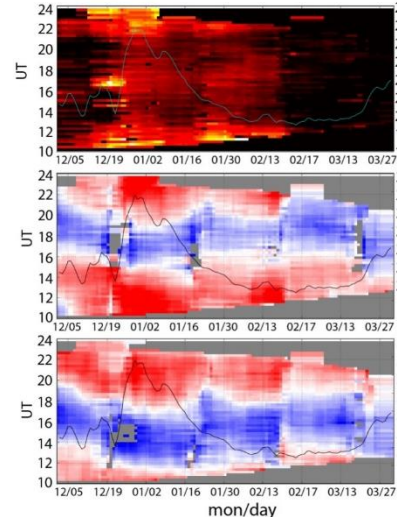


FIGURE 3. Same as figure1, but from November 2018 to March 2019.

Figure 1 shows that two SSW were observed, the first SSW was at the end of January, the second was at the end of February. We see that during SSW, the temperature in the MLT decreased and did not recover to normal winter values. In the behavior of the zonal wind, a reaction is seen on the SSW, namely, the zonal wind was east. We see in the meridional wind the deviation of the minimum values to earlier hours, this indicates a shift in the tidal phase in the meridional wind.

In the winter of 2017-2018, case of SSW was observed in early February and was continuous for about a month (figure 2). SSW in 2017-2018 caused the same effect from 2016-2017 in the zonal wind (reverse from west to east). But there has been an increase in MLT temperature. The meridional wind was more negative during SSW.

In the winter of 2018-2019, one case of SSW was also observed. But SSW occurred in the first half of winter and was also long from mid-December 2018 to mid-January 2019. We see in Figure 3 that the temperature in the MLT did not change significantly during the SSW. The zonal wind also reacted weakly to SSW. Only the meridional wind showed a noticeable reaction.

Figures 1-3 show conflicting results. We see that there is a reaction to SSW in MLT, but it differs from year to year. We hope that further FPI observations will allow us to accumulate more data and make reliable statistical estimates.

Acknowledgments. This work was supported by the Russian Science Foundation, project No. 19-77-00009. The measurements were carried out on the instrument of Center for Common Use «Angara» [<http://ckp-rf.ru/ckp/3056>].

1. J. Holton, G. Hakim, *An Introduction to Dynamic Meteorology*, 2012, V. 88, 552 P.
2. G.V. Vergasova, E.S. Kazimirovsky, External impact on wind in the mesosphere / lower thermosphere / *Solar-terrestrial physics*, 2009, 14, pp. 119–124. [In Russian.]
3. I.V. Medvedeva, A.I. Semenov, M.A. Chernigovskaya, V.I. Perminov, Studying Manifestations of 2008–2011 Sudden Stratospheric Warmings in East-Siberia and European Russia, *Geophysica*, 2012, Vol. 48, No. 1–2, pp. 91–103, 13.
4. I. Medvedeva, A. Medvedev, K. Ratovsky, A. Shcherbakov, M. Tolstikov, Comprehensive study of disturbances of the neutral atmosphere and ionosphere parameters over Eastern Siberia during the 2013 January major sudden stratospheric warming, *Adv. Space Res.*, 2015, Vol. 56, No. 9. pp. 1877–1885, URL: <http://dx.doi.org/10.1016/j.asr.2015.06.008>.
5. R.V. Vasilyev, M.F. Artamonov, A.B. Beletsky, G.A. Zhrebtsov, I.V. Medvedev., A.V. Mikhalev, T.E. Syrenova, Registering upper atmosphere parameters in East Siberia with Fabry—Perot interferometer KEO Scientific “Arinae”. *SolarTerrestrialPhysics*, 2017, 3(3), pp. 61-75, DOI: 10.12737/stp-33201707
6. D. P. Dee, et al., The ERA-Interim Reanalysis: Configuration and Performance of the Data Assimilation System, *Quarterly Journal of the Royal Meteorological Society*, 2011, 137, No. 656, pp. 553-597. doi:10.1002/qj.828.

ON SPACE WEATHER FACTORS WHICH CAN IMPACT TERRESTRIAL ATMOSPHERE PROCESSES

Olga M. Stupishina¹, Elena G. Golovina²

¹ *Saint-Petersburg State University, 198504, Saint-Petersburg, Russia*

² *Russian State Hydrometeorological University, Saint-Petersburg, Russia*

The main idea of our work is to find out the perspective points for the investigation of space factors which can impact terrestrial physical processes.

The presented work contains the description of the Space Weather characteristics for the appearance moments of very long-live (more than 10 days) atmosphere pressure systems on different terrestrial latitude locations. These Long-live Pressure Systems (LPS) are interesting for us because some of them (namely anticyclones) can block pressure fields so they can create some dangerous situations for the human activity. The different terrestrial latitude locations (Fig.1) were: Saint-Petersburg (59°57'N, 30°19'E) and Tambov (52°43'N, 41°27'E). This latitude difference in observations is interesting for us because we know about the different affect of Space Weather variations on northern and southern places so we want to study this difference. The time-intervals were: 1999-2014 years (23-d and 24-th solar cycles) – Saint-Petersburg, 2007-2014 years (24-th solar cycle) – Tambov. We have found only 18 LPS in the Saint-Petersburg area in 16 years of observation and significantly more – 26 LPS in Tambov area in 8 years. Besides we can see only 2 kinds of long-lived baric systems in Saint-Petersburg – cyclones and anticyclones but in Tambov we have registered sometimes LPS for a ridge, a flat field of high or low pressure (Fig.1).

Space Weather parameters description: (1) global variations of Solar Activity (SA) (namely – Solar Spot Number, Radio Flux on 10.7cm, the daily number of Active Regions, the common area of spots on Solar Disk; (2) daily characteristics of the SA flare component in various bands of the electromagnetic spectrum (namely – flares in H α -line, X-Ray flares, radio bursts of Noise Storm type); (3) variations of Interplanetary Space characteristics in Earth vicinity (namely – the level of X-Ray background, characteristics of proton and electron fluxes in different energy bands, characteristics on whole plasma fluxes in Solar Wind, characteristics of Electric Field); (4) variations of characteristics of Geomagnetic Field (GMF) (namely – k-indices on different terrestrial latitudes, characteristics of separate (x,y,z) GMF-components). All parameters are presented by daily statistics (max, min, median, coefficients of variation and oscillation).

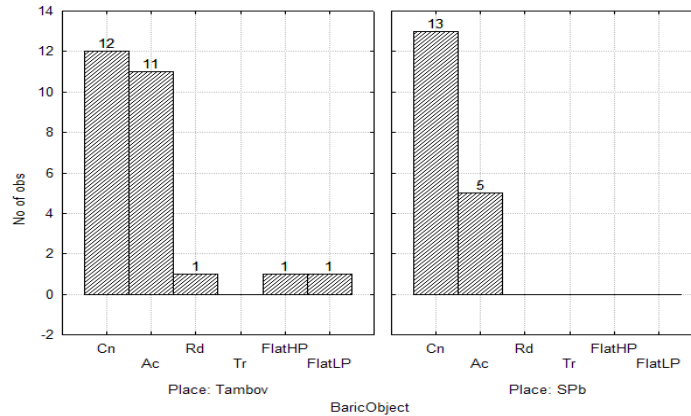


FIGURE 1. The distribution of LPS cases by the kinds of pressure systems in different latitude points. Cn – Cyclone, Ac – anticyclone, Rd – Ridge, Tr – Trough, FlatHP – Flat Field of High Pressure, FlatLP – Flat Field of Low Pressure.

The first part of the presented work contains the description of LPS features those are specific for different latitude points: Saint-Petersburg has these long-lived pressure systems mostly in the fall branch of solar cycle when Tambov has most of them in the solar rise branch (Fig.2).

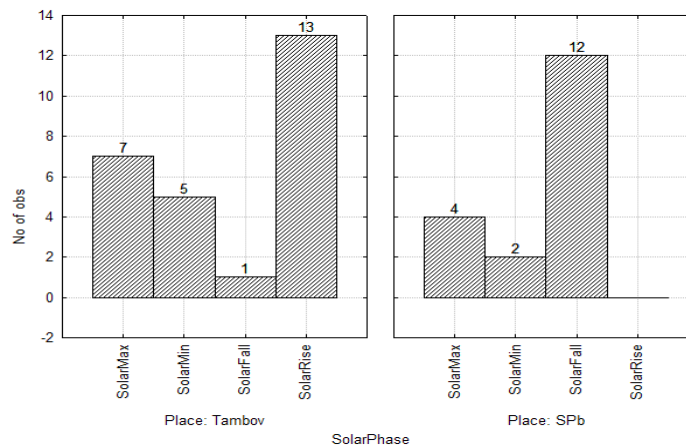


FIGURE 2. The distribution of LPS cases by the solar cycle phases in different latitude points.

We have compared the Space Weather characteristics for follow events: (1) event (the scale is 1 day) of the LPS beginning vs. event of the LPS end; (2) event of the LPS beginning vs. beginning of the Natural (5-7 days) Synoptic Period (NSP).

The second part of the work describes the behavior of selected Space Weather parameters for aforementioned moments in detail. The selection of parameters was done by algorithm that was based on some elementary description statistics plus elements of cluster analysis; the algorithm was specially developed by the authors [1-4].

We have discovered that in different solar cycle phases as well as in different calendar seasons Space Weather factors those match the above events differentiate. Also we have found out such combinations of a calendar season with solar cycle phase in which we can catch the same Space Weather factors for one above mentioned event vs. the other same for another event.

For the appearance moments of LPS we have discovered the interesting behavior for follow Space Weather characteristics: variations of all global SA indices, variations of low energy (C-class) X-ray

solar flares number, variations of proton fluxes of concrete energies, and variations of GMP parameters daily statistics. Also we have discovered the terrestrial-latitude difference in the atmosphere response on the Space Weather impact.

The results of the work may be considered as the base for detail investigation of space-terrestrial connection.

1. O. M. Stupishina, E. G. Golovina, M. S. Mostamandi et al., Meteorological and heliogeophysical information analytics for the medical purposes, *Proceedings of the Russian State Hydrometeorological University*, 2016, 42, p.164 -177.

2. O. M. Stupishina, E. G. Golovina, Investigation of Correspondence between Environmental Parameter Complexes and Human Body Status, *Proceedings of V International conference "Atmosphere, Ionosphere, Safety"*, 2016, pp.263-267.

3. O. M. Stupishina, E. G. Golovina, M. S. Mostamandi, Biometeorological Regime Monitoring of Arkhangelsk Region, *Proceedings of V International conference "Atmosphere, Ionosphere, Safety"*, 2016, pp. 268-272.

4. O. M. Stupishina, E. G. Golovina, Detection and Monitoring of Environmental Factors those can be Responsible for the Cardio-Catastrophes, *Proceedings of VI International conference "Atmosphere, Ionosphere, Safety"*, 2018, pp.235-239.

NON-UNIFORM STRUCTURE OF SHORT WAVES IN THE IONOSPHERE AND ITS INFLUENCE ON THE POLARIZATION CHARACTERISTICS OF SIGNALS

Kristina V. Raubo, Veniamin E. Zakharov

Immanuel Kant Baltic Federal University, Kaliningrad, Russia.

Introduction. The heterogeneous wave structure is understood as the mismatch of the wave front and the wave surface caused by the difference in magnitude and direction between the phase and group wave velocities. Ionospheric plasma exhibits anisotropic properties under the influence of the Earth's magnetic field [1]. In the approximation of weak inhomogeneity of the medium, the method of geometric optics is widely used to study the propagation of electromagnetic waves [2]. The electric E and magnetic H field strengths of the distinguished normal wave are expressed as [2]:

$$E = \Phi f, \quad H = \sqrt{\frac{\varepsilon_0}{\mu_0}} p \times E,$$

where Φ and \mathbf{f} are the complex amplitude and polarization vector of the wave field, p - is the momentum, ε_0 and μ_0 are the permittivity and magnetic permeability of the vacuum, respectively. Using the normalization condition $\mathbf{f}\mathbf{f}^* = 1$, where the sign "*" means the operation of complex conjugation, we find that the components of the polarization vector \mathbf{f} at each observation point in the ionosphere satisfy the system of homogeneous equations

$$(p^2 \delta_{im} - p_i p_m - \varepsilon_{im}) f_m = 0, \quad i, m = 1, 2, 3,$$

where the summation is implied by the twice-occurring index m , are the components of the tensor of the complex relative permittivity of the ionosphere plasma, and δ_{im} is the Kronecker symbol.

In [3], the propagation features of the ordinary and extraordinary mode of short waves in the presence of local inhomogeneities in the ionosphere are considered. In [4], the data of satellite radio sounding of the ionosphere were used to diagnose the heterogeneous structure of the ionosphere. In [5], the formation of ray paths and absorption of short waves in the ionosphere during magnetic storms was studied.

The method of an extended bi-characteristic system allows one to find not only the ray paths and wave absorption themselves, but also the attenuation factor of the wave amplitude [6]. In [7], the

formation of the amplitude and polarization characteristics of short waves in a three-dimensionally inhomogeneous anisotropic ionosphere was studied by integrating the equations of transport of the parameters of the vector of the complex wave amplitude along the ray tubes. To describe the wave propagation medium, experimental models of the neutral atmosphere [8] and ionosphere [9] were used.

The aim of this work is to apply the radio wave propagation model [7] to a numerical study of the influence of the development of an inhomogeneous wave structure on the polarization characteristics of ionospheric signals.

Results of the calculations and conclusions. The emitter is located on the Earth's surface and has geographical coordinates: latitude $\varphi = 15^\circ$, and longitude $\lambda = 290^\circ$. The calculations were made for solstice conditions at high solar activity ($F10,7 = 150$). The universal time is given as UT = 16,65 hour. Day number of the year is set N=172.

Figure 1a presents the results of numerical calculations of the ray path for an ordinary wave (solid line 1) and the ratio of the speed of light to group velocity (dashed line 2) at a frequency $f = 10$ MHz. Coordinate grid: h - is the height above the Earth's surface, and s - is the length along the beam. The elevation angle $\beta = 30^\circ$, and the azimuth $\gamma = 90^\circ$ are set the direction of the reference ray at the location point of transmitter.

Figure 1b shows the calculation results for the angle between the momentum and induction vectors of the geomagnetic field \mathbf{B} and the angle between the group velocity vector \mathbf{v}_{TP} and the momentum vector for the same beam.

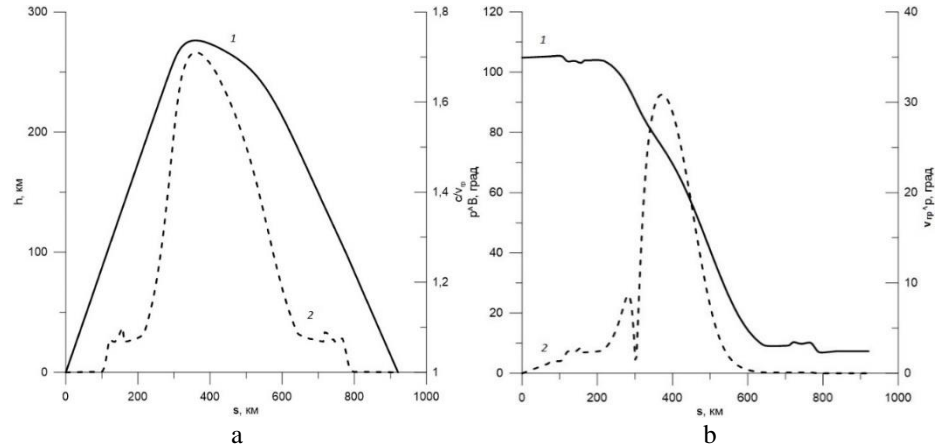


FIGURE 1 The ray path for an ordinary wave in the (h, s) plane at a frequency of 10 MHz (curve 1) and dependence of the ratio of the speed of light to group velocity on s (a). The dependence of the angle between the direction of the group velocity vector and the direction of the geomagnetic field induction vector on s (curve 1) and the dependence of the angle between the direction of the group velocity vector and the momentum vector on s (curve 2) (b).

As seen, when one plunges into each ionospheric layer, the group velocity decreases, and the strongest one is in the vicinity of the beam turning point in the F2 layer of the ionosphere. The mode of wave propagation along the beam gradually changes from quasi-longitudinal to quasi-transverse with respect to the direction of the geomagnetic field. When passing a neighborhood of a point with a transverse propagation regime, a sharp decrease in the level of development of wave inhomogeneity occurs (a decrease in the angle between the direction of the group velocity vector and the momentum vector). As known from the theory of a homogeneous plasma in a constant magnetic field, upon transition to the transverse propagation regime, an ordinary wave with elliptical polarization degenerates into a linearly polarized wave [1].

An extraordinary wave remains elliptically polarized when passing through the transverse propagation regime. Accordingly, in our calculations for an extraordinary wave, there is no effect of a sharp decrease in wave inhomogeneity in the vicinity of the transition through the transverse propagation regime. At each observation point on a distinguished ray path, we introduce a local Cartesian coordinate system. The z axis is directed along the momentum vector \mathbf{p} , and the y axis is located in the plane of the vectors \mathbf{p} and \mathbf{B} .

Figure 2 presents the results of numerical calculations of the modules of the Cartesian projections of the polarization vector, calculated along the beam of an ordinary wave (see Fig. 1(a)). The main ones are $|f_x|$ (curve 1) and $|f_y|$ (curve 2). The appearance of the component $|f_z|$ (curve 3) is a consequence of the development of an inhomogeneous wave structure as the beam sinks deeper into the ionosphere. In the vicinity of the transition through the transverse propagation regime, a sharp decrease in $|f_x|$ and $|f_z|$, the polarization of the wave approaches linear along the y axis.

An ordinary wave in the ionosphere has a left polarization. The restructuring of the polarization ellipse is most significant in the vicinity of the turning point of the ray path. In the case of an unusual wave with right polarization, a change in $|f_x|$ and $|f_y|$ in the vicinity of the beam pivot point, it is opposite in comparison with Fig. 2: for $|f_x|$ a maximum is formed, and for $|f_y|$ - minimum.

Conclusion. The main results of the studies are the following: 1. Using numerical experiments, we simulated the evolution of the complex amplitude vector along the ray paths of normal modes. 2. The consistent formation of the inhomogeneous structure of the waves and their polarization characteristics along the ray paths has been investigated.

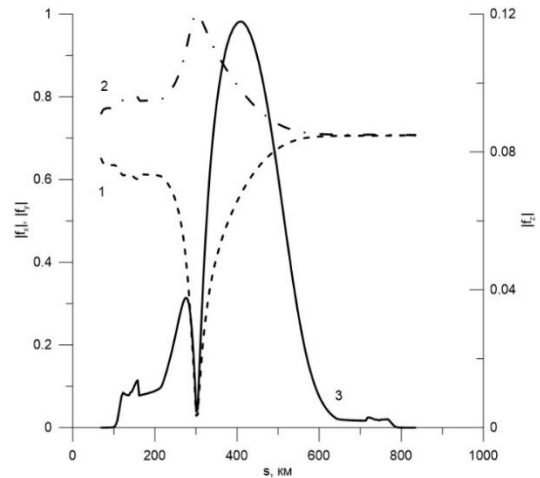


FIGURE 2. Modification of the Cartesian projection moduli of the complex polarization vector f ordinary wave along the radial trajectory Fig. 1.

1. B. E. Brunelli and A. A. Namgaladze, *Physics of the ionosphere*, Nauka, Moscow, 1988, 528 p. (in Russian)
2. Yu. A. Kravtsov, Yu. I. Orlov, *Geometrical optics of inhomogeneous media*, Nauka, Moscow, 1980, 304 p. (in Russian)
3. A. S. Kryukovskii, D. S. Lukin, and D. V. Rastyagaev, Investigation of Peculiarities of Distribution of Short Radio Waves in the Inhomogeneous Anisotropic Ionosphere, *Electromagnetic waves and electronic systems*, 2009, 14(8), pp. 17–26.
4. A. T. Karpachev, G. A. Zhabankov, and V. A. Telegin, Region of Permanent Generation of Large-Scale Irregularities in the Daytime Winter Ionosphere of the Southern Hemisphere, *Geomagn. Aeron.*, 2016, 56(1), pp. 69–76.
5. D. S. Kotova, M. V. Klimenko, V. V. Klimenko, and V. E. Zakharov, Numerical Simulation of the Influence of the May 2–3, 2010 Geomagnetic Storm on HF Radio-Wave Propagation in the Ionosphere, *Radiophysics and Quantum Electronics*, 2014, 57(7), pp. 519–530, doi: 10.1007/s11141-014-9529-2.
6. A. S. Kryukovsky, D. S. Lukin, and K. S. Kiryanova, Method of Extended Bicharacteristic in Propagation Ionospheric Plasma, *Communications technology and electronics*, 2012, 57(9), pp. 1039–1045.
7. V. E. Zakharov, Amplitude Formation and polarization characteristic of short waves for distribution in the ionosphere, *Communications technology and electronics*, 2019, 64(6), pp. 525–534
8. A. E. Hedin, Extension of the MSIS thermospheric model into the middle and lower atmosphere, *J. Geophys. Res.*, 1991, 96(A1), pp. 1159–1172.

9. D. Bilitza, D. Altadill, Y. Zhang et al., The International Reference Ionosphere 2012 – a model of international collaboration, *J. Space Weather and Space Clim.*, 2014, 4(A07), doi:10.1051/2014004.

INFLUENCE OF METEOROLOGICAL STORMS ON THE LOWER IONOSPHERE ACCORDING TO VERTICAL SENSING DATA

Olga P. Borchevskina^{1,2}, Ivan V. Karpov^{1,2}, Mikhail I. Karpov^{1,2}, Nina A. Korenkova¹, Valery I. Vlasov¹ and Vladimir S. Leshchenko¹

¹Pushkov Institute of Terrestrial Magnetism, Ionosphere, and Radio Wave Propagation, West Department, Russian Academy of Sciences, Kaliningrad, 236017 Russia

²Immanuel Kant Baltic Federal University, Kaliningrad, 236041 Russia

Introduction. Despite notable success in interpreting of irregular ionospheric phenomena, the physical mechanisms for the formation of ionospheric inhomogeneities caused by disturbances in the lower atmosphere remain poorly understood. Studies of the relationship of processes in the upper atmosphere and ionosphere with tropospheric and stratospheric meteorological processes are important for creating self-consistent models of the mutual influence of space factors and weather forming processes. The irregular occurrence of disturbed conditions in the lower atmosphere complicates the physical interpretation of the influence these processes on the upper atmosphere and ionosphere. Usually, the hypotheses about the atmosphere-ionosphere coupling are built using the theory generation and propagation of atmospheric waves [1, 2]. One of the sources of atmospheric waves, in particular, acoustic-gravity and internal gravity waves, in the lower atmosphere, which can affect the upper atmosphere and the ionosphere are meteorological disturbances. The importance of meteorological influences on the overall variability of the ionosphere was noted in [3].

Data analysis. In the *E* region the gravity wave investigation have been focused on the *E_s* layers, because gravity waves play some role in their formation [4, 5], probably via enhanced irregular neutral winds associated with gravity waves [6, 7]. The appearance of an inhomogeneous neutral wind can be associated with various dynamic processes in the lower thermosphere [8, 9].

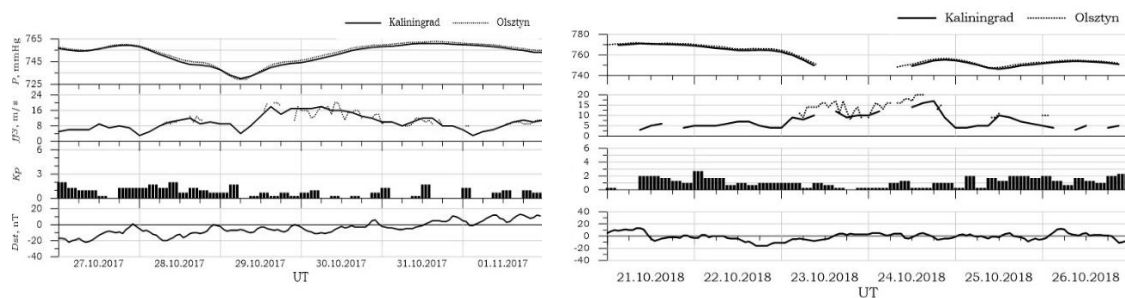


FIGURE 1. Diurnal variation in atmospheric pressure *P*, maximum wind gusts *ff3*, geomagnetic activity indices *Kp* and *Dst* in Kaliningrad and Olsztyn on October 27-November 1, 2017 and October 21-26, 2018.

The work presents the analyses of the lower ionosphere local variations in Kaliningrad (54° N, 20°E) during meteorological events in the region in 2017-2018. Three-hour data on atmospheric pressure and wind gusts were used to describe the meteorological situation (www.rp5.ru). 15-minute measurements of the critical frequency (*foE_s*, MHz), screening frequency *E*-layer (*fbE_s*, MHz) and the minimum effective trace height of the sporadic ionosphere layer (*h'E_s*, km) were used as data for analyzing variations of the sporadic layer *E*, which characterize the main characteristics of the irregular layer,

according to the Parus-A ionosonde of the Kaliningrad branch of IZMIRAN. Two events with the maximum wind speed in Kaliningrad reached 17 m/s or more, and the decrease in atmospheric pressure reached 30 mmHg in a few hours were selected for the analysis. The considered periods were characterized by quiet geomagnetic conditions. The Kp index did not exceed 2 most of the time, and the Dst index, which describes the storm activity, varied from -20 to 20 nT (fig.1).

Two events were selected for analysis: October 29-30, 2017 and October 23-24, 2018. Figure 2 shows daily variations in E_s parameters during the severe weather events on October 2017 and 2018. The high variability of the $\Delta fE_s = f_oE_s - f_bE_s$ parameter should be mentioned, which characterizes the turbulence of a sporadic layer [10].

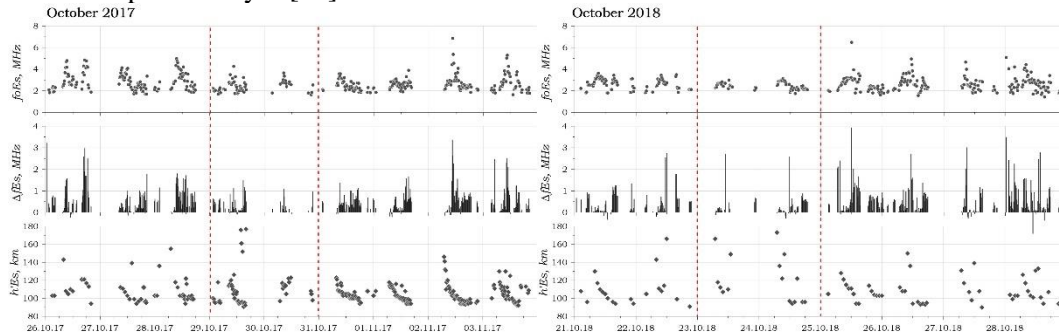


FIGURE 2. Diurnal variation in critical frequency (f_oE_s , МГц), minimum effective track height E_s ($h'E_s$, km), and differences between the critical frequency and the screening frequency ΔfE_s according to the Kaliningrad ionosonde (54.3 N, 20.1 E) during the passage of the meteorological storms on October 2017, 2018.

The main phase of the storm on October 2017 was October 29 from 06 to 23 UT. The disappearance of a layer of increased electron concentration was observed from 17.00 UT on October 29 to 6.00 on October 30 and from 14.00 on October 30 to 07.00 on October 31. The main phase of the storm on October 2018 was October 23 from 00 UT on October 23 till 18 UT on October 24. Scattering at the lower thermosphere altitudes according to vertical sounding data was observed from 14.00 on October 23 till 7.00 on October 24. Before and after the passage of the meteorological disturbance in the troposphere, the E_s observed on ionograms was recorded quite often, and the next day after the storm, there is a regular appearance the layer of increased electronic concentration with a difference between the critical frequency and the screening frequency reaching 1 MHz (fig.2). The disappearance the E_s have been caused by a regional local effect. This circumstance may indicate the possibility that the decrease in the electron density of E_s is related to the effects caused by the passage of a meteorological storm in the troposphere. The disappearance of E_s began about 1-2 hours after the storms approached the area controlled by the ionosonde, which is consistent with the expected times of propagation of the AGWs energy from the troposphere to the thermosphere and ionosphere. AGWs can propagate to the mesosphere and lower thermosphere, including the E region, where they can affect the formation of the E_s layer. The main mechanism of this interaction is the so-called windshear theory [4, 9].

Conclusions. This paper presents the results of observations the troposphere and ionosphere parameters in the Kaliningrad region during the passage of two meteorological storms in October 2017 and 2018. Changes in the behavior of the sporadic layer E during the passage of the storm in the troposphere are demonstrated. There is a disappearance of E_s registration according to vertical sensing data directly during the passage of the storm. It is assumed that the mechanism responsible for this interaction is based on the AGWs action initiated by convective movements in the lower atmosphere and propagating from the storm region into the thermosphere and ionosphere. AGWs propagation and dissipation leads to disturbances in the neutral gas temperature and changes in the electronic temperature at the E region altitudes.

This work was supported by the Russian Foundation for Basic Research and the government of the Kaliningrad region, project No. 19-45-390005 (O.P. Borchevkina, M.I. Karpov) and RFBN grant No. 18-05-00184a (I.V. Karpov).

We express gratitude to the Copernicus Atmosphere Monitoring Service for the meteorology data; the International GNSS Service for access to GNSS data used in this study, as well as the OMNIWeb Plus NASA/Goddard Space Flight Center service for the data on geomagnetic and solar flux indices.

1. E. Kazimirovsky, M. Herraiz, A. D. L. B. Morena, Effects on the ionosphere due to phenomena occurring below it, *Surveys in Geophysics*, 2003, 24(2), pp. 139–184, DOI: 10.1023/A:1023206426746;
2. J. Lastovicka, Forcing of the ionosphere by waves from below, *Journal of Atmospheric and Solar-Terrestrial Physics*, 2006, 68(3), pp. 479–497, DOI: 10.1016/j.jastp.2005.01.018, 2006.
3. J. M. Forbes, S. E. Palo, X. Zhang, Variability of the ionosphere, *Journal of Atmospheric and Solar-Terrestrial Physics*, 2000, 62(8) pp. 685–693, DOI: 10.1016/S1364-6826(00)00029-8.
4. J.D. Matthews, Sporadic E: current views and recent progress, *Journal of Atmospheric and Solar-Terrestrial Physics*, 1998, 60(4), pp. 413–435, DOI: 10.1016/S1364-6826(97)00043-6.
5. C. Scotto, Sporadic-E layer and meteorological activity, *Ann Geophys*, 1995, 38(1), pp. 21–24.
6. M.L. Parkinson, P.L. Dyson, Measurements of mid-latitude E-region, sporadic-E, and TID-related drifts using HF Doppler-sorted interferometry, *Journal of Atmospheric and Solar-Terrestrial Physics*, 1998, 60, pp. 509–522.
7. V. Barta, Ch. Haldoupis, G. Satori, D. Buresova, J. Chum, M. Pozoga, K. A. Berényi, J. Bór, M. Popek, Á. Kis, P. Bencze, Searching for effects caused by thunderstorms in midlatitude sporadic E layers, *Journal of Atmospheric and Solar-Terrestrial Physics*, 2017, 161, pp. 150–159, DOI: 10.1016/j.jastp.2017.06.006.
8. C. Haldoupis, Midlatitude Sporadic E. A Typical Paradigm of Atmosphere-Ionosphere Coupling, *Space Science Reviews*, 2012, 168(1–4), pp. 1–21, DOI: 10.1007/s11214-011-9786-8.
9. A. Pignalberi, M. Pezzopane, E. Zuccheretti, Sporadic E layer at mid-latitudes: average properties and influence of atmospheric tides, 2014, *Ann. Geophys.*, 32, pp. 1427–1440, DOI: 10.5194/angeo-32-1427-2014.
10. V.A. Liporovsky, E.V. Pokhotelov, E.V. Liporovskaya, M. Parrot, C.-V. Meister, O.A. Alimov, Modification of sporadic E-layers caused by seismic activity, *Surveys in geophysics*, 2000, 21, pp. 449–486.

SENSITIVITY OF THE LOWER ATMOSPHERE CIRCULATION TO THE INTERSECTION OF THE SECTOR BOUNDARIES OF THE INTERPLANETARY MAGNETIC FIELD

*Anna A. Kukoleva¹, Nina K. Kononova², Alexey A. Krivolutsky¹,
Alexander I. Pogoreltsev³*

¹*Laboratory for Atmospheric Chemistry and Dynamics, Roshydromet, Central Aerological Observatory, Dolgoprudny, Moscow Region, Russia*

²*Institute of Geography of the Russian Academy of Sciences, Moscow, Russia*

³*Russian state hydrometeorological University, Saint Petersburg, Russia*

Introduction. The purpose of this study is to find the relationship between the circulation of the lower atmosphere of the Northern hemisphere and the change of sectors of the interplanetary magnetic field (IMP) in near-earth space, based on data on the duration of different forms of elementary circulation mechanisms (ECM) according to the classification of B.L. Dzerdzhevsky [1].

In [1], 4 circulation groups were identified: zonal (Z), zonal disturbance (DZ), meridional North (MN), and meridional South (MS). The circulation of Z-group is characterized by nearly zonal flow in the absence of blocking situations, in case MN circulation - the number of blocking anticyclones increases to 3–4, and for MS - without blocking and low pressure at the pole. There are 13 types and 41

subtypes of circulation by this groups. Examples of dynamic diagrams for each group are shown in Fig.1.

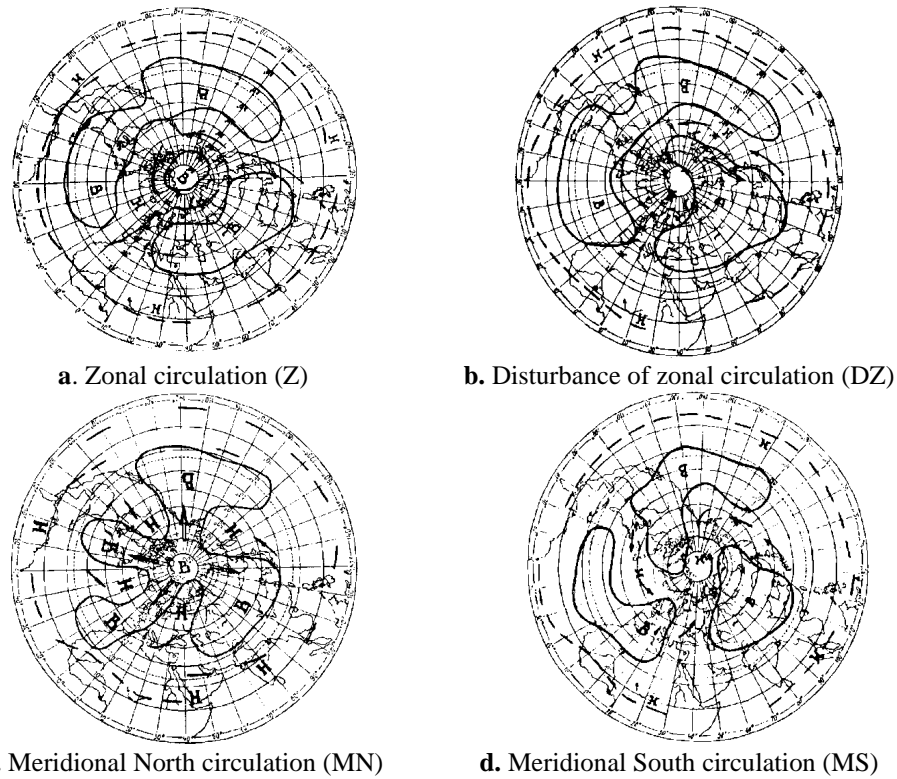


FIGURE 1. Northern Hemisphere atmospheric circulation groups (the dynamic schemes).

Information about the phases of the 27-day cycle of the IMP direction sectors ("+"- from the Sun, and "-" - " - to the Sun) is presented in [2]. The values of the frequency of different forms of circulation in separate phases of the IMP over the Northern hemisphere of the Earth were obtained based on data for 2006-2010, which correspond to the solar activity minimum (between 23 and 24 cycles). Days with disturbed geomagnetic conditions were excluded from consideration. The analysis was made separately for each season. The frequency of

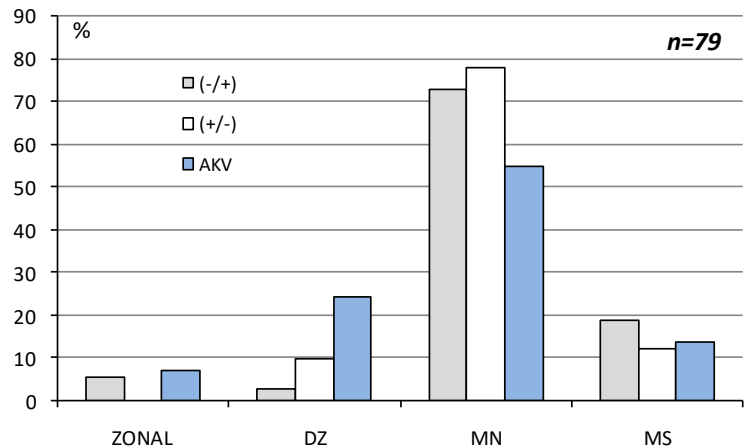


FIGURE 2. The frequency of the circulation groups a day after passing of the IMP sector boundary passage by the Earth. (AKV - average climatic value).

of the circulation groups (Z, NZ, MS, and MU) generally in the entire period corresponds to the average multi-year distribution under review. However, for cold period (December-March) it was found the MN frequency of the circulation group is 19-23% higher than the average value a day after crossing the IMP sector boundary. The DZ group frequency is 14-21% lower than the average climatic value (Fig.2) during this period. These results qualitatively coincide with the conclusions [3, 4]. Wilcox [3] and Hines

and Halevy [4] showed that the area of tropospheric troughs and upper-level tropospheric vorticity area index decreases one day after the Earth crosses the IMP sector boundary. Since the group of MS is characterized by 3-4 blocking in the hemisphere, the area of cyclones, respectively, decreases. Thus, the results obtained qualitatively confirm the conclusions [3, 4].

The next area of work with data is the study of circulation patterns during periods of sudden stratospheric warming (SSW). Data on the average zonal temperature in the polar atmosphere of the Northern hemisphere (87,5 N) were considered in the period 1992-2016 according to data [5, 6]. The total number of SSW events considered is equal 38. The beginning of the SSW was taken as the moment of wind direction changes from West to East at the level of 10 hPa.

The frequency of different circulation groups before, during, and after SSW is shown in Fig.3. The average climate value (ACV) represents the last column of the diagram. The number of corresponding events is shown in parentheses. The frequency of the DZ group was 8% higher before the SSW and 4% lower after the event (1-2 weeks), and the MS group was 9% higher than the average multi-year value after the end of the SSW. Results for other forms within the standard error range ($\sigma = 3-5\%$).

The relationship between the onset of SSW and the change of the MMP sign was also investigated. Slightly more than half of the events ($n = 21$) started in the negative direction of the MMP (towards the Sun) and in $n = 17$ cases the field was positive (from the Sun). The analysis was hampered by the some uncertainty of the SSW beginning and the MMP sign uncertainty in certain periods. Thus, there was no reliable link between MMP and warming.

Previously, it can be concluded the intersection of IMP sector boundary passage affects the formation of blocking situations in the lower troposphere. Perhaps the negative phase of MMP in combination with some forms of circulation is favorable for the SSW occurrence. In order to establish a more reliable connection, it is planned to continue this research in the future.

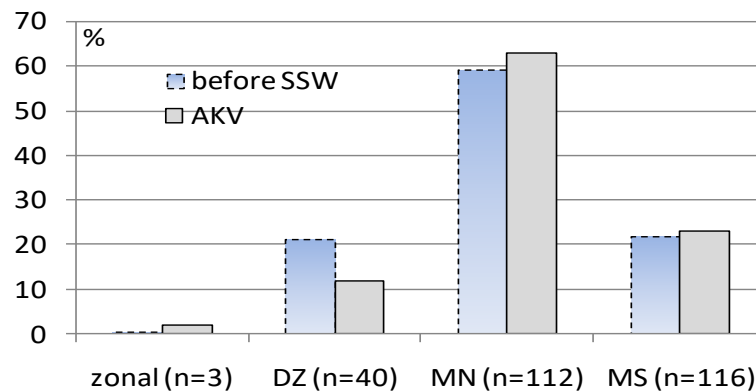


FIGURE 3a. The frequency of the circulation groups before SSW (2 weeks).

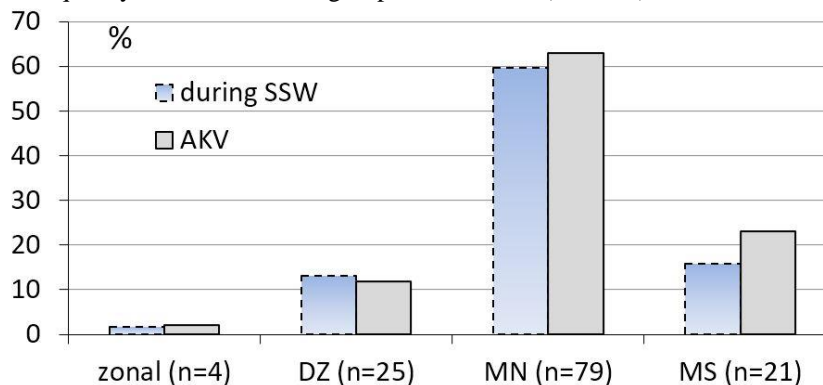


FIGURE 3b. The frequency of the circulation groups during SSW

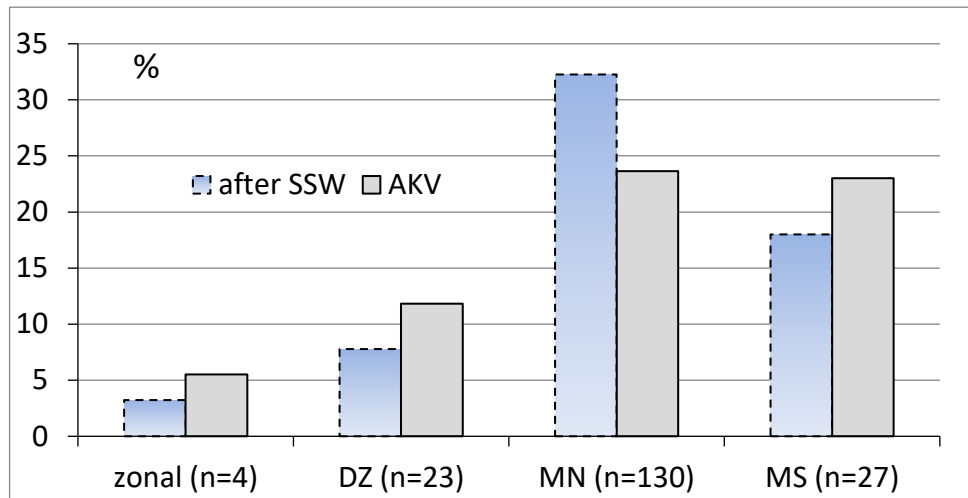


FIGURE 3c. The frequency of the circulation groups after SSW (2 weeks).

1. N. K. Kononova, Classification of circulation mechanisms of northern hemisphere by B.L. Dzerdzeevskii, The russian academy of sciences. Institute of geography, M. Voentehinizdat, 2009, 372 p.
2. <http://www.izmiran.ru/services/saf/archive/ru/>
3. J.M. Wilcox, Solar magnetic structure: Influence on stratospheric circulation, *Science*, 1973, 180, pp. 185-186.
4. C.O. Hines and I. Halevy, On the reality and nature of a certain sun-weather correlation, *J. Atmos. Sci.*, 1977, 34, pp. 382–404.
5. E.N. Savenkova, N.M. Gavrilov, A.I. Pogoreltsev, On statistical irregularity of stratospheric warming occurrence during northern winters, *Journal of Atmospheric and Solar-Terrestrial Physics*, 2017, 163, pp. 14-22, doi: 10.1016/j.jastp.2017.06.007.
6. https://gmao.gsfc.nasa.gov/reanalysis/MERRA/data_access/

NUMERICAL MODELING OF THE SOLAR TERMINATOR AND SOLAR ECLIPSE USING LIDAR DATA

Yuliya A. Kurdyayeva¹, Ivan V. Karpov^{1,2}, and Olga P. Borchevskina^{1,2}

¹West Department of Pushkov Institute of Terrestrial Magnetism, Ionosphere and Radio Wave Propagation Russian Academy of Sciences, Kaliningrad, Russia

² Immanuel Kant Baltic Federal University, Kaliningrad, Russia

Introduction. The propagation of infrasound and internal gravity waves (IGW) from the troposphere to the thermosphere significantly affects the state of the atmosphere and ionosphere at all altitudes. The sources of atmospheric waves in the lower atmosphere can be processes associated with the evolution of meteorological disturbances, seismic activity, the passage of the solar terminator or solar eclipse. In numerous theoretical studies, various problem of generation, propagation, and the influence of atmospheric waves on the state of the atmosphere have been studied in sufficient detail. However, in most works simplified situations are considered, when either the processes of wave interaction with each other and the background state of the atmosphere are neglected, or the real stratification of the atmosphere is not taken into account. Some modern numerical models take these features into account

and allow realistic simulation of the infrasound and IGW propagation taking into account wave processes of different scales with a high time resolution. The paper presents the results of a numerical experiment to simulate the propagation of infrasound and IGW from the lower atmosphere into the upper atmosphere with using the numerical non-hydrostatic atmosphere model “AtmoSym”[1-3]. The observed atmospheric pressure variations during the passage of the solar eclipse on March 20, 2015 over Kaliningrad (54°N, 20°E) are considered as the source of the waves.

Numerical experiment. In a numerical experiment are used minute-by-minute variations of surface pressure set at the lower boundary of the computational domain as a wave source. We used the results of lidar sounding of the lower atmosphere (performed in Kaliningrad (54°N, 20°E) on March 20, 2015) on the day of the passage of the solar eclipse for determine the pressure variations. Lidar observations were carried out from 6:00 to 18:00 LT, which includes the transit time of the morning terminator (6:40 LT), the main phase of the eclipse (10:50 LT) and its end (13:10 LT). It is assumed that variations in lidar signal intensity reflect the frequency characteristics of pressure variations at a fixed height. The amplitude values of the pressure variations were calculated on the assumption that the maximum amplitudes of the changes in the observed scattered signal intensity correspond to the amplitudes of the pressure variations of 10 mmHg. Such change pressure during are normal for spring conditions in Kaliningrad. Numerical calculations were carried out in a computational domain of 2000 km horizontally and 500 km vertically. To set the boundary conditions at the lower boundary it was assumed that the observed variations in the lower atmosphere are created by dynamic sources (solar terminator and solar eclipse) propagating along the lower boundary with the speed of the solar terminator at the latitude of Kaliningrad $V = 270$ m/s.

The discussion of the results. An analysis of the perturbations of the temperature of the thermosphere during the simulation period showed the appearance of variations with periods of infrasound (less than 4 min) and short-period GWs (more than 8-10 min). It was found that variations with short periods appear directly during periods of passage of the solar terminator and eclipse. Such a wave pattern is in good agreement with already existing ideas about the propagation of waves (forming at tropospheric heights) into the upper atmosphere [4,5]. In the range of periods of more than 20 minutes, the spectra of variations show significant differences in the amplitudes of harmonics, which is explained by the more complex nature of the propagation of such waves in the atmosphere. Figure 1 shows the results of a wavelet analysis of temperature variations during the simulation period. As can be seen from Fig. 1, the time of the appearance of variations with periods of about 4-20 minutes at various points along the integration region clearly coincides with the times of the passage of the solar terminator, the beginning and end of the eclipse. This is due to the near to vertical propagation of waves in this frequency range.

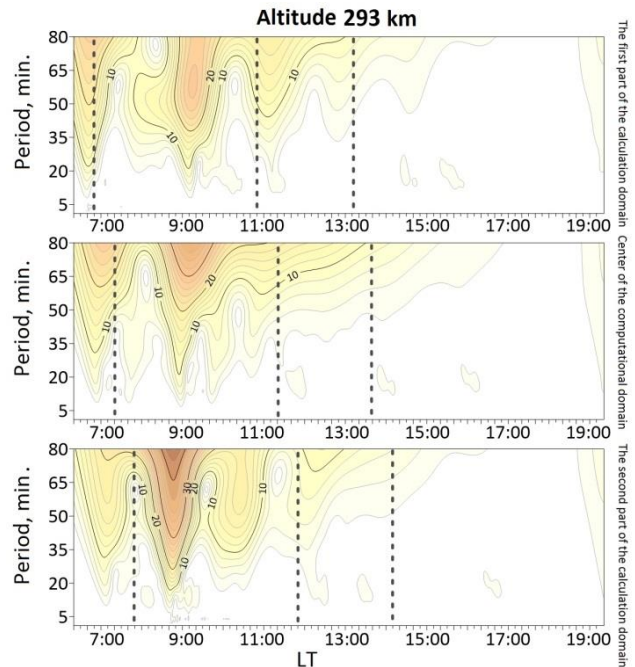


FIGURE 1. The result of a wavelet analysis of temperature perturbations at an altitude of 293 km.

The waveguide nature of propagation can be explaining variations with periods of 8–10 min (Fig. 1). These components of the variations propagate both in the direction of movement of the region of the solar terminator, and in the opposite direction. At the heights of the upper atmosphere, disturbances appear with periods of about 50 minutes. The appearance of such variations in the thermosphere can be explained by the processes of dissipation of short waves in the thermosphere.

Thus, atmospheric waves propagating from the lower atmosphere during periods of passage of the solar terminator and solar eclipse form disturbances at the heights of the thermosphere. The frequency characteristics of the perturbations of the thermosphere are determined by the infrasound waves and the IGW propagating from the lower atmosphere, as well as by the waves excited directly in the thermosphere due to the dissipation of waves arriving from the lower atmosphere.

Temporal variability of thermosphere parameters is formed due to a superposition of various component variations propagating in opposite directions. This leads to a significant complication of the temporal variability of the parameters of the thermosphere after passing through the main sources of disturbances - the solar terminator and eclipse.

Conclusion. The calculation results showed that the indirect use of experimental data on the intensity of the lidar signal, reduced to data on pressure variations in the surface layer, allows us to simulate the waves generated by the solar terminator and solar eclipse. The results of a numerical experiment on modeling perturbations of the parameters of the thermosphere due to the propagation of atmospheric waves excited in the lower atmosphere during the periods of passage of the solar terminator and solar eclipse on March 20, 2015 showed that the generation of infrasound and internal gravitational waves with periods of less than 10 minutes is amplified in the lower atmosphere. The generated waves, propagating almost vertically, reach the heights of the thermosphere and, due to wave dissipation processes, excite large-scale perturbations with a characteristic period of about 50 minutes propagating in the opposite direction, relative to the direction of movement of the terminator region. The results obtained are confirmed by the results of experimental studies of the dynamics of the ionosphere.

Acknowledgments. *The research is supported by the Russian Foundation for Basic Research projects No. 18-05-00184.*

1. S. P. Kshevetskii, Modelling of propagation of internal gravity waves in gases, *Comp. Math. Math. Phys.*, 2001a, 41, pp. 295-310.
2. S. P. Kshevetskii, Numerical simulation of nonlinear internal gravity waves, *Comp. Math. Math. Phys.*, 2001b, 12, pp. 1777-1791.
3. S. P. Kshevetskii, Analytical and numerical investigation of non-linear internal gravity waves, *Nonlinear Proc. Geoph.*, 2001, 8, pp. 37-53.
4. S. P. Kshevetskii, I.V. Karpov, Formation of Large Scale Disturbances in the Upper Atmosphere Caused by Acoustic Gravity Wave Sources on the Earth's Surface, *Geomagnetism and Aeronomy*, 2014, 54, pp. 513–522, 10.1134/S0016793214040173.
5. N. Petrukhin, E. Pelinovsky, E. Batsyna, Reflectionless propagation of acoustic waves through the Earth's atmosphere, *JETP Letters*, 2011, 93, pp. 564-567, 10.1134/S0021364011100110.

INVESTIGATION OF THE WAVE SURFACE AND OF THE RAY TRAJECTORIES EVOLUTION WHILE THE RAY BEAM OF HF WAVES PROPAGATES IN THE NON-UNIFORM ANISOTROPIC ABSORBING IONOSPHERE

Kristina V. Raubo, Veniamin E. Zakharov

Immanuel Kant Baltic Federal University, Kaliningrad, Russia

Numerical experiments were carried out to study the formation of the wave surface and of short wave trajectories during the propagation of a beam of rays in an inhomogeneous anisotropic absorbing ionosphere for normal waves in dependence on the choice of geophysical conditions and of radiation direction.

Introduction. The study of wave propagation in inhomogeneous anisotropic media with dispersion is an urgent problem in modern wave physics. By approximate methods for solving the wave equation, are the geometrical optics method in electrodynamics and the WKB (Wentzel – Kramers – Brillouin) method analogous to it in quantum mechanics. The traditional solution of the wave equation is based on the expansion in an asymptotic series in a small parameter of the problem — the ratio of the wavelength to the scale of the inhomogeneity of the medium. In plasma physics, the study of the formation of ray trajectories in phase space [1], in particular, using variation principles and methods of statistical physics, has spread.

The beginning of these studies was laid by Hamilton. It has been revealed that the use of the eikonal function for approximating the wave phase is local in nature and cannot be used to solve problems such as the study of caustics, wave mode transformations, and the tunneling effect.

In this work, we study the problem of the propagation of short waves in a three-dimensionally inhomogeneous anisotropic ionosphere by solving the following problems: 1) The first task is to study the evolution of the shape of the radial surface and its deviation from the spherical one as the wave propagates from the point emitter on the Earth's surface into the ionosphere by taking refraction into account. 2) The second task is to apply the method of complex geometric optics to the study of the influence of wave absorption in the medium on ray paths under conditions of ionospheric propagation.

1. Numerical algorithm. Ionospheric plasma and neutral atmosphere are described by experimental models IRI2012 [2] and MSIS86 [3]. The geomagnetic field is taken in the dipole approximation. For calculations, a numerical model of the propagation of short waves in the ionosphere was used [4]. The geographic coordinates of the emitter on the Earth's surface are latitude $\varphi = 15^\circ$, and longitude $\lambda = 290^\circ$. The solstice conditions (day number of the year $N = 172$) and high solar activity ($F10.7 = 150$) were selected. Radiated signal wave packet with a given value of the carrier frequency is considered.

Elevation angle β and azimuth angle γ determine the direction of radiation of the reference beam in the beam. The beam of rays is selected in a narrow angular solution ($\Delta\beta, \Delta\gamma$). An example of constructing an approximation of a beam of rays is a set of five rays, when the reference beam is supplemented by four more rays with angular coordinates of radiation ($\beta \pm \Delta\beta, \gamma \pm \Delta\gamma$). An algorithm for integrating the characteristic equations for the eikonal equation as applied to each of the beam rays was carried out by the Runge-Kutta method. We obtain a difference grid of geomagnetic coordinates along the rays of the beam. For each node on the reference beam, the group delay time of the signal from the radiation source to this node is calculated. On each side of beam, the nodes are interpolated so that they correspond to the same grid of delay times as on the reference beam. An element of the wave surface crossing the radiation tube is constructed for each value of the delay time of the signal. Such an element is approximated by a piecewise flat surface composed of triangular elements. The vertices of the triangles correspond to the nodes of the difference grid.

The current cross section $S = S(s)$, where s is the length along the reference beam, is found as the projection of the surface area vector of triangular elements on the direction of the group velocity vector

of the wave in the node of the reference beam. The found function $S = S(s)$ allows us to express the geometric factor of the total attenuation factor of the wave amplitude due to the divergence of the rays in the tube.

2. Results of the calculations and conclusions. Figure 1a presents the results of numerical calculations of the ray paths for an ordinary (solid line) and extraordinary (dashed line) wave at a frequency $f = 10$ MHz.

Coordinate grid: h is the height above the Earth's surface, and s is the length along the beam. The elevation angle $\beta = 30^\circ$ is set, and the azimuth $\gamma = 90^\circ$ of the radiation for the reference beam of the transmitter. The radiation of the transmitter in a beam with a narrow angular solution ($\Delta\beta = 20^\circ$, $\Delta\gamma = 20^\circ$) in the vicinity of the reference beam is considered. World Time UT = 4.65 hours.

Figure 1b represents graphs of the time dependence of the group (curve 1) and phase (curve 2) delay of the signal along the reference beam:

$$\Delta t_{gp} = \int_0^s \frac{ds}{g},$$

$$\Delta t_{\phi} = \frac{1}{c} \int_0^s d\Psi = \frac{1}{c} \int_0^s n' \cos(\mathbf{p} \wedge \mathbf{g}) ds,$$

where n' is the real part of the medium refractive index for the distinguished normal mode, p is the momentum, c is the speed of light, g is the group velocity, and Ψ is the eikonal.

The rationale for the choice of $\Delta\beta$ and $\Delta\gamma$ values was carried out by means of numerical experiments. It is taken into account that a decrease in $\Delta\beta$ and $\Delta\gamma$ increases the accuracy of calculations up to the resolution of the used models of the ionosphere and neutral atmosphere.

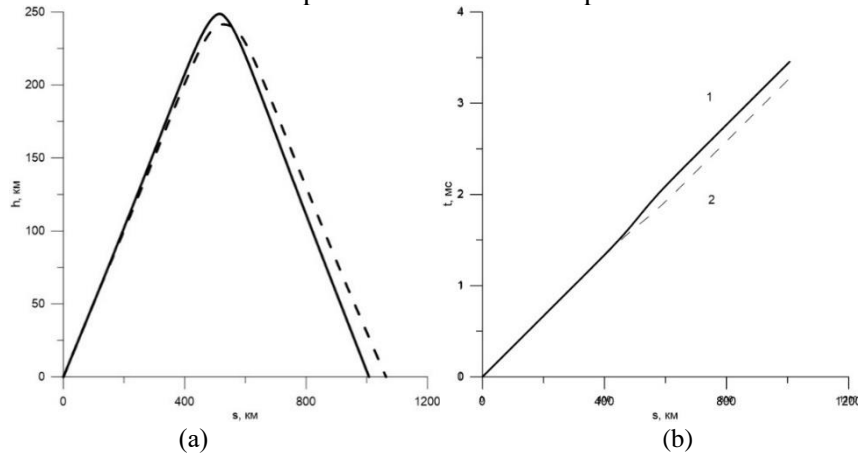


FIGURE 1. Beam paths for an ordinary wave (solid line) and an extraordinary wave (dashed line) in the (h, s) plane at a frequency of 10 MHz – (a); group delay (curve 1) and phase delay (curve 2) along the ray path for an ordinary wave – (b).

The lower boundary of the ionosphere in the model corresponds to an altitude of $h = 60$ km. The refractive index of the neutral atmosphere for short waves at altitudes $0 < h < 60$ km is taken to be unity. Figure 1a shows that when passing from a neutral atmosphere to the ionosphere, the beam experiences birefringence. The turning point of the beam corresponding to an ordinary wave (on a solid line) in the ionosphere is higher than in the case of an unusual wave (on a dashed line).

The results in Figure 1 do not take into account the influence of medium absorption on the formation of ray paths and the inhomogeneity of the wave structure. In [5], the method of complex geometric optics was applied, which made it possible to take into account the coordinated character of the formation of ray paths and wave absorption in a smoothly inhomogeneous medium.

For the illuminated region, the radius vector of the observation point remains a real quantity, but the complex momentum vector $\mathbf{p} = p\mathbf{l}$ is introduced (\mathbf{p} is the complex momentum vector, \mathbf{l} is the unit vector in the direction of the momentum vector), $p = n = n' + jn''$, where n'' is the imaginary part of n . The imaginary part of the refractive index is due to the presence of absorption in the medium. Collisions of particles in a plasma affect both n' and n'' .

In [5], integrating the eikonal equation in the phase space $\{p_i, q_i\}$, $i = 1, 2, 3$, - of the momentum and generalized coordinates, the ray equations were found

$$\frac{dq_i}{d\tau} = \text{Re} \left(\frac{\partial H}{\partial p_i} \right) \left(1 + \left(\frac{\text{Im} \left(\frac{\partial H}{\partial p_i} \right)}{\text{Re} \left(\frac{\partial H}{\partial p_i} \right)} \right)^2 \right), \quad \frac{dp_i}{d\tau} = - \left(1 - j \frac{\text{Im} \left(\frac{\partial H}{\partial p_i} \right)}{\text{Re} \left(\frac{\partial H}{\partial p_i} \right)} \right) \frac{\partial H}{\partial q_i}, \quad (1)$$

where H is the Hamilton function of the system, τ is an independent integration variable along each ray. For a weakly absorbing medium, the problem has a small parameter: $n''/n' \ll 1$. Decomposition up to second-order quantities gives:

$$|p| = \sqrt{(n')^2 + (n'')^2} \approx n' \left(1 + \frac{1}{2} \left(\frac{n''}{n'} \right)^2 \right)$$

and up to the first order of smallness - $|p| \approx n'$ and $p \approx n'l$, where n' depends on the frequency of particle collisions in the medium.

In [6], system (1) was integrated for a one-dimensional model of the ionosphere layer with absorption, but without taking into account plasma anisotropy. For the inclined incidence of the ray paths onto the layer, it was found that as the absorption increases (increase in the ratio n''/n'), the penetration of rays into the layer increases. The reflection of the beam from the layer can be replaced by the passage of the beam through the layer.

In this paper, studies were continued in relation to a three-dimensionally inhomogeneous anisotropic model of the ionosphere plasma. At a radiation frequency that is substantially less than the critical frequency of the ionospheric layer, the effect of absorption on the formation of ray paths is weak. However, the effect is enhanced as the rays penetrate into the vicinity of the maximum electron concentration due to a decrease in the real part of the refractive index of the plasma and an increase in the imaginary part of the refractive index of the ionosphere.

1. E.R. Tracy, A. J. Brizard, A. S. Richardson, A. N. Kaufman, Ray Tracing and Beyond, *Phase Space Methods in Plasma Wave Theory*, Cambridge University Press, 2014. 505 p
2. A. E. Hedin, Extension of the MSIS thermospheric model into the middle and lower atmosphere, *J. Geophys. Res.*, 1991, 96(A1), pp. 1159–1172.
3. D. Bilitza, D. Altadill, Y. Zhang et al., The International Reference Ionosphere 2012 – a model of international collaboration, *J. Space Weather and Space Clim.*, 2014, 4(A07), doi:10.1051/2014004.
4. V. E. Zakharov, Amplitude Formation and polarization characteristic of short waves for distribution in the ionosphere, *Communications technology and electronics*, 2019, 64(6), pp. 525-534. (in Russian).
5. V. E. Zakharov, D. S. Kotova, Short radio wave distribution model in the Ionosphere in the complex approximation geometric optics, *Propagation of radio waves*, 2011, 3, pp.336-339. (in Russian).
6. V. E. Zakharov, D. S. Kotova, Research of beam trajectories, absorption and homogeneous short radio wave structure in the ionosphere, *Propagation of radio waves*, 2011, 3, pp.340-342. (in Russian).

IMPACT OF NATURAL IONIZATION SOURCES ON ATMOSPHERIC ELECTRICITY

Eugene Rozanov^{1,2}, Ilya Usoskin^{3,4}, and Kseniia Golubenko^{4,5}

¹*PMOD/WRC and IAC ETHZ, CH-7260, Davos, Switzerland*

²*West Department of Pushkov Institute of Terrestrial Magnetism, Ionosphere, and Radio Wave Propagation, Russian Academy of Sciences, Kaliningrad, Russia*

³*Space Physics and Astronomy Unit, University of Oulu, Finland*

⁴*Sodankyla Geophysical Observatory, Oulu, Finland*

⁵*St. Petersburg State University, St. Petersburg, Russia*

Introduction. We performed and analyzed several model experiments with the chemistry-climate model (CCM SOCOL) for the 2004-2005 time period. The atmospheric ionization rates produced by Rn-222 and galactic cosmic rays (GCR) were used to calculate the global distribution of the atmospheric conductivity and fair-weather vertical current density (J_z). We also evaluated the impact of the extreme solar proton event (SPE), corresponding to the 774 AD event, on the atmospheric electricity and found that it would lead to a large (up to 6-10 times depending on region) enhancement of J_z on the global scale. The objectives of the work are i) development of the new model version allowing numerical simulations of ionization from Rn-222; ii) calculation of the global distribution of the atmospheric conductivity and fair-weather current density (J_z) using the ionization produced by GCR, SPE, and Rn-222. To reach these objectives we added emission, decay, and advective transport of Rn-222 to the CCM SOCOL. For the convective transport, we apply dry convection scheme for regions with instability layers and wet convection for regions with convective cloudiness [1]. When a column of air is unstable with respect to a dry lapse rate, the air gets mixed uniformly within the column. When a column of air is unstable with respect to a wet lapse rate, 50 % of the air in the lowest layer of the column moves directly to the highest layer at which it is stable, with no entrainment of air from intermediate layers. Then this air mass descends and mixes homogeneously with the air from intermediate layers.

Experiments. We performed several 2-year long model experiments for the 2004-2005 period for two different cases. For the first case, we used the CCM SOCOL to simulate the variability of ionization rates and conductivity in the clean air (ignoring aerosol and clouds), thus considering only galactic cosmic ray flux and radon, the latter affecting only the lower troposphere. We showed that the radon contribution leads to an enhanced variation in ionization rates near the surface. In the free troposphere between 300 and 700 hPa, ionization rates are defined mostly by galactic cosmic rays (GCR). For the second case, we estimate the effects of an extreme SPE, corresponding to the 774 AD event [2], on the atmospheric electricity.

Results. Strong SPEs are very rarely occurring events, while the quiet scenario with the ionization induced only by GCR and Rn-222 is observed during most of the time. In this case (see Figure 1), the atmospheric vertical current density maximizes (reaching ~ 3.8 pA/m²) in radon source regions and in the polar regions, where the GCR induced ionization is the highest. Contribution of Rn-222 is essential in middle- and low-latitude/altitude regions where the GCR-induced air conductivity is significantly lower than that at greater heights/latitudes.

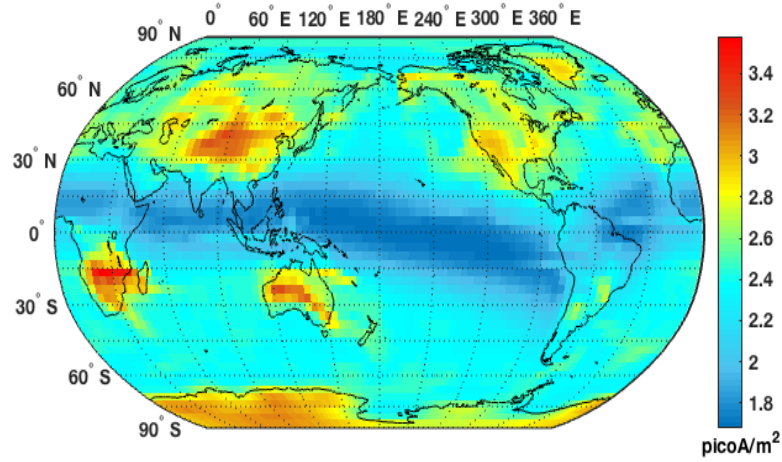


FIGURE 1. Global map of the vertical current density distribution (pA/m^2) for the quiet scenario (GCR+Rn-222).

The maps of the fair-weather vertical current are shown in Figure 2 for the scenario with extreme SPE. In this case, J_z is dramatically enhanced, particularly in high-elevated polar regions (Greenland and Antarctica), of the vertical atmospheric current density, reaching $\sim 90 \text{ pA/m}^2$ in high-elevated polar regions, with only a small enhancement in equatorial regions.

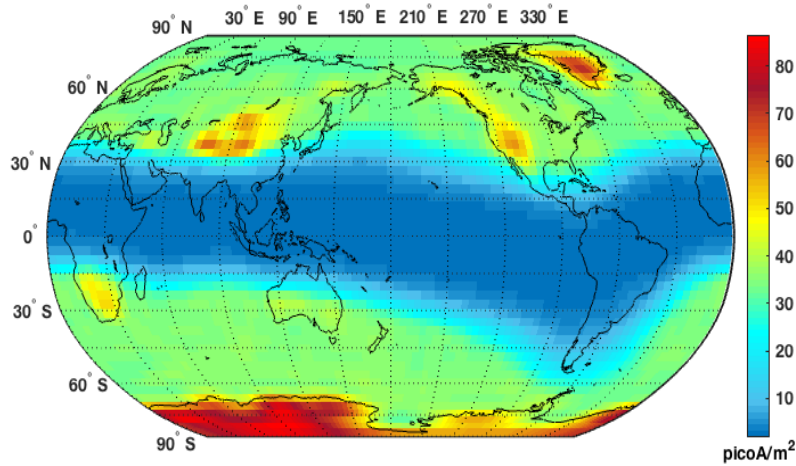


FIGURE 2. Global map of the vertical current density distribution (pA/m^2) for the extreme scenario (GCR+Rn-222+SPE).

We note that only the effects of the increased ionization rate due to solar energetic particles were considered here, while other effects, such as the influence of a geomagnetic storm on the ionospheric potential, were not, making this estimate conservative. It is concluded that an extreme solar particle event may lead to a dramatic (a factor of up to 30) increase of the vertical atmospheric current density, reaching $\sim 90 \text{ pA/m}^2$ in high-elevated polar regions, with only a small enhancement in equatorial regions.

Acknowledgments: This work partially supported by the Academy of Finland (Projects ESPERA no. 321882, CRIPA-X no. 304435, HEAIM no. 314982 and no. 316223). The discussions and short-term science missions of KG and IU to PMOD/WRC supported by European COST Action CA15211

(ELECTRONET) made this work possible. ER work on the ionospheric potential calculation module was supported by the Russian Science Foundation, grant no. 17-17-01060.

1. D. Jacob and M. Prather, Radon-222 as a test of convective transport in a general circulation model, *Tellus B: Chemical and Physical Meteorology*, 1990, 42 (1), pp. 118-134, doi:10.3402/tellusb.v42i1.15196.

2. F. Mekhaldi, Muscheler, R., Adolphi, F. *et al.* Multiradionuclide evidence for the solar origin of the cosmic-ray events of AD 774/5 and 993/4, *Nat Commun*, 2015, 6, pp. 8611, doi:10.1038/ncomms9611.

ARTIFICIAL PRECIPITATION OF ENERGETIC ELECTRONS FROM THE EARTH' RADIATION BELT

Alexander O. Ryabov, Vladimir L. Frolov

Lobachevsky State University of Nizhny Novgorod, Nizhny Novgorod, Russia

Introduction. Modification of the F_2 -region of the ionosphere by powerful HF radio waves of ordinary polarization leads to the development of various nonlinear phenomena and plasma instabilities in it. This causes generation of high-frequency and low-frequency plasma turbulence near the reflection height of the pump wave, strong plasma heating, acceleration of electrons to superheat energies, generation of electric fields and currents, changing the shape of the plasma profile, etc. It also leads to modification of ionospheric-magnetospheric bonds, causing precipitation of energetic electrons from the Earth's radiation belt. The first results directly confirming the possibility of stimulating the precipitation of energetic electrons with energies $E \approx 100$ Kev in the mid-latitude ionosphere were obtained at the SURA stand during an experiment performed on May 12, 2008 [1]. The report presents the results of research on stimulating the precipitation of energetic electrons from the Earth's radiation belt when modifying the mid-latitude ionosphere with powerful O-polarization radio shortwaves continuously emitted by the SURA stand, and the effect of these electrons on the lower layers of the ionosphere. These studies are based on those performed in 2005-2010. Experiments were made at the program of the SURA-DEMETER [2]. Modification of the ionosphere was performed using the SURA heating stand. Data on energetic electrons were obtained using the IDP spectrometer installed on board the Demeter spacecraft, which could measure the energy and flow of electrons in the energy range of 70 keV – 2.5 MeV.

Conditions and results of the experiments. We use the results obtained with the onboard equipment of the *DEMETER* French microsatellite with an orbital height of about 660 km. The SURA heating facility is located to the east of Nizhny Novgorod (56.15° N, 46.1° E). The effective radiation power of the facility monotonically increases with increasing frequency f_r : from 80 MW at $f_r = 4300$ kHz to 280 MW at $f_r = 9300$ kHz.

Experiments. In this paper, we will talk about two blocks of experiments: the first one concerns artificial precipitations over the SURA stand; the second concerns artificial precipitations in the magnetically conjugated region.

Artificial precipitations over the SURA stand. To separate artificial and natural precipitations of energetic electrons near the SURA stand, the results of measurements of energetic electron fluxes were selected and analyzed in the absence of exposure to high-power HF radio radiation on the F_2 -region of the ionosphere. This allowed us to establish that the precipitation of energetic electrons near the SURA stand is recorded at high geomagnetic activity with an index $AE \geq 500$ nT and doesn't fall below latitudes 62 – 65°N at a low level of activity with $AE \leq 200$ nT.

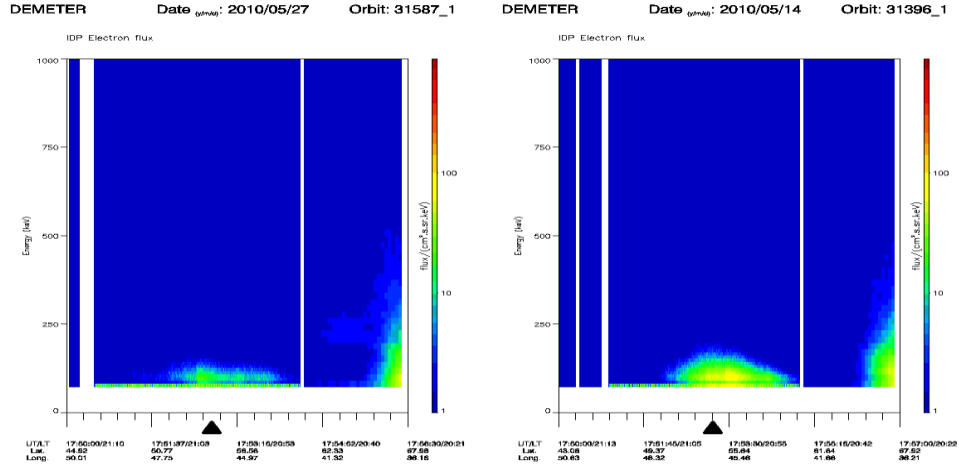


FIGURE 1. Spectral characteristics of precipitating energetic electrons in the presence of a plasma density constant (panel on the left) and in its absence (panel on the right).

The experiments allow us to conclude that artificial precipitations of energetic electrons stimulated by ionosphere modification weren't registered when the conditions for generating intense plasma perturbations near the reflection height of the pump wave weren't met. These conditions fully meet the requirements for generating intense artificial ionospheric turbulence and generating ducts with high plasma density at altitudes of the outer ionosphere [2], although these conditions are not sufficient to stimulate artificial precipitations, for example, when the geomagnetic conditions remained calm for a long time before measurements and there were no energetic electrons in the radiation belt.

Examples of artificial precipitations are shown in Fig. 1, where the panel on the left shows precipitations in the presence of duct with increased plasma density, and the panel on the right shows intense precipitations when the density duct wasn't registered. It can be seen that the presence of duct leads to an increase in both the energy of the precipitating electrons and their flow.

The results of the performed measurements allow us to formulate signs of an artificial precipitations of energetic electrons from the Earth's radiation belt, observed during the modification of the ionosphere by powerful HF radio waves in the late evening and pre-midnight hours. This is: 1) the maximum intensity of precipitations is observed inside the disturbed magnetic force tube (especially in the presence of duct with increased plasma density) or near it; 2) in the plane of the geomagnetic meridian, the intensity of the precipitation gradually decreases towards the north, extending to the region of auroral latitudes, and much more sharply to the south; 3) the energy of the precipitating electrons is on average ~ 100 keV; 4) precipitations occur when the effective radiation power of pump wave exceeds 40 MW and the effective interaction of powerful radio waves with the plasma in the F_2 -region of the ionosphere. The performed research allowed us to establish that the region of energetic electron precipitations stimulated by ionosphere modification has spatial dimensions of ~ 1100 km along the geomagnetic meridian up to 400 km across it with its greater length to the north of the stand.

Artificial precipitations in the magnetically conjugate region (relative to stand SURA). One of the interesting problems associated with the modification of the F_2 -region is the analysis of the ionosphere characteristics in the magnetically conjugate region relative to the region disturbed by ground transmitters.

During the experiments on the generation of precipitation in the magnetically conjugate region, we used different time modes for heating the disturbed region, but usually the heating lasted 30-45 minutes, and was switched on 25-40 minutes before the flight of DEMETER above the stand through a perturbed magnetic force tube. These conditions were very different from experiments where the purpose was to

modify the upper ionosphere directly above the stand, when the heating time was about 15 minutes. This is due to the fact that to create appreciable disturbances in the magneto-conjugate region, we need to stimulate the ionosphere more time than in the case of heating the area above the stand.

An important issue related to the analysis of the experiments was the location of the magneto-conjugate region. There are different models of calculations of magnetically conjugate points (IZMIRAN, IKI RAS, NASA). For the region disturbed by the radio emission of the SURA stand, the magneto-conjugate is the region centered at coordinates 40.5 south latitude, 61.5 east longitude.

In the course of our experiments we determined the conditions of artificial precipitation stimulation:

- $f_{PW} \leq f_{0F2}$ (preferably $f_{0F2} - f_{PW} \geq 0.5$ MHz)
- $P_{eff} \geq 50$ MW
- heating time - more than 40 minutes
- flight - near magnetically conjugate region center

At the Fig. 2 at the left picture shows session when SURA stand was turned off. The black triangle marks the place of maximum convergence with the center of the perturbed power tube. The energy and flux values in this session were small. At the right picture - session when SURA stand was turned on. Energy is equal approximately 200 keV, and flux is 100 conventional units and more. The maximum size of the areas in which artificial precipitation are observed is about 2000 kilometers along the geomagnetic field and 500 kilometers across the geomagnetic field. There have been many such sessions, but these are the most effective.

An important indicator distinguishing artificial precipitation from natural was the more noticeable energy fall between Aurora and the magnetically conjugate region. Of course, this fall is observed in natural conditions too, but in the cases, when SURA works efficiently, it becomes more noticeable.

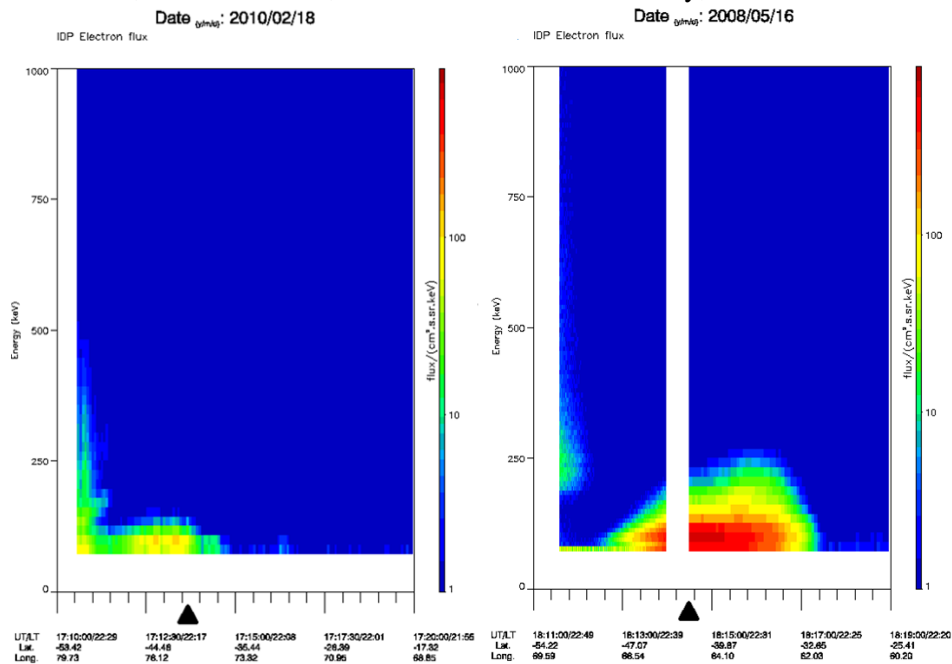


FIGURE 2. Spectral characteristics of precipitating energetic electrons. Left picture – when stand was switched off, right – when stand was switched on.

So, the experiments about stimulation precipitation in magnetically conjugate region gave next results: 1) the values of electron energy is about 200 keV and electron flux is about 100 conventional units, which is more higher than its in nature conditions; 2) the maximum of precipitation is observed

in the center of magnetically conjugate region; 3) There is increase energy fall between Aurora and center of the magnetically conjugate region (46^0 - 53^0 degrees of south longitude).

Conclusion. Comparing two groups of experiments, we can say next. The values of electron energy is close, electron flux is higher in magnetically conjugate region sessions and the size of the precipitation area is larger in magnetically conjugate region sessions (2000 km against 1100 km).

It is assumed that the mechanism of stimulation of precipitation is determined by the interaction of energetic electrons with VLF electromagnetic waves, which are generated in the region of interaction of the pump wave with ionospheric plasma by means of excitation of lower hybrid plasma oscillations and their scattering from small-scale plasma density irregularities [3].

Ryabov's research was carried out with the support of the RFBR (grant № 19-52-15007). Frolov's investigation was made with the support of the RFBR (grant № 20-05-00166A).

1. G.A. Markov, A.S. Belov, V.L. Frolov, et al. Excitation of a magnetospheric maser through modification of the Earth's ionosphere by high-power HF radio emission from a ground-based transmitter, *Journal of Experimental and Theoretical Physics*, 2010, 111(6), pp. 916-920.

2. V.L. Frolov, V.O. Rapoport, E.A. Schorokhova, et al. Features of the electromagnetic and plasma disturbances induced at the altitudes of the Earth's outer ionosphere by modification of the ionospheric F_2 -region using high-power radio waves radiated by the SURA heating facility, *Radiophysics and Quantum Electronics*, 2016, 59(3), pp. 177-198.

3. A. Vartanyan, G. M. Milikh, B. Eliasson, et al. Generation of whistler waves by continuous HF heating of the upper ionosphere, *Radio Sci.*, 2016, 51, pp. 1188–1198, doi:10.1002/2015RS005892.

THE MODELS OF THE QUASISTATIONARY ELECTRIC FIELD PENETRATION FROM THE GROUND TO THE MIDDLE LATITUDES IONOSPHERE

Semen A. Nesterov¹, Valery V. Denisenko¹, Mohammed Y. Boudjada², and Helmut Lammer²

¹ Institute of Computational Modelling, Russian Academy of Science, Krasnoyarsk, Russia

² Space Research Institute, Austrian Academy of Sciences, Graz, Austria

Introduction. Interest in the lithosphere-atmosphere-ionosphere relationship is mainly caused by the need to forecast earthquakes. Since several satellite observations show ionospheric electric field perturbations above seismic regions. Nowadays, the most popular models consider the lithosphere as a generator of an electric current or an electric field in the atmosphere. At the present time, three- and two-dimensional models of a conductor that includes the atmosphere and the ionosphere are known [1, 5]. However, such models are created for a vertical magnetic field, and therefore they are applicable only at high latitudes. Some new models are analyzed in article [4]. The purpose of this work is to build a quantitative model of the penetration of a quasistationary electric field from the Earth's surface into the ionosphere with an inclined magnetic field.

Here we study two cases when the earthquake preparation zone is extended along the magnetic meridian or in the normal direction. The origin of coordinates is located in the epicenter, the x-axis is directed along the tectonic fault, the y-axis is horizontal and normal to the x- and z-axis and is directed from the ground to the ionosphere. In the first model we assume that the distribution of the electric field depends only on the y and z coordinates, and only on the x and z coordinates in the second model.

Basic equation. The basic equations for the steady state electric field \mathbf{E} and current density \mathbf{j} are Faraday's law, the charge conservation law, and Ohm's law, which for the electric potential V can be reduced to the electric conductivity equation

$$-\text{div}(\hat{\sigma} \text{grad } V) = 0, \quad (1)$$

where $\hat{\sigma}$ is the conductivity tensor.

Conductivity. In the main part of the atmosphere up to a height of 50 km, we use the empirical conductivity model [7]. Above 50 km the influence of the magnetic field is manifested, and the conductivity becomes a gyrotropic tensor $\hat{\sigma}$ which components are, respectively, $\sigma_p, \sigma_H, \sigma_{\parallel}$ - Pedersen, Hall and field-aligned conductivities [6]. Since we are considering local phenomena, we neglect the curvature of the Earth's surface. The magnetic induction vector \mathbf{B} is located in the x-z plane. The magnetic inclination I is the angle between the direction to the magnetic north pole and \mathbf{B} vector. Above 90 km we use the model [2], which is based on the empirical models IRI, MSISE and IGRF. Since we consider local phenomena, conductivity is regarded as dependent only on the vertical coordinate z . In the layer $50 < z < 90$ km the values for σ_p and σ_{\parallel} are interpolated, and we use the formula $\sigma_H = (\sigma_p(\sigma_{\parallel} - \sigma_p))^{1/2}$, which is typical for plasma with one predominated kind of charged particles [6].

Boundary value problem. The electric conductivity equation (1) takes shape:

$$-\frac{\partial}{\partial y} \left(\sigma_{yy}(z) \frac{\partial V(y, z)}{\partial y} \right) - \frac{\partial}{\partial z} \left(\sigma_{zy}(z) \frac{\partial V(y, z)}{\partial y} + \sigma_{zz}(z) \frac{\partial V(y, z)}{\partial z} \right) = 0, \quad (2)$$

where $\sigma_{yy} = \sigma_p$, $\sigma_{zy} = \sigma_H \cos I$, $\sigma_{zz} = \sigma_p \cos^2 I + \sigma_{\parallel} \sin^2 I$.

On the surface of the Earth, like many other authors, we assume a given distribution of the vertical component of the perturbation of the electric field strength. This corresponds to the boundary condition of the form

$$E_z|_{z=0} = E_z^0(y) = E_0 \gamma (1 + \cos(\pi y / y_0)) \sin(\pi y / y_0), \quad (3)$$

where a simple horizontal distribution is considered due to the lack of electric field observations. Here $y_0 = 300$ km – typical width of the seismic preparation zone, $E_0 = 100$ V/m, which is typical for a moderate earthquake, $\gamma \approx 0.77$ is normalization factor.

The ionosphere as a conductor is not bounded from above since there is the magnetosphere, which is a rather complicated object. In this work, we do not take into consideration the polar caps and the auroral zones, and so the conjugate ionosphere is considered in our model. The values of the potential at the conjugate points at the upper boundary of the ionosphere, $z = z_{\infty}$, are assumed to be equal due to the high conductivity along magnetic field lines in the magnetosphere. In the conjugate ionosphere, the same equation (2) is valid with the boundary condition

$$E_x(\tilde{y}, \tilde{z})|_{\tilde{z}=0} = 0, \quad (4)$$

which corresponds to the highest conductivity of ground and sea water.

The vertical electric field near the Earth's surface only exists in certain area $|y| < y_0$. We substitute it with the periodicity condition with the large period $2L \gg y_0$, we take $L = 10y_0$. It means the

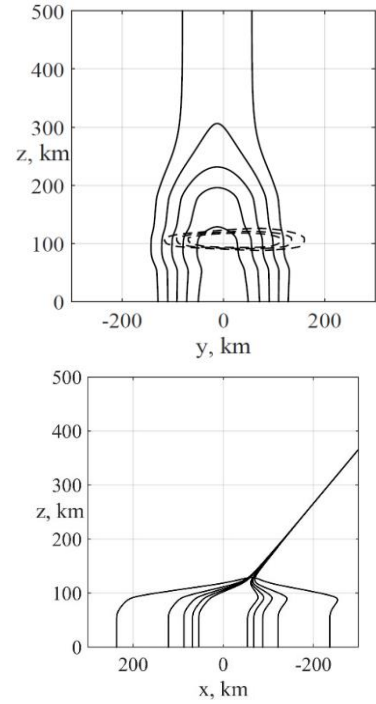


FIGURE 1. Projections in the y-z and x-z planes of the current lines (solid lines) and contour lines of j_x (dashed lines) above the earthquake preparation zone.

periodical continuation over the whole y -axis of the potential $V(y, z)$ and $E_z^0(y)$ (3). The periodical solution for the boundary value problem (2-4) exists and it is unique. We numerically solve this problem using Fourier transform in the same way as in [5].

The main results. Figure 1 shows the projections in the y - z and x - z planes of the current lines (solid lines) when the magnetic field inclination equals $I = 45^\circ$. A current of 0.45 pA/m flows between adjacent lines. The dashed lines indicate the contour lines of the x -component of the current density with a contour interval equal to 1 pA/m². In this model, the electric field strength vector lies in the y - z plane. Therefore, the x -component of the current density is due only to the Hall conductivity. The figure shows that the main part of the j_x current density is concentrated at altitudes of about 100 km, as a result of which the current lines in this area are elongated in the direction of the x -axis.

The bottom panel of Fig. 1 displays the same current lines projections in the x - z plane. The current line passing through the region of the highest concentration of the x -component of the current density is much more extended along the x -axis than the other current lines. Because of $\sigma_{\parallel} \gg \sigma_p$ in the ionosphere E_{\perp} is almost independent of the height and its maximum is about 1.3 μ V/m. The field-aligned component E_{\parallel} is small in the ionosphere in comparison with E_{\perp} .

We have done calculations for different magnetic inclinations. A slight dependence of $E_{\perp}(I)$ maximum value in the ionosphere is obtained, $E_{\perp} \approx 1.37, 1.36, 1.28$ μ V/m for $I = 90^\circ, 55^\circ, 20^\circ$, respectively.

$E_{\perp}(I)$ varies much stronger, approximately as $|\sin I|$ [5] when the earthquake preparation zone is perpendicularly extended to the direction of the magnetic meridian. Generally a 3-D model is necessary when the earthquake preparation zone is finite in both horizontal directions. However one can expect some decrease of $E_{\perp}(I)$ in middle and low latitudes.

It ought to be mentioned that in the vicinity of the geomagnetic equator the models with conductivity tensor (i.e. Cartesian components) depends only on the height cannot be used because of the curvature of the magnetic field lines in this equatorial region.

Conclusions. We find in our preliminary investigation a decrease in the strength of the electric field, penetrating the ionosphere, in low magnetic latitudes. This is in agreement with previous investigations. In the constructed model, the obtained electric field is three orders of magnitude smaller than the field variations observed in the ionosphere before strong earthquakes. Therefore, the model confirms the conclusion about the need to explore other physical mechanism of lithosphere-atmosphere-ionosphere coupling.

The research is supported by Russian Foundation for Basic Research (project 18-05-00195).

1. V. V. Denisenko, M. Ampferer, E. V. Pomozov, A. V. Kitaev, W. Hausleitner, G. Stangl and H. K. Biernat, On electric field penetration from ground into the ionosphere, *J. Atmosph. Solar-Terr. Phys.*, 2013, 102, pp. 341–353, doi: 10.1016/j.jastp.2013.05.019.
2. V. V. Denisenko, H. K. Biernat, A. V. Mezentsev, V. A. Shaidurov, S. S. Zamay, Modification of conductivity due to acceleration of the ionospheric medium, *Ann. Geophys.*, 2008, 26, pp. 2111–2130.
3. V. V. Denisenko, M. Y. Boudjada, M. Horn, E. V. Pomozov, H. K. Biernat, K. Schwingenschuh, H. Lammer, G. Prattes and E. Cristea, Ionospheric conductivity effects on electrostatic field penetration into the ionosphere, *Natural Hazards Earth Syst. Sci.*, 2008, 8, pp. 1009–1017, doi: 10.5194/nhess-8-1009-2008.
4. V. V. Denisenko, M. Y. Boudjada and H. Lammer, Propagation of seismogenic electric currents through the Earth's atmosphere, *J. Geoph. Res.: Space Phys.*, 2018, 123(5), pp. 4290–4297, doi: 10.1029/2018JA025228.

5. V. V. Denisenko, S. A. Nesterov, M. Y. Boudjada and H. Lammer, A mathematical model of quasistationary electric field penetration from ground to the ionosphere with inclined magnetic field, *Journal of Atmospheric and Solar-Terrestrial Physics*, 2018, 179, pp. 527-537, doi: 10.1016/j.jastp.2018.09.002.

6. J. K. Hargreaves, The upper atmosphere and Solar-terrestrial relations, *Van Nostrand Reinold Co Ltd*, NY, 1979.

7. M. J. Rycroft and A. Odzimek, Effects of lightning and sprites on the ionospheric potential, and threshold effects on sprite initiation, obtained using an analog model of the global atmospheric electric circuit, *J. Geophys. Res.*, 2010, 115(A00E37) doi: 10.1029/2009JA014758.

NUMERICAL STUDY OF THE PROPAGATION OF ATMOSPHERIC WAVES FROM THE TROPOSPHERE SOURCE

Sergey P. Kshevenskii¹, Yuliya A. Kurdyeva²

¹*Immanuel Kant Baltic Federal University, Kaliningrad, Russia*

²*West Department of Pushkov Institute of Terrestrial Magnetism, Ionosphere and Radio Wave Propagation Russian Academy of Sciences, Kaliningrad, Russia*

Introduction. Tropospheric heat sources (clouds for example) are a continuous source of atmospheric waves. Such sources can be considered localized or consisting of a combination of many sources, but localized of small sizes (a typical size is from one to several kilometers). When gas is heated by heat sources, there is no determined direction of wave propagation, and therefore at the height of the source, the amplitudes of the waves propagating up and down from the tropospheric heat sources are the same. Reaching the Earth's surface, waves from tropospheric sources change the surface pressure. Reflected from the surface of the Earth, these waves propagate upward, along with the waves propagating upward directly from heat sources. Their propagation upward together with waves propagation directly from tropospheric sources can significantly affect the state of the upper atmosphere.

In paper [1, 2] is proposed used of experimental data on pressure variations on the Earth's surface for the numerical study of the propagation of waves from the lower atmosphere to the upper. However, the question arises of how pressure on the Earth's surface is associated with meteorological processes and what error is introduced when replacing tropospheric meteorological sources with experimentally observed pressure fluctuations on the Earth's surface. This work is devoted to a numerical study of this question.

Numerical experiment. The numerical model "AtmoSym" [3-5] used in the study and it based on solving a system of nonlinear hydrodynamic equations for atmospheric gas in a gravitational field. The dependences of the parameters of the environ (viscosity, thermal conductivity, background density, background temperature) in the numerical model are taken from the empirical model of the atmosphere. The computational grid in the numerical model is non-uniform along the vertical, the optimal vertical grid is constructed by the program based on real stratification of the environ.

A small model tropospheric thermal source was considered and the propagation of waves from it up to the thermosphere was calculated. The peculiarity of this numerical experiment is a two-step approach:

1. Pressure variations near of the Earth surface caused by the work of a heat source are recorded.
2. The obtained pressure variations on the boundary surface are used to new calculate the propagation of waves upward from pressure variations.

The model heat source is set as (1):

$$f(x,z,t)=\exp(-((x-x_0)/D_x)^2-((z-z_0)/D_z)^2)(1-t/\tau)\sin(\omega t). \quad (1)$$

Here, the parameter x_0 is center the location of the source in the computational domain. The parameters z_0 , D_x , and D_z specify the location and dimensions of the heat source, which in our model simulates the

heating / cooling of atmospheric gas during phase transitions of water in the atmosphere. It is assumed that these parameters approximately correspond to the size and location of a typical small cloud, since condensation of water vapor not only entails heat generation, but also leads to the formation of clouds. The parameter $\tau = 300$ second was introduced for slow switching on the source in order to suppress possible processes. We will further solve the problem of the propagation of waves from a source operating at infrasound frequencies, where in this case $2\pi / \omega = 3$ minutes and from a source operating at the frequency of internal gravity waves, where in this case $2\pi / \omega = 30$ minutes. We hope that all other sources working at other frequencies and potentially interesting for our study work qualitatively like some of the sources we analyze, and therefore studying only these two sources is enough.

Discussion. Fig. 1 shows the calculation results for time instants $t=13$ min and $t=19$ min. The upper panel shows the results of numerical calculations of the wave pattern from the tropospheric source $f(x, z, t)$ with a period $=180$ s, the bottom panel shows the wave pattern from the boundary source on the Earth's surface, and the specified boundary pressure fluctuations are obtained from the solution of the first problem. It can be seen that the wave pattern from the tropospheric source and from the surface source are very similar, and the difference in the wave amplitudes does not exceed 10%.

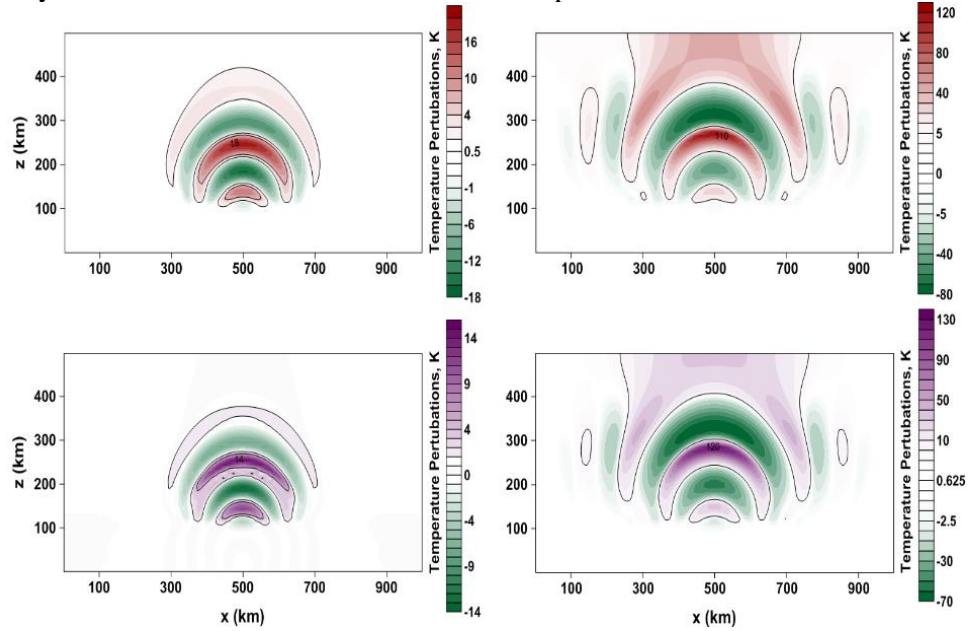


FIGURE 1. Temperature perturbations fields for $t = 13$ min (left) and for $t = 19$ min (right). The wave panel from above (red-green) was made by the heat source $f(x, z, t)$ with an oscillation period of 180 seconds. The wave panel below (violet-green) is from the recorded pressure variations at the lower boundary.

The obtained coincidence of wave patterns from the tropospheric and boundary sources shows that the problem of waves from a tropospheric source above the earth's surface can be replaced by the problem of waves from a boundary source. The problem of waves from a boundary source has the advantage that the pressure on the surface of the earth is experimentally recorded by networks of microbarographs, or the field pressure on the ground can be obtained from some other indirect measurements. At the same time, tropospheric heat sources are located at an altitude of several kilometers, while they have a complex spatial structure, which makes it difficult to obtain detailed experimental information about these sources.

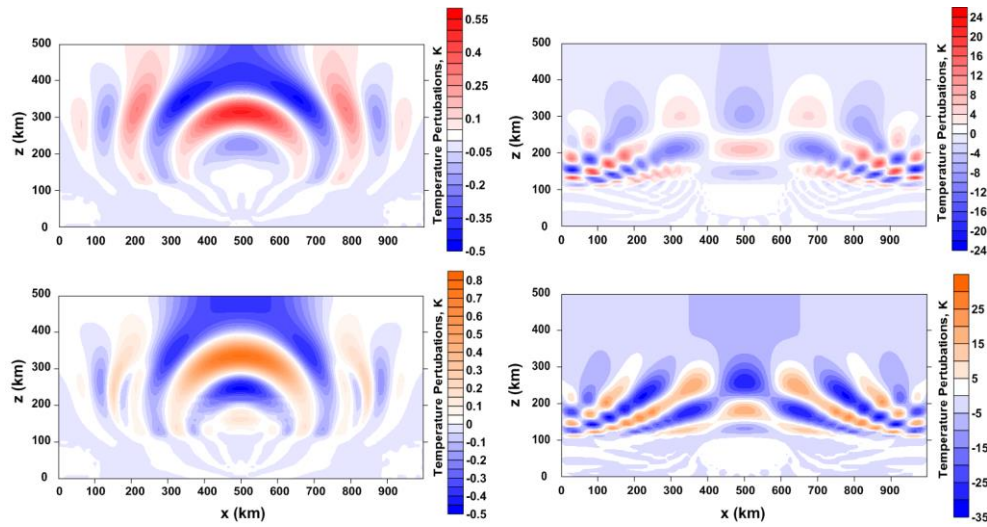


FIGURE 2. Temperature perturbations fields $t=19$ min (left) and for $t=85$ (right). The wave panel from above (red-blue) was making by the heat source $f(x, z, t)$ with an oscillation period of 1800 seconds. The wave panel below (orange-blue) is from the recorded pressure variations at the lower boundary.

If the tropospheric source work at frequencies of internal gravitational waves (Fig. 2), then the general coincidence of the wave pattern from the tropospheric source with the wave pattern from pressure fluctuations on the Earth's surface also have, but the quality of this coincidence is worse.

However, this information is sufficient, for example, to estimate the amplitudes of waves from tropospheric sources reaching heights of the upper atmosphere. For a more exact coincidence of amplitudes and patterns, it is probably possible to use an approach that takes into account the difference in pressure from time, which is equal to twice the propagation time of waves from a source to the Earth's surface

Acknowledgments. *This work was funded by the Russian Foundation for Basic Research and the government of Kaliningrad region (project no. 19-45-390005).*

1. Y. A. Kurdyayeva, S. P. Kshevetskii, N. M. Gavrilo et al., Correct Boundary Conditions for the High-Resolution Model of Nonlinear Acoustic-Gravity Waves Forced by Atmospheric Pressure Variations, *Pure Appl. Geophys.*, 2018, 175, pp. 3639–3652, doi:10.1007/s00024-018-1906-x.

2. Y. Kurdyayeva, S. Kulichkov, S. Kshevetskii et al., Propagation to the upper atmosphere of acoustic-gravity waves from atmospheric fronts in the Moscow region, *Annales Geophysicae*, 2019, 37(3), pp. 447-454, DOI:10.5194/angeo-37-447-2019.

3. S. P. Kshevetskii, Modelling of propagation of internal gravity waves in gases, *Comp. Math. Math. Phys.*, 2001a, 41, pp. 295-310.

4. S. P. Kshevetskii, Numerical simulation of nonlinear internal gravity waves, *Comp. Math. Math. Phys.*, 2001b, 12, pp. 1777-1791.

5. S. P. Kshevetskii, Analytical and numerical investigation of non-linear internal gravity waves, *Nonlinear Proc. Geoph.*, 2001, 8, pp. 37-53.

ANALYTICAL AND NUMERICAL MODELING OF THE ACOUSTIC WAVE DISTURBANCE OF THE ATMOSPHERE BY A GROUND SOURCE AND THE IONOSPHERIC EFFECT

Sergey B. Leble, Ekaterina S. Smirnova

Immanuel Kant Baltic Federal University, Kaliningrad, Russia

Introduction. A lot of investigations aimed at studying the ocean-atmosphere-ionosphere connection is being distinguished. In [1], convincing arguments were presented in favor of the fact that phenomena occurring in the oceans are an important source of waves in the thermosphere, those are acoustic and internal gravitational waves [2], that affects the total electron concentration [3], that proves to be important both in the diagnostics of low atmospheric effects and prognosis.

Important results were obtained for the exponential atmosphere within the linear theory [2]. For instance, the dispersion relations were derived, which provided the basis for the developed concepts and practical recommendations for geophysics. In this paper, compared with previous [4] we modify the boundary problem formulation, obtaining analytical solution of the 1D multi-layer problem of purely acoustic perturbations and their ionospheric effect.

The Fourier method is employed to solve the basic equations and deliver the transformation from the time domain to the frequency domain. The solution of the resulting ordinary differential equations transforms to the time domain by inverse Fourier transform to obtain the final integral form. The corresponding integral contains a rapidly-oscillating function, which paves the way for further asymptotic analysis, that we demonstrate here [5].

Basic equations. The proper decomposition of the perturbation into acoustic and entropy modes in a one-dimensional flow, which is studied in this work, is used as the basis. The equations based on the conservation of momentum, energy, and mass determine the behavior of a fluid, as non-dissipative medium [6]. These nonlinear equations model the dynamics of all possible types of motion that can take place in a gas medium.

We start with linearized conservation equations in terms of pressure and density variations, $p'(z)$ and $\rho'(z)$ as deviations from hydro-dynamically-stable stationary functions $\bar{p}(z), \bar{\rho}(z)$ which are no longer constants for gas in the gravity field. Consider the problem of the propagation of acoustic waves in an exponentially-stratified atmosphere layer. The pressure and density of the unperturbed atmosphere are described by the law:

$$\bar{p}(z) = p_0 \cdot \exp\left(-\frac{z}{H}\right) = \rho_0 g H \cdot \exp\left(-\frac{z}{H}\right); \bar{\rho}(z) = \rho_0 \cdot \exp\left(-\frac{z}{H}\right). \quad (1)$$

Here, $\bar{p}(z)$ is the pressure of the unperturbed atmosphere, p_0 is the pressure at the water–air interface, $\bar{\rho}(z)$ is the density of the unperturbed atmosphere, ρ_0 is the air density at the water–air interface, H is the atmospheric scale height, and z is the current height value.

Let \vec{V} be the velocity vector of the gas flow with the vertical component V_z ; $\gamma = C_p / C_v$; C_p, C_v are molar heat capacities at constant pressure and volume correspondingly; \vec{g} is the gravity acceleration field vector, whose components, in the case of vertical gravitational field, are $g_x = 0, g_y = 0$, and $g_z = g$.

Further, in the context of entropy mode introduction, we enter a new variable φ' :

$$\varphi' = p' - \gamma \frac{\bar{p}}{\bar{\rho}} \rho' \quad (2)$$

Next, we go to the conventional set of variables:

$$P = p' \cdot \exp\left(\frac{z}{2H}\right), \Phi = \varphi' \cdot \exp\left(\frac{z}{2H}\right), U_z = V_z \cdot \exp\left(-\frac{z}{2H}\right), \quad (3)$$

where P, Φ, U_z are the new quantities defined in this way and V_z is the vertical velocity of the flow.

Our main intention to simplify the model relates to the plane waves' case. Therefore, we consider the one-dimensional boundary problem for each layer of our model. For such a case, the system of hydrothermodynamics takes the form:

$$\frac{\partial P}{\partial z} = -\frac{1}{(\gamma-1)g} \frac{\partial^2 \Phi}{\partial t^2} + \frac{\gamma-2}{2\gamma H} P + \frac{\Phi}{\gamma H}, \quad (4)$$

$$\frac{\partial^2 \Phi}{\partial z \partial t} = \frac{\gamma-1}{\gamma H} \frac{\partial P}{\partial t} - \frac{\gamma-2}{2\gamma H} \frac{\partial \Phi}{\partial t}, \quad (5)$$

$$U_z = -\frac{1}{(\gamma-1)\rho_0 g} \frac{\partial \Phi}{\partial t}. \quad (6)$$

Boundary conditions. We set the boundary conditions for the gas velocity:

$$U_z(0, t) = A e^{-\lambda t} \cos \omega_0 t, \quad (7)$$

where λ characterizes the width or duration of the pulse and the factor A is the velocity amplitude.

Next, we use the Fourier transform for the basic quantities. To do this we prolongate the functions on the whole axis t anti-symmetrically:

$$U_z(0, t) = A \theta(t) e^{-\lambda t} \cos \omega_0 t - A \theta(-t) e^{\lambda t} \cos \omega_0 t, \quad (8)$$

where

$$\theta(t) = \begin{cases} 1, & t > 0; \\ 0, & t \leq 0. \end{cases} \quad (9)$$

After a transition into ω -space:

$$u_z(0, \omega) = -\frac{2Ai\omega}{\sqrt{2\pi}} \frac{\lambda^2 + \omega^2 - \omega_0^2}{(\lambda^2 + (\omega - \omega_0)^2)(\lambda^2 + (\omega + \omega_0)^2)}. \quad (10)$$

Solution. The statement of the problem of the propagation of the boundary regime and its solution are described in detail in [4]. Solution in for the velocity in the t -space:

$$U_z(z, t) = \frac{-A}{\pi} \int_{-\infty}^{\infty} \frac{\lambda^2 + \omega^2 - \omega_0^2}{(\lambda^2 + (\omega - \omega_0)^2)(\lambda^2 + (\omega + \omega_0)^2)} \exp \left[i \left(\omega t - z \sqrt{\frac{\omega^2}{\gamma g H} - \frac{1}{4H^2}} \right) \right] d\omega \quad (11)$$

or, using decomposition:

$$\frac{\lambda^2 + \omega^2 - \omega_0^2}{(\lambda^2 + (\omega - \omega_0)^2)(\lambda^2 + (\omega + \omega_0)^2)} = \frac{1}{\lambda + i(\omega - \omega_0)} + \frac{1}{\lambda + i(\omega + \omega_0)} - \frac{1}{\lambda - i(\omega - \omega_0)} - \frac{1}{\lambda - i(\omega + \omega_0)} \quad (12)$$

speed solution can be represented as:

$$U_z(z, t) = I_1 + I_2 + I_3 + I_4 \quad (13)$$

where with the stationary phase approximation:

$$I_1 \approx \frac{A}{4\pi^2} \frac{1}{|\lambda + i(\omega_{dom} - \omega_0)|} \sqrt{\frac{2\pi}{z \left| \frac{d^2 k}{d\omega^2} \right|}} \cos \left(k(\omega_{dom})z - \omega_{dom}t \pm \frac{\pi}{4} \right), \quad (14)$$

$$k(\omega) = \sqrt{\frac{\omega^2}{\gamma g H} - \frac{1}{4H^2}}, \quad (15)$$

$$\omega_{dom} = \frac{t\gamma g}{2\sqrt{Hg\gamma t^2 - z^2}}. \quad (16)$$

The values of the integrals I_2, I_3, I_4 are similar to the integral I_1 according to (12).

Analysis of the Effects at Ionospheric Heights. Neutral gas perturbation. To analyze the neutral gas perturbation effect at the altitudes of the ionosphere, it is necessary to return to the physical quantities and then calculate their changes with increasing altitude for each layer:

$$p' = P \cdot \exp \left(-\frac{z-h}{2H} \right), \varphi' = \Phi \cdot \exp \left(-\frac{z-h}{2H} \right), U_z = V_z \cdot \exp \left(\frac{z-h}{2H} \right). \quad (17)$$

The acoustic wave propagation entering the ionosphere acts on ions.

Ionospheric effect. We develop [4] in two aspects. 1. From IGW we go to action of acoustics 2. Account of ionization variations from sun source during the day. The ionosphere effect, a variation of electron concentration as a function of the vertical coordinate and time, is determined by the vertical component of velocity. In [7], a simple formula for the electron concentration dynamics was derived, its coordinate and time dependence were calculated as the solution of the diffusion equation, parametrized by the acoustic generate neutral gas velocity profile as a coefficient.

Reaction of Ionosphere Plasma to Acoustic Wave. The electron diffusion, forced by neutral gas motion, is described by the equation [8]:

$$n_t - \left[D_0 e^{z/H} \left(n_z + \frac{n}{2H} \right) \right]_z + (nU)_z + \beta_0 n e^{-z/H} = q_1, \quad (18)$$

where n is the electron concentration at the height z , $D_0 = D_a \sin^2 I$, the multiple of ambipolar diffusion coefficient and square Sin of magnetic line inclination I , U is the projection of neutral gas velocity, β_0 is the recombination coefficient at a boundary of the layer under consideration, the height scale of ions is $H_i = 2H$, the power density of the ionization source is approximated by Chapman layer $q_1 = q_0 \sin \Omega t \left(\exp \left[1 - (z - z_0)/H \right] \exp \left[- (z - z_0)/H \right] \right)$ with Ω - frequency of the Earth rotation. The first order perturbation theory expression in wave amplitude is the non-stationary equation (we omit the primes below) [7]:

$$n_t - n_{zz} + z^2 n/4 = -WV(0, z) + q. \quad (19)$$

And the solution:

$$n = V(0, z) + \sum_k \Phi_k(z) e^{\lambda_k t} \int_0^t [q_k(t_1) - W_k(t_1)] e^{\lambda_k t_1} dt_1 \quad (20)$$

where $\Phi_k(z)$ is the basis of Whittaker functions and q_k, W_k can be expressed as projections to $\Phi_k(z)$.

To conclude, we state, that the result gives analytical expression this allows to calculate and plot the electron concentration under the acoustic wave and day variation of ionization source impact.

Acknowledgement. The work is supported by grant RFBR No 18-05-00184.

1. O.A Godin, Air-sea interaction and feasibility of tsunami detection in the open ocean, *J. Geophys. Res.*, 2004, 109, pp. C05002, doi:10.1029/2003JC002030.
2. C.O. Hines, Gravity waves in the atmosphere, *Nature*, 1972, 239, pp. 73–78.
3. I.V. Karpov, S.B. Leble, The analytical theory of ionospheric IW effect in F2 layer, *Geomagn. Aeron.*, 1986, 26, pp. 234–237. (In Russian).
4. S. Leble, E. Smirnova, Tsunami-Launched Acoustic Wave in the Layered Atmosphere: Explicit Formulas Including Electron Density Disturbances, *Atmosphere*, 2019, 10, pp. 629; doi.org/10.3390/atmos10100629.
5. S.Y. Dobrokhoto, D.S. Minenkov, V.E. Nazaikinskii, B. Tirozzi, Functions of noncommuting operators in an asymptotic problem for a 2D wave equation with variable velocity and localized right-hand side, *Oper. Theory Adv. Appl.*, 2013, 228, pp. 95–126.
6. S. Leble, A. Perelomova, Problem of proper decomposition and initialization of acoustic and entropy modes in a gas affected by the mass force, *Appl. Math. Model.*, 2013, 13, pp. 629–635.
7. I.V. Karpov, S.B. Leble, Solution of nonstationary problem of ionospheric response to a thermospheric disturbance (in Russian), *Izv. VUZ, Radiophysica XXVI*, 1983, pp. 1599–1601. (In Russian).
8. V. M. Polyakov, V. V. Rybin, The problem of ionosphere layer dynamics as a Sturm-Liouville problem, *Geomagn. and Aeronomy*, 1975, 15, pp. 806–813. (In Russian).

IONOSPHERIC-MAGNETOSPHERIC RELATIONS

STATISTICAL ANALYSIS OF IONOSPHERIC TOTAL ELECTRON CONTENTS AVERAGED OVER DIFFERENT LATITUDINAL ZONES DURING GEOMAGNETIC STORMS

Konstantin G. Ratovsky¹, Maxim V. Klimenko², Yury V. Yasyukevich¹, Artem M. Vesnin¹, Vladimir V. Klimenko²

¹Institute of Solar-Terrestrial Physics SB RAS, Irkutsk 664033, Russia

²West Department of Pushkov IZMIRAN, RAS, Kaliningrad 236017, Russia

In the paper we continue studying the ionospheric responses to geomagnetic storms based on statistical analysis of different ionospheric characteristics [1, 2]. Previously, we used peak electron density (NmF2) from the ionosondes and global electron content (GEC) from CODE global ionospheric maps (GIM). The statistical analysis of NmF2 [1] gave two main results. The behavior of ionospheric response near the beginning of the geomagnetic storm recovery phase perfectly fits the well-known concept of the seasonal dependence of the ionospheric response to geomagnetic storms: the response is most negative in summer and least negative (or even positive) in winter with intermediate values in spring and autumn. For the isolated and strong geomagnetic storms we revealed the so-called after-storm effects (positive NmF2 disturbances observed during the daytime on the 3-5th day after the beginning of the recovery phase). We showed that after-storm effects are explained by the increase in the atomic oxygen density due to its transport from equatorial to middle latitudes in the after-storm effect phase. In turn, this transport is caused by the additional neutral gas pressure gradient from low to high latitudes, which arises from the appearance of the excess neutral gas density at low latitudes in the geomagnetic storm main phase due to the equatorward transport of oxygen from auroral latitudes. The statistical analysis of GEC [2] for isolated storms showed the clear positive response on the day of the beginning of the recovery phase. This confirmed the hypotheses on positive electron density disturbance formation during the main phase of the geomagnetic storm due to the oxygen transfer. However, the statistical analysis of GEC for strong storms showed both positive and negative responses near the beginning of the recovery phase, requiring additional mechanisms for negative disturbances formation.

In this study as ionospheric characteristics we used regional mean total electron content (TEC) values over five zones of the geomagnetic latitude: equatorial zone ($\pm 30^\circ$), North and South Hemisphere mid-latitude zones ($30^\circ\div 60^\circ$ and $-30^\circ\div -60^\circ$), and North and South Hemisphere high latitude zones ($60^\circ\div 90^\circ$ and $-60^\circ\div -90^\circ$). The statistical analysis was performed as in [1, 2]. We calculated TEC disturbance as a relative deviation of the observed value from the 27-day running mean: $\Delta\text{TEC} = 100\% \cdot [\text{TEC} - \text{TEC}_{\text{mean}}] / \text{TEC}_{\text{mean}}$. As the ionospheric response, we consider the average value of ΔTEC ($\langle\Delta\text{TEC}\rangle$) for the given storm type, season and day before/after the beginning of the geomagnetic storm recovery phase.

Figure 1 shows the variations in $\langle\Delta\text{TEC}\rangle$ for 5 days before and after the beginning of the geomagnetic storm recovery phase for the isolated storms (time interval between adjacent storms more than 5 days).

The main effect in the equatorial zone is positive response on Day 0 (beginning of recovery phase), from $\sim 4\text{-}5\%$ in winter and summer to $\sim 7\text{-}8\%$ in autumn and spring with recovery to an undisturbed level on the 3-4th day after Day 0 (except for spring). This effect is fully consistent with the statistical analysis for GEC [2].

The main effect in the North Hemisphere mid-latitude zone is positive response on Day 0 in winter and autumn ($\sim 11\text{-}13\%$) and negative response on Day 1 (the day after Day 0) in summer ($\sim -10\%$).

Secondary effects are positive response on Day -1 (the day before Day 0) in summer and spring ($\sim 7-8\%$), negative precursor in winter ($\sim -3\%$), negative after-storm effect in winter ($\sim -3\%$) and positive after-storm effect in summer ($\sim 3\%$). All noted effects of the North Hemisphere mid-latitude zone (including secondary effects) are repeated in the Southern Hemisphere, with the only difference being that winter should be replaced by summer, spring by autumn, etc. (i.e., the effects are repeated in terms of local winter, local spring, etc.). The identity of responses for the Northern and Southern Hemisphere in terms of local seasons, apparently, indicates that all the noted effects (including secondary) are the result of magnetic storms and not the result of other factors (influence of processes in the lower atmosphere and short-period variations in solar activity). Indeed, obtaining identical responses from the Northern and Southern Hemispheres in terms of local seasons, we deal with various storms occurring at really different times with different influence of other factors. The quantitative difference is that in the Southern Hemisphere the main effect looks more contrasting, both positive ($\sim 16\%$) and negative ($\sim -13\%$) effects are larger in amplitude.

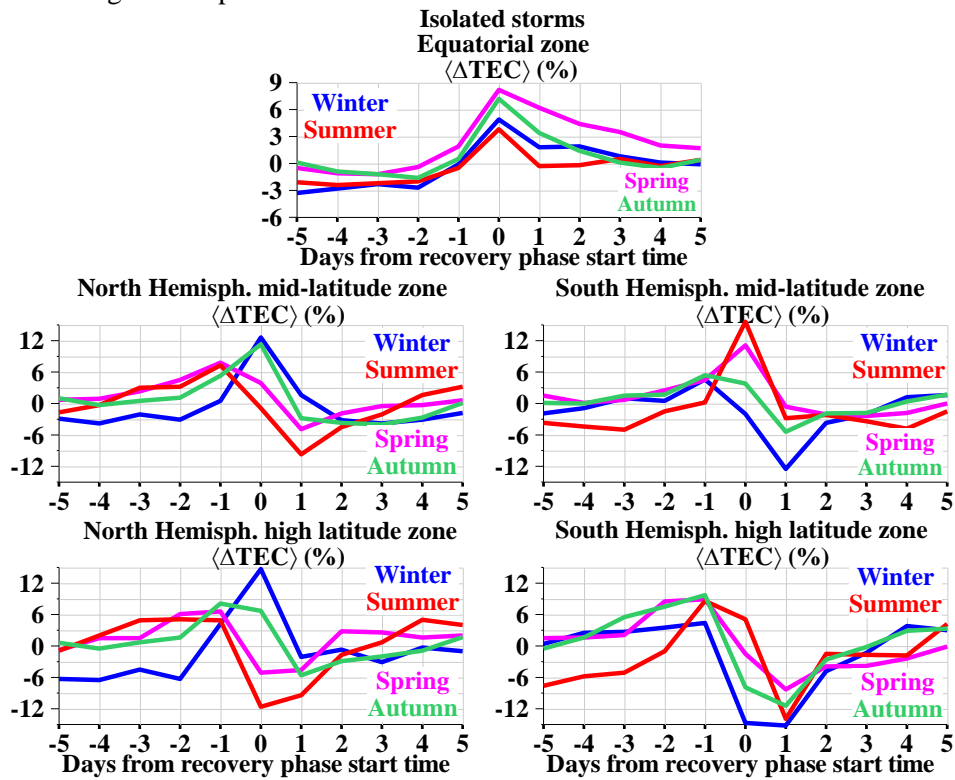


FIGURE 1. Variations in $\langle \Delta \text{TEC} \rangle$ for 5 days before and after beginning of geomagnetic storm recovery phase for isolated storms. Blue, magenta, red, and green curves show results obtained for winter, spring, summer, and autumn, respectively.

At high latitudes, the largest negative responses are seen on Day 0 (up to -12%) or Day 1 (up to -15%), which is expected from the well-known concepts of magnetic storms. But at the same time, at high latitudes, positive responses are also seen on Day 0 (up to 15%) or Day -1 (up to 10%), which is difficult to explain from the well-known concepts of magnetic storms. A possible version of the result is a method for constructing the CODE GIM at high latitudes, in which the effects of middle latitudes are captured by the high latitude zone.

Figure 2 shows the variations in $\langle \Delta \text{TEC} \rangle$ for 5 days before and after the beginning of the geomagnetic storm recovery phase for the strong storms (minimal Dst < -100 nT). Unlike the case of isolated storms, the positive response in the equatorial zone is not concentrated on Day 0, and the positive response

amplitude is less with the exception of winter. As in the GEC analysis [2], the winter case is the result of poor statistics of winter strong storms and the dominant influence of one storm with a large positive response. In contrast to the case of isolated storms, the equatorial TEC response does not repeat the GEC response [2]. The main difference is significant reduction in the negative response seen on Day 1. As shown below, the negative GEC response is mainly due to the negative response in the mid- and high latitudes. The response of the equatorial TEC to strong storms is generally positive, with the exception of summer storms. The analysis of the F10.7 disturbances (calculated by the same method as $\langle \Delta \text{TEC} \rangle$) showed that the negative response to summer strong storms is most likely due to the negative trend in solar activity.

In the case of strong storms, the main effect in the mid-latitude zones is positive response on Day 0 in local winter ($\sim 15\text{-}19\%$) and negative response on Day 1 in local summer ($\sim -18\%$ to -19%). On Day 1, the response is always negative with a sequential increase in amplitude from local winter to local summer. On Day 0, the response is positive only for local winter and autumn. In contrast to the case of isolated storms, the secondary effects for the Northern and Southern Hemispheres are not repeated, and thus, it makes no sense to focus on their analysis.

The main effect of strong storms in the high latitude zones (with the exception of the winter response in the Northern Hemisphere) is negative response on Day 1 for all seasons (from -12% to -21%) and a negative response on Day 0 for all seasons except for a local winter (from -6% to -21%). As mentioned above, the winter response in the Northern Hemisphere is probably the result from poor statistics of winter strong storms and the dominant influence of one storm with large positive response. In general, such a pattern fits into the framework of well-known concepts of geomagnetic storms. Nevertheless, even without the winter response in the Northern Hemisphere, positive responses are observed on Day -1 (up to 10%), which requires an explanation. As in the case of isolated storms, this may be related to a method for constructing the CODE GIM at high latitudes.

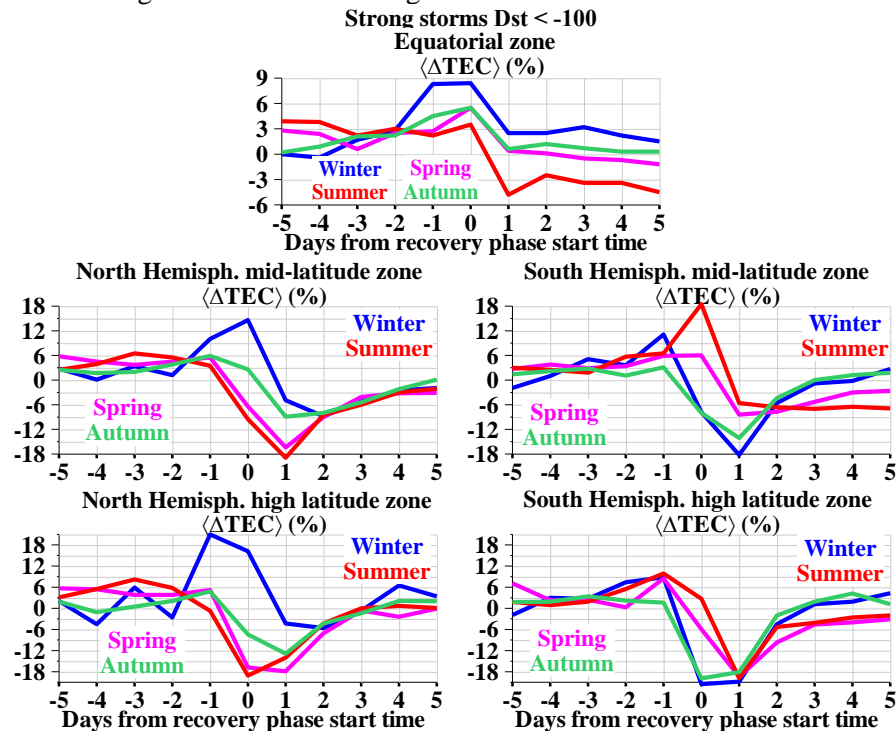


FIGURE 2. Variations in $\langle \Delta \text{TEC} \rangle$ for 5 days before and after beginning of geomagnetic storm recovery phase for strong storms. Blue, magenta, red, and green curves show results obtained for winter, spring, summer, and autumn, respectively.

Acknowledgments. The reported study was funded by RFBR, project number 18-05-00594. In the study we used the methods obtained in the framework of Basic Research program II.12. We are grateful to SPDF for access to the solar and geomagnetic index data and to the CODE laboratory for TEC data.

1. K. G. Ratovsky, M. V. Klimenko, V. V. Klimenko, N. V. Chirik, N. A. Korenkova, D. S. Kotova, After-effects of geomagnetic storms: statistical analysis and theoretical explanation, *Solar Terrestrial Physics*, 2018, 4(4), pp. 26-32, doi:10.12737/stp-44201804.

2. K. G. Ratovsky, M. V. Klimenko, Y. V. Yasyukevich, V. V. Klimenko, Statistical analysis of ionospheric global electron content response to geomagnetic storms, *2019 Russian Open Conference on Radio Wave Propagation (RWP)*, Kazan, Russia, 2019, pp. 183-186, doi:10.1109/RWP.2019.8810392.

DYNAMICS OF MAIN AND RING IONOSPHERIC TROUGHS

Alexander T. Karpachev

Pushkov Institute of Terrestrial Magnetism, Ionosphere and Radio Wave Propagation Russian Academy of Sciences, IZMIRAN, Troitsk, Moscow Reg., Russia

Introduction. Dynamics of the main ionospheric trough (MIT) and the ring ionospheric trough (RIT) during geomagnetic disturbances is considered. RIT is formed at the recovery phase of the geomagnetic storm /substorm at latitudes of the residual magnetospheric ring current of $54\text{--}58^\circ$ GMLat and is associated with it. For analysis, about 120 geomagnetic disturbances with $K_p \geq 4$ were used according to the Cosmos-1809, Cosmos-900, Intercosmos-19 and CHAMP satellites.

Observation data. The data of the in-situ measurements of Ne и Te onboard Kosmos-900 (1977-1979), Ne onboard CHAMP (2001-2010), Te and NmF2 according to Interkosmos-19 (1979-1981) and Kosmos-1809 (1986-1990) were used.

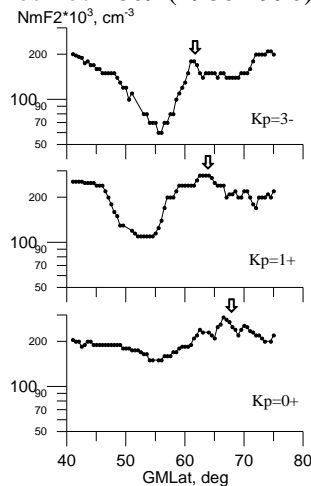


FIGURE 1. Latitudinal NmF2 profiles obtained according to Cosmos-1809 on June 1, 3, and 4, 1987 for 23-02 LT [1].

RIT discovery. Figure 1 shows examples of NmF2 variation with invariant latitude, recorded onboard the Kosmos-1809 [1]. The data were obtained at night over Europe on June 1, 3, and 4, 1987, when the magnetosphere returned to a quiet state after a long perturbed period with $K_p^{\max} = 5$. The arrow indicates the position of the equatorial boundary of auroral diffuse precipitation according to simultaneous observations onboard the DMSP. When a geomagnetic activity decreased from $K_p = 3-$ to $0+$, the auroral oval returned to a quiet state. The trough gradually depleted, but its minimum practically remained in place, at latitudes of $53\text{--}55^\circ$, so that at $K_p = 0+$ it turned out to be $13\text{--}14^\circ$ equatorward from the auroral oval. Thus, the observed trough is not associated with the auroral oval, located at typical latitudes of the residual magnetospheric ring current, and therefore, by analogy, it was defined as a Ring Ionospheric Trough (RIT) [3].

Figure 2 on the left shows the dynamics of MIT and RIT according to the Interkosmos-19 and Kosmos-900 data in the night sector of local time (data were transformed to 00 LT). The trough position and K_p -index variations are consistent according to the trough model [2]. The trough position at the maximum of the main phase of the storm is a slightly below the model position (taking into account a delay of ~ 3 h). During the recovery phase of the storm, the mid-latitude trough is located at the latitudes of the residual ring current, much lower than the position of subauroral MIT. One can only wonder why no one paid attention to such a strong discrepancy. Thus, the trough observed at night during the storm March 29-30, 1979 is RIT. Figure 2

on the right shows examples of simultaneous observations of MIT and RIT (indicated by the numbers 1 and 2). The minimum of each trough corresponds to the Te peak.

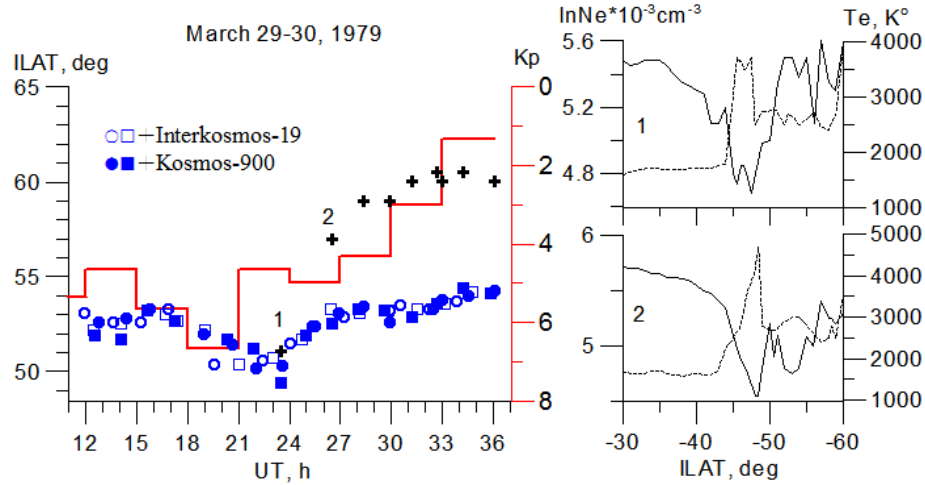


FIGURE 2. On the left: dynamics of MIT (crosses) and RIT (circles in the Northern, squares in the Southern hemisphere) during the storm March 29-30, 1979, according to IK-19 and Kosmos-900. On the right: latitudinal profiles of Ne and Te for satellite paths 1 and 2.

Observation onboard the CHAMP. RIT was the most comprehensive investigated on the basis of a large CHAMP data set. The simplest case was recorded on August 10-11, 2000. The disturbance was quite strong, Kp = 6-. Figure 3 on the left shows the data obtained at midnight in the Southern winter hemisphere. The Kp variations are shifted to the right by 1 hour, which means the trough reaction delay about 1 hour. At the perturbation maximum (Kp = 6), the trough appeared at 48°, which is 5° equatorward from the model position. Examples of fp latitudinal cross-sections are shown on the right. As the geomagnetic activity decreased, the trough shifted to the latitudes of the residual ring magnetospheric current, all the while remaining lower in latitude than follows from the MIT model, i.e. it is RIT. Subauroral MIT was clearly manifested starting from ~30 UT, after which both troughs were observed simultaneously on satellite passes 9-19. After 42-43 UT, the trough position again corresponds to the MIT model. At the same time, it is located at typical latitudes of the residual ring magnetospheric current. Therefore, most likely this is a joint structure: MIT and RIT. Thus, at the recovery phase of the storm, all versions can be observed: one MIT, one RIT, or both troughs simultaneously.

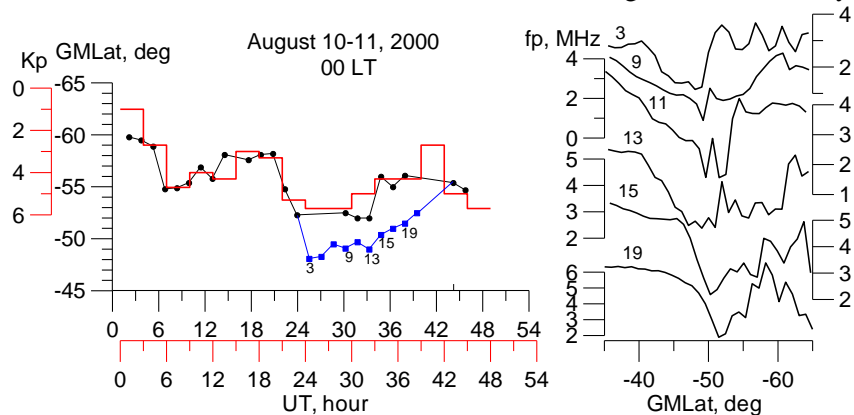


FIGURE 3. On the left: dynamics of the MIT and RIT during a storm on August 10-11, 2000. On the right: latitudinal fp profiles for the most characteristic passes 3-19.

In the next case the trough was located at latitude of $\sim 54^\circ$ for a very long time, regardless of the Kp index variation. Figure 4 shows the dynamics of the trough during the substorm on June 26-27, 2001 with Kp = 4. Satellite data were obtained in the winter Southern hemisphere in the morning sector (6.7 LT). At the substorm development phase, the trough with a delay of about 2 h was shifted to the equator, although for some time a reverse movement was observed, associated with the corresponding variations of the Dst index. When Kp reached its maximum, the trough appeared at latitude of $\sim 54^\circ$, and remained at this latitude for a long time, despite the rapid decrease of Kp. At the substorm maximum, the trough is characterized by a structure typical for MIT, as shown by fp profile 30 (on the right). However, during pass 9, the equatorial wall of the trough becomes flat. This, apparently, is associated with the development of the negative phase of the ionospheric storm, since the day before at this longitude the trough had the usual shape. The flat equatorial wall of the trough remains until path 15, but already on the pass 19, the trough returns to its usual shape: fig. 4, on the right. On the passes 21-25, on the contrary, the polar wall of the trough is degenerate, therefore, the trough is shallow here. The blue curve in fig.4 shows pass 22 recorded on June 26 in approximately the same longitudinal sector. A comparison of the latitudinal profiles of 22 for June 26 and 21-25 for June 27 shows how much the shape of the trough changed during the substorm (shown by the arrow). As a result, the minimum of trough on pass 21 turned out to be 10° below the model position. This is RIT certainly. Note that, in contrast to other cases, only RIT was observed for a long time, and MIT that could clearly separate in latitude from RIT in the range of 30-43 UT did not appear. The MIT appeared only on the path 27 and especially clearly further: at the passes 31 on June 27 and 2-4 on June 28. Thus, during the disturbance on June 26-27, MIT smoothly transformed into RIT, and then RIT jumped into the MIT.

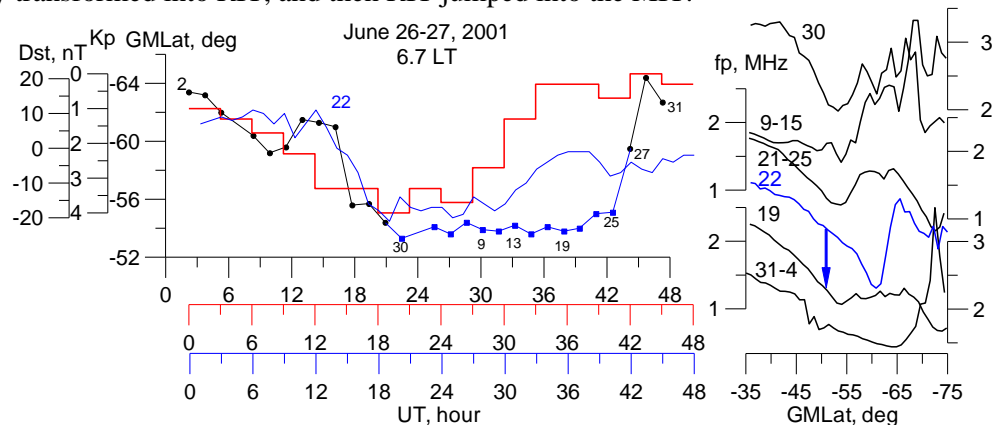


FIGURE 4. On the left: dynamics of the MIT and RIT during the storm on June 26-27, 2001. The blue curve is the Dst variation. On the right: fp latitudinal profiles for the most characteristic turns.

Conclusion. The dynamics of MIT and RIT is very complex during geomagnetic disturbances: troughs can be observed simultaneously and separately, while the MIT can jump into the RIT and vice versa. RIT is observed at latitudes of the residual ring magnetospheric current, therefore, the problem of separation of troughs is especially acute in the morning sector, when the MIT shifts to the lowest possible latitudes.

1. M.G. Deminov, A.T. Karpachev, and L.P. Morozova, Subauroral ionosphere during the SUNDIAL period of June 1987 according to the Cosmos-1809 satellite, *Geomagnetism and aeronomy*, 1992, 32(1), pp. 54-58.
2. A.T. Karpachev, M.G. Deminov, and V.V. Afonin, Model of the mid-latitude ionospheric trough on the base of Cosmos-900 and Intercosmos-19 satellites data, *Adv. Space Res.*, 1996, 18(6), pp. 221-230.
3. A.T. Karpachev, Characteristics of the Ring Ionospheric Trough, *Geomagnetism and aeronomy*, 2001, 41(1), pp. 57-66.

INFLUENCE OF THE SUBSTORM PRECIPITATIONS AND POLAR CAP PATCHES ON THE GPS SIGNALS AT POLAR LATITUDES

Vladimir B. Belakhovsky¹, Yaqi Jin², Wojciech J. Miloch², Alexander V. Koustov³, Ashton Reimer⁴

¹ Polar Geophysical Institute, Apatity, Russia

² Department of Physics, University of Oslo, Oslo, Norway,

³ Department of Physics and Engineering Physics, University of Saskatchewan, Saskatoon, Canada

⁴ SRI International, Menlo Park, California, USA

This study investigates the influence of substorm-related energetic particle precipitations and polar cap patches (PCP) on GPS signal scintillations in the high-latitude ionosphere. These ionosphere disturbances are a most powerful at the high-latitude region. A number of events in 2010-2017 are analyzed when the EISCAT radar data on Svalbard was available. We use data collected by the GPS scintillation receiver (University of Oslo) at Ny-Ålesund. Substorms are identified through IMAGE magnetometer data as well as optical observations in Ny-Ålesund. Occurrence of polar cap patches is determined by using electron density data from the EISCAT 42m radar (as a density increase above 200 km) and by considering optical observations at Ny-Ålesund station at 630.0 nm emission line. For some events, we show the onset of PCPs on the dayside and their propagation into the nightside, where the GPS receiver is located, by considering data from the Resolute Bay (Canada) incoherent scatter radar (RISR) and the SuperDARN radars. Our analyze shows that GPS amplitude scintillation index (S4) practically have no changes during considered events. Our observations suggest that the substorms and PCPs, being different types of the high-latitude disturbances, lead to the development of different types and scales of ionospheric irregularities.

1. Introduction. The Global Navigation Satellite Systems (GNSS) play an important role for the modern society. However, the ionosphere as a medium for the radio waves propagation can have a negative influence on the quality of received signal. Irregularities in the plasma density distribution can lead to fast fluctuations of amplitude and phase of the signal which is referred to as ionosphere scintillations [1]. The strong scintillations reduce the quality of the signal and even lead to the signal loss. Thus, the investigation of GPS scintillations is an important aspect of space weather. The level of scintillations is characterized by the phase ($\sigma\Phi$) and amplitude (S4) scintillation indexes, rate of TEC (total electron content) variations.

The most powerful disturbances in the polar ionosphere are substorms particle precipitation and polar cap patches (PCP). The PCP are identified as a density increase above approximately 200 km. It is well known that the appearance of these structures is accompanied by the increase of the airglow intensity in 630.0 nm spectrum lines [2]. Its origin is caused by the reconnection on the dayside of the magnetosphere and penetration of plasma through the polar cap into the ionosphere [3].

In the present work we address the following question: how substorm disturbances and polar cap influence on the GPS signals in the polar ionosphere?

2. Data. We focused on the geophysical observations on Svalbard. The Ny-Ålesund (NYA) GPS scintillation receiver of the University of Oslo was the main instrument used in our study. Upon availability of data, the Skibotn (Norway, mainland) GPS receiver was also used. The ROT (rate of total electron content) was calculated.

For describing the ionospheric plasma parameters (density, velocity, ion and electron temperature) we used the Svalbard EISCAT 42m radar. The beam of this radar is directed along the geomagnetic field. For some convenient cases the aurora observations of Polar Geophysical Institute, University of Oslo on Svalbard was used. IMAGE magnetometer data was used for the geomagnetic field observations. OMNI database was used for the evaluating the solar wind and interplanetary magnetic

field parameters. We identified more than 100 cases for years 2010-2017 when the data from the EISCAT 42m radar was available, however, in this report we present the typical examples.

3. Data analysis. We demonstrate that substorm-associated precipitations can lead to a strong GPS phase ($\sigma\phi$) scintillations up to ~ 2 radians which is much stronger than those usually produced by PCPs. On the Figure 1 it is shown the substorm growth at 16 UT which lead to the strong phase scintillations (1.5 radian). It was strong polar substorm: the amplitude of the substorm reaches the value more than 1000 nT at Hornsund (HOR) station, at NAL station the amplitude of the substorm was 600 nT. The substorm was accompanied by the strong increase of aurora intensity in different spectrum lines (not shown).

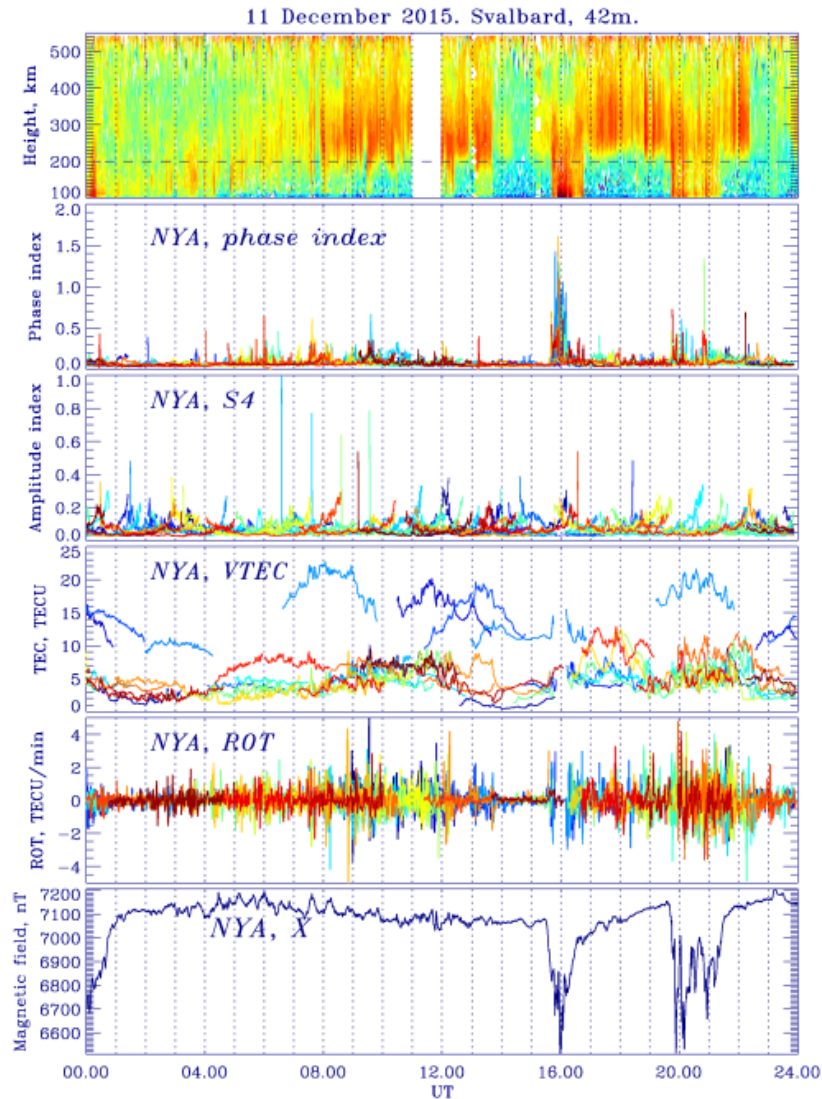


FIGURE 1. The ionosphere plasma density according to the EISCAT 42m radar data on Svalbard; phase, amplitude scintillation indexes from the NYA station; total electron content and rate of TEC from the NYA station; geomagnetic field variations (X-component) on NYA station for the 11 December 2015, 00-24 UT.

The substorm leads to the abrupt increase of the ionosphere plasma density (more than order) at altitudes 100-100 km according to the EISCAT 42m radar data on Svalbard. The substorm leads to the gap in total electron content (TEC) variations according to the GPS receiver data on NYA station.

On the other hand, PCPs can lead to a much faster ROT (rate of total electron content) variations. On Figure 2 the PCPs during the substorm development are shown. Substorm at 19 UT leads to a strong phase scintillations (0.9 radian) while PCPs lead to stronger ROT variations at 20-21 UT.

So our observations suggest that the substorms and PCPs, being different types of the high-latitude disturbances, lead to the development of different types and scales of ionospheric irregularities.

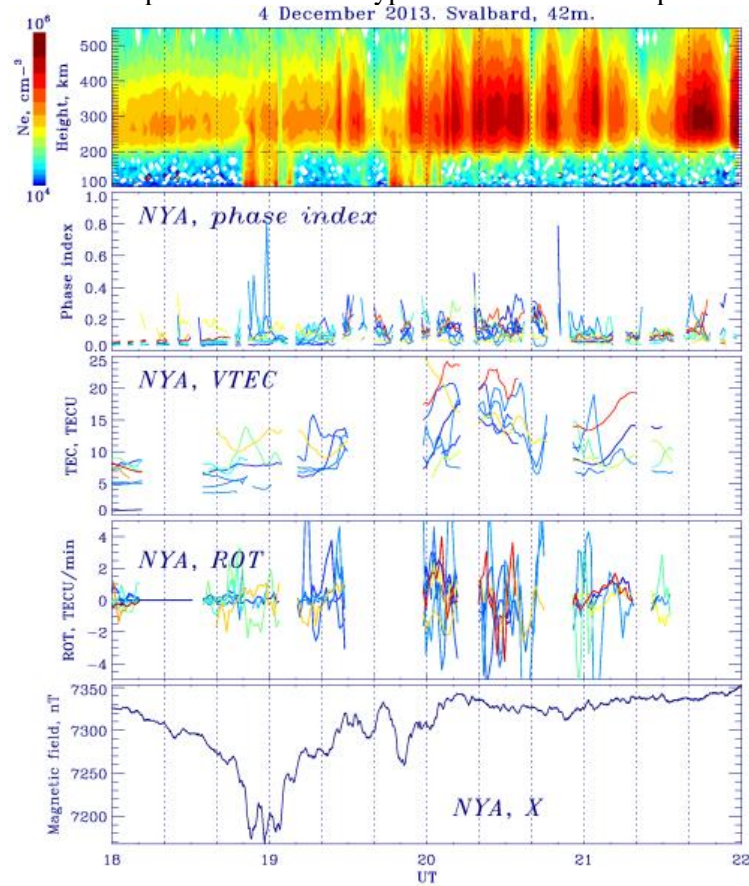


FIGURE 2. The ionosphere plasma density according to the EISCAT 42m radar data on Svalbard; phase scintillation index from the NYA station; total electron content and rate of TEC from the NYA station; geomagnetic field variations (X-component) on NYA station for the 4 December 2013, 18-22 UT .

Acknowledgement. This study was supported by grant of the Russian Science Foundation (project 18-77-10018).

1. S. Basu, K. M. Groves, S. Basu, P.J. Sultan. Specification and forecasting of scintillations in communication/navigation links: Current status and future plans, *Journal of Atmospheric and Solar- Terrestrial Physics*, 64 (16), 1745–1754. 2002.
2. K. Hosokawa, K. Shiokawa, Y. Otsuka, A. Nakajima, T. Ogawa, and J. D. Kelly, Estimating drift velocity of polar cap patches with all-sky airglow imager at Resolute Bay, Canada, *Geophysycal Research Letters*, 33, L15111, doi:10.1029/2006GL026916. 2006.
3. D. A. Lorentzen, J. Moen, K. Oksavik, F. Sigernes, Y. Saito, and M. G. Johnsen, In situ measurement of a newly created polar cap patch, *Journal of Geophysical Research*, 115, A12323, doi:10.1029/2010JA015710. 2010.

MODELING AND ANALYSIS OF IONOSPHERIC PARAMETERS DURING MAGNETIC STORMS (ON THE EXAMPLE OF EVENTS IN 2017-2019)

Oksana V. Mandrikova, Nadezhda V. Fetisova

Institute of Cosmophysical Research and Radio Wave Propagation FEB RAS, Mirnaya str., 7, Paratunka, Kamchatka region, Russia

Introduction. Ionospheric response to non-stationary changes in the near-Earth space environment (solar flares, geomagnetic storms, etc.) is manifested in the form of an anomalous increase (decrease) in electron density [1, 2]. Formed during these periods, ionospheric irregularities have a negative impact on the operation of modern technical systems; therefore, their timely detection is of significant practical importance. The main zones of localization of irregularities are the equatorial and auroral regions, but they can also be observed in the mid-latitudes, and their intensity significantly increases while solar activity increases [1, 3]. Ionospheric disturbances can include a positive and negative phase and their characteristics depend on the intensity of geomagnetic disturbance, registration station, etc. [1]. Despite an understanding of the general behavior of the ionosphere during disturbed periods, at present some questions remain open (for example, the alternation of positive and negative phases of ionospheric storms, their dynamics, etc. [1, 2]) and require additional studies. Therefore, the development of empirical methods for the timely detection of ionospheric disturbances and their further study is of significant importance.

Currently existing methods for analyzing ionospheric data are not effective enough, due to the lack of complete reliable information about the dynamics of ionospheric processes and a complex structure of recorded data [3, 4]. In the paper, we use a generalized multi-component model (GMCM) [3, 4], which allows us to describe the dynamics of the ionospheric parameters during disturbed periods. Using the ionospheric critical frequency data (foF2) of the Kamchatka region (Paratunka station, Russia, 53.0°N and 158.7°E), we carried out a comparison of GMCM with IRI-2016 [5] and the moving median method. The paper shows the possibility of GMCM using to detect anomalies occurring in the ionospheric parameters during increased solar activity and magnetic storms.

Description of the method. The ionospheric parameter time series can be represented as a generalized multicomponent model (GMCM) [3, 4]:

$$f(t) = A^{REG}(t) + U(t) + e(t) = \sum_{\mu=1, \overline{T}} \sum_{k=1, N_{j^{reg}}^{\mu}} s_{j^{reg},k}^{\mu} b_{j^{reg},k}^{\mu}(t) + \sum_{i=1,3} \sum_{\eta,n} P_{i,\eta}(d_{\eta,n}) \Psi_{\eta,n}(t) + e(t), \quad (1)$$

where $A^{REG}(t) = \sum_{\mu=1, \overline{T}} \sum_{k=1, N_{j^{reg}}^{\mu}} s_{j^{reg},k}^{\mu} b_{j^{reg},k}^{\mu}(t)$ ($\mu = \overline{1, T}$ is a component number) is a regular component

describing characteristic variations of calm ionosphere, $s_{j^{reg},k}^{\mu} = \sum_{l=1}^{p_{j^{reg}}^{\mu}} \gamma_{j^{reg},l}^{\mu} \omega_{j^{reg},k-l}^{\mu} - \sum_{n=1}^{h_{j^{reg}}^{\mu}} \theta_{j^{reg},n}^{\mu} a_{j^{reg},k-n}^{\mu}$ is an estimated value of regular μ -th component obtained on the basis of multiresolution analysis (MRA) [6], $p_{j^{reg}}^{\mu}$, $\gamma_{j^{reg},l}^{\mu}$ are the order and parameters of autoregression of the μ -th component, $h_{j^{reg}}^{\mu}$, $\theta_{j^{reg},n}^{\mu}$ are the order and parameters of moving average of the μ -th component, $\omega_{j^{reg},k}^{\mu} = \nabla^{v^{\mu}} \delta_{j^{reg},k}^{\mu}$, v^{μ} is a difference order of the μ -th component, $\delta_{-m^{reg},k}^1 = c_{-m^{reg},k}$, $\delta_{j^{reg},k}^{\mu} = d_{j^{reg},k}$ ($\mu = \overline{2, T}$), $c_{-m^{reg},k}$ are wavelet coefficients of MRA smoothed component, $d_{j^{reg},k}$ are wavelet coefficients of MRA detailing

components, T is the number of modeled components, $a_{j^{reg},k}^\mu$ are residual errors of the μ -th component model, $N_{j^{reg}}^\mu$ is the length of the μ -th component, $b_{-m^{reg},k}^1 = \phi_{-m^{reg},k}$, $b_{j^{reg},k}^\mu = \Psi_{j^{reg},k}$, $\mu = \overline{2,T}$, $\phi_{-m^{reg},k}(t)$ is a scaling function, $\Psi_{j^{reg},k}(t)$ is a wavelet function, $U(t) = \sum_{i=1,3} \sum_{\eta,n} P_{i,\eta}(d_{\eta,n}) \Psi_{\eta,n}(t)$ is an *anomalous component* describing the dynamics of ionospheric parameters during disturbed periods (in case of calm ionosphere, it is assumed that $U(t) = 0$), $e(t)$ is a noise component.

$P_{i,\eta}$ coefficients are determined by following relations:

$$\begin{aligned} P_{1,\eta}(d_{\eta,n}) &= \begin{cases} 0, & \text{if } |d_{\eta,n}| \leq T_{1,\eta} \text{ or } |d_{\eta,n}| > T_{2,\eta} \\ d_{\eta,n}, & \text{if } T_{1,\eta} < |d_{\eta,n}| \leq T_{2,\eta} \end{cases}, \\ P_{2,\eta}(d_{\eta,n}) &= \begin{cases} 0, & \text{if } |d_{\eta,n}| \leq T_{2,\eta} \text{ or } |d_{\eta,n}| > T_{3,\eta} \\ d_{\eta,n}, & \text{if } T_{2,\eta} < |d_{\eta,n}| \leq T_{3,\eta} \end{cases}, \\ P_{3,\eta}(d_{\eta,n}) &= \begin{cases} 0, & \text{if } |d_{\eta,n}| \leq T_{3,\eta} \\ d_{\eta,n}, & \text{if } |d_{\eta,n}| > T_{3,\eta} \end{cases}, \end{aligned} \quad (2)$$

where $d_{\eta,n} = \langle U, \Psi_{\eta,n} \rangle$, $\{\Psi_{\eta,n}\}_{\eta,n \in \mathbb{Z}}$ is a wavelet-basis. $T_{1,\eta}$ threshold determines *ionospheric disturbances of weak-intensity* (class 1), $T_{2,\eta}$ threshold – *of moderate intensity* (class 2), $T_{3,\eta}$ threshold – *of high intensity* (class 3).

Taking into account the significant non-stationarity of the process during disturbed periods, $P_{i,\eta}^{ad}$, $i = \overline{1,3}$ adaptive thresholds were introduced, and in Eq. (1) $d_{\eta,n}$ coefficients were set to:

$$d_{\eta,n} = \begin{cases} d_{\eta,n}^{1+}, & \text{if } P_{1,\eta}^{ad} < (d_{\eta,n} - d_{\eta,n}^{med}) \leq P_{2,\eta}^{ad} \\ 0, & \text{if } |d_{\eta,n} - d_{\eta,n}^{med}| < P_{1,\eta}^{ad} \text{ or } |d_{\eta,n} - d_{\eta,n}^{med}| > P_{2,\eta}^{ad} \\ d_{\eta,n}^{1-}, & \text{if } -P_{2,\eta}^{ad} \leq (d_{\eta,n} - d_{\eta,n}^{med}) < -P_{1,\eta}^{ad} \\ d_{\eta,n}^{2+}, & \text{if } P_{2,\eta}^{ad} < (d_{\eta,n} - d_{\eta,n}^{med}) \leq P_{3,\eta}^{ad} \\ 0, & \text{if } |d_{\eta,n} - d_{\eta,n}^{med}| < P_{2,\eta}^{ad} \text{ or } |d_{\eta,n} - d_{\eta,n}^{med}| > P_{3,\eta}^{ad} \\ d_{\eta,n}^{2-}, & \text{if } -P_{3,\eta}^{ad} \leq (d_{\eta,n} - d_{\eta,n}^{med}) < -P_{2,\eta}^{ad} \\ d_{\eta,n}^{3+}, & \text{if } (d_{\eta,n} - d_{\eta,n}^{med}) \geq P_{3,\eta}^{ad} \\ 0, & \text{if } |d_{\eta,n} - d_{\eta,n}^{med}| < P_{3,\eta}^{ad} \\ d_{\eta,n}^{3-}, & \text{if } (d_{\eta,n} - d_{\eta,n}^{med}) < -P_{3,\eta}^{ad} \end{cases}, \quad (3)$$

where $P_{i,\eta}^{ad} = V_i \cdot St_\eta$; V_i is a threshold coefficient, $St_\eta = \sqrt{\frac{1}{\Phi-1} \sum_{n=1}^{\Phi} (d_{\eta,n} - \overline{d_{\eta,n}})^2}$, $\overline{d_{\eta,n}}$ and $d_{\eta,n}^{med}$ are average value and the median respectively, which, in view of the daily course of the ionospheric data, are calculated in a moving time window of length Φ .

In this case, the intensity of positive ($I^+(n)$) and negative ($I^-(n)$) ionospheric anomalies for each i class at time $t=n$ can be determined as

$$I^{i+(-)}(n) = \sum_{\eta} |d_{\eta,n}^{i+(-)}|. \quad (4)$$

Results and conclusions. Figure 1 shows the results of the foF2 data modeling based on GMCM, the median method and IRI model (https://ccmc.gsfc.nasa.gov/modelweb/models/iri2016_vitmo.php). Analysis of Fig. 1 shows, that on the eve of the magnetic storm, anomalous changes were observed in the ionosphere – a positive anomaly of weak intensity (Fig. 1 d, e) was detected, GMCM errors exceeded the confidence intervals (Fig. 1 c). The initial phase of the storm was accompanied by a slight decrease in the electron concentration (Fig. 1 d, e). During the main phase of the storm, a positive anomaly of moderate intensity was detected in the ionosphere. In the recovery phase, it was replaced by an intense negative ionospheric storm. The period of a significant decrease in the electron concentration (Fig. 1 d, e) was accompanied by long-term (more than 4 days) changes in the ionospheric parameter time course (the exceedance of errors was more than 2.5 standard deviations, Fig. 1 c). A comparison of the results of GMCM with IRI and the median method confirms the efficiency of the proposed method.

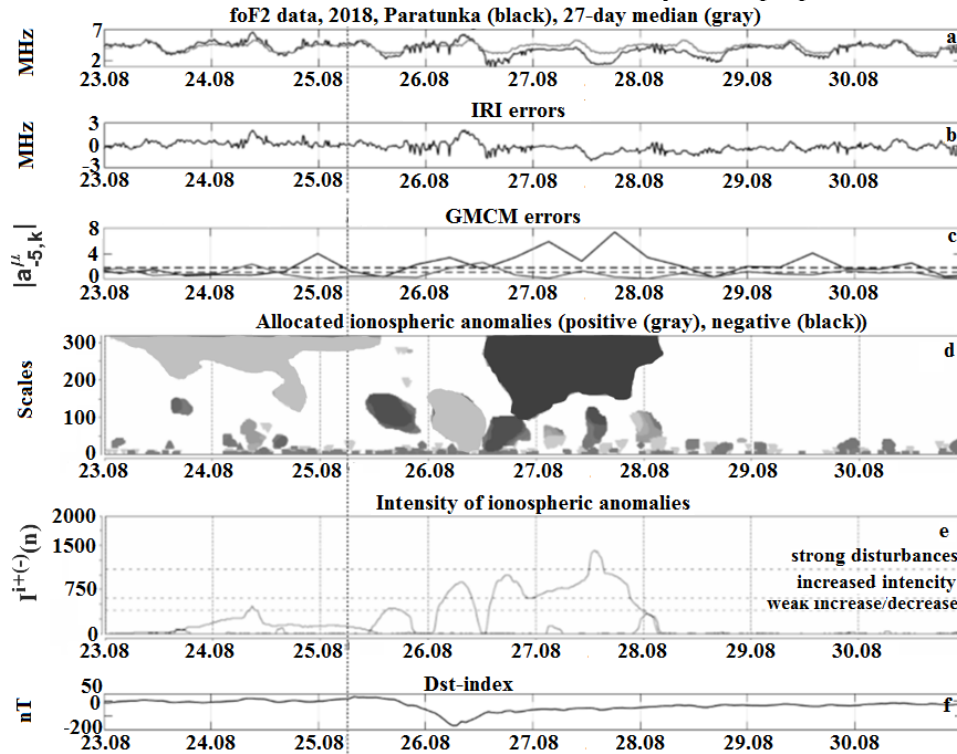


FIGURE 1. Results of the foF2 data analysis during the magnetic storm (vertical dashed line indicates the beginning of the magnetic storm)

Acknowledgements. The work was carried out according to the Subject AAAA-A17-117080110043-4 «Dynamics of physical processes in the active zones of near space and geospheres». The authors are grateful to the organizations recording the data which were applied in the paper.

1. A.D. Danilov, Ionospheric F-region response to geomagnetic disturbances, *Advances in Space Research*, 2013, 52(3), pp. 343–366.
2. G.A. Mansilla, Ionospheric response to the magnetic storm of 22 June 2015, *Pure and Applied Geophysics*, 2017, doi: 10.1007/s00024-017-1741-5.

3. O. Mandrikova, Yu. Polozov, N. Fetisova, T. Zalyaev, Analysis of the dynamics of ionospheric parameters during periods of increased solar activity and magnetic storms, *Journal of Atmospheric and Solar-Terrestrial Physics*, 2018, 181 (B), pp. 116–126, doi: 10.1016/j.jastp.2018.10.019.
4. O.V. Mandrikova, N.V. Fetisova, Y.A. Polozov, I.S. Solovev, M.S. Kupriyanov, Method for modeling of the components of ionospheric parameter time variations and detection of anomalies in the ionosphere, *Earth, Planets and Space*, 2015, 67(1), pp. 131-146. doi: 10.1186/s40623-015-0301-4.
5. D. Bilitza, B.W. Reinisch International Reference Ionosphere 2007: Improvements and new parameters, *Advances in space research*, 2008, 42, pp. 599–609.
6. Mallat S. A wavelet tour of signal processing, London, Academic Press, 1999, 671 p.

SUPERSUBSTORMS DURING TWO STRONG MAGNETIC STORMS

*Irina Despirak¹, Andris Lubchich¹, Natalia Kleimenova², Liudmila Gromova³, Sergey Gromov³,
Liudmila Malysheva^{2 3}*

¹*Polar Geophysical Institute, Apatity, Murmansk region, 184209, Russia*

²*Schmidt Institute of the Earth Physics, Moscow, Russia*

³*IZMIRAN, RAS, Troitsk, Russia*

Introduction. It is known, that substorms can develop during magnetic storms atypically. Recently it was found a specific type of substorms - supersubstorms, observed mainly during geomagnetic storms [1, 2]. They are very intense magnetic substorms, and these extreme events generating considerable interest in terms of an understanding of the physical interaction processes in the solar wind - Earth's magnetosphere - ionosphere system. The term “Supersubstorm” (SSS) was introduced by [1] to designate very strong substorms, when the analysis of ground-based observations from the SuperMAG magnetometer network were carried. SSSs are very intense magnetic substorms when the SML or AL indexes of geomagnetic activity reach very high negative values (< -2500 nT). SSS events are detected during specific conditions in the solar wind, namely, when the long-term southward interplanetary magnetic field, which is usually associated with the solar wind magnetic clouds (MCs) or a SHEATH plasma compression region ahead of a MC [1], [3]. Furthermore, the most SSS events are associated with density jumps and pressure pulses of the solar wind. It was shown that according to the considered SSS classification, occurrence a SSS is associated with interplanetary manifestations of coronal mass ejections (CME) and, in fact, there is no relationship to high-speed streams from coronal holes [3].

The aim of our work is to study the substorm activity during two storms: 7-8 September 2017 and 25-26 August 2018. The first event, 7-8 September 2017, is the large magnetic storm (Dst~-150 nT), registered during the decline phase of 24 solar cycle. Note that there were only few storms during end of this solar cycle, and the occurrence of September 2017 strong storm attracted the attention of many researchers [4-6]. We analyzed the spatial behavior of two supersubstorms events observed during storm on 7-8 September 2017 and one supersubstorm registered during the storm on 25-26 August 2018. For this purpose, the data from the SuperMAG global magnetometer network and Scandinavian magnetometer profile IMAGE were used. It should be noted that great number of examples of the SSS observations may find in the previous works [1, 3], and therefore we did not include the another SSSs in this paper.

Data. We used the OMNI data base and the catalog of large-scale solar wind phenomena (<ftp://ftp.iki.rssi.ru/omni/>) for determination of the solar wind types [7]. Extremely intense substorms (SSS) were determined by SML, based on the data from magnetic ground-based observations of the

SuperMAG network (<http://supermag.jhuapl.edu/>) and Scandinavian IMAGE network (<http://space.fmi.fi/image/>). Supersubstorms are defined as those events with peak SML (AL) < -2500 nT [1, 2]. The latitudinal SSS propagation we defined by the equivalent currents distribution modelled by MIRACLE system. The spatial SSS distribution were examined by maps of the electric field currents from the SuperMAG network.

Results. Supersubstorm determination.

Figure 1 (bottom panel) shows the variations of SML index from 16 UT on 7 September to 22 UT on 8 September 2017. Two supersubstorms were observed: at ~00:25 UT on 8 September, which is marked as SSS-1, and at ~13:08 UT on 8 September, which is marked as SSS-2. The moments of SSS are pointed by blue arrows. Note, that the SSS-1 was more intensive than SSS-2, probably, due to the higher values of B_z component of the Interplanetary Magnetic Field.

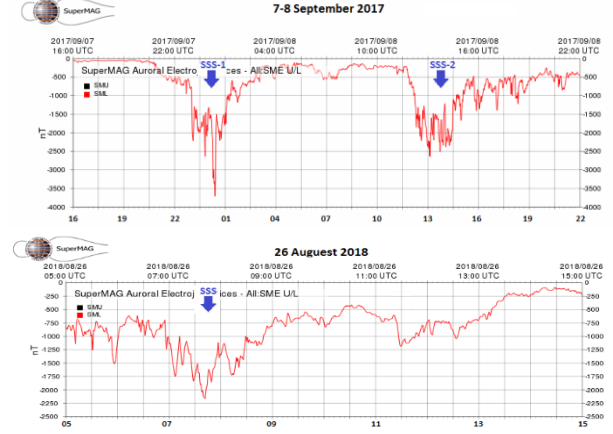


FIGURE 1. The variation of SML index from 16 UT on 7 September to 22 UT on 8 September and from 05 to 15 UT on 26 August 2018.

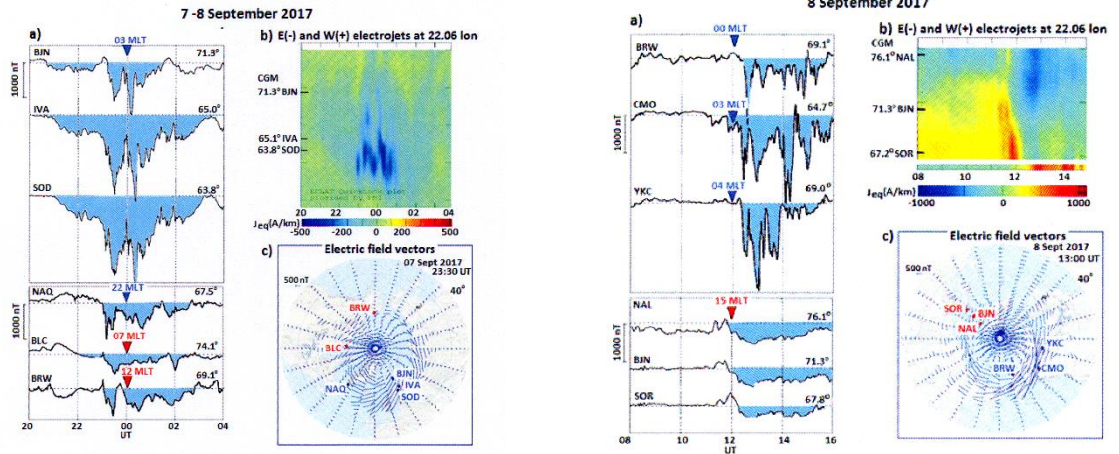


FIGURE 2. Spatial distributions of the magnetic disturbances during SSS-1 and SSS-2: a) Variations of X-component of the magnetic field at the auroral stations BJN, IVA, SOD for SSS-1 and BRW, CMO, YKC for SSS-2 and at the polar stations NAQ, BLC, BRW for SSS-1 and NAL, BJA, SQR for SSS-2; b) map of the equivalent currents by MIRACLE system; c) map of the electric field vectors from SuperMag network.

The third supersubstorm (SSS) was observed at ~ 07:40 UT on 26 August 2018 at the end of the magnetic cloud (MC) in the solar wind, when the B_Y component of the IMF had already changed to the positive values, the B_Z component of the IMF had remained negative for a long time, but it had already begun to decrease slightly. In addition, the solar wind speed was low, and the local of the solar wind pressure jump preceded this supersubstorm.

Longitudinal effects of the westward electrojet during SSS. The left panels of Figure 2 show the spatial distribution of the magnetic disturbances during the first supersubstorm (SSS-1). It is seen that the maximal disturbances were registered at the auroral latitudes, at IMAGE meridian, in the post-midnight sector. Variations of X-component of magnetic field are shown on the top panels of Figure 2a. It is seen the strong magnetic field variations (more ~1000 nT). The development of the westward

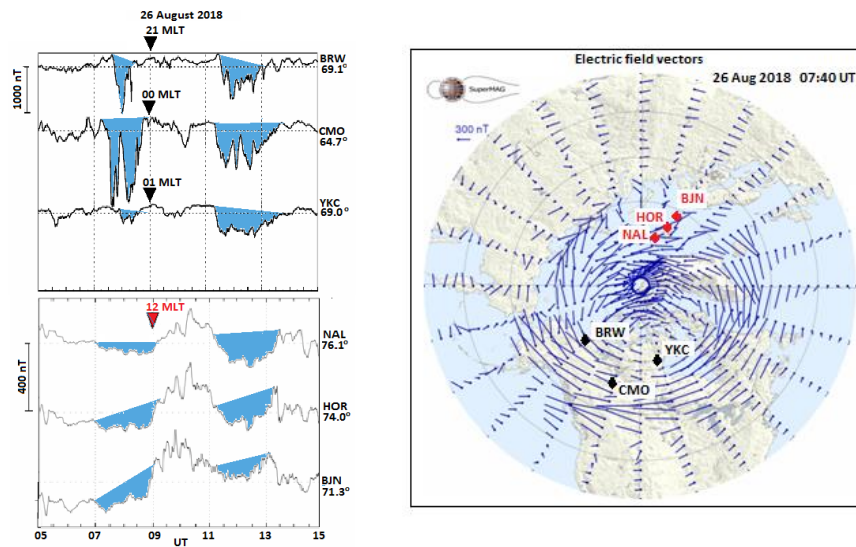


FIGURE 3. Spatial distributions of the magnetic disturbances during SSS-3: a) Variations of X-component of the magnetic field at the auroral stations BRW, CMO, YKC and at the polar stations NAL, HOR, BJN; b) the map of equivalent currents by MIRACLE system; c) the map of the electric field vectors from SuperMag network.

the electric field vectors (Figure 2c) shows that the westward electrojet was developed in the global scale, reaching the day side region.

The same developments of the westward electrojet were registered during SSS-2 and SSS-3 (Figure 2 (right panels) and Figure 3).

Conclusions.

- 1) Three supersubstorms have been observed during two strong magnetic storms on 7-8 September 2017 and on 26 August 2018.
- 2) For the first time, it was found that supersubstorms could develop in the global scale surrounding the Earth.

Acknowledgements. The work was performed as part of a state assignment.

1. B.T. Tsurutani, R. Hajra, E. Echer, J.W. Gjerloev, Extremely intense ($SML \leq -2500$ nT) substorms: Isolated events that are externally triggered?, *Ann. Geophys.*, 2015, 33(5), pp. 519–524.
2. R. Hajra, B.T. Tsurutani, E. Echer, W.D. Gonzalez., J.W. Gjerloev, Supersubstorms ($SML < -2500$ nT): Magnetic storm and solar cycle dependences, *J. Geophys. Res.*, 2016, 121, pp. 7805–7816, doi: 10.1002/2015JA021835.
3. I.V. Despirak, A.A. Lyubchich, N.G. Kleimenova, Supersubstorms and conditions in the solar wind, *Geomag. Aeron.*, 2019, 59(2), pp. 170–176.
4. N.G. Kleimenova, E.E. Antonova, O.V. Kozyreva et al., Strong vfgnetic storm on 7-8 September 2017: high-latitude magnetic variations and geomagnetic pulsations Pc5, *Geomag. and Aeron.* 2018, 58(5), pp. 619–629.
5. A.P. Dimmock, L. Rosenqvist, J.-O. Hall, A. Viljanen, E. Yordanova, I. Honkonen et al., The GIC and geomagnetic response over Fennoscandia to the 7–8 September 2017 geomagnetic storm, *Space Weather*, 2019, 17, <https://doi.org/10.1029/2018SW002132>.
6. D.V. Blagoveshchensky, M.A. Sergeeva, Impact of geomagnetic storm of September 7–8. 2017 on ionosphere and HF propagation: A multi-instrument study, *Advances in Space Research*, 2019, 63, pp. 239–256.
7. Yu.I. Yermolaev, N.S. Nikolaeva, I.G. Lodkina et al., Catalog of large-scale solar wind phenomena for the period 1976-2000. *Cosmic Research (Engl. Transl.)*, 2009, 47, pp. 81–94.

electrojet during SSS-1 shown on the left panel (Figure 2b), presented the equivalent westward and eastward currents. It confirms that development of SSS-1 took place at the auroral latitudes, from $\sim 58^\circ$ to $\sim 71.4^\circ$ CGMLAT.

However, simultaneously the bay-like magnetic disturbances located at the polar latitudes (from $\sim 67^\circ$ to $\sim 74.1^\circ$ CGLAT), at the stations NAQ, BLC (in the morning sector) and BRW (near the noon) (Figure 2a, bottom panels) were observed.

The SuperMAG map of

EFFECT OF STRONG GEOMAGNETIC STORM ON GNSS PRECISE POINT POSITIONING QUALITY

Semen V. Syrovatskii^{1, 2}, Anna S. Yasyukevich¹, Yury V. Yasyukevich¹

¹*Institute of Solar-Terrestrial Physics SB RAS, Irkutsk, Russia*

²*Lomonosov Moscow State University, Faculty of Physics, Moscow, Russia*

Introduction. Global navigation satellite systems (GNSS) like GPS, GLONASS, BeiDou etc. have become tightly integrated into human daily lives and economic activity. The state of the ionosphere is one of crucial factors for the GNSS positioning accuracy. While the navigation signal propagates through the ionosphere, ionospheric irregularities can lead to the signals scattering [1]. The effect is more pronounced when the irregularity scale is of the radiowave first Fresnel zone $\sim(\lambda Z)^{1/2}$ (where λ is the signal wavelength, Z is the distance to the irregularity). It is about 100-300 m in GNSS case, i.e. so-called small-scale irregularities. The scattering leads to radio signal amplitude scintillations and, in the extreme case, may give rise to signal losses-of-lock [2]. Deep signal fades appearing due to small-scale irregularities result in navigation outages [3]. This can decrease the stability of the GNSS service and even arouse inability to provide coordinates to a user.

In quiet geophysical conditions ionospheric irregularities of different scales can appear in high-latitude and equatorial regions. The amplitude scintillations and GNSS signal losses-of-lock are often observed in these regions [4]. Geomagnetic storms are known to be a source for small-scale ionospheric irregularities in wide latitudinal range. Geomagnetic storms, as well, feature occurrence of traveling ionospheric disturbances (TID) propagating from auroral oval toward lower latitudes. TIDs also can be a source for GNSS positioning quality deterioration. Luo et al. [5] studied several strong storms during solar cycle 24, including the 2015 March 17 St. Patrick storm. They reported increase in precise point positioning (PPP) error during the storm up to 0.32 m at medium and above 1 m at high latitudes with respect to only 0.163 m on a quiet day.

In this study, we analyze the dynamics in GNSS positioning error during several strong geomagnetic storms of last decade on a global scale. Our task is to identify the changes in positioning accuracy in different latitudinal-longitudinal sectors depending on the storm evolution and characteristics.

PPP error estimating. We study is based on the data of phase dual-frequency measurements from the worldwide GNSS network [6]. To estimate the changes in positioning accuracy, for every station we calculated GPS precise point positioning (PPP) coordinates in the kinematic mode. The calculating was performed using the GAMP opensource software [7]. Receiver and satellite clock offsets are considered in GAMP PPP solution by applying IGS precise satellite orbit and clock products. Besides, linearized equations of original pseudorange and carrier phase observations take into account line-of-sight (LOS) ionospheric delay, receiver non-calibrated code delay, receiver and satellite non-calibrated phase delays, and zenith wet delay. We used a dual-frequency PPP model, in which the receiver non-calibrated code delays are absorbed by both receiver clock offset and LOS ionospheric delay parameters. The 24-hour averaged values of X, Y, Z coordinates for a station were regarded as reference positions. The total positioning error was calculated as a difference between the reference and the instant position:

$$\sigma_{XYZ} = (\Delta X^2 + \Delta Y^2 + \Delta Z^2)^{1/2} \quad (1)$$

To estimate the dynamics of the error in different latitudinal regions, we calculated zonal mean error values for the European-Asian (0:180°E) and American-Atlantic (-180:0°E) sectors within the latitude bins of 2.5° size.

Results. In the article, as an example, we focused in detail on results for the August 25-26, 2018 geomagnetic storm. The storm is one of the strongest geomagnetic events of the solar cycle 24. The storm was triggered by the August 20, 2018 Coronal Mass Ejection (CME). On August 25, 2018 the CME reached the Earth, giving rise to a strong G3 geomagnetic storm.

Figure 1 provides the distributions in PPP error around the globe at 07:45 UT on August 25 (a, before the storm) and on August 26 (c, during the storm main phase). Pannels b and d in the figure show the intensity in total electron content (TEC) variations filtered within 10-20 min range at the corresponding time instans. These variations are obtained using the SIMuRG tool for collecting, processing, storage and presentation of GNSS TEC data [8].

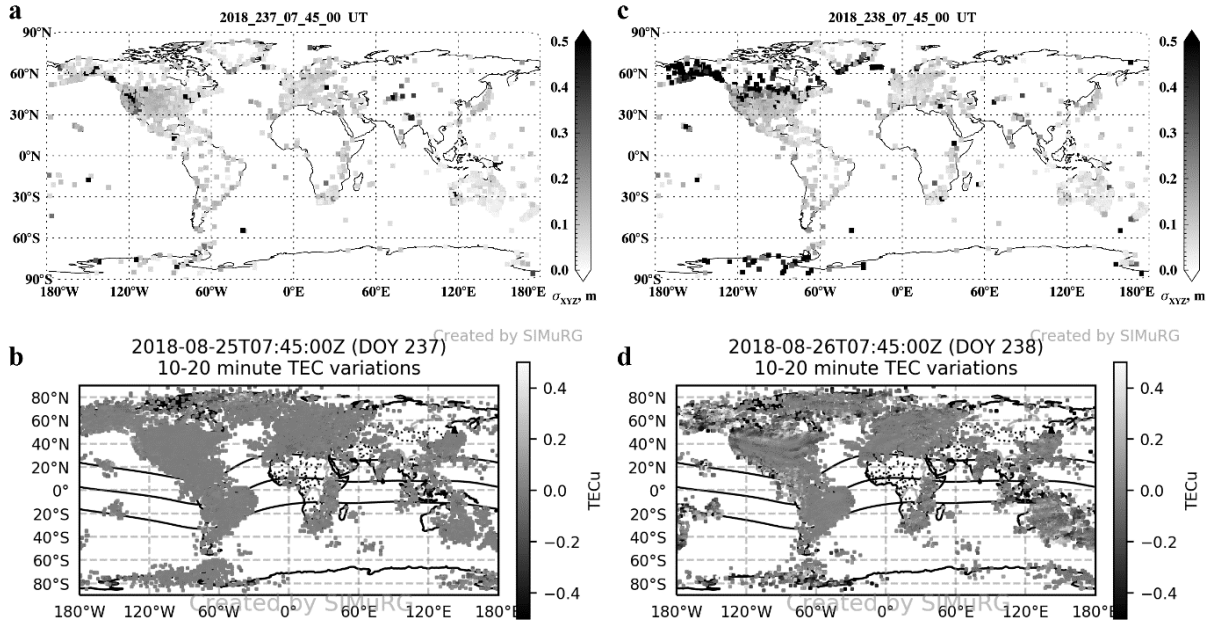


FIGURE 1. Averaged total PPP error σ_{XYZ} vs latitude in the American - Atlantic (a-c) and Asian - European (d-f) longitudinal sectors. The latitude bin size is 2.5° .

In the Fig. 1d, during the storm main phase, we can see a significant enhancement in TEC variation intensity in the areas stretched along the auroral oval boundaries, both in the Northern and Southern hemispheres. In the North American sector, strong disturbances reach 40°N latitude. Increased variations are also observed in the equatorial region. In these same areas, we can observe heightened values of total positioning error σ_{XYZ} that were not recorded in the period before the storm. The error values exceed 0.5 m compared to ~ 0.1 m on a quiet day.

Figure 2 shows the zonal mean values of total PPP error σ_{XYZ} averaged in American - Atlantic (a-c) and Asian - European (d-f) longitudinal sectors. Panels a and d show the dynamics in PPP error for the reference quiet day (August 24, 236 DOY), the panels b and e show the data for the storm beginning day (August 25, 237 DOY) and the panels c and f – for August 26 (238 DOY). Note that the quality of the GAMP PPP solution over 0-2 UT is unsatisfactory and we do not consider this time. The horizontal white strips on the pannels (zero values) mark lack of the data.

The results for the reference day show that the characteristic error in most regions do not exceed 0.1 m. Increased error values are observed over $30\text{--}60^\circ\text{N}$ latitudes in the American - Atlantic sector. The error reaches 0.3 m here even on a quiet day. These PPP error increases are due to satellite geometry or data processing peculiarities. Such effects have similar patterns for both the storm and the reference days.

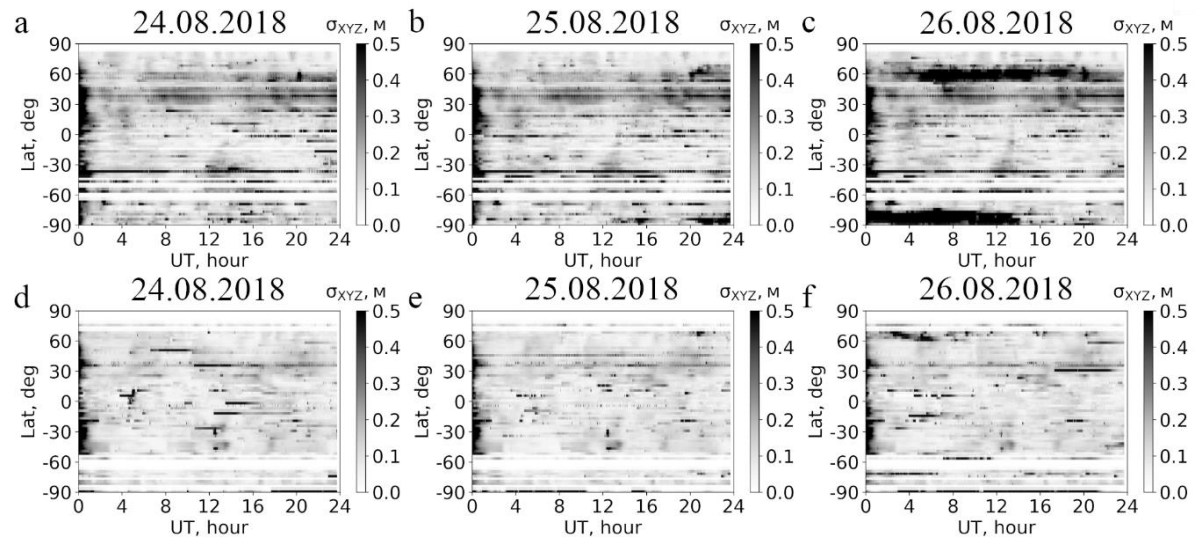


FIGURE 2. Averaged total PPP error σ_{XYZ} vs latitude in the American - Atlantic (a-c) and Asian - European (d-f) longitudinal sectors. The latitude bin size is 2.5° .

After 20:00 UT on August 25 we can notice a slight increase in the average error at $65\text{--}75^\circ\text{N}$ latitudes in the Northern hemisphere both in American-Atlantic and Asia-European sectors. A sharp decrease in the PPP quality is clearly observed during all day on August 26 in the North American sector. The average PPP error is significantly greater than 0.5 m. Also, a noticeable growth in PPP error is visible in high latitudes of the Southern hemisphere until 14 UT. In the European-Asian sector, positioning deterioration is observed at $60\text{--}70^\circ\text{N}$ latitudes till around noon. So, we recorded a precision deterioration, which results in fivefold worse positioning accuracy during the storm. The revealed PPP positioning deterioration is comparable in magnitude with that observed during the September 6, 2018 solar radio flare [9] but lasts much longer. Our analysis has shown that these positioning quality degradation was observed even longer than during the St. Patrick magnetic storm.

The research is supported by the Russian Federation President Grant No. MK-3265.2019.5. We applied data treating methods developed under budgetary funding of Basic Research program II.16. TEC variation maps were obtained via SIMuRG on-line service (<https://simurg.iszf.irk.ru>). The SYM-H index data were provided by the WDC for Geomagnetism, Kyoto (<http://wdc.kugi.kyoto-u.ac.jp/wdc/>). We acknowledge use of NASA/GSFC's Space Physics Data Facility's OMNIWeb service, and OMNI data (<https://omniweb.gsfc.nasa.gov>).

1. K. C. Yeh and C. H. Liu, Radio wave scintillation in the ionosphere, *Proc. IEEE*, 1982, 70(4), doi:10.1109/PROC.1982.12313.
2. P. M. Kintner, B. M. Ledvina, E. R. de Paula, GPS and ionospheric scintillations, *Space weather*, 2007, 5(9), doi:10.1029/2006SW000260.
3. A. O. Akala, P. H. Doherty, C. S. Carrano et al., Impacts of ionospheric scintillations on GPS receivers intended for equatorial aviation applications, *Radio Science*, 2012, 47(4), doi:10.1029/2012RS004995.
4. Y. Jiao and Y. T. Morton, Comparison of the effect of high-latitude and equatorial ionospheric scintillation on GPS signals during the maximum of solar cycle 24, *Radio Sci.*, 2015, 50(9), doi:10.1002/2015RS005719.
5. X. Luo, S. Gu, Y. Lou et al., Assessing the Performance of GPS Precise Point Positioning Under Different Geomagnetic Storm Conditions during Solar Cycle 24, *Sensors*, 2018, 18(6), doi:10.3390/s18061784.
6. J. M. Dow, R. E. Neilan, C. Rizos, "The International GNSS Service in a changing landscape of Global Navigation Satellite Systems," *J. Geodesy*, 2009, 83(3-4), doi:10.1007/s0019000803003.

7. F. Zhou, D. Dong, W. Li et al., GAMP: An open-source software of multi-GNSS precise point positioning using undifferenced and uncombined observations, *GPS Solutions*, 2018, 22(2), doi:10.1007/s10291-018-0699-9.
8. Yu. V. Yasyukevich, I. V. Zhivetiev, A. V. Kiselev et al., Tool for Creating Maps of GNSS Total Electron Content Variations, *Proceedings of 2018 Progress In Electromagnetics Research Symposium (PIERS – Toyama)*, 2018, doi:10.23919/PIERS.2018.8597604.
9. Y. Yasyukevich, E. Astafyeva, A. Padokhin et al., The 6 September 2017 X-class solar flares and their impacts on the ionosphere, GNSS, and HF radio wave propagation, *Space Weather*, 2018, 16(8), doi:10.1029/2018SW001932.

COMPARISON OF THE HF GROUND BACKSCATTER SIMULATED USING IONOSPHERE MODEL UPDATED BY VS AND GIM TEC DATA

Alexey V. Oinats¹, Ilya K. Edemsky¹, Denis D. Rogov²

¹*Institute of Solar-Terrestrial Physics SB RAS, Irkutsk 664033, Russia*

²*Arctic and Antarctic research institute, Saint-Petersburg 199397, Russia*

Introduction. Interpretation of HF radar data (like SuperDARN data) is significantly dependent on the mapping accuracy, when characteristics of the registered echoes are associated with a specific geographical region. All HF radars measure HF propagation delay (slant or oblique range) to a target. A problem arises since we mostly need true ground distance to the target. A number of HF radars can measure also elevation angle. However even in this case HF refraction, which is unknown a priori and can be subject to significant changes depending on ionospheric conditions, can affect the determination of target location.

Researchers use different solutions of the problem depending on required accuracy. One approach is using some effective HF reflection height and simple flat Earth geometry (Breit and Tuve's theorem). For example, in [1] fixed effective height is used to determine traveling ionospheric disturbance (TID) characteristics from SuperDARN data. Other researchers use more complex technique based on empirical height models [2, 3] which are appropriate for specific HF radars.

In the paper we develop another approach which is based on HF wave propagation simulation using empirical ionosphere models updated by real observations. We test a technique for region-based updating IRI-family ionosphere models, such as IRI-2012 [4] and IRI-PLAS [5], using data of vertical sounding (VS) and global navigation satellite systems (GNSS). As input parameters we used critical frequency of F2 layer (foF2) obtained at VS stations (Arti, Amderma, Salekhard, Dikson, and Norilsk) located in the Ekaterinburg HF radar (EKB; 56.4°N, 58.5°E) field-of-view (FOV) and total electron content (TEC) from global ionospheric maps (GIMs). The locations of the radar, its FOV, and VS stations are shown in Figure 1 (left). Updated vertical profiles of electron density are used to simulate HF ground backscatter (GB) in the framework of waveguide approach. HF GB calculation technique [6, 7] is based on adiabatic approach of eigenfunction method [8]. This technique allows us to calculate not only trajectory characteristics but also GB intensity, taking into account the EKB HF radar antenna system specification and ground electrical parameters. However in the current report we compare simulated HF minimum slant range, which is associated with skip distance, with the observed one by the EKB HF radar to test effectiveness of various updating schemes.

For illustration on Figure 1 (right side) the observed range-time-intensity plot (RTI plot, panel (a)) and its simulation (panel (b)) are shown for February 8, 2014 and beam #0 (azimuth -4.3°). Minimum slant range is shown on the figure by crosses.

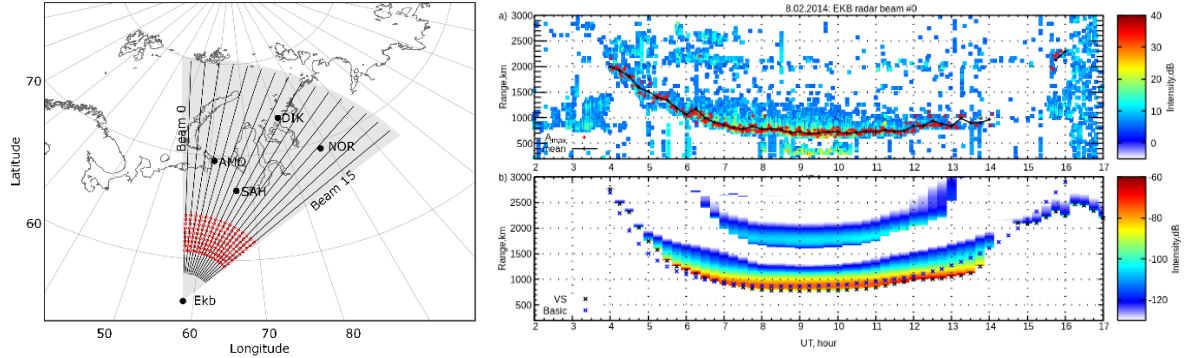


FIGURE 1. The EKB HF radar location and its FOV. Vertical ionosonde locations are shown by black circles with labels. Panel (a) - the EKB HF radar range-time-intensity plot (RTI) observed on February 8, 2014 on beam #0. Red crosses correspond to echoes with maximum intensity. Black line with crosses shows mean slant range dependence. Panel (b) GB intensity calculated using IRI-2012 updated by VS data. Black crosses show minimum range dependence. Blue crosses show minimum range dependence calculated using default IRI-2012

Updating schemes description. IRI-2012 model has a built-in mode in which electron density height profile can be adjusted by user input foF2 value [4]. If one have a set of foF2 measured in spatially separated points for a given time moment, it becomes possible to make a spatial interpolation of the measured values (or their deviations from the model values). Then foF2 values interpolated along a given propagation path can be used as input to calculate updated IRI electron density profiles.

In this study we check three schemes for IRI model updating. In the first one we used foF2 measured by VS to calculate a correction factor which is equal to the ratio of the observed critical frequency to the model one at the ionosonde location

$$r = \frac{foF2_{obs}}{foF2_{model}}. \quad (1)$$

For a set of VS stations we have a set of correction factors spatially distributed in the region under analysis. The factors are interpolated using inverse weighted distance interpolation methods modified for the spherical case. At a point of interest the actual critical frequency is obtained via the correction factor and the model critical frequency in that point.

The second scheme uses GIM TEC maps and IRI-PLAS model [5] for calculation the actual foF2 in a given point. IRI-PLAS has a built-in mode, in which both foF2 and hmF2 (F2 layer peak height) can be updated according to user input TEC value. We used GIM maps provided by Center for Orbit Determination in Europe (CODE) to get TEC for a given point and UT hour.

The third scheme uses foF2 measured at VS station and GIM TEC together. The combined use of actual foF2 and TEC GIM values allow us to make some calibration of the equivalent ionosphere slab thickness [9] provided by IRI-PLAS. First, we calculate the “observed” slab thickness for each VS station

$$\tau_{obs} = \frac{TEC_{GIM} \cdot 10^3}{1.24 foF2_{obs}^2}. \quad (2)$$

Then the proportionality coefficient, r_{obs} , is calculated between τ_{obs} and τ_{model} for VS station location. The coefficient is spatially interpolated, and corrected foF2 are calculated at a point of interest

$$foF2_{calc} = 8.97 \sqrt{\frac{TEC_{GIM}}{r_{obs} \tau_{model}}}. \quad (3)$$

All the schemes described above allow us to reconstruct “actual” foF2 at each point of a given HF propagation path. To calculate electron density profiles which are necessary for subsequent HF propagation simulation we use $foF2_{calc}$ as user input to IRI-2012 model.

Results and discussion. Figure 1a shows RTI plot obtained by the EKB HF radar on beam #0 (azimuth -4.3°) on February 8, 2014. Red crosses show extracted dependence of minimum slant range which corresponds to echoes with maximum intensity. Black line with crosses is averaged observed minimum range. Corresponding simulated HF GB minimum slant range is presented in Figure 1b. Black and blue crosses show dependences for the default IRI-2012 model and the updated one by VS data.

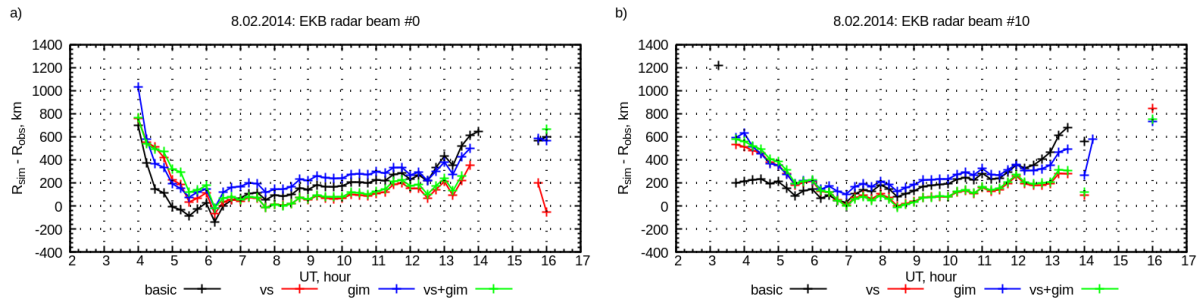


FIGURE 2. Absolute difference between calculated and mean observed minimum range for beam #0 (a) and beam #10 (b). Black, red, blue, and green lines correspond to simulation without updating, VS only, GIM only, and VS + GIM updating schemes

Figure 2 shows difference between simulated GB minimum range and observed one as a function of UT. Black, red, blue, and green lines correspond to the simulation using default IRI-2012 model without updating, VS updating only, GIM only, and VS + GIM updating schemes respectively. Figure 2a and 2b correspond to beam #0 and beam #10 respectively.

As one can see from Figure 2 there is some typical shape of the dependence. Deviation has minimum of about 0–200 km at noon and increases to morning and evening hours. Such dependence can be associated with ionosphere model shortcomings during solar terminator passing hours. On beam #0 deviation reaches values of 600–1000 km. This can be also connected with contamination by the echoes coming from behind the EKB HF radar. These echoes are incorrectly marked by the technique for minimum slant range extraction from the observations.

All simulations mostly overestimate minimum slant range. However deviation calculated without updating (black) is negative during the period 5–7 UT on beam #0, whereas it is positive during the same time interval on beam #10. This may lead to the distortion of the image after mapping, because on one beam the echoes will be mapped closer to the radar, and on the other beam farther.

Finally, VS updating gives the best correspondence with observations. Deviation for VS updating is almost twice less than for default IRI-2012. Combined VS and GIM TEC data gives almost the same deviation as for VS updating scheme. GIM TEC updating scheme gives the worst correspondence with observations.

Acknowledgments. The reported study was funded by RFBR, project number 19-05-00889. In the study we used the methods obtained in the framework of Basic Research program II.12. The results were obtained using the equipment of Center for Common Use «Angara» <http://ckp-rf.ru/ckp/3056/>. We are grateful to the CODE team for the access to GIM TEC data provided from the CODE FTP directory: <ftp://ftp.aiub.unibe.ch/CODE/>.

1. W.A. Bristow, R.A. Greenwald, J.C. Samson, Identification of high-latitude acoustic gravity wave sources using the Goose Bay HF radar, *J Geophys Res*, 1994, 99(A1), pp. 319–331.

2. G. Chisham, T.K. Yeoman, G.J. Sofko, Mapping ionospheric backscatter measured by the SuperDARN HF radars—part 1: a new empirical virtual height model, *Ann Geophys*, 2008, 26, pp. 823–841.

3. T.K. Yeoman, G. Chisham, L.J. Baddeley, R.S. Dhillon, T.J.T. Karhunen, T.R. Robinson, A. Senior, D.M. Wright, Mapping ionospheric backscatter measured by the SuperDARN HF radars—part 2: assessing SuperDARN virtual height models, *Ann Geophys*, 2008, 26, pp. 843–852.
4. D. Bilitza, D. Altadill, V. Truhlik, V. Shubin, I. Galkin, B. Reinisch, and X. Huang, International Reference Ionosphere 2016: From ionospheric climate to real-time weather predictions, *Space Weather*, 2017, 15, pp. 418–429, doi:10.1002/2016SW001593.
5. T.L. Gulyaeva, D. Bilitza, Towards ISO Standard Earth Ionosphere and Plasmasphere Model, *In: New Developments in the Standard Model*, NOVA Publishers, 2012.
6. A.V. Oinats, V.I. Kurkin, K.A. Kutelev, N. Nishitani, The outlook of SuperDARN radars application for monitoring of the ionospheric dynamics in Russia, *Physical Bases of Instrumentation*, 2012, 1(3), pp. 3-18 (in Russian).
7. S. N. Ponomarchuk, N. V. Ilyin, V. V. Khakhinov, V. I. Kurkin, A. V. Oinats, and M. S. Penzin Comprehensive algorithm for calculation of backscatter signals characteristics within the waveguide approach, *Proc. SPIE 11208, 25th International Symposium on Atmospheric and Ocean Optics: Atmospheric Physics*, 112088R, 18 December 2019, doi: 10.1117/12.2539946.
8. V.I. Kurkin, I.I. Orlov, V.N. Popov, Normal Wave Technique in HF Radio Communication Problem, Nauka, Moscow, 1981.
9. R.S. Roger, Measurements of the equivalent slab thickness of the daytime ionosphere, *Journal of Atmospheric and Terrestrial Physics*, 1964, 26(4), pp. 475–497.

AURORAL IONOSPHERE STATIONARY MODEL (E-AIM) UV INPUT PARAMETERS ESTIMATION USING SATELLITE DATA

Vera D. Nikolaeva¹, Evgeny I. Gordeev², Denis D. Rogov¹, Aleksander V. Nikolaev¹

¹ Department of Geophysics, Arctic and Antarctic research institute, Saint Petersburg, Russia

² Department of Earth Physics, Saint Petersburg State university, Saint Petersburg, Russia

The Earth's ionosphere is one of the primary indicators of the solar influence on our planet. This is especially true for the Arctic zone. Investigation of relationships between the solar UV activity and the ionosphere parameters (regular layer E) in the Russian Federation Arctic Region is the main goal of this study.

E-layer Auroral Ionospheric Model (E-AIM) is developed in Arctic and Antarctic research institute to provide temporal and spatial density distribution of the main ionosphere neutral species (NO, N(⁴S), N(²D)), ions (N₂⁺, NO⁺, O₂⁺, O⁺) and electrons in the altitude range from 90 to 150 km. E-AIM model consider solar radiation ionization source, superposed with sporadic precipitation of magnetospheric electrons. The E-AIM model based on E-layer equilibrium state that reaches in chemical reactions between ionospheric species in each location under specific solar and geomagnetic activity conditions. The numerical solution of the continuity equations for the neutrals and ions is implemented using the high-performance Gear method [1] for ordinary differential equation (ODE) systems. Applying the Gear method for solving stiff ODE system strongly reduce the computation time and machine resources comparing to widely used methods and provide an opportunity to calculate the global spatial E-layer ion content distribution. NRLMSISE-00 model [2] is used for neutral atmosphere content and temperature E-AIM input.

The input parameters for the Auroral Ionospheric Model, characterizing solar and magnetic activity, are the sunspot number, the three-hour Ap index, and the daily value of the solar radio emission at the wavelength 10.7 cm (F10.7 index). Calculation of the electron density using the auroral ionosphere model for the daytime is done using two different ways of solar UV radiation input: (1) a theoretically calculated UV spectrum based on Canadian index F10.7 as an input parameter; (2) direct measurements of the solar UV spectra obtained from the TIMED satellite.

(1) Solar activity indices are widely used to estimate the photon flux at the Earth's atmosphere upper boundary. In photoionization calculation, the E-AIM model took into account the solar photons density flux value for various values of the daily solar activity index F10.7. Solar radio emission 10.7 cm (2800 MHz) is suitable for solar activity description and space weather prediction. F10.7 observations series is one of the longest among the solar activity indicators. Daily measurements take place in Canada since 1947 [3]. Due to such a long observation series, this index allows to estimate the solar activity over the course of seven solar cycles [4] and makes it possible to use it in retrospective calculations. Data is provided by the National Research Council of Canada in partnership with Canadian Natural Resources and is publicly available [5].

Using the F10.7 index as an input parameter, the E-AIM model calculates X-ray and UV solar radiation fluxes in the wavelength range from 0.05 nm to 105 nm, including 16 spectral lines. In this range, a separate calculation of hard X-ray radiation (0.05–0.8 nm), soft X-ray radiation (0.8–10 nm), and ultraviolet radiation (10–105 nm) is performed. The background solar X-ray flux from 0.05 to 0.8 nm at the atmosphere upper boundary is produced according to [6]; from 0.8 to 10 nm according to [7]. The calculation of UV radiation at the upper atmospheric boundary for 37 wavelength intervals covering a range from 5 to 105 nm is based on EUVAC Solar Flux Model [8]. The EUVAC model is appropriate for calculating parameters such as ionization rates, but its relatively rough wavelength resolution is not good enough to calculate certain parameters of aeronomic interest adequately, such as detailed photoelectron fluxes, for example.

(2) TIMED satellite (Thermosphere Ionosphere Mesosphere Energetics and Dynamics), designed at Applied Physics Laboratory of John Hopkins University, supported by NASA, launched on December 7, 2001 and is still functioning. One of the scientific tasks of the TIMED mission is to study the dynamics of the mesosphere and lower thermosphere under the influence of UV solar radiation. TIMED satellite data can be used to quantify atmospheric radiative processes, including the effects of solar flares, solar rotation (27 days), and the eleven-year cycle. The SEE (Solar EUV Experiment) device [9] was developed at the University of Colorado for the TIMED mission. The SEE data is publicly available and has a temporal resolution of 97 minutes, which corresponds to the frequency of the satellite position in the sub-solar point. Several measurements within three minutes are taken during each orbital period. TIMED SEE LEVEL 3A data is a solar radiation spectrum from 0.5 to 195 nm with 1 nm channels and 38 emission lines. Thus, satellite data provides high resolution UV and X-Ray data for aeronomic calculations [10]. Also higher solar flux temporal resolution is the only way to estimate UV variation and solar flares effect on the ionosphere [11].

The direct measurements of the TIMED satellite are used to evaluate the accuracy of calculating the electron density of the auroral ionosphere E layer using the E-AIM model with the Canadian index F10.7 as an input parameter. However, the corrected TIMED satellite data appears in the public access with a delay and can be used only for archived data analysis. Calculations of E-AIM model with different input parameters are compared with vertical sounding data from Russian Arctic stations (Gorkovaskaya, Amderma and Dikson) located in the different parts of the auroral zone (Table 1) for the low geomagnetic and solar activity period.

To compare model calculations with different UV input parameters, the period from June 4 to 6, 2019 was chosen. These days are characterized by the almost complete absence of the sporadic layer Es at all the stations. The electron concentration of the E layer of the ionosphere was calculated for each location with an hourly time step. Due to the temporal resolution of the F10.7 index, when calculating using the EUVAC model, the UV source changed every day. UV input according to the TIMED satellite has a resolution of 1.5 hours.

TABLE 1. Geographical and Geomagnetic station coordinates.

	Code	Name	Geog. Lat.	Geog. Long.	Geomag. Lat.	Geom. Long.
1	GRK	Gorkovskaya	60.27	29.38	56.7427	105.5537
2	AMD	Amderma	69.60	60.20	66.0404	136.4837
3	DIK	Dikson	73.52	80.68	69.5847	156.4218

Taking into account the fact that the sounding frequency is directly related to the ionization of the ionosphere, the electron concentration at the maximum of the E layer was converted to the critical frequency by the formula

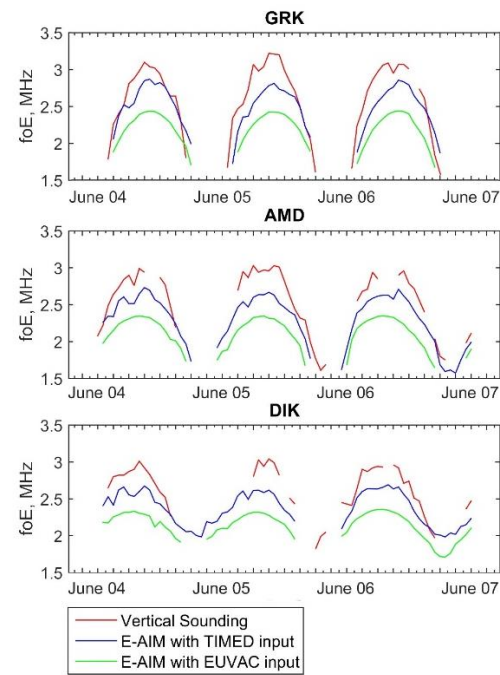
$$f = \sqrt{\frac{N_e}{1.24 \cdot 10^{10}}},$$

where f — sounding frequency [MHz], N_e — electron concentration [m^{-3}].

Figure 1 demonstrates the ionospheric vertical sounding data from Gorkovskaya, Amderma, and Dikson stations (red curves) compared to the E-AIM model results obtained using the TIMED satellite (blue curves) and EUVAC model (green curves) UV input.

Calculations of the E-AIM model using both UV input methods describe well the diurnal variation of the critical frequency of the regular E layer of the auroral ionosphere. Both methods of calculation give continuous underestimation of critical frequencies for all stations, which suggests that the discrepancy magnitude is not related to their location. Maximum discrepancies are observed during local noon and decrease with increasing solar zenith angle. However, in contrast to empirical EUVAC model, the results of E-AIM with directly measured TIMED UV input clearly demonstrate dynamics related to the temporal variation in solar radiation spectrum, which is crucial for sporadic solar flares events.

E-AIM model requires photoionization calculation adjustment to obtain reliable electron concentration values for the auroral ionosphere. A detailed analysis of the discrepancy causes and model adjustment will be carried out in the near future.

**FIGURE 1.** E-AIM model results calculated with the TIMED satellite (blue curves) and EUVAC model (green curves) UV input compared to ionospheric vertical sounding data from Gorkovskaya, Amderma, and Dikson stations (red curves) comparison.

The work is done with the RFBR financial support (project № 18-05-80004).

1. C.W. Gear, Numerical Initial Value Problems in Ordinary Differential Equations. *Prentice-Hall, Upper Saddle River*, 1971.
2. J. M. Picone, A. E. Hedin, D. P. Drob, A. C. Aikin, NRLMSISE-00 empirical model of the atmosphere: Statistical comparisons and scientific issues, *J. Geophys. Res.*, 2002, 107(A12), pp. 1468, doi:10.1029/2002JA009430.

3. A. E. Covington, Microwave solar noise observations during the eclipse of November 23, 1946, *Nature*, 1947, 159, pp. 405–406.
4. K. F. Tapping, J. J. Valdes, Did the Sun change its behaviour during the decline of cycle 23 and into cycle 24?, *Sol. Phys.*, 2011, 272, pp. 337–350.
5. K. F. Tapping, The 10.7 cm solar radio flux ($F_{10.7}$), *Space Weather*, 2013, 11, pp. 394–406, doi:10.1002/swe.20064.
6. GOST 25645.130—86 “Solar X-rays. Amplitude characteristics”. — Moscow.: Publishing House of Standards, 1986
7. GOST 25645.145—88 “Soft X-ray solar radiation. No-flare flux density model”. — Moscow.: Publishing House of Standards, 1990
8. P.G. Richards, J.A. Fennelly, D.G. Torr, EUVAC: a solar EUV flux model for aeronomic calculations, *J. Geophys. Res.*, 1994, 99, pp. 8981.
9. D. L. Woodraska, T. N. Woods, F. G. Eparvier, In-flight Calibration and Performance of the Solar Extreme Ultraviolet Experiment (SEE) aboard the TIMED Satellite, *SPIE Proceedings*, 2004, 5660, pp. 36-47.
10. T. N. Woods, G. J. Rottman, Solar ultraviolet variability over time periods of aeronomic interest, in: Comparative Aeronomy in the Solar System, eds. M. Mendillo, A. Nagy, and J. Hunter Waite, Jr., *Geophys. Monograph Series*, Washington, DC, 2002, pp. 221-234.
11. R. Vaishnav, C. Jacobi, J. Berdermann, E. Schmolter, M. Codrescu, Ionospheric response to solar EUV variations: Preliminary results, *Adv. Radio Sci.*, 2018, 16, pp. 157-165, doi: <https://doi.org/10.5194/ars-16-157-2018>.

INVESTIGATION OF INFLUENCE OF THE DISTURBED HIGH-LATITUDE IONOSPHERE ON THE SLIPS OF THE MAIN PARAMETERS OF GPS NAVIGATION SIGNALS DURING GEOMAGNETIC ACTIVITY

Alexander A. Chernyshov^{1,2}, Victor I. Zakharov³, Wojciech Miloch⁴, Yaqi Jin⁴

¹Space Research Institute of the Russian Academy of Sciences (IKI), Moscow, Russia

²West department of Pushkov Institute of Terrestrial Magnetism, Ionosphere and Radio Wave Propagation, RAS, Kaliningrad, Russia

³Faculty of Physics, Lomonosov Moscow State University, Moscow, Russia

⁴Department of Physics, University of Oslo, Oslo, Norway

Electromagnetic waves transmitted by the Global Navigation Satellite Systems (GNSS) satellites, whose wavelengths are of the order of decimeters, travel through the ionosphere before reaching a ground-based receiver. Thus, free electrons in the ionosphere can have a large impact on the group, phase and amplitude characteristics of such waves. These measurements can be used to obtain values of the total electron content (TEC), which is an integrated electron density along the ray path between the receiver and satellite determined for a tube with a cross section of one square meter. Besides, irregularities in the ionospheric plasma density distort electromagnetic waves during trans-ionospheric propagation and may lead to a poor determination of parameters or even to temporary discontinuation of maintenance (slip) of the GNSS signal. The high-latitude ionosphere is characterized by intense small-scale irregularities and inhomogeneities in the plasma density, which can be related to electric fields and increased precipitation of energetic particles. Thus, it is important to carry out detailed studies of ionospheric effects on the navigation signal propagation at high-latitudes.

The effect of an geomagnetic substorm on the slips on Global Positioning System (GPS) navigation parameters in the polar region is investigated. Optical data from the all-sky imager (ASI), as well as interplanetary magnetic field (IMF) and magnetometer data are used to complete the analysis of the slips occurrence and to monitor the substorm evolution. Two types of operational slips are considered: (i) instrumental slips including losses in the measured phase of the GPS signal, that is, these slips are of a

technical character, reflecting the quality of the electronic components of the radio transmission unit, and can virtually affect the accuracy of navigational positioning and (ii) sharp total electron content (TEC) variations lacking physical explanation or are possibly related to yet unknown processes or phenomena. In the present work, we study in detail the effects of a geomagnetic substorm that occurred on December 23, 2014, between 19:00 and 23:59 universal time (UT), on the slips in phases L_1 and L_2 as well as TEC slips at high latitudes. We focus on the response of the GPS navigation system to the perturbed

ionosphere and study the slips of the main parameters of the GPS navigation signals. To

investigate the spatial variability of the GPS TEC measurements, we use in total 4 GPS receivers in the Scandinavian sector, in Tromsø (TRO1), Skibotn (SKBN), Kiruna (KIRU) and Sondankyla (SODA). For

studying the auroral morphology and the evolution of auroral substorm, we use the ASI located at Skibotn, as well as the OMNI IMF data and the data from the ground-based magnetometer at Tromsø station. ASI records images at wavelengths of 630.0 nm and 557.7 nm every 30 and 15 seconds, respectively. In this

study, we calculate distributions of cycle slips and TEC jumps in time for each observed satellite. Also, we estimate the probability of slips in the parameter " i " (here " i " means L_1 , L_2 , TEC, P_1 and P_2) measured at each receiving station for all visible navigation satellites.

Fig. 1 gives an overview of the studied event. The IMF B_z turned southward from 19 UT and remained negative until 21:20 UT. For this orientation of the IMF, we expect the dayside magnetopause reconnection to occur, and the consequent polar cap expansion. This expansion can be clearly seen in

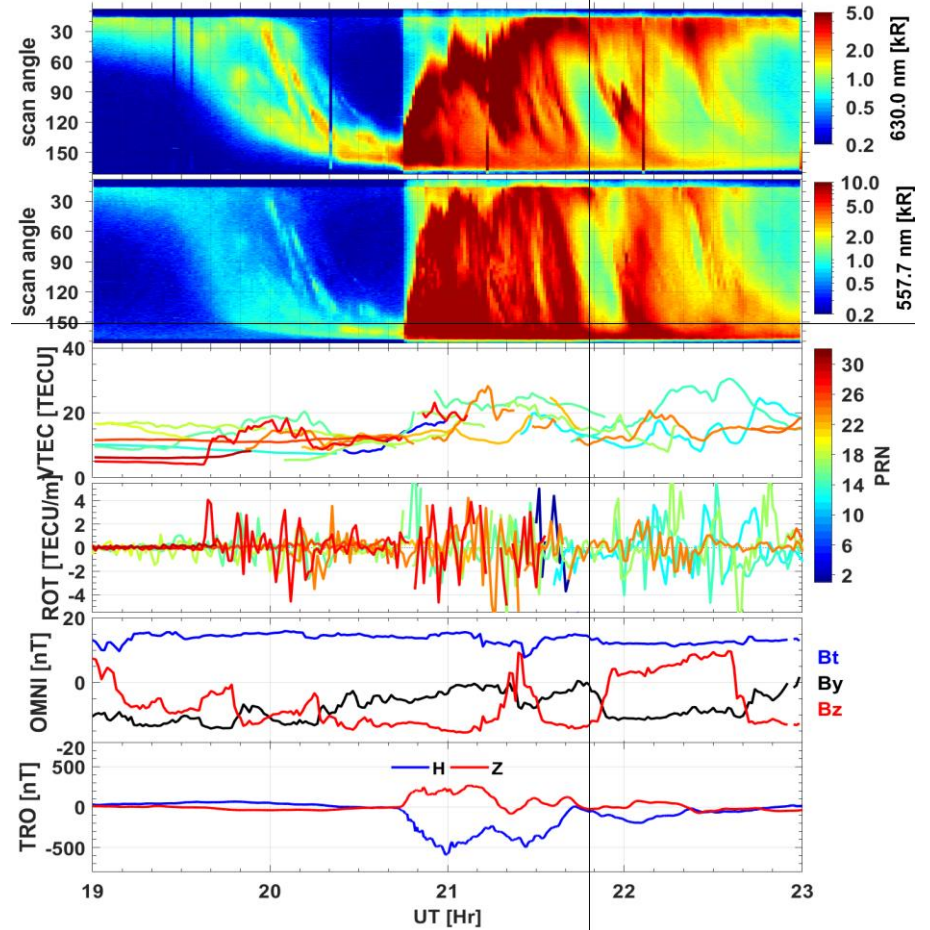


FIGURE 1. Overview of the event on December 23, 2014. From top to bottom: (a-b) the optical data in a keogram format from the all-sky imager at 630.0 nm and 557.7 nm, respectively (the auroral intensity is indicated by the bars on the right side of each panel), (c) GPS TEC from the collocated GPS receiver at Skibotn (the color shows data from different GPS satellites as indicating by the PRN code in the color bar), (d) the rate of change of TEC (ROT), (e) the OMNI IMF data, and (f) the H and Z components of the magnetic field from the ground-based magnetometer in Tromsø.

the equatorward motion of the auroral oval from 19:30 UT in panels (a)-(b). The substorm onset was at around 20:45 UT when the aurora suddenly intensified and expanded poleward, after which the whole sky was covered with the auroral arcs. In addition, one can observe that there are several auroral streamers moving equatorward from the poleward edge of the auroral oval. The corresponding ionospheric currents are reflected in the H and Z components of the magnetic field, which are measured by magnetometers at a nearby station in Tromsø (panel f). The sudden decrease in the H component at around 20:45 UT suggests onset of the magnetic substorm, which developed rapidly, as the H component rapidly reached -500 nT at 21 UT. At the same time, the Z component of the magnetic field increased, implying that the westward auroral electrojet was mainly equatorward of Tromsø. This is consistent with the auroral measurements with the all-sky imager, which show strong aurora in the southern part of the field-of-view. Panels (c) shows TEC from satellites and panel (d) present the GPS TEC Rate Of change of TEC (ROT) measured at the Skibotn station. The GPS TEC are characterized by large-scale fluctuations, which are clearly depicted by the ROT in panel (d). These large-scale TEC fluctuations are likely associated with auroral ionization process.

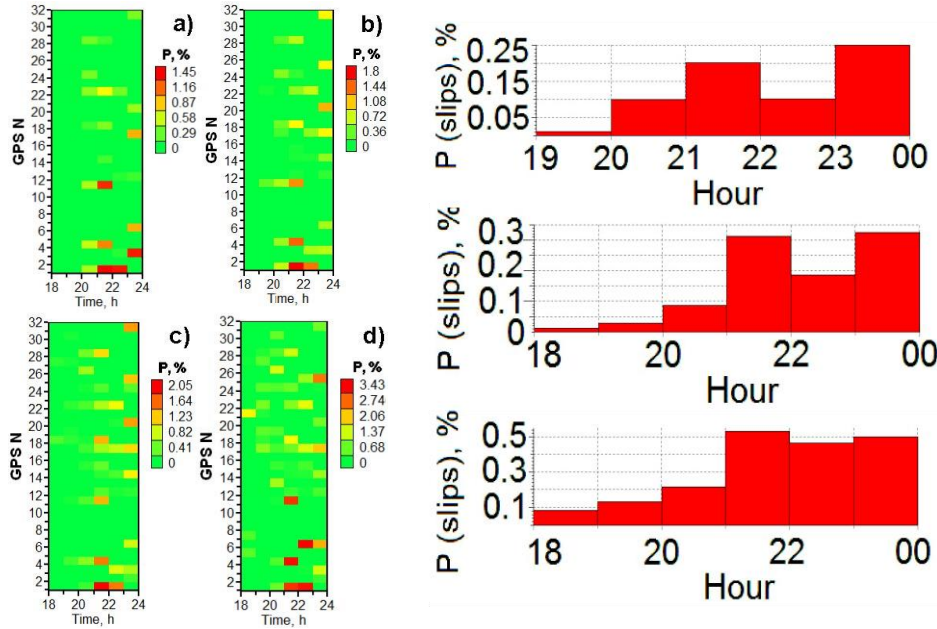


FIGURE 2 (right) Temporal distribution of TEC jumps for all visible GPS satellites at stations: a) *SODA*; b) *KIRU*; c) *TRO1* and d) *SKBN* and (left) Averaged probability of TEC jumps at stations *KIRU*; *TRO1*; and *SKBN* (from top to bottom) for all visible GPS satellites.

substorm onset is at about at 20:45 UT (see Fig. 1), while the auroral oval expansion is observed from 19:30. Probability of the phase cycle slip L_2 increased after 19 UT at SKBN and after 20 UT at SODA. The maximum number of slips on L_2 is between 21 and 23 UT at SKBN and a bit later, between 22 and 23:59 UT at SODA. The maximum values are reached before 23 UT for SKBN and midnight UT on for SODA. Fig. 2 (right) presents data for the jumps in TEC from the four stations. TEC jumps probability increases with the substorm onset (about 20 UT) and peaks during the recovery and growth phases. Thus, the maximum values for stations *SODA*, *KIRU*, *TRO1*, and *SKBN* are respectively 1.4%, 2%, 2%, and 4%. As a criterion of jumps, we take a level of TEC change of more than 1 TECU/min, and present

Having provided a background of geomagnetic conditions, we study cycle slips in the GPS signals (L_1 , L_2), and estimated vertical TEC using the stations TRO1, SKBN, KIRU and SODA. The probability of the phase cycle slip for L_1 increased after 19 UT, and the number of slips L increases substantially between 20 to 23 UT, with the peak between 22 and 23 hours. It should be noted that the magnetic

the example data in Fig.2 (left) and TEC jumps increase 5-10 times during the substorm as compared to a quiet period. Note that TEC jump means in general addition turbulization in the electron concentration on trace of navigation signal.

Our study demonstrates that the operational slips in the GPS signals are mainly related to the auroral particle precipitation that occurs during geomagnetic activity in the polar ionosphere. The auroral particle precipitation produces intensification of optical emissions and therefore a close association of TEC scintillations. A rapidly moving auroral arc in the ionosphere can produce a short duration diffractive scintillation and cause a receiver to lose lock when the GPS ray path crosses the electron density structure associated with the aurora. The GPS frequency L_2 is consistently subject to more slips than frequency L_1 both for quiet and disturbed conditions since the frequency of L_2 is characterized by a smaller signal-to-noise ratio, which makes it a much more sensitive indicator of phase failures. We indicate that the probability of TEC slips is higher than for slips in phase at frequencies L_1 and L_2 . The substorm leads to a growth in slips L_2 at the stations in Sondankyla and Skibotn with a delay of several hours which is probably associated with specific features of plasma turbulence originating from magnetic disturbances. The maximum of slips is observed during the recovery phase of the auroral substorm. This fact reflects the dynamics of the substorm influence on the ionosphere and, most likely, it is associated with the evolution of plasma inhomogeneities and instabilities in the high-latitude ionosphere excited during the geomagnetic activity. The growth of instrumental slips of the phases of the navigation signals L_1 and L_2 and the TEC calculated on their basis during the recovery of the substorm is shown, that is, the dynamics of the development of the substorm is specified, most likely related to the evolution of a developing and relaxing turbulized ionospheric plasma.

This study was supported by Russian Science Foundation (grant 17-77-20009) and by the Norwegian Agency for International Cooperation and Quality Enhancement in Higher Education (Diku) (grant CPRU-2017/10068).

GPS-TEC FLUCTUATIONS AND POSITIONING ERRORS DURING GEOMAGNETIC STORM MARCH 17, 2015 OVER EUROPE

Irk I. Shagimuratov¹, Ivan I. Efishov¹, Mihail V. Filstov², Irina E. Zakharenkova¹, Irina Despirak² and Nadezhda Yu. Tepenitsyna¹

¹ West Department IZMIRAN, 236010, Kaliningrad, Russia

² Polar Geophysical Institute, Apatity, Russia

Introduction. Total electron fluctuations at high latitudes are caused presence in the ionosphere of different scale irregularities. The TEC fluctuations are occurred as phase fluctuations GPS/GLONASS signals. The are numerous papers concerns this problem [1-4]. During auroral disturbances were increased fluctuations transionosperic signals and impact their on navigation measurements in Arctic region [5-7]. The GPS measurements are importance as for investigation of physical processes in the high latitude ionosphere as well as for study of influence on GPS/GLONASS navigation. The strong fluctuations often occurred round magnetic midnight. The TEC fluctuations associated with auroral oval. Strong TEC fluctuations can complicate phase ambiguity resolution and to increase the number of undetected and uncorrected cycle slips and loss of signal lock in GPS navigation and positioning errors. In avroral ionosphere the increase intensity of TEC fluctuations are followed by auroral activity [8]. The relation between intensity TEC fluctuations and GPS positioning errors presented by Jacobsen and

Dahnn [9] over Europe. In this paper the occurrence TEC fluctuations and positioning errors over Europe during geomagnetic storm March 7, 2015 is presented.

Data and method. In this paper we discuss local affects of the St. Patrick's day storm March 17, 2015 on GPS signals which took place from network in the longitude range $\sim 20 - 30^\circ\text{E}$ which covered latitudes the $54 - 70^\circ\text{N}$. The main data were phase measurements provided by the ground-based (IGS) network of GPS receivers. Time-derivative of TEC (ROT, rate of TEC change) used to measure of GPS signal phase fluctuation activity and the Rate of TEC Index (ROTI) used as characteristic of the phase fluctuations intensity to detect the presence of ionospheric irregularities [10] caused by passing of radio signals through them

$$ROTI = \sqrt{\langle ROT^2 \rangle - \langle ROT \rangle^2}.$$

Geomagnetic measurements from the IMAGE network (www.geo.fmi.fi/image) were used for this work and also all-sky camera data over Kiruna (<http://www2.irf.se/allsky/data.html>).

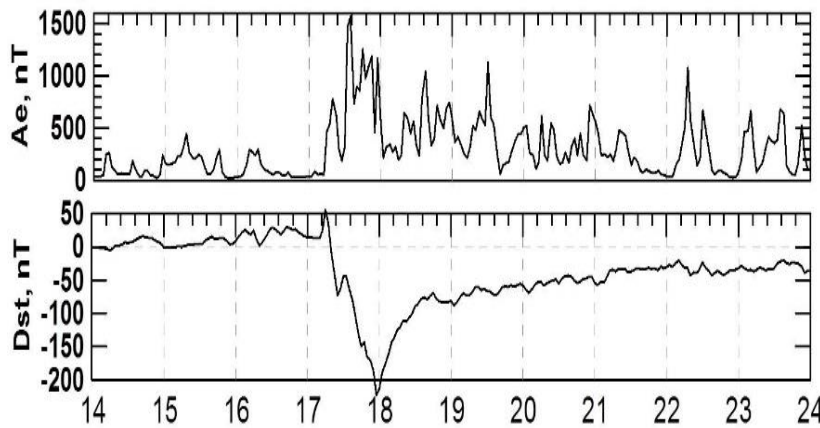
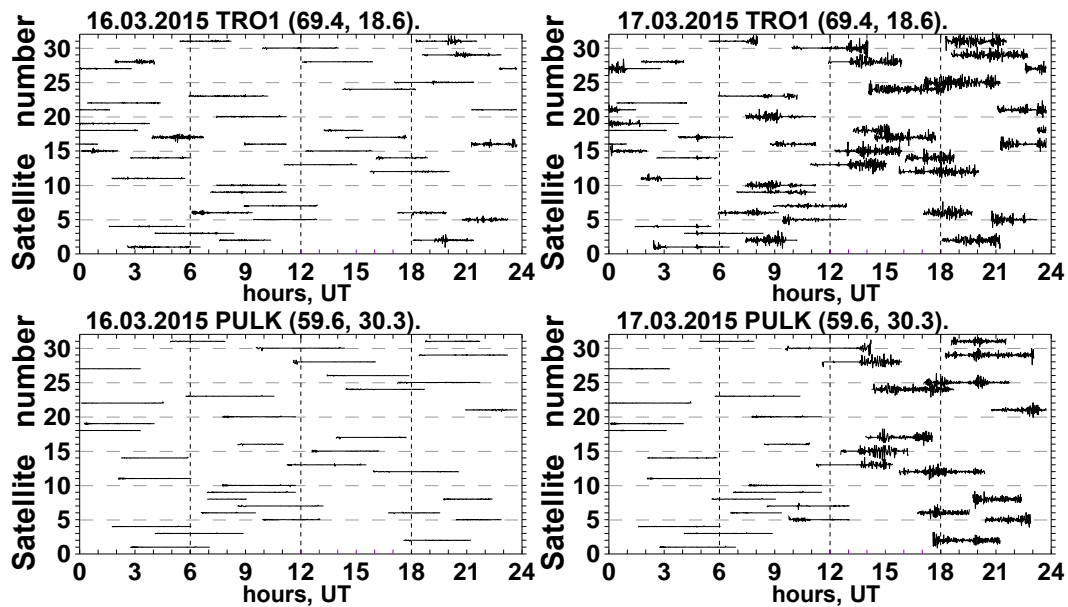


FIGURE 1. Variations Ae and Dst indices on interval 14 - 24 March 2015.

Fig.1 demonstrated development of the storm by time series of global (Dst and Ae) indices. Strong auroral activity occurred after 13 UT.

Storm time occurrence of TEC fluctuations. During the storm the increasing TEC fluctuation activity took place at different latitudes, in partly, auroral, subauroral and midlatitude regions.



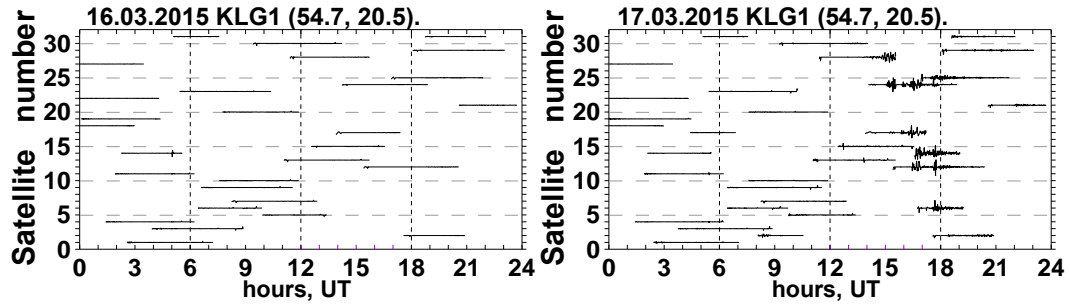


FIGURE 2. Occurrence TEC fluctuations (ROT) all satellite passes on 24-hr interval over auroral, subauroral and midlatitude stations.

The maximal intensity of fluctuations was registered in the period 15-18 UT on March 17, 2015, when intensive auroral disturbance was developed.

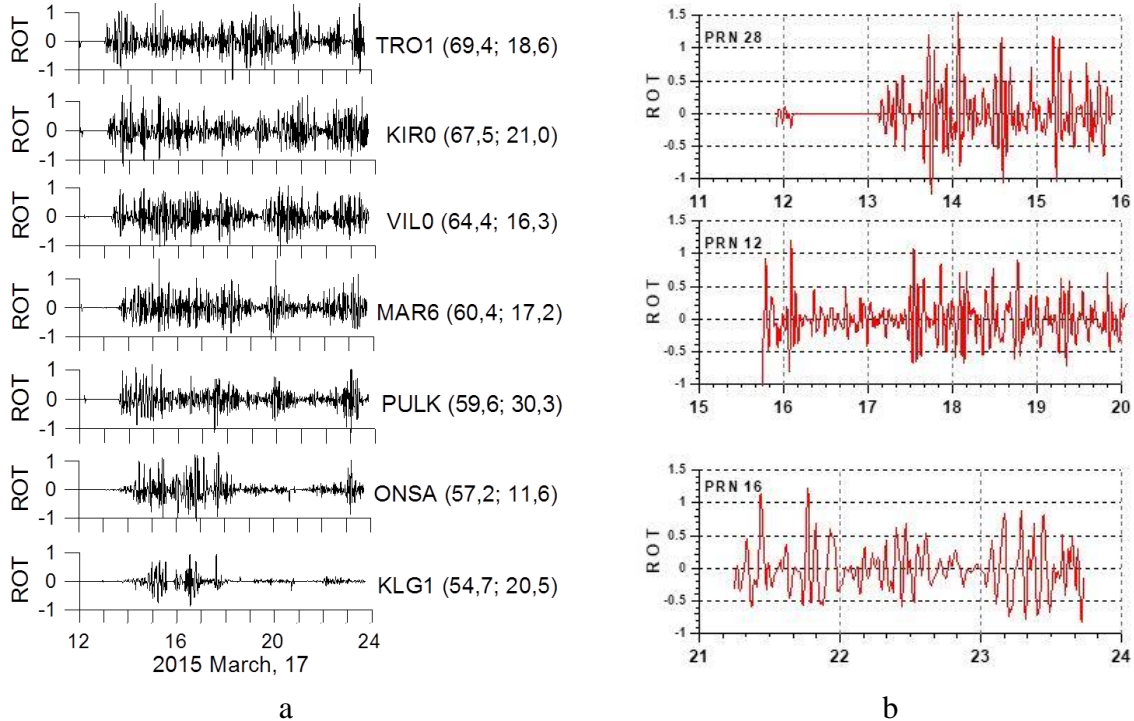


FIGURE 3. TEC fluctuations over Europe (ROT) at different stations (a) and detail variations ROT for individual satellite passes over Kiruna, March 17, 2015 (b).

Occurrence of TEC fluctuations ROT at meridian array stations (Fig. 3a), which shows time development of ROT on basis of navigation signals of selected GPS satellites № 20 and № 21. The fluctuations were registered on latitude until of 54.7°N. The figure 3b shows a detail pictures of development of TEC fluctuations along individual satellite passes over Kiruna during March 17, 2015. On pictures it can see a patch structures of TEC fluctuations. The structures we associated with situation then satellite signal intersect auroral formes which registered all-sky camera over Kiruna (<http://www2.irf.se/allsky/data.html>).

Occurrence positioning errors on different stations. We analyzed positioning errors using Precise Point Positioning (PPP) algorithm on the base of the GIPSY software of the NASA Jet Propulsion Laboratory in kinematic mode (<http://apps.gdgps.net>). The 3D position errors were computed with 30

sec interval. The 3D position error (P_{3D}) was defined as the offset of the detrended coordinate from its median value (x_0, y_0, z_0) and calculated for each epoch

$$P_{3D}(i) = \sqrt{(x(i) - x_0)^2 + (y(i) - y_0)^2 + (z(i) - z_0)^2}.$$

As median value (x_0, y_0, z_0) we used coordinate calculated on 24 hour interval for previous day of the storm.

Figure 4 presents variation 3D errors auroral, subauroral and midlatitude stations. The analysis shows that during quiet conditions the errors do not exceed some cm. During disturbance positioning errors exceed tens of meters. At Kiruna station errors reach 30 m. We associated this effect with auroral structures which were observed over Kiruna in this time.

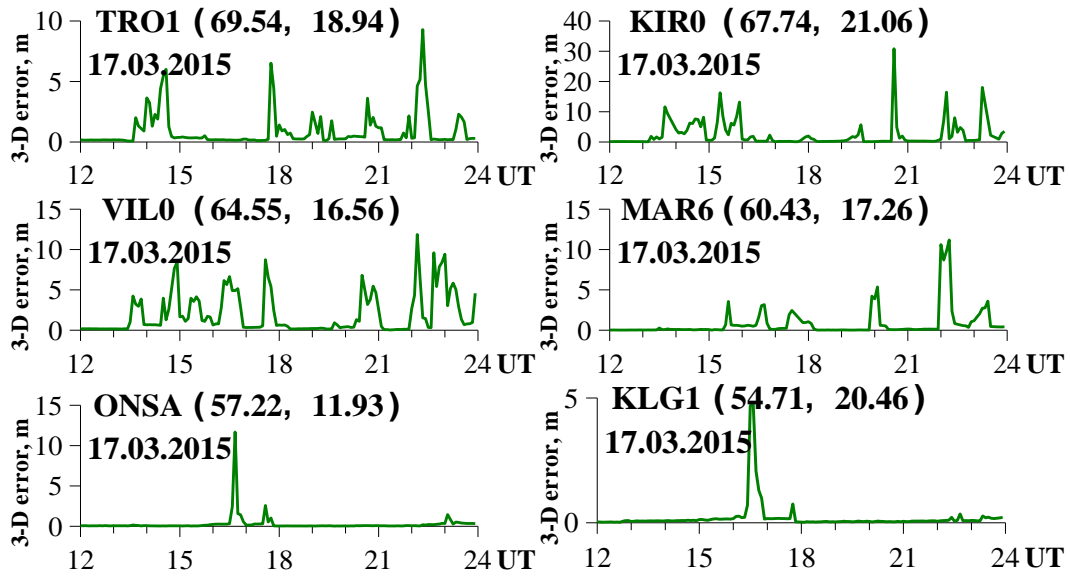


FIGURE 4. 3D positioning errors for different stations associated with the auroral disturbance.

Summary. We analyzed the occurrence of the TEC fluctuations and the positioning errors associated with the auroral disturbances over Europe during the strong storm of March 17, 2015. The auroral disturbances occurred at afternoon. The maximal intensity of the TEC fluctuations took place at the auroral ionosphere. Weak fluctuations were observed over midlatitude stations. The effects were related with the dynamics of the auroral oval. We analyzed also an impact of the geomagnetic disturbances on the Precise Point Positioning errors. The positioning errors were determined using the GIPSY-OASIS software (APS-NASA). Maximal errors took place at Kiruna station. We associated the effect with presence different auroral form over Kiruna in this time.

Acknowledgments. This work was supported by grants RFBR 19-05-00570 and program 28 presidium RAS. The authors thank FMI for all-sky data over Kiruna.

1. J. Aarons, B. Lin, M. Mendillo, K. Liou, M. Codrescu, GPS phase fluctuations and ultraviolet images from the Polar satellite, *Journal Geophysical Research*, 2000, 105, pp. 5201–5213.

2. L. Spogli, L. Alfonsi, G. De Franceschi, V. Romano, M. H. O. Aquino, and A. Dodson, Climatology of GPS ionospheric scintillations over high and mid-latitude European regions, *Ann. Geophys.*, 2009, 27, pp. 3429–3437, doi: 10.5194 angeo-27-3429-2009.

3. P. Prikryl, R. Ghoddousi-Fard, B. S. R. Kunduri, E. G. Thomas, A. J. Coster, P. T. Jayachandran, E. Spanswick, and D. W. Danskin, GPS phase scintillation and proxy index at high latitudes during a moderate geomagnetic storm, *Ann. Geophys.*, 2013, 31 (5), pp. 805–816, doi: 10.5194/angeo-31-805-2013.
4. Iu. Cherniak, I. Zakharenkova, Dependence of the high-latitude plasma irregularities on the auroral activity indices: a case study of 17 March 2015 geomagnetic storm, *Earth, Planets and Space*, 2015, 67 (151), doi: 10.1186/s40623-015-0316-x.
5. S. A. Chernouss, N. V. Kalitenkov, The dependence of GPS positioning deviation on auroral activity, *International Journal of Remote Sensing*, 2011, 32 (1), pp. 3005-3017.
6. S. A. Chernouss, M. V. Shvets, M. V. Filatov, I. I. Shagimuratov, N. V. Kalitenkov, Studying Navigation Signal Singularities during Auroral Disturbances, *Russian Journal of Physical Chemistry B*, 2015, 9 (5), pp. 778-784.
7. S. A. Chernouss, I. I. Shagimuratov, I. B. Ievenko, M. V., Filatov, I. I., Efishov, M. V. Shvets, N. V. Kalitenkov, Aurora as indicator of the ionospheric impact on transionospheric navigation signals, *Proceedings of V International Conference "Atmosphere, Ionosphere, Safety"*, Kaliningrad, Russia, 19 - 25 June 2016, Book of Proceedings, pp. 185-191.
8. I. Shagimuratov, S. Chernouss, Iu. Cherniak, I. Zakharenkova, I. Efishov, Phase fluctuations of GPS signals associated with aurora, *Proceedings 9th European Conference on Antennas and propagation*, Lisbon, Portugal, 12-17 April 2015, paper 1570053943.
9. K. S. Jacobsen and M. Dahnn, Statistics of ionospheric disturbances and their correlation with GNSS positioning errors at high latitudes, *J. Space Weather Space Clim.*, 2014, 4 (A27).
10. X. Pi, A. J. Manucci, U. J. Lindqwister, C. M. Ho, Monitoring of global ionospheric irregularities using the worldwide GPS network, *Geophysical Research Letters*, 1997, 24, pp. 2283-2286.

IONIZATION IN THE ATMOSPHERE IN THE POLAR REGION DURING SOLAR PROTON EVENTS IN SEPTEMBER 2017 ACCORDING TO MEASUREMENTS ON RUSSIAN SPACECRAFT METEOR AND ELECTRO

Evgeny A. Ginzburg ¹, Alexey A. Krivolutsky ², Anna A. Kukoleva ², Irina N. Myagkova ^{2,3}

¹*Institute of Applied Geophysics, Roshydromet, Moscow, Russia*

²*Laboratory for Atmospheric Chemistry and Dynamics, Roshydromet, Central Aerological Observatory, Dolgoprudny, Moscow, Russia*

³*Scobeltsyn Institute of Nuclear Physics, MSU, Moscow*

Protons from solar flares that penetrate The Earth's atmosphere at high latitudes cause it to ionize and thus trigger a chain of chemical reactions that lead to a temporary change in the chemical composition of the atmosphere.

To date, when considering the effects of solar protons on the Earth's atmosphere, data from the American GOES series satellites are used as the main data sources for SCR proton flows. At the same time, there is a fairly long and uniform series of measurements of solar proton fluxes on domestic satellites, primarily on the polar meteor satellites at altitudes of ~800-900 km, and since 2011 – on the geostationary Electro satellites. Most of the measurements are carried out in the energy range from several MeV to several tens of MeV, and protons with energies of more than 600, 800 MeV are registered in the three integral channels of the Cherenkov counter on the Meteor and on the Electro.

The table shows the energy ranges in MeV in the proton channels on the Meteor-3 # 2, Electro-L # 2, and GOES spacecrafts that were used in this work.

TABLE 1. Energy ranges in MeV in the proton channels on the Meteor-3 # 2, Electro-L # 2, and GOES spacecrafts.

Meteor-3 №2	Electro-L №2	GOES13
10-160	9-20	>10
>15	20-40	>30
>25	40-100	>50
>600	>600	>60
>800	-	>100

The first 3 channels on KA Electro are band. Assuming the spectrum in solar proton events to be power with the exponent $|\gamma| > 1$, it is possible to transform band channels into "quasi-integral" channels with a good degree of accuracy by simple addition. Thus, "quasi-integral" channels with threshold energies of 9b 20 and 40 MeV were prepared for Electro-L # 2. For the same reasons, the 10-160 MeV channel on the meteor SPACECRAFT was considered integral with a threshold of 10 MeV. Having the data from the mentioned spacecraft at their disposal, the solar proton events (SPE) of the beginning of September 2017 were considered. A comparative analysis of the time variations and spectra of proton fluxes in these events was carried out (figures 1 and 2). The total SPE consisted of four successive proton events, the starting points of each of them are shown by arrows on the lower graph in figure 1.

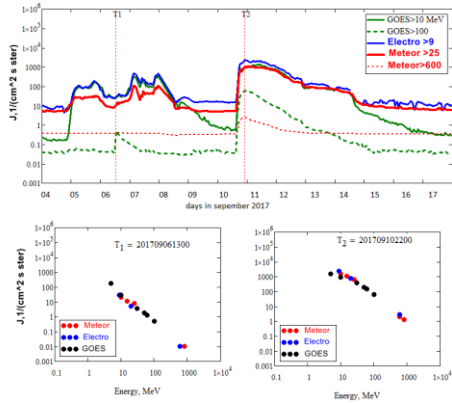


FIGURE 2. The time variations of SCR protons in some channels of Electro, Meteor, and GOES satellites. Electro and Meteor (upper graph) and energy spectra of protons (lower graphs) at moments T1 and T2.

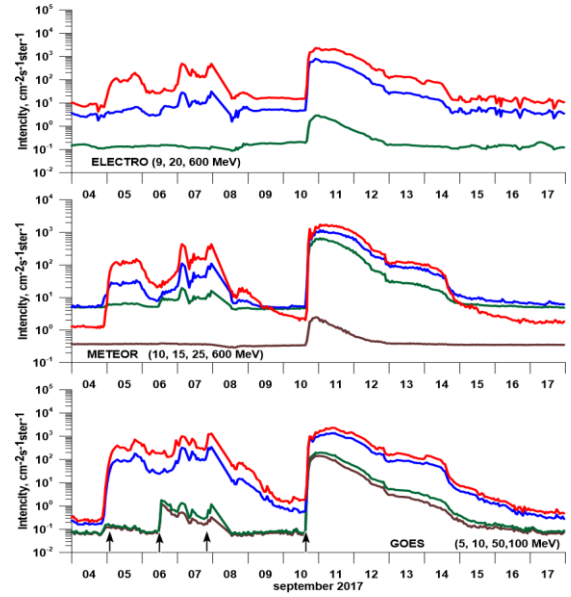


FIGURE 1. The time variations of SCR proton fluxes from September 4 to September 17, 2017 according to the data of the Electro, Meteor, and GOES satellites.

From the proton spectra presented in the lower graphs of fig. 2 at time instants T1 and T2 (the times when the maximum values of proton fluxes of the highest energies reach the 2nd and 4th), it can be seen that the readings from three spacecraft agree with each other and the general spectrum and spectra with each spacecraft is power-law with spectral stiffness indicators consistent with the time course data on the upper graph.

Thus, it can be considered quite justified to calculate the ionization of air in the polar regions separately from the data of each of the satellites, followed by a comparison of the results of calculations. The method described in [1] was used to calculate the ionization rate. The calculation results are presented in fig. 3 in the form of contours

of the ionization rate in time-height coordinates above the Earth's surface.

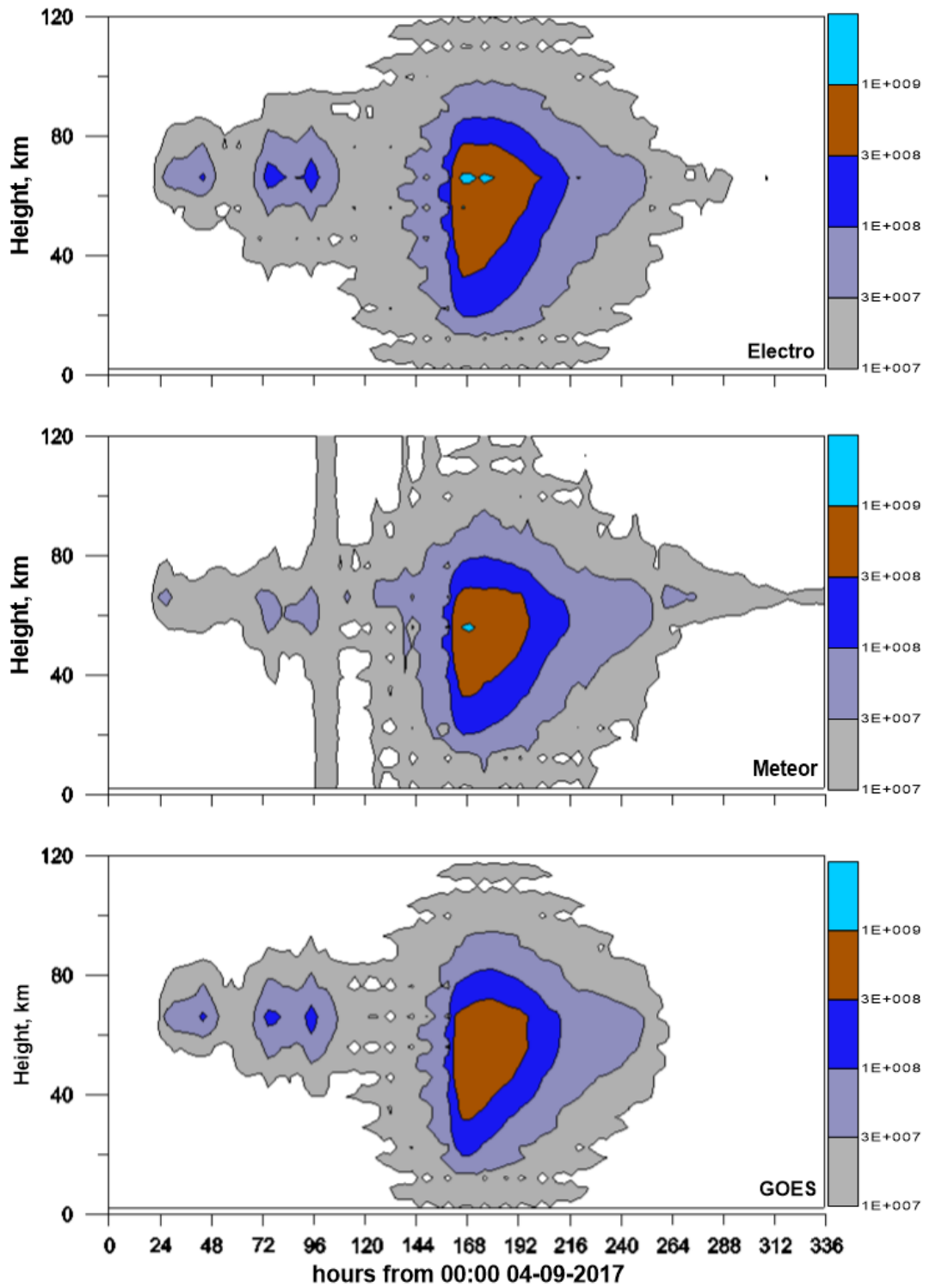


FIGURE 3. Contours of ionization rates under the influence of SCR proton fluxes September 4-17, 2017, calculated from the data of proton measurements on the Electro, Meteor and GOES satellites.

We can see a good agreement both on the time course of the ionization rates, separately calculated from the data of each of the three spacecraft, and on the distribution of the ionization rate by height at each time point.

For a more confident assessment, including a quantitative one, of the results of the ionization calculation, we began to build ionization dependencies on the height for each moment of time and the time course of ionization for each height.

Examples of such constructions are shown in figures 4 and 5, respectively. The time points T1 and T2 in these figures are the same as in figure 2.

We can see a good coincidence of the high-altitude ionization distributions in the maxima of proton fluxes with the highest energies during the 2nd and 4th proton events. The same can be said about the time course of ionization at an altitude of 70 km—close to the height where the ionization rate reaches the highest values.

Thus, we can make a preliminary conclusion that the domestic data of the meteor satellite can be used for calculations of ionization rates in the polar atmosphere and for subsequent calculations of photo-chemical processes using a three-dimensional global transport photochemical model of the troposphere and the middle atmosphere.

1. F.M. Vitt, C.H. Jackman, A comparison of sources of odd nitrogen production from 1974 through 1993 in the Earth's middle atmosphere as calculated using a two-dimensional model, *J. Geophys. Res.*, 1996, 101(D3), pp. 6729-6739.

MUTUAL COMPARISON OF METHODS FOR CALCULATING THE ABSOLUTE VERTICAL TOTAL ELECTRON CONTENT

Anna A. Mylnikova, Yury V. Yasyukevich, Artem M. Vesnin

Institute of Solar-Terrestrial Physics of Siberian Branch of Russian Academy of Sciences, Irkutsk, Russia

Introduction. Global Navigation Satellite Systems (GNSS) have provided vast experimental material for studying the Earth's ionosphere. The main measured parameter is the total electronic content (TEC) calculated from the two-frequency code and phase measurements of the pseudorange [1]. TEC is determined along the oblique beam "satellite - receiver". Moreover, for a number of tasks, it is important

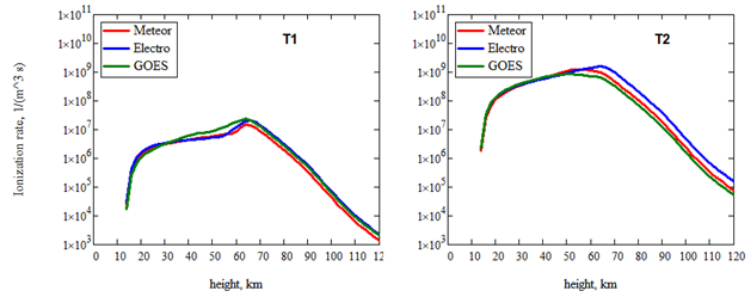


FIGURE 4. Altitude dependences of the ionization rate at time instants T1 and T2 according to proton measurements on the Electro, Meteor, and GOES satellites.

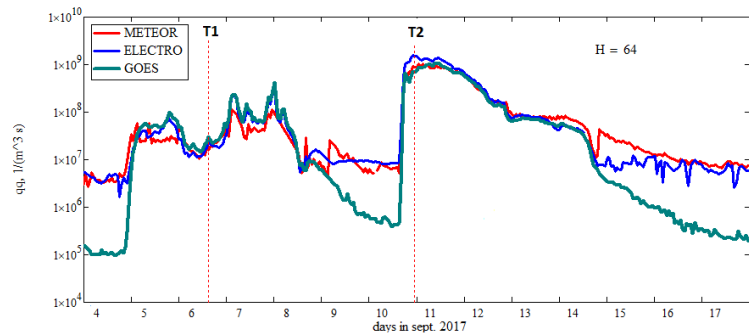


FIGURE 5. The time variations of the ionization rate at an altitude of $H = 64$ km according to proton measurements on the Electro, Meteor and GOES satellites.

to evaluate the vertical absolute TEC based on a set of oblique measurements determined with a systematic error (phase ambiguity and differential code delays).

To solve this problem, a technique was developed for determining the absolute vertical TEC and differential code delays (DCB) according to GNSS receivers and the TayAbsTEC software package was created on its basis [2]. In this work, we compare the results of TayAbsTEC with data obtained using other methods. A comparison was made for the data for the full year 2009 (minimum of solar activity) and 2014 (maximum of solar activity).

Algorithm for determining the absolute vertical TEC and DCB. The developed algorithm has the following structure:

1) The calculation of oblique TEC according to GNSS.

TEC is calculated by phase and group measurements at two frequencies [1].

$$I_{\varphi} = \frac{1}{40.308} \cdot \frac{f_1^2 f_2^2}{f_1^2 - f_2^2} \cdot [(L_2 \lambda_2 - L_1 \lambda_1) + const + \sigma L] \quad (1)$$

$$I_P = \frac{1}{40.308} \cdot \frac{f_1^2 f_2^2}{f_1^2 - f_2^2} \cdot [(P_2 - P_1) - c \Delta \tau + \sigma P] \quad (2)$$

2) Detecting and eliminating the influence of outliers and cycle slip parameters in the TEC data [3].

3) Eliminating the phase measurement ambiguity. The ambiguity is eliminated using the average difference of the group (2) and phase (1) TEC measurements.

4) Evaluation of vertical TEC, gradients, and other parameters based on the model of TEC measurements.

To determine the absolute vertical TEC and DCB, it is necessary to specify a model of TEC measurements, where one of the parameters is the vertical TEC I_V and the TEC error due to DCB $-I_{BIAS}$. Next, you need to evaluate its parameters. Along with I_V and I_{BIAS} model parameters are latitudinal and longitude gradients, the time derivative of TEC.

The TEC measurement model has the following form:

$$I_M = S_j^i \cdot I_V(\varphi, l, t) + I_{BIAS_j} \quad (3)$$

$$I_V(\varphi, l, t) = I_V(\varphi_0, l_0, t_0) + G_{\varphi} \cdot \Delta \varphi_j^i + G_{q_{\varphi}} \cdot (\Delta \varphi_j^i)^2 + G_l \cdot \Delta l_j^i + G_{q_l} \cdot (\Delta l_j^i)^2 + G_t \cdot \Delta t_j^i + G_{q_t} \cdot (\Delta t_j^i)^2$$

It is the expansion of the vertical TEC in a Taylor series in space and time. The model also sets the functional dependence of the vertical TEC on the elevation angle (θ) by means of the projection operator, considering the spherical of the Earth:

$$S_j^i = \left[\cos \left\{ \arcsin \left(\frac{R_E}{R_E + h_{max}} \sin [\alpha \cdot (90 - \theta_j^i)] \right) \right\} \right]^{-1} \quad (4)$$

where R_E is the radius of the Earth, h_{max} is the height of a thin spherical layer (450 km), is the angle of flight of the satellite above the horizon.

Next, the parameters of the model are determined by minimizing the square of the difference in the TEC calculated from the phase measurements considering the phase ambiguity, and the TEC model (3).

Comparison of the daily dynamics of vertical TEC. The paper compares the data obtained using TayAbsTEC with the data of vertical TEC calculated using other methods. For comparison, data calculated using the IONOLAB laboratory software [4], data calculated using the software of a group of scientists led by Gopi Seemala [5], and global ionospheric data GIM Maps, CODE laboratory [6] were selected for comparison.

The chosen methods for calculating the vertical TEC are almost the same as TayAbsTEC. The main differences are that the DCB values in these methods, except for GIM, are not estimated, but are apriori taken from the global ionospheric GIM maps, and spatial gradients are not estimated in these methods, see [7] and [5].

The comparison was made for the data for 2009, the minimum solar activity and for 2014, the maximum solar activity, for five stations located in different parts of the Earth: alrt (82.5° N, 62.34° W), lpal (28.76° N, 17.9° W), irkj (52.22° N, 104.32° E), ntus (1.35° N, 103.68° E), thu2 (76.54° N, 68.82° W).

Figure 1 shows the histograms of the difference in the absolute vertical TEC of the IONOLAB laboratory (a), the Seemala group (b) and the CODE laboratory (c) with the vertical TEC calculated by TayAbsTEC for the data from the lpal station.

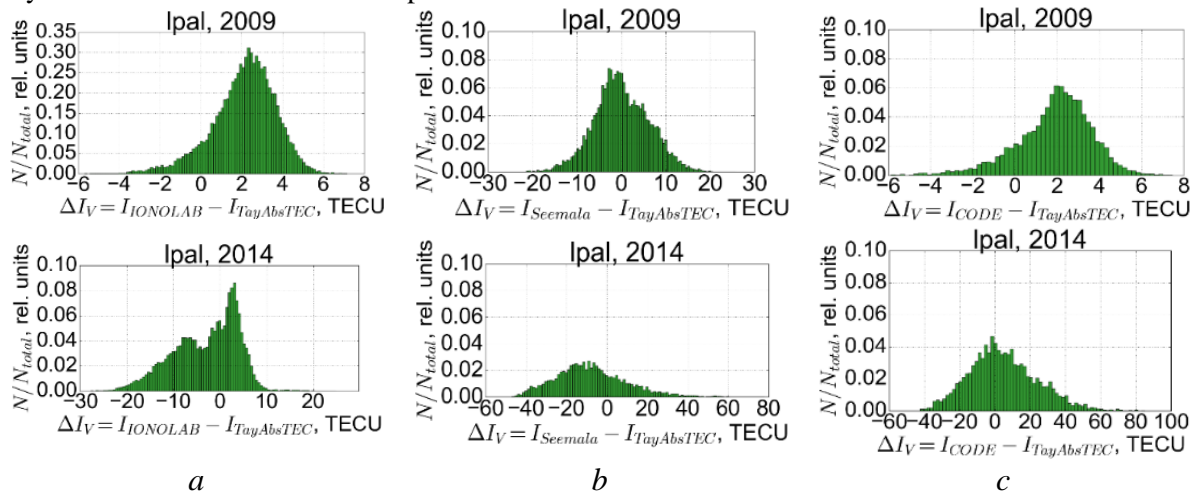


FIGURE 1. Histograms of the difference in the absolute vertical TEC of the IONOLAB laboratory (a), the Seemala group (b) and the CODE laboratory (c) with the vertical TEC calculated by TayAbsTEC for 2009 (upper row) and 2014 (lower row) of the year, lpal station.

All histograms in the figure have the form of a Gaussian distribution, there is a systematic and random error. The values of the mode and standard deviation (σ) for the year of maximum solar activity (2014) are larger than for the year of minimum solar activity for all compared methods. The values of the modes and the standard deviation of the differences are presented in Table 1. A synchronous increase in deviations with all methods in 2014 indicates that all the considered methods work equally well under conditions of high solar activity. The greatest deviations in the TayAbsTEC method are observed with the results of the Seemala method, the smallest – with the data from the CODE laboratory.

TABLE 1. The value of the difference mode.

	2009 year		2014 year	
	Mode	σ	Mode	σ
IONOLAB-TayAbsTEC	2.5 TECU	1.5 TECU	-5 TECU	7 TECU
Seemala-TayAbsTEC	-5 TECU	6 TECU	-10 TECU	18 TECU
CODE-TayAbsTEC	2 TECU	1.8 TECU	0 TECU	19 TECU

Conclusion. A statistical comparison was made of the absolute vertical TEC values calculated using the TayAbsTEC method with the TEC values calculated by the IONOLAB laboratory, Seemala group, and TEC from CODE laboratory. All distributions of differences have the form of a normal distribution,

there is a systematic and random error. The systematic error for the difference in the values of the vertical TayAbsTEC and IONOLAB TEC is ~ 5 TECU for 2014 (2.5 TECU for 2009). For the difference with the Seemala group results, the systematic error is ~ 10 TECU (5 TECU for 2009), for the difference with the CODE systematic error is ~ 0 TECU for 2014 (2 TECU for 2009).

The study is supported by the Russian Foundation for Basic Research Grant No. 18-35-2003.

1. E. L. Afraimovich, E. I. Astafyeva, V. V. Demyanov, et al., A review of GPS/GLONASS studies of the ionospheric response to natural and anthropogenic processes and phenomena, *J. Space Weather Space Clim.* 2013, 3(27).
2. Yu. V. Yasyukevich, A. A. Mylnikova, V. E. Kunitsyn, A. M. Padokhin, Influence of GPS/GLONASS differential code biases on the determination accuracy of the absolute total electron content in the ionosphere, *Geomagnetism and Aeronomy*, 2015, 55(6), pp. 790-796. doi:10.7868/S0016794015060176.
3. G. Blewitt, An automatic editing algorithm for GPS data, *Geophys. Res. Lett.*, 1990, 17(3), pp. 199–202.
4. IONOLAB laboratory website, <http://www.ionolab.org>.
5. G. K. Seemala, M. Yamamoto, A. Saito, C.-H. Chen, Three-dimensional GPS ionospheric tomography over Japan using constrained least squares, *J. Geophys. Res. Space Physics*, 2014, 119, pp. 3044– 3052, doi:10.1002/2013JA019582.
6. J. M. Dow, R. E. Neilan, C. Rizos, The international GNSS service in a changing landscape of global navigation satellite systems, *J. Geodesy*, 2009, 83(3–4), pp. 191–198.
7. F. Arkan, C. B. Erol, O. Arkan, "Regularized estimation of vertical total electron content from Global Positioning System data", *Journal of Geophysical Research-Space Physics*, 2003, 10, pp. 1469-1480.

FEATURES OF SOLAR ACTIVITY INDICES FOR THE IONOSPHERE IN THE SOLAR CYCLE 24

Marat G. Deminov, Elena V. Nepomnyashchaya, and Vladimir N. Obridko

Pushkov Institute of Terrestrial Magnetism, Ionosphere, and Radio Wave Propagation, Russian Academy of Sciences, Troitsk, Moscow, Russia

Introduction. It is believed that solar cycles 23 and 24 correspond to a transition to a new long-term regime of low solar activity, the properties of which are not well understood, since a similar regime was apparently observed more than 100 years ago [1]. A study of some features of the solar activity indices for the ionosphere in cycles 23 and 24 was performed by us recently [2]. The goal of this work was to continue these studies to determine the characteristics of the amplitude and shape of cycle 24 from these solar activity indices.

Solar activity indices. The monthly mean values of the solar activity indices (the flux of the solar radio emission at a wavelength of 10.7 cm, F , and the new version of the relative sunspot number Ri) and of the ionospheric index of that activity T within the interval from January 1947 to November 2019 were the initial values for the analysis. The ionospheric index is based on $foF2$ measurements, so it is more accurate than the solar indices for the $foF2$ median [3]. This makes it possible to use the T index as a $foF2$ characteristic, and this index is measured in the scale (measurements units) of Rz . It is reasonable also to reduce the F and Ri indices to the scale of Rz in order to provide comparability of these indices. The following regression equations were used for this [4]:

$$Rr = 0.708Ri - 0.3, \quad Rf = 33.5(85+F)^{1/2} - 410 - 15\exp(-0.1(F-65)), \quad (1)$$

where Rr and Rf are Ri and F in the Rz scale.

A filter with the weighted function

$$W(t) = \exp(-x^2/2) - (3 - x^2/2)\exp(-2) \quad (2)$$

is used in the analysis of the amplitude and shape of the solar cycle [5], where $x = t/12$, t is measured in months and varies from $t = -23$ to $t = 23$, and $t = 0$ is a given month. Note that $W(t) = 0$ at $|t| = 24$, so the filter with the weighted function $W(t)$ is called a 24-month Gaussian filter [5]. Such a filter almost completely excludes fluctuations on time scales shorter than 1–3 years and provides one distinct maximum of the solar activity cycle for every 24 solar cycles [5]. The smoothed values of the solar activity indices obtained with such filter based on the initial data (the monthly mean values of these indices) are denoted as Rr_{24} , Rf_{24} , and T_{24} .

The difference between the Rr_{24} , Rf_{24} , and T_{24} indices is insignificant in the interval of 1948-1979. That is why the 1948-1979 interval is called a reference interval. The beginning of a solar cycle is usually determined by the minimum of the relative sunspot number in the changes of this index with time. In the given case, November 2008 was the beginning of the 24th cycle according to the Rr_{24} data. The end of the 24th cycle is expected at the end of 2020 or in the beginning of 2021 [6]. To analyze this cycle, we used the data of the indices Rr_{24} , Rf_{24} , and T_{24} until December 2017.

The shapes of solar cycles for these smoothed solar activity indices are almost universal, i.e., they are applicable to any of the complete cycles [5]:

$$dR = ax^3/(\exp(x^2) - 0.71), \quad (3)$$

where [5, 7]

$$dR = Rr_{24} - (Rr_{24})_0, \quad x = (t - t_0)/b, \\ a = dR_{\max}/0.5038, \quad b = (37 + 1700/dR_{\max})/1.0807,$$

t is the time in months, counting from the beginning of the cycle, t_0 , $(Rr_{24})_0$ is the Rr_{24} value for $t = t_0$, $dR_{\max} = (Rr_{24})_{\max} - (Rr_{24})_0$ is the amplitude of the cycle. For the reference interval 1948-1979, equation (3) is also applicable for the indices Rf_{24} and T_{24} , since in this interval the indices Rr_{24} , Rf_{24} , and T_{24} practically coincide. One of the goals of this paper was to evaluate the applicability of equation (3) for cycle 24.

Results. In the 24th solar cycle, the Rf_{24} and T_{24} indices nearly coincided, and the difference between them was less than 5 (Fig. 1). In this cycle, the difference between the Rf_{24} and Rr_{24} indices could reach 20, and the hysteresis effect was pronounced clearly enough. This effect reached a maximum for $Rr_{24} = 50$, when $Rf_{24} = 56$ and $Rf_{24} = 66$ in the growing and declining phases of the solar cycle, respectively.

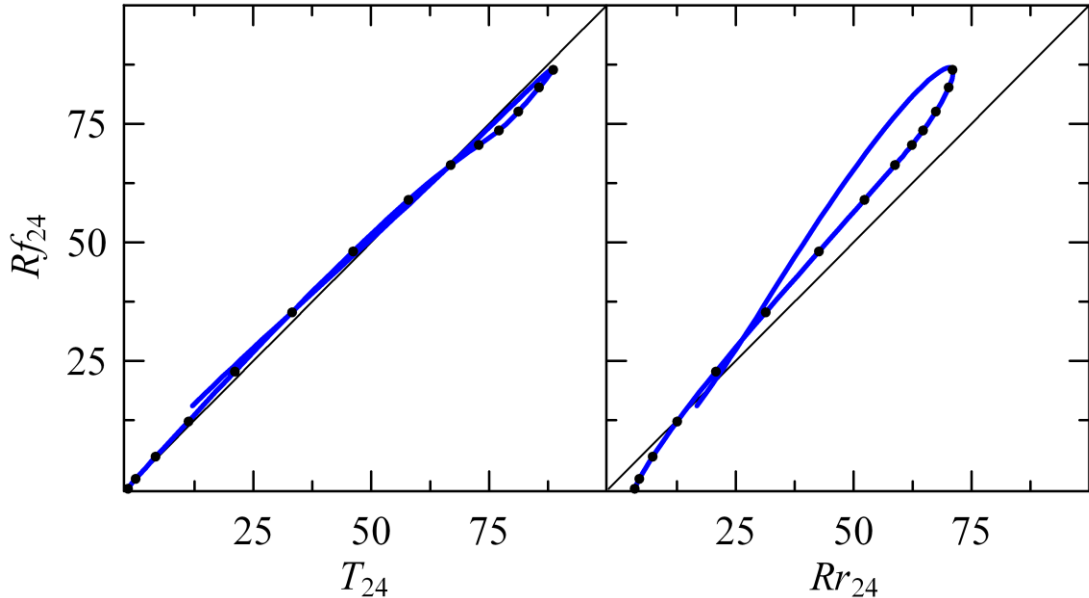


FIGURE 1. Relation of the smoothed index Rf_{24} to the T_{24} and Rr_{24} indices for the 24th solar cycle. The growing phase of the cycle is marked by dots.

Therefore, the Rf_{24} index is a more accurate than Rr_{24} indicator of solar activity for the median $foF2$, which is consistent with the results obtained previously from other data sets [2, 4].

The indices Rf_{24} and Rr_{24} show the different nature of the change in the shape of the solar cycle. Figure 2 shows comparisons of the shape of the solar cycle 24 according to experimental data and according to equation (3) for these indices. In equation (3), the start time of the cycle and its amplitude were set according to experimental data.

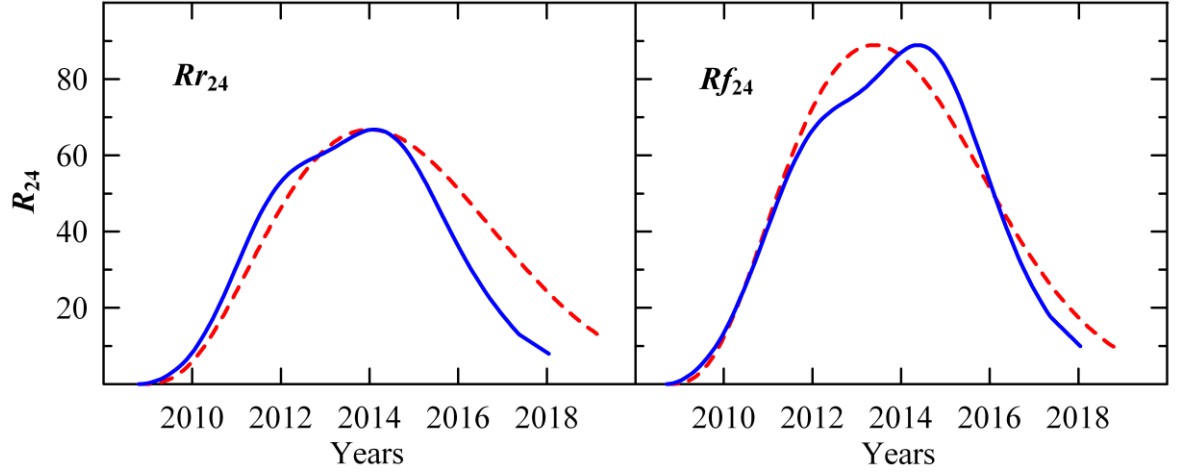


FIGURE 2. Solar activity indices Rr_{24} and Rf_{24} for the 24th solar cycle according to experimental data (solid lines) and according to equation (3) (dashed lines).

From the data in Figure 2 it can be seen that for the Rr_{24} index, the times of the onset of the cycle maximum according to experimental data and according to equation (3) practically coincided. In the declining phase of the solar cycle, the difference between these data is significant. Equation (3) reflects a stable pattern of changes in the shape of the solar cycle. Therefore, for the Rr_{24} index, this regularity was violated during the recession phase of the solar cycle.

For the Rf_{24} index, the maximum of cycle 24 according to the experimental data occurred approximately 1 year later than according to equation (3). This is one of important properties of cycle 24, since for the reference interval (1948–1979) this difference did not exceed 3 months. The shape of the solar cycle 24 for the Rf_{24} index differed from the typical average value due to a shift in the time of the onset of the maximum of this cycle.

Conclusion. The characteristics in changes in the solar activity indices (the solar radio emission flux at a wavelength of 10.7 cm, F , and the new version of the relative sunspot number Ri) and the ionospheric index of that activity T in the 24th solar activity cycle were analyzed. The smoothed with a 24-month filter values of these indices were used for the analysis. The following conclusions were derived.

1. The relation between F and T in cycle 24 remained stable and did not differ from the typical average relation for previous cycles.
2. The relation between F and Ri in cycle 24 differed from a typical average relation. In addition, a distinct hysteresis effect was observed for cycle 24, when different values of F corresponded to a fixed value of Ri in the phases of growth and decline of the solar cycle
3. The shape of cycle 24 differed from a typical average pattern for all analyzed indices. For index F , the cycle maximum occurred approximately 1 year later than the typical time of the onset of this maximum. For the Ri index, this difference was much smaller.

Acknowledgments. Data on the solar activity indices were taken from the sites: <http://sidc.oma.be/silco> (WDC-SILSO, Royal Observatory of Belgium, Brussels), <http://www.sws.bom.gov.au> (Space Weather Services, Australia), <http://www.spaceweather.gc.ca> (Space Weather Canada). The work is supported in part by the Russian Foundation for Basic Research (grants no. 20-05-00050) and Program no. 28 of the RAS Presidium.

1. L. Svalgaard, W.W. Hansen, Solar activity - past, present, future, *J. Space Weather Space Clim.*, 2013, 3(A24), doi: 10.1051/swsc/2013046.
2. M.G. Deminov, E.V. Nepomnyashchaya, V.N. Obridko, Solar activity indices for ionospheric parameters in the 23rd and 24th cycles, *Geomagn. Aeron.*, 2020, 60(1), pp. 1-6.
3. J. Caruana, The IPS monthly T index, *Solar-Terrestrial Prediction: Proc. Workshop at Leura, Australia (October 16-20, 1989)*, 1990, 2, pp. 257-263.
4. M.G. Deminov, G.F. Deminova, Solar activity index for the long-term prediction of the F2 layer critical frequency, *Geomagn. Aeron.*, 2019, 59(2), pp. 177-184.
5. D.H. Hathaway, The solar cycle, *Living Rev. Sol. Phys.*, 2015, 12(4), doi:10.1007/lrsp-2015-4.
6. L.A. Upton, D.H. Hathaway, An updated solar cycle 25 prediction with AFT: The modern minimum, *Geophys. Res. Lett.*, 2018, 45, pp. 8091-8095, doi: 10.1029/2018GL078387
7. M.G. Deminov, E.V. Nepomnyashchaya, V.N. Obridko, Properties of solar activity and ionosphere for solar cycle 25, *Geomagn. Aeron.*, 2016, 56(6), pp. 742-749.

GPS-TEC RESPONSE TO THE SOLAR ECLIPSE OF AUGUST 21, 2017 OVER AMERICA AND ECLIPSE IMPACT ON GPS POSITIONING PERFORMANCE

Irk I. Shagimuratov, Irina E. Zakharenkova, Galina A. Yakimova, Nadezhda Yu. Tepenitsyna, Ivan I. Efshov

West Department IZMIRAN, Kaliningrad, Russia

Introduction The total solar eclipse on 21 August 2017 was observed during daytime hours (16:00–20:00 UTC) across the continental United States. The ionosphere undergoes essential changes during a solar eclipse. As a consequence, a solar eclipse can significantly influence radio wave propagation. The irregular horizontal gradients caused by an eclipse complicate phase-ambiguity resolutions in GPS dual-frequency measurements. The gravity wave generated by an eclipse can also lead to trans-ionospheric signal degradation and can impact the performance of satellite-based radio-telecommunication and navigation systems [1].

There are some discrepancies in the occurrence of the eclipse effect in GPS TEC. For the total solar eclipse August 11, 1999, the depression of TEC varied from a few TECU to only 0.2-0.3 TECU at middle latitudes [2-5]. Many researchers have studied the ionospheric variations caused by the solar eclipse of 20 March 2015 [6-8].

In this paper, we present the response of GPS TEC to August 21, 2017 total solar eclipse over America. We used the multi-site GPS observations of several international permanent networks (IGS, UNAVCO, CORS) to analyze spatial and temporal variations of GPS TEC over America. In this report, the GPS positioning errors associated with the solar eclipse are also discussed.

Estimation technique. We applied different approaches to analyze the GPS TEC behavior during the eclipse. The single-site technique was employed to obtain the diurnal TEC variations over permanent GPS stations in the American region. While forming the diurnal TEC variation, the GPS measurements from all visible satellites were averaged. For a more detailed consideration of the eclipse effects in the TEC behavior, we analyzed the variation of the absolute TEC along individual passes over representative stations. The multi-site technique was used to produce the TEC maps with a 5-

min interval. The maps yielded the pattern of changes in the spatial structure of the ionosphere during the eclipse.

The eclipse effect in diurnal variations of TEC. The single-site technique was used to examine the diurnal variations of TEC. The GPS measurements of all satellites observed from a single station during a 24-hr period were taken into account.

Figure 1 presents the diurnal changes of TEC over single stations for the eclipse day (August 21, 2017) and quiet days (August 20, 2017). The reference quiet days enable to evaluate the eclipse effect against day-to-day variations of TEC. The absolute levels of TEC for the eclipse day were lower relative to the reference days. For these GPS stations, the eclipse effect occurred as a trough-like depression of TEC. Around the maximum phase of the eclipse, for the corresponding stations, TEC values reached its localized and short-term minima. The minimal level of TEC was registered for ~30-50 min, and then it slowly recovered to its regular level during 2-3 hours. The depression of TEC down to 4-5 TECU was maximal near the eclipse totality path at the eastern coast of North America. We note that a post-eclipse TEC enhancement occurred at all longitudes.

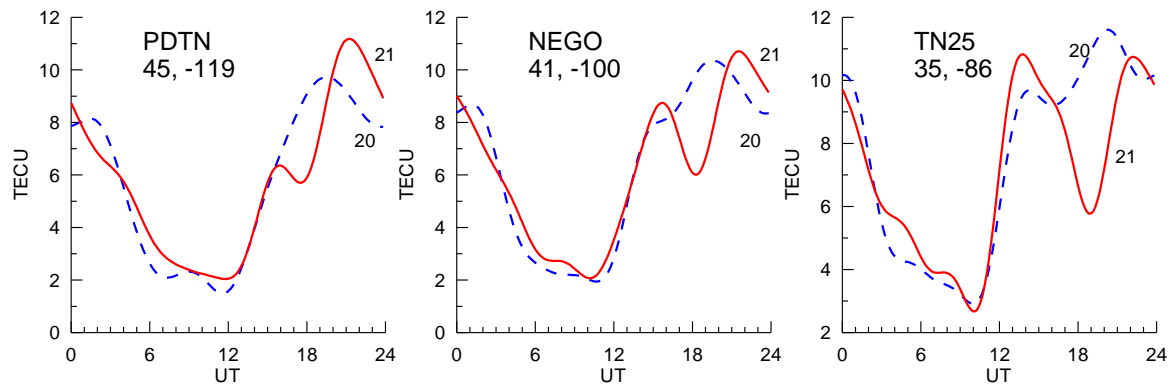


FIGURE 1. Diurnal variation of TEC at different longitudes for the eclipse day (red) and control day 20 August (blue).

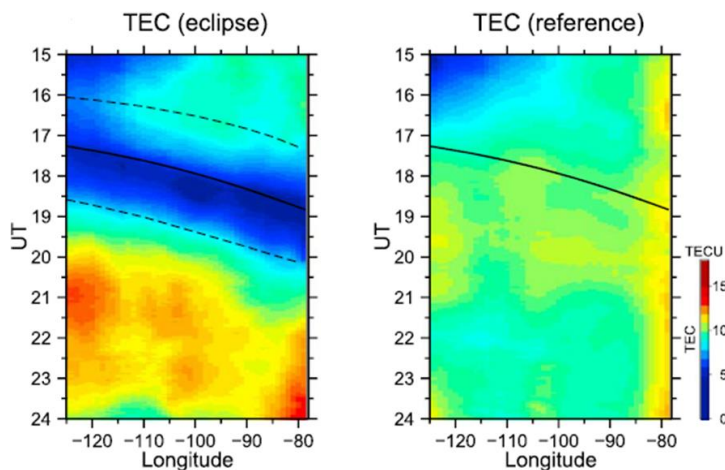


FIGURE 2. TEC variation along totality path as a function of UT and longitude for eclipse and reference day. Solid line shows totality path; dashed lines show begin and end of partial eclipse. The total solar eclipse started at the western coast of North America on 16:04:58 UT and ended at the eastern coast at 20:13:21 UT.

Figure 2 presents absolute TEC values, calculated with 0.5° step along the totality path as a function of UT and longitude for the eclipse and reference days. For the eclipse day, we find that eclipse started in different LT conditions, TEC depression occurred during eclipse time at all longitudes.

The eclipse effect in variations of TEC along satellite passes.

Figure 3 presents, as example, the variations of TEC along satellite passes over single stations for the eclipse day (August 21, 2017) and reference quiet day (August 20, 2017). The absolute levels of TEC for the eclipse day were lower with respect to the reference day. For

representative stations, the eclipse effect occurred as a trough-like depression of TEC. Around the maximum phase of the eclipse, TEC values reached their minima. The minimal level of TEC persisted for ~30-50 min and then it slowly recovered to its regular level during 2-3 hours. The TEC depression reached ~4-5 TECU.

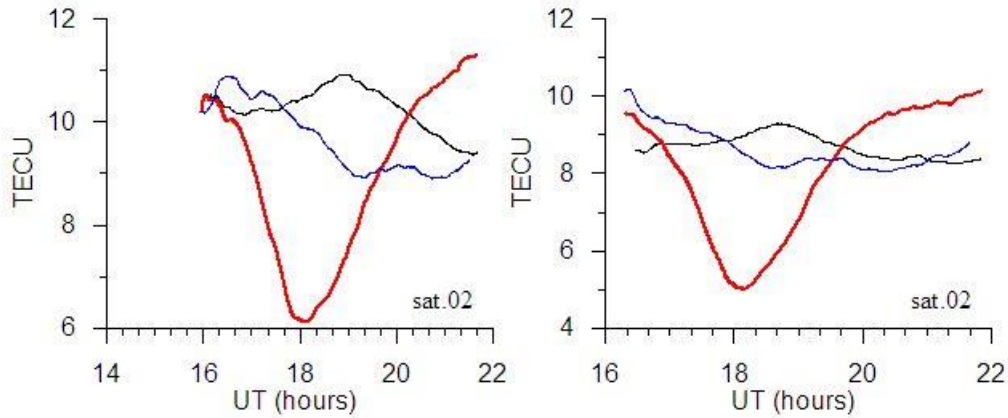


FIGURE 3. GPS TEC variations along satellite passes PRN 02 over stations AMC2 (38.62, -104.52) and BSMK (46.63, -100.82)

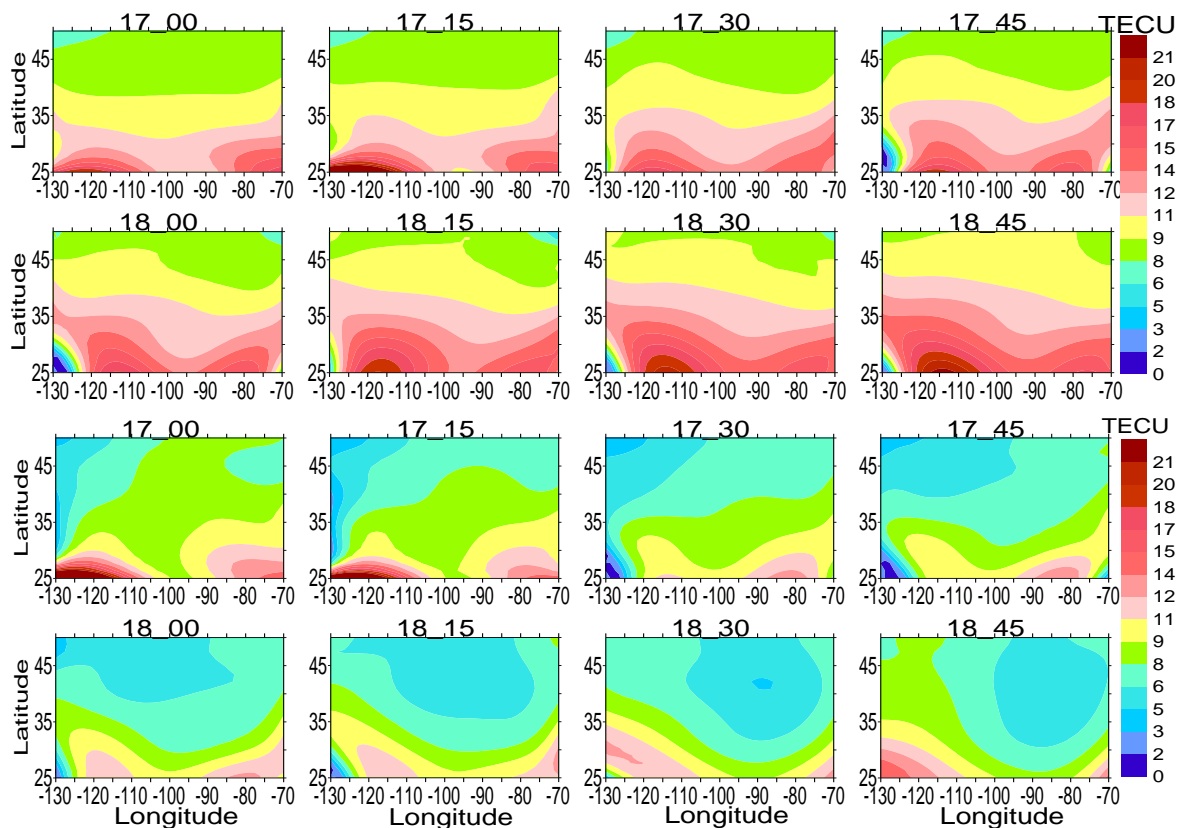


FIGURE 4. GPS TEC maps with a 5-min interval for 20 August (top panel) and eclipse day of 21 August 2017 (bottom panel).

Spatial distribution of TEC during the eclipse. To analyze spatial distribution of TEC during the eclipse, we constructed and examined GPS TEC maps for the North America region (Figure 4). We used the GPS measurements collected from 110+ GPS stations. In the multi-site algorithm, the simultaneous GPS measurements from all stations are used to obtain the spatial pattern of the ionosphere modification during the eclipse. The TEC maps demonstrate a clear TEC depression with a progression of the total solar eclipse.

GPS positioning performance during the eclipse. We analyzed positioning errors using the Precise Point Positioning (PPP) algorithm with the GIPSY software of the NASA Jet Propulsion Laboratory in the kinematic mode (<http://apps.gdgps.net>). The 3D position errors were computed with a 30-sec interval. The 3D position error (P_{3D}) is defined as an offset of the detrended coordinate from its median value (x_0, y_0, z_0) and calculated for each epoch:

$$P_{3D}(i) = \sqrt{(x(i) - x_0)^2 + (y(i) - y_0)^2 + (z(i) - z_0)^2}$$

As a median value (x_0, y_0, z_0), we used coordinates calculated on 24-hr interval for the quiet previous day. Figure 5 presents, as example, the 3D positioning and vertical errors for PDTN station associated with the solar eclipse. The analysis shows that the errors did not exceed 20 cm. The value of the error cannot be detected if regular background level of PPP errors for individual GPS station is higher than these values.

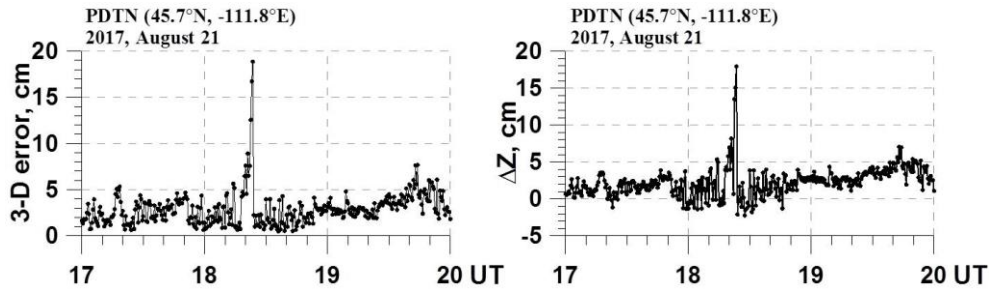


FIGURE 5. 3D positioning and vertical (ΔZ) errors for PDTN station associated with the solar eclipse.

Summary. The pattern of the GPS TEC changes over America during the eclipse was analyzed using the observations from 110+ GPS stations. The trough-like variations with a gradual decrease and followed by a recoveral increase of TEC at the time of the eclipse were observed over the whole continental U.S.

The depression of TEC reached down to 4-5 TECU. The maximum depression was observed over all stations located at the totality path of the solar eclipse. The TEC maps demonstrate that the depression of TEC reached 20-30% during the eclipse day with respect to the previous day. The delay of the minimum level of TEC with respect to the maximum phase of the eclipse was 20-30 min. The time lag of the TEC response to the eclipse increases with the distance from the eclipse path. The response of TEC to the solar eclipse depends on latitude, longitude, and LT. The positioning errors associated with eclipse did not exceed 20 cm.

Acknowledgments. This work was supported by grant RFBR 19-05-00570-a and program 28 presidium RAS.

1. N. Jakowski, S. M. Stankov, D. Klaehn, Operational space weather service for GNSS precise positioning, *Annales Geophysicae*, 2008, 23(9), pp. 3071-3079.
2. F. Ding, W. Wan, B. Ning, L. Liu, H. Le, G. Xu, et al., GPS TEC response to the 22 July 2009 total solar eclipse in East Asia, *Journal of Geophysical Research*, 2010, 115, pp. A07308, doi: 10.1029/2009JA015113.

3. L.W. Baran, I. I. Efishov, I. I. Shagimuratov, V. P. Ivanov, A. F. Lagovsky, The response of the ionospheric total electron content to the solar eclipse on August 11, 1999, *Advances in Space Research*, 2003, 31(4), pp. 989-994.
4. R. A. Bamford, The effect of the 1999 total solar eclipse on the ionosphere, *Physics and Chemistry of the Earth, Part C: Solar, Terrestrial & Planetary Science*, 2001, 26(5), pp. 373-377.
5. E. L. Afraimovich, E. A. Kosogorov, and O. S. Lesyuta, Effects of the August 11, 1999 total solar eclipse as deduced from total electron content measurements at the GPS network, *J. Atmos. Sol. Terr. Phys.*, 2002, 64, pp. 1933-1941.
6. S. M. Stankov, N. Bergeot, D. Berghmans, Multi-instrument observations of the solar eclipse on 20 March 2015 and its effects on the ionosphere over Belgium and Europe, *J. Space Weather Space Clim.*, 2017, 7(A19), doi: 10.1051/swsc/2017017.
7. M. M. Hoque, D. Wenzel, N. Jakowski, T. Gerzen, J. Berdermann, Ionospheric response over Europe during the solar eclipse of March 20, 2015, *J. Space Weather Space Clim.*, 2016, 6(A36), doi: 10.1051/swsc/2016032.
8. I. I. Shagimuratov, G. A. Yakimova, N. Yu. Tepenitsyna, I. I. Efishov, and L. M. Koltunen, Effects of the solar eclipse of March 20, 2015 on the total electron content over Europe, *Russian Journal of Physical Chemistry B*, 2018, 12(3), pp. 568-575.

CONTRIBUTION OF THE PLASMASPHERE TO TOTAL ELECTRON CONTENT AT MIDDLE AND HIGH LATITUDES

Anna S. Yasyukevich¹, Yury V. Yasyukevich¹, Maxim V. Klimenko², Artem M. Vesnin¹

¹*Institute of Solar-Terrestrial Physics SB RAS, Irkutsk, Russia*

²*West Department of Pushkov Institute of Terrestrial Magnetism, Ionosphere and Radio Wave Propagation, RAS, Kaliningrad, Russia*

Introduction. Global Navigation Satellite Systems (GNSS) measurements have been actively used in ionospheric researches. The GNSS data have several advantages (time resolution, spatial coverage, availability). However, the measured total electron content (TEC) is the sum of the ionosphere (IEC) and plasmasphere (PEC) electron contents along the satellite-receiver line-of-sight (LoS) up to ~ 20000 km altitude. Therefore, the data contain information about both the ionosphere and the plasmasphere. Herewith, in a number of applications (satellite positioning, for example) it is important to consider the plasmasphere contribution. Thus, it is essential to properly describe typical cycles in the plasmasphere, as well as the effects of the near-Earth space on this atmospheric layer.

It is impossible to separate the ionosphere and plasmasphere contribution to TEC from GNSS measurements only. There are different approaches to evaluate the plasmasphere electron content, including radio occultation measurements [1-3], satellite altimeters [4], radio plasma imagers [5-6]. Belehaki et al. [7] proposed the method for estimating the plasmasphere contribution to TEC using the combination of GNSS data and ionosonde measurements [7].

Data and methods. To calculate TEC data, we use the measurements from dual-frequency GNSS receivers of international IGS network [8]. The receivers are located at middle (IRKJ, 52°N, 104°E) and high (NRIL, 69N, 88E) latitudes. We analyze the data for the 2010-2013 period. The period is characterized by a sharp increase in solar activity. From the initial data, we calculate series of vertical TEC values by the method described in [9].

To estimate ionospheric electron content, we additionally involved measurements from ionosondes located in Irkutsk and Norilsk, close to the GNSS stations. Ionosphere electron content is obtained from experimental electron density profiles by the procedure described in [10]. The authors [10] showed that the calculated IEC values in Millstone Hill, Wallops Island and Jicamarca were in good agreement with the measurements from the incoherent scatter radar and the TOPEX satellite. To separate the ionosphere and plasmasphere contributions we applied a method proposed in [7]. We define plasmasphere electron

content as the difference between TEC and IEC values: $PEC = TEC - IEC$. The temporal resolution of the obtained TEC and PEC values is 15 minutes.

Results. Figure 1 presents the dynamics in daytime (black dots) and nighttime (gray dots) PEC values (a, c) and PEC/TEC ratio (b, d) at Irkutsk (a, b) and Norilsk (c, d) for 2010-2013. Changes in the solar UV central flux (0.1-50 nm) are shown on the panels by black thin lines. Daytime PEC values follow the changes in the solar activity level. There are pronounced semiannual variations with maxima during equinoxes in daytime PEC dynamics. The maxima of semiannual variations depend on the solar activity level. Nighttime PEC values have the different seasonal variations with maximum values in summer and minimum values in winter.

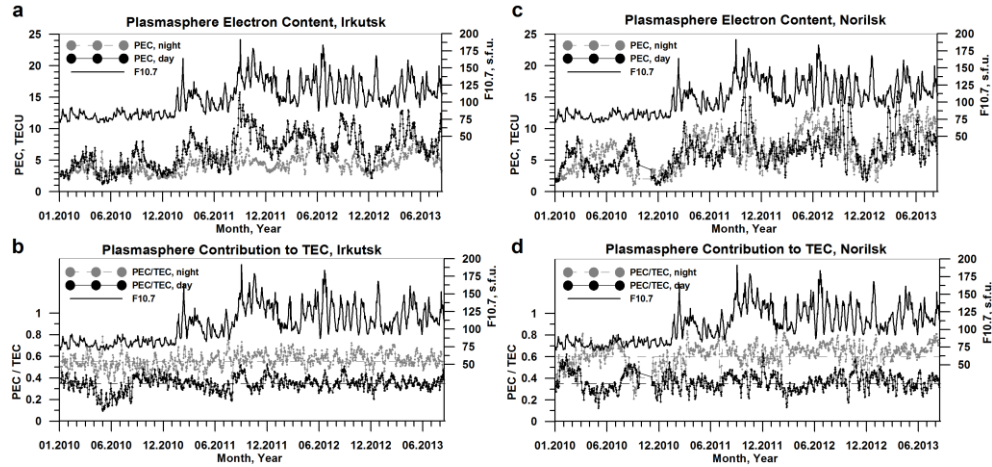


FIGURE 1. Changes in daytime (black dots) and nighttime (gray dots) PEC values (a, c) and PEC/TEC ratio (b, d) in Irkutsk (a, b) and Norilsk (c, d) for the 2010-2013 period. Thin black lines show dynamics in the solar UV central flux.

PEC/TEC ratio varies significantly within local time. On daytime, PEC is 25-30% of TEC. At nighttime, the plasmasphere contribution increases substantially. It averages about half of TEC value and, in some periods, reaches 70%. At high-latitude station the nighttime plasmasphere contribution is higher than at mid-latitude one. Note that PEC/TEC ratio practically does not change with increase in solar activity. It fluctuates around 0.35 at midday and ~0.55-0.6 at night.

Figure 2 presents the local time versus day-of-year distributions of PEC/TEC ratio in Irkutsk (a) and Norilsk (b) averaged for 2010-2013 years. Panels c and d show the same distributions but obtained from the IRI-Plas model [11] simulations. Dashed lines show the time of solar terminator at 100 and 300 km altitudes. PEC/TEC ratio distributions feature significant diurnal variations. The maximum contribution of the plasmasphere to TEC is registered before sunrise in most

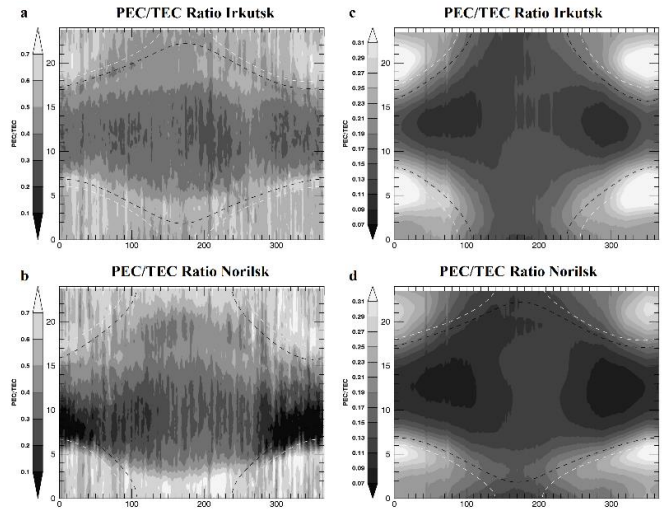


FIGURE 2. Local time versus day-of-year distributions of PEC/TEC ratio from experimental data (a, b) and IRI-Plas model simulation (c, d). Dashed lines show the time of solar terminator at 100 and 300 km altitudes.

cases. The smallest plasmasphere contribution to TEC is observed after sunrise in Norilsk in winter and is about 10 %.

The dynamics in plasmasphere contribution to TEC from experimental data and IRI-Plas model are close in general. However, the model significantly underestimates the level of the plasmasphere contribution, especially at night. According to the model results, the plasmasphere contribution is about 10-15 % in daytime and does not exceed 34 % at night.

The authors are grateful to the IGS service for the GNSS data and to NCEI NOAA and WDC, Kyoto services for solar and geomagnetic data. The ionosondes data were recorded by the Angara Multiaccess Center facilities at ISTP SB RAS (<http://ckp-angara.iszf.irk.ru/>). The study is supported by the Russian Foundation for Basic Research Grant No. 18-35-20038. We used data processing techniques developed within the base financing of FR program II.16.

1. P. Chen, Y. Yao, Research on global plasmaspheric electron content by using LEO occultation and GPS data, *Adv. in Space Res.*, 2015, 55, pp. 2248–2255, doi: 10.1016/j.asr.2015.02.004.
2. S. Heise, N. Jakowski, A. Wehrenpfennig, et al., Sounding of the topside ionosphere/plasmasphere based on GPS measurements from CHAMP: Initial results, *Geophys. Res. Lett.*, 29, 2002, 14, 1699, doi 10.1029/2002GL014738.
3. M. V. Klimenko, V. V. Klimenko, I. E. Zakharenkova, I. V. Cherniak, The global morphology of the plasmaspheric electron content during Northern winter 2009 based on GPS/COSMIC observation and GSM TIP model results, *Adv. Space Res.*, 2015, 55(8), pp. 2077–2085, doi: 10.1016/j.asr.2014.06.027.
4. H.-B. Lee, G. Jee, Y. H. Kim, J. S. Shim, Characteristics of global plasmaspheric TEC in comparison with the ionosphere simultaneously observed by Jason-1 satellite, *J. Geophys. Res. Space Phys.*, 2016, 118, pp. 935–946, doi: 10.1002/jgra.50130.
5. T. Gerzen, J. Feltens, N. Jakowski, et al., Validation of plasmasphere electron density reconstructions derived from data on board CHAMP by IMAGE/RPI data, *Adv. in Space Res.*, 2015, 55, pp. 170–183, doi: 10.1016/j.asr.2014.08.005.
6. X. Huang, B. W. Reinisch, P. Song, et al., Developing an empirical density model of the plasmasphere using IMAGE/RPI observations, *Adv. in Space Res.*, 2004, 33, pp. 829–832, doi: 10.1016/j.asr.2003.07.007.
7. A. Belehaki, N. Jakowski, B. W. Reinisch, Plasmaspheric electron content derived from GPS TEC and digisonde ionograms, *Adv. in Space Res.*, 2004, 33, pp. 833–837, doi: 10.1016/j.asr.2003.07.008.
8. J. M. Dow, R. E. Neilan, C. Rizos, The International GNSS Service in a changing landscape of Global Navigation Satellite Systems, *J. Geodesy*, 2009, 83, pp. 191–198, doi: 10.1007/s00190-008-0300-3.
9. Yu. V. Yasyukevich, A. A. Mylnikova, A. S. Polyakova, Estimating the total electron content absolute value from the GPS/GLONASS data, *Results in Phys.*, 2015, 5, pp. 32–33, doi: 10.1016/j.rinp.2014.12.006.
10. X. Huang, B. W. Reinisch, Vertical electron content from ionograms in real time, *Radio Sci.*, 2001, 36(2), pp. 335–342, doi: 10.1029/1999RS002409.
11. T. L. Gulyaeva, International standard model of the Earth's ionosphere and plasmasphere, *Astronomical & Astrophysical Transactions*, 2008, 22(4-5), pp. 639–643, doi: 10.1080/1055679030856 5760.

MULTI-INSTRUMENTAL OBSERVATIONS OF IONOSPHERIC PLASMA DENSITY DISTURBANCES DURING GEOMAGNETIC STORMS

Irina E. Zakharenkova¹ and Iurii V. Cherniak²

¹West Department of IZMIRAN, Kaliningrad, Russia

²COSMIC Program Office, UCAR, Boulder, USA

Introduction. In general, the midlatitude ionosphere is considered being relatively free from the strong ionospheric irregularities and plasma density gradients. But during strong geomagnetic disturbances, the midlatitude ionosphere becomes more complicated since structures of different scales

can appear here with excitation and equatorward propagation of large-scale traveling ionospheric disturbances (TIDs), equatorward extension of a zone of intense auroral irregularities and a poleward expansion of storm-induced equatorial ionospheric irregularities.

Methods. We present results of a comprehensive analysis of storm-induced plasma density disturbances based on a combination of in-situ and remote sensing techniques including 6100+ ground-based GNSS stations, in situ plasma observations onboard Swarm, C/NOFS, and DMSP satellites, COSMIC GPS scintillations, and up-looking GPS observations onboard Swarm mission.

Results and Conclusion. In this paper, we discuss the major features of the storm-induced ionospheric disturbances — large-scale and medium-scale TIDs and expanded ionospheric irregularities — that occurred at midlatitudes during strong geomagnetic storms of 2015-2017. We also report a new pattern of storm-induced ionospheric irregularities behavior at midlatitudes — poleward-streaming plasma density depletions. Under disturbed conditions, they appear at North America low-latitudes as a part of extended postsunset equatorial plasma bubbles and further, they are streaming from low-latitudes in a northwestward, poleward direction toward the main ionospheric trough and auroral irregularities zone. The channels of poleward-streaming plasma depletions were stretched from low-latitude base towards higher latitudes—they found to occur for geomagnetic storms under specific combination of steady southward IMF, sub-auroral polarization streams (SAPS) electric fields, and enhanced westward drifts at midlatitudes resulted in northwestward plasma transportation equatorward of the SAPS region. The poleward-streaming plasma depletions form an illusion of TIDs moving in a poleward, northwestward direction—this propagation direction is opposite to typical equatorward propagation of storm-induced LSTIDs generated in the auroral zone and propagated towards the equator. This phenomenon is accompanied by strong ionospheric irregularities occurred over both edges of plasma depletion channel, posing a localized threat for GPS-based positioning applications. Even moderate-to-intense storms (Dst minimum -145 nT) can promote such effects at midlatitudes.

Acknowledgments. This work was supported in part by RFBR grant No. 19-05-00570-a.

SIMULATION OF OBLIQUE SOUNDING IONOGRAMS DURING ST. PATRICK'S DAY 2015 GEOMAGNETIC STORM: VALIDATION AND INVESTIGATION OF THE INFLUENCE OF THE EARTH'S MAGNETIC FIELD

Daria S. Kotova^{1,2}, Maxim V. Klimenko¹, Artem M. Vesnin^{3,4}, Vladimir V. Klimenko¹, Veniamin E. Zakharov⁵, Denis D. Rogov⁶, and Donat V. Blagoveshchensky⁷

¹West Department of Pushkov Institute of Terrestrial Magnetism, Ionosphere and Radio Wave Propagation RAS, Kaliningrad, Russia

²Department of Physics, University of Oslo, Oslo, Norway

³Institute of Solar-Terrestrial Physics SB RAS, Irkutsk, Russia

⁴Irkutsk State University, Irkutsk, Russia

⁵Immanuel Kant Baltic Federal University, Kaliningrad, Russia

⁶Arctic and Antarctic research institute, Saint-Petersburg, Russia

⁷Saint-Petersburg State University of Aerospace Instrumentation, St. Petersburg, Russia

Introduction. Most publications about radio waves propagation are devoted to studies in the medium described by the empirical IRI model [1-3], or locally created averaged ionospheric model for mid-latitude region [4]. Therefore, the model medium is median and does not have sharp gradients in the electron density. However, it is precisely the gradients of electron density and ionospheric inhomogeneities that significantly affect the propagation of HF radio waves. One of the sources of the formation of plasma inhomogeneities of various scales is geomagnetic storms. At high latitudes, during

the period of geomagnetic disturbances, a strong Es layer is quite often formed, which shields the HF signal [5]. In addition, there is the question of the need to take into account anisotropy in the simulation of HF radio communications [6]. Therefore, it is necessary to study the influence of the Earth's magnetic field on the features of the propagation of HF both during quiet conditions and geomagnetic disturbances.

Technique description. This paper presents a study of the influence of the Earth's magnetic field on the formation of ray trajectories and paths obtained during the strongest geomagnetic storm in the current solar cycle on March 17–18, 2015. Since the geomagnetic storm sudden commencement began on March 17 at ~05:00 UT from the fall of the Dst index to -223 nT at ~ 23:00 UT, the time 12:02 UT on March 16 was selected as quiet conditions, and 12:02 UT on March 17 and March 18 as disturbed conditions, and 12:02 UT on 19 March as recovery phase conditions. For the study, we used the previously developed algorithm of the three-dimensional shooting method [7], as well as a consistent computational algorithm that uses propagation media model and calculates HF radio waves propagation parameters [8]. To describe quiet and disturbed conditions we used the parameters of the ionosphere and neutral atmosphere at heights of 80–800 km obtained using Global Self-consistent Model of the Thermosphere, Ionosphere and Protonosphere (GSM TIP) [9, 10]. The GSM TIP model was previously successfully used by us to study the effect of geomagnetic storms on the propagation and absorption of HF radio waves [11].

Results and conclusion. Using the three-dimensional shooting method [7] for various frequencies (up to the maximum usable frequency (MUF)), modeled paths were found between the Lovozero and Gorkovskaya stations taking into account the influence of the Earth's magnetic field. Figure 1 shows the modeled oblique sounding ionograms that was obtained for time 12:02 UT taking into account absorption for quiet conditions on March 16, during the storm time on March 17 and 18, and in the recovery phase on March 19, 2015.

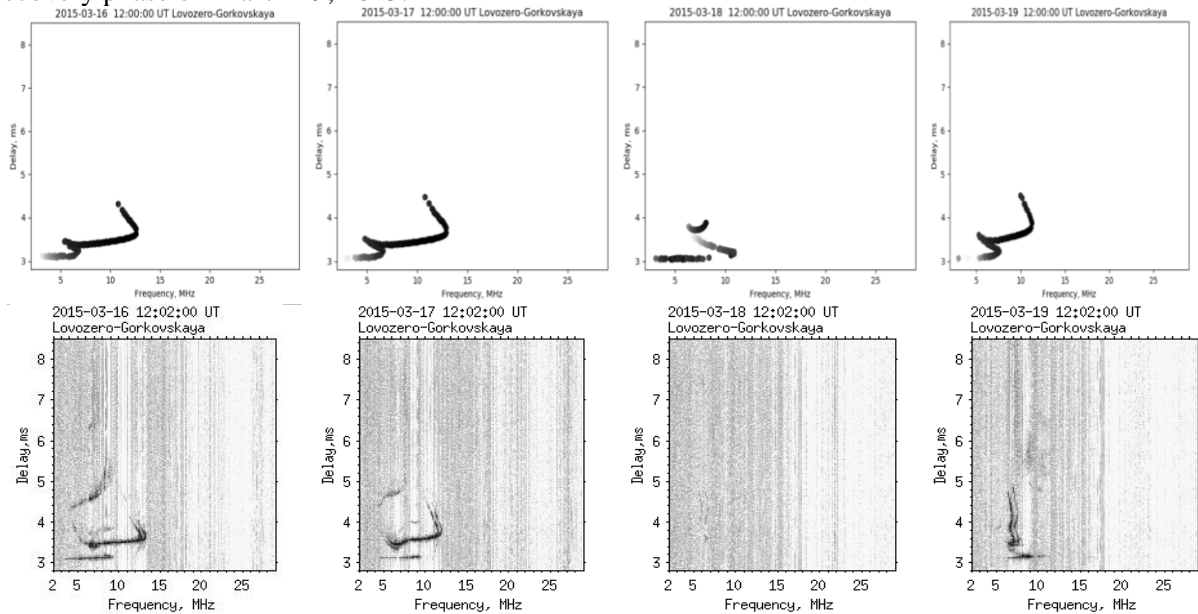


FIGURE 1. Model (top) and experimental (bottom) oblique sounding ionograms on the trace Lovozero - Gorkovskaya at time 12:02 UT for March 16-19, 2015.

It can be seen that the GSM TIP model qualitatively reproduces changes in the E and F regions during the geomagnetic storm under consideration: the F2 layer MUF for quiet conditions corresponds to the observed one (of the order of 12.6 MHz), the Es layer gain is reproduced for March 18 and 19 (MUF Es

increases from 6.6 MHz up to 10.9 MHz and 7.6 MHz, respectively). The delay time, which means the height of the layers corresponds to the experimental data. The ionogram for the 18th is partially reproduced. Due to the strong absorption in the experimental ionogram, traces of reflections are practically invisible. However, the F region decreased: MUF F2 dropped to 7 MHz, which is reproduced in the model calculations results - 8 MHz. The greatest discrepancy was obtained for March 19, when the model environment was practically restored to its original conditions, which is not observed in the experiment.

The angular characteristics (azimuth and elevation angle) of each obtained path were used by us as initial conditions for calculating the ray paths in the absence of the Earth's magnetic field. In Fig. 2 presents the results. It is clearly seen that, without taking into account the Earth's magnetic field, not only the reflection height changes (it becomes 35 km lower on average), but also the behavior of the rays near the reflection point - the radius of curvature of the ray path decreases. It can be seen that the rays go on completely different trajectories and the practical ones do not come to the receiving point. In case the absence of taking into account the influence of the Earth's magnetic field for the lower rays reflected from the F2 layer, we can note the formation of a common intersection point of rays near with 58° geomagnetic latitude. A similar point is formed for the lower rays reflected from the E region. However, for all the high rays shown by solid black lines, this pattern is not observed.

Such a result is illustrative and shows that when solving the problems of radio wave propagation, it is important to take into account the Earth's magnetic field.

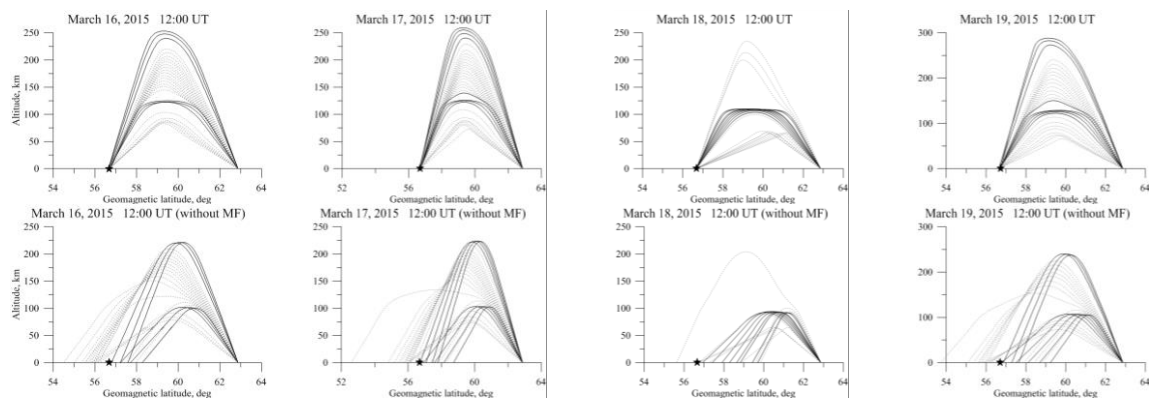


FIGURE 2. The ray paths obtained during the execution of the shooting method for simulation of the ionograms (left). Ray-paths obtained for the same frequencies and angular characteristics (azimuth and elevation angle), but in the absence of an external magnetic field, are presented to the right. The upper rays are shown by a solid black line, the gray dashed line shows of lower rays. An asterisk indicates the position of the receiving point (Gorkovskaya).

Ray tracing simulation was performed (D. S. Kotova) with the financial support of the Grant of the President of Russian Federation for young scientists (MK- 2584.2019.5). The study of the influence of the Earth's magnetic field on the radio waves propagation (M. V. Klimenko, D. S. Kotova) was supported by the Russian Science Foundation (project №17-77-20009).

1. N. Y. Zaalov, E. V. Moskaleva, and T. S. Burmakina, Application of the IRI model to the HF propagation model with optimization of the ionosphere parameters to day-to-day variation, *Adv. Space Res.*, 2017, 60(10), pp. 2252-2267, doi: 10.1016/j.asr.2017.08.018.

2. I. A. Nosikov, M. V. Klimenko, P. F. Bessarab, and G.A Zbankov, Application of the nudged elastic band method to the point-to-point radio wave ray tracing in IRI modeled ionosphere, *Adv. Space Res.*, 2016, pp. 491-497, doi: 10.1016/j.asr.2016.12.003.

3. M. Fagre, B. S. Zossi, J. Chum et al., Ionospheric high frequency wave propagation using different IRI hmF2 and foF2 models, *J. Atmos. Sol. Terr. Phys.*, 2019, 196, 105141, doi: 10.1016/j.jastp.2019.105141.
4. L. R. Cander and B. Zolesi, Ionospheric Monitoring and Modeling Applicable to Coastal and Marine Environments, *Physical Processes and Numerical Modelling*, 2019, DOI: 10.5772/intechopen.90467.
5. D. V. Blagoveshchensky, O. A. Maltseva, M. M. Anishin, and D. D. Rogov, Sporadic E S Layers at High Latitudes During a Magnetic Storm of March 17, 2015 According to the Vertical and Oblique Ionospheric Sounding Data, *Radiophysics and Quantum Electronics*, 2017, 60(6), pp. 456–466, doi:10.1007/s11141-017-9814-y.
6. M. Fagre, B. S. Zossi, E. Yiğit et al., Effects of Earth's magnetic field variation on high frequency wave propagation in the ionosphere, *Ann. Geophys. Discuss.*, 2019, doi:10.5194/angeo-2019-27.
7. D. S. Kotova, Algorithm of the three-dimensional shooting method based on a numerical model for HF radio waves propagation in the ionosphere, *Physics of Auroral Phenomena*, 2018, 41, pp. 129-130. (in Russian).
8. D. S. Kotova, M. V. Klimenko, V. V. Klimenko, and V. E. Zakharov, Numerical simulation of the influence of the May 2–3, 2010 geomagnetic storm on HF radio-wave propagation in the ionosphere, *Radiophysics and Quantum Electronics*, 2014, 57(7), pp. 467–477, doi: 10.1007/s11141-014-9529-2
9. A. A. Namgaladze, Yu. N. Korenkov, V. V. Klimenko et al., Global model of the thermosphere-ionosphere-protonosphere system. *PAGEOPH*, 1988, 127 (2/3), pp. 219–254, <http://dx.doi.org/10.1007/BF00879812>;
10. M. V. Klimenko, V. V. Klimenko, I. V. Despirak et al., Disturbances of the thermosphere-ionosphere-plasmasphere system and auroral electrojet at 30° E longitude during the St. Patrick's Day geomagnetic storm on 17–23 March 2015, *J. Atmos. Sol. Terr. Phys.*, 2018, doi:10.1016/j.jastp.2017.12.017.
11. D. S. Kotova, M. V. Klimenko, V. V. Klimenko, and V. E. Zakharov, Influence of Geomagnetic Storms of September 26–30, 2011, on the Ionosphere and HF Radiowave Propagation. II. Radiowave Propagation, *Geom. Aeron.*, 2017, 57, pp. 288-300, doi: 10.1134/S0016793217030100.

F2 LAYER IONOSPHERIC RESPONSE TO THE GEOMAGNETIC STORMS DUE TO THE GLOBAL THERMOSPHERE REDISTRIBUTION

Vladimir V. Klimenko¹, Maxim V. Klimenko¹, Konstantin G. Ratovsky², Yury V. Yasyukevich²,
Irina E. Zakharenkova¹, Roman V. Vasiliev²

¹West Department of Pushkov Institute of Terrestrial Magnetism, Ionosphere and Radio Wave Propagation RAS, Kaliningrad, Russia

²Institute of Solar-Terrestrial Physics SB RAS, Irkutsk, Russia

Introduction. Considerable debate on mechanisms of the ionospheric storms [1-2] have not yet led to a unified point of view on this issue. In the given paper we present the investigation of thermosphere-ionosphere coupling processes during geomagnetic storms. We present an overview of the upper atmospheric response to strong geomagnetic storm occurred on March 17-23, 2015 as well as some results of statistical data analysis.

Methods. The results were obtained from both the satellite and ground-based observations (ionosondes, GPS receivers, Fabry-Perrot interferometer), and from the computer simulation using the Global Self-consistent Model of the Thermosphere, Ionosphere, and Protonosphere (GSM TIP). The GSM TIP [3] was developed in the WD IZMIRAN.

Results and Conclusion. We consider the major features of the positive and negative ionospheric storms development at low-, mid-, and high-latitudes. GSM TIP simulations have revealed: 1) the stratification of the storm-enhanced tongue of ionization during 2015 St. Patrick geomagnetic storm that is explained by combine effect of neutral tongue structure and storm-time thermospheric wind disturbances; 2) strong increase of global electron content at the initial stage of geomagnetic storm development due to effects of thermospheric wind and neutral composition; 3) after-storm positive ionospheric response in mid-latitude F region ionospheric density. GSM TIP model results show an

after-storm increase in the $n(\text{O})/n(\text{N}_2)$ ratio and a decrease in the $n(\text{N}_2)$ that results in the daytime positive effects in the f_oF2 .

The reported study was funded by RFBR according to the research project No. 18-55-52006.

1. N. Balan, H. Alleyne, Y. Otsuka, et al. Relative effects of electric field and neutral wind on positive ionospheric storms, *EPS*, 2009, 61(4), pp. 439–445, doi:10.1186/BF03353160.
2. B.T. Tsurutani, A.J. Mannucci, O.P. Verkhoglyadova, and G.S. Lakhina. Comment on “Storming the Bastille: the effect of electric fields on the ionospheric F-layer” by Rishbeth et al. (2010), *Ann. Geophys.*, 2013, 31, doi:10.5194/angeo-31-145-2013.
3. A. A. Namgaladze, Yu. N. Korenkov, V. V. Klimenko et al., Global model of the thermosphere-ionosphere-protonosphere system. *PAGEOPH*, 1988, 127 (2/3), pp. 219–254.

EFFECTS OF IONIZATION OF THE ATMOSPHERE. NATURAL AND TECHNOGENIC DISASTERS

DOUBLE ELVES MEASURED BY THE TUS SPACE DETECTOR

Pavel A. Klimov, Sergei A. Sharakin, Margarita A. Kaznacheeva

Skobeltsyn Institute of Nuclear Physics of Lomonosov Moscow State University, Moscow, Russia

Introduction. Elves (“ELVE” stands for Emission of Light and Very Low Frequency perturbation from an Electromagnetic Pulse) are the type of transient luminous events (TLEs) that represent expanding luminous ring in the ionosphere at the height of 80-90 km. For the first time they were observed and described in [1]. First ground based observations were made in [2].

The duration of elve is less than 1 ms and they can expand over 300 km laterally. Elves are the most common type of TLEs: according to the ISUAL global experimental data the number of elves is about 50% of all TLE statistics [3]. Elves are the result of ionospheric electrons heating by the upward electromagnetic impulse radiated by the lightning discharge current [4].

Number of experiments measured elves with more complicated spatial structure - events which have two rings and called them double elves [5]. In the work [6] simulations of double elves were made and it was demonstrated that these elve doublets are the ionospheric signature of compact intracloud discharges (CIDs).

CIDs are extremely powerful compact discharges that are thought to occur near the tops of some thunderclouds. These discharges have durations of 20-30 μ s. The phenomena is known to be the source of a very intensive electromagnetic pulses (EMP).

In this paper we present elves observations by the TUS detector from space in the nadir direction which allows one to see the spatial structure and measure temporal waveforms with a high time resolution. A method to estimate the altitude of a source based on temporal structure of elve is developed and applied to the TUS data.

The TUS detector. The TUS detector is a part of scientific payload on board the Lomonosov satellite launched on 28.04.2016 from Vostochny cosmodrom (Russian Federation) to the orbit with height 470-500 km and inclination 97.3°. The telescope comprises two main parts: the mirror-concentrator and photo detector in its focal plane. Photo detector consists of 256 channels (pixels) with square windows of 15 × 15 mm covering field of view (FOV) of 9° × 9°. Pixel sensor is the photoelectron multiplier tube (PMT) R1463 of Hamamatsu with cathode diameter of 13 mm. Using PMT as a sensor and large mirror (area of ~2 m²) provide high sensitivity of measurements with high temporal resolution (0.8 μ s) and spatial resolution in the atmosphere near 5 km. The detector measures atmospheric radiation in the near UV wavelength band 300-400 nm which is determined by the UV filter UFS1 and PMTs photo cathode quantum efficiency.

The TUS detector is designed to measure very faint fluorescence and scattered (reflected) Cherenkov radiation of extensive air showers produced by ultra-high-energy cosmic rays. Its high sensitivity and temporal resolution can be efficiently used for measurements of various atmospheric phenomena like, for example, elves. For more details of the TUS telescope, see [7].

Double elves measured by the TUS detector. During approximately two years of operation of the TUS detector it has registered 26 events that can be classified as elves due to space-time structure of the image: “ring” moving with a high speed across the field of view. In the TUS data a number of elves with more complicated space-time pattern were found: so called double elves. One example of double elve, measured on April 10, 2017 at 13:06:59 UTC is presented in Fig.1. On the pixel map two separated

rings are obviously seen. These rings correspond to two peaks in the waveforms shown in the right part of figure (signals of two channels are given for comparison). The first ring is brighter - it corresponds to interaction of ionosphere with a direct electromagnetic wave from lightning. The second ring is caused by a reflected from ground electromagnetic emission of lightning.

The elve is located above the West coast on New Britain (coordinates of the TUS FOV center are 5.68S, 148.40E). To analyze thunderstorm activity at the time of registration, data from the ground-based lightning location network Vaisala GLD360 [8] were used. A thunderstorm with numerous lightning discharges was measured to the north of the detector location which corresponds to the direction of the elve arrival.

Estimation of the double elve source altitude.

Telescope TUS is placed on the satellite and looking at nadir direction. In this case double elve develops in the plane which perpendicular to the optical axis and represents two rings crossing FOV one after another and separated in time. The first ring is created in the ionosphere by the direct EMP which arrives to a pixel FOV with a time delay l_1/c ; the second ring is created by the ground reflection with a delay from initial EMP l_2/c (l_1 and l_2 – pathlength of the direct and reflected EMP, c – speed of light). Thus the delay Δt between two rings of the double elve is simply calculated from a geometry of measurements, $c\Delta t = [L^2 + (H+h)^2]^{1/2} - [L^2 + (H-h)^2]^{1/2}$, and depends on L - distance between pixel FOV center and projection of the source position on the ground, H - altitude of the ionospheric layer where elve is developed and h - the EMP source altitude.

If we measure Δt then we can determine the h given the H and L . The estimation of H is well known from numerous elves observations. For example in the work [9] it was shown that elves heights during individual nights ranges between 83 and 93 km and the overall median altitude is 87.1 km.

The uncertainty of L is much bigger. Thunderstorm occupies a large area (more that 100 km in diameter) which means a large area of cloud coverage as well. In this case it is difficult to determine L accurately. For this reason a method based on probabilistic inference was developed.

In accordance with Bayes theorem the posterior probability of unknown parameters $P(\Theta|D)$ is proportional to a product of a prior probability $P(\Theta)$ and a likelihood function $P(D|\Theta)$ derived from statistical model for the observed data. Here D is observed data which are represented by set of time delay $\{\Delta t_i\}$ ($i=1,...,N$, where N – the number of hit pixels), and $\Theta = \{h, \varphi, \lambda, \sigma\}$, where first three parameters are the EMP source altitude and its geographical coordinates (latitude and longitude), and we introduce the additional nuisance parameter σ as typical error of delay estimation.

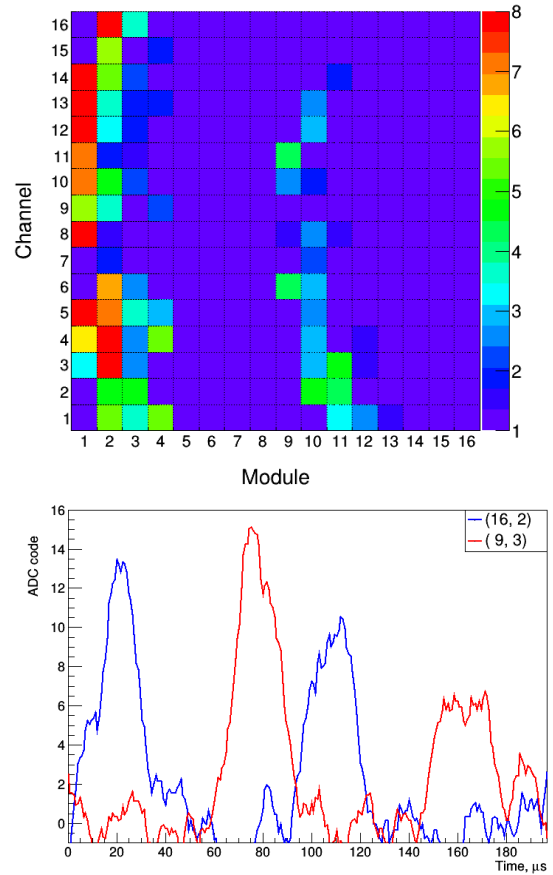


FIGURE 1. A double elve measured by the TUS detector on April 10, 2017. Top: pixel map, two bright rings are seen. Bottom: the waveforms of two channels (blue and red lines), each comprise two peaks with a time delay of $\sim 85 \mu s$.

Geographical coordinates of the source define the L value for each pixel. Assuming that the signal fluctuations in each pixel are independently distributed, we can make a hypothesis that Δt_i in $P(D|\Theta)$ are normally distributed with the theoretical mean $\Delta T_i(h, \varphi, \lambda)$ and unknown (but the same) for all hit pixels variance σ^2 .

The prior distribution function $P(\Theta)$ consists of two independent parts: $P(\Theta) = P(\varphi, \lambda) P(h)$, where the first factor comprises the information for the geographical location of the EMP source which we obtained from Vaisala GLD360 network. The prior $P(h)$ was based on previous CID altitude measurements [10] and was chosen as normal distribution with the mean $h_0 = 15$ km and rather wide standard deviation $\sigma_0 = 15$ km.

As a result, the value of the most probable source altitude (mode) h_{mode} and its accuracy σ_h given a data $\{\Delta t_i\}$ can be obtained for each double elve event. For the event registered at April 10, 2017 we thus obtain: $h_{\text{mode}} = 25.3$ km, $\sigma_h = 7.2$ km.

Conclusions. The TUS detector is capable to measure atmospheric luminous phenomena with a high temporal resolution (0.8 μ s). This allows us to select rare observed previously type of TLEs - so called double elves. Measurements of temporal profile in various channels of the detector makes it possible to determine the altitude of the source of EMP causing such an event. A new method of the EMP height estimation based on Bayesian inference was developed and implemented for the TUS data analyses. This method gives source altitude $h = 25.3 \pm 7.2$ km for the elve presented in this work. The error is rather big and it is related to properties of the TUS data. The developed method is sensible to a number of channels used for the analyses and Δt determination accuracy. Besides the TUS data suffers from a number of dead pixels, weak channels and signal saturation. Obtained value is higher than a typical thunderstorm cloud altitude (below tropopause), but events with such high altitude were measured and reported [11, 12].

The work was done with partial financial support from the State Space Corporation ROSCOSMOS, M.V. Lomonosov Moscow State University through its Prospects for Development program (Perspektivnye Napravleniya Razvitiya). The authors wish to thank Vaisala Inc. company for providing the data on lightning strikes employed in the present study.

1. W. L. Boeck, O. H. Vaughan, Blakeslee, et al., Lightning induced brightening in the airglow layer, *Geophys. Res. Lett.*, 1992, 19 (2), pp. 99-102, doi: 10.1029/91GL03168.
2. H. Fukunishi, Y. Takahashi, M. Kubota, et al., Elves: Lightning-induced transient luminous events in the lower ionosphere, *Geophys. Res. Lett.*, 1996, 23 (16), pp. 2157-2160, doi: 10.1029/96GL01979.
3. A. B. Chen, C.L. Kuo, Y.J. Lee, et al., Global distributions and occurrence rates of transient luminous events, *J. Geophys. Res. Space Physics*, 2008, 113, pp. A08306, doi: 10.1029/2008JA013101.
4. U. S. Inan, T. F. Bell, J. V. Rodriguez, Heating and ionization of the lower ionosphere by lightning, *Geophys. Res. Lett.*, 1991, 18 (4), pp. 705-708, doi: 10.261.1029/91GL00364.
5. R. T. Newsome, U. S. Inan, Free-running ground-based photometric array imaging of transient luminous events. *J. Geophys. Res. Space Physics*, 2010, 115 (A7), doi: 10.1029/2009JA014834
6. R. A. Marshall, C. L. Silva, V. P. Pasko, Elve doublets and compact intracloud discharges. *Geophys. Res. Lett.*, 2015, 42 (14), pp. 6112-6119, doi: 10.1002/2015GL064862
7. P. A. Klimov, M. I. Panasyuk, B. A. Khrenov, et al., The TUS detector of extreme energy cosmic rays on board the Lomonosov satellite, *Space Science Reviews*, 2017, pp. 1-17, doi: 10.1007/s11214-017-0403-3.
8. R. Said, M. Murphy, GLD360 upgrade: Performance analysis and applications, 2016, 24th Int. Lightning Detection Conf. and Sixth Int. Lightning Meteorology Conf.
9. O. A. Velde, J. Montany, Statistics and variability of the altitude of elves, *Geophys. Res. Lett.*, 2016, 43 (10), pp. 5467-5474. doi: 10.1002/2016GL068719.
10. A. R. Jacobson, M. J. Heavner, Comparison of Narrow Bipolar Events with Ordinary Lightning as Proxies for Severe Convection, *Monthly Weather Review*, 2005, 133, pp. 1144, doi: 10.1175/MWR2915.1.

11. A. Nag, V. A. Rakov, Cramer, J., Remote measurements of currents in cloud lightning discharges, *IEEE Transactions on Electromagnetic Compatibility*, 2011, 53, pp. 407-413.

12. D. A. Smith, M. J. Heavner, A. R. Jacobson, et al., A method for determining intracloud lightning and ionospheric heights from VLF/LF electric field records, *Radio Science*, 2004, 39 (1), doi: 10.1029/2002RS002790.

LARGE-SCALE EARTHQUAKE OF EARLY 2010 ON HAITI: THE LOCALIZATION AND RELATIONSHIP OF IONOSPHERIC IRREGULARITIES WITH CERTAIN SEISMIC SOURCES

Maria A. Titova^{1,3,5}, Victor I. Zakharov^{2,4}, and Sergey A. Pulinets^{1,3}

¹Space Research Institute of the Russian Academy of Sciences, Moscow, 117997, Russian Federation

²Faculty of Physics, Lomonosov Moscow State University, Moscow, 119991, Russian Federation

³Federal Research Center Institute of Applied Physics, Nizhny Novgorod, 603950, Russian Federation

⁴Obukhov Institute of Atmospheric Physics, Moscow, 119017, Russian Federation

⁵Pushkov Institute of Terrestrial Magnetism, Ionosphere and Radio Wave Propagation, Moscow, Troitsk, 108840, Russian Federation

Introduction. Large-scale earthquake occurred of early 2010 on the island of Haiti with a magnitude of M 7.0, the epicenter coordinates were lat. 18.443° N, long. 72.571° W, and the depth of the seismic center was 13 km, according to USGS (U.S. Geological Survey). The power of earthquake have attracted to it close attention from the geophysicists [1-6], because it allows a carefully to consider the interaction of the lithosphere–atmosphere–ionosphere at amid quiet geomagnetic activity up to 20 nT, according to WDC, Kyoto (<http://wdc.kugi.kuoto-u.ac.jp/dstae>) during the seismic events. Therefore, the changes have registered in the ionosphere structure, these cannot be explained only by variations in the Earth's magnetic field and solar activity. Thus, the work is focused on the study of the earthquake, which is the source of atmospheric and ionospheric disturbances by the using GPS data.

GPS system in the study ionosphere. A group delay and a phase advance of radio navigation signals are used to take values the total electron content (TEC, 1TECU=10¹⁶ electron/m²), that are being made along the line of sight between the receiver on the ground and the transmitters on-board the GPS system satellites at two coherently-coupled frequencies [7, 8, 12]. The error in determining TEC variations from phase measurements is less than 0.1% relative to the background concentration [9].

Using data from the global specialized networks of stations IGS and UNAVCO. Applying data from the networks of IGS (International Geophysical Survey) and UNAVCO (University Navstar Consortium) for the TEC calculation method has allowed to obtain sufficient spatial resolution. For example, the Fig. 1 shows a map on that displays the joint location of GPS–receiving stations (gray and black small circles) IGS and UNAVCO networks, as well as seismic events in the region (squares).

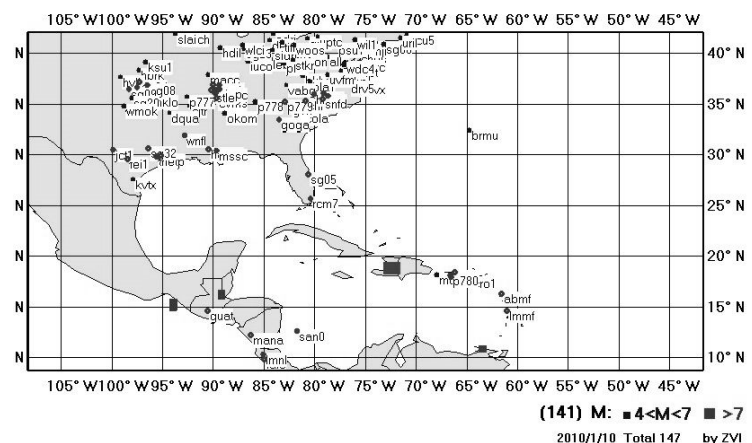


FIGURE 1. The location of IGS and UNAVCO stations (gray and black small circles) and seismic events in the region (squares).

Method of GPS-interferometry for ionosphere research. To get the deviation of TEC parameter from the average values, the combination the registered of phases at the two operating frequencies L_1 and L_2 , and subsequent filtration of high-frequency noise (with period 3 to 5 minutes), and assessment of velocity of the change parameter TEC in time are used in this study [7, 10, 12]. The method has the angle dependence signal amplitude from the sight direction to the satellite. [11, 12].

The complex algorithm have implemented in the CRASS GPS application programs, which were created at the Department of Atmospheric Physics in the Physics Faculty by at Lomonosov Moscow State University for processing data arrays [10].

Results. More than 7.5 thousand hours of individual observations, that is, over 4.3 million phase measurements were processed to analysis of earthquakes in Haiti for the period January 1-15, 2010.

Figure 2 shows the daily seismic rate of an earthquake. The mainshock was preceded by a series of foreshocks that began on January 2 with a magnitude of 4.2 and extended with increasing intensity until January 9. The quake of M 5.1 was recorded on January 11, 2010. More than forty aftershocks with a M 4.2 and higher magnitudes were registered after the main shock. Figure 3 shows the energy logarithm temporal dependence had estimated by the formula Kanamori, i.e.

$$\lg E = 1.5M + 11.8, \quad (1)$$

where E is the earthquake energy in joules, M is the magnitude. The sampling period is 6 hours. The dispersion value is indicated by a slim horizontal lines, relatively the average value, which is marked by a bold horizontal line on the graph. The discrete line on the figure indicate the largest shock time. It can be seen that the region earthquake is accumulating energy of the order of 10^{15} J.

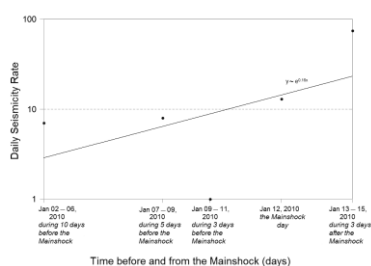


FIGURE 2. The daily seismic rate.

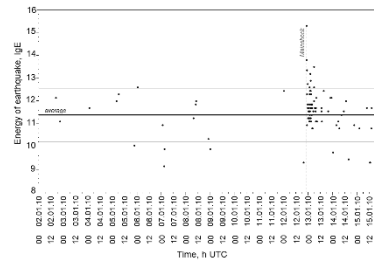


FIGURE 3. The temporal dependence of the energy logarithm.

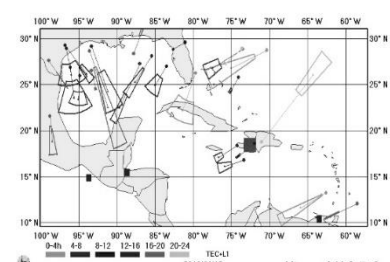


FIGURE 4. The subionospheric points January 12, 2010.

On the earthquake day the analysis made it possible to identify several structures associated with the epicenter-Fig. 4. The figure shows the subionospheric points locations and the segments indicate the estimates of velocity, and azimuth deviation for each structure.

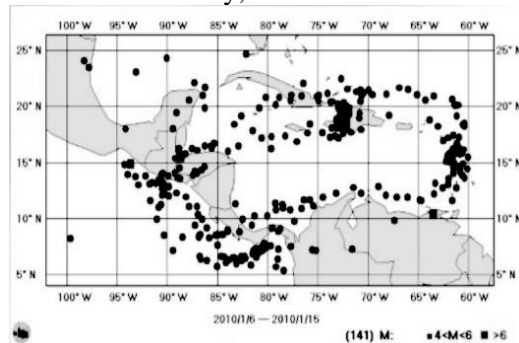


FIGURE 5. The monitoring period 10 days in Caribbean Plate.

The geophysical analysis obtained results interpretation is presented in Fig. 5. for the earthquake in Haiti. Basically subionospheric points are distributed at the event epicenter, as well as, according to the boundaries of active continental and oceanic transform faults, subduction zone. It should be noted that the methodical accuracy of subionospheric points localization is 50-100 km [12].

Conclusions. Intensive changes the parameters ionosphere occur over seismically active regions, relative to the indicators of their regular variability (quiet-time ionosphere), not only during the main

shock, but the earthquakes preparation, as well as after their active phase.

It has been established that the irregularities structures ionosphere detected by the GPS-interferometry method on the selected observational network are geographically related to the orographic disturbances location. The source of inhomogeneous structures is the entire region of earthquake preparation for example an faults.

Acknowledgments to the Russian Science Foundation under grant 18-12-00441 for partially supported this work.

1. M. A. Titova, V. I. Zakharov, S. A. Pulinets Detection of ionospheric disturbances above the Haiti region on January 1–15, 2010, according to GPS data obtained in quiet geomagnetic conditions, *Geomagnetism and Aeronomy*, 2019, 59(6), pp. 791–800.
2. A. A. Namgaladze, O. V. Zolotov, B. E. Prokhorov, Numerical simulation of the variations in the total electron content of the ionosphere observed before the Haiti earthquake of January 12, 2010, *Geomagnetism and Aeronomy*, 2013, 53(4), pp. 522–528.
3. S. A. Pulinets, K. G. Tsybulya, Unique variations of the total electron content in the preparation period of Haitian earthquake (M7.9) on January 12, 2010, *Geomagnetism and Aeronomy*, 2013, 50(5), pp. 686–689.
4. M. Akhoondzadeh, M. R. Saradjian, TEC variations analysis concerning Haiti (January 12, 2010) and Samoa (September 29, 2009) earthquakes // *Adv. Space Res.*, 2011, 47(1), pp. 94–104.
5. V. I. Zakharov, V. E. Kunitsyn, M. A. Titova, Opportunities and some the ionosphere regional monitoring results by GPS-interferometry, Proceedings of 23rd Russian Open Conference Radio Waves Propagation, Mari State University. Yoshkar-Ola, Russian Federation, vol. 1, pp. 204–207, 2011. (in Russian).
6. V. I. Zakharov, V. E. Kunitsyn, M. A. Titova, Possibilities and some results of the ionosphere regional monitoring by GPS-radio interferometry, Published in: 2011 30th URSI General Assembly and Scientific Symposium, doi: 10.1109/URSIGASS.2011.6050959
7. B. Hofmann-Wellenhof, H. Lichtenegger, J. Collins, GPS Theory and practice, New York: Springer-Verlag Vienna, 1998, pp.389
8. X. Pi, A. J. Mannucci, U. J. Lindqwister, C. M. Ho, Monitoring of global ionospheric irregularities using the worldwide GPS network, *Geophys. Res. Lett.* 1997, 24(18), pp. 2283–2286.
9. V. E. Kunitsyn, E. D. Tereshchenko, E. S. Andreeva, Ionospheric Radio Tomography, Moscow: Nauka, Russian Federation, 2007, pp. 335. (in Russian).
10. V. I. Zakharov, A. S. Zienko, V. E. Kunitsyn, The propagation of GPS radio signals for the different solar activity, *Electromagnetic waves and electronic systems*, 2008, 13(8) pp. 51–57. (in Russian).
11. C. Mercier, Observations of atmospheric gravity waves by radiointerferometry, *J. Atmos. Terr. Phys.*, 1986, 48(7), pp. 605–624.
12. E. L. Afraimovich, N. P. Perevalova, GPS–monitoring of the Earth high atmosphere. Institute of Solar–Terrestrial Physics, Siberian Division Russian Academy of Sciences, 2006. pp. 480. (in Russian).

RANDOMNESS AND DETERMINISM IN EARTHQUAKE PREDICTION

Sergey A. Pulinets

Space Research Institute of RAS, Moscow, Russia

Earthquake preparation processes, as catastrophic phenomena, do not fit into a linear causal chain. Catastrophic phenomena are essentially non-linear, and their behavior is described by non-linear equations [1]. Moreover, the set of solutions of the nonlinear equation corresponds to the set of evolution paths of the system [2]. The openness of the system adds complexity to the situation due to additional external sources and sinks of energy, trigger processes that accelerate or slow down the development of catastrophic phenomena [2]. That is why, in solving the problem of short-term earthquake prediction, we observe a confrontation between two antagonistic positions: on the one hand, it is argued that a short-

term earthquake forecast is impossible in principle [3], on the other hand, an approach based on monitoring of precursors is poured into pure determinism [4]. As recent studies show, both of these positions can be challenged, and their reasonable symbiosis can lead to a solution to the problem. This report is just a demonstration of how to resolve this long-standing contradiction, or at least indicate ways to eliminate or mitigate it using various examples of multi-parameter monitoring of recent destructive earthquakes.

The objective of this study is to try to demonstrate, using concrete examples of the development of processes at the final stage of strong earthquakes preparation, the implementation of the theory of nonequilibrium processes in open dissipative media: how geophysical parameters behave, for example, in terms of limiting the phase space of a strange attractor, the formation of regimes with escalation which synchronizes the pace of evolution of subsystems, the presence of autocatalytic processes, etc.

Recently, much attention has been paid to trigger processes. We are trying to show how to combine triggers with precursors, which seems like a logical paradox.

All recent results give hope for the formation of a new approach, the result of which will be a symbiosis of probabilistic theories and a real deterministic forecast.

This work is financially supported by the Ministry of Science and Higher Education of the Russian Federation in accordance with subsidy Agreement signed 10.22.2019 No. 075-11-2019-015. The unique identifier of the project is RFMEFI58519X0008.

1. V.V. Kuznetsov, Physics of terrestrial catastrophic phenomena, *Proceedings of the Institute of Geology and Geophysics SB RAS*, 1992, 809, ed. "Science", Siberian Branch, Novosibirsk, pp. 95.
2. S.P. Kurdyumov, E.N. Knyazeva, Features of nonequilibrium processes in open dissipative media, in the book. *Problems of Geophysics of the XXI Century*, Moscow, Nauka, 2003, pp. 37-65.
3. R.J. Geller, D.D. Jackson, Y.Y. Kagan, F. Mulargia, Earthquakes Cannot Be Predicted, *Science*, 1997, 275, pp. 1616–1618.
4. S.A. Pulinets, K.A. Boyarchuk, Ionospheric precursors of earthquakes, *Springer, Berlin, Heidelberg, New York*, 2004, 315 p.
5. P. Shebalin, Combining Probabilistic Seismicity Models with Precursory Information, in: *Pre-Earthquake Processes: A Multidisciplinary Approach to Earthquake Prediction Studies*, Editors(s): *Dimitar Ouzounov, Sergey Pulinets, Katsumi Hattori, Patrick Taylor*, Publisher: *AGU/Wiley*, 2018, pp. 77-98, doi: 10.1002/9781119156949.ch10.

IONOSPHERE EFFECTS DURING STRONG METEOROLOGICAL EVENTS IN KALININGRAD REGION IN 2010–2018

Mikhail I. Karpov^{1,2}, Ivan V. Karpov^{1,2}, Olga P. Borchevkina^{1,2}, Galina A. Yakimova¹, Nina A. Korenkova¹

¹*Pushkov Institute of Terrestrial Magnetism, Ionosphere, and Radio Wave Propagation, West Department, Russian Academy of Sciences, Kaliningrad, 236016 Russia*

²*Immanuel Kant Baltic Federal University, Kaliningrad, Russia*

Introduction. The passage of atmospheric fronts, the formation of cyclones and anticyclones, the formation of mesoscale turbulence, jet streams and other meteorological processes in the lower atmosphere are the sources of generation of acoustic-gravitational waves (AGWs) with periods close the Väisälä-Brent period. Propagating from the excitation region almost vertically, they can reach the heights of the thermosphere and ionosphere, and dissipation of such waves leads to the formation of local heating regions of the thermosphere, which affects the dynamics and ionization-recombination processes of the ionosphere [1–3]. Experimental studies of the state and dynamics of the ionosphere

over during extreme meteorological events, such as hurricanes and typhoons, demonstrate the formation of various kinds of effects, including trailing ionospheric disturbances, disturbances in the electric field, total electron content (TEC), occurrence of optical emissions, F-scattering phenomena, etc. [4–7]. In case of typhoons, TEC and $foF2$ disturbances reach up to 4–6 TECU and 1.5–2.0 MHz, respectively, which corresponds to 35–50% relative to median values [8]. Studies of less extreme events also show 15–30% deviations in $foF2$ [9–10]. Studies of less extreme events also show a change in critical frequencies. The purpose of this work is to identify, based on long-term observations, ionospheric variations during enhanced meteorological activity in Kaliningrad region in 2010–2018.

Methods. To describe the meteorological situation, we used three-hour measurements of the maximum wind gusts in Kaliningrad, as well as atmospheric pressure, reduced to average sea level, according to www.rp5.ru. The ionosphere response was studied by analyzing $foF2$ hourly measurements and TEC averaged over a 10-min interval. As an additional data source, we used the observations made at the meteorological station located in Olsztyn, Poland (53° N, 20° E), and the International GNSS Service in Lamkovko. For a comparative analysis, TEC observations at station HERS/HERT (50° N, 0° E) were used.

Only events with the maximum surface wind speed 17 m/s or more (score of 8 or more on the Beaufort scale) were selected. Event occurred during the moderate or high geomagnetic activity have been excluded. The criteria for calm geomagnetic conditions were $Kp\text{-index} \leq 3$ and $-20 \leq Dst\text{-index} \leq 20$ nT on the event day and on the previous day. Furthermore, only those events were analyzed, when $Dst\text{-index}$ did not change by more than 20 nT, and AU and AL indices didn't exceed 150 nT on peak days of meteorological activity.

Results. In total, six events with 1–3 days duration were selected for the final analysis according to the indicated criteria. The table summarizes the data for each event, including maximum gusts of wind ($ff3$, m/s) and mean atmospheric pressure (p , mmHg), as well as perturbations of TEC and $foF2$ expressed in standard deviation (σ) and in percent relative to moving median values with the window ± 13 days. For disturbances less than 1.5σ , a dash is indicated in the table.

TABLE. Average atmospheric pressure, maximum speed of wind gusts, deviations of TEC and $foF2$ in Kaliningrad, Olsztyn and UK during the considered meteorological events of 2010–2018.

Event	Kaliningrad/Olsztyn		ΔTEC KLG/LAMA		$\Delta foF2$ KLG		ΔTEC HERS/HERT	
	$ff3$, m/s	p , mmHg	σ	%	σ	%	σ	%
27.03.2010	17/14	748/750	-	-	1,8	-18	-	-
26.12.2011	16/16	766/768	1,9	-28	-	-	-	-
27.12.2011	17/17	767/769	2,1	-34	-	-	1,7	-17
06.12.2013	17/20	734/738	1,6	-28	no data		-	-
15.03.2014	19/22	746/747	2,0	-18	1,9	-13	1,9	-17
16.03.2014	16/14	746/747	1,6	-22	1,6	-18	1,6	-15
17.03.2014	20/25	748/750	1,8	-37	2,3	-28	-	-
29.10.2017	18/20	737/738	-	-	-	-	-	-
30.10.2017	18/20	751/754	2,0	64	-	-	-	-
23.10.2018	12/17	757/758	-	-	-1,6	-	1,8	16
24.10.2018	17/20	753/753	2,4	20	-	16	-	-

Figures 1 shows an examples of atmosphere and ionosphere parameters variations for events occurred in March 2014, which is notable for the highest amplitudes of gusts of wind speed, amounting to 19–20 m/s in Kaliningrad and 22–25 m/s in Olsztyn. In the noon hours of March 15, 2014, when atmospheric pressure dropped below 740 mmHg and wind gusts exceeded 20 m/s for about 7–8 h, decrease in TEC and $foF2$ reached 18 and 13% (2.0 and 1.9 standard deviations), respectively. In the

next two days of unstable meteorological conditions on March 16 and 17, negative perturbations of TEC and foF2 persisted and reached -37% and -28%, respectively.

Discussion. In all cases considered, ionospheric disturbances over the meteorological storm region were observed for at least 3 hours. In four out of six cases, the disturbances doubled the standard deviation and amounted to 18–64% for TEC and 13–28% for foF2. At UK stations located over 1000km to the west from Kaliningrad, TEC disturbances were either absent or were noticeably weaker and did not exceed 2σ and 17%.

Detected changes in the state of the ionosphere over Kaliningrad are due to the processes accompanying the development of meteorological storms. The enhancement of AGW generation processes under such meteorological conditions is, apparently, the most important factor determining the disturbance of the state of the ionosphere. The vertical propagation and dissipation of AGWs in the upper atmosphere leads to the formation of local perturbations of the temperature and density of the thermosphere, which in turn affects the ionization-recombination processes in the thermosphere.

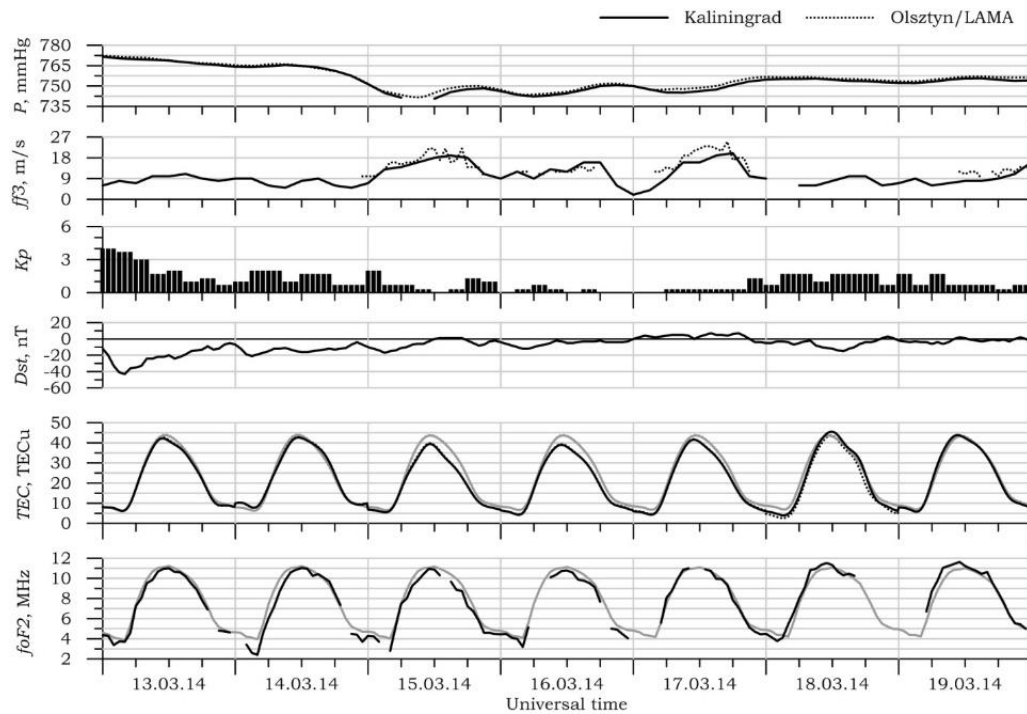


FIGURE 1. Atmospheric pressure (P , mmHg), maximum gusts of wind ($ff3$, m/s), Kp - and Dst -indices, as well as TEC and $foF2$ in Kaliningrad and Olsztyn from March 25 to 30, 2010. Gray lines indicate the median values of TEC and $foF2$.

In addition, as shown in [Snively and Pasko, 2003], meteorological sources excite relatively short-period AGWs, which can enhance turbulent processes at the heights of the lower thermosphere. An increase in turbulence at the heights of the lower thermosphere leads to significant changes in the gas composition of the thermosphere and, in particular, to a decrease in the concentration of atomic oxygen. The effect of these processes on the ionosphere is manifested in an increase in recombination processes and a decrease in the efficiency of ionization processes, which leads to negative effects in the dynamics of TEC and $foF2$. As follows from the observations, in most cases the reaction of the ionosphere to meteorological disturbances is manifested in a decrease in the daily values of TEC and $foF2$, which is consistent with the idea of the influence of AGW on the thermosphere. The reasons for the appearance of positive perturbations, apparently, are associated with more complex processes. In the observations

presented in [Karpov et al. 2019a, 2019b], it was shown that positive ionospheric effects occur at the boundary of the meteorological disturbance zone. It can be assumed that the causes of such ionospheric effects can be associated with plasma transfer processes from the region of large-scale thermospheric disturbances formed above the epicenter of a meteorological storm located north of Kaliningrad.

Conclusions. The results of the analysis of ionospheric disturbances initiated by meteorological storms in the Kaliningrad region for 2010–2018 are summarized as follows:

1. In all cases considered, the ionospheric disturbances observed over the meteorological storm region over a period of at least 3 hours.

2. In four of the six cases, the amplitude of the perturbation of the ionospheric parameters TEC and $foF2$ doubled the standard deviation from the median values, and in two cases ranged from 1.6 to 2.0 standard deviations.

3. The most frequently occurring ionospheric disturbances were manifested in a decrease in the daily values of TEC and $foF2$ and less frequently in an increase in these parameters.

4. Perturbations in TEC were more pronounced (18–64%) than disturbances in $foF2$ (13–28%).

This work was supported by the Russian Foundation for Basic Research and the government of the Kaliningrad region, project No. 19-45-393002.

1. D.C. Fritts, M.J. Alexander, Gravity wave dynamics and effects in the middle atmosphere, *Rev. Geoph.*, 2003, 41(1), pp. 1–68.

2. R. Plougonven, F. Zhang, Internal gravity waves from atmospheric jets and fronts, *Rev. Geoph.*, 2014, 52(1), pp. 33–76.

3. I. Karpov, S. Kshevetskii, Numerical study of heating the upper atmosphere by acoustic-gravity waves from a local source on the Earth's surface and influence of this heating on the wave propagation conditions, *J. Atmos. Sol.-Terr. Phys.*, 2017, 164, pp. 89–96. 2017.

4. C.R. Martinis, J.R. Manzano, The influence of active meteorological systems on the ionosphere F region, *Ann. Geofisica*, 1999, 42(1), pp. 1–7.

5. N.V. Isaev, V.M. Sorokin, V.M. Chmyrev, et al., Disturbance of the electric field in the ionosphere by sea storms and typhoons, *Cosmic Res.*, 2002, 40(6), pp. 547–553

6. A.S. Polyakova, N.P. Perevalova, Comparative analysis of TEC disturbances over tropical cyclone zones in the north-west pacific ocean, *Adv. Space Res.*, 2013, 52, pp. 1416–1426.

7. M. Chou, C. Lin, J. Yue, et al., Concentric traveling ionosphere disturbances triggered by Super Typhoon Meranti (2016), *Geoph. Res. Letters.*, 2017, 44(3), pp. 1219–1226.

8. W. Li W., Yue J., Wu S., et al. Ionospheric responses to typhoons in Australia during 2005–2014 using GNSS and FORMOSAT-3/COSMIC measurements // *GPS Solutions*. V. 22. N 61. 2018.

9. V.H. Depuev, A. H. Depueva, Reaction of the critical frequency of the F2 layer to a sharp depletion in atmospheric pressure, *Geomagnetism and Aeronomy*, 2010, (50), pp. 804–813.

10. I.V. Karpov, O.P. Borchevkina, M.I. Karpov, Local and Regional Ionospheric Disturbances During Meteorological Disturbances, *Geomagnetism and Aeronomy*, 2019, 59(4), pp. 458–466.

STATISTICS OF EARTHQUAKES IN RELATION TO SOLAR AND GEOMAGNETIC ACTIVITY

Tamara V. Gaivoronskaya, Alexander T. Karpachev

Institute of Terrestrial Magnetism, Ionosphere and Radio Wave Propagation (IZMIRAN) Troitsk, Moscow, Russia

Introduction. The paper presents the periodic variations of global number of earthquakes during the tree 11-year solar cycles (1976–2008) with the subdivision of earthquakes according to their magnitudes from $M=6.0$ to $M=8.0$ and more. The results have shown that the seismic activity follows

the solar activity and is late by far. By the geomagnetic data the probable dependence of seismic events on the level of magnetic disturbances is considered. It is constructed the statistical distributions of number of earthquakes in dependence on the index K_p of geomagnetic activity.

The periodic variations of annual number of large earthquakes have been compared with the solar and geomagnetic activity. During the century from 1910 to 2010 including 11-year cycles of solar activity with 15 on 23, the earthquakes with great magnitude $M \geq 7$ are considered earlier [1-3].

In present for three 11-year solar cycles the variations of global number of earthquakes have been considered in details, taking into account their stratification on magnitude. The catastrophic earthquakes with magnitude $M \geq 8$ are registered rarely, the number of earthquakes with $M \geq 7$ is not greater than 30-40, and earthquakes with magnitude $M \geq 6$ occur in a year 100-200 times. The Fig.1 shows the variations of annual number of earthquakes with $M \geq 6$ and $M \geq 7$ during a few solar cycles. Above the arrows indicate the years when the earthquakes with $M \geq 8$ have place. Here the flowing curve defines the long-term course of solar activity, derived by smoothing the sunspot number R on 11-year moving periods. The statistics of earthquakes with $M \geq 6$, on the whole corresponding to the planetary seismic situation, testifies that trends of seismic and solar activity are opposite. It is not so clearly for the 11-year seismic variations, but the long-term trends are well visible. While solar activity is declining, seismic one is growing.

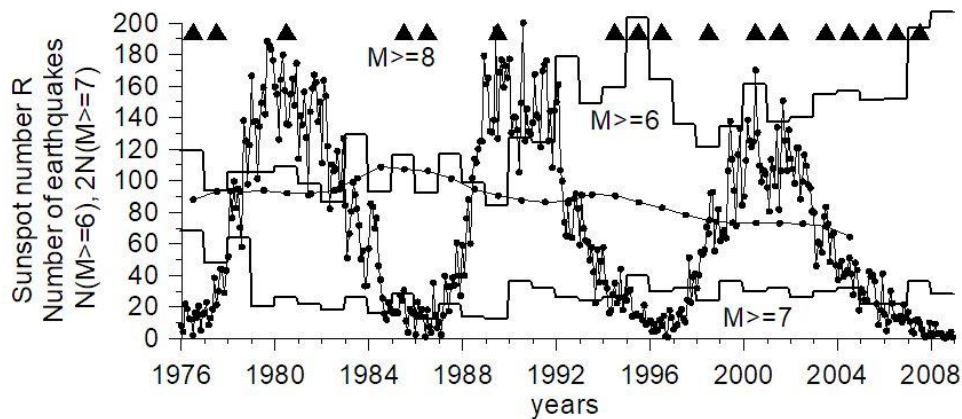


FIGURE 1. The variations of the global number of earthquakes with magnitudes $M \geq 6$, $M \geq 7$ and $M \geq 8$ for the last three 11-year solar cycle.

In addition to the long-term variations, the relationship day by day between the geomagnetic storms caused by solar activity and the large seismic events is considered. It has been constructed the statistical distributions of number of earthquakes with magnitude $M \geq 6$ in dependence on the geomagnetic disturbances.

The geomagnetic disturbance in any given day characterizes by a maximum value of index K_p ($K_p=0,1,\dots,9$) in the day. By the data for 1992, with the middle solar activity, it has been constructed the distributions of number of days in dependence on the geomagnetic disturbance, $N(K_p)$. Then, the number of days characterized by geomagnetic index K_p has been estimated in condition that the earthquakes with magnitude $M \geq 6$ have occurred those days. Both distributions $N(K_p)$ and $N(K_p/Eq)$ are shown in Fig.2.

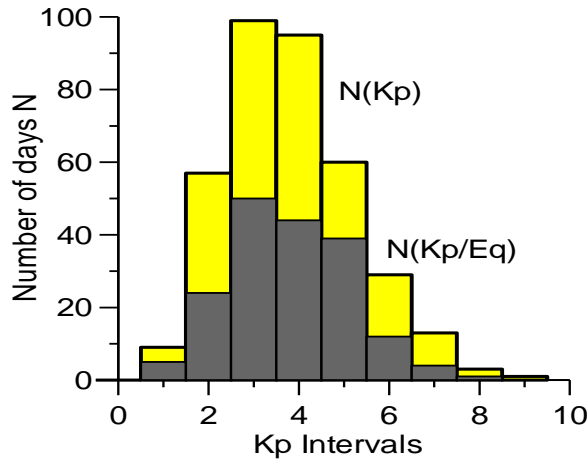


FIGURE 2. The distribution $N(Kp)$ of the number of days with the geomagnetic index Kp and the conditional distribution $N(Kp/eq)$ of the same days, accompanied by the earthquakes with $M \geq 6$.

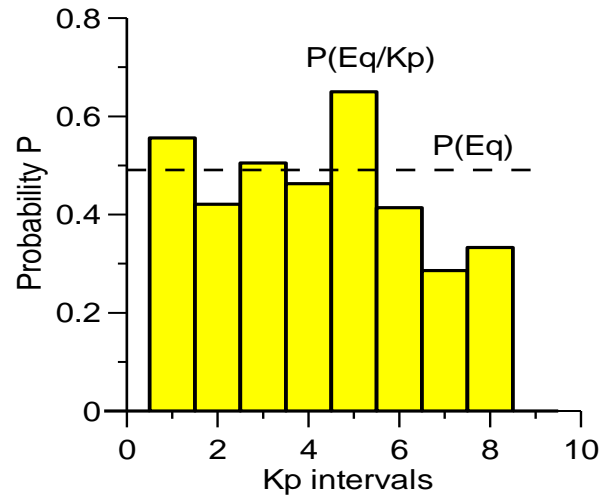


FIGURE 3. The conditional probability $P(eq/Kp)$ of the occurrence of earthquake with magnitude $M \geq 6$ when the current geomagnetic disturbance has the index Kp .

The probability $N(Kp \cap eq)$, when both events, the geomagnetic disturbance with certain index Kp and the earthquake with magnitude $M \geq 6$, happen in the same day, may be presented as follows:

$$N(Kp \cap eq) = P(Kp/eq)P(eq) = P(eq/Kp)P(Kp),$$

where the probability $P(Kp) = N(Kp)/N$ and the conditional probability $P(Kp/eq) = N(Kp/eq)/N$ is determined by distribution $N(Kp)$ and $N(Kp/eq)$ constructed above, N – number of days per year. The probability $P(eq)$ of realization of earthquake with magnitude $M \geq 6$ is calculated as the ratio of total number of earthquakes per year to the number of days N .

Now, the conditional probability $P(eq/Kp)$ that the earthquake with magnitude $M \geq 6$ will happen on the day of the geomagnetic disturbances with index Kp , can be found from the equation (1). The resulting distribution $P(eq/Kp)$ is shown in Fig.3. From the distribution one can see that the probability of coming of earthquake surpasses the mean statistical value $P(eq)$ by the geomagnetic disturbance $Kp=5$ and, in general, it is more in the days with small geomagnetic activity. In the time of strong geomagnetic storms with $Kp=6-8$ the probability of earthquakes is fallen. Therefore it is possible to suppose that the seismic events occur more often either on the falling of geomagnetic storms or in the quiet time. Thus, the conditional probability of occurrence of earthquakes in dependence on the geomagnetic situation observed day by day, is not contrary to the above mentioned long-term trends of solar and seismic activity.

1. T.V. Gaivoronskaya, A.T. Karpachev, Variations of seismic activity on the ground of solar cycles, *Conference "Astronomy-2018", Section: Solar-Earthly Physics*, October 22-26, 2018, MSU, Moscow.

2. T.V. Gaivoronskaya, A.T. Karpachev, Statistical characteristics of ionosphere variations in the time of seismic activity, *Proceedings of VI International Conference "Atmosphere, Ionosphere, Safety" (AIS-2018), Kaliningrad, Part 1*, pp.142-144

3. T.V. Gaivoronskaya, Periodic variations of seismic and geomagnetic activity, *International Symposium in memory of Prof. Galperin "Auroral Phenomena and Solar-Terrestrial Relations"*. February 4-7, 2007, Space Research Institute, Moscow, pp.96.

EFFECTS OF STORM EVENTS ON THE UPPER ATMOSPHERE ON THE BALTIC SEA

Olga P. Borchevkina^{1,2}, Yuliya A. Kurdyaveva¹, Mikhail I. Karpov^{1,2}, Boris V. Chubarenko³, Dmitry A. Domnin³, Nina A. Korenkova¹ and Ivan V. Karpov^{1,2}

¹Pushkov Institute of Terrestrial Magnetism, Ionosphere, and Radio Wave Propagation, West Department, Russian Academy of Sciences, Kaliningrad, 236017 Russia

²Immanuel Kant Baltic Federal University, Kaliningrad, 236041 Russia

³Institute of Oceanology RAS, Moscow, Russia

Introduction. The influence of processes in the lower atmosphere from meteorological sources on the state and dynamics of the upper atmosphere should not be underestimated. Thus, according to estimates the contribution of such sources is about 15–30% of all the factors of variability of the ionosphere in a quiet geomagnetic environment [1, 2]. Ionospheric disturbances occur quite quickly (a few hours after the beginning of the meteorological disturbance) which indicates the wave nature of the processes that implement the connections of phenomena in different layers of the atmosphere. The hypotheses about the mechanisms of the influence of processes in the lower atmosphere on the state of the ionosphere and upper atmosphere are based on the concept of generation of atmospheric gravity waves (AGW) in the lower atmosphere and their vertical propagation into the upper atmosphere [3, 4]. Such waves can transfer energy from the perturbation region in the lower atmosphere to the ionosphere altitudes and influence the local electron density through ion-neutral collisions, leading to ionospheric perturbations and TID [5].

Methods and results of observations. Three-hour measurements of the maximum values of wind gusts and atmospheric pressure were used to describe the meteorological situation. Hourly measurements of the critical frequency of the F2 layer of the ionosphere (f_oF2 , MHz) of the Kaliningrad branch IZMIRAN were used as data for analyzing the ionosphere response (54° N, 20° E), as well as averaged over a 10-minute interval measurements of the total electronic content (TEC) according to the GPS signal receiver. As an additional data source, measurements from the Olsztyn meteorological station (53° N, 20° E), Poland and International GNSS Service LAMA stations (53.7° N, 20.6° E) were used. To analyze the f_oF2 and TEC perturbations, deviations of these values were determined relative to the moving median centered on the day of the day in question, with a window of 13 days before and after the time point in question.

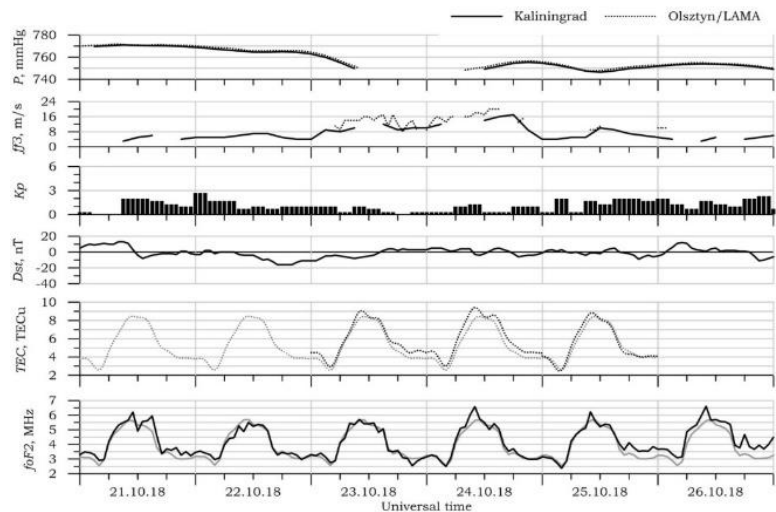


FIGURE 1. Diurnal variation in atmospheric pressure P , maximum wind gusts $ff3$, geomagnetic activity indices Kp and Dst in Kaliningrad and Olsztyn, as well as TEC in Olsztyn and f_oF2 in Kaliningrad on October 21-26, 2018. The gray lines indicate the median values of TEC and f_oF2 .

Figure 1 presents measurements of atmospheric pressure, maximum wind gusts, KP and Dst geomagnetic activity indices, as well as TEC and f_oF2 data in Kaliningrad and Olsztyn from 21 to 26 October 2018. The gray lines indicate the median values of TEC and f_oF2 . On the night of October 24, there was an increase in the electron concentration, and by 09: 00 UT, the increase in TEC reached 20% relative to the average values, which corresponded to 2.4 standard deviation σ . The increase in the critical frequency of the F2 layer was 19% or 1.6 σ .

Wavelet analysis methods were applied to the observation data of the full electronic content determined from the signals of the flying GPS satellites to determine the frequency characteristics of variations in the ionosphere parameters over the area of meteorological disturbance. The results of this analysis provide information about the energy distribution in the signal spectrum and information about the time of occurrence of certain frequency components.

Figure 2 presents TEC periodograms obtained from observations of PRN 9 and PRN 23 satellite signals over station VIS0 (57.5 N, 18.4 E) on October 21-26. The threshold value of the angle of the Sun's location for analyzing the response of the ionosphere to meteorological disturbances in the troposphere was determined to be 30°. The main attention was paid to the allocation of TEC variations with periods of 2-20 minutes in the observations. AGWs with such periods propagate almost vertically from the perturbation region in the troposphere. Days of meteorological disturbance in the troposphere were accompanied by amplification the TEC variation amplitudes with periods of 12-20 minutes on October 23. This increase may be due to an increase in AGWs activity spreading from the area of the weather storm.

Modeling. To assess the AGWs effect on the upper atmosphere excited in the troposphere during a meteorological storm, a simulation was performed using the numerical model “Atmosym” [6]. The method of conducting such a numerical experiment is presented in [7]. In a numerical experiment to study the disturbances in the upper atmosphere on the Baltic region from meteorological sources, two-minute data on temperature changes in the Baltic sea were used. The data were reduced to pressure variations and used as a lower boundary condition in model calculations.

Atmospheric pressure disturbances at the lower boundary in the model reproduced conditions in which pressure variations in the region with $x < 1000$ km were determined from data obtained above the water surface, and in the region with $x > 1000$ km from observations on land. The model source moves from the start of the left border of the calculated area to the middle (1000 km) and continues to work on this section for the rest of the time. Figure 3 shows the spatial distributions of temperature wave disturbances in the upper atmosphere from a source in the lower atmosphere. The results of calculations showed that such a source generates mainly infrasound waves with small amplitudes. Against the background of a sharp drop in pressure around 5 a.m. local time, there is a sharp increase in temperature, which can be associated with the AGWs arrival with a period ~ 15 min.

The wave additive (fig. 3) exceeds the values corresponding to calm meteorological conditions [7] by almost 2 times. Because the data used for pressure variations are obtained indirectly, the actual heating of the atmosphere can be significantly higher. The proposed physical mechanisms of disturbances in the upper atmosphere are described in detail in [8].

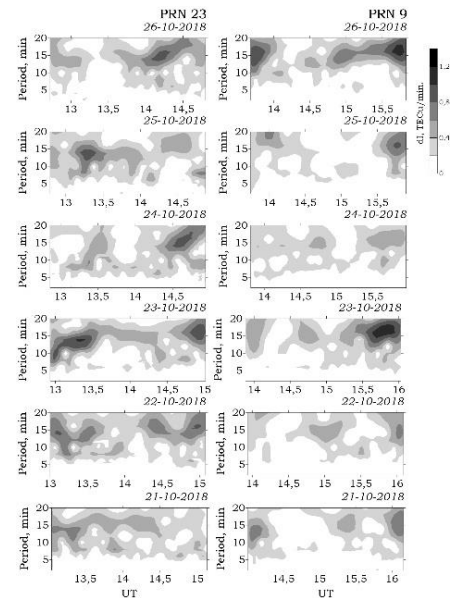


FIGURE 2. TEC variations spectra on October 21-26, 2018 at the VIS0 station (57.5° N, 18.4° E).

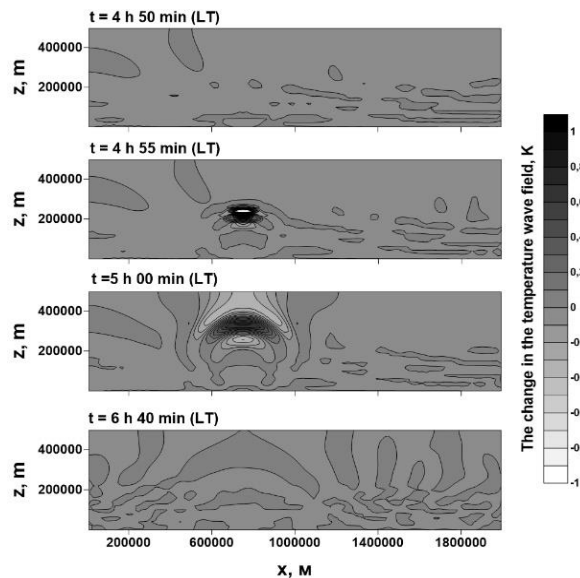


FIGURE 3. Wave perturbations in temperature in the upper atmosphere from a AGWs ground source.

Conclusions. The analysis from observations in atmospheric and ionospheric parameters during the development of a meteorological storm on the Baltic sea on October 2018 shows that rapid changes in wind velocity and ground pressure lead to an increase in the TEC to 2.4 standard deviations and the critical frequency F2 layer to 1.6 standard deviations directly above the area of meteorological disturbances. The processes AGWs generation in the lower atmosphere is increased in the conditions of meteorological storms. The AGWs propagation into the upper atmosphere leads to the formation of perturbations in the thermosphere state on spatial scales determined by the duration and spatial dimensions of the region located in the meteorological perturbation area. The appearance of such regions affects the circulation and electrodynamic processes in the thermosphere and ionosphere. The model study

confirms the supposed physical mechanisms the influence of meteorological storms on the upper atmosphere and ionosphere.

This work was supported by the Russian Foundation for Basic Research and the government of the Kaliningrad region, project No. 19-45-390005 (O.P. Borchevkina, M.I. Karpov) and RFBN grant No. 18-05-00184a (I.V. Karpov).

We express gratitude to the Copernicus Atmosphere Monitoring Service for the meteorology data; the International GNSS Service for access to GNSS data used in this study, as well as the OMNIWeb Plus NASA/Goddard Space Flight Center service for the data on geomagnetic and solar flux indices.

1. C.R. Martinis, J.R. Manzano, The influence of active meteorological systems on the ionosphere F region, *Ann. Geofisica*, 1999, 42(1), pp. 1–7.
2. J. M. Forbes, S. E. Palo, X. Zhang, Variability of the ionosphere, *Journal of Atmospheric and Solar-Terrestrial Physics*, 2000, 62(8) pp. 685-693, DOI: 10.1016/S1364-6826(00)00029-8.
3. O.P. Borchevkina, I.V. Karpov, Ionospheric irregularities in periods of meteorological disturbances, *Geomagnetism and Aeronomy*, 2017, 57(5), pp. 624-629.
4. I. Azeem, M. Barlage, Atmosphere-ionosphere coupling from convectively generated gravity waves, *Adv. Space Res.*, 2018, 61(7), pp. 1931-1941.
5. K. Hocke, K. Schlegel, A review of atmospheric gravity waves and travelling ionospheric disturbances: 1982-1995, *Annales Geophysicae*, 1996, 14, pp. 917-940.
6. N.M. Gavrilov, S.P. Kshevetskii, Numerical modeling of propagation of breaking nonlinear acoustic-gravity waves from the lower to the upper atmosphere, *Advances in Space Research (includes Cospar Information Bulletin)*, 2013, 51(7), pp. 1168-1174.
7. Y. Kurdyeva, S. Kulichkov, S. Kshevetskii, O. Borchevkina, E. Golikova, Propagation to the upper atmosphere of acoustic-gravity waves from atmospheric fronts in the Moscow region, *Ann. Geophys.*, 2019, 37, pp. 447–454.
8. I.V. Karpov, O.P. Borchevkina, M.I. Karpov, Local and Regional Ionospheric Disturbances During Meteorological Disturbances, *Geomagnetism and Aeronomy*, 2019, 59(4), pp. 458-466.

ELEMENTARY PROCESSES IN THE UPPER ATMOSPHERE AND IONOSPHERE

AB INITIO CALCULATIONS OF THE $1\Sigma_g^+$ AND $1\Sigma_u^+$ STATES OF Na_2

Sergey O. Adamson¹, Daria D. Kharlampidi², Gennady V. Golubkov^{1,3}, Yury A. Dyakov¹, Maxim G. Golubkov¹

¹Semenov Federal Research Center for Chemical Physics, Russian Academy of Sciences, Moscow, Russian Federation

²Moscow State Pedagogical University, Institute of Biology and Chemistry, Department of General Chemistry, Moscow, Russian Federation

³National Research Center "Kurchatov Institute", Moscow, Russian Federation

Introduction. The main role in the radio waves propagation at 60-110 km altitudes from the Earth is assigned to the processes passing through the formation of intermediate highly excited (Rydberg) states of diatomic molecules [1-6]. To elaborate a correct theoretical approaches for the description of these processes it is advisable to consider a contributions from the long-range Rydberg states localized in the range of internuclear distances larger than $5R_e$, where R_e is the equilibrium internuclear distance of the ground electronic state [7].

At first it seems that the Na_2 molecule is suitable object for the test study, because its spectra have been investigated experimentally and theoretically over a century [7-10]. The achievements include an *ab initio* calculations of more than eighty adiabatic electronic states of the Na_2 in the range of internuclear distances $\sim 2.6 - 21.2 \text{ \AA}$ with a high accuracy [11,12,13,14]. Unfortunately, this range is insufficient to calculate the properties of the rovibrational states lying higher than the $5^1\Sigma_g^+$ state dissociation limit. Thus, the goal of our study is to build the adiabatic potential energy curves of the $1\Sigma_g^+$ and $1\Sigma_u^+$ states in a larger range of internuclear distances than presented in work [12].

Method of the calculations. The calculations were performed with the Na pseudopotential [15], supplemented by (7s6p5d4f)/[7s6p5d4f] atomic orbital (AO) basis set (Table 1). The core-valence electron correlation was taken into account using the core polarization potential (CPP) with $\alpha_s = 0.9947$, $\rho_s = 0.9605 \text{ a.u.}$ [16,17]. The AO set optimization was started from the total energy minimization using the four s-type Gaussian functions, and then the exponents of the remaining functions were optimized in order to better reproduce the energies of the excited 3p - 4f atomic states. For the optimized AO set the maximum difference from the experimental sodium excitation energies [18] is about 11 cm^{-1} for the $^2D(4d)$ state. As in previous works [11,12,14,19], the two-electron wave function of the Na_2 molecule was constructed in full configuration interaction approach (FCI). All calculations were performed using the MOLPRO program package [20].

TABLE 1. AO basis set for Sodium.

AO	Exponent
<i>s</i>	2.662241, 0.853282, 0.273488, 0.087656, 0.028095, 0.009492, 0.002746
<i>p</i>	1.048871, 0.325736, 0.106338, 0.031416, 0.006500, 0.002500
<i>d</i>	0.314937, 0.065639, 0.022201, 0.009123, 0.003435
<i>f</i>	0.053883, 0.016108, 0.005857, 0.002130

Results and discussion. The combination of CPP potential with the new [7s6p5d4f] sodium AO basis set allows to construct adiabatic potential curves of $1\Sigma_g^+$ and $1\Sigma_u^+$ states in the range of internuclear

distances of 1.7 - 50 Å. (Figure 1). The lowering of the left interval boundary from 2.6 Å to 1.7 Å made it possible for the repulsive branches of the potential curves to reach the energies exceeding the (3s + 5p) dissociation limit energy. The right boundary position of 50 Å was sufficient to detect the avoided-crossing of (10-11) $^1\Sigma_g^+$ states.

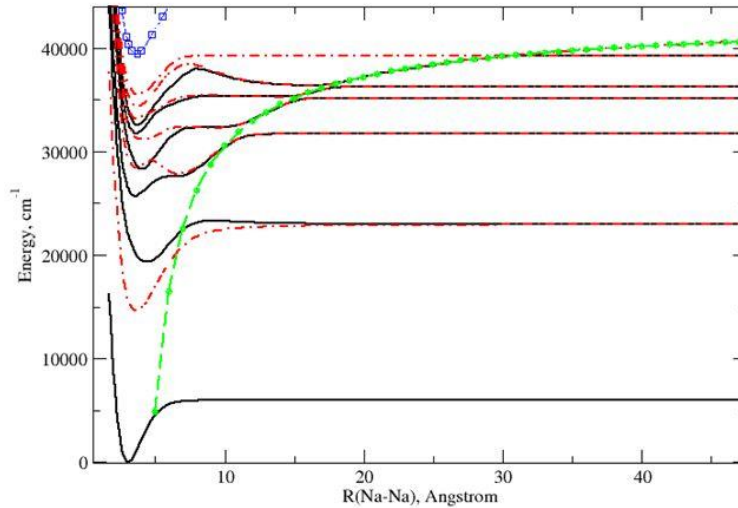


FIGURE 1. Adiabatic electronic (1-6) $^1\Sigma_g^+$ (solid lines) and (1-6) $^1\Sigma_u^+$ (dash-dotted lines) states of Na_2 . The dashed lines denote the ground state of the Na_2 ion ($^\circ$) and the empirical diabatic ionic curve (\bullet). The reference point of the energy scale is the position of the minimum energy of the ground electronic state (cm^{-1}).

It is found that the obtained values of the electronic terms (T_e) and dissociation energies of (D_e) (1-6) $^1\Sigma_g^+$ and (1-2) $^1\Sigma_u^+$ states are in a better agreement with the experimental ones than the results of the previous calculations [12] (Table 2,3). The calculated values of the equilibrium internuclear distances (R_e) turn out to be less than experimental ones by ~ 0.01 Å. An error in the calculated R_e values is most likely a consequence of the adiabatic approach use, which does not take into account non-adiabatic and relativistic effects. Only the experimental term T_e is known for the $3^1\Sigma_u^+$ state, which is in satisfactory agreement with the calculated one (Table 2,3).

TABLE 2. Molecular constants of the electronic (1-6) $^1\Sigma_g^+$ states. Equilibrium internuclear distances R_e are presented in Å, electronic terms T_e and dissociation energies D_e — in cm^{-1} .

	State						Source
	$1^1\Sigma_g^+$	$2^1\Sigma_g^+$	$3^1\Sigma_g^+$	$4^1\Sigma_g^+$	$5^1\Sigma_g^+$	$6^1\Sigma_g^+$	
Limit	3s+3s	3s+3p	3s+4s	3s+3d	3s+4p	3s+5s	
R_e	3.080 ^a	4.450 ^b	3.569 ^c	4.074 ^d	3.638 ^e	3.735 ^f	
	3.085	4.445	3.556	4.069	3.625	3.710	[12] ^g
	3.069	4.446	3.551	4.061	3.626	3.698	PW ^h
T_e	0 ^a	19338 ^b	25692 ^c	28327 ^d	31770 ^e	32563 ^f	
	0	19349	25615	28240	31700	32460	[12] ^g
	0	19325	25662	28277	31737	32506	PW ^h
D_e	6022 ^a	3658 ^b	6070 ^c	6868 ^d	4525 ^e	6660 ^f	
	5892	3509	6035	6825	4464	6643	[12] ^g
	5987	3623	6075	6883	4522	6691	PW ^h

a) experiment, ref. [21]; b) experiment, ref. [22]; c) experiment, ref. [23,24]; d) experiment, ref. [25]; e) experiment, ref. [26]; f) experiment, ref. [27,28]; g) theory, method A, ref.[12]; PW – theory, present work.

TABLE 3. Molecular constants of the electronic (1-6) $^1\Sigma_u^+$ states. Equilibrium internuclear distances R_e are presented in Å, electronic terms T_e and dissociation energies D_e — in cm^{-1} .

	State							Source
	$1^1\Sigma_u^+$	$2^1\Sigma_u^{+a}$	$2^1\Sigma_u^{+b}$	$3^1\Sigma_u^+$	$4^1\Sigma_u^+$	$5^1\Sigma_u^{+a}$	$6^1\Sigma_u^+$	
limit	3s+3p	3s+4s	3s+4s	3s+3d	3s+4p	3s+5s	3s+4d	
R_e	3.635 ^c	3.660 ^d	6.736 ^d					
	3.630	3.651	6.742	4.001	3.646	3.752	3.662	[12] ^f
	3.624	3.643	6.724	3.973	3.635	3.713	3.717	PW ^g
T_e	14680 ^c	28454 ^d	27839 ^d	31248 ^e				
	14575	28345	27790	31118	33059	34351	35448	[12] ^f
	14588	28383	27836	31178	33105	34341	35511	PW ^g
D_e	8310 ^c	3308 ^d	3923 ^d	3947 ^e				
	8284	3305	3861	3947	3105	4752	5005	[12] ^f
	8351	3353	3901	3981	3155	4857	4726	PW ^g

a) inner well; b) outer well; c) experiment, ref. [29]; d) experiment, ref.[30]; e) experiment, ref. [31]; f) theory, method A, ref. [12]; g) PW – theory, present work.

At large internuclear distances, an *ab initio* or Rydberg – Klein – Rees (RKR) potentials can be extended by long-range (asymptotic) potentials, which form depends on the nature of the dissociating system. As it was shown for (3-5) $^1\Sigma_g^+$ states of Na_2 the left boundary of the asymptotic region can be estimated using the modified Le Roy radius ($R_{\text{LR-m}}$) [7,32]. Comparing the $R_{\text{LR-m}}$ with the avoided-crossing positions you can to see that the $R_{\text{LR-m}}$ radius lowers the asymptotic boundary (Figure 1) for the (5-6) $^1\Sigma_g^+$ states.

Conclusion. The calculations using a new basis of valence atomic orbitals made it possible to refine the properties of the adiabatic electronic (1-6) $^1\Sigma_g^+$ and (1-6) $^1\Sigma_u^+$ states in a wide range of internuclear distances, including an avoided-crossings.

These results can be used to calculate the cross section of the quenching process in the collision of Rydberg sodium atoms. In the future, the similar calculations must be carried out for systems containing nitrogen and oxygen atoms. It should be remembered that the cross sections and rate constants of the main processes that determine the parameters of a nonequilibrium atmospheric plasma strongly depend on the density of the neutral species [33-35].

Acknowledgments. This work was carried out in the framework of State Assignment of the Ministry of Science and Higher Education of the Russian Federation (project AAAA–A19–119010990034–5).

1. G. V. Golubkov, M. G. Golubkov, I. V. Karpov, Microwave Radiation of the atmosphere Induced by a Pulsed Gamma Source, *Russ. J. Phys. Chem. B.*, 2011, 5(3), pp. 412, doi:10.1134/S1990793111030067.

2. G. V. Golubkov, M. G. Golubkov, M. I. Manzhelii, Microwave and IR Radiation of the Upper Atmosphere during Periods of Enhanced Solar Activity, *Dokl. Phys.*, 2012, 57(2), pp. 461, doi: 10.1134/S102833581212004X.

3. G. V. Golubkov, M. G. Golubkov, M. I. Manzhelii, Additional Background Radiation of the Atmosphere D Layer within the Frequency Range from 0.8 to 6.0 GHz, *Dokl. Phys.*, 2013, 58(10), pp. 424, doi: 10.1134/S1028335813100066.

4. M. G. Golubkov, G. K. Ozerov, S. O. Adamson et al., Reaction of associative ionization $\text{N} + \text{O} \rightarrow \text{NO}^+ + \text{e}^-$ at slow collisions of atoms, *Chem. Phys.*, 2015, 462, pp. 28, doi: 10.1016/j.chemphys.2015.07.037.

5. G.V. Golubkov, M. I. Manzhelii, A. A. Berlin et al., Fundamentals of radio-chemical physics of the Earth's atmosphere, *Russ. J. Phys. Chem. B.*, 2016, 10(1), pp. 77, doi:10.1134/S1990793116010024.
6. V. V. Kuverova, S. O. Adamson, A. A. Berlin et al., Chemical physics of D and E layers of the ionosphere, *Adv. Space Res.*, 2019, 64(10), pp. 1876, doi: 10.1016/j.asr.2019.05.041.
7. W. C. Stwalley, Up and away in the potential landscape of diatomic molecule potential energy curves, *J. Mol. Spectr.*, 2016, 330, pp. 14, doi:1016/j.jms.2016.10.009.
8. K. K. Verma, J. T. Bahns, A. R. Rajaei-Rizi et al., First observation of bound–continuum transitions in the laser-induced $A^1\Sigma_u^+ - X^1\Sigma_g^+$ fluorescence of Na_2 , *J. Chem. Phys.*, 1983, 78(6), pp. 3599, doi:10.1063/1.445188.
9. K. M. Jones, E. Tiesinga, P. D. Lett, P. S. Julienne, Ultracold photoassociation spectroscopy: Long-range molecules and atomic scattering, *Rev. Mod. Phys.*, 2006, 78(2), pp. 483, doi:10.1103/RevModPhys.78.483.
10. N. Jayasundara, R.B. Anunciado, E. Burgess et al., Ro-vibrational level dependence of the radiative lifetime of the Na_2 $4^1\Sigma_g^+$ shelf state, *J. Chem. Phys.*, 2019, 150(6), pp. 064301, doi:10.1063/1.5053107.
11. G. H. Jeung, Excited states of Na_2 dissociating into $3d+3s$, $4p+3s$, and $5s+3s$, *Phys. Rev. A*, 1987, 35(1), pp. 26, doi:10.1103/PhysRevA.35.26.
12. S. Magnier, Ph. Millié, O. Dulieu, F. Masnou-Seeuws, Potential curves for the ground and excited states of the Na_2 molecule up to the $(3s+5p)$ dissociation limit: Results of two different effective potential calculations, *J. Chem. Phys.*, 1993, 98(9), pp. 7113, doi:10.1063/1.464755.
13. S. Magnier, M. Aubert-Frkon, O. Bouty et al., Structures in the long range potential curves of the Na_2 molecule: comparison between ab initio and asymptotic calculations, *J. Phys. B: At. Mol. Opt. Phys.*, 1994, 27(9), pp. 1723, doi:10.1088/0953-4075/27/9/012.
14. A. Sanli, B. Beser, J.R. Edwardson et al., Electronic transition dipole moment and radiative lifetime calculations of sodium dimer ion-pair states, *J. Chem. Phys.*, 2015, 143(10), pp. 104304, doi:10.1063/1.4929925.
15. D. Maynaud, J. P. Daudey, Alkali Dimers Ground-State Calculations Using Pseudopotentials, *Chem. Phys. Lett.*, 1981, 81(2), pp. 273, doi:10.1016/0009-2614(81)80251-5.
16. W. Müller, J. Flesch, W. Meyer, Treatment of intershell correlation effects in ab initio calculations by use of core polarization potentials. Method and application to alkali and alkaline earth atoms, *J. Chem. Phys.*, 1984, 80(7), pp. 3297, doi:10.1063/1.447083.
17. W. Müller, W. Meyer, Ground-state properties of alkali dimers and their cations (including the elements Li, Na, and K) from ab initio calculations with effective core polarization potentials, *J. Chem. Phys.*, 1984, 80(7), pp. 3311, doi:10.1063/1.447084.
18. J. E. Sansonetti, Wavelengths, Transition Probabilities, and Energy Levels for the Spectra of Sodium (Na I – Na XI), *J. Phys. Chem. Ref. Data*, 2008, V37(4), pp. 1659, doi:10.1063/1.2943652.
19. A. Sanli, X. Pan, S. Magnier et al., Measurement of the Na_2 $5^1\Sigma_g^+ \rightarrow A^1\Sigma_u^+$ and $6^1\Sigma_g^+ \rightarrow A^1\Sigma_u^+$ transition dipole moments using optical-optical double resonance and Autler–Townes spectroscopy, *J. Chem. Phys.*, 2017, 147(20), pp. 204301, doi:10.1063/1.5002726.
20. Werner H.-J., Knowles P.J., Knizia G., Manby F.R., Schütz M., and others // MOLPRO, version 2010.1, a package of ab initio programs, <http://www.molpro.net>.
21. W. T. Zemke, W. C. Stwalley, Analysis of long range dispersion and exchange interactions between two Na atoms, *J. Chem. Phys.*, 1994, 100(4), pp. 2661, doi:10.1063/1.467249.
22. C. Effantin, J. d'Incan, A. J. Ross et al., Laser-induced fluorescence spectra of Na_2 : the $(3s, 3p)^1\Sigma_g^+$, $(3s, 3p)^1\Pi_g$ and $(3s, 4s)^1\Sigma_g^+$ states, *J. Phys. B*, 1984, V.17(8), pp. 1515–1523, doi:10.1088/0022-3700/17/8/013.
23. Chin-Chun Tsai, Thou-Jen Whang, J. T. Bahns, W. C. Stwalley, The $3^1\Sigma_g^+$ “shelf” state of Na_2 , *J. Chem. Phys.*, 1993, 99(11), pp. 8480, doi:10.1063/1.465624.
24. Chin-Chun Tsai, J. T. Bahns, He Wang et al., Optical–optical double resonance spectroscopy of the $4^1\Sigma_g^+$ “shelf” state of Na_2 using an ultrasensitive ionization detector, *J. Chem. Phys.*, 1994, 101(1), pp. 25, doi:10.1063/1.468178.
25. H. Wang, T.-J. Whang, A. Lyyra et al., Study of the $4^1\Sigma_g^+$ “shelf” state of Na_2 by optical–optical double resonance spectroscopy, *J. Chem. Phys.*, 1991, V.94(7), pp. 4756, doi:10.1063/1.460560.
26. Chin-Chun Tsai, J. T. Bahns, W. C. Stwalley, Optical–optical double resonance spectroscopy of the $4^1\Sigma_g^+$ “shelf” state of Na_2 using an ultrasensitive ionization detector, *J. Chem. Phys.*, 1994, 100(2), pp. 768, doi:10.1063/1.466559.
27. T. Laue, P. Pellegrini, O. Dulieu et al., Observation of the long-range potential well of the $(6)^1\Sigma_g^+ (3s+5s)$ state of Na_2 , *Eur. Phys. J. D*, 2003, 26(2), pp. 173, doi: 10.1140/epjd/e2003-00221-7.

28. Chin-Chun Tsai, J. T. Bahns, W. C. Stwalley, Optical-optical double resonance spectroscopy of the $6^1\Sigma_g^+$ “shelf” state of Na_2 using an ultrasensitive ionization detector, *J. Mol. Spectr.*, 1994, V.167(2), pp. 429, doi:10.1006/jmsp.1994.1247.
29. P. Qi, J. Bai, E. Ahmed et al., New spectroscopic data, spin-orbit functions, and global analysis of data on the $A^1\Sigma_u^+$ and $b^3\Pi_u$ states of Na_2 , *J. Chem. Phys.*, 2007, 127, pp. 044301, doi:10.1063/1.2747595.
30. A. Pashov, W. Jastrzebski, W. Jasniecki et al., Accurate Potential Curve for the Double Minimum $2^1\Sigma_u^+$ State of Na_2 , *J. Mol. Spectr.*, 2000, 203(2), pp. 264, doi:10.1006/jmsp.2000.8181.
31. G.-Y. Yan, A. L. Schawlow, Experimental observation of the $(3)^1\Sigma_u^+$ state of Na_2 by deperturbation of the $C^1\Pi_u-X^1\Sigma_g^+$ system, *J. Opt. Soc. Am. B*, 1989, 6(12), pp. 2309, doi:10.1364/JOSAB.6.002309.
32. Bing Ji, Chin-Chun Tsai, W. C. Stwalley, Proposed modification of the criterion for the region of validity of the inverse-power expansion in diatomic long-range potentials, *Chem. Phys. Lett.*, 1995, 236(3), pp. 242, doi:10.1016/0009-2614(95)00216-Q.
33. G. V. Golubkov, G. K. Ivanov, E. M. Balashov et al., l-mixing and dissociation of Rydberg molecules accompanying slow collisions with inert-gas atoms, *J. Exp. Theor. Phys.*, 1998, 87(1), pp. 56, doi:10.1134/1.558644.
34. G. V. Golubkov, G. K. Ivanov, M. G. Golubkov, Perturbation of the states of Rydberg atom A^{**} by neutral particles at intermediate distances, *Khim. Fiz.*, 2005, 24(6), pp. 3. (in Russian).
35. G. V. Golubkov, G. K. Ivanov, M. G. Golubkov, Highly excited electronic states of nanoscaled systems, *Khim. Fiz.*, 2005, 24(9), pp. 3. (in Russian).

TO ATOMIC OXYGEN CONCENTRATION IN THE E REGION OF THE IONOSPHERE

Vladimir L. Bychkov¹, Timur A. Maslov¹, Olga P. Borchevskina^{2,3}, Sergey O. Adamson⁴, Gennady V. Golubkov^{4,5}, Yuri A. Dyakov⁴, Maxim G. Golubkov⁴

¹M.V. Lomonosov Moscow State University, Moscow, Russia

²Pushkov Institute of Terrestrial Magnetism, Ionosphere, and Radio Wave Propagation, West Department, Russian Academy of Sciences, Kaliningrad, Russia

³Immanuel Kant Baltic Federal University, Kaliningrad, Russia

⁴N.N. Semenov Federal Research Center for Chemical physics, Russian Academy of Sciences, Moscow, Russia

⁵National Research Center Kurchatov Institute, Moscow, Russia

Introduction. Information on the characteristics of atmospheric plasma at various altitudes and possible conditions for its formation is of great importance for the preparation of flight tests using gas-discharge devices, for improving the operation of satellite positioning devices. In this work, we determined the concentration of oxygen atoms of the background plasma at an altitude of 95–105 km, the appearance of which is caused by photo dissociation processes at these altitudes, the main processes that lead to the production of oxygen atoms and their death in the processes of three-particle atom recombination are identified. Their concentrations have been calculated, allowing a comparison with the results of existing experiments and find out the reliability of theoretical calculations of the contributions of spectral intervals to the photodissociation rate at these heights presented in the well-known monograph [1].

Calculation of the altitude concentration of Oxygen atoms. A small contribution to photodissociation at an altitude of 90 km is made by the region of the Schuman – Runge bands (1925–1760 Angstroms). At an altitude of 100 km, short-wave radiation (1020 Angstroms) can also influence dissociation. This can explain the fact that the calculated concentration of atomic oxygen is 2–4 times higher than the measured P151H [1]. The Lyman - α line plays a secondary role in this area of the ionosphere.

Knowing the coefficients (rate constants) of photodissociation presented in [1], it is possible to determine the altitude concentrations of oxygen atoms, which are of interest from the point of view of ionosphere chemistry.

To take into account the death of oxygen atoms, we choose the main recombination channels of these atoms at heights of 90-105 km using the well-known work [4], namely, the reaction of recombination of oxygen atoms into a molecule (with the participation of an oxygen molecule) $O + O + O_2 \rightarrow O_2 + O_2$ with a reaction rate constant of $K_{rec, O1} = 2.45 \cdot 10^{-31} \cdot T^{-0.63} \text{ cm}^6/\text{s}$ [4]; and also the recombination reaction of oxygen atoms into a molecule (with the participation of a nitrogen molecule) $O + O + N_2 \rightarrow O_2 + N_2$ with a reaction rate constant – $K_{rec, O2} = 2.76 \cdot 10^{-34} \cdot \exp(720/T) \text{ cm}^6/\text{s}$ [7].

Then one can write an equation describing the change in the concentration of atomic oxygen over time

$$\frac{dn(O)}{dt} = 0 = K_{di} \cdot n(O_2) - K_{rec, O1} \cdot n(O) \cdot n(O_2) - K_{rec, O2} \cdot n(O) \cdot n(O) \cdot n(N_2) \quad (1)$$

At real times, the concentration of atomic oxygen can be considered unchanged, i.e. under quasi-stationary conditions (the rate of change in the concentration of atomic oxygen is assumed to be zero), and equation (1) takes the form

$$K_{di} \cdot n(O_2) = n(O)^2 \cdot (K_{rec, O1} \cdot n(O_2) + K_{rec, O2} \cdot n(N_2)),$$

where $n(O)$ is the concentration of atomic oxygen; $n(O_2)$ is the concentration of molecular oxygen; $n(N_2)$ is the concentration of molecular nitrogen. Whence it follows that

$$n(O) = \sqrt{\frac{K_{di} \cdot n(O_2)}{K_{rec, O1} \cdot n(O_2) + K_{rec, O2} \cdot n(N_2)}} \quad (2)$$

To obtain the concentration values, we will use the data for the concentration of molecules N and gas temperature T at the studied heights [1] see Table 1.

Table 2 shows the values of dissociation coefficients for different parts of the spectrum obtained from processing data from [1].

TABLE 1.

Alt., km	T, K	N, (cm ⁻³)
90	187	6,98·10 ¹³
95	188	2,9·10 ¹³
100	195	1,19·10 ¹³
105	209	5,2·10 ¹³

TABLE 2. The values of the photodissociation coefficients K_d , (s⁻¹) for different parts of the spectrum of solar radiation.

Alt, km	$K_d(1)$	$K_d(2)$	$K_d(3)$	$K_d(4)$	$K_d(1-4)$
90	10 ⁻⁹	5·10 ⁻⁹	1,5·10 ⁻⁸	3,3·10 ⁻⁸	6,2·10 ⁻⁸
95	10 ⁻⁹	5·10 ⁻⁹	10 ⁻⁷	6,0·10 ⁻⁸	2,2·10 ⁻⁷
100	10 ⁻⁹	5·10 ⁻⁹	8,7·10 ⁻⁷	7,0·10 ⁻⁸	8,8·10 ⁻⁷

Contributions taken into account: 1 - Herzberg Continuum; 2-lines Lyman - α ; 3-Continuum of Schumann - Runge; 4- Stripes of Schumann - Runge; contribution of all channels, K_d (1-4).

Knowing the components of the atmosphere by altitude, we can compile a Table 3 for concentrations of these components.

TABLE 3. Dependence of the concentrations of oxygen and nitrogen molecules on altitude.

Alt, km	$n(\text{cm}^{-3})$	$n(\text{cm}^{-3})[O_2]$	$n(\text{cm}^{-3})[N_2]$
90	6,98·10 ¹³	1,4·10 ¹³	5,5·10 ¹³
95	2,9·10 ¹³	0,6·10 ¹³	2,3·10 ¹³
100	1,19·10 ¹³	0,24·10 ¹³	0,9·10 ¹³

TABLE 4. Values of the concentration of atomic oxygen.

$n(\text{cm}^{-3})$ [O] (1)	$n(\text{cm}^{-3})$ [O] (2)	$n(\text{cm}^{-3})$ [O] (3)	$n(\text{cm}^{-3})$ [O] (4)
1,29·10 ¹¹	2,88·10 ¹¹	5·10 ¹¹	10 ¹²
1,32·10 ¹¹	2,95·10 ¹¹	1,32·10 ¹²	1,97·10 ¹²
1,4·10 ¹¹	3,13·10 ¹¹	3,89·10 ¹²	4,2·10 ¹²

The recombination coefficients were obtained from [4] at different gas temperatures? Corresponding to altitude. Using the data from Tables 2-3, and the quasi-stationary expression for the concentration of

oxygen atoms (2), we obtain the following values of the concentration of atomic oxygen, presented in Table 4.

The contribution to the photodissociation coefficient is taken into account: 1-Herzberg Continuum; 2-lines Lyman - α ; 3-Continuum of Schumann - Runge; 4- Bands of Schumann - Runge. When taking into account the contribution of all 4x components, we have the following dependence of the oxygen atom concentration on height, presented in Table 5:

TABLE 5. Dependence of the oxygen atom concentration

Alt, km	$n(\text{cm}^{-3}) [\text{O}]$
90	$1,02 \cdot 10^{12}$
95	$1,9 \cdot 10^{12}$
100	$4,18 \cdot 10^{12}$

The obtained above expression allows one to obtain the distribution of the concentration of oxygen atoms at altitudes of 90 - 100 km. Figures 1 shows a comparison of those calculated by us and those experimentally obtained in [3]. In Fig.1b a comparison of the results obtained by us and in the experiments [3] is presented. [CIRA] and P151H are the names of rockets containing photometers and ionization chambers that measure the attenuation (absorption) of solar radiation by the atmosphere, in particular Lyman- α (121.6 nm) and sent into flight in November 28, 1975.

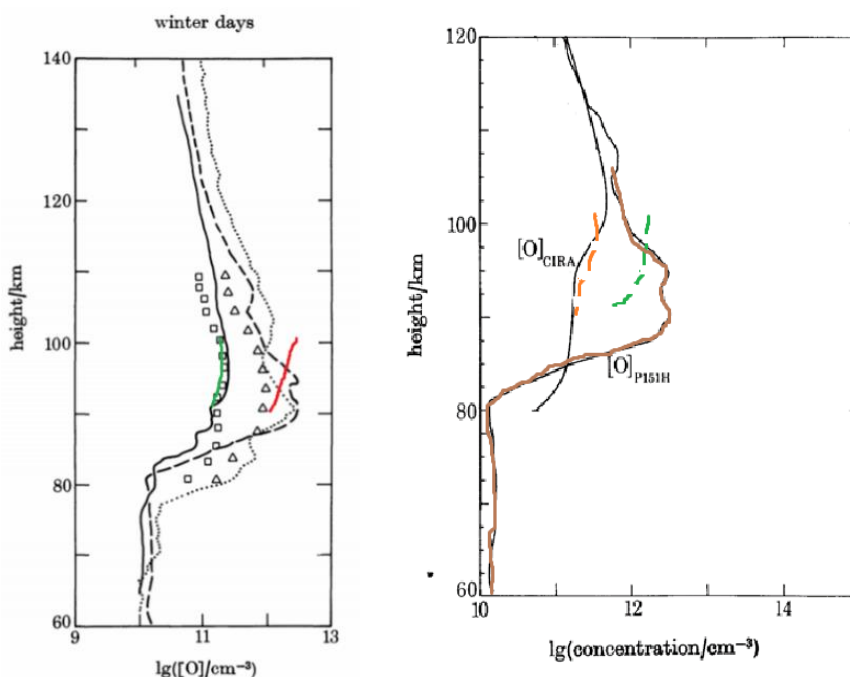


FIGURE.1. Comparison of O atoms calculated by us and measured in [3]. a) Green line– The Lyman – alpha line contribution to oxygen atoms formation. Red line – sum of 1 – 4 contributions to oxygen atoms formation. b) Orange line – The Lyman – alpha line contribution to oxygen atoms formation; Green line— sum of 1 – 4 contributions to oxygen atoms formation.

Conclusion. Results of comparison show that presented simplified model demonstrate good agreement with experimental data the Lyman – α line contribution to O atoms formation and satisfactory agreement with experimental data of the total sum of 1 – 4 contributions to O atoms formation.

1. G.B.Brasseur, S. Solomon, Chemistry and physics of the Stratosphere and Mesosphere. D. Reidal publishing company. 1984. Dordrecht, Holland.
2. L. Thomas, Recent developments and outstanding problems in the theory of the D region, *Radio Science*, 1974, 9(2), pp.121-136.
3. P. H. G. Dickinson, W. C. Bain, L. Thomas, E. R. Williams, D. B. Jenkins and N. D. Twiddy, The determination of the atomic oxygen concentration and associated parameters in the lower ionosphere. *Proc. R. Soc. Lond. A*, 1980, 369, pp. 379-408. doi: 10.1098/rspa.1980.0006.

4. I.A. Kosygi, A.Y. Kostinsky, A.A. Matveev, V.P. Silakov, Kinetic scheme of the non-equilibrium discharge in nitrogen-oxygen mixtures. *Plasma Sources Sci. Technol.*, 1992, 1(3), pp. 207.

PHOTOCHEMICAL PROPERTIES OF PENTALENE AND ITS DERIVATIVES: AROMATICITY, ANTIAROMATICITY, AND CHANGING OF CHEMICAL ACTIVITY AFTER THE SINGLE AND DOUBLE IONIZATION

Yurii A. Dyakov¹, Sergey O. Adamson¹, Gennady V. Golubkov^{1,2}, Dina P. Gubanova³,
Mishik A. Kazaryan⁴, Maxim G. Golubkov¹

¹Semenov Federal Research Center for Chemical Physics RAS, Moscow, Russia

²National Research Center "Kurchatov Institute", Moscow, Russia

³A.M. Obukhov Institute of Atmospheric Physics RAS, Moscow, Russia

⁴P.N. Lebedev Physics Institute RAS, 53, Leninskiy Prospekt, 119991 Moscow, Russia

Introduction. The hypothesis that soot microparticles, which are present in the air of cities and industrial centers, are extremely toxic and cause many dangerous diseases, was experimentally confirmed by the known study of the effects of atmospheric pollution by microparticles on people health in 6 largest American [1] and in European cities. As was discovered, microparticles with a size of less than 2.5 microns are most dangerous [2]. They freely penetrate through the walls of the capillaries of the lungs into the blood and are able to destroy human organs. Soot microparticles mostly consist from the mixture of various polyaromatic hydrocarbons (PAHs), and the smaller their size, the greater the potential negative impact for the body. Possessing high chemical activity, they are responsible for the rapid growth of respiratory, cardiovascular and oncological diseases observed in recent years [3,4]. These particles also causing the formation of toxic substances in atmosphere like smog, fog and other phenomena. Therefore, the reducing of emissions of PAH into the atmosphere as a result of the combustion reaction in engines and other devices, as well as the destruction or neutralization of formed particles, is one of the most important in medicine, ecology, and climate control.

One of the main stages of the synthesis and destruction of PAHs is the formation of five- and six-membered ring fragments of aromatic molecules. They are either radicals or chemically active neutral compositions, so-called antiaromatic compounds, which contain $4n$ π -electrons, where n is any integer. In recent years, a large number of theoretical and experimental studies have been carried out, proving the key role of this mechanism in the synthesis and destruction of unsaturated hydrocarbons, in particular PAHs [5–15].

The concepts of “aromaticity” and “antiaromaticity” were introduced by Hückel in 1931 [16] to determine the stability of cyclic planar unsaturated hydrocarbon compounds and their reactivity. Aromatic compounds are called planar cyclically conjugated systems containing $4n + 2$ π -electrons. Usually they are chemically stable. Antiaromatic compounds contain $4n$ π -electrons, and, on the contrary, are chemically very active.

Pentalene is a typical anti-aromatic polycyclic hydrocarbon consisting of two linked cyclopentadiene rings. It has the chemical formula C_8H_6 with 8 π -electrons ($4n$ π -electrons, $n = 2$). Chemically, it is extremely active and does not observed in nature, however, it is a key intermediate in many reactions and plays an important role in the formation and destruction of polyaromatic hydrocarbons. Pentalene has two other known isomers: phenylacetylene and benzocyclobutadiene. Phenylacetylene, unlike pentalene, is a typical aromatic hydrocarbon containing a benzene ring with an acetylene moiety instead of one of the hydrogen atoms. This substance is widely used in the chemical and pharmaceutical industries, and its photochemical properties are well studied. Benzocyclobutadiene is an intermediate isomer that contains both the aromatic benzene ring and the antiaromatic four-unit cyclobutadiene cycle.

Pentalene is currently poorly studied due to instability and high chemical activity. But, as mentioned above, it is an important link in various chemical reactions, both in the synthesis and destruction of PAHs, and in reactions on the surface of microparticles contained in the atmosphere.

In this article we consider the basic photochemical properties of pentalene and its isomers, as well as the change of these properties after the ionization. Our study is also has a fundamental scientific interest, since ionization changes the number of conjugated π -electrons and, accordingly, violates the "aromaticity" or "antiaromaticity" of these molecules, which inevitably should affect their chemical properties.

Computational details. In order to investigate the dissociation and isomerization mechanisms of studied molecules, quantum chemical calculations of potential energy surfaces (PES) were performed using the G3(MP2,CCSD) *ab initio* computational scheme, which was described in details earlier [6-9]. Initial geometry optimizations were performed using the B3LYP/6-31G* method. The energies of all species then were refined by the G3(MP2,CCSD) scheme. All *ab initio* calculations have been performed by the GAUSSIAN 09 package [17].

Results and Discussion. Potential energy surfaces (PES) of isomerization reactions between neutral pentalene, benzocyclobutadiene and phenylacetylene, as far as between their cations and dications are presented in Figure 1 and 2, respectively. We can see that pentalene in its neutral form is the less energetically stable isomer, whereas phenylacetylene is the most stable in agreements with Hückel's rule. Benzocyclobutadiene demonstrates intermediate properties. But all these isomers can be rearranged into each other. The main dissociation channel is the acetylene elimination, which occurs from benzocyclobutadiene with barrier's height of 108.4 kcal/mol (is not shown on the Figure 1). The next defragmentation channel is hydrogen atom loss from phenylacetylene with the energy of 114.5 kcal/mol.

After the single ionization (is not shown on the Figures), i.e. after destroying the aromatic and anti-aromatic properties of all isomers, pentalene becomes the most stable molecule, whereas energy level of phenylacetylene becomes noticeably higher. The height of barriers decreases, especially for the pentalene – benzocyclobutadiene rearrangement reaction. H atom elimination reaction from phenylacetylene becomes the most probable (105.8 kcal/mol), although acetylene loss from benzocyclobutadiene could also give some effect (113.1 kcal/mol).

After double ionization that produces dications, theoretically should change the situation with aromaticity/anti-aromaticity in the opposite condition.

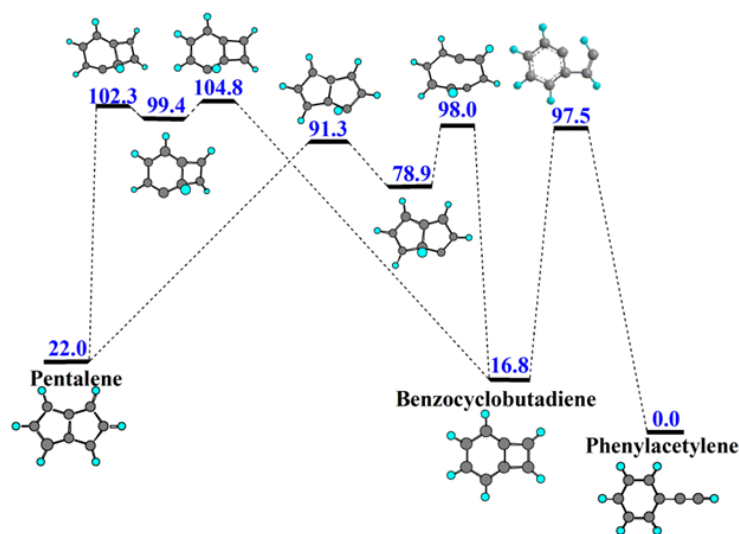


FIGURE 1. Isomerization PES for neutral pentalene, benzocyclobutadiene and phenylacetylene

Pentalene in dication form has 6 π -electrons and become an aromatic molecule. At the same time phenylacetylene loose two electrons and becomes 4 π -electrons anti-aromatic system. According to the Figure 2, pentalene and benzocyclobutadiene decisively becomes aromatic and energetically stable, whereas phenylacetylene is very unstable and, likely, anti-aromatic.

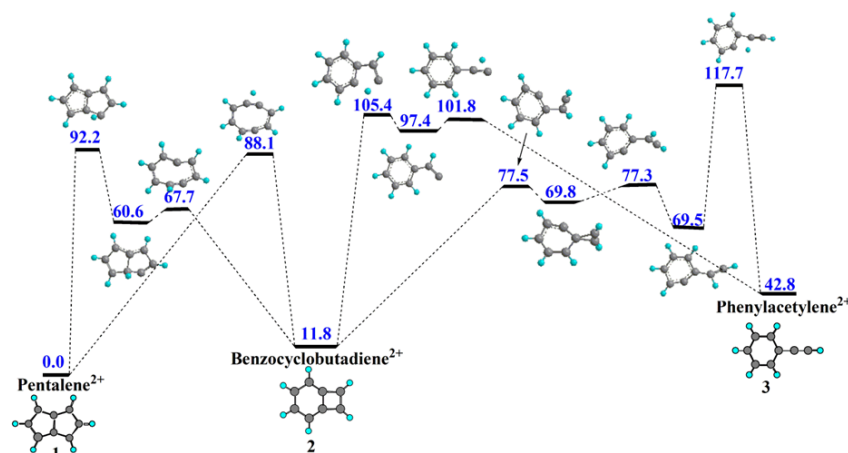


FIGURE 2. Isomerization PES for dicationic form of pentalene, benzocyclobutadiene and phenylacetylene

But in the case of dications, the molecules are exposed by strong electric field, which can initiate additional decomposition reactions, including the Coulomb explosion, and are not followed by the expected neutral molecular behavior. The influence of double and triple ionizations has been studied earlier [18-20].

Conclusion. The effect of changing of aromaticity of planar cyclic hydrocarbons on the example of pentalene, benzocyclobutadiene, and phenylacetylene after single and double electron loss have been investigated. It was found that initially being anti-aromatic, pentalene becomes to demonstrate aromatic properties. *Vice versa*, phenylacetylene, the typical aromatic molecule, become anti-aromatic and chemically unstable after the double ionization.

Acknowledgements. This work was carried out in the framework of State Assignment of the Ministry of Science and Higher Education of the Russian Federation (project AAAA-A19-119010990034-5).

1. D.W. Dockery, C.A. Pope, X. Xu, J.D. Spengler, J.H. Ware, M.E. Fay, B.G. Ferris, F.E. Speizer, An association between air pollution and mortality in six U.S. cities, *The New England Journal of Medicine*, 1993, 329, pp. 1753-1759.
2. F.J. Miller, D.E. Gardner, J.A. Graham, Jr. R.E. Lee, W.E. Wilson, J.D. Bachmann, Size considerations for establishing a standard for inhalable particles, *Journal of the Air Pollution Control Association*, 1979, 29, pp. 610-615.
3. K. Siegmann, H.C. Siegmann, Molecular precursor of soot and quantification of the associated health risk. In: *Moran-Lopez, editor. Current problems in condensed matter*, New York: Plenum Press, 1998, pp. 143-60.
4. H. Richter, J.B. Howard, Formation and consumption of single-ring aromatic hydrocarbons and their precursors in premixed acetylene, ethylene and benzene flames, *Progress in Energy and Combustion Science*, 2000, 26, pp. 565-608.
5. H. Richter, J.B. Howard, Formation of polycyclic aromatic hydrocarbons and their growth to soot - a review of chemical reaction pathways, *Physical Chemistry Chemical Physics*, 2002, 4, pp. 2038-2055.
6. Y.A. Dyakov, C.K. Ni, S.H. Lin, Y.T. Lee, A.M. Mebel, Photodissociation of azulene at 193 nm: Ab initio and RRKM study, *Journal of Physical Chemistry A*, 2005, 109, pp. 8774-8784.
7. Y.A. Dyakov, C.K. Ni, S.H. Lin, Y.T. Lee, A.M. Mebel, Acetylene elimination processes from neutral and positively charged azulene: ab initio and RRKM study, *Journal of the Chinese Chemical Society*, 2006, 53 (1), pp. 161-168.

8. Y.A. Dyakov, C.K. Ni, S.H. Lin, Y.T. Lee, A.M. Mebel. Ab initio and RRKM study of photodissociation of azulene cation, *Physical Chemistry Chemical Physics*, 2006, 8, pp. 1404-1415.
9. V.V. Kislov, A. M. Mebel, The Formation of naphthalene, azulene, and fulvalene from cyclic C5 species in combustion: An ab initio/RRKM study of 9-H-fulvalenyl (C5H5-C5H4) radical rearrangements, *Journal of Physical Chemistry A*, 2007, 111, pp. 9532-9543.
10. M.F. Lin, C.M. Tseng, Y.A. Dyakov, C.K. Ni, Photostability of amino acids: Internal conversion versus dissociation, *Journal of Chemical Physics*, 2007, 126, pp. 241104.
11. Y.A. Dyakov, A. Bagchi, Y.T. Lee, C.K. Ni, Photodissociation dynamics of benzoic acid, *Journal of Chemical Physics*, 2010, 132, pp. 014305.
12. A.M. Mebel, A.Landera, Product branching ratios in photodissociation of phenyl radical: A theoretical ab initio/Rice–Ramsperger–Kassel–Marcus study, *Journal of Chemical Physics*, 2012, 136, pp. 234305.
13. G.R. Galimova, V.N. Azyazov, A.M. Mebel, Reaction mechanism, rate constants, and product yields for the oxidation of Cyclopentadienyl and embedded five-member ring radicals with hydroxyl, *Combustion and Flame*, 2018, 187, pp. 147–164.
14. L. Zhao, R.I. Kaiser, B. Xu, U. Ablikim, M. Ahmed, M.V. Zagidullin, V.N. Azyazov, A.H. Howlader, S.F. Wnuk, A.M. Mebel, VUV photoionization study of the formation of the simplest polycyclic aromatic hydrocarbon: naphthalene (C10H8), *Journal of Physical Chemistry Letters*, 2018, 9, pp. 2620–2626.
15. Y.A. Dyakov, S.O. Adamson, G.V. Golubkov, D.P. Gubanov, M.A. Kazaryan, S.M. Kazaryan, O.S. Andrienko, M.G. Golubkov, Changing the aromaticity properties of small organic molecules after the ionization, *Proc. of SPIE 11322, XIV International Conference on Pulsed Lasers and Laser Applications*, 2019, 11322, pp. 113221Q.
16. E. Hückel, Quantum-theoretical contributions to the benzene problem. I. The electron configuration of benzene and related compounds, *Z. Phys*, 1931, 70, pp. 204–286.
17. M. J. Frisch, G.W. Trucks, H. B. Schlegel, G. E. Scuseria, M.A. Robb, J.R. Cheeseman, G. Scalmani, V. Barone, G.A. Petersson, H. Nakatsuji, X. Li, M. Caricato, A.V. Marenich, J. Bloino, B.G. Janesko, R. Gomperts, B. Mennucci, H. P. Hratchian, J.V. Ortiz, A.F. Izmaylov, J.L. Sonnenberg et. al., *Gaussian, Inc., Wallingford CT. Gaussian 09, Revision A.02*, 2009.
18. T.S. Zyubina, Y.A. Dyakov, S.H. Lin, A.D. Bandrauk, A.M. Mebel. Theoretical study of isomerization and dissociation of acetylene dication in the ground and excited electronic states, *J. Chem Phys.*, 2005, 123, pp. 134320.
19. A.M. Mebel, T.S. Zyubina, Y.A. Dyakov, A.D. Bandrauk, S.H. Lin, Potential energy surfaces in coulomb explosion of polyatomic molecules: Benzene and cyclohexane trications and acetylene dication, *Int. J. Quantum Chem.*, 2005, 102, pp. 506-519.
20. Q.Q. Wang, Y.A. Dyakov, D. Wu, D.D. Zhang, M.X. Jin, F.C. Liu, H. Liu, Z. Hu, D.J. Ding, H. Mineo, Y. Teranishi, S.D. Chao, S.H. Lin, X.H. Cheng, O.K. Kosheleva, A.M. Mebel, Ionization/Dissociation Processes of Methyl-Substituted Derivates of Cyclopentanone in Intense Femtosecond Laser Field, *Chem. Phys. Lett.*, 2013, 586, pp. 21-28.

PRACTICAL GLOBAL FORECASTS OF ATMOSPHERE PARAMETERS BASED ON EXPERIMENTAL TECHNOLOGY WITH OZONE PHOTOCHEMISTRY (FOROZ MODEL)

Alexei A. Krivolutsky¹, Tatyana Yu. Vyushkova¹, Maxim V. Banin¹ and Mikhail A. Tolstykh^{2,3}

¹Laboratory for Atmospheric Chemistry and Dynamics, Roshydromet, Central Aerological Observatory, Dolgoprudny,
Moscow Region, Russia

²Hydromedcenter, Moscow, Russia

³Institute of Applied Mathematics, RAS, Moscow, Russia

The results of numerical seasonal forecasts of temperature, calculated with the help of two interactively working numerical global models are presented: photochemical model CAO CHARM (0-90 km) [2] and the model of seasonal forecast PLAV (0-30 km) [1]. Merging together fields of wind

and temperature at the height of more than 30 km was carried out with the use of the model of general circulation CAO ARM [3]. The comparison of the results of the forecast with the reanalysis data was made. As a result of the conducted calculations it is registered that a new united model FOROZ (Forecast with Ozone) has shown stability while doing numerical scenarios and calculations. The comparison of seasonal forecasting fields of temperature of the model PLAV and of the united model FOROZ with reanalysis data is similar in low troposphere and is different in stratosphere. The united model FOROZ makes better forecast of temperature in the upper strata of the troposphere and stratosphere.

Short model description. The united model FOROZ (Forecast with Ozone) is a complex of models, providing the calculation of ozone in the diapason of altitude 0-90 km with the help of CHARM [2], ARM [3] and PLAV [1] models. The ARM model makes it possible to realize fully fledged ozone calculations higher than the upper limit of PLAV model.

When merging CHARM and PLAV models together the temperature data transmission is realized: once during a model day the transmission of three-dimensional ozone fields into PLAV model takes place, and from PLAV model the transmission of global fields of wind speed components and global temperature fields into CHARM model takes place. The difference between model resolutions gets over with the help of interpolation, because CHARM model has a rougher resolution.

The difference between Sigma coordinate system in PLAV model and geometrical altitude in CHARM model also gets over with the help of interpolation. Vertical speeds are recounted by known formulae while getting over from Sigma coordinate system to geometrical ones.

Initialization of photochemical CHARM model consists in getting «chemical climate» for all small gas components of the model (including Ozone), namely in getting their global three-dimensional distribution inside internal model grid nodes for every day of a year. Thus, these fields can be used as initial ones while realizing forecasts.

Forecasting results for summer and winter seasons. Within the limits of implementation of numerical experiments some numerical forecasts with the help of PLAV model and united FOROZ model for winter and summer (relatively) scenarios were realized. Initial data of the year 1999 were used. Quarterly forecasts in both models were made. April and October were last months of models run results scenarios. Initially calculations by a photochemical model were made in order to initialize three-dimensional ozone fields for every month of the year, which in its turn helps to use this database while realizing other scenarios.

The comparison of models in temperature field is shown in Table 1. Average difference between calculations in two models in the global field of grid nodes is presented for every high-altitude level of PLAV model. 28 different levels of PLAV model attitude are numbered in the first column.

As it seen from Table 1, the difference between the initial PLAV model and the united FOROZ model is decreasing in altitude as far as models move off from the place of their «merging». When estimating the results of fulfilled work a very important aspect was understanding of the fact whether the forecast became better (or worse) after merging the models. With that end in view the comparison of the forecast results with the reanalysis data was made. The comparison results as well as the forecast results are given in figures below.

TABLE 1. The comparison of FOROZ and PLAV models in temperature field for all altitudes.

PLAV model levels	Altitude/pressure (mbar)	April, 1999		October, 1999	
		Average difference	Standard deviation	Average difference	Standard deviation
1	9	-6.3	2.6	-7.51	1.77
2	19	-6.27	2.49	-9.41	1.73
3	32	-2.11	2.56	-6.58	3.22
4	~20 km 49	3.1	3.24	-1.53	4.27

5	~18 km	70	5.71	2.96	2.26	3.66
6		94	5.72	2.75	3.82	2.51
7		120	4.9	2.83	4.08	2.16
8	~14 km	150	3.82	2.59	3.67	2.09
9		184	2.65	2.1	2.88	1.80
10		223	1.6	1.61	1.98	1.35
11	~10 km	269	0.86	1.32	1.23	1.16
12		320	0.48	1.36	0.80	1.33
13		375	0.29	1.59	0.58	1.51
14	~5 km	432	0.21	1.78	0.51	1.60
15		491	0.19	1.89	0.47	1.65
16		550	0.18	1.96	0.46	1.69
17	~3 km	610	0.17	2.01	0.43	1.74
18		669	0.12	2.05	0.40	1.75
19		725	0.05	2.08	0.38	1.76
20	~1.5 km	778	0.01	2.11	0.36	1.75
21		825	-0.03	2.14	0.36	1.74
22		866	-0.06	2.14	0.38	1.73
23		901	-0.07	2.1	0.39	1.70
24		931	-0.06	2.04	0.35	1.65
25		955	-0.05	1.94	0.33	1.52
26		974	-0.05	1.79	0.31	1.40
27		990	-0.05	1.69	0.31	1.36
28		1000	-0.05	1.69	0.31	1.36

Forecast comparison for summer and winter seasons of 1999 years with reanalysis data. The database of “NCEP Daily Global Analyses” was used for comparing model results with empirical data. Figure 1 shows global monthly mean distribution of ozone mixing ratio (ppm v) simulated with CHARM-I. This result is in good correspondence with observations and with simulations with other models (but without ions) [6]. Thus, we can conclude that model reproduces neutral species well. It should be mentioned that CHARM-I is the development of the model CHARM which does not include ion chemistry.

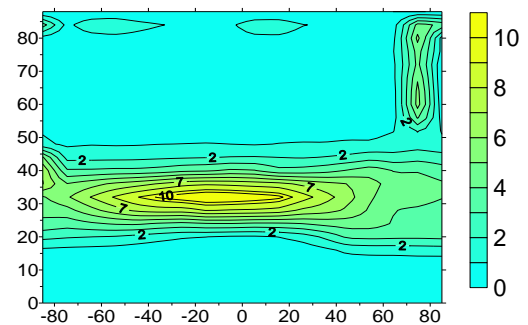


FIGURE 1. Global distribution of ozone mixing ratio (simulation with CHARM-I)

The difference for average month fields in stratosphere (18 km) for April 1999 between reanalysis data NCEP and model forecasts is shown in Figure 2. The difference is calculated in grid nodes of NCEP field, which has 2.5°x2.5° resolution horizontally. Figure 2a shows difference with PLAV model, Figure 2b shows difference with FOROZ model. As it can be seen, the difference is rather big: average deviation of forecasts in models compared with reanalysis data is 6.5 K. Average square deviation from reanalysis data for PLAV and FOROZ models is 6.5K and 6.1K accordingly. Thus, the forecast of united FOROZ model reproduces the temperature field of reanalysis a bit better.

Similarly, Figure 3 shows difference between model forecasts and reanalysis data in troposphere at an altitude of 5 km for April 1999. The deviation of model fields in troposphere from reanalysis data is less. The average deviation for PLAV model is 6K, for FOROZ model is 5.8K. The main differences are in the regions with developed orography.

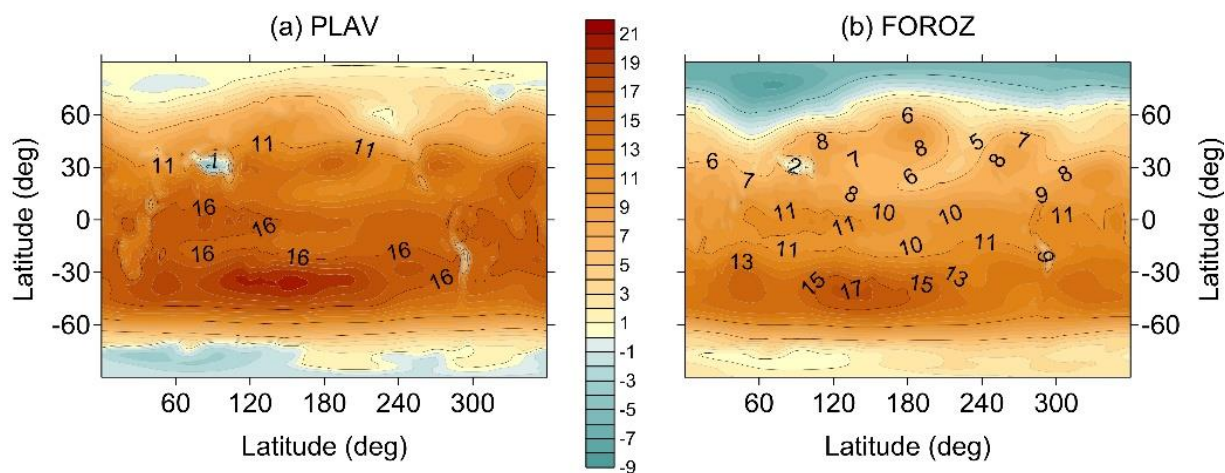


FIGURE 2. The difference for average month fields in stratosphere (18 km) for April 1999 between NCEP data and model forecasts. Figure a) shows difference between NCEP data and PLAV model forecast: minimum is -5 K, maximum is 20.6 K, average deviation from NCEP data is 9.7 K, average square deviation is 6.5 K. Figure b) shows difference between NCEP data and FOROZ model forecast: minimum is -8.2 K, maximum is 17.4 K, average deviation is 6.5 K, average square deviation is 6.1 K.

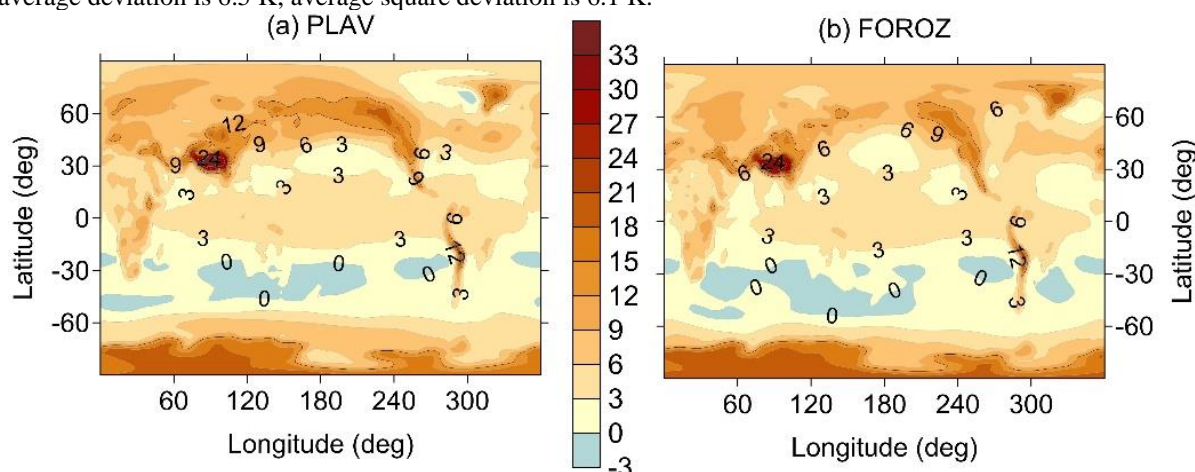


FIGURE 3. The difference between NCEP data and model forecasts in troposphere at an altitude of 5 km for April 1999. Figure a) shows difference between NCEP data and PLAV model forecast: minimum is -2.4 K, maximum is 35 K, average deviation from NCEP data is 6 K, average square deviation is 5.1 K. Figure b) shows difference between NCEP data and FOROZ model forecast: minimum is -2.4 K, maximum is 32.5 K, average deviation is 5.8 K, average square deviation is 5.3 K.

Concluding remarks. Presented results of test forecasts by using new experimental technology (i.e. there is a new created version of model forecast) with connected photochemical module in which calculation of three dimensional global ozone fields takes place which is based on the solution of total photochemical system of equations and with regard for global spatial transfer of chemically active admixture, as well as calculation results comparison, have shown that the model works stable.

It seems, that the main deviation with reanalysis data is caused by orography. It may be necessary to analyze the work of the corresponding module in more details.

It should be noted that as a perspective of the work development in this direction it would be important to raise the upper limits of PLAV model in order to make forecast on the stratosphere levels and to achieve a more complete compliance with the work of photochemical block which has the upper

limit at 90 km. In our view it would be more valuable to use ARM model of general calculation as one more additional resource (direction).

1. M.A.Tolstykh: Global Semi-Lagrangian hydrodynamic model PLAV for medium and long range forecasting. Obninsk, 2010
2. A.A. Krivolutsky, L.A. Cherepanova, T.Yu. Vyushkova, A.I. Repnev, The Three-Dimensional Numerical Model CHARM-I: The Incorporation of Processes in the Ionospheric D-region, *Geomagnetism and Aeronomy*, 2015, 55(4), pp. 468-487.
3. A.A. Krivolutsky, L.A. Cherepanova, T.Yu. Vyushkova, A.I. Repnev, A.V. Klyuchnikova, Global circulation of the Earth's atmosphere at altitudes from 0 to 135 km simulated with ARM model. Consideration of the solar activity contribution. *Geomagnetism and Aeronomy*, 2015, 55(6), pp. 468-487.
4. A.A. Krivolutsky, T.Yu. Vyushkova, L.A. Cherepanova, A.A. Kukoleva, M.V. Banin, The Three-Dimensional Photochemical Model CHARM. Incorporation of Solar Activity, *Geomagnetism and Aeronomy*, 2015, 55(1), pp. 59-88.
5. M. Prather, Numerical advection by conservation of second-order moments, *J. Geophys. Res.*, 1986, 91, pp. 6671-6681.
6. G. Brasseur and S. Solomon. *Aeronomy and Physics of the Middle Atmosphere*, Springer, 644 p., 2005.

ANALYSIS OF THE EVENTS OF LARGE-SCALE DISTURBANCES IN AEROSOL INDEX DISTRIBUTION CAUSED BY FOREST FIRES IN SIBERIA (2016-2019)

Oleg A. Tomshin¹, Vladimir S. Solovyev^{1,2}

¹Laboratory of Atmospheric Optics, Yu.G. Shafer Institute of Cosmophysical Research and Aeronomy of SB RAS, Yakutsk, Russia

²M.K. Ammosov North-Eastern Federal University, 677013, Yakutsk, Russia

Introduction. Forest fires play an important role in natural cycles, performing the ecological functions of natural forest renewal and maintaining a balance of biodiversity. The release of biomass combustion products into the atmosphere has a significant effect on the physical and chemical processes occurring in it [1-4]. Under conditions of observed climate warming, an increase in the frequency and area of fires and, consequently, the volume of emissions of combustion products is expected [5]. The paper analyzes the cases of the formation of large-scale disturbances in the distribution of the aerosol index (AI) caused by forest fires in Siberia (2016-2019).

Data. Data on forest fires (hotspots) was obtained from MODIS radiometer. Aerosol index variations were analyzed by VIIRS data. MODIS and VIIRS data were obtained from NASA's open online resources [6]. The direction and speed of the winds at an altitude of ~ 1.5 km (850 mbar) and the deviations of the atmospheric pressure values at sea level from the long-term average (Δ SLP) were taken from the NCEP reanalysis [7]. The aerosol index, calculated from measurements at wavelengths of 331 nm and 360 nm, is most sensitive to the presence of aerosols (soot and dust particles) that absorb UV radiation in the atmosphere.

Discussion. A significant fraction of forest fires in 2016-2019 occurred in Western and Eastern Siberia. The observed fire situation in the years under review was promoted by high temperature values and low relative humidity.

In fig. 1a, b, maps of the spatial distribution of the considered parameters for July 23, 2016 are presented: a) daily average values of the aerosol index, b) deviations of daily average values of pressure at sea level from mean annual values (Δ SLP); on the right side of the figure are color scales of AI and Δ SLP values; black dots mark MODIS hotspots. In the spatial distribution of the aerosol index, large heterogeneity is observed over the Central Siberian Plateau. The source of the observed AI disturbances turned out to be wildfires in the Krasnoyarsk and the Irkutsk regions (July-August 2016).

The observed configuration of pressure fields and winds (Fig. 1b) led to the formation of large inhomogeneity, which was the result of the accumulation of smoke aerosols in the stagnant region for several days (low pressure and low wind speeds). Aerosol heterogeneity was observed at a great distance from the fire sources for several days after their cessation.

In fig. 1c, d, the events of August 10, 2017 are presented - forest fires on the western border of Yakutia and large AI heterogeneity. Designations are similar to the previous figures. Increased forest fire activity in the considered area was observed from the second half of July 2017, while the northeastern direction of aerosol particle removal was relatively constant. The greatest distance from the fire sources was several thousand kilometers, and the lifetime of the aerosol inhomogeneity was 4-5 days after the termination of the wildfires.

In 2019, increased forest fire activity was observed in Eastern Siberia. In fig. 2a shows the distribution of the aerosol index on July 23, 2019. The formed configuration of air flows and low wind speeds led to the formation of large-scale inhomogeneity, which spread to the territory of Eastern Siberia to Western Siberia.

In fig.2c shows the spatial distribution of the aerosol index on August 11, 2019. Most of the forest fires detected on that date were placed on the territory of the Irkutsk region and Yakutia. The cyclone established above the southern part of the Central Siberian Plateau promoted the transfer of

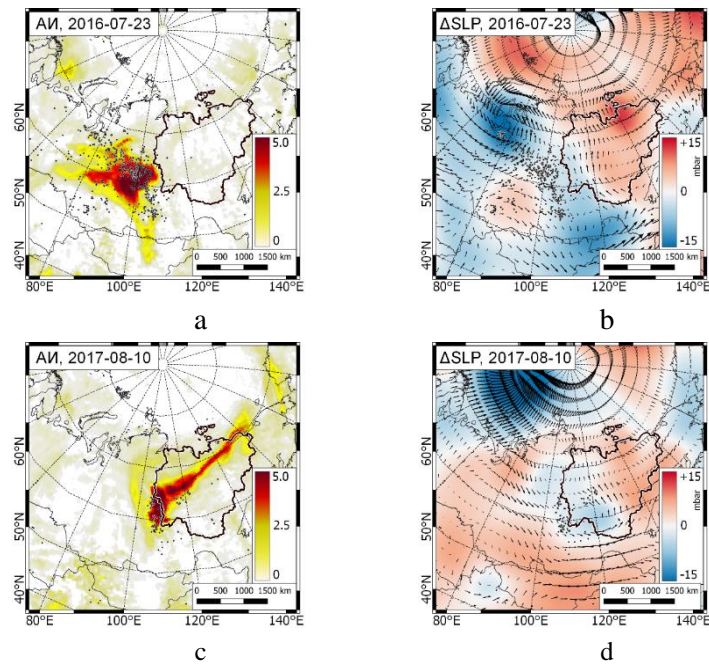


FIGURE 1. The distribution of daily average values of AI (a, c) and Δ SLP and the wind field at 850 mbar (b, d), for a-b) 23.07.2016, c-d) 10.08.2017. Black dots mark positions of MODIS hotspots.

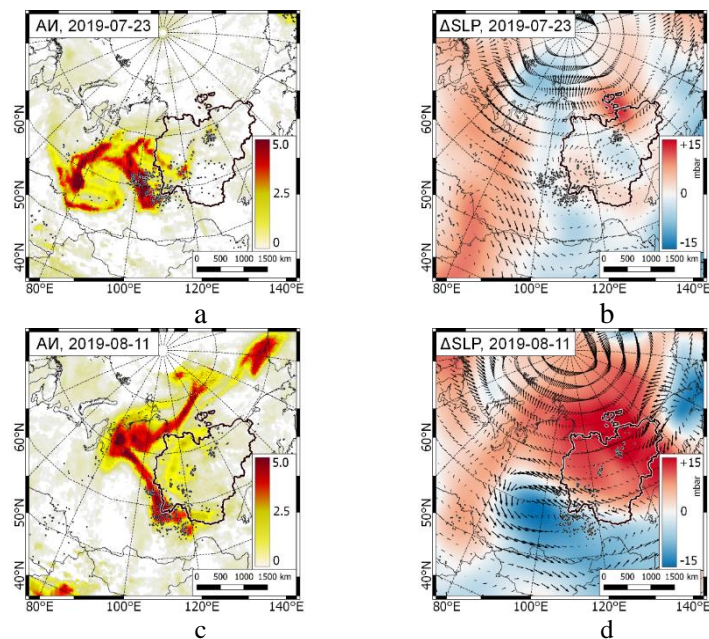


FIGURE 2. The distribution of daily average values of AI (a, c) and Δ SLP and the wind field at 850 mbar (b, d), for a-b) 23.07.2019, c-d) 11.08.2019. Black dots mark positions of MODIS hotspots.

smoke aerosols to the northeast, where for some time emissions were accumulated and further transported in the northeastern direction, towards the North American continent. High AI values persisted throughout the entire period of increased drug activity in the region for two weeks. The emission transfer range during the wildfires was at least 4,500 km.

Conclusion. The analysis shows that during the fire hazard season, the main factor determining the spatio-temporal distribution of AI in the Asian part of Russia is large-scale forest fires.

Under certain meteorological conditions, the formation of stagnant regions in the atmosphere, which are characterized by low wind speeds, is possible. Aerosol particles can accumulate in such areas, which can lead to the formation of large-scale inhomogeneities. Such heterogeneities are characterized by high AI values and a lifetime from several days to about a week after the cessation of the forest fires.

Airborne transport of aerosol particles from forest fires in Siberia and the Far East can take place over considerable distances. So, in particular, aerosol plumes from forest fires 2016-2019 in Siberia were carried by air currents through the Pacific Ocean, reaching the territory of North America.

1. Babintseva R.M., Titova Y.V. Effects of Fire on the Regeneration of Larch Forests in the Lake Baikal Basin, *Fire in Ecosystems of Boreal Eurasia*, 1996, pp. 358–365.

2. Kasischke E.S., Hyer E.J., Novelli P.C., Bruhwiler L.P., French N.H.F., Sukhinin A.I., Hewson J.H., Stocks B.J. Influences of Boreal Fire Emissions on Northern Hemisphere Atmospheric Carbon and Carbon Monoxide, *Glob. Biogeochem. Cycles*, 2005, 19, pp. 1–16.

3. Tomshin O.A., Solovyev V.S. The impact of large-scale forest fires on atmospheric aerosol characteristics, *International Journal of Remote Sensing*, 2014, 35(15), pp. 5742–5749.

4. Arshinov M.Y., Afonin S.V., Belan B.D., Belov V.V., Gridnev Y.V., Davydov D.K., Fofonov A.V., Nédélec P., Paris J.-D. Comparison between Satellite Spectrometric and Aircraft Measurements of the Gaseous Composition of the Troposphere over Siberia during the Forest Fires of 2012, *Izvestiya. Atmospheric and Oceanic Physics*, 2014, 50(9), pp. 916–928.

5. Shvidenko, A. Z., Schepaschenko, D. G. Climate Change and Wildfires in Russia, *Contemporary Problems of Ecology*, 2013, 6(7), pp. 683–692.

6. Acker J.G., Leptoukh G. Online Analysis Enhances Use of NASA Earth Science Data, *Eos, Transactions AGU*, 2007, 88(2), pp. 14–17.

7. Kalnay E., Kanamitsu M., Kistler R., Collins W., Deaven D., Gandin L., Iredell M., Saha S., White G., Woollen J., Zhu Y., Leetmaa A., Reynolds R., Chelliah M., Ebisuzaki W., Higgins W., Janowiak J., Mo K.C., Ropelewski C., Wang J., Jenne R., Joseph D. The NCEP/NCAR 40-year reanalysis project, *Bull. Amer. Meteor. Soc.*, 1996, 77, pp. 437–470.

ATMOSPHERIC PROCESSES INVOLVING CHLORINE-CONTAINING PARTICLES

Igor I. Morozov¹, Evgenii S. Vasiliev¹, Nikolai D. Volkov¹, Valerii V. Lunin², Sergei V. Savilov²

¹Semenov Federal Research Center for Chemical Physics RAS, Moscow, Russia

²Lomonosov Moscow State University, Moscow, Russia

Introduction. Adopted in recent decades, international protocols and conventions, such as the Montreal Protocol, oblige developed countries and countries with economies in transition to phase out some substances that cause harm to the environment. These include, in particular, perchlorocarbons. Studies in different countries have shown that when they are transformed in the atmosphere, toxic halogen-containing acids are formed. Oxidation of halogenated hydrocarbons in the atmosphere leads to generation of a number of secondary pollutants, including halogenated organic acids and aldehydes. Halogenated acetic acids and aldehydes are toxic compounds. Tropospheric transformation of the halogenated aldehydes is the competition of gas-phase reactions with photolysis and with wet deposition, while transfer into liquid phase dominates for halogenated acids. The most important oxidant

in both the tropospheric gas and aqueous phase is the OH radical. Studies have shown [24] that chloroacetic acids form naturally in the atmosphere in chemical reactions involving some organochlorine compounds, mainly chloroethylene, tetrachlorethylene, chloroethane, which are oxidized in the presence of ozone, hydrogen oxides, nitrogen, and carbon. Chloroacetic acid (MCA), dichloroacetic acid (DCA) and trichloroacetic acid (TCA) are products of atmospheric degradation of 1,1,1-trichloroethane and tetrachlorethylene, which are widely used in production. Haloacetic acid, tend to accumulate in natural waters.

Information about the behavior of DCA and MCA in an aqueous medium is not sufficient, especially considering their resistance is in a state of aqueous solution. The same situation with reactions in the gas phase.

Figure 1 shows a diagram of the oxidation of chloroethylene to chloroacetic acid. In the first act, OH radical breaks a double C = C bond. The resulting radical reacts with atmospheric oxygen. As a result of further adjustment, toxic chloroacetic acid is formed.

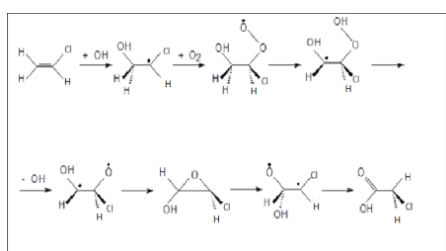


FIGURE 1. Oxidation of chloroethylene in the atmosphere

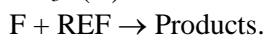
The rate constant for the gas-phase reaction with hydroxyl radical, OH, which is a main atmospheric oxidizer, is known only for trifluoroacetic acid TFA. Using a pulse radiolysis absolute rate technique, rate constants at 315 K was determined to be $(1.6 \pm 0.4) \times 10^{-13} \text{ cm}^3 \text{ molecule}^{-1} \text{ s}^{-1}$. In another study, this rate constant was determined over the temperature range 283–323 K using a relative rate technique, providing a close value of $1.2 \times 10^{-13} \text{ cm}^3 \text{ molecule}^{-1} \text{ s}^{-1}$. Thus, the gas-phase reaction of OH radicals with trifluoroacetic acid may provide a sink for this compound in the troposphere

that cannot be totally neglected. Later, relative rate techniques were used to study the kinetics of the reactions of OH radicals with a homologous series of perfluorinated acids, $\text{F}(\text{CF}_2)_n\text{COOH}$ ($n = 1, 2, 3, 4$), in 700 Torr of air at 296 K. Atmospheric lifetimes of fluorinated acids $\text{F}(\text{CF}_2)_n\text{COOH}$ with respect to reaction with OH radicals were estimated to be approximately 230 days for $n = 1$ and 130 days for $n > 1$, stating that reaction with OH radicals is a minor atmospheric fate of $\text{F}(\text{CF}_2)_n\text{COOH}$. The major atmospheric removal mechanism for $\text{F}(\text{CF}_2)_n\text{COOH}$ is believed to be wet and dry deposition, which by rough estimations occurs on a time scale of days.

For other halogenated acids, the rate constants with OH radical were not determined. Other oxidizing agents may be halogen atoms. In our example, we used fluorine atoms.

Experimental section. Kinetics of the reaction of F-atoms with trichloroacetic acid was studied at 293 K using a low-pressure flow reactor. Reactant concentrations were monitored by mass-spectrometry combined with molecular beam sampling. Rate constant was determined using a standard method of competing reactions. Below, the experimental procedure will be described in more detail using the reaction of F atoms with benzene as an example.

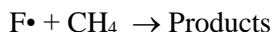
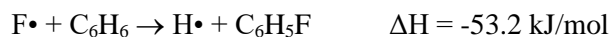
Different concentrations of the compound under study (TCA) and a reference compound (REF) were introduced into the reactor, where two parallel reactions took place:



The kinetic study of the reaction of TCA with F-atom consisted of four sets of experiments, in which measurements of the k_1/k_{ref} ratio for competing reactions of F-atoms with 1,1,1-trichloroethane, ethanol, cyclohexane, and 2-fluoroethanol were carried out. The literature rate constants for the reference compounds are discussed below in the corresponding sections. To monitor the TCA concentration, it was necessary to determine mass-spectral lines which suited for its identification, as described in the next section. The reaction rate constant obtained was $k = (4.4 \pm 0.5) \times 10^{-11} \text{ cm}^3 \text{ molecule}^{-1} \text{ s}^{-1}$. This is an average value determined by relative method employing four reference reactions of F-atoms: with 1,1,1-

trichloroethane, ethanol, cyclohexane, and 2-fluoroethanol, for which rate constant ratios $k/k_{\text{ref}} = 7.4 \pm 1.2$, 0.24 ± 0.02 , 0.28 ± 0.02 and 0.34 ± 0.04 , respectively, were obtained. The resultant rate constant is compared with the rate constants for the related fluoro-substituted acids.

Another example of an important atmospheric reaction is the reaction of F atoms with benzene: $\text{F} \cdot + \text{C}_6\text{H}_6 \rightarrow \text{HF} + \cdot\text{C}_6\text{H}_5$ $\Delta H = -108.4 \text{ kJ/mol}$



The experiments were performed using a low-pressure flow reactor connected to a mass spectrometer. Reagents and reaction products were analyzed in a molecular beam inlet mass spectrometer. The pyrex cylindrical reactor was 50 cm long and had an internal diameter of 2.3 cm. A controlled flow of helium

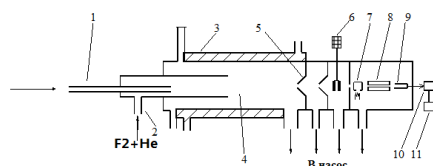


FIGURE 2. Flow reactor with mass spectrometer. 1 - injector, 2 - high-frequency discharge, 3 - jacket with coolant, 4 - reaction zone, 5 - inlet cone, 6 - modulator, 7 - ion source, 8 - mass spectrometer, 9 - electron multiplier, 10, 11 - ion current detection system.

carrier gas in a mixture with fluorine atoms flowed through the reactor tube. A cylindrical tube 1.7 cm in diameter is located along the axis of the reactor. A gas mixture consisting of benzene and a competing reagent, methane, was fed into the reactor through it. The typical gas flow rate in the reactor was 2.7 m/s, and the total pressure in the reactor was 1.0 mbar. Fluorine atoms were obtained in a high-frequency discharge of a mixture of F_2 and He (He 99%). The concentration of substances in the reactor was calculated by measuring the flows of gas mixtures of methane, benzene and molecular fluorine. The degree of fluorine dissociation was 97%. Sampling from the reaction zone to the mass spectrometer was carried out in the form of a modulated molecular beam. At

different concentrations, benzene and a competing reaction substance in mixtures with an excess of helium carrier gas entered a flow reactor through a central tube, where two reactions proceeded together.

From the number of transformations of both substances, the ratio of the rate constants of the investigated reaction (k) and the competing reaction (k_{ref}) was determined according to equation 1:

$$\ln ([\text{C}_6\text{H}_6]_0 / [\text{C}_6\text{H}_6]) / \ln ([\text{REF}]_0 / [\text{REF}]) = k / k_{\text{ref}} \quad (1)$$

$[\text{C}_6\text{H}_6]_0$, $[\text{REF}]_0$ and $[\text{C}_6\text{H}_6]$, $[\text{REF}]$ are the concentrations of benzene and the substance of the competing reaction before the introduction of atomic fluorine into the reaction mixture and after receipt of the latter, respectively.

Before the start of the kinetic experiment, the mass spectrum of the electron impact of benzene ($M/z = 78$,) was measured, Fig. 3 shows the spectra of the 20 most intense peaks. The competing reaction was chosen so that benzene could be detected by the molecular peak of the mass spectrum. The superposition of mass spectra of benzene and methane did not occur. The result of measurements of the benzene conversion depth with respect to the methane conversion depth is shown in Fig.4. The results were obtained at a temperature of 293 K.

The kinetics of the reaction between fluorine atoms and benzene has been studied experimentally at room temperature $T = 293 \text{ K}$. The method of competing reactions was applied to determine the reaction rate constant. The reaction was studied in a low-pressure flow reactor;

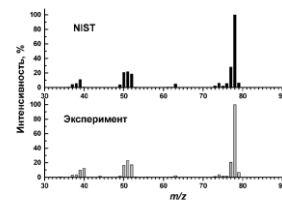


FIGURE 3. Mass spectrum of electron impact of benzene during inlet in the form molecular beam. Literature Data (NIST).

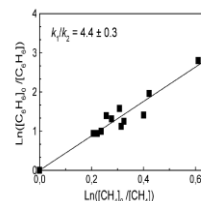


FIGURE 4. Dependence of the benzene conversion depth on the methane conversion depth in reactions with a fluorine atom at a temperature of 293 K.

the mass spectral method was used to determine the concentration of the reactants and the reaction products. The reaction of fluorine atoms with methane was used as a competing reaction, the ratio of the rate constants of the studied reaction (k_1) and the competing reaction (k_2) was determined, $k_1/k_2 = 4.4 \pm 0.3$. The rate constant for the reaction of F atoms and benzene was calculated with the literature data, $k_1(293\text{ K}) = (2.7 \pm 0.5) \times 10^{-10} \text{ cm}^3 \text{ molecule}^{-1} \text{ s}^{-1}$.

A separate discussion is planned to be presented on processes with chlorine-containing acids in water. This will include the processes of hydration of chlorine-containing molecules and their reactions in water under various tropospheric conditions in temperature and concentration.

Acknowledgments This work was supported by the RFBR grant No. 19-05-50076 (MIKROMIR. Modification of the experimental setup was performed as part of the state task of Russia (V.45.12, 0082-2014-0012, № AAAA-A20-120021390044-2).

1. E.S. Vasiliev, I.I. Morozov, G.V. Karpov, Rate constant for the reaction of F-atoms with trichloroacetic acid, *Int. J. Chem. Kinet.*, 2019, 51(12), pp. 909-917.
2. E. S. Vasiliev, A. G. Syromyatnikov, D. K. Shartava, G. V. Karpov, I.I. Morozov, Mass-spectrometric study of dichloroacetic acid, *Chem. Saf.*, 2018, 2(1), pp. 206-212, <http://chemsafety.ru>.
3. E.S. Vasiliev, V.D. Knyazev, G.V. Karpov, I.I. Morozov, Kinetics and Mechanism of the Reaction of Fluorine Atoms with Pentafluoropropionic Acid, *J. Phys. Chem. A*, 2014, 118, pp. 4013-4018.
4. E.S. Vasiliev, V.D. Knyazev, E.S. Savelieva, I.I. Morozov, Kinetics and mechanism of the reaction of fluorine atoms with trifluoroacetic acid, *Chem. Phys. Lett.*, 2011, 512, pp. 172-177.
5. I. Morozov, S. Gligorovski, P. Barzaghi, D. Hoffmann, Y. G. Lazarou, E. Vasiliev, H. Herrmann, Hydroxyl Radical Reactions with Halogenated Ethanol in Aqueous Solution: Kinetics and Thermochemistry, *Int. J. Chem. Kinet.*, 2008, 40, pp. 174-188.

THE ORIENTATIONAL ISOMERISM IN NEUTRAL WATER HEXAMERS IN THE GAS PHASE

Ekaterina A. Shirokova¹, Alexey G. Razuvaev¹, Alexey V. Mayorov², Bálint Aradi³, Thomas Frauenheim³, and Stanislav K. Ignatov¹

¹N. I. Lobachevsky State University of Nizhny Novgorod, Nizhny Novgorod, Russia

²National Institute of Standards and Technology, Gaithersburg, MD, USA

³BCCMS, University of Bremen, Bremen, Germany

Introduction. The increased interest in water clusters is caused by their role in a number of important atmospheric properties and processes, such as energy distribution, hydrolysis and hydration reactions [1, 2], and the propagation of electromagnetic radiation. As a result, the multimolecular complexes of water, which are found everywhere in the Earth's atmosphere, make a significant contribution to the climate formation and change [3, 4].

(H₂O)_n clusters are formed due to the combination of n water molecules with hydrogen bonds. For the same n , two types of isomerism can be formed: (1) the isomerism of the oxygen “skeleton” (that is the structure formed by oxygen atoms) and (2) the isomerism of the hydrogen bond network for the same skeleton, which is due to the fact that the formation of the most favorable hydrogen bond in a cluster obeys the rules similar to the Bernal–Fowler rules for an ice crystal. Two types of isomerism are shown in Fig. 1, which demonstrates the isomeric structures of the (H₂O)₆ cluster, which differ in the oxygen skeleton (Fig. 1a) and the network of hydrogen bonds for the same oxygen skeleton (Fig. 1b).

The structural and thermodynamic parameters of (H₂O)_n clusters with $n = 2-10$ are currently actively studied using both experimental and theoretical methods; there are also studies of large water clusters up to 200–300 molecules in size [5–7]. The data obtained for (H₂O)_n clusters with $n = 3-5$ are in good

agreement with experimental studies but for larger clusters the estimates of the thermodynamic characteristics and equilibrium concentrations in the gas phase vary significantly. In particular, the influence of the clusters' structural diversity on their thermodynamic characteristics remains unclear.

In order to estimate the effect of orientational isomerism on the thermodynamic parameters and concentrations of water clusters in the gas phase, 133 isomeric structures of water hexamer (H_2O)₆ have been studied.

Calculation details. The thermodynamic parameters of neutral hexamers of water (H_2O)₆ were determined by direct calculation of a large number of isomers differing in a network of hydrogen bonds. A sample of 96 isomers (H_2O)₆ of *book* conformations, 27 of *cage* type isomers, 10 of *prism* isomers was considered. The initial structures were selected using an original program that generates orientation isomers for a given "skeleton" of oxygen atoms. The program generated all possible coordinates of hydrogen atoms for a given skeleton and selected structures that satisfy the modified Bernal–Fowler rules.

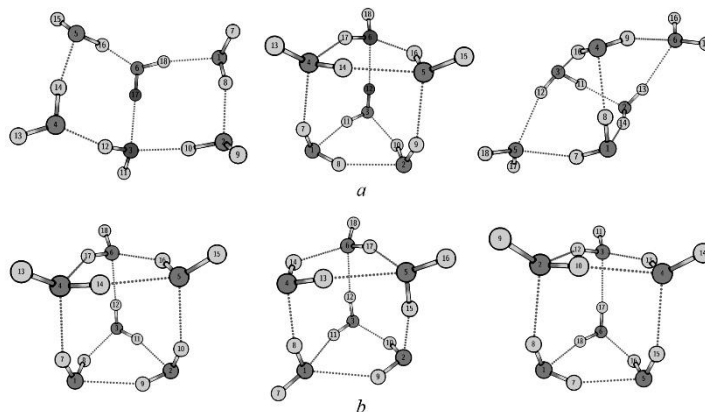


FIGURE 1. (a) – *book*, *prism*, and *cage* (left to right) conformations of the oxygen skeleton of (H_2O)₆; (b) – examples of orientational isomers in the *prism* conformation (H_2O)₆.

The geometry optimization of 133 cluster structures, their energies, vibrational frequencies, and thermodynamic parameters were calculated using the DFT (B3LYP/6-311++G(2d,2p)), G4, W1BD, DFTB, and MB-pol calculations. For each cluster structure under consideration, the thermodynamic quantities E_{tot} (total energy of the molecule), $E_{\text{tot}} + \text{ZPE}$ (total energy with the zero-point energy), $U^0_{298\text{ K}}$, $H^0_{298\text{ K}}$, $G^0_{298\text{ K}}$ (the total energy with thermal corrections to the standard internal energy, enthalpy, and Gibbs energy) were calculated. Thermodynamic functions were calculated in the "rigid rotor – harmonic oscillator" approximation for the ideal-gas state of the system. Using these values, the thermodynamic functions of the cluster formation from individual molecules $\Delta_r \varepsilon$ ($\Delta_r E_{\text{tot}}$, $\Delta_r E_{\text{tot}} + \text{ZPE}$, $\Delta_r U^0_{298\text{ K}}$, $\Delta_r H^0_{298\text{ K}}$, $\Delta_r G^0_{298\text{ K}}$) were calculated.

The obtained values of thermodynamic parameters are averaged according to two schemes:

(1) the arithmetic mean:

$$\langle \Delta_r \varepsilon \rangle_{\text{av}} = \frac{1}{k} \sum_{i=1}^k \Delta_r \varepsilon_i,$$

(2) the Boltzmann average:

$$\langle \Delta_r \varepsilon \rangle_{\text{td}} = \frac{\sum_{i=1}^k \Delta_r \varepsilon_i \exp\left(-\frac{\Delta_r \varepsilon_i}{RT}\right)}{\sum_{i=1}^k \exp\left(-\frac{\Delta_r \varepsilon_i}{RT}\right)},$$

where R is the universal gas constant, and T is temperature.

We analyzed also the binding energy per monomer $\Delta_b E = -\Delta_r E_{\text{tot}}/6$ and other binding thermodynamic functions per monomer.

Using the obtained values of $\Delta_r G^0_{298\text{ K}}$, the equilibrium constant of reaction $6\text{H}_2\text{O} \rightarrow (\text{H}_2\text{O})_6$ and the concentration of clusters in the gas phase were calculated.

Results. During the geometry optimization, new oxygen “skeletons” appeared, different from the original *cage*, *book*, and *prism*. Some of them were described previously in other studies and have generally accepted names.

The results obtained by different calculation methods differ slightly. This confirms the correct choice of basis for calculating DFT with the B3LYP functional.

Figure 2 shows the histograms of the binding energy per monomer values $\Delta_b E$ calculated at the DFT, G4 and DFTB levels for the whole set of calculated clusters. As it is evident from this figure, the energy distributions for $(\text{H}_2\text{O})_6$ clusters differ significantly from the normal ones. They have (a) the compact single-modal group of the clusters closest to the lowest state with the energy dispersion typically in the range of 0.5 kcal/mol and (b) the long “tail” of less favorable structures extending up to 2–3 kcal/mol higher than the minimum energy. The similar energy distributions are observed for all used calculation methods.

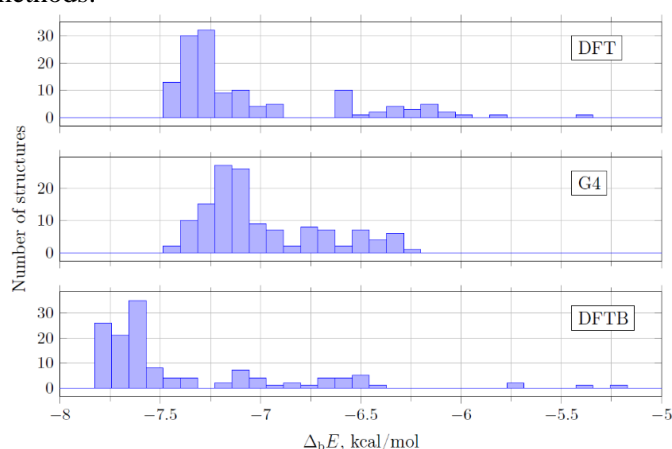


FIGURE 2. The distribution of the structures by $\Delta_b E$.

relative concentrations in percent are given as the ratio of C_{sum} concentration to the concentration of monomeric molecules in a saturated water vapor $C_{\text{H}_2\text{O}}$.

TABLE 1. Concentrations of clusters of all considered types (molecules/cm³) estimated by various averaging methods at different theory levels. Thermodynamic conditions: ideal gas state at $T = 298.15$ K and monomer pressure 3200 Pa ($P^0 = 10^5$ Pa).

	C_{sum}	C_{min}	C_A	C_B	$C_{\text{sum}}/C_{\text{H}_2\text{O}}, \%$
DFT	$8.17 \cdot 10^5$	$2.82 \cdot 10^4$	$6.10 \cdot 10^2$	$2.88 \cdot 10^3$	$1.05 \cdot 10^{-10}$
W1BD	—	$1.65 \cdot 10^3$	—	—	—
G4	$1.61 \cdot 10^3$	$1.37 \cdot 10^2$	$7.99 \cdot 10^{-1}$	$2.91 \cdot 10^0$	$2.07 \cdot 10^{-13}$
DFTB	$1.68 \cdot 10^9$	$9.35 \cdot 10^7$	$1.88 \cdot 10^5$	$3.78 \cdot 10^6$	$2.16 \cdot 10^{-7}$

Conclusion. It was found that taking into account the orientational isomerism leads to the values of water cluster gas-phase concentrations different by 1–2 orders of magnitude from the results obtained when only single or several most energetically favorable structures are considered. The concentrations of all the considered hexamer structures in the saturated water vapor at $T = 298.15$ K are estimated as $1.61 \cdot 10^3$ (G4) and $8.17 \cdot 10^5$ (DFT) molecules/cm³.

This work was supported by the Russian Foundation for Basic Research (RFBR) and the government of Nizhny Novgorod region of the Russian Federation (project 18-43-520012); and RFBR (project 20-03-00282). NIST Raritan Cluster was used to perform Gaussian16 calculations. E. A. Shirokova is

grateful to the Deutsche Forschungsgemeinschaft for the financial support during her internship at BCCMS (project DFG-RTG 2247).

1. S. K. Ignatov, P. G. Sennikov, A. G. Razuvaev et al., Ab-initio and DFT study of the molecular mechanisms of SO₃ and SOCl₂ reactions with water in the gas phase, *J. Phys. Chem. A*, 2004, 108(16), pp. 3642–3649.
2. S. K. Ignatov, P. G. Sennikov, A. G. Razuvaev et al., Theoretical study of the reaction mechanism and role of water clusters in the gas-phase hydrolysis of SiCl₄, *J. Phys. Chem. A*, 2003, 107(41), pp. 8705–8713.
3. V. Vaida, Perspective: Water cluster mediated atmospheric chemistry, *J. Chem. Phys.*, 2011, 135(2), pp. 020901.
4. J. M. Anglada, G. J. Hoffman, L. V. Slipchenko et al., Atmospheric significance of water clusters and ozone-water complexes, *J. Phys. Chem. A*, 2013, 117(40), pp. 10381–10396.
5. K. D. Jordan and K. Sen, Theoretical Studies of Neutral and Charged Water Clusters, *Chemical Modelling*, 2016, 13, pp. 105–131.
6. M. D. Tissandier, S. J. Singer, J. V. Coe, Enumeration and evaluation of the water hexamer cage structure, *J. Phys. Chem. A*, 2000, 104(4), pp. 752–757.
7. J. Bourgalais, V. Roussel, M. Capron et al., Low Temperature Kinetics of the First Steps of Water Cluster Formation, *Phys. Rev. Lett.*, 2016, 116(11), pp. 1–5.

INFLUENCE OF ELEMENTARY PROCESSES IN DRY AIR ON PARAMETERS OF THE COULOMB'S LAW

Vladimir L. Bychkov¹, Vladislav O. Gotovtsev¹, and Oleg A. Olkhov²

¹M.V. Lomonosov, Moscow State University, Moscow, Russia

²N.N. Semenov Federal Research Center for Chemical physics, Russian Academy of Sciences, Moscow, Russia

Introduction. The occurrence of ion-molecular processes in air in presence of charged particles affects the change in the parameters of the Coulomb law. As is known [1,2], historically this law was obtained without any idea of the properties of charges in air, of the properties of air itself [3] in the presence of background ionization. The modern interpretation of this law [2] does not take into account specific atmospheric conditions, as if the experiments were carried out in a vacuum. It is not described that in experiments there always occurs an interaction of charges on the surface of conductors with molecular ions, which are always present in air and determine the rate of charge neutralization. The lack of discussion of these issues creates a perverse picture of the manifestation of this law and limitations on its experimental implementation, while the discussion of such details becomes unexpected for many researchers.

In order to clarify and highlight the processes that affect the manifestation of the Coulomb law in atmospheric conditions and show their dependence on pressure and ambient temperature, we performed the corresponding calculations taking into account the effect of ion-molecular processes on the real manifestation of the Coulomb law. This work is devoted to determining the corresponding times for model atmospheric pressure air compositions. First, we determine the main air ions that can affect the change in the charges of the elements, and then move on to their influence on the formulation of the law.

The original formulation of the Coulomb's law. Consider the well-known formula of the Coulomb law (in SI) [1, 2]

$$F = \frac{q_1 \cdot q_2}{4 \cdot \pi \cdot \epsilon \epsilon_0 \cdot r_{12}^2}, \quad (1)$$

where F is the force acting on point ones charges q_1 , q_2 are placed on experimental carriers (which we call elements), i.e. charges the distance between which can be considered much larger sizes of the

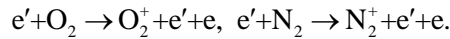
carriers themselves, ε is the dielectric constant of air, ε_0 is the dielectric constant of vacuum, r_{12} is the distance between the carriers. It describes the force arising between carriers, and implicitly assumes that the action of the charges comes from the center of their location on the elements, the distance between which is r_{12} .

In atmospheric air, formula (1) implicitly includes the parameters of elementary processes taking place in a gas. So, the number of charges located on the spherical elements varies in time, due to the fact that charged particles of the atmospheric background - ions will move to (or from) these elements, changing the electric charge initially placed on the element.

Each element will have a charge that varies over time. Moreover, due to the fact that the ionic composition of the atmosphere changes with humidity, the characteristic time that describes the stationary state of charged elements will change with humidity and will be different for dry and humid air, we do not say that changes in air pressure and temperature also affect the speed of charging and discharging elements.

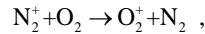
The basic elementary processes involving ions in dry air. Here are the reactions that occur during ionization of molecules by electrons, electron attachment to oxygen molecules, and electron detachment from negative oxygen ions [3–7] in dry air in the pressure range 100–760 Torr:

Atmospheric background ionization by fast electrons [3,8] with rate Q

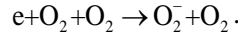


with the formation of molecular ions N_2^+ and O_2^+ and plasma electrons e

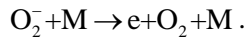
Charge-exchange of ions N_2^+ in a collision with ions O_2^+



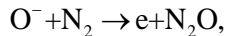
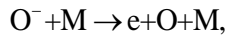
Three-body adhesion of slow electrons to oxygen molecules [9-11] with frequency ν_{tr} :



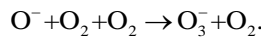
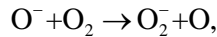
We also take into account the process of electron detachment from molecular oxygen ions in collisions with neutral molecules of the air mixture [11]



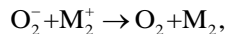
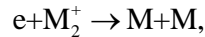
But we do not take into account the processes of electron detachment from ions O^- and O_3^- in air, at low values of the external electric field [9]



and ions O_2^- and O_3^- that appear in reactions



The balance of positively charged particles is determined by the processes of electron-ion and ion-ion recombination



where M_2^+ is the positive ion.

The balance of charged particles. At atmospheric pressure at low ion concentrations, usually velocity of attachment is greater than velocity of electron ion recombination $\nu_{tr} \gg \alpha_{ei} \cdot N_{O_2^+}$, and [3]

$Q = \alpha_{ii} \cdot N_{o_2^-} \cdot N_{M_2^+}$, where α_{ii} is coefficient of ion-ion recombination, $N_{o_2^+}$, $N_{o_2^-}$, $N_{M_2^+}$ are respectively concentration of ions. Under stationary conditions for the background ions, the plasma quasineutrality condition is satisfied $N_{o_2^-} \approx N_{o_2^+}$, whence $N_{o_2^-} = \sqrt{Q / \alpha_{ii}}$. At atmospheric conditions, it is usually $Q = 4 \text{ cm}^{-3} \cdot \text{s}^{-1}$ [4,8], but can vary depending on seismic conditions; $\alpha_{ii} \approx 2 \cdot 10^{-6}$, cm^3/c [3, 6], the ion concentration is of the order of the experimentally observed $N_{o_2^-} \approx 1.4 \cdot 10^3$, cm^{-3} .

The concentration of ions in the law of Coulomb. Using results obtained in the previous section, we write the expression for the Coulomb law

$$F = \frac{q_1(t) \cdot q_2(t)}{4 \cdot \pi \cdot \epsilon \epsilon_0 \cdot r_{12}^2}.$$

Here the time dependencies of q_1 and q_2 are taken into account.

To determine the time dependencies of the charges on the elements, we write the corresponding equations describing the changes in the initial charges on the elements

$$\frac{d q_i}{d t} = -4 \cdot \pi \cdot r^2 e \cdot \left(D \frac{\partial N}{\partial r} - b_i \cdot E \cdot N \right), \quad (9)$$

where r is the distance from the center of the particle; N is the density of ions at a distance r ; D and b_i are coefficient of diffusion and mobility of the ion; E is electric field of the particle.

$$e \cdot D = b_i \cdot k T$$

is relation between diffusion and Townsend mobility coefficients, e is electron charge.

It can be shown that $D \frac{\partial N}{\partial r} \ll b_i \cdot E \cdot N$ for $r \sim 1 \text{ cm}$ of the element, $N \sim 10^4 \text{ cm}^{-3}$ ions at infinity and $q_i > 10^{-11} \text{ Cu}$, which are performed in experiments in air

$$\frac{d q_i}{d t} = -4 \cdot \pi \cdot r^2 e \cdot b_i \cdot E \cdot N$$

where is the ion charge modulus taken. Then we obtain

$$\frac{d q_i}{d t} = -e \cdot b_i \cdot \frac{q_i}{\epsilon \epsilon_0} \cdot N \quad \text{or} \quad q_i = q_{i0} \exp \left(-e \cdot b_i \cdot \frac{N}{\epsilon \epsilon_0} \cdot t \right).$$

Then the formula of Coulomb's law will take the form

$$F = \frac{q_1 \cdot q_2 \exp \left(-e \cdot \frac{N}{\epsilon \epsilon_0} (b_1 + b_2) \cdot t \right)}{4 \cdot \pi \cdot \epsilon \epsilon_0 \cdot r_{12}^2}. \quad (10)$$

We substitute the ion concentration into this expression and obtain

$$F = \frac{q_1 \cdot q_2 \exp \left(-e \cdot \frac{\sqrt{Q / \alpha_{ii}}}{\epsilon \epsilon_0} (b_1 + b_2) \cdot t \right)}{4 \cdot \pi \cdot \epsilon \epsilon_0 \cdot r_{12}^2} = F_{class} \cdot \exp \left(-e \cdot \frac{\sqrt{Q / \alpha_{ii}}}{\epsilon \epsilon_0} (b_1 + b_2) \cdot t \right),$$

where F_{class} is the force from expression (1). The formula shows that measurements of the coulomb force depend on conditions in the atmosphere: on the background ionization rate, ion mobility, and the value of the ion-ion recombination rate constant.

We introduce the characteristic particle discharge time

$$\tau = \frac{\epsilon \epsilon_0}{e \sqrt{Q / \alpha_{ii}} (b_1 + b_2)}. \quad (11)$$

The mobility of oxygen ions in the atmosphere in the limiting case of a c^{-1} zero electric field at a gas temperature of 300 K was experimentally obtained $b_1 = 2,24 \text{ cm}^2 \cdot \text{V}^{-1} \text{s}^{-1}$ $b_2 = 2,16 \text{ cm}^2 \cdot \text{V}^{-1} \text{s}^{-1}$ [12]. Thus, the characteristic time of the discharge of a particle in the atmosphere according to the formula (11) is $\tau = 89.8 \text{ s}$. We see that if we consider the Coulomb law for a time longer than the characteristic time of the discharge of the particle, it is necessary to take into account the discharge of particles and use formula (11).

Conclusions. We see that a rather simplified formula that takes into account the role of atmospheric ions in the Coulomb law significantly changes its appearance.

1. Yu.A. Lyubimov Essays on the history of electromagnetism and dielectrics. M. Binom 2008.
2. V.A. Aleshkevich Electromagnetism. M. Fizmatlit. 2014.
3. B.M. Smirnov Ions and excited atoms in plasma. M.: Atomizdat. 1974.
4. N. Ardelyan, V. Bychkov, D. Bychkov and K. Kosmachevskii 2013 Plasma assisted combustion, gasification and pollution control vol 1, Ed I Matveev (Denver, Colorado: Outskirts press) pp. 183-372
5. Y Akishev, A. Deryugin, V. Karalnik, I. Kochetov, et.al. 1994 *Plasma Phys. Rep.* 20, pp. 511-524
6. I. Kossyi, A. Kostinsky, A. Matveyev, and V. Silakov. 1992 *Plasma Sources Sci. Technol.* 1. pp. 207-220
7. B. Smirnov 2008 Reference Data on Atomic Physics and Atomic Processes. (Berlin: Springer-Verlag).
8. V. Konovalov and E. Son, *Plasma chemistry*, 1987, 14, pp. 194-227.
9. A. Mnatsakanyan, G. Naidis, *Reviews of Plasma Chemistry*, 1991, Ed. B Smirnov (New York: Consultants Bureau), pp. 259–285.
10. N. Aleksandrov, *Plasma chemistry*, 1981, 8, Ed B Smirnov (Moscow: Energoizdat), pp. 90-122.
11. A. Ponomarev, N. Aleksandrov, *Plasma Sources Sci. Technol.*, 2015, 24, pp. 03501.
12. I. McDaniel, E. Mason, Mobility and diffusion of ions in gases. *Moscow: Mir*, 1976.

ELECTROMAGNETIC AND OPTICAL PHENOMENA IN THE ATMOSPHERE INCLUDING LONG-LIVED AND PLASMA OBJECTS

MEASUREMENT OF COLD NEUTRON FLUX AND SOFT X-RAY RADIATION IN HETEROGENEOUS PLASMOID

Anatoly I. Klimov, Nikita K. Belov, Boris N. Tolkunov

Joint Institute for High Temperature RAS, Moscow, Russia

Experimental results on registration of the different radiations from a heterogeneous plasmoid (HP) created by pulsed- repetitive discharge in the experimental set up PVR are considered in this work. Intensive cold neutron flux, and soft X- radiation ($E < 10$ KeV) are recorded in our experiment with a heterogeneous plasmoid. It was revealed that there is high voltage threshold $U_d > 3.8$ kV in the electric discharge for the creation of intensive neutron flux. Hypothesis about possible analogy between a long-lived HP and ball lightning is considered.

Experimental results. Heterogeneous plasmoid (HP) is created in the experimental setup PVR by a pulsed repetitive electric discharge in a swirl gas flow. Experimental set and diagnostic instrumentation were described in our works [1, 2]. The typical HP (3) in a water steam vortex flow is shown in the figure 1. This HP (3) consists of nucleus (metal micro-droplets) and plasma halo around it. Note that cathode and anode are manufactured from Nikole.



FIGURE 1. Heterogeneous plasmoids (3) created by pulsed- repetitive electrical discharge (2) in the experimental setup PVR. Cathode-injector (4) - right, anode (1) - left. Erosive metal micro droplets-5

The experimental conditions are the followings: - argon mass flow rate 1,4-2 G/sec, water steam mass flow rate 1- 2 G/sec, mean electric current 2 A, mean input electrical power 1 kW, cathode electrode mass flow rate 1mG/sec. The following diagnostic instrumentation is used in our experiments:- neutron radiometer – KPAH- 1, neutron detector on the base of He3 – CPIIC, X – ray films with aluminum filters for registration of quantum energy 1-10 KeV, X – ray spectrometer AMPTEK X-123 (USA) and X – ra spectrometer БДЭР (Russia) for registration of quantum energy range $E = 0,1 - 30$ KeV, X-ray detector CPIIC for registration of quantum energy range $E > 20$ KeV.

Registration of Low Energy Neutrons and X- Ray Radiation. Neutron detector CPIIC on the base of He3-detector is used in these experiments. Radiometer KPAH-1 is used for neutron flux measurement also. These detectors are calibrated by a radioactive tablet Am^{95}_{243} with

Be- convertor in Nuclear Center (Dubna). Scheme of this experiment is shown in the figure 2. Detectors CPIIC and KPAH-1 are arranged near PVR's nozzle. The distance L of their locations are varied from 2 cm up to 200 cm from plasma jet axis. The angle of their registration is varied in the range of $\alpha = 00 - 900$. The different neutron absorbers are used near these detectors such as Polyethylene plates, water cells and others in some experiments. The typical signals from these detectors are shown in the figure 3.



FIGURE 2. General view of the experimental set up PVR with detector CPIIC and radiometer KPAH-1

It is revealed that neutron's signal amplitude is higher than background one at the definite conditions only:

- Distance $L < 30 \div 40$ cm.
- Angle $\alpha = 90^\circ$. Visualization direction of the detector is perpendicular to plasma jet axis. The signal amplitude has background level at the angle $\alpha = 0^\circ$.
- Neutron absorber decreases signal's amplitude considerably.
- Strong X-ray radiation is absent in these experiments.



FIGURE 3. Neutron's signal (down) and γ -radiation signal (top) measured CPIIC-detector.

The second result proves the absence of electromagnetic interference in these experiments. Note that battery power supplies are used in these detectors. So, electromagnetic interference from electrical circuit should be negligible in these experiments.

One can see (figure 3, down) that there is a non-stationary neutron signal from HP measured by neutron detector. There are some maximums and minimums in this signal. Note

that the beginning of this neutron signal has some time delay $\tau \sim 30 \div 140$ sec from plasma switch on.

It is revealed that strong γ - photons ($E > 20$ KeV) are not created by HP in these experiments, figure 3 (top).

It is obtained that there is definite voltage threshold $U_d > 3,6 \div 4,2$ kV of neutron creation by pulsed electric discharge.

The typical value of neutron flux measured by the radiometer KPAH-1 is about of $S_n = 10^5 \div 10^6$ neutron/sec. This value S exceeds the background value S_b during time interval $20 \div 30$ sec at plasma off.

It is obtained that neutron flux S_n is non-homogeneous in space and non-stationary in time. Space distribution of this neutron flux is not spherical. The value S_n is minimal one in the perpendicular direction to plasma jet axis.

It is revealed that induced radiation from the Indium sample activated by HP's neutron flux is very small (closed to zero).

Soft X-Ray Radiation. Two beryllium windows ($10\ \mu\text{m}$) are arranged in PVR's quartz tube to measure a soft X-ray radiation. The typical X-ray spectrum recorded by BDER- spectrometer is shown in the figure 4 (left). One can see two maximums in this spectrum:- the first maximum is about of $E \sim 1.0\ \text{KeV}$ and the second one is about of $4.0\ \text{KeV}$. The typical traces of a «strange» particles in the exposed film are shown in the fig. 4 (right). One can see several black broken lines in this film.

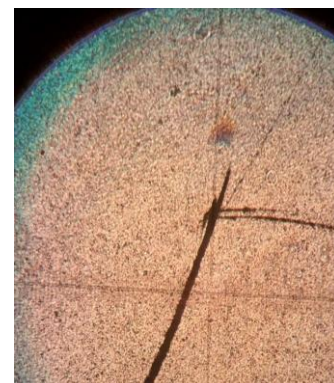
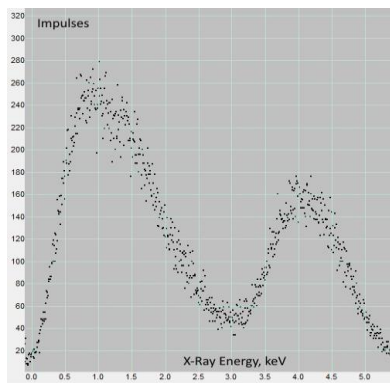


FIGURE 4. Soft X-ray spectrum measured by BDER- spectrometer (left). Exposed film with black broken lines (right).

Conclusions.

1. Neutron-like particles are recorded by radiometer KPAH-1 and radiometer CIIPC with He-3 detector. Total intensity of these particles is about of $S_n = 10^5 \div 10^6$ neutron/sec.
2. It is revealed that there is high voltage threshold $U_d > 3,6 \div 4,2\ \text{kV}$ in the electrical discharge for the neutron flux creation in the HP.
3. Intensive soft X-ray radiation ($E < 4\ \text{keV}$) from HP is measured by spectrometer Amptek X-123.

1. A. Klimov, Vortex Plasmoids Created by High-Frequency Discharges, *Atmosphere and Ionosphere: Dynamics, Processes, Monitoring*, Springer, Berlin, 2013, pp. 251.
2. A. Klimov, A. Grigorenko, A. Efimov, N. Evstigneev, O. Ryabkov, M. Sidorenko, A. Soloviev and B. Tolkunov, High-energetic Nano-cluster Plasmoid and its Soft X-ray Radiation, *J. Condensed Matter Nucl. Sci.*, 2016, 19, pp. 1–10.

THE FLICKERING NATURE OF BALL LIGHTNING SHINING

Anatoly I. Nikitin, Vadim A. Nikitin, Alexander M. Velichko,
Tamara F. Nikitina

V.L. Talrose Institute for Energy Problems of Chemical Physics at N.N. Semenov Federal Research Center for
Chemical Physics, Russian Academy of Sciences, Moscow, Russia

In July 2016 near Blagoveshchensk, Russia, a video of ball lightning (BL) with a normal exposure was obtained, on which the flickering of its radiation and its structure — the core and the shell — were clearly visible [1]. Two BL were observed about 5 minutes. One of them had faded, was invisible during 20–40 s, and then had flashed again. The video was shot by Oleg Pesterev and Margarita Rabusova with Huawei smartphone, total time of recording was 77 s.

The first part of the video (from 0 to 33 s) was shot through a double-glazed window. In the period from 0 to 5 s, the image of BL moves from the lower left corner of the frame to its center. Due to overexposure, the colour of the ball appears white. However, one can notice the flickering of its light. At the end of this period, the exposure approaches normal, and the structure of BL in the form of a core and an outer ring, between which dark ring is located, becomes visible (see Fig. 1). In the period from 6 to 9 seconds, the light of BL flickers, its brightness decreases, and the colour takes on an orange tint. From 10 to 11 seconds, the size of BL sharply decreases to a point that continues to flicker. Perhaps this is due to the rapid removal of the object from the observer. Then very quickly, in 1/15 of a second, the size of the ball becomes the same. In the range of 12-15 s, the ball is fixed with normal exposure. This interval was analyzed frame by frame each 1/30 s (see Fig. 3). From 15 to 33 seconds, the same thing happens: the light intensity of BL changes randomly, while its size and structure remain the same. From 33 to 43 seconds, the observer moves with the camera to the balcony, at the end of the interval, the sound of rain becomes audible. In the initial period of shooting from the balcony, there is no image of BL in the frames. Black space is visible, which should lead to an automatic increase in exposure. At the end of the interval, the image of BL in the form of a strongly overexposed ball with a “crown” falls into the frame. Interval 53-60 s: the image of BL is strongly overexposed, but flicker is noticeable, mainly in the light of the “crown”. In the interval 60-71 s, BL is again removed, but not as far as the first time, and not so fast. Then it returns to its former place. Interval 72-73 s: BL flashes, a bright spot occupies the corona area (flash lasts 0.5 s). After the flash, the brightness of the ball decreases, and again becomes visible ring structure of the image, similar to the structure observed when shooting through the window. During 0.5 seconds, BL goes out. In the interval 73-77 s there is nothing in the frame, the sound of rain is heard.

Figure 1 shows a view of BL taken through a window during the period when the camcorder switched from overexposure mode to normal mode. The image shows a disk in the form of a light ring and a bright core, which are separated by a dark ring. Figure 2 shows the brightness distribution of the disk along its diameter; for it, the ratio of the intensities of the glow of the core and the dark ring (contrast) is $\gamma = 1.27$.

Figure 3 is a graph of changes in the intensity of luminosity of its core in the period from 12th to 15th seconds. It is seen that intensity of the glow varies greatly from frame to frame. Sometimes the glow of BL “turns off” for only 1/30 second, and then abruptly restored. The intensities of the glow of the core and shell change synchronously. The search for signs of periodicity using the Fourier analysis showed its absence (see Fig. 4). In the indicated interval (from 12th to 15th s), weakly pronounced maxima fall at frequencies of 1 Hz, 4 Hz, 9 Hz, and 12 Hz. This is consistent with the result of photometry of negative of BL photo, made by Ryabtsev and Stakhanov [2] (4 - 6 Hz), but an order of magnitude smaller than the result obtained in [3] (100 Hz). Note that during periods of minimum glow, ball lightning retained its size and shape.

In our opinion, the most significant result of our analysis is the discovery that BL can “turn off” for a few seconds, and then begin to shine again. This property, as well as shown by us “flickering” nature of its glow, indicate that during the absence of glow the energy in BL remains unchanged. Only the rate of “expenditure” of this energy is reduced. Another result of observation is that BL, which has

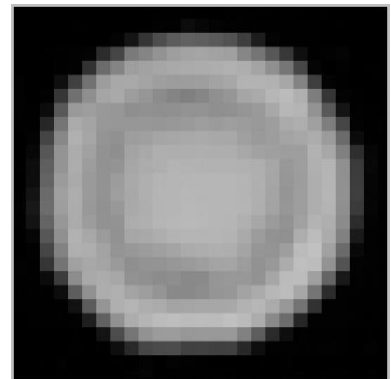


FIGURE 1. Image of ball lightning

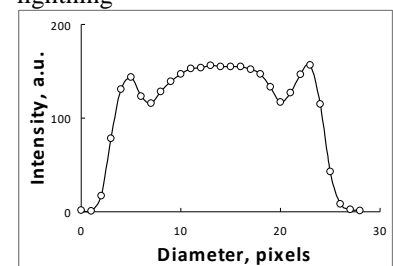


FIGURE 2. The distribution of image brightness along the diameter

a large supply of energy, can be not emitting light for a long time and remain invisible. Moving at a speed of 10-50 m/s, in 10 seconds it can move away from the place of its formation at 100-500 m and, starting to shine, will be perceived by observers as “being appeared out of nowhere”. The cases of BL appearing as if “from thin air” are described in [4-6]. Apparently, the ability of ball lightning to remain invisible can explain the cases of observation of “black” BL [7].

All of the above leads to the paradoxical assumption that the “most invisible” state may be the “most profitable” style of BL existence. Apparently, the “strategy” of BL is to live losing as little energy as possible. If, indeed, a mode of existence of BL with a minimum rate of energy loss is possible, then this significantly increases interest to it as a promising energy storage device (of course, for this one needs to learn how to get it in a laboratory).

In the most natural way, the mechanism of “dosing” of energy losses can be explained by the “electrodynamic model” of ball lightning [8-11]. According to this model, relativistic electrons moving in circular orbits are

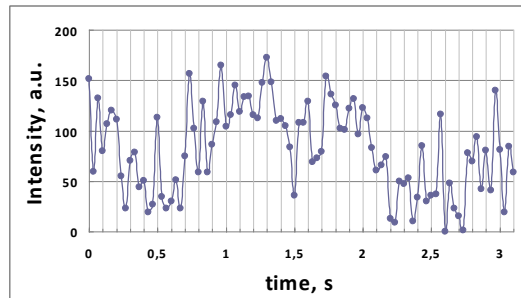


FIGURE 3. The type of change in the intensity of the glow of ball lightning from 12th to 15th seconds

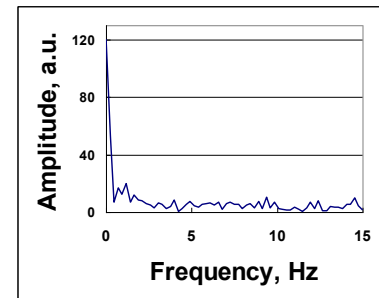


FIGURE 4. The result of the Fourier analysis of frequency of intensity oscillations of ball lightning glow

the generator of electromagnetic radiation of ball lightning (in the radio and optical ranges). With a large number of electrons in orbit and their uniform arrangement along the orbit, the electron ring does not radiate electromagnetic energy at all [12]. In this case, the kinetic energy of the electrons is conserved. Electrons will radiate energy only if the uniformity of their distribution in the orbit is violated, which depends on the external influence. The extent of this effect may vary randomly. With a strong violation of the uniform filling of the orbit with electrons, they can radiate energy in the form of a powerful electromagnetic pulse. Note that the release of energy in the form of a radiation pulse is not the equivalent of the death of BL.

In our case the Fourier analysis of time dependence of the brightness of the glow showed an almost complete absence of signs of the periodicity of its radiation. This casts doubt on the reliability of the conclusion of the authors of the article [3] about the presence of modulation of radiation intensity of the object, which they identified with BL, with a frequency of 100 Hz. It is possible that the object, shot by Chinese researchers, was an electric discharge, initiated by linear lightning between the wires of a high-voltage (35 kV) electric line, which passed 20 m from the place of the linear lightning strike [6]. In this regard, it is likely that the detection lines of silicon, iron and calcium in the spectrum of the observed object was caused by the glow of the discharge, into which a dust, deposited on the wires and insulators of the electric line, was turned out. So this spectrum has nothing to do with ball lightning.

Acknowledgements. We are grateful to Oleg Pesterev, Margarita Rabusova and Andrei Rabusov for useful information and permission to use the film they shot. This work was developed within the framework of the Program for Basic Research of the Russian State Academy of Sciences for 2013-2020 and supported by the Ministry of Sciences and Higher Education (agreement GZ No.007-00269-18-00).

1. A. Rabusov, 2016. Ball lightning. <https://www.youtube.com/N8y8IN0Gu-c>.

2. A. N. Ryabtsev, I.P. Stakhanov, Analysis of the photograph image of ball lightning. *Zh. Techn. Fiz.* 1987. 57 (8), pp. 1583-1587 (in Russian).
3. J. Cen, P. Yan, S. Xue, Observation of the optical and spectral characteristics of ball lightning. *Phys. Rev. Letters.* 2014, 112, pp. 035001.
4. W. Brand, *Der Kugelblitz*. Henry Grand, Hamburg, 1923.
5. D. J. Turner, Ball lightning and other meteorological phenomena. 1998. 293, 2-60.
6. H. Boerner, *Ball Lightning. A Popular Guide to a Longstanding Mystery in Atmospheric Electricity*. Springer Nature, Switzerland AG., 2019.
7. S. Singer, *The Nature of Ball Lightning*. Plenum Press, New York, 1971.
8. A. I. Nikitin, Electrical capacitor as the element of the power core of ball lightning. *Electrical Technology Russia.* 1998. 4, pp. 70-85.
9. A. I. Nikitin, The dynamic capacitor model of ball lightning. In: *Proc. 6th Intern. Symp. On Ball Lightning (ISBL99)*. 1999. Antwerp, Belgium. pp. 91-95.
- 10 A. I. Nikitin, Electrodynamical model of ball lightning. *Russ. J. Chem. Phys.* 2006. 25 (3), pp. 38-62 (in Russian).
11. A. I. Nikitin, Possible process of ball lightning training in nature. *Journ. Atm. Solar-Terr. Phys.* 2019. 190, pp. 54-61.
12. L. A. Artsimovich, S. Yu. Lukianov, *Motion of Charged Particles in the Electric and Magnetic Fields*. Nauka, Moscow, 1978 (in Russian).

PROPERTIES OF COMPACT LONG-LIVED LUMINOUS FORMATIONS IN THE ATMOSPHERE

Andrey V. Chistolinov

Joint Institute for High Temperatures of the Russian Academy of Sciences, Moscow, Russia

Introduction. In this paper, we consider the properties of compact long-lived luminous formations in the atmosphere, known as ball lightnings. The history of scientific research of ball lightning, if we count it from the famous work of Francois Arago [1], has more than 180 years. However, to this day there is no neither a generally accepted theory of this phenomenon, nor even any consensus about its nature.

Currently, more than 200 different models of ball lightning have been proposed. Unfortunately, the vast majority of these models are not able to predict the characteristics of its behavior. As noted in [2], the problem with most theories is that they do not predict the observed properties of ball lightning, and many, on the contrary, predict unobservable properties.

The situation is no better with attempts to reproduce ball lightning in laboratory conditions. The various luminous formations that are produced in laboratories today have little in common with natural ball lightnings. So, in terms of life time, they barely reach 1-2 seconds, while natural ball lightnings live for tens of seconds or even minutes and sometimes manage to make a path of tens of meters during their life. Natural ball lightnings demonstrate the ability to bypass obstacles, pass through cracks and small holes, move against the wind and still maintain their integrity. Nothing similar can be obtained in the laboratory.

But, even worse, ball lightning does not have, generally speaking, a strict definition [2, 3]. This allows each researcher to define it in a convenient way and explore a convenient object, calling it a ball lightning.

This paper attempts to introduce some standards for defining a ball lightning. To do this, we introduce a set of basic properties of ball lightning, the reliability of each of which is confirmed by observation statistics. The basic properties of ball lightning are the minimum set of ball lightning properties required for: evaluating the conformity of theoretical models to the real ball lightning that

were recorded in nature, and evaluating the conformity of objects obtained in laboratory experiments to natural ball lightning.

I would like to emphasize that the basic properties are not the properties that a particular ball lightning has, but the properties that a ball lightning has as a phenomenon. In other words, we do not claim that all these properties can appear simultaneously in the same ball lightning, but they can appear definitely as the statistics of observations show. Therefore, any theoretical model that claims to explain this phenomenon must demonstrate its ability to predict all the basic properties, without exception. The same applies to laboratory experiments. Any laboratory analog that claims to reproduce a natural ball lightning must demonstrate the reproduction of all its basic properties.

Basic properties of ball lightning. To date, there are quite detailed studies of a large observational material on the problem of ball lightning [2-9]. This work is based on two major data banks of ball lightning observation data [3] and [4], containing 2000 and 5315 of observed cases, respectively. When selecting the basic properties of ball lightning, their presence in other independent banks of ball lightning observational data was also checked [2, 5-9].

We assumed that the basic properties of ball lightning must meet the following criteria:

1. The specificity of the properties for ball lightning.
2. Availability of observational statistics for this property.
3. Unambiguity of property interpretation.
4. The reliability of determining the properties by using the human senses.

Based on these criteria, 20 basic properties of ball lightning were identified, which are presented in Table 1. The list of the basic properties of ball lightning did not include properties that we did not consider specific to this object (that is, distinguishing it from other similar objects or phenomena), for example, the ability to exist for less than a certain time, emit a light flux less than a certain value, have a size less than a specified one, the ability to extinguish quietly, etc.

Also, this list did not include properties that are not reliably determined by human perception, such as the brightness of the ball lightning and its color characteristics.

Some properties of ball lightning, which are fairly reliably determined using human perception organs and for which there are sufficient statistics of observations, were not included in the list due to the fact that they cannot be unambiguously interpreted. Such properties, for example, include the speed of a ball lightning, since it is impossible to make an unambiguous conclusion about the nature of the speed of this movement from the available statistics [3, 4] – whether it is the speed of the ball lightning relative to the air or the speed of the air that carries the ball lightning.

At the same time, it should be noted that a number of properties of ball lightning can be included in the list of basic properties in the future, if sufficient detailed statistics of observations appear on them.

Such properties of ball lightning, for example, include:

1. The ability to interact in a certain way with metal, wood, and soil.
2. The ability to move relative to the air at a certain speed.
3. The ability to have a specific internal structure.
4. The ability to make certain sounds.

Analysis of ball lightning models shows that many models have common problems. Like, models of ball lightning with an internal energy source face serious difficulties when trying to explain such basic properties of ball lightning as: stable levitation in the air, the ability to exist for 100 seconds or more, the ability to rotate during the observation time, the ability to pass through the glass without destroying it. At the same time, ball lightning models with an external power source are currently unsatisfactory, mainly because this external source continues to remain undetected.

TABLE 1. The list of the basic properties of ball lightning.

№	Property	Observations, %*	Number of cases**	Source
1	Preservation of the volume	96	1990	[4]
2	The stability of the spherical shape	91	1830	[4]
3	The absence of any significant heat flow at a distance < 1 m	91	270	[3]
4	Stable levitation in the air	75	1310	[4]
5	The ability to be born on metallic conductors	66	750	[4]
6	The ability to explode	46	1390	[4]
7	The ability to emit luminous flux ≥ 3000 lm	10	60	[3]
8	The ability to maintain stability when the diameter is ≥ 0.5 m	9,3	90	[3]
9	The ability to exist for ≥ 100 s	7,1	70	[3]
10	The ability to ignite flammable substances that come in contact with them	6,4	130	[4]
11	The ability to spin during the observation time	5,1	90	[4]
12	The ability to produce chemical changes in the air	5,0	100	[4]
13	The ability to be born during lightning phenomena in the clouds	4,3	50	[4]
14	The ability to be attracted to long conductors	3,9	70	[4]
15	The ability to avoid obstacles	2,6	50	[4]
16	The ability to pass through the slit with width less than its own diameter	2,0	100	[4]
17	The ability to bounce off the surface of objects when in contact with them	1,7	90	[4]
18	The ability to create radio interference	1,3	30	[4]
19	The ability to pass through the glass without damaging it	0,8	42	[4]
20	The ability to make holes in the glass	0,5	26	[4]

*Percentage of the sample in which this property is marked

** Rounded to tens with the exception of the last two properties.

Conclusion. The paper considers the properties of compact long-lived luminous formations in the atmosphere, known as ball lightnings. The set of the basic properties of a ball lightning selected by criteria is presented: their specificity for a ball lightning, availability of observation statistics for them, unambiguity of interpretation and reliability of determination by means of human perception organs. In total, it is possible to identify 20 basic properties of ball lightning. The criterion for the reliability of these properties is the presence of a sufficiently large observation statistics for each of them and their presence in independent data banks of ball lightning observations. The presented properties can be useful for evaluating theoretical models of ball lightning, as well as for evaluating the degree of compliance of laboratory analogues of ball lightning with the natural original.

1. F. Arago, Thunder and lightning. Paris. 1838. SPb, 1885.
2. M. Stenhoff, Ball lightning: An unsolved problem in atmospheric physics. New York. Kluwer Academic and Plenum Publishers, 1999.
3. I.P. Stakhanov, On the physical nature of ball lightning. M. Nauchny`j mir, 1996.
4. A.I. Grigoryev, Ball lightning. Yaroslavl. YarSU, 2010.
5. W. Brand, Der Kugelblitz. Hamburg. H.Grand, 1923.
6. S. Singer, The nature of ball lightning. New York. Plenum, 1971.
7. J. D. Barry, Ball lightning and bead lightning: Extreme forms of atmospheric electricity. New York. Plenum, 1980.

8. I. M. Imyanitov, D. J. Tihy, Beyond the laws of science. M. Atomizdat, 1980.
9. B.M. Smirnov, Observational properties of ball lightning, *Sov. Phys. Usp.*, 1992, 35 (8), pp. 650–670.

ON ELECTRIC FIELD DISTRIBUTION THE NEAR A CHARGED SPHERE. HIGH-ENERGY BALL LIGHTNING AND ITS BIG CHARGE

Vladimir L. Bychkov^{1,2}, Igor I. Esakov² and Denis V. Shestakov³

¹M.V. Lomonosov, Moscow State University, Moscow, Moscow, Russia

²Moscow Radiotechnical Institute RAN, Moscow, Russia

³N.N. Semenov Federal Research Center for Chemical physics, Russian Academy of Sciences, Moscow, Russia

Introduction. Estimates of the electric field strength near charged spheres with the parameters of the observed high-energy ball lightning [1] raise the question of why there is no realization of a discharge to the ground and its runoff. A similar question arises in the study of the corona discharge. Such studies [2] show that at high fields near the tip of the charged electrode, fields of the order of 10^8 V/m are created, comparable to fields near the surface of the BL, and the discharge begins to pulsate (Trichel pulsations), and there is no breakdown to the Earth. The, so-called, impossibility of this, is often used to show that ball lightning is an uncharged or weakly charged object. The presence of a high electric field on the sphere allows one to explain its levitation at high values of its own weight.

The electric field of a strongly charged sphere. We will study this situation from the point of view of electrostatics and plasma physics. Consider a charged sphere in an electric field created by a high intrinsic charge. Moreover, the electric field on the surface of the sphere is large due to the presence of a large charge and is able to ionize the air.

It is known from electrostatics that the electric field near a charged sphere changes depending on the distance R from it, as

$$E = E_s (r_s / R)^2, \quad (1)$$

where E_s and R are the electric field at the surface of the sphere and the distance to the sphere respectively, r_s is the radius of the sphere. The value of the electric field E_s is associated with the electric charge on the sphere Q and the radius of the sphere with a known relation $Q = 4\pi\epsilon_0 \cdot r_s^2 E_s$, and in the absence of plasma the relation is (Coulomb's law)

$$E = \frac{Q}{4\pi \cdot \epsilon_0 \cdot R^2}, \quad (2)$$

where ϵ_0 is the dielectric constant of air.

If the initial electric field is greater than the so-called breakdown field, at which the rate of ionization processes is compared with the rate of electron death, then the field on the sphere is related to the breakdown field by the relation following from (1)

$$r_{br} = r_s (E_s / E_{br})^{0.5}, \quad (3)$$

is the distance from the center of the sphere to the ionization boundary, is the breakdown electric field (in air $E_{br} \approx 2,8 \cdot 10^6$ [3]). A plasma layer is formed in the space around the charged sphere $r_s < r < r_{br}$, which shields the electric field of the charged sphere.

At high electric field strengths in air, as shown by calculations [4], a plasma is formed in air consisting mainly of NO^+ ions and electrons; therefore, the electron concentration for estimates can be determined on the basis of a simplified equation

$$\frac{dn_e}{dt} = q + \nu_i \cdot n_e - \alpha_{dr} \cdot n_e^2. \quad (4)$$

Here t is time, q is the rate of production of electron-ion pairs in air due to fast background particles, $\nu_i = \nu_i(E/N)$ is the frequency of ionization of air molecules by electrons in an electric field (its value depending on the parameter E/N (N -concentration of gas particles) can be found in [5], α_{dr} is the coefficient of dissociative recombination of electrons and molecular ions, for estimates $\alpha_{dr} = 2 \cdot 10^{-7} (T_g/T_e)^{0.5}$, cm^3/s [5], T_g , T_e the temperature of the gas and electrons, respectively. Under conditions of quasi-neutral plasma $n_e = N_i$, N_i is the concentration of positive ions. In the plasma layer occurs creation of charged particles wherever $E \geq E_{br}$. For further discussion from [5] follows, for example, that at $E=4 \text{ MV/m}$ ($E/N=150 \cdot 10^{-15} \text{ V cm}^2$), the characteristic time of an increase in the electron concentration up to $n_e \sim 10^{21} \text{ cm}^{-3}$ is $t \sim 3 \cdot 10^{-9} \text{ s}$.

Determine how plasma affects the electric field in the layer $r_s < r < r_{br}$. According to [15], the potential of a charged sphere in a plasma is defined by the expression

$$\varphi = \frac{Q}{4\pi \cdot \varepsilon \cdot R} \cdot \exp(-R/r_D), \quad (5)$$

where at high voltage electrodes r_D is the radius of Poisson [9]

$$r_D = (\varepsilon_0 \cdot U / e^2 n)^{0.5}.$$

Here e is the electron charge, n is the concentration of plasma particles, U is high voltage.

The absolute value of the electric field determined on the basis of the expression (5) has the form

$$E_p = \frac{Q}{4\pi \cdot \varepsilon_0 \cdot R^2} \cdot \exp(-R/r_D) (1 + R/r_D). \quad (6)$$

Estimates show that for breakdown fields $n \approx 10^{15} \text{ cm}^{-3}$ [4], and $U \sim 30 \text{ kV}$ in this case (6) simplifies and takes the form

$$E_p = \frac{Q}{4\pi \cdot \varepsilon_0 \cdot R^2} \cdot R/r_D \cdot \exp(-R/r_D) \equiv \frac{Q}{4\pi \cdot \varepsilon_0 \cdot R^2} \cdot F,$$

where explicitly

$$F \equiv 10^x = R/r_D \cdot \exp(-R/r_D) = R \cdot \left(\frac{e^2 \cdot n}{\varepsilon_0 U} \right)^{0.5} / \exp R \cdot \left(\frac{e^2 \cdot n}{\varepsilon_0 U} \right)^{0.5}.$$

In Table 1 can see the values of x (U , eV, n , cm^{-3})

TABLE 1.

$U / n, \text{eV} \cdot \text{cm}^3$ R, cm	10^{-11}	10^{-10}	10^{-9}
10	$-4.25 \cdot 10^3$	$-1.34 \cdot 10^3$	$-4.26 \cdot 10^2$
50	$-2.13 \cdot 10^4$	$-6.73 \cdot 10^3$	$2.12 \cdot 10^3$

F has a small quantity and it tends to zero; therefore, we can assume that the plasma field $E_p = 0$. So

$E_p = 0$ in the range $r_s < r < r_{br}$ of the sphere radius and for all the concentration of plasma particles. Thus, plasma processes turn off the electric field. Plasma at high fields appears during times $t = 10^{-9}$ and smaller, so the electric field turns off. Therefore, no breakdown phenomena in this spatial region occurs. At $r \geq r_{br}$ the electric field is again expressed by the law of Coulomb $E = \frac{Q}{4\pi \cdot \varepsilon_0 \cdot R^2}$. At

$r = r_{br}$, $E = E_{br}$ the thickness of the layer where electrons and ions are generated is of the order of the plasma oscillation length - the Debye thickness (in our case, see above). In this layer in the stationary

case from (4) follows $0 = q + v_i \cdot n_e - \alpha_{dr} \cdot n_e^2$, or $n_e = \frac{v_i}{2\alpha_{dr}} + \frac{1}{2} \cdot \sqrt{\left(\frac{v_i}{\alpha_{dr}}\right)^2 + 4 \frac{q}{\alpha_{dr}}}$.

A specific value of the electron concentration at a near breakdown electric field $E=3,3$ MV/m turns out to be [13] under stationary conditions of the order of $n_e \sim 5 \cdot 10^{15} \text{ cm}^{-3}$, when $T_e \sim 3 \text{ eV}$, and the Debye radius turns out to be $r_D = 1,8 \cdot 10^{-5} \text{ cm}$. This layer can manifest itself by a barely visible halo in the air, which often presents in observations.

Conclusions. The presence of a sphere with a high charge and electric field larger than breakdown one will significantly affect the ability of the sphere to ionize the surrounding air. Air breakdown in the area between the surface of the sphere and the radius of the breakdown field will not occur. This increases the lifetime of a charged ball relative to neutralization by air ions. The movement of the sphere can have features when the sphere approaches the surface of the Earth.

1. A.I. Nikitin, V.L. Bychkov, T.F. Nikitina, A.M. Velichko, and V.I. Abakumov Sources and components of ball lightning theory. *International Interdisciplinary Conference "Euler Readings MRSU 2017" IOP Publishing IOP Conf. Series: Journal of Physics: Conf. Series*, 2018, 996, pp. 012011, doi :10.1088/1742-6596/996/1/012011.

2. Yu.S. Akishev, M.E. Grushin, I.V. Kochetov, A.P. Napartovich, N.I. Trushkish. Establishment of Trichel pulses in the negative corona in the air. *Plasma Physics*, 1999, 25(11), pp.1-6.

3. N.V. Ardelyan, V.L. Bychkov, I.V. Kochetov, K.V. Kosmachevskii, Prebreakdown air ionization in the atmosphere, in *The Atmosphere and Ionosphere: Elementary Processes, Monitoring and Ball Lightning*, V. Bychkov, G. Golubkov, A. Nikitin, Eds. Springer, 2014, pp. 69-111.

4. N.V. Ardelyan, V.L. Bychkov, K.V. Kosmachevskii On Electron Attachment and Detachment Processes in Dry Air at Low and Moderate Constant Electric Field. *IEEE Transactions on Plasma Science*, 2017, 45(12), pp. 3118-3124, doi: 10.1109/TPS.2017.2773021.

5. N.V. Ardelyan, V.L. Bychkov, D.V. Bychkov, K.V. Kosmachevskii CHAPTER 3. Electron-beam and non-self-maintained driven plasmas for PAC. In *Plasma assisted combustion, gasification and pollution control*. Ed. I.B. Matveev. Outskirts press. Denver, Colorado, 2013, 1, pp. 183-372.

6. B.M. Smirnov Introduction to plasma physics. Moscow. Nauka. 1982.

7. Y. P. Raiser, Physics of gas discharge. Moscow. Nauka, 1992.

8. Tables of physical quantities. Handbook Ed. Kikoin I.K. Moscow. Atomizdat 1976.

9. Kudryavtsev A.A., Smirnov A.S. Tsendin L.D. Physics of glow discharge. Saint-Petersburg. Lan-Publishers. 2010.

ATMOSPHERIC ELECTRODE MICROWAVE DISCHARGE IN ARGON FLOW: EXCITATION MODES AND SPATIO-TEMPORAL PATTERN

Vladimir M. Chepelev, Sergey N. Antipov, Makhach Kh. Gadzhiev

Joint Institute for High Temperatures RAS, Moscow, Russia

Introduction. A non-equilibrium plasma is a plasma where the energy of an electric field is transferred first to the electrons of a weakly ionized gas and then – to neutral particles. This stimulates certain atomic-molecular transformations and a whole spectrum of radicals and excited particles with high reactivity is formed. The main feature of the generation of non-equilibrium plasma is that electrical energy is used mainly for the production of high energy electrons without significant heating

of gas. For a long time, low-pressure glow discharges (for example, capacitive RF discharges) were used in order to treat various surfaces with a non-equilibrium plasma. Such type of plasma is characterized with a low density of atoms in the gas phase and, therefore, with a low collision frequency between electrons and heavy particles. Recently, non-equilibrium plasma processes have been increasingly studied in microwave discharges and plasma jets on their base, which have a much higher charge density and, as a consequence, higher reactivity compared to RF discharges [1]. In this case, the temperature of the gas in the jet can be reduced to almost room temperature. This allows plasma treatment of heat-sensitive material surfaces including biological objects. The development of microwave plasmatrons in recent years has received increased attention [2-4].

In this work, we study spatio-temporal features of a microwave discharge and the plasma jet on its base in continuous and pulse-periodic magnetron operating modes.

Experimental apparatus and results. A prototype of a multipurpose microwave plasma torch previously developed allows generating a cold atmospheric pressure plasma jet in the external portable discharge chamber (plasma torch) with a wide outlet of about 5 cm² in cross-sectional area on the basis of a microwave electrode discharge. The microwave plasmatron operates at a frequency of 2.45 GHz, has a microwave power in the waveguide of up to 2.5 kW, power in the burner of up to 200 W and includes the following components (Fig. 1):

- 380/220 V high-voltage power supply,
- microwave unit, including water-cooled magnetron,
- waveguide system (sectional, with two sets of flanges with gaskets) with splitter and water cooling,
- 50 Ohm coaxial cable 2 m long with two N-connectors,
- plasma torch with six electrodes in common chamber.

The splitter is a coupling loop located on the narrow wall of the waveguide and loading the N-type coaxial connector. The design of the splitter allows you to change the magnitude of coupling by rotating the plane of the loop.

At the maximum coupling magnitude (the loop plane is perpendicular to the wide walls of the waveguide) about 10% of the microwave generator power is withdrawn to the coaxial line (taking losses into account). The plasma torch represents a payload and is connected to the splitter using a cable assembly.

The torch consists of a cylindrical discharge chamber containing 6 rod electrodes placed parallel to each other which form an equilateral hexagon in cross section.

A microwave discharge is initiated when a plasma-forming gas flows through the torch, and the discharge channels are formed between the rod electrodes and the inner wall of the discharge chamber near the chamber outlet (6 channels). It should be noted that the low-temperature argon plasma generator MicroPlaSter β by ADTEC Plasma Technology Co Ltd is a closest analogue of the developed plasma torch [5]. However, this generator is a highly specialized device designed for biomedical applications. Its use in laboratory research is difficult: MicroPlaSter β has large weight and size, non-portable design and limited ranges of operating parameters.

The characteristics of the microwave discharge mostly depend on the magnetron operating modes, which are determined by a power supply. The operation of the magnetron from a conventional AC network with a frequency of 50 Hz and a voltage of 220 V can be simplified as follows. The magnetron power supply unit is designed to generate the necessary voltages driving a magnetron, namely anode voltage and filament voltage. Its main high-voltage elements are: a transformer, a booster capacitor and a diode. The last two elements double the voltage of a high-voltage transformer. Such a high voltage is necessary on the anode of a magnetron for its normal operation. Let us briefly describe the process of voltage doubling. In the first half-cycle a high voltage from the transformer charges the capacitor through the open diode. At that, the voltage on the magnetron is zero since the

open diode shunts it. In the second half-period the diode is closed, the capacitor voltage is applied to the magnetron and the voltage of the negative half-period of the high-voltage winding of the transformer is added as well. These two voltages are summed and create a high operating voltage on the magnetron. When a sufficient voltage is reached on the magnetron anode, the magnetron starts operating at a frequency of 2.45 GHz. When the voltage on the magnetron drops below the threshold value, the magnetron stops generating. Then, at the end of the half-wave, voltage drops to zero due to a decrease in the voltage amplitude of the high-voltage transformer winding and discharge of the booster capacitor. Thus, the magnetron operates (generates) in a pulse mode (50 pulses per second) and only in one half-cycle of high-voltage transformer. In each pulse magnetron outputs a 2.45 GHz wave packet (50-Hz modulated 2.45-GHz microwaves).

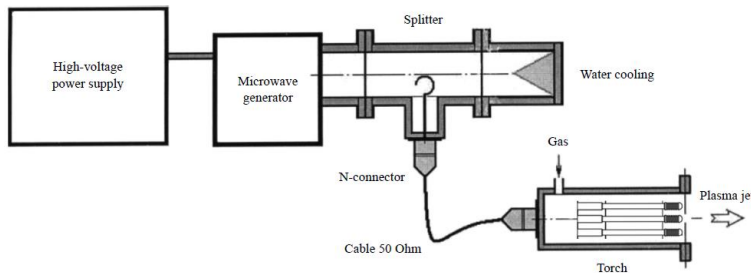


FIGURE 1. Sketch and a view of the microwave plasmatron with an external plasma torch [2, 4].

an oscilloscope, the probe of which was placed in the region of the cold plasma jet near the torch outlet. The signal level reached several volts. It was found that the pulse-periodic mode was carried out with a frequency of 50 Hz, and pulse duration of 15 ms. In the continuous mode, the floating potential oscillated weakly around a constant value depending on the distance to the torch with amplitude of about 15-20%.

A general view of the discharge channels from the outlet of the plasma torch is shown in Fig. 2. In continuous mode, imaging was carried out by means of the VS-FAST high-speed color video camera with a frame rate of up to 10000 frames per second. In the pulse-periodic mode, in addition to the excitation of the discharges “electrode-chamber”, the occurrence of spark channels “electrode-electrode” was

For the plasmatron developed, three-phase AC circuit is used with three step-up transformers and three diode arms. The circuit makes it possible to conduct the operation of the magnetron in a continuous mode. In order to implement a pulse-periodic mode of magnetron operation, one of the diode arms in the circuit was switched off.

High purity Ar (99.998%) is used as a plasma-forming gas. Ar flow rate is regulated in the range from zero to several slm. For diagnostics of plasma generation in the jet we used floating potential measuring by means of

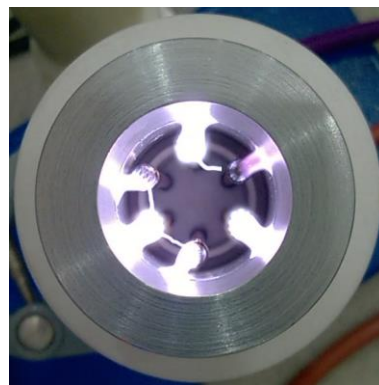


FIGURE 2. Microwave discharges in the plasma torch (outlet view) at pulse-periodic (left) and continuous (right) magnetron operation modes

observed. In the continuous mode, spark discharges did not occur, and the discharges between the electrodes and the inner wall of the chamber were glow type.

Conclusion. A prototype of a multipurpose microwave 2.45-GHz-plasmatron with an external portable discharge chamber (plasma torch) with 6 rod-like electrodes and wide 2.5-cm-diameter output was described. A spatio-temporal pattern of electrode microwave discharges in continuous and pulse periodic modes of magnetron power supply was studied by means of high-speed video imaging. Temporal features of plasma generation in a cold plasma jet on the base of the discharge were investigated by means of probe floating potential measuring by oscilloscope. In the continuous mode the formation of diffuse channels of a glow type between the electrodes and the inner wall of the chamber was observed. In the pulse-periodic mode, in addition to glow discharges, spark electrode-electrode and electrode-chamber channels arise.

The work is supported by the Russian Foundation for Basic Research №19-08-00844.

1. S.V. Dresvin, A. A. Bobrov, V. M. Lelevkin, et al., VCh- i SVCh-plazmotrony (RF and microwave plasmatrones), Novosibirsk: Nauka, 1992 [in Russian].
2. A.V. Prokopenko, K.D. Smirnov, *Prikladnaya Fizika* (Applied Physics), 2011, 5, pp. 64-68 [in Russian].
3. V.N. Tikhonov, S.N. Aleshin, I.A. Ivanov, et al., *J. Phys.: Conf. Ser.*, 2017, 927, pp. 012067.
4. S. Antipov, A. Chistolinov, V. Chepelev, et al., in "Microwave Discharges: Fundamentals and Applications", Proc. of the X Int. Workshop on Microwave Discharges (MD-10), Moscow: Yanus-K, 2018, pp. 205-210.
5. T. Shimizu, T. Nosenko, G. Morfill, et al., *Plasma Proc. and Polym.*, 2010, 7 (3-4), pp. 288-293.

HYDRODYNAMIC MODEL OF COMPACT LONG-LIVED LUMINOUS FORMATIONS IN THE ATMOSPHERE

Andrey V. Chistolinov

Joint Institute for High Temperatures of the Russian Academy of Sciences, Moscow, Russia

Introduction. In this paper, we consider a hydrodynamic model of compact long-lived luminous formations in the atmosphere, known as ball lightnings. Ball lightning according to the most complete definition, which we will adhere to here is a natural, compact, long – lived, self-luminous formation, floating freely in the air, preserving its volume and close to spherical shape, the occurrence of which correlates with thunderstorm activity.

Ball lightning is rarely at rest. As a rule, ball lightning moves horizontally at a speed from tenths to several meters per second. Moreover, this seems to be the speed of movement relative to the air, since such speeds are also recorded in rooms where the speed of air movement, as a rule, does not exceed a few tenths of a meter per second. In addition, there are a number of reports that describe the movement of ball lightning in the open air against the wind [1,2]. But this is not the most surprising feature of the ball lightning movement. According to some reports, ball lightning can pass through the glass without damaging it. This ability of ball lightning was first described in [3]. Later, this ability of ball lightning was confirmed by a large number of observations (42 observations) in [2]. A discussion of this effect can also be found in [4].

To date, most of the proposed models assume that the horizontal movement of a ball lightning can be explained either by air flows or electric fields.

However, this assumption is poorly consistent with the numerous cases when the ball lightning moves along an almost closed trajectory in a room with one open entrance. For example, when it enters a room through an open door or window, and then goes around the room and leaves it through

the same entrance [1]. The speed of horizontal movement of the ball lightning can be almost an order of magnitude higher than the typical speed of air movement in a closed room. Electric forces, in this case, cannot be the cause of such a movement, since due to the potentiality of the electric field, the work of electrostatic forces in a closed circuit is zero.

In addition, the movement of ball lightning was repeatedly observed in all-metal aircraft [5], which also contradicts the hypothesis that the electric field is the main cause of the movement of ball lightning.

Finally, a charged body under the influence of electric fields or air currents is obviously not able to pass through the glass without making a hole in it.

Model. With a fairly large number of different hypotheses about the nature of ball lightning, the number of models describing its behavior is very small. As a rule, there are hydrodynamic models based on the assumption that the ball lightning substance is a homogeneous liquid phase with a density close to that of air [6-13].

In this paper, we will try to develop this approach and show that a hydrodynamic model can be used to construct a theory from which all the key features of ball lightning dynamics known from observational data can be derived.

The most developed of the hydrodynamic models is the model of N.I. Gaidukov [6-11]. In his works, ball lightning is modeled as "an ideal incompressible liquid of limited volume with a density equal to the density of air ... and the problem of ball lightning movement in air streams is reduced to the study of the flow of this liquid in a moving viscous air medium" [8].

The Gaidukov ball lightning model allows numerical modeling of the behavior of ball lightning when it interacts with obstacles, the passage of ball lightning through small holes or slits, and so on [6-11].

However, it can be shown that the Gaidukov model incorrectly describes the dynamics of ball lightning. In the Gaidukov model, ball lightning moves only under the influence of air streams and electric fields. It is known that both of these factors do influence the movement of ball lightning [2], however, as shown above, they are not enough to explain the movement of ball lightning. As for the passage of a ball lightning through the glass without damaging it, it is generally impossible in the Gaidukov model.

If we want the model to correctly describe the observations of ball lightning, then the ball lightning substance must be able to pass through objects such as glass, that is, in general, it must be able to pass through an atomic substance. In other words, the substance of ball lightning and air should be considered as two mutually permeable media.

However, the correct dynamic model must also describe the rotation of the ball lightning. Thus, according to [2], this rotation is observed in 5.1% of cases, which is about 90 cases. This number of cases of rotation observation can hardly be attributed to an error.

At first glance, the problem of ball lightning rotation is solved in the Gaidukov model. In fact, in this model, ball lightning matter is considered as an ideal liquid that experiences neither internal friction nor friction with atomic matter. Thus, in the Gaidukov model, the moment of rotation of the ball lightning will be preserved.

However, from the point of view of modern physics, the Gaidukov model is inconsistent. Indeed, according to modern ideas about matter, there are no ideal liquids in the Eulerian sense. Only a quantum liquid can have the properties of an ideal liquid. So, if the particles that make up the liquid are bosons, then in the case of quantum degeneration, it will go into a superfluid state (the bose-liquid state). In such a liquid, the rotational movement will persist for a long time.

Therefore, in order to correctly describe all the dynamic properties of a ball lightning, the ball lightning substance in the proposed model is considered as a light incompressible bose-liquid that can move through an atomic substance.

This hydrodynamic model, in addition to the translational movement of the ball lightning and changes in its shape, also describes the rotation of the ball lightning and its passage through solid obstacles, such as glass. Thus, it includes all the main features of ball lightning dynamics known from observational data. This is actually most important for the empirical model.

We will introduce a special term for the ball lightning substance in this model – we will call this substance tied matter (TM). The system of equations for tied matter can be written on the basis of L.D. Landau's system of equations for bose-liquid [14, 15]. It can be shown that tied matter cannot be any of the known types of condensed matter. The possible physical nature of tied matter, as well as its behavior in the approximation of classical hydrodynamics, was discussed in [16].

In [16] it is shown that the proposed model of tied matter explains the features of the translational motion of a ball lightning in the approximation of classical hydrodynamics [2]. In particular, an interesting feature of the proposed model is that in the case that the temperature of the tied matter of ball lightning is above the ambient temperature (and this is a necessary condition for the existence of ball lightning), the system of equations of tied matter and air environment has no stable stationary solutions in the reference system of air. A stable solution exists only for the motion of the ball lightning relative to the air at a certain speed, which is determined by the temperature of the tied matter of the ball lightning. And this speed is equal to:

$$u_b = \sqrt{\frac{2\gamma \varepsilon}{7\mu kT_a}} \quad (1)$$

where

- u_b is velocity of the ball lightning relative to the air for a homogeneous air medium,
- μ is coefficient of friction of TM with atomic matter, per one molecule of atomic matter,
- γ is binding energy of a single molecule of atomic matter with TM,
- ε is heat flow from tied matter to atomic matter per molecule of atomic matter,
- T_a is temperature of the atomic matter.

Thus, according to the proposed model, a ball lightning cannot be at rest for a long time – it must move, which is in good agreement with the observational data [2]. And it will move until it runs out of all of its energy.

Moreover, this movement will largely depend on the inhomogeneities of the air environment. In particular, it will be controlled by temperature gradients existing in the surrounding air [16], which, as shown in the works of V. P. Torchigin [17, 18], explains such features of the behavior of ball lightning, known from observations, as the ability to bypass obstacles and the ability to find holes in obstacles.

The rotation of the ball lightning. According to the proposed model, the rotation of the ball lightning is explained by the rotation of the superfluid component of the tied matter of the ball lightning [16] and, thus, cannot be described in the framework of classical hydrodynamics. In the simplest case, the rotation of the superfluid component is described by a system of equations (2) [14, 15]:

$$\begin{cases} \nabla \times \vec{u}_s = 0 \\ \nabla \cdot \vec{u}_s = 0 \end{cases} \quad (2)$$

The system of equations (2) excludes the possibility of existence of rotation of the superfluid component without singularities. The rotation of the superfluid component, as is known from the theory of superfluidity [14, 15], occurs due to the appearance of vortex filaments in the liquid volume. The solution of the system (2) for a single straight-line vortex thread in a boundless medium, taking into account the quantization of the angular momentum, has the form [15]:

$$\vec{u}_s = \frac{l\hbar}{mr^2} \vec{r} \times \vec{e}_z, \quad (3)$$

where $l = 1, 2, 3, \dots$, \vec{e}_z is unit vector, m is effective mass of a particle of tied matter.

In this case, only values with $l = 1$ correspond to a stable quantum vortex thread according to [15]. That is, the consequence of quantization of the angular momentum and the requirement of sustainability is that all vortex filaments in the superfluid component of tied matter are the same.

According to L.D. Landau's theory of superfluidity, the motion of vortex filaments occurs together with the superfluid component of tied matter [14, 15]. That is, when the ball lightning rotates due to the rotation of the superfluid component of the tied matter, the vortex threads will rotate with it. In real conditions, the rotation of a ball lightning as a whole will always be overlaid with a complex vortex pattern of the flow of a superfluid component of tied matter. This type of flow of the superfluid component is called quantum turbulence. A ball lightning containing vortex threads of tied matter, due to the complex nature of the motion of the superfluid component, will have an internal structure like a rotating ball of entangled threads. And this picture of the internal structure of the ball lightning is indeed often noted by eyewitnesses [2].

Conclusion. The paper proposes a hydrodynamic model of compact long-lived luminous formations in the atmosphere, known as ball lightnings. The proposed model predicts such features of the ball lightning behavior as: the ability to move relative to air, the ability to bypass obstacles in its movement, the ability to find holes in obstacles, the ability to pass through the glass without destroying it, the ability to rotate without noticeably slowing down the speed of rotation. In addition, this model explains the appearance of an internal structure in the form of a tangle of threads in a rotating ball lightning.

1. Stakhanov I.P. On the physical nature of ball lightning, M. Nauchny`j mir, 1996.
2. Grigoryev A.I. Ball lightning, Yaroslavl, YarSU, 2010.
3. Brand W. Der Kugelblitz, Hamburg, H.Grand, 1923.
4. Bychkov V.L., Nikitin A.I., Ivanenko I.P., Nikitina T.F., Velichko A.M., Noisikov I.A. Ball lightning passage through a glass without breaking it, *J. of Atmospheric and Solar-Terrestrial Physics*, 2016, 150, pp. 69-76.
5. Singer S. The nature of ball lightning, New York, Plenum, 1971.
6. Gaidukov N.I., *Zhurnal Tekhnicheskoi Fiziki*, 1986, 56(9), pp. 1797-1801.
7. Gaidukov N.I., *Zhurnal Tekhnicheskoi Fiziki*, 1987, 57(10), pp. 1899-1903.
8. Gaidukov N.I., *Zhurnal Tekhnicheskoi Fiziki*, 1989, 59(2), pp. 88-94.
9. Gaidukov N.I., *Zhurnal Tekhnicheskoi Fiziki*, 1991, 61(11), pp. 49-56.
10. Gaidukov N.I., *Zhurnal Tekhnicheskoi Fiziki*, 1992, 62(2), pp. 27-33.
11. Gaidukov N.I., *Zhurnal Tekhnicheskoi Fiziki*, 1992, 62(9), pp. 130-135.
12. Natyaganov V.L. An electrocapillary eddy model of ball lightning, *Dokl. Phys.*, 2003, 48(6), pp. 319-322.
13. Nickel K.L. A fluid dynamical Model of Ball lightning and bead lightning. Science of Ball Lightning. Ed. Y.-H. Ohtsuki, World Scientific, Singapore, 1989.
14. Halatnikov I.M. The theory of superfluidity, M. Nauka, 1971.
15. Putterman S. Superfluid hydrodynamics, Amsterdam, North-Holland Pub. Co., 1974.
16. Chistolinov A.V. Atmosphere, Ionosphere, Safety. Proceedings of VI International conference. Part 1, Kaliningrad, 2018, pp.326-330.
17. Torchigin V.P., Torchigin A.V., Behavior of self-confined spherical layer of light radiation in the air atmosphere, *Phys. Lett. A*, 2004, 328, 189.
18. Torchigin V.P., How ball lightning finds out slots and holes to penetrate through them, *Optik*, 2019, 194, 163126.

STUDY OF NON-STATIONARY PROCESSES AND COMPACT LUMINOUS FORMATIONS IN A DISCHARGE WITH A LIQUID CATHODE

Andrey V. Chistolinov¹, Roman V. Yakushin², Maksim A. Khromov¹ and Mikael A. Sargsyan¹

¹Joint Institute for High Temperatures of the Russian Academy of Sciences, Moscow, Russia

²D. Mendeleev University of chemical technology of Russia, Moscow, Russia

Processes occurring in discharge systems in which one of the electrodes is a liquid have been studied to a much lesser extent than the corresponding processes in discharge systems with solid electrodes [1]. In this paper, a DC discharge with a liquid cathode was investigated.

An important feature of the DC discharge with liquid cathode is that this type of discharge creates nonequilibrium mass transfer of the liquid cathode into the gas phase under the action of ion bombardment of liquid cathode similar to cathode sputtering process in a classical glow discharge [2, 3]. At the same time, according to direct measurements carried out in [4], about 500 molecules of atomized water fall on the surface of an aqueous solution per ion. It is assumed that the intensive transfer of the liquid cathode material to the gas phase determines the nature of gas streams in the discharge zone.

In this paper, non-stationary processes in the discharge plasma with a liquid cathode were studied using high-speed imaging methods. A tungsten electrode with a diameter of 2 mm, located above the surface of the conducting liquid, was used as the anode in the discharge system. A solution of sodium hydroxide in deionized water with a concentration of 60 mg/l (specific electrical conductivity of 330 $\mu\text{S}/\text{cm}$) was used as a liquid cathode. The discharge occurred at atmospheric pressure in air. The experiment used a flow-through discharge cell. The average temperature of the solution in the discharge cell was maintained at 12 ± 1 °C. High-Speed video recording was performed using the Phantom VEO 410S colored video camera, with a recording speed of up to 10,000 frames per second.

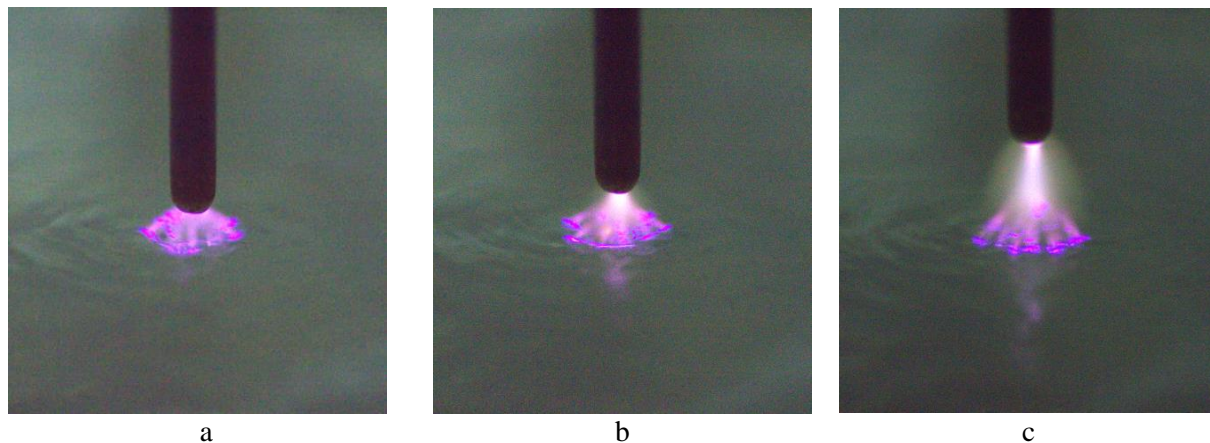


FIGURE 1. Images of a discharge with a liquid cathode in the presence of external lighting. Exposure 250 microseconds, discharge current 100 mA, distance between the electrode and the liquid surface: a) 1 mm, b) 2mm, c) 4mm.

High-speed video recording showed the presence of heterogeneity of the discharge, which is manifested most strongly near the surface of the liquid. According to the data of high-speed video recording near the surface of the liquid cathode, the discharge channel is divided into separate filaments Fig. 1. The same discharge channel near the metal electrode can remain undivided Fig. 1b, 1c.

At the same current, the distance between the branching point of the discharge channel into the filaments and the liquid surface practically does not depend on the distance between the electrode and

the liquid surface, if this distance is greater than the distance between the branching point and the liquid surface Fig. 1B, 1C. Otherwise, the growth of filaments begins directly from the electrode Fig. 1A.

High-speed video shows that filaments and the cathode spots move randomly along the surface of the liquid. Typical speeds are on the order of a few meters per second. In this case, the number of filaments and cathode spots does not remain constant, but fluctuates over time around a certain average value.

The study of high-speed images showed that each cathode spot bends the surface of the liquid and is located in a small deepening (cavity). It is assumed that the presence of cavities under the cathode spots is due to jets of non-equilibrium steam that flow from the area of the cathode spots as a result of ion bombardment. When the cathode spots move along the surface of the liquid, these cavities follow them. As a result, capillary waves are formed on the surface of the liquid, which diverge concentrically from the discharge zone Fig. 1A-1C.

Interestingly, when using a solution of sodium hydroxide in deionized water with a concentration of 60 mg/l at the studied currents (up to 100 mA), there is no characteristic yellow glow of the discharge, which occurs even with a very small impurity of sodium in the gas-discharge plasma. As shown by spectral measurements, the characteristic sodium line of 589 nm in the emission spectrum of the discharge plasma is completely absent. This suggests that sodium ions are practically not transferred to the gas phase under such conditions.

However, the study of high-speed video recordings showed that from time to time in the discharge zone in various places, flashes of the characteristic yellow color suddenly appear Fig. 2.

High-speed video footage show that the duration of these flashes is in most cases less than 100 microseconds. Apparently, the appearance of these flashes is associated with the ejection of microdrops from the surface of the liquid into the discharge zone. Since the solution contains sodium ions, the evaporation of microdrops in the plasma leads to yellow flashes caused by the glow of the sodium line when it enters the plasma. The mechanism for ejecting such microdrops into the discharge zone remains unclear.

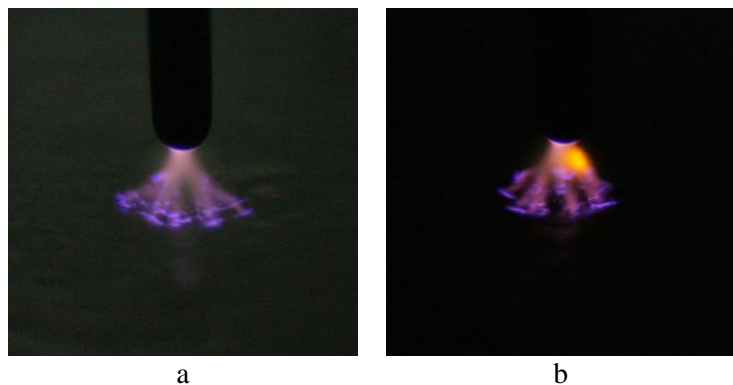


FIGURE 2. Images of a discharge with a liquid cathode in the absence of external lighting. Exposure 250 microseconds, discharge current 100 mA, distance between the electrode and the liquid surface 2 mm. a) normal combustion, b) yellow colored flash

As a result of electrophysical measurements, the values of the cathode potential drop and the field strength in the discharge for the test solution at given discharge currents were estimated. The dependence of the voltage at the discharge cell on the distance between the electrode and the solution surface was close to linear Fig. 3. The linearity of this relationship allows us to extrapolate the voltage drop at the discharge cell to the zero distance between the electrode and the liquid surface.

The cathode potential drop can be estimated as the difference between the extrapolated value of the voltage drop at the zero value of the discharge gap and the value of the voltage drop on the discharge cell when the electrode actually touches the solution. In the studied current range (50-100 mA), the cathode potential drop was found to be independent of the discharge current value and equal to 610 ± 50 V. The average field strength in the discharge gap was determined

by the angle of the straight line on the graph of the dependence of the voltage drop on the discharge gap value Fig. 3.

For a discharge current of 50 mA, it was about 600 V/cm, for a discharge current of 100 mA, about 500 V/cm. The obtained values of the cathode potential drop and the field strength in the discharge gap indicate that this type of discharge is not an arc discharge, but is closest in its electrophysical characteristics to a glow discharge. At the same time, the non-stationary processes observed in this type of discharge are atypical for a glow discharge and are caused, as we believe, by an intensive process of non-equilibrium transfer of the liquid cathode material to the gas phase in the discharge zone.

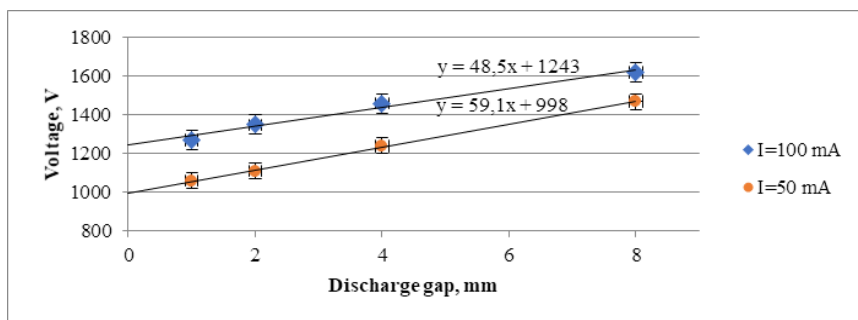


FIGURE 3. Dependence of the voltage drop at the discharge cell on the size of the discharge gap for a discharge with a liquid cathode at different currents

This work was partially supported by the Russian Foundation for Basic Research grant № 20-08-00898.

1. A.M. Kutepov, A.G. Zakharov, A.I. Maksimov, Vacuum-plasma and plasma-solution modification of polymeric materials, M. Nauka, 2004. 497 p.
2. P. Bruggeman, C. Leys, Non-thermal plasmas in and in contact with liquids, *J. Phys. D: Appl. Phys.*, 2009, 42(5), pp. 1-28.
3. P. Bruggeman, M. Kushner, B. Locke et al., Plasma-liquid interactions: a review and roadmap, *Plasma Sources Sci. Technol.*, 2016, 25, pp. 053002.
4. N.A. Sirotkin, D.L. Gurina, Effect of transfer processes of liquid cathode components on the properties of DC discharge at atmospheric pressure, *International journal of applied and fundamental research*, 2016, 11, pp. 94-99.

MICRO BALL LIGHTNING AND STATES, EFFECTS, AND DIRECTIONS FOR RESEARCH

Edward Lewis

<http://www.scientificrevolutions.com>

Introduction In 1992, based on Matsumoto's earliest descriptions of micrometer-sized ring traces associated with excess energy/apparent elemental changes in a palladium electrode as well as changes of morphology of the electrode that are reminiscent of reported ball lightning effects such as in this reference[1], I proposed to Matsumoto and Ken Shoulders that the experiment was producing micrometer-sized ball lightning. Matsumoto quickly believed the idea. Around this time, Ken Shoulders started investigation on transmutation effects associated with the micro ball lightning that he called "EVs."

Through studying the available ball lightning literature around 1990, I realized that the idea of microscopic-sized ball lightning was a new idea that no one else researched. The smallest size of ball lightning that anyone had proposed or described in the scientific literature and ISBL Proceedings was

perhaps 2 millimeters in size. This makes sense because natural ball lightning or electrical sparks smaller than this would be difficult to see, or they would go unnoticed as something important. Especially, the micrometer-sized ones are difficult to see unless they are brightly shining and move slowly.

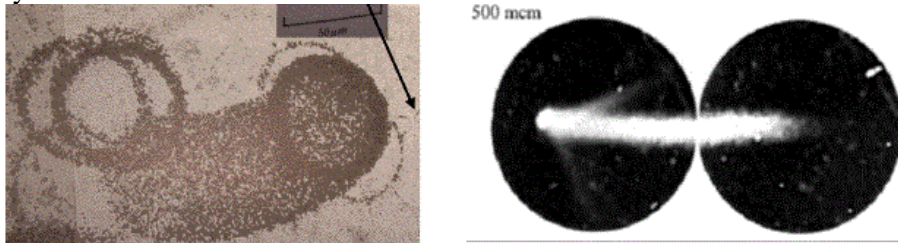


FIGURE 1. Left: Example of Matsumoto's hopping and skimming ring traces. 50 micrometers in diameter [2]. Right: Example of Urutskoev comet-like traces, a kind of trace that Matsumoto had previously called "white holes" [3]

In 1992, I imagined what is the minimum size of ball lightning that is possible. I didn't see any reason that they should not be atomic-scale or even smaller in size

since their internal structure and makeup is really not known. Various people had proposed models such as tokamak-looking toroids, but there was no evidence. So I started to propose that even atoms themselves might convert to become ball lightning. Then, I imagined that if this were so, then the unusual properties of ball lightning we see exhibited on the macroscopic scale is mirrored in atomic behavior in the atomic scale. So the micro ball lightning idea can explain many anomalies.

For example, I wrote a paper called "Considerations about Plasmoid Phenomena and Superconductivity Phenomena"[4] and proposed that just as it is known that ball lightning can go through glass and perhaps other insulators without damaging them, micro ball lightning might be used to carry electricity from one place to another through materials and that this is an origin of superconductivity phenomena. I also proposed that maybe patches of atoms or aligned "filaments" of atoms in materials that were in the ball lightning (or "plasmoid") state in materials might themselves also transmit electricity superconductively with little loss of electricity.

After reading about Ken Shoulder's research extensively such as by reading his patents and after getting into correspondence with him, I believed that his research was very important for ball lightning and transmutation researchers to understand.

But to my surprise, in the 1990s, instead of transmutation researchers getting interested, they largely ignored him, Matsumoto and me. They would not allow him to present at the ICCFs even though he had already published the most ground-breaking articles in *Fusion Technology* and also had the most numerous articles published in that journal. So Matsumoto started to only attend the ISBLs in the late 1990s, and he published there for a few years. After about the year 2000, interest in the transmutation field died away significantly. Then, as you know, the ISBLs were discontinued due to lack of interest.

Current Russian Research Progress Various groups have been studying the behavior of microplasmoids. Especially, Bogdanovich et. al's experimental research [5] describes amazing slowly moving plasmoids or plasmoid atomic patches and the plasmoid cluster configuration shown. I hope researchers replicate his results.

Future Research Avenues The Ohmase-type gases, whatever they are, actually produce microplasmoids when burned as evidenced by the effects on the metals and other materials that Bob Greenyer tested. This is a mysterious phenomena. I don't even know what the gas is, but gases with similar behaviors have various names including Brown's gas. That is a research topic. The gas or at least the flame or parts of the flame may be "plasmoid state" atoms (not regular plasma, but atoms in the plasmoid state). This would help explain the ball lightning traces.

The atoms of materials such as Tungsten contacted with the approximately 100 degree Celsius flame "slosh" like liquid, and I suggest that the atoms temporarily exist in the plasmoid state. For information on the plasmoid atomic state hypothesis and evidence, see, for example, this reference [6]. I think that the plasmoid state is the 7th state of matter including the BEC and Fermi states and the 5th natural state of atoms discovered so far.

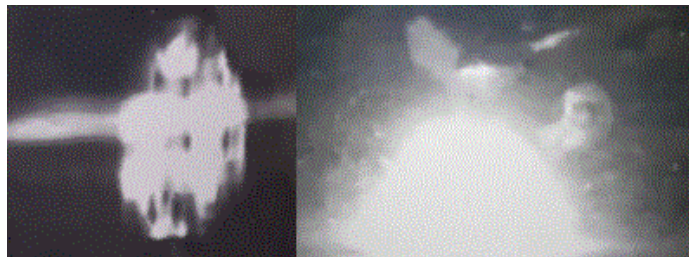


FIGURE 2. Left: The microplasmoid cluster by Bogdanovich is about 10 millimeters long and 5 millimeters wide.[5] Right: Is the dark plasmoid a hexagonal dark-state plasmoid? [5].

A theoretical advance would be to understand the structure and behavior of the micro ball lightning more. In Russia, in the late 1990s, Urutskoev reported discovering the emission of micrometer sized "strange particles" and elemental transmutation similar to Matsumoto's research.[3] He proposed that these are "Lochak monopoles," and this became the main hypothesis of most of the Russian experimental researchers.

However, many of the experimenters ignore the concept that these are microplasmoids like ball lightning. I don't have space here to explain the reasons, but the "monopole" hypothesis is not correct. This point of view overlooks the unusual behaviors of micro ball lightning such as the "black state" properties. So I hope that researchers study more about Ken Shoulders' experimental research and broaden the scope of their understanding of ball lightning.

Safety: Russian medical researchers have been in the forefront of trying to understand the medical effects of these micro ball lightning. This is important. Shoulders and Bostick both died of cancer. Until it is clear what their effects are, please be cautious. I think that these travel further than several tens of centimeters. Both Shoulders and Urutskoev wrote that some traveled more than a meter. It is clear that some natural ball lightning travel maybe 100s of meters or kilometers at times. Shoulders showed experimentally that there are black and white states. He warned that regular shielding materials don't stop black state ones [7].

Energetic and Destructive Behaviors The energy concentration of microplasmoids like ball lightning is astonishingly high. The electrical charge density of single micrometer-sized ball lightning-like plasmoids was too high to be believed by physicists such as Richard Feynman when Shoulders started to try to quantify energy density in the late 1970s. However, Feynman later said that he believed that the theoretically impossible energy density was valid based on the experimental evidence.[8] Many physicists such as W. Bostick noticed that the energetic effects could not be explained by known physics.

Urutskoev concluded that "monopoles" (or micro ball lightning) may have caused the Chernobyl disaster because he had previously found the same kinds of traces that he had found in materials impinged on by the tiny objects emitted from parts of his experimental devices at the site of the Chernobyl disaster [9].

The instrumental atomic behavior for the anomalies is the state shift from normal dormant atoms to ball lightning (or plasmoid) state atoms. In this state, the behavior of atoms is very different than normal, so transmutation and material motion happen at low temperatures. Just as ball lightning behave, atoms in such a state behave.

If researchers continue to discover the energetic behavior and fundamental structure of ball lightning, they'll see how some patches of long-lived ball lightning state materials without energy stimulation continue to emit destructive plasmoids that create tunnels through materials and pitting and trenches on materials and how they can destroy electronics long after an experiment is over. It is

known that they may explode, and as plasmoid-state patches or ball lightning travel around, they can transmute elements changing the chemical composition of materials they touch. In my opinion, people are just beginning to understand plasmoids, and it may be decades before people understand their properties well and can use them well, so I think any physical modeling is premature.

Another theoretical advance would be to try to understand the similar plasmoid/ball lightning effects happening around the universe since it is more and more evident that not only are plasma and electrical effects happening everywhere in our universe that we can observe and in and on the sun, but as I tried to show in a recent article [10] and video [11], there are plasmoid markings similar to those made by micro ball lightning objects all over the planets, moons, and asteroids wherever we look. In this era, it does seem to be that the fundamental structure of the universe is plasmoids.

1. T. Matsumoto, Observation of gravity decays of multiple-neutron nuclei during cold fusion, *Fusion Technology*, 1992, 22(1).
2. T. Matsumoto, Artificial Ball-Lightning – Photographs of Cold Fusion, 1995.
3. L.I., V.I. Liksonov, and V.G. Tsinoev, Observation of transformation of chemical elements during electric discharge, *Annales de La Fondation Louis de Broglie*, 2002, 27(4), <http://aflb.ensmp.fr/AFLB-274/aflb274p701.pdf>
4. E. Lewis, Considerations about Plasmoid Phenomena and Superconductivity Phenomena, manuscript 1995, <http://www.padrak.com/ine/ELEWIS5.html>
5. B.Yu. Bogdanovich, N.V. Volkov, N.A. Len, and A.V. Nesterovich, Video recording of long-lived plasmoids near objects exposed to remote and direct effects of high-current pinch discharges, *Technical Physics*, 2019, 64 (4).
6. E. Lewis, Traces of ball lightnings in apparatus, *Unconventional Electromagnetics and Plasmas*, 2008, Vol. 1&2.
7. K. Shoulders, Shielding from the Inevitable, manuscript 2006, <http://www.rexresearch.com/shoulders/ShieldingFromTheInevitable.pdf>
8. K.G. Jaehning and J. Roberts, The frontiersman, *Science History Institute*, 2016, <https://www.sciencehistory.org/distillations/the-frontiersman>
9. L.I. Urutskoev and V.N. Gerasko, On the possible mechanism of Chernobyl accident, http://www.recom.hotmail.ru/CHER_INC_1.doc
10. E. Lewis, “Strange particles”: plasmoids and the need for a paradigm change in physics, *Infinite Energy*, issue 147, September 2019.
11. E. Lewis, Plasmoids and Paradigms, November 3, 2019 <https://www.youtube.com/watch?v=TYvyBcpP1jE>.

“STRANGE” RADIATION AND BALL LIGHTNING

Anatoly I. Nikitin, Vadim A. Nikitin, Alexander M. Velichko, Tamara F. Nikitina

N.N. Semenov Federal Research Center for Chemical Physics, Russian Academy of Sciences, Moscow, Russia

In 2000, Urutskoev et al. [1] discovered “strange” particles appearing at an electric explosion of titanium foil in distilled water. These particles leaved long traces on photographic film, wrapped in black paper. The velocity of these “strange” particles was estimated as 20-40 m/s and their energy as 700 MeV. Traces were located inside the photographic emulsion, this led to the conclusion that the source causing the blackening of the film flew in a plane parallel to the plane of the emulsion. The similar tracks were repeatedly observed by other researchers.

Fig. 1 shows a trace of a strange particle appeared during test of industrial high-voltage equipment accompanied by the formation of an open electric arc [2]. The trace has a form of a dotted line consisted of elements of complex shape. Many models of such “strange” particles have been proposed

– hydrogen clusters, magnetic monopoles, dark matter, plasma drops, etc. However, the authors of the proposed models do not even try to answer questions: 1) Why these particles fly strictly along the emulsion? 2) Why, moving at a speed of only 20 m/s, they are able to act on the emulsion as particles with the energy about 1 GeV? 3) What is the mechanism of their action on the emulsion? 4) Why does the appearance of the tracks look like prints on the ground of car tire treads? 5) Why does the spot area change along the track? 6) Why curved tracks are recorded along with direct tracks? The common thing that unites the authors of the models is that almost all of them emphasize the analogy of the behavior of objects with the behavior of ball lightning and even call them “microscopic ball lightning”.

Indeed, there is such an analogy. Natural ball lightnings have an energy reserve, an uncompensated electric charge and are able to move along the surface of conductors and dielectrics. Ball lightning continuously loses the charge. As ball lightning approaches the conductor, this charge flows in the direction of this conductor. A mechanical impulse acquired by carriers of a falling charge when moving in the field of the main charge is transmitted to ball lightning. This allows to it “push off” from the conductor and move at a certain distance from it.

In [3] the forces acting in the shell of water molecules, surrounding a cavity with ions, are calculated. It was shown that two opposite forces act on the molecule in the shell: a force F_a , attracting the molecule to electric charge of ions, and a force F_r , repelling the molecule from the shell. Let us consider what a cluster can be with a total charge of ions $Q_1 = 4.5 \cdot 10^{-12}$ C. Such a charge, for example, is possessed by $n = 2.8 \cdot 10^7$ hydroxyl ions $(OH)^-$. Let the ion diameter be $4 \cdot 10^{-10}$ m, the area occupied by one ion, $s = 16 \cdot 10^{-20}$ m², and the ions are placed on the surface of a sphere of radius R . The surface area of the sphere is $S = 4\pi R^2 = s \cdot n$, hence $R = (s \cdot n / 4\pi)^{1/2} = 6 \cdot 10^{-7}$ m. The electric field created by the charge $Q = 4.5 \cdot 10^{-12}$ C at a distance $R = 6 \cdot 10^{-7}$ m, $E = Q / 4\pi\epsilon_0 R^2 = 10^{11}$ V/m, which is greater than $E_{min} = 2 \cdot 10^9$ V/m, determined by the Langevin criterion $E_{min} > 2 \cdot 10^9$ V/m [3]. This means that the water molecules in the shell are completely polarized. Ions stretch the shell with the force $F_Q = Q^2 / 8\pi\epsilon_0 R^2 = 2.53 \cdot 10^{-1}$ N. The water molecule with dipole moment $p = 6.327 \cdot 10^{-30}$ C·m is attracted to the charge placed in the center of the sphere with the force $F_a = pQ / 2\pi\epsilon_0 R^3 = 2.37 \cdot 10^{-12}$ N.

At the same time, it is pushed out from the shell by neighboring molecules with a force $F_r = 2.69 \cdot 10^{-9} \cdot (R - R_0)^{-1.3} = 2.69 \cdot 10^{-9} \cdot (6004.5)^{-1.3} = 3.3 \cdot 10^{-14}$ N. (Here R and R_0 are in angstroms (10^{-10} m) and $R_0 = -4.5$ [3]). The resulting force, acting on the molecule, is $F_t = F_a - F_r = 2.337 \cdot 10^{-12}$ N. On the surface of the shell with a radius $R = 6 \cdot 10^{-7}$ m, $n_w = 2.82 \cdot 10^7$ water molecules can fit. The compression force of the shell with one layer of water molecules is $F_\Sigma = F_t \cdot n_w = 6.59 \cdot 10^{-5}$ N. This force is 3840 times less than the force F_Q . The F_Q force can be compensated if the number of layers of water molecules in the shell is equal to 3840, and its thickness is $a = 4 \cdot 10^{-10} \times 3840 = 1.54 \cdot 10^{-6}$ m. As a result, we obtained a cluster with a cavity radius $R = 6 \cdot 10^{-7}$ m and an outer radius of $R_1 = R + a = 2.14 \cdot 10^{-6}$ m. The mass of the cluster M_1 is equal to the mass of the shell. Its volume is $V_{sh} = 4\pi [(R + a)^3 - R^3] / 3 = 4 \cdot 10^{-17}$ m³, and the mass $M_{sh} = \rho_w V_{sh} = 4 \cdot 10^{-14}$ kg. (Here $\rho_w = 10^3$ kg / m³ is the density of water).

Let us consider a possible scenario for the formation of traces on photographic films. Suppose that a cluster with radius $R_1 = 2.14 \cdot 10^{-6}$ m, charge $Q_1 = 4.5 \cdot 10^{-12}$ C and mass $M_1 = 4 \cdot 10^{-14}$ kg moves in the direction of the film. When the edge of the cluster is at a distance $L = 15 \cdot 10^{-6}$ m from the film surface, a small cluster is separated from it with charge $q_1 = 4.5 \cdot 10^{-14}$ C and mass $m_1 = 4 \cdot 10^{-16}$ kg and begins to move to the film. This cluster moves under the action of the force $F_{q1} = Q_1 q_1 / [4\pi\epsilon_0 (R_1 + x)]^2$, where x varies from 0 to L . Having passed the path L , the small cluster will gain energy $W_{q1} = (Q_1 q_1 / 4\pi\epsilon_0) \cdot [1/R_1 - 1/(R_1 + L)] = 7.447 \cdot 10^{-10}$ J = $4.65 \cdot 10^9$ eV. Its speed is $v_1 = (2W_{q1} / m_1)^{1/2} = 1.929 \cdot 10^3$ m/s, and the impulsive moment is $m_1 \cdot v_1 = 7.7184 \cdot 10^{-13}$ kg·m/s. The large cluster will acquire the same moment, it will begin to move upward from the film at a speed $V_1 = (m_1 \cdot v_1) / M_1 = 19.3$ m/s and gain energy $W_{Q1} = M_1 V_1^2 / 2 = 7.45 \cdot 10^{-12}$ J.

A cluster with a charge $Q_1 = 4.5 \cdot 10^{-12}$ C creates an electric field $E_1 = Q_1/4\pi\epsilon_0 L^2 = 1.8 \cdot 10^8$ V/m at a distance $L = 15 \cdot 10^{-6}$ m. Such field is comparable in magnitude with the intensity $E_{min} = 2 \cdot 10^9$ V m, determined by the Langevin criterion [3]. Therefore, we can assume that there will be a polarization of the film material, and a force will act on the cluster, which will inhibit its movement. When the work of this force becomes equal to the kinetic energy of the cluster, it will stop and begin to “fall” onto the film. The force acting on the cluster from the side of the polarized film is $F_d = P_1 Q_1 / 2\pi\epsilon_0 R^3$, where P_1 is the dipole moment of the polarized film section, and R is the distance between the center of charge and the film. The work of this force on the portion of the trajectory dR is equal to $dA = F_d \cdot dR$, and the full work until the cluster stops

$$\int_{R_0}^R F_d dR = -\frac{P_1 Q_1}{4\pi\epsilon_0} \cdot \frac{1}{R^2} \Big|_{R_0}^R = \frac{P_1 Q_1}{4\pi\epsilon_0} \left[\frac{1}{R_0^2} - \frac{1}{(R_0 + \Delta R)^2} \right]. \quad A = \quad (1)$$

Here $R_0 = 10^{-4}$ m is the cluster height above the film surface at the moment of the beginning of the upward movement, and $R = (R_0 + \Delta R)$ is the height that it will reach.

Figure 2 shows the result of a numerical calculation of the change in cluster height above the level of separation of a small cluster from it $L = 15 \cdot 10^{-10}$ m. For the parameters of the cluster and the film, the values $Q_1 = 4.5 \cdot 10^{-12}$ C, $M_1 = 4 \cdot 10^{-14}$ kg, $D_1 = 4.28 \cdot 10^{-6}$ m are assumed. It is believed that for a separated small cluster, the charge $q_1 = Q_1/100 = 4.5 \cdot 10^{-14}$ C and the mass $m_1 = M_1/100 = 4 \cdot 10^{-16}$ kg are one a percentage of the initial values of the charge and mass of the main cluster, and these values remain unchanged despite the fact that Q_1 and M_1 decrease with each “jump”. For the dipole moment of the polarized film, the value $P_1(t) = Q_1(t) \times 2 \cdot 10^{-8}$ C·m (the decrease in charge Q_1 is taken into account for each act of separation of a small cluster). It is accepted that at $t = 0$ the lower edge of the cluster is at a distance of $1.5 \cdot 10^{-6}$ m from the emission height of the small cluster and its velocity is zero. One can notice that after five “jumps” the system switches to the alternating mode of short (0.5 μ s long) and long (1.4 μ s long) jumps with an average period of 1.86 μ s. The height of the “jump” and the duration of the “flight” increases with time. This can be explained by a gradual decrease in the charge of a large cluster and the magnitude of the induced dipole moment of the film. The reason for the alternation of long (high) and short (low) “jumps” is as follows. When a cluster “falls” from a large height, it acquires a great speed. To stop the cluster and reverse the direction of its velocity vector, it is necessary to spend a significant part of the pulse acquired by it when a small cluster was emitted. As a result, the cluster begins to move up at a low speed and, accordingly, “falls” also at a low speed. The next impulse of interaction of charges of a large and small cluster “throws” it to a large height. If a charged cluster has a velocity component directed along the film plane, it will leave a chain of double spots on it, separated by large intervals. These spots can merge due to the spreading of the charge and form complex traces of the type shown in Fig.1.

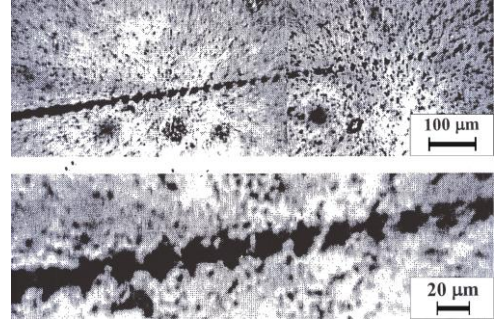


FIGURE 1. A trace of a “strange” particle on photographic film [2].

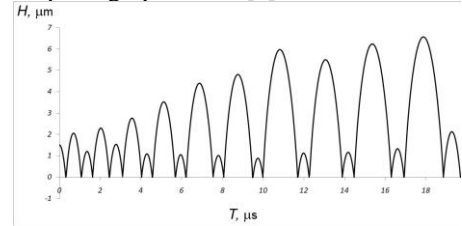


FIGURE 2. Dependence of the cluster elevation height above the level $L = 15 \mu\text{m}$ of separation of a small charge from it. Cluster parameters: charge $Q_1 = 4.5 \cdot 10^{-12}$ C, mass $M_1 = 4 \cdot 10^{-14}$ kg, diameter $D_1 = 4.28 \cdot 10^{-6}$ m. (Calculation results).

1. L. I. Urutskoev, V. I. Liksonov, and V. G. Tsinoev. Observation of transmutation of chemical elements during electric discharge. *Annales de la Fondation Louis de Broglie*. 2002, 27, 701-726.
2. A. S. Agapov, V. A. Kalensky, I. B. Kaitukov, A. V. Malyshev, R. V. Ryabova, A. V. Steblevsky, L. I. Urutskoev, and D.V. Filippov, Observation of “strange emission” and titan isotopes distortion at testing of the industrial electric equipment. In: *Proc. 12th Russian Conference on Cold Nuclear Transmutation of Chemical Elements and Ball Lightning*. Moscow, NIC FTP “Erzion”. 2005, 24-40 (in Russian).
3. A. I. Nikitin, A. M. Velichko, V. A. Nikitin, and T. F. Nikitina, Forces in the charged cluster. *Proc. 15th International Symp. on Ball Lightning (ISBL-20)*. 7-13 June 2020. Zelenogradsk, Kaliningrad Region, Russia, 2020, 70-83.

EFFECTS ARISING AT SHOOTING OF BRIGHT OBJECTS

Anatoly I. Nikitin, Vadim A. Nikitin, Alexander M. Velichko, Tamara F. Nikitina

N.N. Semenov Federal Research Center for Chemical Physics, Russian Academy of Sciences, Moscow, Russia

The main data on ball lightning properties have been derived from the descriptions of observers. However, for various reasons (emotional agitation, difficulties in verbal description, forgetfulness, etc.), these descriptions are often incomplete, contradictory, and devoid of details. Therefore, photographs and videos on which ball lightning is found are of great value. These materials allow a detailed analysis of images in the laboratory, which helps to increase the reliability of obtaining data on the properties of ball lightning. In recent years, thanks to the widespread use of digital video cameras and smartphones, a large number of images of natural luminous objects have appeared on the Internet, which has provided new opportunities for analyzing the properties of these objects. In this regard, it is necessary to discuss the specific features of photographing and image processing of these objects. What is common to all these shootings is that almost always shooting is made without aiming in the absence of time to determine and set the correct exposure. Sometimes it results in appearance of additional traces next to the image of ball lightning caused by the reflection of light from the lens. When using digital cameras and video cameras, shooting is in most cases automatic, when the exposure level is determined not by the brightness of the object, but by the total brightness of the frame. In this case, overexposure of the luminous object inevitably occurs, which results in the impossibility to reveal the details of its structure. In this regard, digital photographic equipment is absolutely inferior to film technology. For the latter, thanks to the logarithmic law of blackening of the film, there is always a hope to somehow correct the overexposed image. However for digital technology, when the level of full charge of the cell of the photosensitive array has been already reached, the subsequent action of the light only worsen the image due to the leakage of the charge to the neighboring cells. The described difficulties of image processing are not comparable with other “surprises” that may appear when using digital photo equipment. The most trivial example is the appearance of “mysterious” balls during photography in a humid atmosphere. The reason for this effect is the shooting of raindrops illuminated by the flash, which were near the camera. In the frames of the video shot in 2009 in Dolgoprudny, ball lightning looks like a bright yellow disk surrounded by a crimson-colored halo (see Fig. 1a) [1].

The first “obvious” conclusion is that a yellow ball lightning, surrounded by a corona discharge region, was shot [2]. The presence of the luminous shell of ball lightning (corona discharge) is considered as one of the properties of ball lightning, confirmed by a number of observations. However, this conclusion cannot be considered as correct. Indeed, coloring analysis of a ball lightning image showed that the RGB color receptors are off scale and most likely the true color of ball lightning was the color of the halo, the appearance of which was caused by the scattering of light in

the air. Another common image defect when shooting bright objects is the appearance of black contours around them (see Fig. 1b) [1].

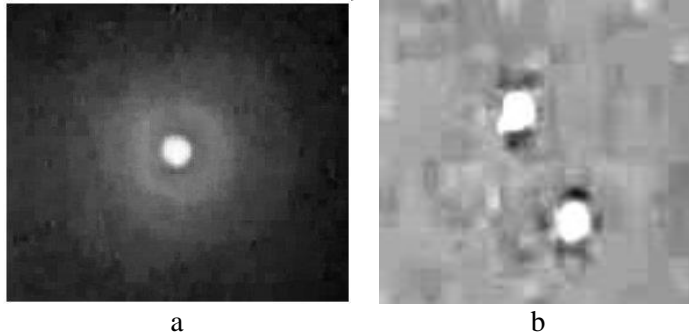


FIGURE 1. a) A view of ball lightning with a bright halo shot in Dolgoprudny. b) Image of ball lightning, separated into two parts.

image is digitally processed using a special algorithm. This algorithm includes a “sharpening” program to collect information from a 2×2 pixel field into a 1×1 pixel field. This method is called “Unsharp Mask”. The method is based on optical illusion for the human eye, which sees a sharper border, if to increase the brightness of the light region near the border and reduce the brightness of the dark region. If there is a bright object in the picture, then a dark outline appears around it, which was not there before. This procedure is also used in “Photoshop” when processing digital photographs to increase image contrast. When using the “Unsharp Mask” program, the program analyzes the image for differences between neighboring pixels. If they differ markedly from each other in brightness, the program defines these pixels as elements of the contour of the object and makes them even more contrast. All pixels surrounding light pixels become brighter, and those that surround dark pixels become darker.

Note that “digital post-processing” of the image is not the only reason for the appearance of distortion at the borders of bright objects. Local overexposure, which leads to a super-saturation of photo-electric cells with subsequent spreading of the charge on neighboring elements, can have a greater effect. This can lead to a distortion of the shape of a bright object in the direction of breaking the “roundness”, since the reading of “overexposed” pixels occurs horizontally or vertically. Therefore, the spilled charge will look like horizontal or vertical rays or angles. Well and, of course, these distortions will intensify after applying the “Unsharp Mask”.

Fig. 2a shows a view of an object shot on July 27, 2015 in the Moscow region Mitino using the NTS Desire 600 Dual Sum smartphone [3]. The image on the photosensitive matrix of the camera is presented as a slightly stretched spot surrounded by a dark outline. However, the operator stated that he had seen exactly the round object, which he called ball lightning. In this regard, the question arises: what should be trusted more: the visual impressions of observers or the “picture” created by the



FIGURE 2. a) View of a luminous object shot in Mitino [3]. b) Image of Mitino's ball lightning after digital processing a sequence of video frames [4].

video camera? This question is not pointless, since when using methods of processing “noisy” images like Fig. 2a one can find in them details resembling drone propellers (see Fig. 2b) [4].

Thus, when analyzing photographic materials, one should always take into account the possibility of the appearance of instrumental distortions of images and at the same time take into account additional information received from observers of the event. The footage should be accompanied by a description of the conditions of observation and shooting of ball lightning – weather conditions, events, preceding the appearance of ball lightning, and its behavior at a time when shooting has not yet begun. Beyond that, the contact and conversation with the authors of photos and videos can prevent the use of hoaxes and fakes, which are quite common on the Internet.

The main information that can be obtained by analyzing videos of ball lightning is data on the features of its movement, the constancy or variability of the intensity of its glow, its size and lifetime. When receiving data on the dynamics of its radiation, it is desirable to have a correctly exposed image, and to determine its size, you need to know the angular size of the ball and the distance to it. The angular dimensions are easily determined by comparing the image of ball lightning with the image of objects with known angular dimensions that fell into the video frame [3]. Well, determining the distance to the subject (and, therefore, estimating its size) is a rather difficult task. It is possible to solve this problem precisely only in rare cases, for example, when shooting was carried out by several operators with a known location [3]. However, in the overwhelming majority of cases, shooting is done by one person, and the value of its result is not high enough [1]. Fortunately, there are rare cases when the result of processing an image of a bright object, shot with a single camera, made it possible to simultaneously determine the distance to the object and its size. For instance, at 2015 on the Voronezh River a bright object, reflecting in the river, was shot. Processing of the photo allowed determine a distance to this object and its size [5].

1. S. Nikolaev, Ball lightning in Dolgoprudny. 2009.
<http://rutube.ru/tracks/3787124.html?v=f37c6f3d5dd780052a6bca48c0825685>
2. V. L. Bychkov, and A. I. Nikitin, Ball lightning: a new step in understanding. In: Bychkov V. L., Golubkov G. V., Nikitin A. I. (Eds). *The Atmosphere and Ionosphere. Elementary Processes, Monitoring, and Ball Lightning*. Springer, Cham, 2014. pp. 201-367.
3. A. I. Nikitin, A. M. Velichko, T. F. Nikitina, and I. G. Stepanov, Analysis of the unique case of ball lightning observation in Mitino, the northwest district of Moscow. *Journ. Atm. Solar-Terr. Phys.* 2018. V.179, pp. 97-104.
4. P. Kocksholt, 2019. Private communication.
5. A. I. Nikitin, A. M. Velichko, T. F. Nikitina, and I. G. Stepanov, Observation of ball lightning on the river Voronezh. In: *Proc. 5th Intern Conf. Atmosphere, Ionosphere, Safety (AIS-2016)*. 2016. P. 284-287.

BASIC STUDY OF MULTIPLE BALL LIGHTNINGS IN LINE BY LEADER TIP MODELS

Satoshi Kawano

3-1-11 Kotobuki-cho Hakata-ku Fukuoka-city 812-0884, Japan

Introduction. The author hypothesizes that Ball Lightning (BL) is a corona discharge from the leader tip which is floating in the air. BL is categorized to two types. One is a corona discharge from the positive or negative leader tip (type-1) as shown in Figure 1a. Another is a Space Stem (SS) which is a luminous plasma nucleus ahead of the negative leader tip as shown in Fig. 1b. The leader will propagate along the ambient electric field (EF) of its tip [1]. Therefore if the EF is reduced to zero, the leader tip will float in the air. Further the proper discharge from its tip will sustain the high ionization

and conductivity of the leader so that the leader is almost invisible. The ionization of the streamer is lower than that of the leader so that the streamers are luminous. Figure 1c shows the corona discharge from the needle tip that is a simple simulation of BL type-1. SS is considered a fictitious electrode in the gap [2]. This paper proposes the hypotheses of the feasible mechanism how these models produce multiple BLs.

Basic structure classification of multiple BLs. The author proposed the basic structure classification of multiple BLs on the proceedings of ISBL99 as follows.

Siamese twin Ball Lightnings (dumbbell type

Ball Lightning). Strange twin BLs have been often witnessed. Paul Sagan described that dual vertical balls rarely have a glowing filament or strand between them [3].

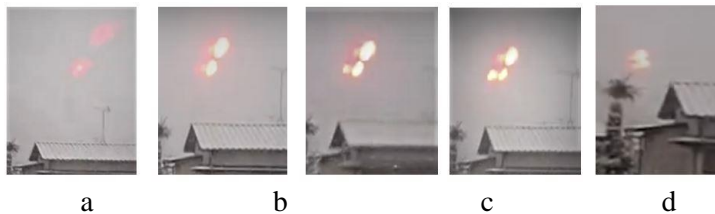


FIGURE 3. Pale red vertical twin BLs moved rapidly from an upper side and floated (a); Suddenly they changed the color from pale red to bright yellow (b); They started to spout the jet to the left side (c); The jet of lower side BL gradually became powerful, and it almost formed new BL beside it (d); Unfortunately, before forming perfect new BL, the jet lost the power, so that they returned to former twin BL (e).

to the leader and the fan shaped discharge corresponds to new BL.

Multiple Ball Lightnings in line. Most BLs which form a line will be classified into the series type in Fig. 2a. As the result of the investigation of some videos, the author categorized such BLs into two groups due to the distance of the interval between each other as below.

1) Multiple Ball Lightnings with short intervals. The intervals between each BL are under a few times of its diameter.

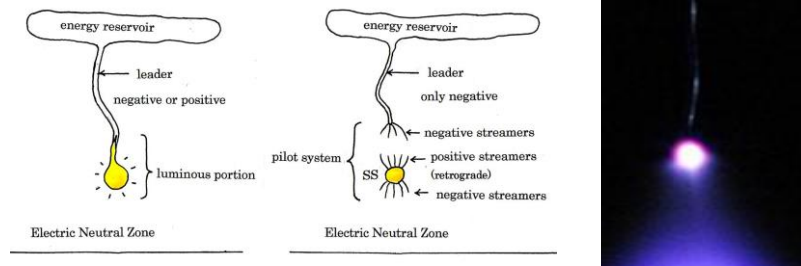


FIGURE 1. BL type 1 positive/negative (a), BL type 1 negative (b), corona discharge from conductive wire tip (c).

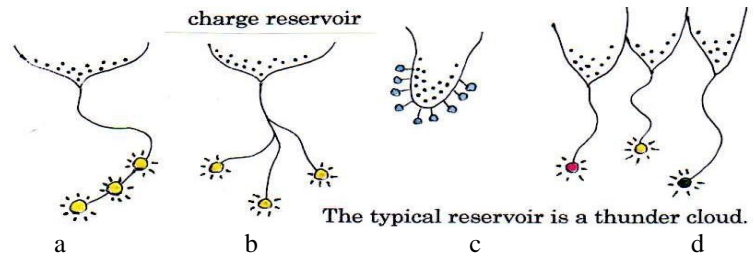


FIGURE 2. BLs which are connected in series by the leader (a). (b) indicates multiple BLs which are connected in parallel by the stepped leader. (c) shows many corona discharges with the small leader on the surface of the electric charge reservoir. Therefore each BL will have the peculiar properties.

This video suggests how multiple BLs are produced. There is a similar phenomenon in Lichtenberg figure of the surface discharge, which is termed Grite Buschel as shown in Fig.13. If the applied voltage duration gets longer, the streamers under the highest EF grow into the leader, which propagates outside of the primary discharge circle to form the new fan shaped discharge. This suggests the jet from BL is a bundle with streamers which will develop

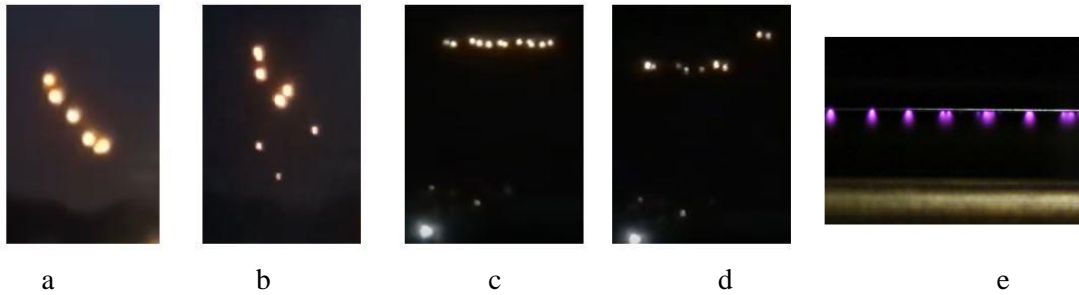


FIGURE 4. They will be positive BLs, because their diameter is large in size and the rim is fuzzy. As soon as BL of the rear disappeared, new BL emerged at the short distance ahead of BL at the head. It is queer that some BLs started to glow again soon after they had vanished once (a); Curiously, small BLs, one after another were born and fell down to the ground slowly. The following phenomena which are forms by the nature are often mistaken for the multiple BLs. (b); (c) is a superior mirage. It shows a towering phenomenon peculiar to the mirage. (d) shows the negative corona discharges on the wire. It simulates the photospheres formed on the middle part of the leader. Since they differ in the origin, they should be categorized into another type of lined BLs.

2) Multiple BLs with long intervals.

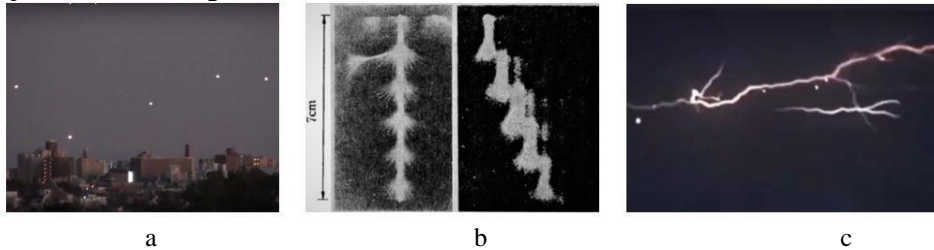


FIGURE 5. The distance between each BL is more than about 50 meters and their intervals are about the same (a).

Generally, they seem to appear at higher altitude than that of BLs with short intervals. The positive leader cannot propagate such a long distance in one step compared to negative one. Hence the author surmises that such BLs are the survivors of SS which stepped to propagate the leader. If the leader bends extremely, they change their outline into the polygon, so that it becomes hard to classify the type of the structure.

Conclusion. The author considers how multiple BLs in line are formed as follows. BL at the head propagates the leader ahead and this leader tip forms new BL of corona discharge. It is similar to the step-wise propagation of negative surface discharge along the small ditch as shown in 5b. Such a process is repeated until the electric charge from the reservoir and the discharge from all BLs become equilibrium, thus multiple BLs in line chained by the leader are produced. Curious small BL in 4b which drops downward is formed by the inflow of the comparatively small surge caused by the potential fluctuation of the reservoir. Some videos show that BL not only at the head but also at various positions van-ish and appear again at same position after a while. This will be caused by the individual changing condition of BL but not by the fluctuation of inflow electric charge to lined BLs. Further, the rear existing BLs survive at the same position without disappearing after new BL is formed. Th Ree et al. reported that SS which seemed to have died due to the decrease of the inflow electron to SS revived again by its recovery [4]. 5c shows that such balls near the lightning channel are reactivated by the inflow lightning charge. They are considered to be the plasma balls which have pretended to be dead like SS. BL is also considered the plasma ball which has such survival capability.

This author proposes on this paper that the leader tip BL models have a possibility to produce multiple lined BLs theoretically.

1. T Ohnishi and J Suganuma, Numerical simulation of BL as standing lightning, in proceedings, *5th ISBL*, 1997.
2. Les Renardieres Group, Negative discharge in long air gaps at Les Renardieres, *Electra* 74, 1981.
3. Paul Sagan, Ball Lightning Paradox of physics, iUniverse, Inc., New York, Lincoln, USA, pp. 219-290, 2004.
4. Th Reess et al., An experimental study of negative discharge in a 1.3 m point-plane air gap: the function of the Space Stem in the propagation mechanism, *J. Phys.*, 28, pp. 2306-2313, 1995.

ELECTROPHYSICAL PHENOMENA IN DIELECTRIC FLUIDS AND CLAY UNDER INFLUENCE OF CORONA DISCHARGE

Vladimir L. Bychkov¹, Vladimir A. Chernikov¹, Kirill I. Deshko¹, Pavel A. Goryachkin¹,
Tamara O. Mikhailovskaya¹, Alexander P. Shvarov¹ and Vladimir L. Shapovalov²

¹M.V. Lomonosov, Moscow State University, Moscow, Russia

²N.N. Semenov Federal Research Center for Chemical physics, Russian Academy of Sciences, Moscow, Russia

Introduction. Interest in effects of plasma in air on the surface of various dielectric materials is of a practical nature. It is associated with the study of the behavior of particles on the Earth's surface under various conditions under the influence of an electric field in thunderstorms, and in the field of action of various devices for transporting electric energy. Such studies are also of interest for solving the environmental problems of disinfecting liquids and powders, changing their conductivity, chemical composition, generating active particles in liquids and in the surface layers of dispersed materials, dispersing powders with electric discharges, in plasma chemistry, as well as activating combustibles. The fundamental question is the possibility of the appearance of structures on the surface of a liquid or dispersed material under the influence of an electric field, which belongs to the field of electrohydrodynamics [1-4], where various instabilities are considered, leading to the formation of particles, jets of other objects.

Similar objects appear in the processes of thunderstorm activity, and are manifested in the appearance of so-called ball lightning [5] with jets, protrusions and other formations on the surface. The studies carried out on the development of electro-hydrodynamic phenomena are quite extensive [1-4]. However, there is little work on plasma exposure in order to obtain information about changes in the physical and mechanical properties of the surface. We restrict ourselves to considering the effect of discharges, and primarily corona, on the surface of materials. In our previous works, attention was focused on electrohydrodynamic (EHD) features of the liquid surface under the action of corona discharge [6-9].

In [6-9], we performed the first experiments on the effect of corona discharge plasma on the surface of liquids. It has been shown that funnels appear on the surface of liquids, and for liquids such as alcohol, a mixture of alcohol and

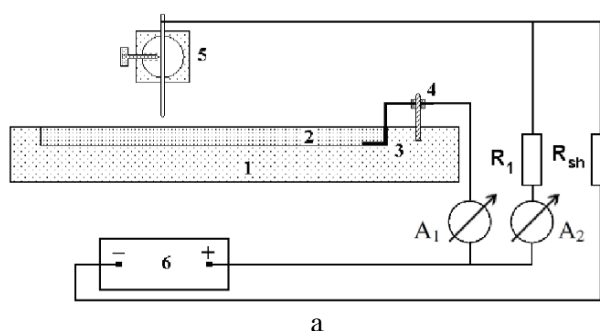


FIGURE 1. a. Schematic diagram of the experiment with a corona discharge above the surface of a liquid: 1 - dielectric cell. 2 - liquid. 3 - copper anode. 4 - rack. 5 - copper cathode. 6 - power source. b. The device of a multi-needle corona (19 needles).

glycerol, jets appear directed towards the upper electrode. Often these jets decay into droplets, which we associated with the development of the Tonks – Frenkel and Rayleigh instabilities [6]. Explanations of the causes of the appearance or non-appearance of columns of liquid did not find an explanation. In this work, we continued the study of the formation of structures in the corona discharge above the surface of liquid butyl glycol and clay powder for studying electrodynamic instabilities in order to answer the above questions.

Experimental setup. As in [6], a schematic diagram of an experimental setup with a single electrode and a photograph of a setup with several electrodes are shown in Fig. 1. The installation consists of a filled cell with liquid or dispersed material (clay) and an electrical circuit. The upper electrode has a diameter of 0.9 mm (with a radius of curvature of the tip of the needle 0.2 mm). The upper electrode (electrodes) was located at a height of 5-15 mm above the surface of the material (see Fig. 1). The electrodes were at positive or negative potential. Depending on the statement of the problem, the cells were either metal or dielectric. The discharge current was measured using a milliammeter A1, and the electrical voltage was measured using a circuit consisting of a resistance R1 and a milliammeter A2. Ampere-Volt – discharge characteristics were measured and presented in ampere-volt² coordinates, which were convenient for analyzing the properties of the corona discharges [12]. A photograph of a multi-needle device (19 needles) is shown in Fig.1b. The material for analysis was located in the cell and an electrode with negative or positive polarity was placed above the liquid perpendicular to its surface.

A high voltage generator was used as a power source, which allowed us to change the voltage of the electrode from 2 to 30 kV in increments of 250 V. The characteristic voltage was in the range of 5–50 kV. The ballast resistance was an axis of 100 MΩ. The current passing through it had a value of 50–100 μA. A discharge (ion flow [6]) was formed between the upper electrode and the surface of the liquid.

Experimental results. Electrohydrodynamic columns above the surface of butyl glycol. In this work, we used a negative corona, because, as shown in [6, 11], the results of experiments when the electrode with a positive potential was a corona electrode were in many respects similar to the results of experiments with a negative corona. In particular, it was possible to obtain funnels on the surface of all used liquids under the high-voltage electrode, as well as the stable state of two columns above the surface of butyl glycol, a photograph of which is shown in Fig. 2. Columns appeared along the edges of the funnel. Such surface behavior is similar to the behavior of columns and jets on the surface of alcohol [6].

The discharge voltage was of the order of 10 kV at currents of the order of 50 μA. Destruction of the columns into droplets did not occur at these low voltage values, since the development range of the Tonks – Frenkel instability [6], which leads to the decay of drops for alcohol, glycerol, and butyl glycol, is in the range of 17–25.

It should be noted that in experiments with a discharge above the surface of tap water, columns and their disintegration into droplets were not observed, due to its significant electrical conductivity.

Experiments with clay powder. Clay from Selivanovsky district, Vladimir region was used for research. According to the classification [5], the initial clay sample corresponds to light clay.



FIGURE 2. Columns above the surface of butyl glycol. Negative corona. The distance from the end of the needle to the surface of the liquid is 7 mm. $V = 10$ kV.

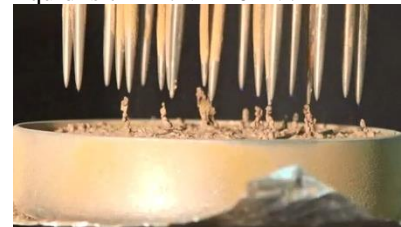


FIGURE 3. Columns under the surface of clay. Negative corona.

Under the influence of the corona discharge on clay powder with a thickness of 10 mm, under the needles at a distance of 5-10 mm from the surface under the influence of a negative corona voltage of 5-10 kV. with a current of 230 μ A, columns appeared under the 19-needle high-voltage electrode bars. Some time after turning on the discharge (1-2 frames of the video camera), nothing noticeable happened. Then, the blowing out of small particles of silt, fine and medium clay, creating a cloud (1-2 frames of a video camera). This blowing is due to the ionic wind, a corona discharge moving particles. In this case, the ion wind pressure reaches 40 Pa [6]. During the deposition of cloud particles, columns, sometimes conical, consisting of clay particles, from 1 to 7 mm high in an amount of up to 8 pieces, appeared on the clay surface (see Fig. 6c.). They were quite stable and existed without collapsing for more than 1 min. If the cloud of small particles of clay was not blown, then the columns did not form. Also, column formation was not observed when using solid powders with a particle diameter of 0.25–0.05 mm.

Conclusions. The results of experiments on the production of electrohydrodynamic structures in ethyl glycol and clay defect are presented. An essential role of the ponderomotor force is shown when an electric field acts on the dielectric particles of the studied substances in a strongly inhomogeneous field of a high-voltage corona discharge electrode.

1. G.A. Ostroumov, The interaction of electric and hydrodynamic fields. Moscow. Nauka. 1979.
2. L.D. Landau, E.M. Lifshitz, Electrodynamics of continuous media. Moscow: Nauka. 1982.
3. D.F. Belonozhko, S.O. Shiryayeva, A.I. Grigoriev, Nonlinear waves on a charged surface of a liquid. Yaroslavl Publishing House of Yaroslavl University. P.G. Demidova. 2006.
4. V.A. Saranin, Yu.V. Ivanov, Equilibrium of liquids and its stability, M.-Izhevsk: Research Center Regular and chaotic dynamics, 2009.
5. A.I. Grigoriev, Ball lightning. Yaroslavl Publishing House of Yaroslavl University. P.G. Demidova. 2006.
6. A.F. Alexandrov, V.L. Bychkov, Electrohydrodynamic features of the interaction of a corona discharge with a liquid surface, *Vestnik of Moscow University. Series 3. Physics. Astronomy*, 2011, 4, pp.67-74.
7. V. L. Bychkov, A.P. Ershov, and V.A. Chernikov, Negative Corona Discharge Over a Surface of Alcohol, *IEEE Transactions on Plasma Science*, 2008, 36(4), Part 1, pp. 1140-1141.
8. V. L. Bychkov, V. A. Chernikov et. al., Corona Discharge Over liquids with Powder Addition, *IEEE Transactions on Plasma Science*, 2011, 39(2), pp. 2640-2641.
9. V.L. Bychkov, V.A. Chernikov, et. al, Multi-Electrode Corona Discharge Over liquids, *IEEE Transactions on Plasma Science*, 2011, 39(2), pp. 2642-2643.

ON FORCE-FREE EIGENSTATES FOR BALL LIGHTNING

Geert C. Dijkhuis

Convectron N.V., Rotterdam, The Netherlands

Abstract. For ball lightning and bosonic plasmas we derive force-free solutions in quaternion form. The quaternion matrix of electromagnetic potentials enforces zero magnetic field by regularity rules. St. Elmo's fire on windshields caused a 2006 ball lightning event inside a small jet plane. We model it as elementary Bessel function in quaternion form. Our 3D solution plots scalar and vector potentials in the formation phase of this plasma ball.

Linked streamers modeling ball lightning share field topology with Bose-Einstein condensate of ultra-cold atoms trapped by lasers [1, 2]. Flux knots found in thermonuclear fusion plasmas inspired Rana's magnetohydrodynamic model of ball lightning [2]. His formulas for field, current and energy ensure stability by conservation of helicity. Threading cool ambient plasma, hot streamers with 0.05-0.20 mm width and 2-8 m length radiate like laboratory plasma torches [2]. Initial magnetic field

values 1-3 T suffice for lifetimes 3-22 s, in line with global data for ball lightning [3]. For laboratory tests Ranada suggests two transverse discharges with electrodes in rapid rotation.

AUS team created similar linked-field textures in tenuous clouds of Rubidium atoms [1]. External magnetic fields control precession of atomic spins forming skyrmion textures in their test facility. Figure 1(D) shows magnetic field topology linking each loop just once with all other loops as in the elementary Hopffibration. The topology of helical electric field lines in Fig. 1(E) shows four junctions on the polar axis, tiling concentric spheres with helicity reversal in between. Thus laser-trapped ultra-cold quantum spinscopy flux knots tied in ultra-hot fusion plasmas confined by magnetic fields.

In [1] and [2] spherical Bessel function j_0 scales the field solutions. The mathematical properties of j_0 , its higher orders j_n , their modified forms y_n and extension into complex planes are readily available [4]. Earlier electric profiles treat ball lightning as charged eigenstate of elementary quaternion functions in real matrix form [5]. Its threshold surface field secures invariant size and total charge, with central potential as evolutionary parameter. Below magnetic field adds force-free electrodynamic solutions possibly relevant to silent decay of ball lightning as in an airborne event discussed by Kawano [6]. Newroth observed ball lightning formation on the windscreen of a small jet plane underway from Las Vegas to St. Paul, USA [7]. Flying between two storms the plane was racing to avoid bad weather. From his jump seat in the cockpit between two pilots he saw St. Elmo's fire playing on the inside of the windshield before him. Just as the pilots called the St. Elmo's fire very aggressive, sparks joined together into a perfect ball at face level straight ahead of him, the ball passed his head and disappeared through the door supporting his seat. Afterwards shaken pilots downplayed the event. Newroth's cockpit-born 'perfect ball' dovetails nicely with Jennison's 'perfect sphere' floating down the isle of a commercial airliner four decades earlier.

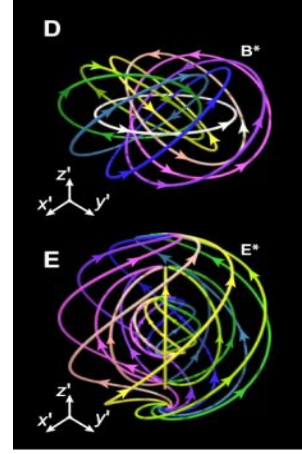


FIGURE 1. Skyrmion state links magnetic loops in (D) and twists electric field lines in (E) [1].

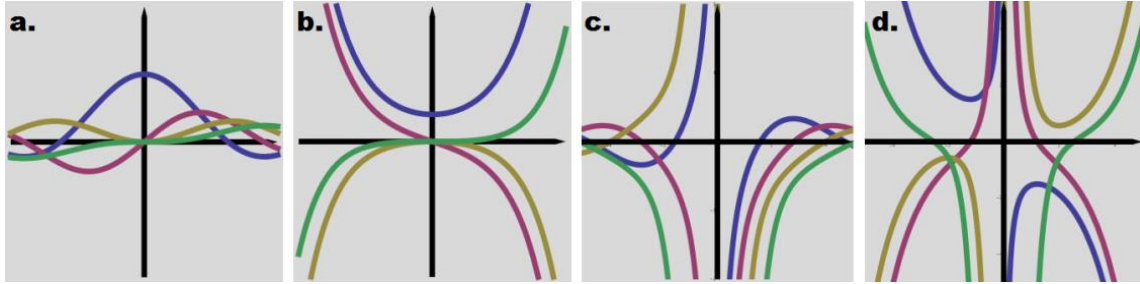


FIGURE 2. From left to right: (a) $\text{Re}[j_n(w)]$, (b) $\text{Im}[j_n(x)]$, (c) $\text{Re}[y_n(w)]$, (d) $\text{Im}[y_n(x)]$. Panels (a,b) plot real and imaginary parts of spherical Bessel functions j_n . Panels (c,d) likewise for modified versions y_n . The co-ordinate domains are $-3\chi w \chi 3$. Blue, red, yellow, green labels orders $n=0,1,2,3$.

Let Cartesian co-ordinates in a 4-vector $\{w, \mathbf{x}\}$ with $\mathbf{x}=\{x,y,z\}$ span a quaternion space [5,9]. Combine $\Phi(w, \mathbf{x})$ as scalar potential of electric field \mathbf{E} with $\mathbf{A}(w, \mathbf{x})$ as vector potential of magnetic field \mathbf{B} into 4-vector $\{\Phi, \mathbf{A}\}$ for the potentials. Define 4×4 potential tensor $\mathbb{P}(w, \mathbf{x})$ in (1) with $\mathbb{P}(w, \mathbf{x})$ in (2) as its leading 3×3 minor through:

$$\mathbf{E} \equiv \text{grad } \Phi; \quad \mathbf{B} \equiv \text{rot } \mathbf{A}; \quad -u \equiv i^2 \equiv j^2 \equiv k^2 \equiv i \cdot j \cdot k; \quad \mathbb{P} \equiv u\Phi + iA_x + jA_y + kA_z, \quad (1)$$

$$\mathbf{E} = \partial \mathbf{A} / \partial w; \quad \mathbf{B} = 0; \quad \mathbf{x} \times \mathbf{A} = 0; \quad \mathbb{P} \cdot \mathbf{x} = \mathbf{x} \partial \Phi / \partial w. \quad (2)$$

with elementary matrices u, i, j, k from **Appendix A** extending complex calculus into quaternion space. By the regularity conditions in (2) $\mathbf{B}=0$ guarantees solutions without Lorentz forces, while $\mathbf{x} \times \mathbf{A} = 0$

aligns co-ordinate vector \mathbf{x} with vector potential \mathbf{A} . Conditions (2) also connect the potentials Φ and \mathbf{A} via their w -derivatives, with $\partial\Phi/\partial w$ emerging as eigen value of minor tensor \mathbb{P} .

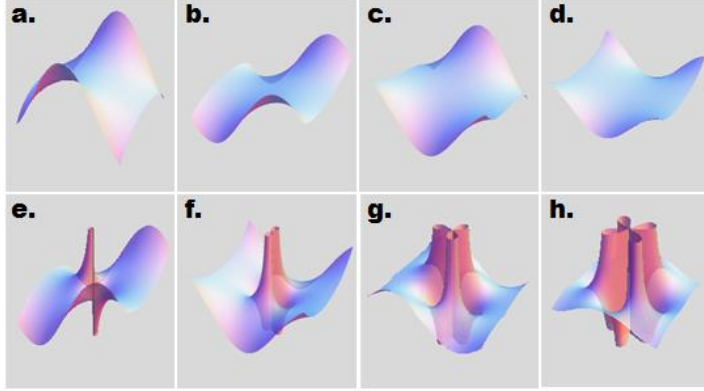


FIGURE 3. Panels ((a): $j_0(w+ix)$ (b): $j_1(w+ix)$; (c): $j_2(w+ix)$; (d): $j_3(w+ix)$) plot spherical Bessel functions j_0, j_1, j_2, j_3 in complex (w,x) -planes, and likewise for the modified versions y_0, y_1, y_2, y_3 in panels ((e): $y_0(w+ix)$; (f): $y_1(w+ix)$; (g): $y_2(w+ix)$; (h): $y_3(w+ix)$). Co-ordinate domain of w and x is $-3\chi w \chi 3$ throughout.

By quaternions space charge enters 3D solutions for atmospheric electricity [9]. Quaternion arctangents plots dipolar potential rings for thundercloud electrification. Meissner-type cusps in a ball plasma result from quaternion inversion. Swirling solutions from split-quaternions increase plasma stability by conservation of chirality [10]. Our quaternion model finds natural ball lightning deeply rooted in Hamiltonian dynamics [11]. MHD textbooks present a force-free solution for pinched plasma columns by Bessel functions [12,13]. Ball lightning as a force-free plasma sphere leads to complex Bessel functions of fractional order [4]. The explicit expressions for spherical Bessel functions j_n and modified versions y_n read:

$$j_n(\zeta) = a_n \sin(\zeta) - \beta_n \cos(\zeta); \quad y_n(\zeta) = a_n \cos(\zeta) + \beta_n \sin(\zeta); \quad \zeta = w + ix, \quad (3)$$

$$a_0 = 1/\zeta; \quad a_1 = 1/\zeta^2; \quad a_2 = 3/\zeta^3 - 1/\zeta; \quad a_3 = 15/\zeta^4 - 1/\zeta^2, \quad (4)$$

$$\beta_0 = 0; \quad \beta_1 = -1/\zeta; \quad \beta_2 = -3/\zeta^2; \quad \beta_3 = -15/\zeta^3 + 1/\zeta, \quad (5)$$

where (3) and (4) lists amplitudes α_n and β_n for orders 0 to 3 as polynomials of $1/\zeta$. Notably j_n defines y_n by switching sine and cosine in (3) with a change in sign, and vice versa.

Panel (a) in Fig.2 shows pole-free profiles for real parts of j_n along the real w -axis, where as such profiles for their imaginary parts in panel (b) diverge to infinity along the imaginary x -axis. For y_n in panels (c,d) all corresponding profiles cluster poles at the origin, and diverge to infinity along either co-ordinate axis. Underneath parametric plots in panels (a-d) of Fig. 3 illustrate pole-freedom and divergences of j_n -sheets in the complex (w,x) -plane. For y_n dipolar singularities in panels (e-h) cluster sector-wise at the origin.



FIGURE 4. Aggressive St. Elmo's fire on central cockpit window triggered Newroth's ball lightning event.

Pictures in Fig. 4 detail a jet plane like the one carrying Newroth. On the flight and cockpit photos a central windshield window as formed his ball lightning is visible. Inside their plate glass usually a thin metallic layer serves for electric de-frosting and de-icing at high altitudes

[6]. Boundary layer flow just outside the windscreen recalls our discharge nozzle tests for investigation of ball lightning [14].

For 3D plots we bring the leading modified Bessel function $y_0 = \sin(w+ix)/(w+ix)$ in quaternion form. By the addition formulas for sine and cosine the 4-vector potentials Φ and \mathbf{A} read:

$$\{\Phi, \mathbf{A}\} = j_0 = \{aw, b\mathbf{x}\}, \quad a = (-w \cos(w) \cosh(r) + r \sin(w) \sinh(h))/(w^2 + r^2), \quad r^2 = \mathbf{x} \cdot \mathbf{x}$$

$\mathbf{A} \equiv (A_x, A_y, A_z)$, $a = (w \sin(w) \sinh(r)/r + \cos(w) \cosh(h))/(w^2 + r^2)$, $\mathbf{x} \equiv \{x, y, z\}$, (6) with hyperbolic functions $\sinh(r) \equiv \frac{1}{2}(e^r - e^{-r})$ and $\cosh(r) \equiv \frac{1}{2}(e^r + e^{-r})$ that blow up along imaginary axes in Fig.2 and 3. Remarkably the 3D zero-potential sheets at $w=0$ in Eq. 6 avoid infinities in panels a,b,c,d of Fig. 5, and poles at the origin. Shape and smoothness qualify such sheets as precursors of ball lightning formation by St. Elmo's fire on flat dielectric surface as witnessed by Newroth.

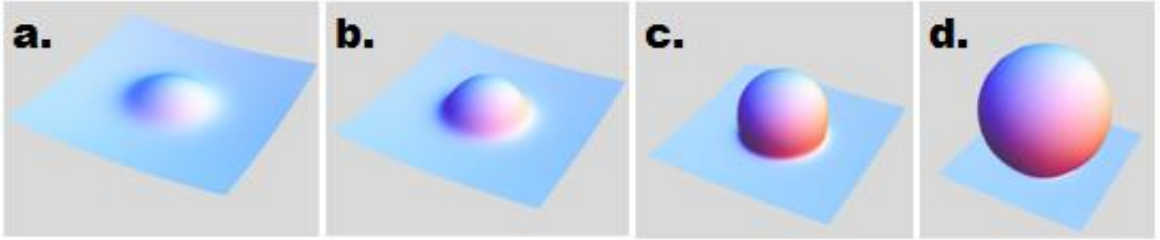


FIGURE 5. Panels ((a): $\mathbf{A}(w=0, x, y, z=1)$; (b): $\mathbf{A}(w=0, x, y, z=0, 7)$; (c): $\mathbf{A}(w=0, x, y, z=0, 4)$; (d): $\mathbf{A}(w=0, x, y, z=0, 4)$; plot successive 3D zero-potential sheets via vector potential \mathbf{A} as modified Bessel-function y_0 in quaternion form. Co-ordinates w, x, y, z are Cartesian. The domain for x and y is $\{-3, 3\}$.

Appendix A. Quaternion form for force-free electromagnetic potentials. Relativistic theory combines electromagnetic fields $\mathbf{E} = \{E_x, E_y, E_z\}$ and $\mathbf{B} = \{B_x, B_y, B_z\}$ in a traceless 4×4 tensor form through [15]:

$$\mathbb{F} \equiv \begin{bmatrix} 0 & -E_x & -E_y & -E_z \\ E_x & 0 & B_z & -B_y \\ E_y & -B_z & 0 & B_x \\ E_z & B_y & -B_x & 0 \end{bmatrix}, \quad \mathbb{f} \equiv \begin{bmatrix} 0 & B_z & -B_y \\ -B_z & 0 & B_x \\ B_y & -B_x & 0 \end{bmatrix}, \quad \begin{aligned} \Delta \mathbb{F} &= (\mathbf{E} \cdot \mathbf{B})^2 \\ \Delta \mathbb{f} &= 0 \end{aligned} \quad (7)$$

Field determinant $\Delta \Phi$ is positive or zero, and the magnetic entries in minor determinant $\Delta \phi$ always cancel. Remarkably the anti-symmetric signature of field tensor Φ returns in regular quaternion form. Replace zeroes in Φ by scalar potential Φ , and likewise the vectors \mathbf{E} , \mathbf{B} in Φ by vector potential $\mathbf{A} = \{A_x, A_y, A_z\}$. Then potential tensor Π and minor tensor π result as:

$$\mathbb{P} \equiv \begin{bmatrix} \Phi & -A_x & -A_y & -A_z \\ A_x & \Phi & A_z & -A_y \\ A_y & -A_z & \Phi & A_x \\ A_z & A_y & -A_x & \Phi \end{bmatrix}, \quad \mathbb{P} \equiv \begin{bmatrix} \Phi & A_z & -A_y \\ -A_z & \Phi & A_x \\ A_y & -A_x & \Phi \end{bmatrix}, \quad \begin{aligned} \Delta \mathbb{P} &= (\Phi^2 + \mathbf{A} \cdot \mathbf{A})^2 \\ \Delta \mathbb{P} &= \Phi \sqrt{\Delta \mathbb{P}}, \end{aligned} \quad (8)$$

with $\mathbf{E} = -\text{grad} \Phi$ and $\mathbf{B} = \text{rot} \mathbf{A}$ as standard definitions of the electromagnetic fields. We find determinant $\Delta \Pi$ as positive or zero, and its minor π as a real number. Four partial derivatives of Π define four 4×4 elementary matrices u, i, j, k in (9) that restore Π to traditional quaternion form in (10) through:

$$u \equiv \partial \mathbb{P} / \partial \Phi, \quad i \equiv \partial \mathbb{P} / \partial A_x, \quad j \equiv \partial \mathbb{P} / \partial A_y, \quad k \equiv \partial \mathbb{P} / \partial A_z, \quad (9)$$

$$-u = i^2 = j^2 = k^2 = i \cdot j \cdot k; \quad \mathbb{P} = u\Phi + iA_x + jA_y + kA_z, \quad (10)$$

with u as 4×4 unit matrix. In explicit and in vector form our twelve conditions for regularity read:

$$\begin{aligned} \partial_x \Phi &= -\partial_w A_x & \partial_y A_z &= \partial_z A_y & y A_z &= z A_y & x \partial_w \Phi &= x \partial_x A_x + y \partial_y A_x + z \partial_z A_x \\ \partial_y \Phi &= -\partial_w A_y & \partial_z A_x &= \partial_x A_z & z A_x &= x A_z & y \partial_w \Phi &= x \partial_x A_y + y \partial_y A_y + z \partial_z A_y \\ \partial_z \Phi &= -\partial_w A_z & \partial_x A_y &= \partial_y A_x & x A_y &= y A_x & z \partial_w \Phi &= x \partial_x A_z + y \partial_y A_z + z \partial_z A_z \\ \mathbf{E} &= \partial \mathbf{A} / \partial w; & \mathbf{B} &= 0; & \mathbf{x} \times \mathbf{A} &= 0; & \mathbb{P} \cdot \mathbf{x} &= \mathbf{x} \partial \Phi / \partial w, \end{aligned} \quad (11)$$

ensuring 3D force free electromagnetic solutions by extension of any complex functions. A well-known analogy links electromagnetics as above with 3D vortex flow in incompressible viscous fluids.

1. W. Lee, A. Gheorghe, K. Tiurev et al., Synthetic electromagnetic knot in a three-dimensional skyrmion, *Science Advances*, 2018, 4.
2. A. F. Ranada, M. Soler, J. L. Trueba, A model of ball lightning as a magnetic knot with linked steamers, *J. Geophys. Res.*, 1998, pp. 309-313.
3. B. M. Smirnov, The properties and the nature of ball lightning, *Phys. Rep.*, 1987, 152, pp. 177-226.
4. M. Abramowitz and I. A. Stegun, *Handbook of Mathematical Functions*, Dover Pubs., 1968, pp. 437-445.
5. G. C. Dijkhuis, Ball lightning as thermodynamic limit of the Periodic System, *The Atmosphere and Ionosphere: Dynamics, Processes and Monitoring*, 2010, pp. 349-354.
6. S. Kawano, Proposal of how ball lightning emerges in fuselage and of how it gets electric energy, *Proceedings of 2nd International Symposium on Lightning and Storm-related Phenomena*, 2017.
7. M. Newroth, Ball lightning in the cockpit of a small jet plane, Posted on The Weird Science Pagedatabase of Ball Lightning Reports, 2006, <http://www.amasci.com/weird/unusual/blll.html>.
8. R. C. Jennison, *Ball lightning*, *Nature*, 1969, 224, p. 895.
9. G. C. Dijkhuis, On 3D potential field solutions for atmospheric charge distributions, *PIERS Online*, 2010, 6(4), pp. 300-306.
10. G. C. Dijkhuis, On ball lightning formation by soliton waves. *Proceedings of the 13th International Symposium on Ball Lightning*, 2014.
11. G. C. Dijkhuis, On canonical eigenstates for ball lightning, *Proceedings of 2nd International Symposium on Ball Lightning and Storm-related Phenomena (ISL-SRP)*, 2017.
12. J. P. Freidberg, *Ideal MHD*, Cambridge University Press, 2014, p. 98.
13. P. H. Roberts, *An Introduction to Magnetohydrodynamics*, Longmans Green, London, 1967, p. 110.
14. G. C. Dijkhuis and J. Pijpelink, Performance of high-voltage test facility designed for investigation of ball lightning, *Science of Ball Lightning (Fireball)*, 1989, pp. 325-337.
15. H. P. Robertson and T. W Noonan, *Relativity and Cosmology*, W.B. Saunders Company, 1968, p. 87.

ANALYSIS OF FORCES IN THE CHARGED CLUSTER

Anatoly I. Nikitin, Alexander M. Velichko, Vadim A. Nikitin, Tamara F. Nikitina

N.N. Semenov Federal Research Center for Chemical Physics, Russian Academy of Sciences, Moscow, Russia

The presence of ions in the atmosphere can facilitate the nucleation and growth of aerosol particles. From the time of the Wilson's experiments [1] to the present day, the process of cluster formation around an ion is usually assumed as a symmetrical enveloping of an ion with a "fur coat" of water molecules polarized by the centrally symmetric electric field of the ion. However, recent calculations of the processes of cluster nuclei formation on sodium and chlorine ions by the Monte Carlo method have shown that, as the number of water molecules in a cluster increases, the ion is displaced to its boundary [2]. In this article, we attempted to find a physical explanation for the effect of displacement of an ion from a cluster. At the same time, studies of the properties of clusters formed by water molecules symmetrically located around an ion (or group of ions) remained interesting to us. Such clusters can appear during the force introduction of charges into an existing shell of water molecules. These processes can occur when strong currents flow through water in natural (thunderstorm) or industrial events.

Let us consider the configuration when exactly 6 water molecules are placed around the ion of diameter $4 \cdot 10^{-10}$ m (see Fig. 1). Let the water molecule is a sphere with diameter $d_w = 4 \cdot 10^{-10}$ m, and its dipole moment ($p = 6.327 \cdot 10^{-30}$ C·m) is represented by a dipole of length $l = 0.587 \cdot 10^{-10}$ m with the charges at its ends $q_e = 1.078 \cdot 10^{-19}$ C. Our task is to find the radial component of the force acting on the upper dipole **1** from the other dipoles (**2** - **6**). Due to symmetry of the system, the force of "pushing" of dipole **1** by dipole **2** is equal to the force of its pushing by dipole **6**, and the components

of the forces perpendicular to the radius are mutually compensated. For a three-dimensional system, one must find the number of molecules x equivalent in position to molecules **2** or **3**, which can fit in a cluster, and multiply the value of the interaction force of dipoles **2** and **1** (or **3** and **1**) by x . To determine x , you need to find the perimeter of the x -gon, in the corners of which the centers of molecules of type **2** and **6** are located, and divide it by W (the distance between the centers of the neighboring dipoles). Let denote the sides of the trapezoid $GA = W_b$ and $KB = W_s$.

In a right triangle BOE, the angle at the vertex O is $\varphi/2$. The length of the hypotenuse is $BO = R - l/2$, hence $KB = W_s = 2(R - l/2) \sin \varphi/2$. Similarly, from the triangle ADO we find $GA = W_b = 2(R + l/2) \sin \varphi/2$. The angle ψ is found from the triangle BEO: $\psi = (\pi/2 - \varphi/2)$. Let us draw a line from point K perpendicular to the axis OA. In the triangle AKC, the side $AC = l + BC$. From the triangle BKC we find $BC = W_s \cos \psi$, therefore $AC = l + W_s \cos \psi$. In the triangle KCB cathetus $KC = W_s \sin \psi$. From the triangle AKC we find D_i – the length of the diagonal of the trapezoid: $(AK)^2 = (D_i)^2 = (KC)^2 + (AC)^2 = (W_s \sin \psi)^2 + (l + W_s \cos \psi)^2 = (W_s)^2 [(\sin \psi)^2 + (\cos \psi)^2] + l^2 + 2 W_s \cos \psi = (W_s)^2 + l^2 + 2 W_s \cos \psi$. Angle ξ_1 : $\cos \xi_1 = AC/D_i = (l + W_s \cos \psi)/D_i$. To determine the angle ξ_2 , we draw a straight line GF perpendicular to the axis OA. We get triangles BGF and AGF. From the triangle BFG: $\cos \xi_2 = (BF - l)/D_i$. From the triangle AGF: $AF = W_b \cos \psi$, hence $BF = W_b \cos \psi - l$ and $\cos \xi_2 = (W_b \cos \psi - l)/D_i$. For two dipoles lying on the OA axis, the distances D_r between charges of the same sign are, respectively, $D_{r1} = 2R + l$ and $D_{r2} = 2R - l$, and the distance between charges of different polarity is $D_a = R$.

Substituting the values of the distances W_b , W_s , D_i , D_{r1} , D_{r2} and D_a for each dipole in the formula $F = k/r^2$ and taking into account the angles ψ , ξ_1 , ξ_2 and the signs of the forces acting on the charges and using Excel, one can find the sum of the forces acting on a separate dipole from the remaining dipoles (here $k = (q_e)^2/4\pi\epsilon_0$, if r is in angstroms (10^{-10} m), then $k = 1.044 \cdot 10^{-8}$ N). Figure 2 shows the dependence of the force F_r , pushing the dipole out of the sphere, on the radius of the sphere R . The dependence $F_r(R)$ is well approximated by the curve

$$F_r = 2.69 \cdot 10^{-9} (R - R_0)^{-1.3} \text{ (N)}, \quad (1)$$

(R is in angstroms (10^{-10} m), and $R_0 = -4.5$). Let us compare the force F_r with the force F_a of the attraction of the dipole with a moment $p = 6.327 \cdot 10^{-30}$ C·m to the central charge $q = 1.6 \cdot 10^{-19}$ C. The force $F_a = p \text{ grad } E$, where E is the electric field created by the charge q :

$$F_a = p \cdot \text{grad } (q/4\pi\epsilon_0 R^2) = -2pq/4\pi\epsilon_0 R^3. \quad (2)$$

The force F_a is directed toward the center of the cluster and decreases more steeply with increasing R than $F_r(R)$ (see Fig. 2). At $R = 4 \cdot 10^{-10}$ m, $F_a = 2.84 \cdot 10^{-10}$ N, which is 1.65 times greater than F_r , but already at $R = 6 \cdot 10^{-10}$ m, $F_a = 0.843 \cdot 10^{-10}$ N, which less than the value of F_r ($1.27 \cdot 10^{-10}$ N).

Thus, we conclude that a cluster with $R = 4 \cdot 10^{-10}$ m can form in the electric field of an elementary charge, however, further cluster growth, apparently, occurs without significant participation of the electric field of the central charge. The calculation shows that when the molecules are in close contact, the attraction force of a dipole, forming the second layer of the shell with a radius of $R_2 = 8 \cdot 10^{-10}$ m, to the dipole “sitting” on the shell ($F_{d2} = 0.874 \cdot 10^{-10}$ N), is in 2.45 times more than the force F_a of its attraction to the central charge $q = 1.6 \cdot 10^{-19}$ C ($0.357 \cdot 10^{-10}$ N). Therefore, it can be expected that further cluster growth will occur by attaching molecules to the ends of previously joined dipoles.

It is clear that repulsive force of the dipoles in the shell can be decreased by increase of the radius of the shell. This may be accompanied by increase of number of ions. To analyze this possibility, let us consider a spherical cavity with an inner diameter of $R_{i1} = 100$ angstroms (10^{-8} m), inside which 1000 ions of the same sign are placed (with a total charge of $Q = 1.6 \cdot 10^{-16}$ C). Due to Coulomb repulsion, the ions “stick” to the wall of the cavity and will stretch it with a force:

$$F_q = Q^2 / 8\pi\epsilon_0 R_{i1}^2. \quad (3)$$

For the above values of Q and R_{i1} , the force $F_{q1} = 1.15 \cdot 10^{-6}$ N. Let the cluster wall consist of a certain number of layers of water molecules polarized by the charge Q field. The electric field of the

charge $Q=1.6 \cdot 10^{-16}$ C at a distance of $R_{i1}=10^{-8}$ m is $1.4 \cdot 10^{10}$ V/m, this is 7 times greater than $E_{min} = 2 \cdot 10^9$ V/m, necessary for total polarization of water molecules on the shell [3]. According to formula (1), the force of pushing out a water molecule from a shell of radius $R_{i1} = 10^{-8}$ m is $F_{r1} = 6.3 \cdot 10^{-12}$ N.

By formula (2), the force of its attraction to the central charge $Q = 1.6 \cdot 10^{-16}$ C is $F_{a1} = 1.82 \cdot 10^{-11}$ N, which is 3 times more than F_{r1} . The resulting force acting on the water molecule is $F_{res1} = F_{a1} - F_{r1} = 1.2 \cdot 10^{-11}$ N. Let us define n_1 – the number of water molecules in the spherical layer with a radius of $R_{i1} = 10^{-8}$ m. To do this, find the shell area $S_1 = 4\pi R_{i1}^2$ and divide it by the size of the area occupied by one molecule $s = 1.6 \cdot 10^{-19}$ m²: $n_1 = S_1/s = 7.85 \cdot 10^3$. Multiplying F_{res1} by n_1 , we find the total compressive strength of the shell with one layer of molecules $F_{tot1} = 9.42 \cdot 10^{-8}$ N. This is 12 times less than the tensile strength of the shell by a thousand ions. The force F_{q1} can be compensated by increasing the number of layers of water molecules in the cluster shell to 12. The thickness of the cluster shell will be $a_1 = 12 d_w = 4.8 \cdot 10^{-9}$ m, and its diameter $D_{c1} = 2 (R_{i1} + a_1) = 2.96 \cdot 10^{-8}$ m.

If there is a charge $Q_2 = 10^{-8}$ C inside a cavity with an internal radius $R_{i2} = 10^{-4}$ m, the tensile strength of the cluster shell will increase to $F_{q2} = 44.96$ N. In this case, the force of attraction of a single dipole to the center of the cavity F_{a2} will become $1.14 \cdot 10^{-15}$ N. The area of the inner surface of a sphere with a radius 10^{-4} m is $1.256 \cdot 10^{-7}$ m², it can accommodate $n_2 = 7.85 \cdot 10^{11}$ water molecules. Multiplying F_{a2} by n_2 we find the total force with which dipoles of one layer of water molecules compress the shell, $F_{sh2} = 8.68 \cdot 10^{-4}$ N. To compensate the force F_{q2} , it is sufficient to have a shell consisting of $5.18 \cdot 10^4$ layers of water molecules. The thickness of this shell will be $a_2 = 2 \cdot 10^{-5}$ m, and the cluster diameter – $D_2 = 240$ μ m.

It can be assumed that such multi-charged clusters can be formed when strong currents pass through water. T. Matsumoto [4] studying discharges between thin metal wires (0.1–0.2 mm) and a copper anode, lowered into an electrolyte, observed objects with a diameter of about 50 μ m, which left ring traces on a nuclear film.

1. C. T. R. Wilson, Condensation of water vapour in the presence of dust-free air and other gases. *Phil. Trans. Roy. Soc. (London)* A. 1897, 189, 265-307.
2. S. V. Shevkunov, Influence of chlorine ions on stability of nucleation centers in the condensed water vapour. *Journ. Fiz. Khimii*. 2011, 85 (9), 1702-1709 [in Russian].
3. J. S. Blakemore. *Solid State Physics*. Cambridge: Cambridge University Press, 1985.
4. T. Matsumoto, Ball lightning during underwater spark discharges and the Matsumae earthquakes. In: *Proc. 5th Intern. Symp. on Ball Lightning (ISBL97)*. Tsugawa-Town, Niigata, Japan. 1997. p. 193-201.

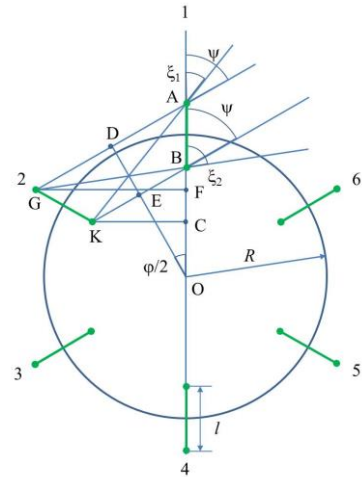


FIGURE 1. Scheme for calculating the forces acting between dipoles AB and GK.

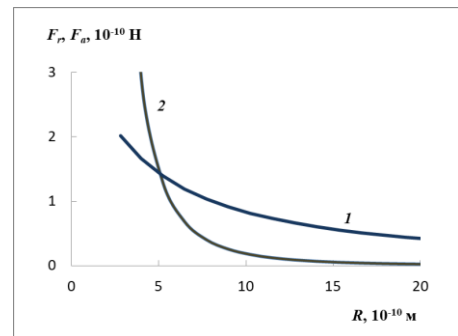


FIGURE 2. 1 – force F_r pushing a water molecule from a sphere of radius R covered with a layer of water molecules. 2 – force F_a of attraction of a water molecule to an ion with a charge $1.6 \cdot 10^{-19}$ C.

NOVEL METHODS FOR ENVIRONMENTAL CONTROL AND MONITORING

INFLUENCE OF LOW-FREQUENCY SONOLYSIS ON THE STABILITY OF CHEMICAL REACTIONS INVOLVING ASSOCIATES

Tatiana P. Kulagina, Lev P. Smirnov, Zoya S. Andrianova

Institute of Problems of Chemical Physics RAS, Semenov prospect, Chernogolovka, Moscow region, Russia

Introduction The influence of low-frequency sonolysis on the kinetics bimolecular liquid-phase reactions was studied with due regard for the association dimers and trimers) of starting reagents. At a research the method of mathematical model operation of temporary instability of reaction found two types of oscillations of concentration of intermediat (harmonic and relaxational) characterized significantly by the differing times [1-4]. Influence of external periodic mechanical action of low frequency on temporary stability of the modes of a bimolecular reaction in liquid at a molecular association of both reagents is theoretically studied. At achievement by amplitude of influence of some size, in a reaction system there are no trimers, there are only dimers, and reaction stops. Model operation of process showed a possibility of speed control of reaction at external low-frequency acoustic influence.

Mathematical model. At model operation assumed that reagent A forms a dimer of A₂ and a trimer of A₃:



where k_i and k_{-i} are the kinetic constants of a straight line (i) and inverse (-i) reactions,



For reagent B in the reactionary scheme considered only its monomer B and a dimer B₂ received in a reversible test



The product of reaction C is formed at interaction



On condition of a quasi-steady state on B₂ dimer the system of the kinetic equations for intermediat of this reaction has an appearance

$$d[A_2]/dt = k_1[A]^2 - k_{-1}[A_2] - k_2[A][A_2] + k_{-2}[A_3] - k_3[A][A_2][A_3], \quad (6)$$

$$d[A_3]/dt = k_2[A][A_2] + k_3[A][A_2][A_3] - k_{-2}[A_3] - k_4k_5[B]^2[A_3]\{k_{-4} + k_5[A_3]\}^{-1}$$

It is almost convenient to create in a reaction system the density fluctuation, uniform in space, at the expense of external periodic force, influencing system a sound wave.

At the action of a sound wave with a frequency ν the stretching σ and compression created in system lead to change of kinetic constants $k(\nu)$ and destruction of associates.

This constant has view:

$$k(\nu)_{-i} = k_{-0i} \exp[(-E_{-i} + \gamma\sigma)/RT], \quad (i = 1, 2) \quad (7)$$

where γ – is a structure-sensitive coefficient, σ – is the strenuous which changes under the law $\sigma = P_0 \sin(2\pi \nu t)$.

Thus, on condition of a quasi-steady state on B₂ dimer the system of the kinetic equations for intermediats of this reaction has an appearance:

$$d[A_2]/dt = k_1[A]^2 - k(\nu)_{-1}[A_2] - k_2[A][A_2] + k(\nu)_{-2}[A_3] - k_3[A][A_2][A_3],$$

$$d[A_3]/dt = k_2[A][A_2] + k_3[A][A_2][A_3] - k(\nu)_{-2}[A_3] - k_4k_5[B]^2[A_3]\{k_{-4} + k_5[A_3]\}^{-1}. \quad (8)$$

At the initial stage of work model operation of influence of external impact only on a kinetic constant of a reverse reaction of formation of dimers is carried out $k(v)_{-1}$.

Having rewritten sets of equations (8) in more convenient look, in an assumption of constant values of temperature of T and activation energy we have:

$$\begin{aligned} dx/dt &= \mu - a_1 \exp(P_0 \sin(2\pi \nu t)) x - ax + by - uxy, \\ dy/dt &= ax - by \exp[(\gamma_2 P \sin(\omega t)] + uxy - my(g + y)^{-1} \end{aligned} \quad (9)$$

where $x = [A_2]$, $y = [A_3]$, $\nu = k_1[A]^2 \text{ mol} \cdot (\text{ls})^{-1}$, $a_1 = k_{-1}$, $a = k_2[A]$, $b = k_{-2}$, $u = k_3[A]$, $m = k_4[B]^2$, $g = k_{-4} k_5^{-1}$.

Speed of w of formation of product of reaction C is described by the equation

$$w = d[C]/dt = dz/dt = my(g + y)^{-1} = k_4 k_5 [B]^2 [A_3] \{k_{-4} + k_5 [A_3]\}^{-1}, \quad (10)$$

where $z = [C]$,

Results and discussion. In work the problem was solved with the help of mathematical model operation of process in open system for a case $[A] = [B] = \text{const}$. Model operation is carried out at variation of all parameters of a task. The most unusual options are given below. At the same time in all options of calculations believed $a_1 = 0.005 \text{ s}^{-1}$, $a = 0.5 \text{ mol}(\text{ls})^{-1}$ and $g = 1.6 \text{ mol}(\text{l})^{-1}$. Величины остальных параметров в зависимости от варианта расчета принимали равными Values of other parameters depending on option of calculation accepted equal: $\mu = 35 \text{ mol}(\text{ls})^{-1}$, $b = 1 \text{ s}^{-1}$, $u = 0, 10$ or $40 \text{ l}^2 \text{ mol}^{-2} \text{ s}^{-1}$, $m = 100$ or $200 \text{ mol}(\text{ls})^{-1}$. In all options of calculation believed in an initial instant that $x(0) = 1.8 \text{ mol}(\text{s})^{-1}$ and $y(0) = 0.23 \text{ mol}(\text{s})^{-1}$. The characteristic of a singular point calculated by the known technique [2] from a linearized set of equations (8).

It is established that for $\text{mol}(\text{ls})^{-1}$ values of parameters $\mu = 35 \text{ mol}(\text{ls})^{-1}$, $b = 1.0 \text{ s}^{-1}$, $u = 40 \text{ l}^2 \text{ mol}^{-2} \text{ s}^{-1}$ and $m = 200 \text{ mol}(\text{ls})^{-1}$ and without external action in system formation of fluctuations of an unusual look is observed: the macroscopic maximum of amplitudes changes harmoniously (as it is characteristic of the steady mode of the central type) with quite larger frequency period (Fig. 1). In system there is a mode of a combination of fluctuations of the central type with steady and unstable fluctuations of nodal type.

The set of equations (9) contains a large number of parameters therefore at the choice of key parameters when carrying out calculations proceeded from need for work to define influence of mechanical impact on associate structure of the reactionary environment. Such parameters are the μ and m parameters characterizing the supermolecular structure by a generation rate of associates A_2 и B_2 , respectively. Calculation is given below for $\mu = 35 \text{ mol}(\text{ls})^{-1}$ and $m = 200 \text{ mol}(\text{ls})^{-1}$. Other parameters same, as given above without external influence. Investigated kinetic regularities of reaction (a generation rate of product of reaction and associates, concentration of a dimers $x(t)$

and a trimers $y(t)$) at variation of values of amplitude P and frequencies $\omega = 2\pi \nu \text{ c}^{-1}$ from periodic influence, since $\omega = 0.1 \text{ s}^{-1}$, before essential change of a type of curves $x(t)$ and $y(t)$. The character kinetic curves are given for concentration of a dimer $[A_2]$ as qualitatively kinetic curves for a trimer and a generation rate of a product have the same appearance [2]. as it follows from the equation (10).

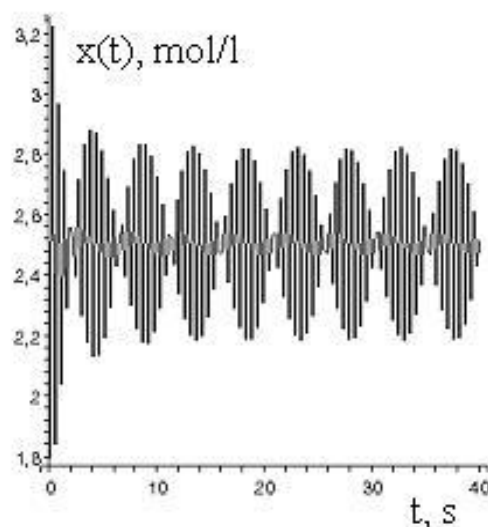


FIGURE 1. The dependence of concentrations $x = [A_2]$ on time t without external action at $\mu = 35 \text{ mol}(\text{ls})^{-1}$, $a_1 = 0.005 \text{ s}^{-1}$, $a = 0.5 \text{ mol}(\text{ls})^{-1}$, $b = 1.0 \text{ s}^{-1}$, $u = 40 \text{ l}^2 \text{ mol}^{-2} \text{ s}^{-1}$, $m = 200 \text{ mol}(\text{ls})^{-1}$, $g = 1.6 \text{ mol}(\text{l})^{-1}$.

On the example of model system it is shown that essential structural changes of oscillations happen at action of waves to the frequency equal to the frequency of the eigentones of system without external influence describing a condition of the reactionary environment ($\omega_0 = 0.4 \text{ s}^{-1}$), and such change is possible already with an influence amplitude $P > 4$. With increase in amplitude of impact of change of concentration $x(t)$ and $y(t)$ in time are described by the composite curves including sites both with low - and with high-frequency oscillations (Fig. 2). Kinetic curve generation rates of termination products of reaction counted on the equation (10). Increase in an oscillation frequency leads to damped oscillations concerning equilibrium position like unstable focus (Fig. 2) and to the reaction termination.

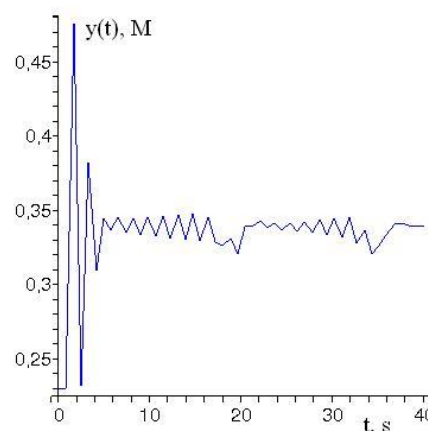


FIGURE 2. The dependence of concentrations $y = [A_3]$ on time t at the external action with the frequency of own fluctuation $\omega = 0.4 \text{ s}^{-1}$ with an influence amplitude $P = 4$.

Influence of association of reagents on kinetics of chemical reactions needs to be considered both in fundamental, and in applied the relations. Further development of researches in this area will cause creation of scientific bases of control of a kinetics of chemical reactions, structure and properties of products.

Work is performed on the theme of the state task of FASO № 0089-2019-0002.

1. L. P. Smirnov, T. P. Kulagina, Features of the Kinetics of Chemical Reactions in a Nanostructured Liquid, *Russian Journal of Physical Chemistry. B*, 2017, 11(5), pp. 786-797.
2. L. P. Smirnov, T. P. Kulagina, Z.S. Andrianova, Influence of low frequency vibrations on the chemical reaction rate in the liquid phase for reagent association, *Russian Chemical Bulletin*, 2017, 66 (1), pp. 2494--2496.
3. T.P. Kulagina, L.P. Smirnov, Z.S. Andrianova, Mathematical Simulation of Low-Frequency Mechanical Action on Bimolecular Reaction Kinetics in a Structured Liquid, *Russian Journal of Physical Chemistry B*, 2018, 12(4), 657-662.
4. T.P. Kulagina, L.P. Smirnov, Z.S. Andrianova, Low-Frequency Mechanical Effect of Concentrations of Bimolecular Reaction Intermediates on Oscillations in Structured Liquid, *Russian Journal of Physical Chemistry B*, 2019, 13(4), 573-576.

ISOTOPE EFFECTS IN COMPRESSED MOLECULES

Natalia N. Breslavskaya^{1,2}, Anatoly L. Buchachenko^{2,3}

¹Institute of General and Inorganic Chemistry RAS, Moscow, Russia

²N.N. Semenov Federal Research Center for Chemical physics, Russian Academy of Sciences, Moscow, Russia

³Scientific Center in Chernogolovka, Chernogolovka, Moscow region, Russia

Introduction. The cavity inside fullerenes provides a unique environment for the study of isolated atoms and molecules [1 and references therein]. Hydrogen molecules have been entrapped in C_{60} in macroscopic quantities [2]. Water normally exists in hydrogen-bonded environments, but a single molecule of H_2O without any hydrogen bonds was completely isolated within the confined subnano space inside fullerene C_{60} [3]. When a mixture of H_2O and D_2O , instead of pure H_2O , was applied, it was possible to obtain a mixture of $H_2O@C_{60}$, $HDO@C_{60}$, and $D_2O@C_{60}$.

At this paper structure and properties of H_2 and H_2O molecules encapsulated in the C_{60} fullerene cage with spherical compressing electric potential are studied. The most reliable means and almost the only measure of compression are isotope effects arising from the differences of zero point energies (ZPE). They are computed for the isotope molecules H_2 , D_2 , H_2O , D_2O ; these results are supposed to be of particular importance for understanding molecular machines – enzymes, which are known to compress reagents and switch on electron transfer as a new, recently discovered spin-selective, and magnetically controlled mechanism of enzymatic catalysis.

Calculation procedure. Calculations of the energy characteristics with full optimization of geometry for all structures were performed using density functional theory (DFT) with M06-2X functional and routine split valence basis set 6-31G*. The M06-2X functional developed for calculating the non-covalent interactions was earlier effectively used in studies of different complexes [4, 5]. It should be noted that noncovalent interaction plays a major role in the stabilization of guest molecule inside fullerene. The calculations were carried out using the Gaussian 2009 program. The results of vibration frequency calculations of all complexes characterize the optimized structures as the energy minima.

Results. The optimized geometries of $H_2@C_{60}$ and $H_2O@C_{60}$ are shown in Figure. The interatomic distance H–H as well as H–O does not undergo significant changes upon encapsulation. The oxygen atom of the encapsulated H_2O molecule is located about at the center of the C_{60} cage. This positioning is like that seen for $H_2@C_{60}$.

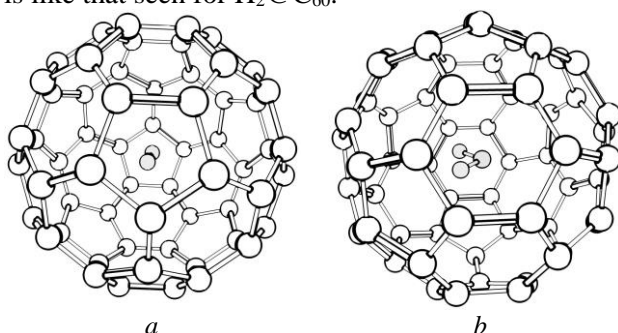


FIGURE 1. Calculated structures of complexes $H_2@C_{60}$ (a); $H_2O@C_{60}$ (b).

Zero point energies of isotopic molecules H_2 , D_2 , T_2 and HOH , HOD , HOT , free and encapsulated in the C_{60} fullerene cage, are calculated. The ZPE of compressed molecule ϵ_c is defined as the difference between the ZPE of caged molecule and ZPE of the cage itself; thus, for H_2

$$\epsilon_c(H_2) = ZPE[H_2@C_{60}] - ZPE(C_{60});$$

for HOH

$$\epsilon_c(HOH) = ZPE[HOH@C_{60}] - ZPE(C_{60}).$$

The difference in energy of compressed and free molecules, that is the excess $\Delta\epsilon$ of ZPE acquired by compressed molecule under compression, is determined as $\Delta\epsilon = \epsilon_c - \epsilon_f$ where ϵ_f is ZPE of the free molecule. Evidently, the compression of molecules in C_{60} increases their ZPE by 2-3 kcal/mol.

The compression induced isotope effect of H_2 and D_2 is determined by the difference

$$\epsilon^* = \Delta\epsilon(H_2) - \Delta\epsilon(D_2);$$

isotope effect on the dissociation rate constant of compressed and free molecules is the value $K^H/K^D = \exp(\epsilon^*/RT)$. Some values of ϵ_c , $\Delta\epsilon$, ϵ^* and the relations of the constants K^H/K^D are presented in the Table.

TABLE 1. Magnitudes of ZPE, ϵ_c , $\Delta\epsilon$, ϵ^* and the ratios of the constants K^D/K^H .

Molecules	ZPE, kcal/mol	ϵ_c kcal/mol	$\Delta\epsilon$ kcal/mol	ϵ^* kcal/mol	K^H/K^D (300K)
C_{60}	238.93	–	–	–	–
H_2	6.46	–	–	1.89	23.1
$H_2@C_{60}$	248.78	9.85	3.39	2.66	84.2
D_2	4.57	–	–	–	–
$D_2@C_{60}$	246.12	7.19	2.62	–	–

HOH	13.52	–	–	1.82	20.8
HOH@C ₆₀	255.02	16.09	2.57	2.00	28.0
HOD	11.70	–	–		
HOD@C ₆₀	253.02	14.09	2.39		

In compressed molecules isotope effects of the dissociation increases by 2-3 times with respect to those of free molecules; this result may be significant for understanding abnormally large isotope effects in enzymatic reactions, where they are attributed to tunneling, but may be caused by the compression of molecules in the catalytic sites of enzymes. This alternative may be significant for physics of enzymatic reactions.

1. A.L.Buchachenko, Compressed Atoms, *J. Phys. Chem. B.*, 2001, 105(25), pp. 5839-5846, doi.org/10.1021/jp003852u.
2. K. Komatsu, M. Murata, Y. Murata, Encapsulation of Molecular Hydrogen in Fullerene C₆₀ by Organic Synthesis, *Science*, 2005, 307, pp. 238-240, doi: 10.1126/science.1106185.
3. K. Kurotobi, Y. Murata, A Single Molecule of Water Encapsulated in Fullerene C₆₀, *Science*, 2011, 333, pp. 613-616, doi: 10.1126/science.1206376.
4. E. R. Kevin, M. Pitonak, P. Jurecka, P. Hobza, Stabilization and Structure Calculations for Noncovalent Interactions in Extended Molecular Systems Based on Wave Function and Density Functional Theories, *Chem. Rev.*, 2010, 110(9), pp. 5023-5063, doi: 10.1021/cr1000173.
5. Y. Zhao, D. G. Truhlar, The M06 suite of density functionals for main group thermochemistry, thermochemical kinetics, noncovalent interactions, excited states, and transition elements: two new functionals and systematic testing of four M06-class functionals and 12 other functionals, *Theor. Chem. Acc.*, 2008, 120, pp. 215-241, doi: 10.1007/s00214-007-0310-x.

POROUS BIODEGRADABLE COMPOSITES FOR REGENERATIVE MEDICINE

Timofei E. Grigoriev¹, Christina G. Antipova¹, Yuri D. Zagoskin¹, Elena .A. Khramtsova²,
Sergei V. Krashennnikov¹, Ksenia I. Lukanina¹, Sergey N. Chvalun¹

¹ National Research Centre "Kurchatov Institute", Moscow, Russia

² N.M.Emanuel Institute of Biochemical Physics Russian Academy of Sciences, Moscow, Russia

Regenerative medicine is the most active and intensively developing trend of the modern science. It is hard to overestimate the social and economic effects of artificial organs both for transplantation and new drug and cosmetic testing. The recent development of new approaches in molecular and cell biology has a great impact in methodics of reparative medicine. However many problems need to be overcome. One of the most important is choice of appropriate scaffold “skeleton construction” for the cells of the artificial organ or tissue. Application of the scaffolds of natural origin - as xenogeneic and allogeneic decellularized tissues reveals wide range of technical and legal problems such as immune response of the patient body and the problem of the initial matrix source, potential biomechanical problems. Development of synthetic scaffolds can solve such problems and move possibly artificial organs from the “art” area to the more or less routine (commercial) product. Scaffolds can be fabricated from biocompatible restorable or nonresorbable synthetic and natural polymers and should have appropriate morphology and tunable physicochemical and mechanical properties. Nevertheless morphology and biochemical composition of decellularized remains the best for cell cultivation indeed. Decellularized allografts retain mechanical and structural properties of native biological tissue such as tensile strength and unique structure of extracellular matrix. So the best scaffold should fit

biomechanical behavior of natural ECM and mimic in general its structure providing the best conditions for cell adhesion and proliferation.

Sponge materials based on biodegradable polymers are currently being actively developed. However, often materials based on polymers with the necessary physicochemical properties do not possess the required physicomachanical characteristics. One way to solve this problem - improving structure and properties of the materials obtained by introducing micro- and nanoscale filler into the polymer matrix, which will allow fine-tune of the required level of mechanical properties.

In the framework of this work, the effect of nanosized anisotropic fillers on the structure and properties of collagen and chitosan sponge materials was investigated. The effectiveness of using chitosan and chitin to modify the properties of collagen spongy materials was shown.

Gamma irradiation technique is widely used for preparation of membranes for biomedical applications due to its safe and ease. In particular, radiation processing of naturally occurring polymers such as chitosan has immense implications. Radiation processing has become a method of choice for modification of polysaccharides for being safer, environmental friendly and easier method to modify polymers. Irradiation of chitosan with gamma rays is very efficient and the product formed can be directly used for downstream applications without any further processing.

It is well known that the main chemical effects on polymers subjected to ionizing radiation are crosslinking and chain scission. Both processes occur simultaneously and their yields determine the final results of irradiation. But with appropriate strategy, the radiation-induced crosslinking is expected to enhance to get the chitosan sponge materials with improved mechanical properties and thermal stability.

In this paper, the main goal was to study the effect of radiation on chitosan sponges with and without chemical crosslinking, to study the physicochemical and mechanical properties of materials after irradiation, and to determine the optimal radiation dose at which the crosslinking effect of irradiation prevails over the degradation one.

During the work, highly porous materials based on chitosan (Primex, Iceland) with a molecular mass of 600 kDa were obtained using the lyophilization process. Half of the samples were chemically crosslinked with glutaraldehyde. Chitosan sponges were irradiated in glass ampules at ambient temperature, with doses of 15, 25, 40 and 50 kGy.

Mechanical compression tests of the irradiated materials were carried out on an Instron 5965 universal tensile testing machine. The materials stress-strain curves were analyzed and the Young's modulus values were calculated from the experimental data. Physicochemical characteristics of the materials were investigated using gel permeation chromatography technique. The kinetics of swelling of the materials after irradiation was studied. Analysis of the morphology of the samples was carried out using a scanning electron microscopy.

Mechanical studies showed the presence of an optimal radiation dose at which a maximum increase in the Young's modulus of the material is observed. For non-crosslinked material it is 40 kGy, and for pre-crosslinked material it is 15 kGy. A further increase in the radiation dose leads to a deterioration in the mechanical characteristics of the samples.

Also, the structure formation of fundamentally new highly porous composite materials - sponge-fibrous based on natural polymers (chitosan, collagen) and non-woven fibers from polymers of natural and synthetic origin obtained by electroforming was also systematically studied. It was shown that the introduction of an insignificant (less than 5%) amount of chitosan into the fibrous base leads to an increase in the elastic modulus by 1.5–2 times. During the formation of a continuous spongy structure in the matrix of fibrous material, a 20-fold increase in the elastic modulus is observed. Modification of electroformed non-woven materials based on synthetic polymers with collagen leads to a significant increase in the biocompatibility of the resulting composites.

The work was supported by NRC “Kurchatov institute” (Order No. 1362 of 06/25/2019) and RSF grant 17-13-01376 in part of electron microscopy sponge-fibrous materials investigation.

SIMULATING ROUGH SURFACES OF NANOAEROSOLS AND ITS INFLUENCE ON SURFACE ENERGY CHARACTERISTICS AND THE ISOTHERMS AND KINETICS OF ADSORPTION

Elena S. Zaitseva, Yuriy K. Tovbin

Kurnakov Institute of General and Inorganic Chemistry, Russian Academy of Science, Moscow, Russia

Introduction. An approach of modeling the structure of a rough surface of aerosol particles obtained from a liquid droplet upon its rapid cooling is formulated. The vapor–liquid interface creates the thermal heterogeneity of the surface on which gas-phase molecules are adsorbed after cooling. An approach is developed for studying polymolecular adsorption on the aerosol rough surface. The effect of adsorption on the surface tension of aerosol surface is examined.

Aerosols have a developed surface, and their state is determined by all surface physical and chemical processes [1]. Traditionally, in the theory the aerosols surfaces structure is simplified to a monolayer interface [2], although on practice they have multy-layer roughness, which depends on the formation conditions [1].

The purpose of the study is modeling the rough surface of aerosol and its surface tension, as well as the adsorption process on aerosol particles. Research task is to use the lattice gas model (LGM) [3] (its uniqueness is the uniform accuracy of description of bulk and surface properties) in theoretical calculations with their practical application in studying the physicochemical properties of aerosols for the environmental issues [4-5]. LGM surpasses existing methods in accuracy and speed of calculations. These circumstances allow one to perform all the necessary calculations on a personal computer instead of expensive supercomputers.

In [6-7], we formulated an approach for the theoretical description of the structure of the aerosol rough surface obtained from a drop both during its rapid cooling and in a relaxed state. The figure 1 shows the distribution of particles A (gray squares) and vacancies V (white squares) in the transition region of the rough surface on the flat lattice. The clusters with the central vacant node and its nearest nodes are identified. The cluster type is determined by the number of particles A, m^* , in it. The value m^* defines the Henry law constant for the central node.

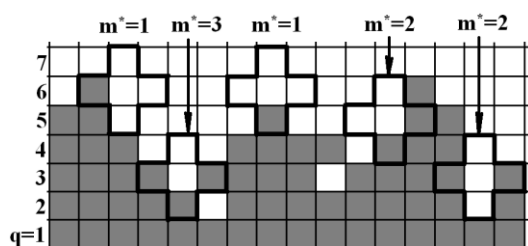


FIGURE 1. Diagram of the rough surface on the flat lattice

the transition region t_{qp}^{VA} are calculated (t_{qp}^{ij} – the probability that j is located in monolayer p near i in monolayer q), $p = q, q \pm 1$.

The main data for calculating the characteristics of the rough surface of the aerosol is the concentration profile of vacancies θ_q^V and particles A θ_q^A (θ_q^i – probability that there is i in the monolayer q), which calculating is described in [3], in the transition region dense phase – vapor divided into monolayers q , $0 \leq q \leq \kappa$ (q – the number of the monolayer, $q = 1$ – the monolayer with the dense phase, $q = \kappa$ – the monolayer with the vapor). According to the concentration profile θ_q^V , all paired functions within

These functions are used in calculating the characteristics of rough surface: $\Theta_q^V(\{m_{qp}\})$ and $\Theta_{qh}^{VV}(\{m\})$ – the probabilities of clusters with one and two central nodes respectively.

The probability $\Theta_q^V(\{m_{qp}\})$ that there is a vacant central node in a monolayer q and m_{qp} number of particles A and $(z_{qp} - m_{qp})$ number of vacancies V (z_{qp} is number of pairs of a node from a monolayer q with nodes from a monolayer p) in monolayers $p = q, q \pm 1$ equals:

$$\Theta_q^V(\{m_{qp}\}) = F_q \theta_q^V \prod_p C_{z_{qp}}^{m_{qp}} (t_{qp}^{VA})^{m_{qp}} (t_{qp}^{VV})^{z_{qp} - m_{qp}},$$

where F_q is the ratio of nodes of the monolayer q in the transition region, $C_{z_{qp}}^{m_{qp}}$ is the number of combinations.

The probability $\Theta_{qh}^{VV}(\{m\})$ that there is two vacant central nodes in monolayers q, h and $\{m_{qp}\}$, $\{m_{hk}\}$ is number of particles A in monolayers $p, k, p = q, q \pm 1, k = h, h \pm 1$, respectively equals:

$$\Theta_{qh}^{VV}(\{m\}) = F_q \theta_{qh}^{VV} \prod_p C_{z_{qp} - \Delta_{ph}}^{m_{qp}} (t_{qp}^{VA})^{m_{qp}} (t_{qp}^{VV})^{z_{qp} - \Delta_{ph} - m_{qp}} \times \\ \times \prod_k C_{z_{hk} - \Delta_{kq}}^{m_{hk}} (t_{hk}^{VA})^{m_{hk}} (t_{hk}^{VV})^{z_{hk} - \Delta_{kq} - m_{hk}}, \Delta_{ph} = \begin{cases} 1, & p = h \\ 0, & p \neq h \end{cases} \text{ и } \Delta_{kq} = \begin{cases} 1, & k = q \\ 0, & k \neq q \end{cases}$$

Using the modeled structure of the rough transition region of the aerosol, the proposed approach allowed us to calculate [6-7] important characteristics of aerosols, such as the capacity of the monolayer, and to obtain isotherms of physical adsorption and chemo-sorption for the modeled surface [7-8].

The figure 2 shows the general isotherms of multilayer adsorption B on the rough surface A and its dependence on the model parameters. Fig. 2 shows the dependences of the amount of the adsorbate Γ , normalized by the monolayer capacity M_{mon} of the adsorbent, on the normalized adsorbate pressure P^B/P_s^B (P_s^B – saturated pressure) with relation of interaction energy $\varepsilon_{BB} = 0.8\varepsilon_{AA}$ and $\varepsilon_{AB} = 1.3$ (curves 2 and 3) and $2.5\varepsilon_{BB}$ (curve 1) and with aerosol radius $R_{\text{dr}} = 20$ (curve 3) and 800 (curves 1 and 2) monolayers. Squares on the curves indicate inflection points.

The theory is compared with experimental data on the adsorption of argon atoms and nitrogen molecules on silica gels [2,7,8].

The presence of adsorbate B on the surface of aerosol A changes the molecular distributions of A [9] and hence the surface energy of the aerosol [10]. Figure 3 shows the dependencies of the excess values F (curves 1, 2) and U (curves 3, 4), normalized by the value F_A for pure A, on fig. 3a and the normalized surface tension σ/σ_A (σ_A – surface tension for pure A) on fig. 3b on the normalized pressure B, P^B/P_s^B . On the fig. 3a curves 1, 3 refer to the equilibrium surface A with B, F_b and U_b , curves 2, 4 refer to non-equilibrium analogues F_{ne} and U_{ne} .

Modeling the surface tension in aerosol particles allows us to determine the minimum stable dimensions of particles and their components distribution. Modeling of adsorption processes on the aerosols surface will allow one to create the best deposition methods with particle growth due to adhesion or coagulation, since the probability of adhesion depends on the surface properties, and the stability of the aerosol depends on collisions with other aerosols.

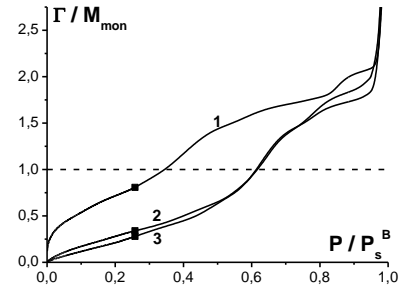


FIGURE 2. The general isotherms of multilayer adsorption on aerosol.

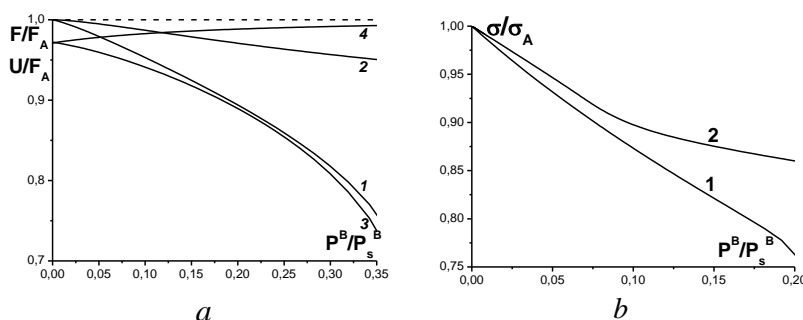


FIGURE 3. Isotherms of excess energy characteristics of the aerosol surface in the presence of adsorbate B with pressure P^B

reaction, an equation should be obtained for the equilibrium distribution of the components of the reaction mixture, which directly follows from constructing an equation in the equilibrium theory. The concept of self-consistency is fundamental when choosing a model to describe experimental data.

The study of physicochemical processes using computer modeling can significantly increase the productivity of scientific research, since most of the experiments related to the selection of the optimal composition will be carried out within the computer.

The work was carried out within the framework of the state task of the Kurnakov Institute in the field of fundamental scientific research.

This work was supported by the Russian Foundation for Basic Research, project code 18-03-00030a

1. P. Barret, *Cinetique Heterogene*, Paris: Gauthier-Villars, 1973.
2. S.J. Gregg, *Adsorption, surface area and porosity*, Academic press inc., 1982.
3. Yu.K. Tovbin, Lattice – gas model in kinetic theory of gas – solid interface processes, *Progress in Surface Science*, 1990, V. 34, pp. 1-236.
4. Kanakidou M., Seinfeld J.H., Pandis S.N. *et al.*, Organic aerosol and global climate modeling: a review, *Atmos. ChemPhys*, 2005, V. 5, No. 4, pp. 1053-1123.
5. Seinfeld J.H., Pandis S.N. *Atmospheric Chemistry and Physics: From Air Pollution to Climate Change*, New York: 2nd John Wiley & Sons, 2006, 1248 p.
6. Yu. K. Tovbin, E.S. Zaitseva and A.B. Rabinovich, Simulating the Surface Relief of Nanoaerosols Obtained via the Rapid Cooling of Droplets, *Russian Journal of Physical Chemistry A*, 2018, Vol. 92, No. 3, pp. 585-594.
7. E.S. Zaitseva and Yu. K. Tovbin, Polylayer Adsorption on Rough Surfaces of Nanoaerosols Obtained via the Rapid Cooling of Droplets, *Russian Journal of Physical Chemistry A*, 2018, Vol. 92, No. 5, pp. 1011-1017.
8. E.S. Zaitseva and Yu. K. Tovbin, Nonuniform Surfaces and the Inflection Point in Polylayer Adsorption Isotherms, *Protection of Metals and Physical Chemistry of Surfaces*, 2018, Vol. 54, No. 4, pp. 557-564.
9. Yu. K. Tovbin, E.S. Zaitseva and E.E. Gvozdeva, Effect of Adsorption on the Energy Characteristics of a Rough Solid, *Russian Journal of Physical Chemistry B*, 2019, Vol. 13, No. 3, pp. 427-437.
10. E.S. Zaitseva, E.E. Gvozdeva, A.B. Rabinovich, and Yu. K. Tovbin, Effect of Adsorption on the State of Equilibrium Rough Surfaces at Interfaces, *Protection of Metals and Physical Chemistry of Surfaces*, 2019, Vol. 55, No. 5, pp. 807-816.
11. E.S. Zaitseva and Yu. K. Tovbin, Self-Consistency in Calculating the Rates of Adsorption and Desorption and an Isotherm of Adsorption on a Rough Surface of Aerosols, *Russian Journal of Physical Chemistry A*, 2019, Vol. 93, No. 4, pp. 631-638.
12. E.S. Zaitseva and Yu. K. Tovbin, Self-Consistent Calculation of the Rates of Dissociative Adsorption and Desorption with the Adsorption Isotherm on the Rough Surface of an Adsorbent, *Kinetics and Catalysis*, 2019, Vol. 60, No. 4, pp. 410-419.

Within the developed model, the rates of adsorption and desorption on rough surfaces were calculated and their self-consistency with the corresponding adsorption isotherm was checked [11,12]. The essence of the self-consistency lies in the fact that by equating the expressions for the rates of the forward and reverse directions of the

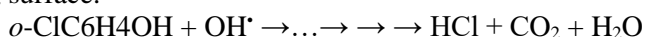
PHOTODEGRADATION OF CHLOROORGANICS CATALYZED BY NANO-TiO₂ PHOTOCATALYSTS

Alexander I. Kokorin¹, Anatoly I. Kulak²

¹N.N. Semenov Federal Research Center for Chemical Physics, RAS, Moscow, Russia

²Institute of General and Inorganic Chemistry NASB, Minsk, Belarus

Photodegradation of toxic chloroorganic compounds on nanostructured TiO₂ photocatalysts including those doped with metal ions or non-metal atoms is of great fundamental interest with possible practical applications for chemical safety, water purification, and environmental protection [1-3]. The following complex reaction describes the process of photocatalytic degradation of *ortho*-chlorophenol on the TiO₂ surface:



The main goal of this paper is to describe the structure, properties and applications of TiO₂-based nanosized and thin-film photo- and photoelectrocatalysts.

The photocatalytic activity of TiO₂ nanoparticles of different size has been studied by following the photodegradation of dichloroacetic acid (DCA), and was tested by measuring the initial rate of the H⁺ and Cl⁻ ions formation [4]. The catalyst efficiency was found to be in correlation with the specific surface area of the semiconductor particles. The efficiency of the nanocrystalline TiO₂ photocatalyst could be increased by doping the particles with copper ions. The structure and the partitioning of different surface Cu(II) complexes has been studied using EPR technique. The influence of the pH value of the solutions and of the adsorbed copper ion content on the efficiency of the DCA photodegradation will be discussed in the presentation [4].

The passage from photocatalytic destructive conversion of aromatic and aliphatic chloroorganic substances to photoelectrochemical can be accompanied by cardinal modifications of the mechanism of photosensitized transformations owing to loss the possibility for participation in multistage photoinduced responses on the semiconductor surface of carriers from conduction band. As the consequence, efficiencies of photocatalytic systems during destruction of aromatic organic substances in defined cases can appear more than photoelectrochemical, in spite of the fact that within the framework of last is achieved formally more high photogeneration level. This was illustrated to be by us on the *o*-chlorophenol that it is necessary to take into account a possibility of the photo- and electropolymerization during photocatalytic destruction reducing in significant modifications of surface activity of semiconductor electrode [5].

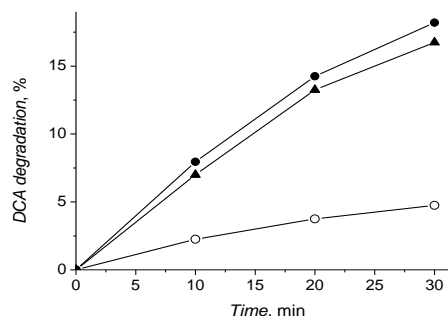


FIGURE 1. Kinetic curves of DCA degradation recorded at pH 3.0 (O, X) and 6.0 (Δ) using the Chloride Ion Selective Electrode in the presence of nano-sized TiO₂ photocatalysts prepared at 200°C (X, Δ) and 500°C (O). T = 298 K, [DCA]₀ = 1 mM, [TiO₂] = 2.5 g/l.



FIGURE 2. Pilot installation for water purification under sun light irradiation. 100 m² installed at HIDROCEN (Madrid, Spain).

Structural characteristics measured from EPR spectra for all paramagnetic centers were measured according to recommendations of [6, 7].

Acknowledgments: Authors thank Russian Foundation for Basic Research (Grant № 20-53-00017).

1. Photocatalytic Purification and Treatment of Water and Air, D. F. Ollis, H. Al-Ekabi, Eds., Elsevier, Amsterdam, 1993, 380 p.
2. J. Schneider, M. Matsuoka, M. Takeuchi, et al, Understanding TiO₂ photocatalysis: mechanisms and materials, *Chem. Rev.*, 2014, 114, pp. 9919–9986.
3. H. Zhang, G. Chen, D. Bahnemann, Photoelectrocatalytic materials for environmental applications, *J. Mater. Chem.*, 2009, 29, pp. 5089–5121.
4. D. W. Bahnemann, S. N. Kholuiskaya, R. Dillert, A. I. Kulak, A. I. Kokorin, Photodestruction of dichloroacetic acid catalyzed by nano-sized TiO₂ particles, *J. Appl. Catal. B*, 2016, 36(1), pp. 161-169.
5. A. I. Kulak, in *Chemical Physics of Nanostructured Semiconductors*; A. I. Kokorin, D. W. Bahnemann, Eds.; VSP–Brill Acad. Publ.: Utrecht, Boston, 2003, pp. 153–182.
6. A. I. Kokorin, V. I. Pergushov, A. I. Kulak, EPR Evidence for Dynamic Rearrangements of Vanadium Paramagnetic Centers on the Surface of V-Doped Titanium Dioxide, *Catal. Lett.*, 2020, 150(1), pp. 263–272.
7. T. V. Sviridova, L. Yu. Sadovskaya, et al. Photoaccumulating TiO₂–MoO₃, TiO₂–V₂O₅, and TiO₂–WO₃ Heterostructures for Self-Sterilizing Systems with the Prolonged Bactericidal Activity *Catal. Lett.*, 2019, 149(1), 147-153.

NANO-DOPANTS IN MECHANOCHEMICAL SYNTHESIS OF COPPER-CERIA CATALYSTS FOR H₂ PURIFICATION

Olga S. Morozova¹, Alla A. Firsova¹, Iliya A. Leipunsky¹, Galina A. Vorobjeva¹, Galina Yu. Ostaeva², Ekaterina A. Eliseeva² and Andrey V. Bukhtiyarov³

¹Federal Research Center of Chemical Physics RAS, Moscow, Russia

²Moscow Automobile and Road Construction State Technical University, Moscow, Russia

³Federal Research Center Boreskov Institute of Catalysis, Novosibirsk, Russia

Introduction. Copper-ceria catalysts are widely used in different industrial and ecologically important processes including H₂ purification from CO and the alkanes catalytic combustion. The first is necessary for preventing the Pt electrode poisoning in modern fuel cells. The second is used in different heating devices. Much evidence point to the key role of CuO/CeO₂ interface responsible for multiple catalytic activities. As it is shown, the presence of Cu²⁺ - Cu¹⁺ and Ce⁴⁺ - Ce³⁺ mixed valence states are especially important because of synergetic effect of Cu ions on reversible oxygen absorption into CeO₂ lattice and removal from fluorite structure of CeO₂ [1]. Previously we showed that mechanochemical treatment is a promising way to synthesized mixed oxide catalysts because of fast, non-waist and low-cost procedure [2]. High concentration of surface and bulk defects being a special feature of mecanochemical synthesis stimulates (1) reagent sorption, (2) oxygen diffusion from the bulk to the surface and from gas phase through the surface to the bulk [3]. As follows from Mars and Van Krevelen mechanism, oxygen from CeO₂ lattice plays a key role in all types of oxidation processes realizing on ceria-containing catalysts [4]. CeO₂ surface modification by Cu ions from standard Cu metal and copper oxide dopants can be successfully carried out under mechanochemical treatment because of high local pressure and temperature. Usually it takes 60 – 90 min. to reach the optimal modification degree of 4 – 5 mass %. In this work we tested Cu metal and Cu₂O nanopowders as additives to CeO₂ to check the dopant size effect on both the synthesis procedure and catalytic activity of the samples obtained.

Experimental. Nano-Cu powder was produced by levitation-in-flow Gen-Miller technique from Cu wire of 99.9% purity. Nano-Cu₂O was prepared through direct reduction of CuSO₄ * 5H₂O water solution (0.2 mol/l) by *tert*-butylamine borane at 20 °C. Cu-containing – CeO₂ composites (8 mass% of Cu or 9 mass% of Cu₂O, respectively) were synthesized in a stainless still ball mill with an average energy intensity of 1 Wt/g at atmospheric pressure in air. The milling time was chosen as 30 min. The catalysts were tested in H₂ purification from CO (CO-PROX reaction) without pretreatment in the temperature range of 50 to 400 °C. Reaction mixture: 98 vol% H₂, 1 vol% CO and 1 vol% O₂ was blown through the reactor with a flow rate of 40 ml/min. Reaction products were analyzed with the use of a gas-chromatograph. The original and as-milled powder morphology and microstructure were studied by a scanning electron microscopy (SEM) and X-ray diffraction (XRD), respectively. The lattice oxygen reactivity towards H₂ was tested under temperature-programmed reduction conditions (H₂-TPR). Simultaneously, differential scanning calorimetric analysis (DSC) and thermo-gravimetric analysis (TG) on a TG-DTA/DSC apparatus (NETZSCH STA 449C, Germany) equipped with a mass-spectrometer (MS) AEOLOS-32 was carried out in a temperature range of 50 – 500 °C with a heating rate of 10°/min. Reaction mixture was 10 vol.% H₂/Ar-He. A flow rate was 80 ml/min. The surface composition, chemical and electronic states of Cu, O and Ce atoms were studied by X-ray photoelectron spectroscopy (XPS). XPS spectra were recorded with SPECS (Germany) spectrometer (MgK_α (hν = 1253.6 eV, 150 Wt) radiation). Binding energies were referenced to Au 4f_{7/2} - 84.0 eV and Cu 2p_{3/2} - 932.67 eV.

Results and Discussion. Figure 1 shows temperature dependence of CO conversion in H₂ excess on copper-ceria composites. The catalytic properties of the samples prepared from nano- Cu and Cu₂O powders is compared with the properties of the sample produced from standard electrolyte (dendrite) Cu powder, which original size is significantly larger than that of nano-Cu (Figure 2). Results obtained for nano-dopants are very similar contrary to these for Cu(dendrite)-CeO₂ mechanically activated during the same 30 min. 50% of CO conversion was reached at 110 °C and 137 °C, respectively.

The major reason of such a remarkable difference in catalytic activity are (1) a perfect distribution of nano-powders in CeO₂ matrix and (2) chemical interaction of nano-dopants (Cu, Cu₂O) with a matrix (CeO₂). Figure 3 shows XRD

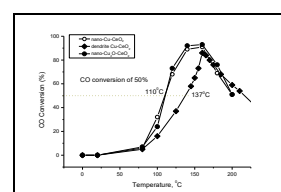
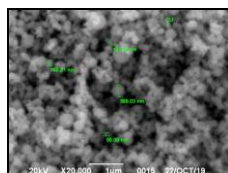
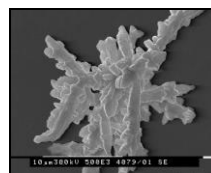


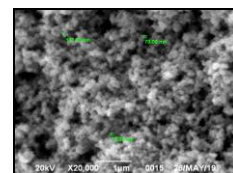
FIGURE 1. Temperature dependence of CO conversion on nano-Cu-, Cu₂O-CeO₂ and Cu(dendrite)-CeO₂



a



b



c

FIGURE 2. SEM micrographs of original a - nano-Cu, b - Cu(dendrite) and c - nano-Cu₂O powders

patterns recorded for nano-Cu₂O- nano-Cu- and Cu (dendrite)-CeO₂ powders after 30 min of mechanochemical synthesis. No Cu₂O XRD peaks are detected (Fig. 3, curve 1) that indicates XRD amorphous-like dopant state and/or its accumulation in CeO₂ grain boundaries. Both Cu-CeO₂ samples contain the same metal fraction of 8 mass% (Fig. 3, curves 2 and 3, respectively). The broad and low intensity Cu peaks in nano-Cu-ceria composition also point to (1) amorphous-like dopant state and/or (2) its accumulation in CeO₂ grain boundaries. XPS data (Figure 4) shows CeO₂ surface modification by Cu¹⁺ and Cu²⁺ ions under the milling conditions, as well as partial reduction of Ce⁴⁺ to Ce³⁺ (not shown) that indicates Cu⁰ and Cu ions oxidation by CeO₂ surface oxygen. A special oxygen state, different from this in oxide lattice is also present. Such a state is usually attributed to low-coordinated oxygen, oxygen localized nearby oxygen vacancies, etc [5].

In our previous work [2] we attributed this new type of surface oxygen to “active” oxygen participating in CO and H₂ oxidation at low temperatures. Figure 5 shows change in ion current intensity (m/e = 18, H₂O) recorded during H₂-TPR for nano-Cu-CeO₂ (curve 1) and Cu (dendrite)-CeO₂ (curve 2). Peak intensity was normalized to composite weight. The low-temperature peak was assigned to reactivity of oxygen localized in Cu – O – Ce surface structures. The high-temperature peak was related to reduction of Cu-oxide nano-fragments or clusters appeared under mechanical treatment. As is estimated from the peak area, the total amount of reactive oxygen in nano-Cu-CeO₂ sample is approximately twice larger than that in standard Cu (dendrite)-CeO₂. The surface “active” oxygen content in nano-Cu-CeO₂ sample exceeds this in Cu (dendrite)-CeO₂. This oxygen is more active in H₂ oxidation: T_{max} = 175 °C instead of T_{max} = 193 °C.

According to XPS data obtained earlier [2], “active” surface of Cu-CeO₂ has to contain Cu¹⁺ ions (Fig. 4, curve 3). This suggestion was in line with a number of publications and was a reason why we choose nano-Cu₂O as dopant to CeO₂. As follows from our current results, the combination Cu⁰ and Cu¹⁺ on CeO₂ surface is not enough for the successful catalytic activity in CO-PROX reaction. It is much better to create the complicate surface containing all kinds of Cu states (Cu⁰, Cu¹⁺ and Cu²⁺, as well as Ce⁴⁺ and Ce³⁺). The latter can be easily formed under the milling conditions through Cu metal oxidation by oxygen from CeO₂ lattice. The other important thing following from comparison of nano-Cu-CeO₂ and standard Cu (dendrite)-CeO₂ catalytic activity is the crucial effect of dopant powder size. The smaller is particle size of dopant, the less milling time is required to prepare catalyst with an adequate activity, due to shorter time for dopant particles crushing and distribution in CeO₂ matrix. More over: dopant particles localization in CeO₂ “body” is rather stable and virtually independent on milling prolongation after some minimal time. In our case, this time is 30 min (dose of 1.8 kJ).

Conclusions. Nano-Cu₂O and nano-Cu dopants application for mechanochemical synthesis of copper-ceria catalysts significantly reduced the procedure duration. The reason was an effective distribution of fine powder particles in CeO₂ matrix (probably, without crushing) accompanied by chemical interaction between dopant and CeO₂. As a result, CeO₂ surface was easily modified by Cu¹⁺ and Cu²⁺. Partial reduction of Ce⁴⁺ to Ce³⁺ was also observed. The formation of reactive low-coordinated oxygen yielded the catalytic activity in CO-PROX higher as compared to composites prepared from standard additives.

Acknowledgements. This work was partially supported by Russian Foundation for Basic Research (Projects n.n. 19-03-00358), FASO Program (Program V.46.13, 0082-2014-0007, № AAAA-A18-118020890105-3) and by the Ministry of Science and Higher Education of the Russian Federation (State assignment No. 0701-2020-0010). We also thank A.V. Leonov, Lomonosov MSU, for XRD measurements and N.G. Berezkina for SEM measurements.

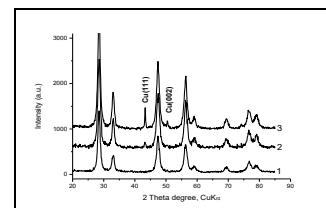


FIGURE 3. XRD patterns of composites 1- nano-Cu₂O-CeO₂, 2 - nano-Cu-CeO₂ and 3-Cu (dendrite)-CeO₂

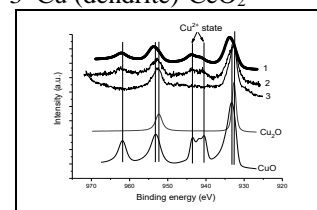


FIGURE 4. Cu₂p XPS spectra for 1 - nano-Cu₂O-CeO₂; 2 - nano-Cu-CeO₂ and 3 - Cu (dendrite)-CeO₂

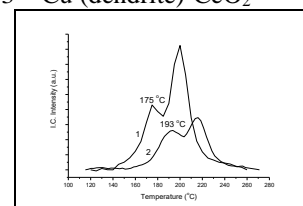


FIGURE 5. H₂-TPR MS curves m/e = 18 (H₂O) for 1 - nano-Cu-CeO₂ and 2-Cu (dendrite)-CeO₂:

1. A. Martínez-Arias, D. Gamarra, A.B. Hungría, M. Fernández-García, G. Munuera, A. Hornés, P. Bera, J.C. Conesa, A.L. Cámara, Characterization of active sites/entities and redox/catalytic correlations in copper-based catalysts for preferential oxidation of CO in H₂-rich streams, *Catalysis*, 2013, 3, pp. 378–400.
2. Ch. Borchers, M.L. Martin, G.A. Vorobjeva, O.S. Morozova, A.A. Firsova, A.V. Leonov, E.Z. Kurmaev, A.I. Kukharensky, I.S. Zhidkov, S.O. Cholakh, Cu-CeO₂ nanocomposites: Mechanochemical synthesis, physico-chemical properties, CO-PROX activity, *J. Nanopart. Res.*, 2016, 18, pp. 344–359.
3. M.-F. Luo, Yu-P. Song, Ji.-Q. Lu, X.-Yu Wang, Zh.-Y. Pu, Identification of CuO Species in High Surface Area CuO–CeO₂ Catalysts and Their Catalytic Activities for CO Oxidation, *J. Phys. Chem. C*, 2007, 111, pp. 12686–12692.
4. C. Doornkamp, V. Poncet, The universal character of the Mars and Van Krevelen mechanism, *Molecular Catal.*, 2000, 162(1-2), pp. 19-32.
5. Zh. Ren, F. Peng, J. Li, X. Liang, B. Chen., Morphology-Dependent Properties of Cu/CeO₂ Catalysts for the Water-Gas Shift Reaction, *Catalysts*, 2017, 7(2), pp. 48-60.

LIGHT INDUCED MYOPIA IN JAPANESE QUAIL CHICKS BY ACOUSTIC MICROSCOPY

Elena A. Khramtsova¹, Pavel P. Zak¹, Julia S. Petronyuk^{1,2}, Natalia N. Trofimova¹,
Sergey V. Krasheninnikov³, Sergey A. Titov^{1,2}, Tamara S. Gurieva⁴, Olga A. Dadasheva⁴,
Timofey E. Grigoriev³, Vadim M. Levin¹

¹N.M.Emanuel Institute of Biochemical Physics Russian Academy of Sciences, Moscow, Russia

²Scientific and Technological Center of Unique Instrumentation Russian Academy of Sciences, Moscow, Russia

³National Research Centre "Kurchatov Institute", Moscow, Russia

⁴Research Center Institute of Biomedical Problems, Russian Academy of Sciences, Moscow, Russia

Introduction. The childhood myopia is one of the most important problems of the twenty-first century. In Southeast Asia, about 60% of children are nearsighted; in the United States and Europe - about 40%. The development of ways and methods for the prevention of childhood myopia requires animal models with short life time cycle and eye structures similar to human. Domestic chickens are widely used animal models of various eye disorders [1]. Elongation of the anterior-posterior axis of the eye globe, influenced by long-wave red light, was shown on domestic chickens [2]. At the same time, blue light shortens axis of the eye globe and even slows down the development of myopization caused by red light. In this case, it is relevant to assess the role of the blue light range on possible prevention of myopization of the children's eyes. Melatonin, synthesized by retina, may be the band between lighting conditions and the development of eye structures [3, 4].

Materials and methods. The objects of the investigation were Japanese quail *Coturnix coturnix japonica* dom. Quails are widely used experimental animals in biomedical researches with extremely high production of retinal melatonin [5]. Japanese quail life time is 50 times shorter than human. Two groups of birds have been selected: 10-30 days old chicks have been used for investigation of the eyes' development in childhood, and adult quails older than 100 days have been studied for observing age-related changes in the optical system of the eyes. The birds have been placed under LED lighting with different spectrum and irradiation energy of 0.004 mW/cm². In this investigation were used red LED light with wavelength 630 nm and blue LED light with wavelength 450 nm. The daily rhythm of the lighting was 9 hours of darkness (night) and 15 hours of lighting (day).

Acoustic microscopy have been chosen as the main method for analysis of lighting influence on eye geometry. The method has several advantages. Ultrasound studies in ophthalmology have proven themselves well; ultrasound technique is non-invasive, intravital and allows to observe biological objects in dynamics during the life time. Moreover, acoustic images provide not only information

about shape and size of the object under investigation, but also they depict the variation of elastic properties.

The scanning impulse acoustic microscope SIAM-2011 (Acoustic Microscopy Lab, IBCP RAS, Moscow, Russia) with nominal operation frequency range of 50-100 MHz has been employed for 3D imaging bulk microstructure of the quail eyes [4]. Long-focus (low-aperture) objectives were used. The frequency of 50 and 100 MHz is optimum for observation of the integral microstructure - moderate ultrasound attenuation and sufficient penetration depth in biological objects. The technique provides layer-by-layer imaging of the 3D internal microstructure as a set of gray-scale raster horizontal images (C-scans) at any depth within the depth range up to a few millimeters and images of vertical cross-sections with dynamic focusing (B/D-scans) [6].

Instron model 5965, equipped with a load sensor ± 5000 N series 2580-108 was performed for study the mechanical parameters of sclera. The data of sclera elastic parameters were measured with acoustic microscopy also. The acoustic data analysis needed the sclera density measurement that was found with using hydrostatic weighing.

Results and discussion. Acoustic images of the eyes were obtained by C- and B/D-scanning of control and experimental groups *in situ* (Fig.1). The sizes of eye globe and of the anterior and posterior eye chambers were determined by A-scanning *in vivo*, the data were confirmed by optical microscopy.

Measurement data for all bird ages are shown in Table 1. It was shown that all the eye' linear sizes increase with animal age.

Cornea and sclera form the fibrous cover of the eye globe, the cover is highly rigid to external and internal condition changes and has constant thickness and fibrillar composition [7, 8]. The elastic and mechanical properties of the sclera were measured by acoustic microscopy and mechanical testing by Instron (Fig.2). The preliminary results show that the measured values are 5 and 8 MPa - across and along the sclera thickness, accordingly.

TABLE 1. Linear sizes of eye globe and its structural elements at different stage of postnatal development of chicks. Interval of measurement error is ± 0.05 mm.

Age, days	Eye axial size, mm	Eye equatorial diameter, mm	Corneal thickness, mm	Anterior eye chamber, mm	Lens axial size, mm	Posterior eye chamber, mm	Scleral thickness, mm
10	5.80	8.30	0.13	0.55-0.80	1.70	3.25	0.12
20	6.60	8.70	0.14	0.56-0.90	1.85	3.95	0.12
30	7.10	10.10	0.17	0.23-0.70	1.90	4.40	0.14
>100	8.50	10.80	0.23	0.95	2.50	4.70	0.15

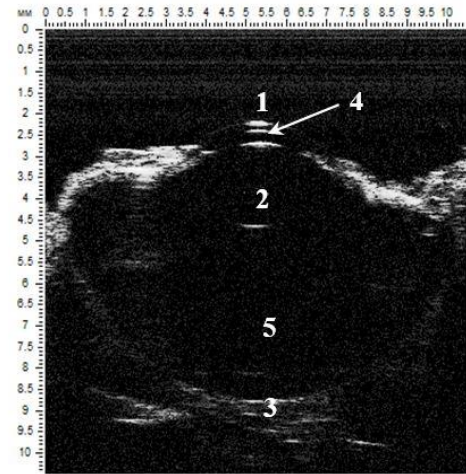


FIGURE 1. Acoustic image (B/D-scan) of quail eye *in situ*. 1 – cornea, 2 – lens, 3 – sclera, 4 – anterior chamber, 5 – posterior chamber.

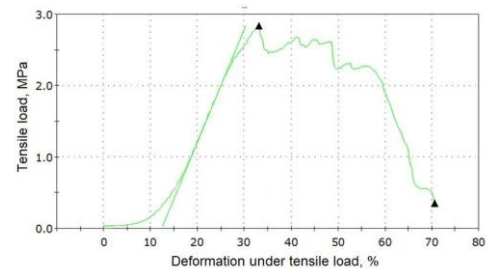


FIGURE 2. Loading curve of quail sclera (control group).

Presented in this paper acoustic microscopy approaches for monitoring of eyes' changes caused by different light spectrum, are effective and perspective. Acoustic microscopy provides visual and quantitative information about linear sizes and elastic properties of biological tissues.

The study of rate of eyes emmetropization analysis and reversibility of normal elastic and mechanical sclera properties after restoration of the daylight spectrum looks promising for future investigations.

Research partially supported by the RFBR grant № 17-04-00708.

1. C. Wisely, J. Sayed, H. Tamez, C. Zelinka, M. Abdel-Rahman, A. Fischer, C. Cebulla, The chick eye in vision research: An excellent model for the study of ocular disease, *J. Prog Retin Eye Res*, 2017, 61, pp. 72-97.
2. F. Rucker, Monochromatic and white light and the regulation of eye growth, *Exp. Eye Res.*, 2019; 184, pp. 172–182.
3. L. Ostrin, Ocular and systemic melatonin and the influence of light exposure, *Clin. Exp. Opt.*, 2019, 102, pp. 99–108.
4. N. Sereznikova, L. Pogodina, T. Lipina, N. Trofimova, T. Gurieva, P. Zak, Age-related adaptive responses of mitochondria of the retinal pigment epithelium to the everyday blue LED lighting, *Doklady Biological Sciences*, 2017, 475 (1), pp. 141-143.
5. E. Khramtsova, E. Morokov, K. Lukanina, T. Grigoriev, Y. Petronyuk, A. Shepelev, E. Gubareva, E. Kuevda, V. Levin, S. Chvalun, Impulse acoustic microscopy: A new approach for investigation of polymer and natural scaffolds, *Polymer Engineering and Science*, 2017, 57(7), pp. 709-715.
6. E. Morokov, E. Khramtsova, E. Kuevda, E. Gubareva, T. Grigoriev, K. Lukanina, V. Levin, Noninvasive ultrasound imaging for assessment of intact microstructure of extracellular matrix in tissue engineering, *Artif Organs*, 2019, 43(11), pp. 1104-1110.
7. J. Summers Rada, S. Shelton, T. Norton, The sclera and myopia, *Experimental Eye Research*, 2006, 82, pp. 185-200.
8. P. Fratzl (eds), *Collagen: Structure and Mechanics*, Springer, Boston, 2008, pp. 359-397.

METHODS AND TECHNIQUES FOR REMOTE SENSING AND IDENTIFICATION OF HAZARDOUS CHEMICALS IN THE ATMOSPHERE AND DIFFERENT SURFACES

ENSEMBLE OF HARMONIC DAMPED OSCILLATORS AS A MODEL OF VARIOUS TYPES OF INTERACTION OF RADIATION WITH MATTER

Dmitry R. Anfimov, Igor L. Fufurin, Igor S. Golyak, Anastasiya S. Tabalina

Bauman Moscow State Technical University, Moscow, Russia

Introduction. Choosing of the most effective method of experimental data processing is one of the main tasks of spectroscopy. The reflectance spectra aren't-selective enough, so we should use some additional mathematical operations to obtain more information from experimental spectra. For example, we could use Kramers-Kronig relations for calculation of extinction coefficient and transmittance spectrum [1-2]. Due to the approximate nature of the spectra conversion methods, their applicability was verified on the set of real substances. The applicability and accuracy of the proposed method for the transformation of the optical coefficients have been verified by the simulations with the model substances representing an ensemble of damped harmonic oscillators [3].

To verify the applicability and efficiency of the described algorithm of spectra conversion, a set of model problems has been solved, and the reflectance and transmittance spectra have been calculated based on a certain model of a substance. In this section, we regard the Kramers–Kronig transformation as a semiempirical procedure, part of whose justification rests on the agreement between phases or optical constants obtained from the model with values measured more directly.

Complex electric permittivity is represented by its real ε' and imaginary ε'' parts. Based on the Lorentz dispersion model, we treat a molecule as an ensemble of damped harmonic oscillations (DHO model) [4]:

$$\varepsilon' = n_0^2 + \sum_j \frac{B_j(\omega_j^2 - \omega^2)}{(\omega_j^2 - \omega^2)^2 + \lambda_j^2 \omega^2}, \quad \varepsilon'' = \sum_j \frac{B_j \lambda_j \omega}{(\omega_j^2 - \omega^2)^2 + \lambda_j^2 \omega^2},$$

where ω_j , B_j and λ_j are the oscillator resonant frequency, the strength, and attenuation coefficient, respectively, for the j -th oscillator of the ensemble; n_0 – is a constant.

The spectral indices of refraction n and extinction k can be obtained from the real and imaginary parts of the dielectric constant as follows:

$$k = \left\{ \frac{1}{2} \left[\left(\varepsilon'^2 + \varepsilon''^2 \right)^{1/2} - \varepsilon' \right] \right\}^{1/2}, \quad n = \left\{ \frac{1}{2} \left[\left(\varepsilon'^2 + \varepsilon''^2 \right)^{1/2} + \varepsilon' \right] \right\}^{1/2},$$

To provide closer resemblance of the model spectra to the real substances that will be tested in real applications, we have generated a model spectrum on the base of diethyl benzene-1,2-dicarboxylate [diethyl phthalate (DEP)]. Using the experimentally measured diffuse reflectance spectrum $R(\nu)$ of the drop of the test substance, the DHO model coefficients ω_j , B_j and λ_j have been determined by the least square method in the range of 1050 to 1400 cm^{-1} . Table 1 presents the calculated values of the coefficients. The value of additive constant entering Eq. (1) is $n_0=2,71$.

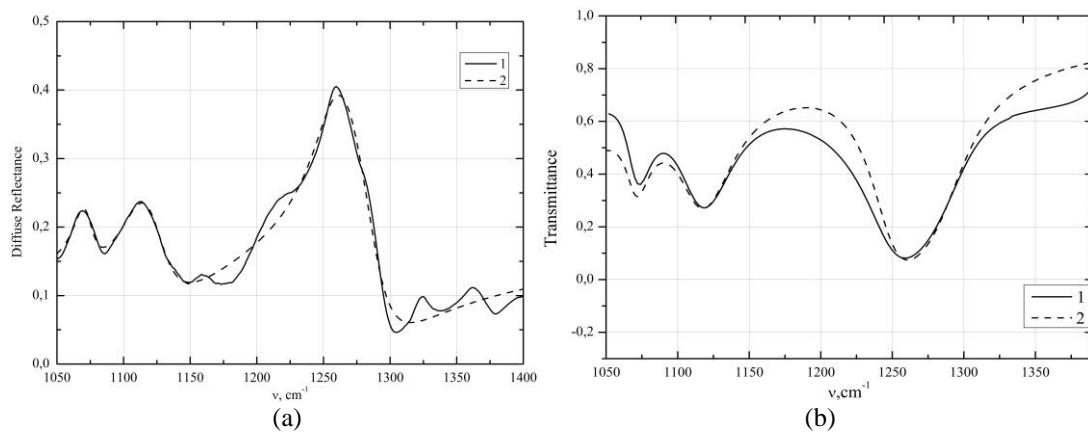
TABLE 1. Fitted DEP model parameters

$\omega_j (cm^{-1})$	$B_j \times 10^4 (cm^{-2})$	$\lambda_j (cm^{-1})$
807.46	308.31	157.36
1070.21	3.99	16.22
1114.15	12.37	33.41
1254.73	37.92	31.48

To test the proposed method for calculating the spectral extinction coefficient from the reflectance spectrum using the Kramers–Kronig relations, we have conducted the following numerical experiment. For the ensemble of harmonic oscillators with parameters from Table 1 representing the model of liquid DEP, we have calculated the reflectance spectrum using in the limited range of 1050 to 1400 cm^{-1} and applied the procedure described above to obtain the transmittance spectrum.

Then, we have modeled the transmittance spectrum directly from Eq. (2) (Fig. 1 curve 2b) and calculate transmittance spectrum (Fig. 1 curve 1b) using Kramers-Kronig Eqs. from a modeled reflectance spectrum. The correlation coefficient for the obtained transmission spectra for the same substance is 0.96, which confirms the reliability of the suggested method for converting optical characteristics.

Figure 1(a) shows the experimental (1a) and modeled (2a) diffuse reflection spectra. Figure 1(b) shows the calculated (1b) and modeled (2b) transmission spectra.

**FIGURE 1.** (a) Experimental and (b) modeled DEP spectral characteristics.

Based on the Fresnel equation for the case of normal incidence of a wave on the interface between two media and the Kramers–Kronig relations for the real and imaginary parts of the complex refractive index, the numerical algorithm was suggested to extract the reflectance and extinction indices of a test substance from the measured diffuse reflection coefficient. The algorithm includes the methods of extrapolation and phase correction of the experimental spectra. The method for registering reflectance spectra and procedures of spectra processing and substance identification is a novel approach for remote detection and identification.

The applicability and efficiency of the suggested algorithm for spectra conversion and identification have been proven on the set of model examples based on the ensemble of damped harmonic oscillators (Lorentz dispersion model). The consistency of calculated and measured spectral characteristics, as well as the accuracy of spectra reconstruction, has been shown.

The reported study was funded by RFBR according to the research project №18-29-02024

1. I. L. Fufurin, A. S. Tabalina, A. N. Morozov, I. S. Golyak, S. I. Svetlichnyi, D. R. Anfimov, I. V. Kochikov, Identification of substances from diffuse reflectance spectra of a broadband quantum cascade laser using Kramers–Kronig relations, *Optical Engineering*, 2020, 59(6), p. 061621. doi: 10.1117/1.OE.59.6.061621.
2. Ig. S. Golyak, A. N. Morozov, S. I. Svetlichnyi et al., Identification of chemical compounds by the spectra of the scattered radiation in the range 5,3 – 12,8 μm measured by tunable quantum cascade laser, *Russian Journal of Physical Chemistry B*, 2019, 38(7), p. 3–10, doi:10.1134/s0207401x19070057.
3. G. Andermann, A. Caron, and David A. Dows, Kramers–Kronig Dispersion Analysis of Infrared Reflectance Bands, *Journal Of The Optical Society Of America*, 1965, 55(10), p. 1210-1216, doi: 10.1364/JOSA.55.001210.
4. B. Hapke, Theory of reflectance and Emittance Spectroscopy, *Cambridge University Press*. 2012. 508 p.

STATIC FOURIER SPECTROMETER

Ivan B. Vintaykin^{1,2}, Pavel A. Korolev²

¹Bauman Moscow State Technical University, Moscow, Russia

²Center of applied physics Bauman Moscow State Technical University, Moscow, Russia

Introduction. In this paper we describe results based on using the spectrometer based on static Michelson interferometer. This spectrometer was build special for registration infrared spectra using algorithms of passive absorption spectrometry [1]. To get infrared radiation with a wavelength of 8 to 14 μm LWIR camera were used. To confirm the operability, a spectra of chemicals was obtained, which was compared with the reference one.

Static Fourier-spectrometer (SFS) [2] is used for measure spectra and to identify the substance. The main element of SFS is special beam splitter. Mirrors beam splitter are inclined at a small angle. Image of the interferogram is formed due to inclination of mirrors. Image of interferogram is formed on focal plane of sensor by projection optics. Infrared camera is used as infrared sensor. Then the lines of the two-dimensional interferogram are summed. Then the result is Fourier transformed [1]. Various versions of such a spectrometer are being developed [3,4]. However, the construction of a classical dynamic Fourier spectrometer with moving mirror based on a microbolometric matrix failed. According to the author [5], this failure is associated with a low dynamic range and high granularity of the ADC in the camera they use.

After assembling the interferometer, together with the infrared matrix, it is necessary to determine the method for calculating the wave numbers during spectrum reconstruction. To correctly recalculate the wave numbers, we took the ammonia spectrum obtained using a gas cell and blackbody. Based on the recorded spectrum and the spectrum from the NIST database, the coefficients of affine transformation to wave numbers are obtained. As a result, the correspondence of the spectra shown in Figure 1a is obtained.

The transmission spectra of ethanol, isopropanol and methanol were also obtained using a spectrometer. The

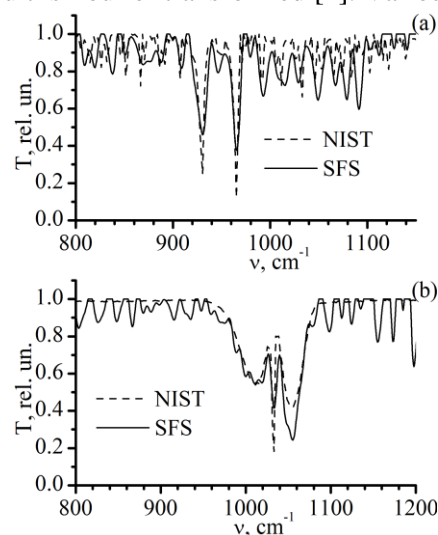


FIGURE 1. Spectra of transparency of ammonia (a) and methanol (b).

methanol spectrum is compared with the spectra from the NIST base (Figure 1b). The possibility of field use of this spectrometer in conditions of natural contrasts was also tested. Tests have shown the possibility of using this device in the field.

This work is supported by the The Russian Foundation for Basic Research (RFBR): grant №. 19-29-06009.

1. A.N. Morozov, S.I. Svetlichnyi, Fundamentals of Fourier spectroradiometry, Moscow, Nauka, 2006.
2. I.B. Vintaykin et al., Raman spectrometer based on a static michelson interferometer, «*Proceedings of the Russian Academy of Sciences. Power Engineering*» Journal, 2016, 6, pp. 144-152.
3. N. Wang, J. Wu, H. Meng, J. Gao, Z. Fan, M. Zhang, Y. Li, J. Li., Performance of a long-wave infrared Fourier Transform imaging spectrometer using a corner-cube Michelson interferometer and an uncooled microbolometer array, *Proc. SPIE*, 2015, 9674, doi:10.1117/12.2197096.
4. M. Schardt, C. Schwallera, A. J. Tremmela, A. W. Kocha, Thermal stabilization of static single-mirror Fourier transform spectrometers, *Proc. of SPIE*, 2017, 10210, doi: 10.1117/12.2261924.
5. T. Svensson, D. Bergström, L. Axelsson, M. Fridlund, T. Hallberg, Design, calibration and characterization of a low-cost spatial Fourier transform LWIR hyperspectral camera with spatial and temporal scanning modes, *Proc. SPIE*, 2018, 10644, doi: 10.1117/12.2304628.

THE DYNAMIC FOURIER-SPECTROMETER FOR RAMAN STAND-OFF DETECTION OF CHEMICAL COMPONENTS

Anatoly A. Balashov², Ilya S. Golyak^{1,2}, Andrey N. Morozov^{1,2}

¹Bauman Moscow State Technical University, Moscow, Russia

²Center of applied physics Bauman Moscow State Technical University, Moscow, Russia

Introduction. Raman spectroscopy is widely used to detect and identify chemical compounds. This is because it has a higher selectivity [1-4], which makes it possible to distinguish very similar molecules and chemical compounds. A disadvantage of the method using Raman spectroscopy is a small scattering cross section. Therefore, registration of Raman spectra requires to use high-aperture system. For the analysis of Raman spectra, diffraction spectrometers are mainly used. Instead of diffraction spectrometers, static [6-8] or dynamic Fourier spectrometers [4, 9] can be used. They can provide a large luminosity [4, 5]. It is important for remote analysis or analysis of a small amount of substance.

The layout of a dynamic Fourier spectrometer for distance obtaining Raman spectra in visible and near-IR spectral range is presented in this work.

Layout is shown in Fig.1. The spectrometer consists of four main parts: a measuring channel, a "white light" channel, a reference channel and a Raman attachment for excitation and collection Raman scattering of light, Fig.1.

The emission spectra are observed in the wavelength region 1000-1500 nm, which corresponds to frequencies of 240-3,500 cm⁻¹.

To excite the Raman spectra, a wavelength-stabilized diode laser with a wavelength $\lambda = 976$ nm, optical power 27mW is used. A laser spectral line width is $\delta\lambda = 0.5$ nm (at a level 90 %). To stabilize the laser, a temperature and current controller is used. Laser is stabilized at temperature 25 degree, which provided the position and spectral line width of the laser line.

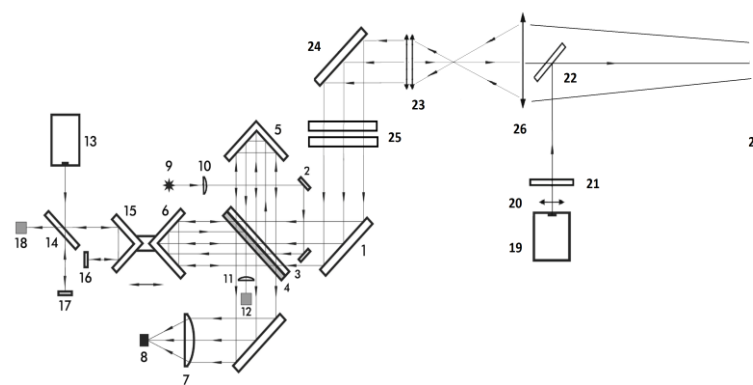


FIGURE 1. Layout of dynamic Fourier-spectrometer

A high sensitivity single-element photodetector IG17X3000T9 with cooling systems is used as a photodetector for registration Raman scattering. Cooling system allows to cool photodetector to minus 20 degrees.

The noise equivalent power (NEP) and detectivity (D^*) are $1,10 \cdot 10^{13} \sqrt{\text{Hz}} \cdot \text{cm/W}$ and $1,3 \cdot 10^{-14} \text{ W}/\sqrt{\text{Hz}}$

In the construction of the interferometer corner reflectors with a second accuracy of the deviation between the incident and reflected rays are used as mirrors. It provides reliability and high stability of the spectrometer in long-term measurements [10, 11].

To accumulate of interferograms and correct summation when a weak signal is registered "white light" channel is implemented. It allows to increase the signal / noise ratio in \sqrt{M} , there M - the number of summed interferogram.

Also a reference channel with a sampling frequency of $\lambda/4$ was realized, that further leads to an increase stability and the expansion of the spectral range of work [11].

With the use of the developed spectrometer, experiments of registration interferograms and reconstructing the Raman spectrum spectra from test sample was carried out. As a test substance was used stilbene ($\text{C}_{14}\text{H}_{12}$), acetylsalicylic acid ($\text{C}_9\text{H}_8\text{N}_2\text{O}_4$). These substances was chosen because their spectrum is well known and their Raman cross section is week [10 - 12].

In the developed Fourier spectrometer, a two-sided interference with a total number of points 34000 are recorded. It ensures a spectral resolution of 2 cm^{-1} .

An example of a recorded two-sided interferogram of stilbene Raman scattering is shown in Fig. 2. The full interferogram is shown in Fig.2 (a), the central part of the interferogram – in Fig.2 (b).

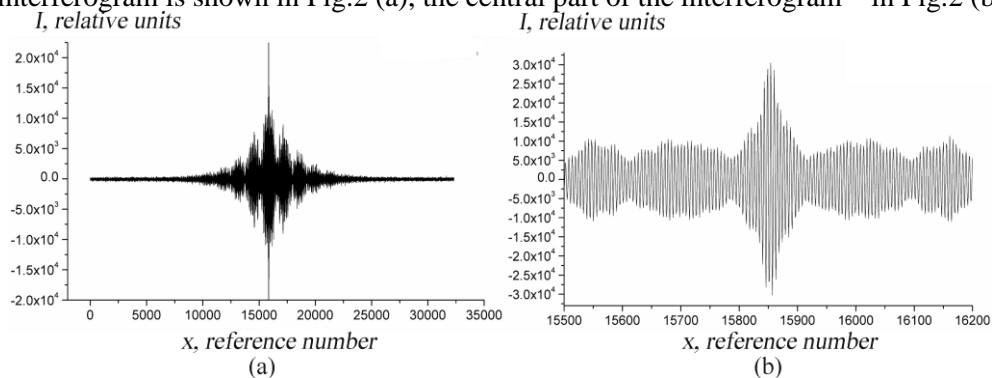


FIGURE 2. Registered interferogram

To reconstruct the Raman spectrum, a full Fourier transform is used [4]. The Raman spectra of the acetylsalicylic acid and stilbene are shown on Fig.3. The samples were located at a distance of 2 meters. The spectrum were obtained by summing over 16 samples.

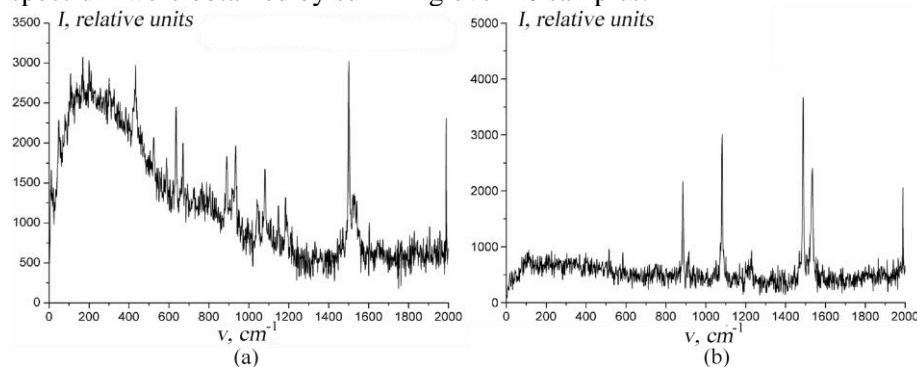


FIGURE 3. Raman spectrum of acetylsalicylic acid (a) and stilbene (b)

On the shown spectrum, separate emission peaks, which correspond to the Raman scattering of test sample, are observed. The main emission peaks in the Raman spectrum of stilbene are located at the following frequencies ν : 1641 cm^{-1} , 1597 cm^{-1} , 1196 cm^{-1} , 1000 cm^{-1} , and the main peaks of acetylsalicylic acid are located on frequencies ν : 3068 cm^{-1} , 2936 cm^{-1} , 1604 cm^{-1} , 1297 cm^{-1} , 1042 cm^{-1} , 748 cm^{-1} , 552 cm^{-1} . Location and number of main peaks in the Raman spectrum, obtained on a dynamic Fourier spectrometer, corresponds to the reference spectrum. Signal noise relation are 39,4 for stilbene and 23,4 for acetylsalicylic acid.

The reported study was funded by RFBR according to the research project №19-29-06009.

1. R.L. McCreery, Raman Spectroscopy for Chemical Analysis, *John Wiley & Sons*, 2005, 420 p.
2. P. Vandenabeele, Practical Raman Spectroscopy: An Introduction, *John Wiley & Sons*, 2013, 161 p.
3. P.R. Griffiths, J.A. De Haseth, J.D. Winefordner, Fourier Transform Infrared Spectrometry, *2nd Edition*, Wiley, 2007, 560 p.
4. A.N. Morozov, S.I. Svetlichnuj, Foundations of Fourier spectroradiometry, *2nd ed. Moscow: Nauka Publ.*, 2014, 456 p.
5. R.J. Bell, Introductory Fourier transform spectroscopy, *Moscow: Mir*, 1975, 380 p.
6. I.B. Vintaykin, N.S. Vasil'ev, Ig.S. Golyak, Il.S. Golyak, A.A. Esakov, A.N. Morozov, S.I. Svetlichnyi, S.E. Tabalin, I.L. Fufurin., Raman spectrometer based on a static michelson interferometer, «*Proceedings of the Russian Academy of Sciences. Power Engineering*» Journal, 2016, 6, pp. 144-152.
7. N.S. Vasil'ev, I.B. Vintaykin, Ig.S. Golyak, Il.S. Golyak, I.V. Kochikov, I.L. Fufurin, Recovery and analysis of raman spectra obtained using a static fourier transform spectrometer, *Computer Optics*, 2017, 41, 5, pp. 626-635.
8. L.V. Egorova, A.S. Anufriev, An imaging dynamic shearing Fourier spectrometer, *Journal of Optical Technology*, 2013, 80, 11, pp. 703-705.
9. A.A. Balashov, V.A. Vaguine, Il.S. Golyak, A.N. Morozov, A.I. Khorokhorin, Multichannel dynamic IR fourier-spectrometer, *Journal of Applied Spectroscopy*, 2017, 84, 4, pp. 643-647.
10. A.A. Balashov, Ig.S. Golyak, Il.S. Golyak, A.N. Morozov, A.I. Nesteruk, A.I. Khorokhorin. Recording Raman Spectra Using a Dynamic Fourier Transform Spectrometer. *J. of App. Spec*, 2018, 85, 5, pp. 923-930.
11. A.A. Balashov, Ig.S. Golyak, Il.S. Golyak, A.N. Morozov, A.I. Khorokhorin, Dynamic type Fourier spectrometer development for Raman spectra detection, *Journal of Physics: Conference Series*, 2019, 1348, pp. 4.
12. Chemical BooK [Electronic resource]. – Access mode: https://www.chemicalbook.com/CASDetailList_15400_EN.htm.

MATHEMATICAL METHODS FOR THE ANALYSIS OF MULTICOMPONENT GAS MIXTURES TO STUDY THE COMPOSITION OF HUMAN BREATH FOR THE PRIMARY DIAGNOSIS OF DISEASES

Igor S. Golyak, Igor L. Fufurin, Andrey N. Morozov

Bauman Moscow State Technical University, Moscow, Russia

Introduction. There is an increasing interest in the measurement of volatile organic compounds (VOCs) in exhaled breath for diagnosis and management of respiratory diseases [1]. Especially in respiratory medicine, to distinguish disease phenotype and enable treatment. Nowadays, gas chromatography with mass spectrometry (GC-MS) is the main instrument for VOCs identification. However, this technique has disadvantages, such as the necessity for expensive equipment, the molecules fragmentation, and sample preconcentration. With the advent of quantum cascade lasers, it has become possible to create a tunable quantum cascade laser-based spectroscopy for the primary diagnosis of diseases [2–6]. This technique enables fast recognition of whole molecules and also has great potential for miniaturization. However, the separation of components from a gas mixture is a non-trivial task due to low molecule concentrations in exhaled air. In environmental monitoring, different methods are actively applied that can be used to analyze exhaled air [7–10].

Experimental results. To test the possibility of applying gas mixture recognition methods, we create the following model. The carbon dioxide concentration in the dried cell of exhaled air (EA) is 0.03%, which corresponds to approximately 300 ppm. Consider the next gas mixture model:

- CO_2 – 300 ppm;
- Acetone – 2 ppm;
- Ethanol – 1 ppm;
- Methanol – 0.1 ppm.

In this case, the concentration of the target substances is 2–3 orders of magnitude lower than the concentration of carbon dioxide. Also, overlapping characteristic lines of methanol and ethanol (see Fig. 1).

We consider a different value of SNR. A sinc filter with a half-width of the window of 2 cm^{-1} is applied to the noisy signal. Model gas mixture examples are shown in Fig. 2

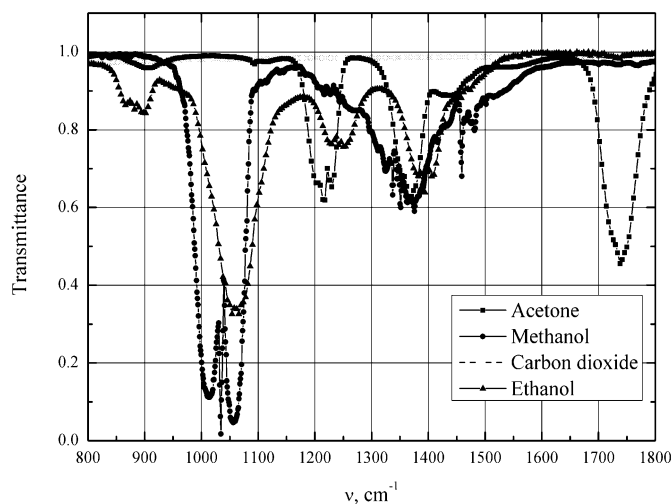


FIGURE 1. The spectra of the components of the mixture in the range $800\text{--}1800\text{ cm}^{-1}$.

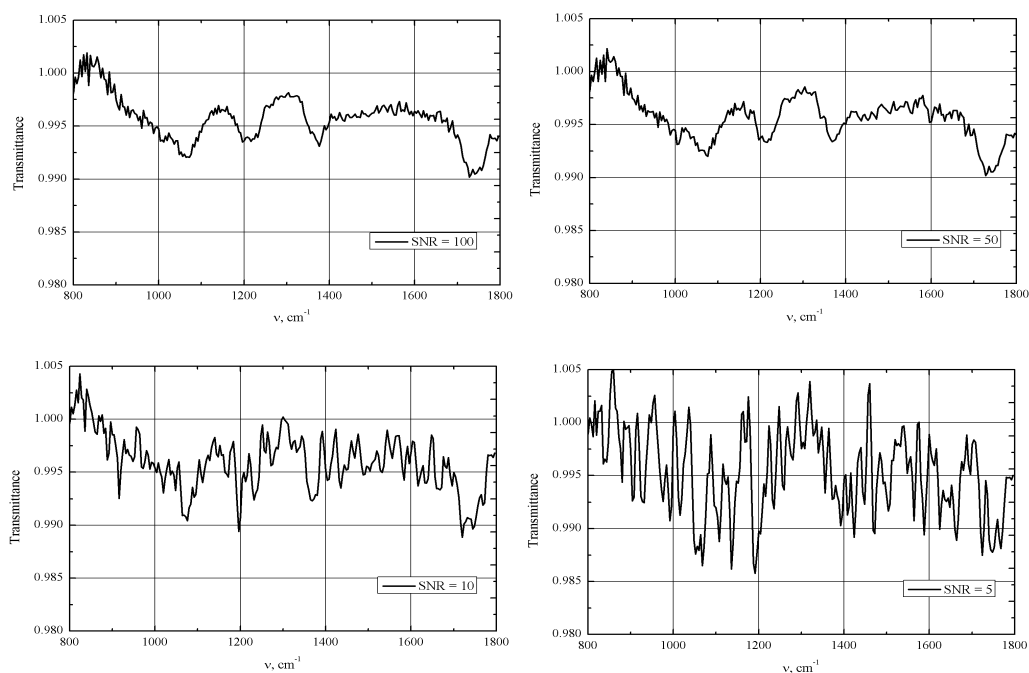


FIGURE 2. Model mixture spectra at different SNR. Sinc half-width filtering with 2 cm^{-1} .

Consider the next methods: the projection method, the method of Bayesian decision estimation, and the method of parametric multidimensional optimization. Table 1 shows the results averaged over 100 numerical experiments.

TABLE 1. The results of the identifier and the relative error in the restoration of concentration.

SNR/Method	Projection method	Bayesian score		Parametric optimization	
100	CO ₂ – 62% CO – false positive Pentane – false positive	Acetone	93%	CO ₂	8%
		Ethanol	92%	Acetone	23%
		Methanol	59%	Ethanol	69%
				Methanol	32%
50	CO ₂ – 52% CO – false positive Phenol – false positive	Acetone	95%	CO ₂	8%
		Ethanol	94%	Acetone	23%
		Methanol	64%	Ethanol	72%
				Methanol	60%
10	CO ₂ – 52% CO – false positive Ethane – false positive	Acetone	98%	CO ₂	8%
		Ethanol	98%	Acetone	21%
		Methanol	60%	Ethanol	79%
				Methanol	44%
5	CO ₂ – 103% CO – false positive Ethane – false positive	Methanol	95%	CO ₂	1%
		Ethylene – false positive		CO – false positive	
		Acetone	64%	Acetone	27%
				Pentane – false positive	

The most accurate of these methods is the parametric optimization method. However, it gives too many errors in the reconstruction of concentration.

To obtain more accurate results, we consider a two-stage method: predicting the component composition and then refining the concentration of each component by the parametric optimization method. The results are shown in Table 2.

TABLE 2. The results of the identifier and the relative error in the restoration of concentration with Multidimensional optimization.

SNR\Method	Double Multidimensional optimization	
100	CO ₂	8%
	Acetone	13%
	Ethanol	29%
	Methanol	49%
50	CO ₂	8%
	Acetone	7%
	Ethanol	25%
	Methanol	49%
10	CO ₂	8%
	Acetone	11%
	Ethanol	46%
	Pentane – false positive	
5	CO ₂	6%
	CO – false positive	
	Acetone	23%
	Pentane – false positive	

In general, the recalculation of the concentration increases by several percents the accuracy of calculating the concentration.

The reported study was funded by RFBR according to the research project №18-29-02024.

1. M. Barker, M. Hengst, J. Schmid, H-J. Buers, B. Mittermaier, D. Klemp, R. Koppmann, Volatile organic compounds in the exhaled breath of young patients with cystic fibrosis, *European Respiratory Journal*, 2006, 27(5), pp. 929–936, doi:10.1183/09031936.06.00085105.

2. M. R. McCurdy, Y. Bakhirkin, G. Wysocki, R. Lewicki, and F. K. Tittel, Recent advances of laser-spectroscopy-based techniques for applications in breath analysis, *Journal of Breath Research*, 2007, 1(1), pp. 14001, doi: 10.1088/1752-7155/1/1/014001.

3. F. M. Schmidt, O. Vahtinen, M. Metsälä, M. Lehto, C. Forsblom, P-H. Groop, L. Halonen, Ammonia in breath and emitted from skin, *Journal of Breath Research*, 2013, 7(1), pp. 17109, doi: 10.1088/1752-7155/7/1/017109.

4. J. Mandon, M. Högman, P. J. F. M. Merkus, J. van Amsterdam, F. J. M. Harren, S. M. Cristescu, Exhaled nitric oxide monitoring by quantum cascade laser: comparison with chemiluminescent and electrochemical sensors, *Journal of Biomedical Optics*, 2012, 17(1), 17003, doi: 10.1117/1.jbo.17.1.017003.

5. E. van Mastrigt, A. Reyes-Reyes, K. Brand, N. Bhattacharya, H.P. Urbach, A.P. Stubbs, J.C. de Jongste, M.W. Pijnenburg, Exhaled breath profiling using broadband quantum cascade laser-based spectroscopy in healthy children and children with asthma and cystic fibrosis, *Journal of Breath Research*, 2016, 10(2), pp. 26003, doi: 10.1088/1752-7155/10/2/026003.

6. A. Reyes-Reyes, Z. Hou, E. van Mastrigt, R. C. Horsten, J. C. de Jongste, M. W. Pijnenburg, H. P. Urbach, N. Bhattacharya, Multicomponent gas analysis using broadband quantum cascade laser spectroscopy, *Optics Express*, 2014, 22(15), pp. 18299, doi: 10.1364/OE.22.018299.

7. I.L. Fufurin, A.S. Tabalina, A.N. Morozov, I.S. Golyak, S.I. Svetlichnyi, D.R. Anfimov, I.V. Kochikov, Identification of substances from diffuse reflectance spectra of a broadband quantum cascade laser using Kramers–Kronig relations, *Opt. Eng.* 2020, 59(6), pp. 061621, doi: 10.1117/1.OE.59.6.061621.

8. N.S. Vasil'ev, I.B. Vintaykin, I.S. Golyak, I.S. Golyak, I.V. Kochikov, I.L. Fufurin, Recovery and analysis of Raman spectra obtained using a static Fourier transform spectrometer, *Computer Optics*, 2017, 41(5), pp. 626–635, doi: 10.18287/2412-6179-2017-41-5-626-635.

9. M. Belov, Quantitative gas analysis of complex multicomponent mixtures, *Science and Education of the Bauman MSTU*, 2013, 13(10), pp. 233-255, doi:10.7463/1013.0615247.

10. V.I. Kozintsev, M.L. Belov, V.A. Gorodnichev, Iu.V. Fedotov, *Osnovy kolichestvennogo lazernogo analiza* [Fundamentals of quantitative analysis of the laser], Bauman MSTU Publ, Moscow, 2006, pp. 464.

INFRARED SPECTROSCOPIC SYSTEM FOR HUMAN BREATH ANALYSIS

Igor L. Fufurin, Andrey N. Morozov, Elizaveta R. Kareva, Anastasiia S. Tabalina

Bauman Moscow State Technical University, Moscow, Russia

Introduction. The development of fast non-invasive screening systems that enable pathology to be detected at an early stage of evolution is one of the important scientific and technological problems in the field of medicine. One of the approaches that can ensure non-invasive diagnosis of diseases in real time is an express analysis of human exhaled air [1]. The development of laser technologies in the field of creating widely tunable quantum cascade lasers (QCLs) provides new opportunities for creating fast, relatively compact and effective systems for diagnosing diseases according to the composition of exhaled air.

1. Prospects of using QCL. As exhaled air is a complex gas mixture, analysis of its microstructure requires high selectivity for the detection of target substances; insensitivity to nitrogen and oxygen, the concentration of which are tens of percent; selectivity for water vapor and CO₂. The mid-infrared range, which contains the spectral lines of vibrational-rotational transitions, is very informative [2]. A wide range of QCL rearrangements will make it possible to analyze simultaneously a large number of different biomarker molecules.

2. Experimental setup. It is proposed to use an experimental setup, the circuit diagram of which is shown in Fig. 1. Two main modules can be distinguished in the scheme: the radiation analysis module (Fig. 1a) and the sample supply module (Fig. 1b).

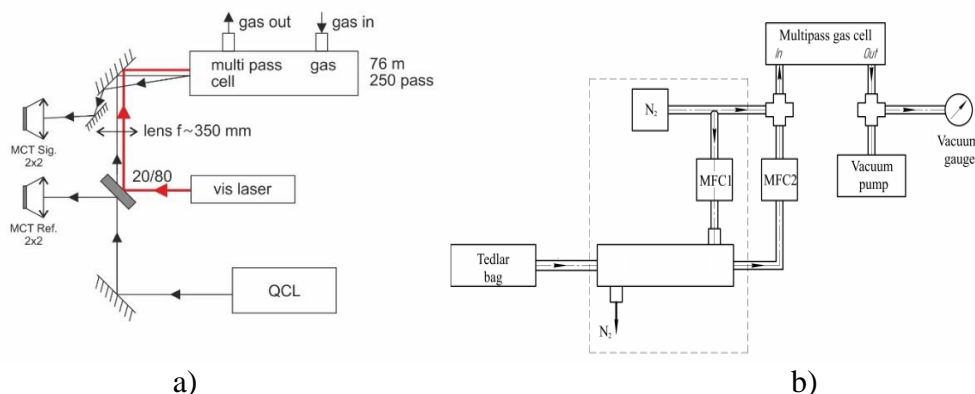


FIGURE 1. Schematic diagram of the experimental setup. a) radiation analysis circuit b) flow pattern of the test sample: MFC – mass flow gas controller.

The following main technical solutions are proposed to achieve the highest possible sensitivity: use of a reference photodetector; study of the sample inside an astigmatic multi-pass gas cell with an optical path length of up to 76 m; removal of water from the test sample; evacuation of a gas cell to eliminate the possibility of any atmospheric fluctuations.

3. Experimental results. Using QCL spectra of test membranous simulators and gas mixtures were recorded in a multi-pass cell. Experimental sensitivity-estimations for certain chemical compounds,

including biomarkers, were performed for setup based on QCL and multi-pass gas cell (table 1) [10]. These results were obtained for the optical path length of 6 m.

TABLE 1. The sensitivity of the experimental setup based on QCL with a multi-pass cell. [10].

Substance	Detection limit
Methane	0.5 ppm
Formaldehyde	2.1 ppm
Ammonia	0.9 ppm

4. Expected results. A number of computational experiments were performed to test methods for processing experimental data. A simplified model of a drained sample of exhaled breath was considered (Fig. 2). The main component of model mixture (carbon dioxide) had nominal concentration 300 ppm.

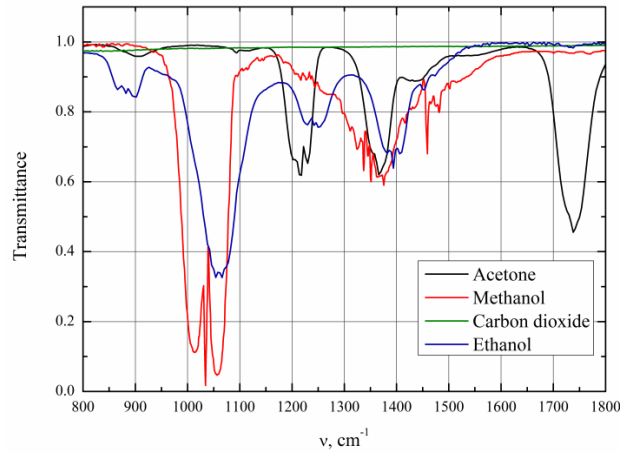


FIGURE 2. Base spectra of mixture components (NIST).

Examples of model mixtures are shown on Fig. 3. In this work for mixture analysis we considered 3 methods: method of Bayes estimation, parametric optimization and double parametric optimization. Table 2 shows results of model mixtures analyzing for the test spectral database for SNR=100.

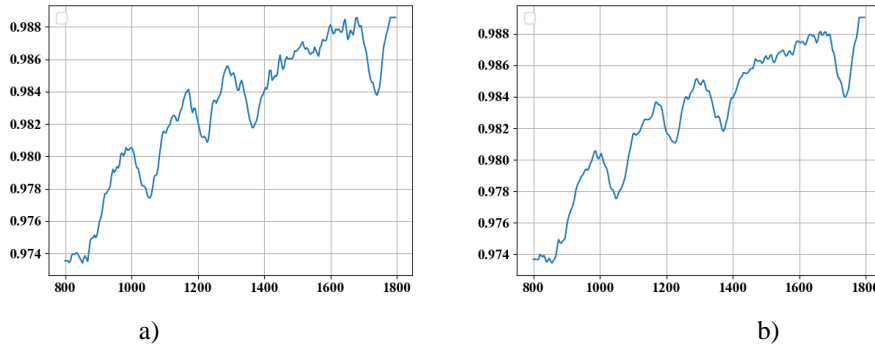


FIGURE 3. The spectra of the model mixture for various SNR: a) SNR = 50; b) SNR = 100.

TABLE 2. Results of computational experiments.

SNR	Bayes estimation	Parametric optimization	Double parametric optimization
100	Acetone $c = 0.14$ ppm $\delta = 93\%$; Ethanol $c = 0.08$ ppm $\delta = 92\%$;	Acetone $c = 1.53$ ppm $\delta = 23\%$; Ethanol $c = 0.32$ ppm $\delta = 68\%$;	Acetone $c = 1.65$ ppm $\delta = 18\%$; Ethanol $c = 0.68$ ppm $\delta = 32\%$;

	Methanol c = 0.04 ppm $\delta = 59\%$	Methanol c = 0.06 ppm $\delta = 40\%$	Methanol c = 0.03 ppm δ $= 71\%$
--	--	--	--

Conclusions. The main goal of medical diagnostic systems is to provide a practicing doctor with a tool for effective diagnosis and monitoring of the course of the disease. Methods of absorption spectroscopy, which are the basis for the design of the radiation analysis module, will ensure the operation of the system in real time.

The reported study was funded by RFBR according to the research project №18-29-02024.

1. M. Phillips, Breath tests in medicine, *Scientific American*, 1992, 267(1), pp. 74-79.
2. L. A. Wallace, E. D. Pellizzari, T. D. Hartwell, C. M. Sparacino, L. S. Sheldon, H. Zelon., Personal exposures, indoor-outdoor relationships, and breath levels of toxic air pollutants measured for 355 persons in New Jersey, *Atmospheric Environment* (1967), 1985, 19(10), pp. 1651-1661, doi: 10.1016/0004-6981(85)90217-3.
3. E.V. Stepanov, Diode laser spectroscopy and analysis of biomarker molecules. *M.: FIZMATLIT*, 2009, 416 p.
4. C. Wang, P. Sahay, Breath analysis using laser spectroscopic techniques: breath biomarkers, spectral fingerprints, and detection limits, *Sensors*, 2009, 9(10), pp. 8230-8262, doi: 10.3390/s91008230.
5. M. R. McCurdy, Y. Bakhirkin, G. Wysocki, R. Lewicki, F. K. Tittel, Recent advances of laser-spectroscopy-based techniques for applications in breath analysis, *Journal of breath research*, 2007, 1(1), pp. 014001.
6. D.A. Samsonov, A.S. Tabalina, I.L. Fufurin, QCL spectroscopy combined with the least squares method for substance analysis, *Journal of Physics: Conference Series*, 2017, 918(1), pp. 012034, doi: 10.1088/1742-6596/918/1/012034.
7. I. L. Fufurin, A. S. Tabalina, A. N. Morozov, I. S. Golyak, S. I. Svetlichnyi, D. R. Anfimov, I. V. Kochikov, Identification of substances from diffuse reflectance spectra of a broadband quantum cascade laser using Kramers-Kronig relations, *Opt. Eng.*, 2020, 59(6), pp. 061621, doi: 10.1117/1.OE.59.6.061621.
8. I.L. Fufurin, O.A. Nebritova, A.S. Tabalina, Methodology for identification biomarker molecules in human expired air, *Acoustooptical and radar methods for measuring processing information. Ser. "Materials of the 12th international scientific and technical conference"*, 2019, pp. 89-92.
9. A. N. Morozov, I. L. Fufurin, A. S. Tabalina, Technique of substances identification by scattering spectra, acquired by quantum cascade laser (QCL), *Proc. of ARMIMP-2018*, 2018, pp. 93-7.
10. I. S. Golyak, A. N. Morozov, S. I. Svetlichny, A. S. Tabalina, I. L. Fufurin, Identification of chemical compounds by scattered radiation spectra in the wavelength range of 5.3-12.8 microns using a tunable quantum cascade laser, *Russian Journal of Physical Chemistry B*, 2019, 38(7), pp. 557-564, doi: 10.1134/S1990793119040055.

AUTOMATIC ALIGNMENT OF THE TRACE FOURIER SPECTROMETER

Pavel P. Demkin, Igor L. Fufurin

Bauman Moscow State Technical University, Moscow, Russian Federation

Introduction. The identification of hazardous chemical compounds in the air is one of the most important tasks in ensuring safety, preventing terrorist threats and preventing emergency situations.

Systems based on active and passive Fourier spectrometers have found widespread use in this area, and their high aperture allows the target substances to be detected in air at a distance of several kilometers [1-2]. A distinctive feature of active methods is the use of a backlight, which allows to increase the contrast between the cloud of the target substance and the underlying surface, thereby

reducing the likelihood of false positives [3]. The main disadvantage of this type of system is the relatively slow system sweep speed when working in the field. Significant time is spent on adjusting the relative position of the infrared source (IS) and the receiving device. The complexity of the adjustment in this case, the greater the longer the control path. In this report, we propose an algorithm for automatic adjustment of the system based on an active Fourier spectrometer using data obtained from the IR and visible channels of the system.

Scheme of an active Fourier spectrometer. The algorithm was developed for an environmental monitoring system based on an active Fourier spectrometer, the scheme of which is shown in Fig. 1.

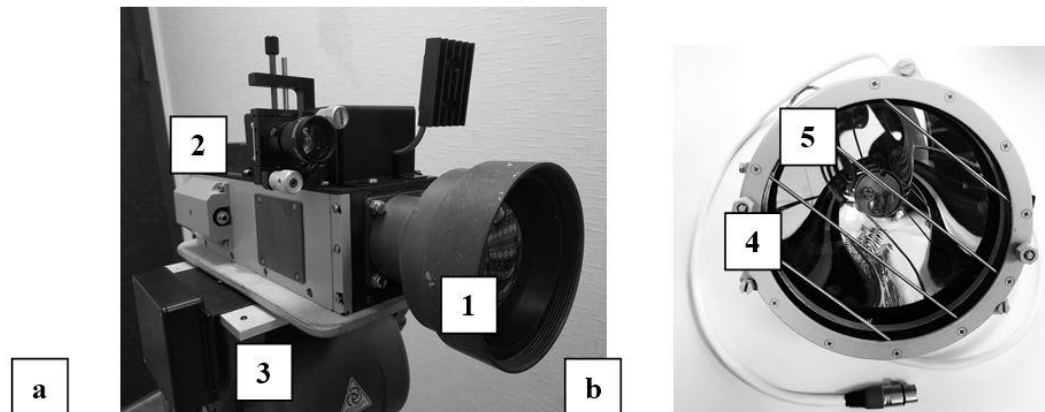


FIGURE 1. Appearance of the main modules of the environmental monitoring system: a) wholesale mechanical unit: 1– Fourier spectrometer; 2 - television sight; 3 - slewing ring; b) radiation source block: 4 – nichrome spiral; 5 - parabolic reflector.

Two main modules can be distinguished in the system: the wholesale mechanical module (see Fig. 1a) and the infrared source module (IS) (see Fig. 1b). The structure of the wholesale mechanical module includes, directly, a Fourier spectrometer (1), a television sight (2), and also a slewing ring with high positioning accuracy (3). The IS module is a parabolic reflector with an incandescent spiral located in the center. The image of the control path is received from the television sight through the “video” channel, and the recorded interferogram is transmitted from the Fourier spectrometer through the “IR” channel.

Setting the relative position of the wholesale mechanical module and the IS in order to obtain the maximum range of the interferogram is the main task of adjusting the system.

System alignment automation technique. Automatic adjustment of the system can be carried out both by the image received from the television sight (that is, by the “visible” channel), and by the intensity of the recorded interferogram (by the “IR” channel). In this paper, we implement an algorithm for adjusting the system based on data from both channels of the Fourier spectrometer. In this case, the adjustment is carried out in two stages.

The primary alignment of the system occurs on the “visible” channel. In the image of the route, the algorithm determines an area colored in region (1). The area of the proposed position of the spiral is highlighted (Fig. 2 (1)). Relative to the selected region (1), based on the known data on the geometry of the IS and its radiation pattern (see Fig. 3a), the coordinates are determined and the region (2) is selected, along which the second stage of the system guidance will take place.

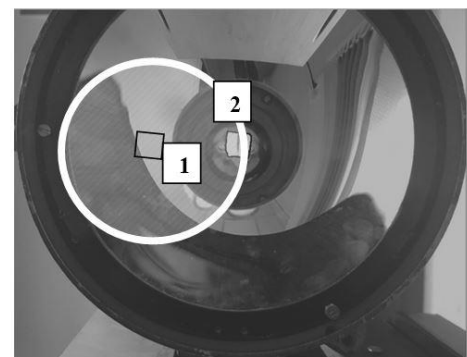


FIGURE 2. Alignment by the “video” channel of the system.

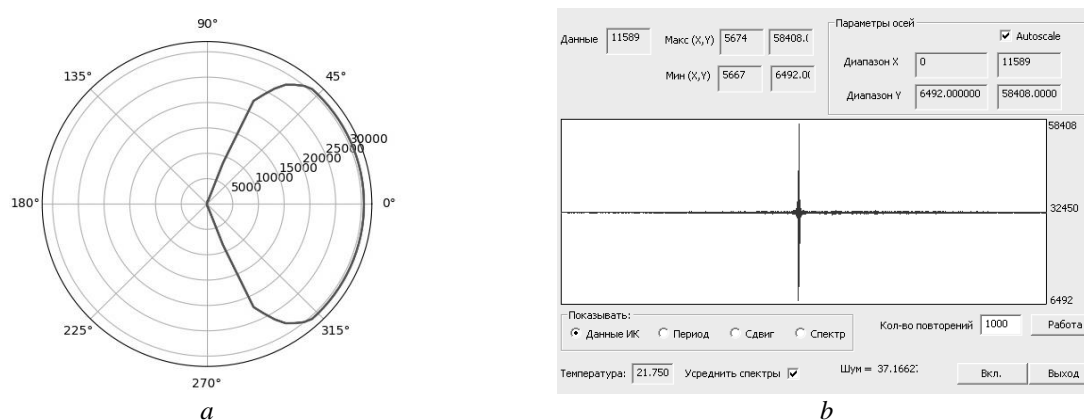


FIGURE 3. a) IS radiation pattern; b) Registration of the span of the interferogram.

Using the slewing ring and the calculated coordinates, the system adjusts to the center of the selected area. At the second stage of the system adjustment, the optimal position of the wholesale mechanical module is adjusted for operation. Inside the region (2), using the rotary support device, the control path is scanned to determine the position corresponding to the largest interferogram span (see Fig. 3b). After the scan is completed, the slewing device returns the system to the coordinates corresponding to the recorded maximum of the interferogram [4].

Conclusion. The described algorithm was worked out in laboratory conditions, with a control track length of 20 m. In the future, it is planned to conduct tests in the field and with increasing distance between the IS and the receiving device.

At the next stage of development, it is planned to further improve the alignment algorithm in order to ensure effective system tuning in the field with a track length of up to 500 m.

1. S.V. Bashkin, A.Yu. Boiko, V.N. Kornienko, I.V. Kochikov, M.V. Lel'kov, A.I. Mironov, A.N. Morozov, A.A. Pozvonkov, A.S. Samorodov, S.I. Svetlichnyi, S.Ye. Tabalin, I.L. Fufurin, P.E. Shlygin, Experimental results of investigating panoramic Fourier transform infrared spectrometer, *Herald of the Bauman Moscow State Technical University. Series Natural Sciences*, 2016, 65(2), pp. 495, doi: 10.18698/1812-3368-2016-2-51-64. (in Russian)

2. A. N. Morozov, S. E. Tabalin, I. L. Fufurin, and S. I. Svetlichnyi, Physical principles of the design of an interferometer with a rotating plate, *Journal of Optical Technology*, 2013, 80(8), pp 495-498, doi:10.1364/JOT.80.000495.

3. A.N. Morozov, I.L. Fufurin, S.I. Svetlichnyi, Correction of wavenumbers in a FTIR imaging spectrometer, *Doklady Physics*, 2015, 60(9), pp. 388-391.

4. L. Kral Automatic beam alignment system for a pulsed infrared laser, *Review of Scientific Instruments*, 2009, 1(80), pp. 13102.

DETERMINATION OF THE SENSITIVITY OF A MICROBOLOMETER CAMERA AS PART OF A STATIC FOURIER SPECTRORADIOMETER

Pavel A. Korolev¹, Ilya S. Golyak^{1,2}, Andrey N. Morozov^{1,2}

¹Center of applied physics Bauman Moscow State Technical University, Moscow, Russia

²Bauman Moscow State Technical University, Moscow, Russia

Introduction. Remote detection of dangerous toxic substances is critically important in ensuring security. One of the most effective methods of solving this situation is the use of IR spectrometers, which allow for sampling-free analysis of the air environment. Static interferometer devices designed on the basis of the Michelson interferometer have a number of advantages compared to dynamic ones using a movable mirror. But on the other hand, they have special requirements for the use of a photodetector designed for detecting IR radiation. The photodetection device (FDD) must be a matrix of photosensitive elements capable of detecting IR radiation. Moreover, to ensure the ability to recognize gases such as Ammonia and Ethanol in the air, specific requirements are imposed on the photodetection device - the operating range of which should be 7-13 microns.

In this paper, a microbolometer camera is used as a photodetector for IR radiation. The measurements of its main parameters are given: the sensitivity of the FDD and the signal-to-noise ratio (SNR) of the receiver. These values are used for setting up microbolometer camera modules in the device. As a result of the experiment, the sensitivity of the camera was 80 mK, which was worse than the stated one, and the SNR of the device, reduced to one degree, is equal to 342 units. The dependence of the signal-to-noise ratio on the shutter frequency of the microbolometer camera is obtained. To confirm the efficiency, the ammonia spectrum was obtained, which was compared with the reference one.

Microbolometer matrices are used in various configurations of the Fourier spectrometer [1, 2]. IR cameras are a matrix of microbolometer detectors combined in a linked system. Bolometers work by changing the electrical resistance of a thermosensitive element when it is heated [3]. The signal-to-noise ratio in the device depends on the illumination of the detector, on the change in the temperature of the FDD during self-heating, and on the ambient temperature. These problems are solved by introducing new temperature coefficients for calibration of spectral errors [4].

To compensate for temperature changes in the IR matrix, the camera needs to periodically calibrate using a mechanical shutter to avoid distortion of the inhomogeneous pixel sensitivity in the interferogram image. A mechanical gate that is an absorbing surface placed in front of the detector. It is an internal compensator that the microbolometer requires, for example, to compensate for pixel drifts. Adjusting the inter-frame and intra-frame delays contributes to the stable operation of the shutter and the device [5].

Patent [6] is a microbolometer detector for detecting IR radiation in two spectral ranges. Thin layer of tantalum provides a wide absorption with peak at 8-9 microns and the another one in the range of 3-5 microns. Silicon nitride, which is part of the film, absorbs in the range of 9-13 microns and has an absorption peak of 11-13 microns. According to the authors, this invention allows maintaining equal absorption coefficients without reducing the resolution. Based on [6], a Russian-made microbolometer matrix design was created [7].

The purpose of this work is to determine the sensitivity of the IR camera, as well as the placement of wave numbers using the reference spectrum of ammonia. In the process of writing this paper, the following tasks are solved: building a signal-to-noise ratio curve from time between two calibrations, determining the noise-equivalent temperature difference (NETD) in the interference pattern horizontally and vertically, and arranging wave numbers along the abscissa axis to construct the

ammonia spectrum. The signal-to-noise ratio reduced to 1 Kelvin in the interferogram recorded by the device is determined.

Experimental part. For the experiment, a radiation source is a blackbody model - “АЧТ-6А”, a power supply - an ATN-2333 device, and a microbolometer camera with a 40 mm f/1 lens mounted on it were used. The microbolometer camera has a size of 640-480 pixels: 640 columns and 480 rows.

During the experiment, radiation from a completely black body was measured. In this case, the temperature difference of 3K between the aft emitter and the environment was provided, and noise was recorded, both from the signal measured on a surface with the same temperature, and from the surface of the emitter and the adjacent substrate having the ambient temperature. The difference of signals between the surface of the radiator and the adjacent substrate with the ambient temperature was also recorded.

Figure 1 shows an IR image from the blackbody. It was represented as a matrix of integers. Sensitivity was determined by the rows and columns of the matrix.

To determine the sensitivity, the noise-equivalent temperature difference was calculated. During the experiment, the signal-to-noise ratio was calculated for different settings of the microbolometer camera: exposure, gain, and offset.

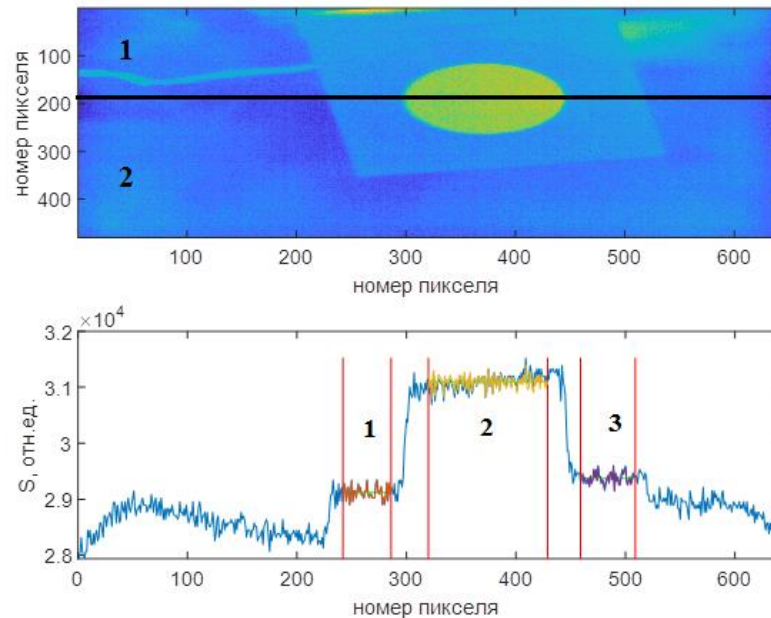


FIGURE 1. Top picture - Snapshot of the black body model in the far IR range, the exposure time is 10 microseconds, the signal gain is 16, temperature difference is 3 K; Bottom picture - dependence of the signal on the element number in the line.

The results of experiments to determine the sensitivity of the IR camera for rows of the matrix are presented in Table 1. Each column of the table has its own exposure time (10, 30, 50 and 70 microseconds). Each line corresponds to a sensitivity value for a different combination of signal amplification (16, 32, 64) and a temperature difference of 1 or 3 K.

TABLE 1. The sensitivity of the IR camera in the rows of the matrix

Signal amplification	Temperature difference (ΔT), K	Exposure time, uSec			
		10	30	50	70
32	1	0,185691	0,106442	0,082690	-

32	3	0,162483	0,089238	0,079497	0,090776
64	1	0,187500	0,108897	0,100421	-
64	3	0,161461	0,097723	0,082787	-
16	3	0,180488	0,113742	0,093468	0,093797

Conclusion. The calculated sensitivity parameters of the microbolometer camera in the horizontal position were higher than the one stated in the passport (80 MK instead of 50 MK), the calculated signal-to-noise ratio is 342 units. The dependence of the signal-to-noise ratio on the time between calibrations in a static Fourier Spectroradiometer found from the experiment showed that as the time between calibrations increases, the signal-to-noise ratio decreases due to the loss of relevance of the calibration data.

1. T. Svensson, D. Bergström, L. Axelsson, M. Fridlund, T. Hallberg, Design, calibration and characterization of a low-cost spatial Fourier transform LWIR hyperspectral camera with spatial and temporal scanning modes, *Proc. SPIE*, 2018, pp. 10644, doi: 10.1117/12.2304628.
2. Nan Wang, Jianghui Wu, HeminMeng, JiaoboGao, Zhe Fan, Mingxuan Zhang, Yu Li, Jianjun Li, Performance of a long-wave infrared Fourier Transform imaging spectrometer using a corner-cube Michelson interferometer and an uncooled microbolometer array, *Proc. SPIE*, 2015, 9674, doi:10.1117/12.2197096.
3. S. V. Mikheev, Basics of infrared technology: studies.manual for students. SPb., 2017. Access mode <https://books.ifmo.ru/file/pdf/2262.pdf> (accessed 30.03.2019).
4. M. Schardt, C. Schwallera, A. J. Tremmela, A. W. Kocha, Thermal stabilization of static single-mirror Fourier transform spectrometers, *Proc. of SPIE*, 2017, 10210. doi: 10.1117/12.2261924.
5. J. Peeters, E. Louarroudi, D. DeGreef, S. Vanlanduit, J. J. J. Dirckx, G. Steenackers, Time calibration of thermal rolling shutter infrared cameras, *Infrared Physics&Technology*, 2017, 80, pp. 145-152. <https://doi.org/10.1016/j.infrared.2016.12.001>.
6. S. A. Denim, B. V. Troshin, S. A. Zhukova, V. E. Turkov, Fast-Acting wide-range infrared microbolometer detector: Pat. RU 2574524 C1. 2016.
7. S. A. Zhukova, V. E. Turkov, S. A. Demin, A. A. Solodkov, Sensitive elements of infrared vision systems based on microbolometer matrices of 640480 pixels format, *Nano - and Microsystem technology*, 2017, 19 (2), pp. 105-113.

OPTICAL METHODS FOR DETECTING AND TRACKING UNMANNED AERIAL OBJECTS AGAINST THE BACKGROUND OF NATURAL OBJECTS

Andrey N. Morozov, Andrey L. Nazolin, and Igor L. Fufurin

Bauman Moscow State Technical University, Moscow, Russia

Introduction. In the past few years, the technology of unmanned aerial vehicles (UAV) significantly improved. UAV have got application in various areas of urban infrastructure. There is a high probability of penetration of third-party UAV to protected objects or to crowded places, and there is also the possibility of carrying a variety of including dangerous load on board the UAV. Detection and identification of AUV and recognition of a dangerous load is an important research. Currently, a large number of papers and projects are underway in this and related areas.

The analysis of the prior research. In paper [1], the classification of UAV by type, size, and technical characteristics is given, as well as the main methods for detecting UAV based on the analysis of radio-frequency and video signals. In paper [2], as well as in US patent 9,715,009 B1, limitations on the use of radar systems for detecting modern miniature UAVs such as ZALA 421-08, DJI Phantom 2

and the like are given. It is shown that for the detection and identification of such types of UAV, an effective approach is the use of optical location methods, including in conjunction with sensors based on the analysis of the radio frequency spectrum and acoustic waves. Also, in paper [3], it was shown that when using radar methods for detecting small UAV for distances of 250-700 m, there is a dead zone, and in this case, the use of optical methods for detecting UAV is necessary.

There are two approaches to detecting objects by infrared image in world practice. The first approach [4] is associated with the identification of an object by its own radiation using thermal imagers. The object self-radiation spectrum has bands in the spectral range of 7-14 μm . Modern thermal imagers have a sensitivity for brightness temperature of about 0.05 K. In the future, such systems need to be equipped with a zoom lens up to 10-20 times. The second approach involves the use of active infrared laser illumination, for example, an IR laser of 903 nm or 1560 nm [5] for detecting and identifying an object, topographic terrain, followed by the allocation of moving UAVs against the background of moving wildlife. To be able to detect UAV at a distance of up to 2 km, the authors propose using 1560 nm with a pulse duration of 1 ns, a repetition rate of 1 MHz and a pulse power of 700 kW. The angular field of the laser beam is -0.5×0.5 deg. The system is equipped with a matrix photodetector (150x20 pixels) and an optical system such that the FOV of the matrix photodetector corresponds to the angular field of the laser beam. In other words, the system works by fixing the reflected signal from the UAV in the given angular space by matrix photodetector. The scanning system is equipped with a high-speed galvanometric mirror ($f = 1$ kHz) for sequential scanning of the laser backlight field. Similar systems also serve as a laser rangefinder - lidar.

In [6], the possibility of detecting UAV using IR cameras in the warm air emitted by the UAV engine or the battery is described. To visualize the laser lidar data, 3D topographic methods of the OctoMap type are used [7]. There is a whole class of methods for the dynamic analysis of the background and the allocation of moving obscure objects [8]. To analyze images and 3D pictures (such as a hypercube), graph theory methods and neural networks are used [9]. Since 2012, the Convolution neural Network (CNN), which can detect objects in real time with high accuracy, has been developed in the field of deep learning.

Currently, the most popular networks used in deep learning to solve this problem are the networks FasterR-CNN [10], YOLO [11], SSD [12]. Each model depends on a basic classifier that affects the quality of the model [13]. In 2013, the R-CNN model [14] was developed, which improved the accuracy of detection to 58 points.

Methods of optical location of the UAV suggest the allocation of parts of the image of the object and a set of characteristic features. On the other hand, spectral optical methods are used in the world practice to analyze the chemical composition of the material from which the UAV coating is made, as well as to detect trace amounts of substances on the surface of an object. So, for example, luminescent methods using ultraviolet illumination can be used to analyze biological objects [15]. Such approaches make it possible to distinguish objects of animate and inanimate nature from a distance, which, for example, can make it possible to distinguish UAV from birds and serve as an additional detection channel.

The monograph [16] provides an overview of existing laser methods for the analysis of chemical compounds. Among the most relevant spectral methods for analyzing trace amounts of substances on the surface of a test object at a distance are luminescent spectroscopy with UV illumination, Raman spectroscopy, differential absorption spectroscopy based on a tunable UV laser, spectral imaging method (hyper / multispectral images), laser diffuse reflectance spectroscopy using infrared tunable quantum cascade lasers (QCL).

So, in [17] it was shown that for a source at a wavelength of 532 nm with an energy of 100 mJ per pulse and using a telescope with an aperture of 203 mm, chemical compounds were detected at a distance of several hundred meters. In [18], the results of using a quantum cascade laser with a tuning

of 7.6–11.4 μm with a radiation power of 100 mW/cm^2 are presented and it is shown that by constructing hyperspectral images it is possible to detect trace amounts of substances up to 10 $\mu\text{g}/\text{cm}^2$ at a distance of 20 m. The possibility of creating lidars of diffuse reflectance of IR radiation based on IR QCL for remote detection of substances on surfaces was shown in [19]. It was shown in [20] that using QCL peak power 150mW and spectral range 5.3-12.8 μm with Peltier-cooled MCT photodetector minimum detection limit is of about 10 $\mu\text{g}/\text{cm}^2$ at a distance of about 1 m.

Detecting system. Assessment of the limiting detection distances and tracking of UAVs by optical methods requires additional fundamental scientific research. The purpose of such studies should be to develop the scientific foundations of remote detection, identification, tracking and determination of UAV parameters and UAV membership in various groups by optical location methods and optical spectroscopy, as well as automatic optical recognition in various environments against the background of moving objects of wildlife.

In the first part of our research we focus on video images analysis in order to identify UAV, tracking and determining their characteristics, including the distance to them. For their implementation, it is proposed to use special equipment as part of a video camera with IR sensitivity ranges for night time operation, an IR illumination system using a laser such as M976-140-F135, a zoom of at least 20 times, precision rotary platform with positioning accuracy ~ 1 mrad, laser rangefinder at a wavelength of 1540 nm with a pulse duration of not more than 25 ns, a radiation divergence of not more than 1 mrad and a radiation energy of not less than 15 mJ.

Then, it is planned to study the possibility of creating a hybrid lidar complex for identifying UAVs and transported cargo, as well as diagnosing vortex formations, consisting of the following main devices: a luminescent lidar with a 266 nm UV laser with a pulse duration of 8 ns, a repetition rate of 20 Hz and radiation energy not less than 10 mJ; industrial camera 1 MP in the range of 120-1100 nm type IStar DH334T; differential absorption lidar based on a tunable UV laser in the wavelength range 193 - 2600 nm with a pulse repetition rate of 1 kHz and a pulse energy of at least 40 μJ type NT 242; Raman lidar based on a pulsed laser with a wavelength of 532 nm and pulse energies of at least 50 mJ of type LD75-G; diffuse light reflectance lidar based on a quantum cascade laser and a KRT-Peltier photodetector; lidar of diffuse light reflectance based on a tunable IR laser with a wavelength of 4400 - 18000 nm pulse energy of at least 1 mJ, radiation divergence of not more than 1 mrad type NT 373-XIR and a KRT-ISS photodetector; infrared lidar for recording the characteristics of vortex formations during the movement of UAV.

Conclusions. To create a UAV control system, it is necessary to combine methods of optical location and spectral analysis, methods of statistics, graphs theory, machine learning, neural networks, and automatic control methods, which is an complex fundamental scientific task.

The reported study was funded by RFBR according to the research project No. 19-29-06009.

1. E. Filin E., Kirichek R.: Approaches to the Detection Micro Air Vehicle Based on the Analysis of the Electromagnetic Spectrum // *Telecom IT*, 2018, 6(2), pp. 87–93 (in Russian).
2. V. Stary, V. Krivanek, A. Stefek, Optical Detection Methods for Laser Guided Unmanned Devices, *Journal of Communications and Networks*, 2008, 20(5), pp. 464-472, doi: 10.1109/JCN.2018.000071.
3. J. J. Farlik, M. Kratky, J. Casar and V. Stary. Radar cross section and detection of small unmanned aerial vehicles, 2016, *17th International Conference on Mechatronics - Mechatronika (ME)*, Prague, 2016, pp. 1-7.
4. B. H. Kim, M. Y. Kim, Anti-saturation and contrast enhancement technique using interlaced histogram equalization (IHE) for improving target detection performance of EO/IR images, *Pros. 17th International Conference on Control, Automation and Systems (ICCAS)*. IEEE, 2017, doi: 10.23919/iccas.2017.8204254.
5. B. Kim, D. Khan, C. Bohak, W. Choi, H. Lee, M. Kim, V-RBNN Based Small Drone Detection in Augmented Datasets for 3D LADAR System, *Sensors*, 2018, 18(11), pp. 3825. doi:10.3390/s18113825.

6. T. Müller, Robust drone detection for day/night counter-UAV with static VIS and SWIR cameras, *B T. Pham & M. A. Kolodny (Editor), Ground/Air Multisensor Interoperability, Integration, and Networking for Persistent ISR VIII. SPIE*, 2017, doi: 10.1117/12.2262575.
7. A. Hornung, K. M. Wurm, M. Bennewitz, C. Stachniss, W. Burgard, OctoMap: an efficient probabilistic 3D mapping framework based on octrees, *Autonomous Robots*, 2013, 34(3), pp.189–206, doi:10.1007/s10514-012-9321-0.
8. C. Wang, T. Wang, E. Wang, E. Sun, Z. Luo, Flying Small Target Detection for Anti-UAV Based on a Gaussian Mixture Model in a Compressive Sensing Domain, *Sensors*, 2019, 19(9), pp. 2168, doi:10.3390/s19092168.
9. K. Klasing, D. Wollherr, M. Buss, A clustering method for efficient segmentation of 3D laser data, *Pros. IEEE International Conference on Robotics and Automation*, 2008, doi: 10.1109/ROBOT.2008.4543832.
10. S. Ren, K. He, R. Girshick et al Faster R-CNN: Towards Real-Time Object Detection with Region Proposal Networks, *arXiv*, 2015, arXiv:1506.01497
11. J. Redmon, A. Farhadi, YOLO9000: Better, Faster, Stronger, *arXiv*, 2016, arXiv:1612.08242.
12. W. Liu et al., SSD: Single Shot MultiBox Detector, *Computer Vision – ECCV*, 2016, pp. 21–37, doi:10.1007/978-3-319-46448-0_2.
13. X. Li, Y. Zhou, Z. Pan, J. Feng, Partial Order Pruning: for Best Speed/Accuracy Trade-off in Neural Architecture Search, *arXiv*, 2019, arXiv:1903.03777.
14. G. Gkioxari, B. Hariharan, R. Girshick et al, R-CNNs for Pose Estimation and Action Detection, *arXiv*, 2014, arXiv:1406.5212.
15. A. Lefcourt, M. Siemens, P. Rivadeneira, Optical Parameters for Using Visible-Wavelength Reflectance or Fluorescence Imaging to Detect Bird Excrements in Produce Fields, *Applied Sciences*, 9(4), pp. 715. doi:10.3390/app9040715.
16. L. Skvortsov, *Laser methods for remote detection of chemical compounds on the surface of bodies*, Technosphere. Moscow, 2014, pp. 207.
17. A. Misra et al., A Two Components Approach for Long Range Remote Raman and Laser-Induced Breakdown (LIBS) Spectroscopy Using Low Laser Pulse Energy, *Applied Spectroscopy*, 2018, 73(3), pp. 320–328, doi:10.1177/0003702818812144.
18. S. Hugger et al., Quantum cascade laser based active hyperspectral imaging for standoff detection of chemicals on surfaces, *Quantum Sensing and Nano Electronics and Photonics XIII, SPIE*, 2016, doi:10.1117/12.2210913.
19. T. Rayner et al., Remote explosive and chemical agent detection using broadly tunable mid-infrared external cavity quantum cascade lasers, *Optics and Photonics in Global Homeland Security III, SPIE*, 2007, doi:10.1117/12.727700.
20. I. Fufurin, A. Tabalina, A. Morozov et al. Identification of substances from diffuse reflectance spectra of a broadband quantum cascade laser using Kramers–Kronig relations. *Optical Engineering*, 2020, 59(6), pp. 061621, doi:10.1117/1.OE.59.6.061621.

ESTIMATION OF THE LEVEL OF ELECTROMAGNETIC NOISE IN THE IONOSPHERE

Leonid S. Chudnovsky

Open Joint-stock Company "Research-and-Production Corporation "Precision System and Instruments", Moscow, Russia

The intensity of the noise electromagnetic radiation of the ionosphere varies greatly with latitude. It is determined by both solar insolation and the density of magnetic field lines. Noise emission occurs at the time of ionization of molecules with the release of an electron and attachment / recombination of electrons to a molecule or ion. Such radiation is called microdipole, radiation physics is described in [1]. During the intrusion of the ionizing radiation of the Sun, the level of electron concentration in the

ionosphere increases and at the same time the radiation situation on Earth increases. A high concentration of electrons in arctic latitudes, especially during the invasion of solar fluxes, leads to an increased value of the intrinsic noise radiation of the ionosphere, which complicates the passage of short waves. For an airborne terrestrial environment, there is a cutoff of the intensity of microdipole radiation at frequencies below 30 MHz, which is associated with the small mean free path of electrons in the air.

Consider the noise emission in the ionosphere. The radiation intensity is proportional to the speed and concentration of free electrons and inversely proportional to their lifetime, which is proportional to the density of molecules. The electronic temperature of free electrons for altitudes from 60 to 105 km is on average 200 K, which corresponds to a velocity of $V = 105 \text{ m/s}$. The product of the electron concentration and the concentration of molecules depends on the height, reaching a maximum at heights of 100-110 km [2].

We turn to the radiation model [1]. A free electron leaves the molecule with a velocity V and completely loses its velocity along the mean free path. The electric field E of such an event is

$$E = \frac{eV}{4\pi R \epsilon_0 c^2} [\delta(t) - \delta(t - \tau)]$$

where e is the electron charge; V is the electron velocity; τ is the electron lifetime; ϵ_0 is the dielectric constant of vacuum; c is the speed of light; R is the distance from the noisy layer of the ionosphere to the receiving point.

Given the distribution of electrons n_e and along the height h for an elementary volume $\Delta v = \Delta S \Delta h$ we obtain the following estimate of the noise spectral density

$$\langle E^2(\Delta v, t - t') \rangle = \left(\frac{e^2 V^2}{4\pi^2 \epsilon_0^2 c^4 R^2} \right) \frac{n_e}{\tau} \delta(t - t')$$

The total noise level of the ionosphere will be equal

$$\langle E^2(\tau) \rangle = \int_{\Delta v} \langle E^2(\Delta v,) \rangle dv$$

Thus, the ionosphere noise starting at frequencies $\omega > \tau^{-1}$ is white noise. At altitudes from 60 to 130 km, the value $(\frac{n_e}{\tau})^{1/2} = 2(10^6 \div 10^7)$. Therefore, heights of 65-110 km make the main contribution to the noise of the ionosphere. After calculating, we obtain the following estimate of the ionosphere noise in the daytime

$$(\langle E^2 \rangle)^{1/2} = 7[\mu\text{V} / \text{m MHz}^{1/2}]$$

In arctic latitudes, this value reaches $70 \mu\text{V} / \text{m MHz}^{1/2}$. With the invasion of ionizing fluxes, the noise level can reach up to $300 \mu\text{V} / \text{m MHz}^{1/2}$. The rms noise level of an antenna with a resistance of 50 ohms is $0.9 \mu\text{V} / \text{mMHz}^{1/2}$. Thus, registration of noise of the ionosphere by an antenna with an effective height of more than one meter is quite possible.

The intrusion of ionizing radiation (gamma) is detected by the system [3] faster than the flow of electrons and heavy particles. The level of radiation threats can be estimated by the ground-based complex for recording ionosphere noise in the VHF range. The use of several phased antennas will make it possible to control the zones of the ionosphere most susceptible to ionization. Open Joint-stock Company "Research-and-Production Corporation "Precision System and Instruments has experience creating such VHF receivers.

1. L. S. Chudnovsky, K. S. Mozgov, S. A. Panov, Microdipole electromagnetic radiation induced by a powerful pulse of gamma quanta, *Chemical Physics*, 2013, 32(11), pp. 23-25.
2. E.L. Stupitsky, Ionization of the atmosphere during a nuclear explosion, in the collection *Physics of a Nuclear Explosion*, 1997, 1, pp.368-397.

MATHEMATICAL METHODS FOR THE DETECTION OF UNMANNED AERIAL VEHICLES BY SIGNALS FROM OPTICAL DETECTION SYSTEMS

Anastasiya S. Tabalina, Igor L. Fufurin, Andrey N. Morozov, Andrey L. Nazolin

Bauman Moscow State Technical University, Moscow, Russian Federation

Introduction. Nowadays, significant progress in UAV technology made it possible to find a lot of applications for drones within the city: from delivering products to taking photographs and videos. Modern drones – affordable, convenient devices that is gaining popularity among private sector persons. As a result, threats of drone attacks have been increasing. The goal of our investigation is to develop remote detection system, that provides UAV identification and tracking within the city. For this purpose, we suggest usage of methods of optical location, optical spectroscopy and methods of automatic identification by visible and IR images of target objects.

In this paper, the methods of processing the visible image obtained from the detection system are discussed. The variety of shapes, proportions and types of UAVs, as well as the small size of the target, wide range of possible backgrounds (including those with low contrast to the object) create significant difficulties in detecting and identifying the drone in the image. Examples of processing images are shown on Figure 1.

Methods of UAV detection.

One of the simple approaches to our task is an expert system [1], where feature selection is assigned to the operator, who analyzes the image and selects features from a pre-defined table. The program based on the selected parameters makes a comparison with the database and determines the most appropriate UAVs model.

Other traditional methods for UAV detection purposes is edge based approaches. Contours/shape descriptors have been extracted and compared with a series of methods, including including hidden Markov models, feature points, tangent/turning functions, curvature maps, shock graphs, Fourier descriptors, etc. [2]. They have their benefits and drawbacks, regarding computational complexity, precision capabilities, implementation issues, robustness and scalability.

Other edge based approaches include Chamfer distance based methods [3] for recognizing objects through smaller shape fragments. These methods generally work by converting the high level metrics into a distance function based comparison, which in turn works by using some kind of chain code shape representation. They incorporate scale and rotation invariance on the high level.

Methods of computer vision. Computer vision is an interdisciplinary scientific field that deals with how computers can be made to gain high-level understanding from digital images or videos. Computer vision tasks are (Fig 2):

- Classification;
- Semantic Segmentation;
- Object Detection;



FIGURE 1. Examples of target UAV.

- Instance Segmentation.

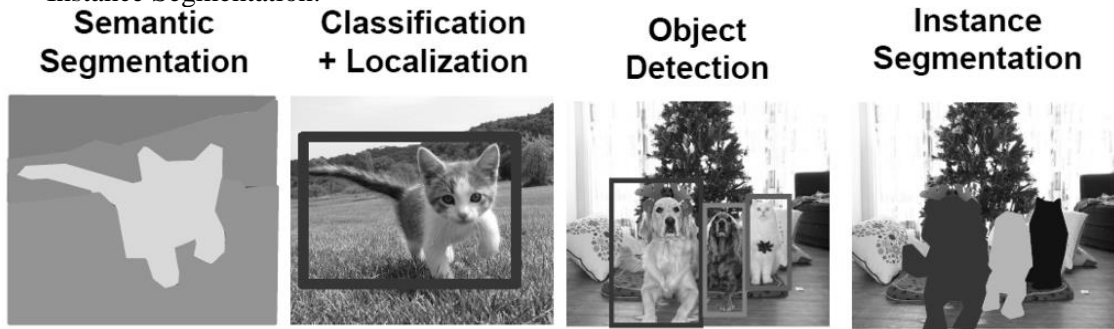


FIGURE 2. Computer vision tasks.

With the advent of convolutional neural networks (CNN), there has been a significant breakthrough in object detection algorithms. Most often, such convolutional neural network architectures as Faster R-CNN, YOLO, SSD are used for detection tasks.

You only look once (YOLO) [4] is an object detection system targeted for real-time processing. The major concept of YOLO is to treat image detection as a regression task, not as classification task. YOLO build a CNN network to predict a tensor and performs a linear regression using two fully connected layers to make box predictions.

Single Shot Detector (SSD) [5] is an architecture uses single CNN for predicting the location of boxes and their classes.

Faster R-CNN [6] performs object detection in two stages. In the first stage, a region proposal network (RPN) takes feature maps of a given image at some intermediate layer as input and outputs a set of rectangular object proposals. Then, Fast R-CNN [7] classifies the object proposals in the second stage.

Faster R-CNN solving the task of object detection. Mask R-CNN develops the Faster R-CNN architecture by adding another branch that predicts the position of the mask covering the found object, and thus solves the instance segmentation task.

Mask-R-CNN application. In this work we consider Mask R-CNN architecture [8] and possibilities of it's application for task of UAV-detection.

At the first stage, CNN was trained on a test data set of 1000 images, validation dataset contained 100 images. Model was trained two main ways (Table 1 The first method was to train CNN from scratch. The second way was to use transfer training. In other words, "transfer training" means that we start with a Weight file that has been pre-trained on some data set. In our case, it was COCO. Although the COCO dataset does not contain a UAV class, it contains many other images (~120K), so trained Scales have already learned many features common in natural images that could improve the accuracy of detection results.

For accuracy measurements mean average precision (mAP) metric was used. Average precision computes the average precision value for recall value over 0 to 1.

TABLE 1 Comparison of models trained in one of two ways.

Iterations	mAP on the validation dataset	
	Learning from scratch	Learning from pre-trained weights
100 epochs, 100 steps per epoch	0.43	0.66
200 epochs, 100 steps per epoch	0.61	0.77



FIGURE 3. UAV detection on the validation images.

Conclusion. Nowadays CNNs are one of the most advanced approaches to machine vision tasks, which include detection and segmentation of objects in the image. The Mask R-CNN architecture for solving the problem of detecting UAVs was considered. The model was trained on a small test dataset of 1000 images. In further investigations we plan to consider the architectures of YOLO and SSD and perform a comparative analysis of them.

This work is supported by Russian Foundation for Basic Research (RFBR) grant №19-29-06009.

1. V. P. Goncharenko, Solving practical problems of UAV image recognition based on the application of natural classification, *Minsk: BGUIR*, 2016. (In Russian)
2. L. Kovács, C. Benedek, Visual real-time detection, recognition and tracking of ground and airborne targets, *Proc. SPIE 7873, Computational Imaging IX*, 2011, pp. 787311, doi: 10.1117/12.872314.
3. J. Shotton, A. Blake, R. Cipolla, Multi-scale categorical object recognition using contour fragments, *IEEE Tr. on Pattern Analysis and Machine Intelligence*, 2008, 30(7), pp. 1270-1281.
4. J. Redmon, A. Farhadi, YOLO9000: better, faster, stronger, *Proceedings of the IEEE conference on computer vision and pattern recognition*, 2017, pp. 7263-7271, doi: 10.1109/CVPR.2017.690.
5. W. Liu, D. Anguelov, D. Erhan, Ch. Szegedy, S. Reed, Ch.-Y. Fu, A. C. Berg, SSD: Single shot MultiBox detector, *Proceedings of the European Conference on Computer Vision (ECCV)*, 2016, 9905, doi: 10.1007/978-3-319-46448-0_2.
6. S. Ren, K. He, R. Girshick, J. Sun, Faster R-CNN: Towards real-time object detection with region proposal networks, *Advances in neural information processing systems*, 2015, 28, pp. 91–99.
7. R. Girshick, Fast R-CNN, *Proceedings of the IEEE international conference on computer vision*, 2015, pp. 1440–1448, doi: 10.1109/ICCV.2015.169.
8. Matterport's Mask R-CNN library (Added Ship Detection sample) for object detection and instance segmentation on Keras and TensorFlow: [github.com]. URL: https://github.com/gabrielgarza/Mask_RCNN

THE POLLUTION OF THE ATMOSPHERIC AIR AND ITS CONNECTION WITH THE BRONCHOPULMONARY DISEASES IN CHILDREN IN THE YAROSLAVL REGION

Pavel V. Berezhansky¹, Sergey O. Turchaninov²

¹ State budgetary healthcare institution of the Moscow region "Odintsovo regional hospital"

² Bauman Moscow State Technical University

Introduction. The respiratory diseases in the structure of the morbidity of the population of Yaroslavl take one of the first places among all the age groups. For the children of different ages this figure is 68%, and for the adult population – 44% [1].

The pollution of the atmospheric air in the Yaroslavl region is formed by the combined influence of the industrial and motor transport emissions. The main share of the chemicals is made by the motor transport, oil refining and Yaroslavl motor plant. In the Yaroslavl region as of January 01, 2015, the number of the enterprises with the stationary sources of the pollutant emissions having the approved standards of the permissible emissions (MPE) is 1261 un.

In 2013 in the Yaroslavl region in accordance with the statistical report 2-TP (air) "The information on the protection of the atmospheric air", the statistical survey covered 14028 units of the stationary sources of the emissions of the pollutants [2].

According to the data from the official website of the Yaroslavl regional center for hydrometeorology and environmental monitoring – CGMS – the branch of the FGBU "Central UGMS" (yacgms.ru), the monitoring of the atmospheric air pollution is carried out in Yaroslavl – at 5 posts, in Rybinsk – at 2 posts, in Pereslavl-Zalessky – at 1 post [3].

In 2020 the Department of the environmental protection and environmental management has developed a qualitatively new approach in the issues of the monitoring of the state of the air environment of the Yaroslavl region. Together with the specialists of the State budgetary institution "The center of the environment for the Yaroslavl region" the list of the problem zones in the districts of the Yaroslavl and the region is determined where the measurement of the indices of the air environment is carried out on a regular basis, including in the evening and at night. The collection of the analytical data is carried out, on the basis of which the register of the places for different pollutants will be formed. Such work will allow to more accurately determine the possible source of pollution according to the data of the road trips of the mobile ecoanalytical laboratory [4].

The predominant pollutants are: nitrogen dioxide, phenol, formaldehyde, benzopyrene in the concentrations above the maximum permissible coefficient in 0.96 – 6.3 times. Along the main highways and factories the exceeding of the maximum permissible coefficient is registered in the air in 1.9 – 7.2 times for nitrogen dioxide, carbon monoxide, formaldehyde. The highest of the total anthropogenic pollution of the atmosphere was revealed in the areas of the highest traffic intensity – the district of Neftestroy, Dzerzhynsky district and in the vicinity of the largest industrial facilities located within the city (in 6.2 times), and the lowest in the areas remote from the city of Yaroslavl (2.06 times), where the traffic intensity is average and there are no large industrial facilities. The average levels of the content of the harmful substances in the atmospheric air in the residential areas exceed the maximum permissible concentrations by 1.48 – 2.03 times for hydrogen fluoride, by 2.78 times for formaldehyde, by 3.02 times for benzopyrene [5].

In the unfavorable areas direct correlation was found between the bronchopulmonary and allergopathological morbidity of children and the level of pollution (in the places where the children live). The number of children with asthma is higher in the areas with the increased content of nitrogen dioxide and benzopyrenes ($r=0.82$, $p<0.05$), and the number of pollinosis is higher in the regions with

the increased content of the carbon monoxide in combination with the increased content of hydrogen fluoride ($r=0.82$, $p<0.05$).

According to regression ratios the increase of the incidence of children with pneumonia, chronic bronchitis, acute and chronic tonsillitis, bronchial asthma was revealed with the increased concentration of the pollutants in the atmospheric air ($p<0.05$). The greatest degree of the influence of atmospheric impurities to the incidence of the respiratory diseases was observed in the age groups of children from 1 to 2 years and from 3 to 6 years.

The study involved 125 children at the age from 1 to 6 years who have suffered several attacks of acute obstructive bronchitis or were diagnosed with asthma and pollinosis. All the children at the time of the inclusion on the study had no signs of acute viral infection for 2 months. All the children were observed in the catamnesis for 36-48 months. The state of the capillary bed was assessed in all the children by the method of computer capillaroscopy, the following parameters were determined: the remodeling coefficient (RC), the coefficient of the transverse deformation of the arterial section (CTDAS), the arteriolo-venular coefficient (AVC), the distance between the capillaries (L) and the length of the perivascular space (LPS) [6].

All the children were divided into 2 groups: 1 group – 73 children from the district with the increased content of nitrogen dioxide, benzopyrenes and hydrogen fluoride in the atmospheric air, 2 group. – 52 children from the district with the maximum permissible content of these substances in the atmospheric air. All the children had the confirmed diagnoses according to the MCD – 10.

In the patients of the 1 and 2 groups there were initially the changes in the capillary bed in the form of weakly differentiated 2 and 3 echelons of capillaries, the presence of morphological changes, the increase of perivascular zone and the curvature of the arterial department, but in the 1 group they were more pronounced. Venular dilatations were observed in both groups.

In the catamnesis it was found that some changes were correlated with the content in the atmospheric air: benzopyrenes and CTDAS ($r = 0.52$; $p < 0.03$), and AVC ($r = 0.75$; $p < 0.003$), nitrogen dioxide and RC ($r = 0.81$; $p < 0.005$), hydrogen fluoride and LPS ($r = 0.59$; $p < 0.03$).

Also in the catamnesis in 56% of the children of the 1 group, there were more pronounced changes in the microcirculatory bed which correlated with the clinical manifestations of the disease.

The statistical methods were used to determine the indicators of the capillary bed with which the worsening of the conditions and the exacerbation of the disease are revealed: RC – more than 9.8 conv. un., CTDAS – more than 1.7 con. Un., AVC - less than 0.45 con. un., L – less than 40.2 mcm and LPS. – more than 110 mcm.

During the catamnestic examination it was found that the patients with the exacerbation retained the microcirculatory changes determined during the initial examination and these changes depended on the content of the substances in the atmospheric air.

Thus, in the Yaroslavl region the atmospheric air is a decisive factor in the formation of the environmental problems for the children with allergopathology. On the territory of the Yaroslavl region there is no method of assessing the risk of causing damage to health depending on the pollution of the atmospheric air which requires further study.

Acknowledgments. The reported study was funded by RFBR according to the research project №18-29-02024.

1. I. S. Sinitsyn, The assessment of the influence of the pollution of the atmospheric air of Yaroslavl on the respiratory diseases, *Yaroslavl pedagogical bulleting*, 2011. 3(1). pp. 190–194.
2. ROSPRIRODNADZOR. On the environmental situation in the Yaroslavl region. <http://76.rpn.gov.ru/node/5918>
3. Yaroslavl regional center for hydrometeorology and environmental monitoring. <http://www.yacgms.ru/struktura/nabludatel'naya-set/pnz/>

4. The Department of environmental protection and nature management. <https://www.yarregion.ru/depts/doosp/Pages/Monitoring-vozduha.aspx>

5. The recorded excess of the sanitary standards in the cities of the region <https://www.yacgms.ru/monitoring-zagryazneniya-okruzhayushhej-sredy/obzor-sostoyaniya-i-zagryazneniya-okruzhayushhej-sredy-za-mesyats/sostoyanie-atmosfernogo-vozduha/>

6. The patent for invention N 2580970 RF of 26.12.2014. The method of predicting of the development of the decompensation of the microcirculatory bed and the worsening of the course of the allergic pathology of the respiratory tract in the children of early age with the burdened allergeanamnesis, Auth. Berezhansky P.V., Turchaninov S.O. – Published: 10.04.2016 Bul. N 10.

APPLICATION OF THE CAUSALITY RELATIONS FOR THE IDENTIFICATION OF SUBSTANCES FROM REFLECTED INFRARED RADIATION

Igor L. Fufurin, Anastasia S. Tabalina, Andrey N. Morozov, Igor S. Golyak

Bauman Moscow State Technical University, Moscow, Russia

Introduction. Identification of chemical compounds is one of the most important tasks in a large field of studies and technologies. Physicochemical characteristics of the test substances, as well as environmental conditions determine experimental techniques for studying the chemical composition of substances [1]. Optical spectroscopy is a widely used technique for analyzing the composition and structures of substances in laboratory and field studies. [2].

The most common optical spectroscopy methods are Fourier spectroscopy (FTIR spectroscopy) [3], nondispersive infrared spectroscopy (NDIR) [4], Raman spectroscopy [5], Terahertz spectroscopy [6] and methods of photoluminescence [7].

For non-laboratory studies of liquids and solids, Raman spectroscopy is widely used. This method is highly selective and sensitive; it allows the identification of substances in optically transparent packages without sampling. A significant drawback of this method is the small quantum efficiency of the Raman scattering radiation, as well as the high level of intrinsic fluorescence for some substances and the necessity to use sufficiently powerful sources of exciting radiation. Since the middle of the 20th-century, analysis of diffusely reflected radiation was used to study the chemical composition of substances, for which broadband infrared sources and monochromators were used, and later Fourier spectrometers. Recently significant progress in laser technologies occurred in connection with the development of quantum cascade lasers (QCL). Modern QCLs are capable of generating laser radiation with a tuning range of up to 1000 cm⁻¹ in the mid-IR range with a pulse power of more than 100 mW and physical laser chip size less than an inch.

Usage of the quantum cascade lasers and sensitive infrared photodetectors makes it possible to create portable spectrometers that allow recording the spectra of diffusely reflected IR radiation [8]. The described technique allows the non-sampling identification of substances in liquid and solid states, in laboratory or field conditions. This method has several principal advantages such as possibility of real-time remote sensing on natural surfaces, insensitivity to external illumination, safety (both for the researcher and for the test sample), possibility of forming a wide beam of probe radiation to scan the surface.

In laboratory conditions, the developed technique can complement the ATR and DRIFTS methods; in field analysis the method complements and competes with Raman spectroscopy. However, it must be remembered that diffuse reflectance spectra for most substances have relatively low selectivity. The Kramers–Kronig relations connect the real and imaginary parts of the complex reflectivity of an

electromagnetic wave entering the Fresnel equations. They allow reconstructing the absorption spectrum from an experimentally observed diffuse reflectance spectrum.

Further detection and identification of substances can be performed both by analysis of the experimental diffuse reflectance spectra and calculated absorption spectra [9]. It can significantly increase the reliability of identification for some classes of substances.

Experimental data analysis. Fig. 1 shows typical diffuse reflectance spectra obtained using experimental setup.

The Pearson correlation coefficient for the two diffuse reflectance spectra of Aspirin is 0.99, which indicates good reproducibility of the measured spectra. The instability of the spectral lines' intensity is caused by the fluctuations of laser power.

In the case of normal incidence of an electromagnetic wave on the interface between two media, according to the Fresnel equations, algebraic relations take place for the reflection, its amplitude and phase as $\ln[r(\nu)] = \ln[\eta(\nu)] + i\varphi(\nu)$. Functions $\ln[\eta(\nu)]$ and $\varphi(\nu)$ are real and imaginary parts of a complex function. According to the causality principle, they must satisfy the Kramers-Kronig relations.

The data in Table 1 was obtained when the spot of exciting laser radiation 2×4 mm² was completely filled with the test substance.

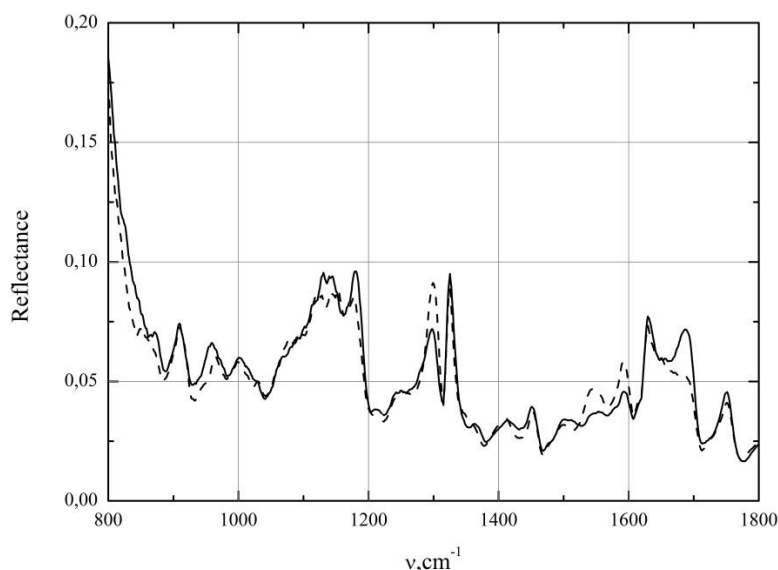


FIGURE 1. Typical view of two diffuse reflectance spectra of Aspirin crystals with sizes from 100μm to 1mm

TABLE 1. Sensitivity of experimental setup.

Test substance	Using reflectance spectra		Using Kramers-Kronig relations	
	Identification threshold, mg	Pearson correlation	Identification threshold, mg	Pearson correlation
Aspirine	6.38	0.9	0.03	0.5
L-Tyrosine	0.75	0.9	0.04	0.6

Estimations. We suggest using a QCL with peak power about 0.2 W, tuning range 7 to 11 μm and repetition frequency ~1 MHz; MCT photodetector with detectivity $D^* \sim 8 \times 10^9$ cm Hz^{1/2}/W, and 2×2 mm² size. Laser radiation on a beam splitter is divided into two parts: the first part goes directly to the reference detector and the second part via telescopic system falls on the test substance on the background, reflects from the test substance, and goes to the signal detector via telescopic and collecting optics. If we use accumulation of 100 spectra, we can obtain reflectance spectra with the SNR $\sim 10^4 \times \alpha$ for small distances from the test substance, where α is the reflection coefficient of the test substance. For test substances with scattering cross-section $\sigma \sim 10^{-19}$ cm² and molecular mass $m \sim 10^{-22}$ g, we can obtain reflectance spectra at a distance of $L \sim 1$ m with the SNR ~ 5 . These estimates

correspond to the possibility of remote detection and identification of test substance with a surface density of $10 \mu\text{g}/\text{cm}^2$ at a distance 1 m.

Conclusion. We present a real-time automated system for remote substance identification on various surfaces without preliminary sample preparation. It can be used as an alerting system to signal the presence of some contaminants. The main components of the system are diffuse reflectance spectra acquisition module, data processing module, and identification module. To achieve better system selectivity recognition and identification algorithms were based on the absorption and transmission spectra calculated from the recorded diffuse reflectance spectra. Spectra conversion algorithms employed Kramers–Kronig relations, phase spectra extrapolation, and phase correction. The experiments showed that the usage of transmittance spectra significantly improved the sensitivity of the identification method; the remote identification limit of $30 \mu\text{g}$ acetylsalicylic acid has been experimentally confirmed. For updated experimental setup such limit was estimated as $10 \mu\text{g}/\text{cm}^2$ at a distance of 1 m.

The reported study was funded by RFBR according to the research project №18-29-02024.

1. H. Lin, F. Gao, Y. Ding, C. Yan, S. He, Methane detection using scattering material as the gas cell, *Applied Optics*, 2016, 55(28), pp. 8030, doi: 10.1364/AO.55.008030.
2. A. Morozov and S. Svetlichnyi, *Osnovy Fur'e-spektroradiometrii. Moskva: Nauka*. 2014. (in russian).
3. A. N. Morozov, S. E. Tabalin, I. L. Fufurin, and S. I. Svetlichnyi, Physical principles of the design of an interferometer with a rotating plate, *Journal of Optical Technology*, 2013, 80(8), pp. 495-498, doi:10.1364/JOT.80.000495.
4. F. Yi, X. Tan, A. Yang, J. Li, H. Liu, Narrowband plasmonic metamaterial absorber integrated pyroelectric detectors towards infrared gas sensing, *Smart Photonic and Optoelectronic Integrated Circuits XX*, 2018, E.-H. Lee and S. He, Eds., SPIE. doi: 10.1117/12.2286437.
5. N. S. Vasil'ev, I. B. Vintaykin, I. S. Golyak, I. S. Golyak, I. V. Kochikov, I. L. Fufurin, Recovery and analysis of Raman spectra obtained using a static Fourier transform spectrometer, *Computer Optics*, 2017, 41(5), pp. 626–635, doi: 10.18287/2412-6179-2017-41-5-626-635.
6. K. I. Zaytsev, A. A. Gavdush, V. E. Karasik, V. I. Alekhovich, P. A. Nosov, V. A. Lazarev, I. V. Reshetov, S. O. Yurchenko, Accuracy of sample material parameters reconstruction using terahertz pulsed spectroscopy, *Journal of Applied Physics*, 2014, 115(19), pp. 193105. doi:10.1063/1.4876324.
7. N. S. Vasil'ev, I. S. Golyak, A. N. Morozov, An algorithm for identification of substances using a finite set of secondary-emission spectra, *Optics and Spectroscopy*, 2015, 118(1), pp. 151–156, doi: 10.1134/S0030400X1412025X.
8. I. S. Golyak, A. N. Morozov, S. I. Svetlichnyi, A. S. Tabalina, I. L. Fufurin, Identification of chemical compounds by the reflected spectra in the range of $5.3\text{--}12.8 \mu\text{m}$ using a tunable quantum cascade laser, *Russian Journal of Physical Chemistry B*, 2019, 13(4), pp. 557-564, doi: 10.1134/S1990793119040055.
9. I. L. Fufurin, A. S. Tabalina, A. N. Morozov, I. S. Golyak, S. I. Svetlichnyi, D. R. Anfimov, I. V. Kochikov, Identification of substances from diffuse reflectance spectra of a broadband quantum cascade laser using Kramers–Kronig relations, *Optical Engineering*, 2020, 59(6), pp. 061621, doi: 10.1117/1.OE.59.6.061621.

PROSPECTS FOR CREATING AN INFRARED FOURIER SPECTROMETER BASED ON A ROTATING PLATE INTERFEROMETER

Anastasiya V. Scherbakova¹, Igor L. Fufurin¹, Sergey I. Svetlichnyi²

¹ Bauman Moscow State Technical University, Moscow, Russia

² Russian Academy of Sciences, Chernogolovka Branch of the N.N. Semenov Federal Research Center for Chemical Physics

Introduction. This paper presented the design of an interferometer with a rotating plate. Models of convolution of interferograms with various Apodization functions such as Rectangle, Max, Fock, Berthier, Blackman-Harris, Hann–Hansel are presented. It is shown that when the plate is rotated by more than a critical angle, the linearity of the wave path difference is violated. Estimates of the critical angle for a plate with a thickness of 10 mm are made. Possible ways to overcome the nonlinearity of the wave path difference are discussed.

The main part. Currently most Fourier spectrometers are based on the Michelson interferometer. However, there are other concepts that have a number of advantages over existing ones. You can reduce the mass and size of the Fourier spectrometer using an interferometer with a rotating plate. 1 Its design is presented in Figure 1.

The optical difference of paths of waves in such an interferometer will be determined by the expression [1]:

$$L = 2(n(OA - OB) + AC) \quad (1)$$

where n is the refractive index of the plate, and OA , OB , and AC are the lengths of the corresponding line segments (determined from geometric considerations shown in Figure 2).

$$OA = \frac{d}{\cos \gamma}; \quad \sin \gamma = \frac{\sin \beta - \alpha}{n} \quad (2)$$

$$OB = \frac{d}{\cos \varphi}; \quad \sin \varphi = \frac{\sin \alpha + \beta}{n} \quad (3)$$

$$AC = d * (\tan \gamma + \tan \varphi) * \frac{\sin \alpha}{\sin \beta} \quad (4)$$

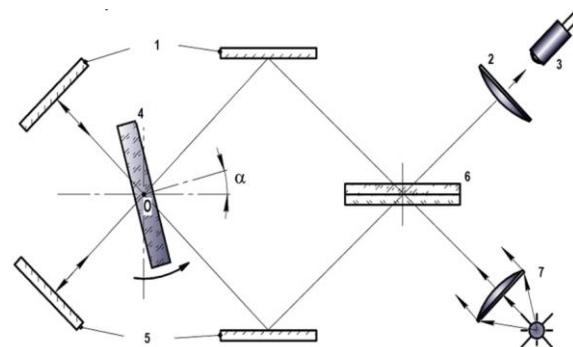
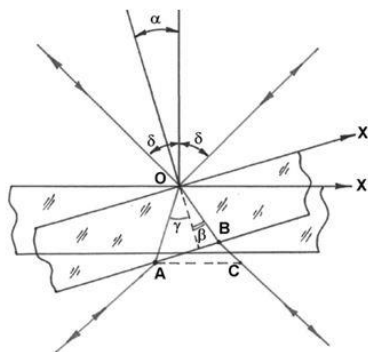


FIGURE 1. Design of an interferometer with a rotating plate. 1,5 – mirrors; 2 – gathering team; 3 – photodetector; 4 – rotating plate; 6- beam splitter; 7 – radiation source

FIGURE 2. Optical diagram of the ray path in the interferometer plate.

With this expression (1), we can construct a model spectrum considering the ideal interferogram of a monochromatic radiation source with a wavelength of 10 microns ($\nu_0=1000$ 1/cm). The Fourier image of the interferogram will be a Dirac delta function at 1000 1/cm .By convolved interferograms with Apodization functions, we obtain a Fourier image $B(\nu)$:

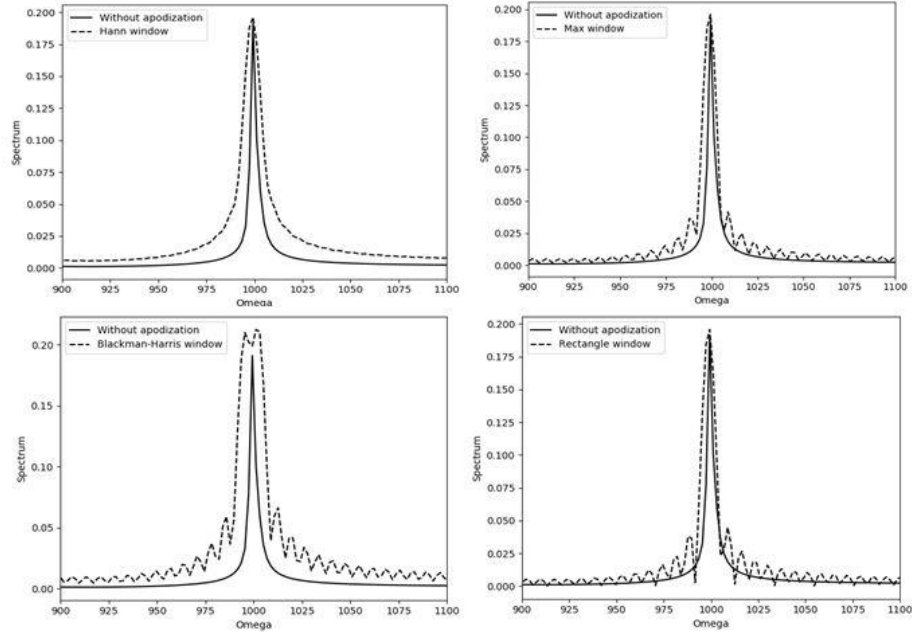


FIGURE 3. Fourier images of interferograms convolved with various. Apodization functions.

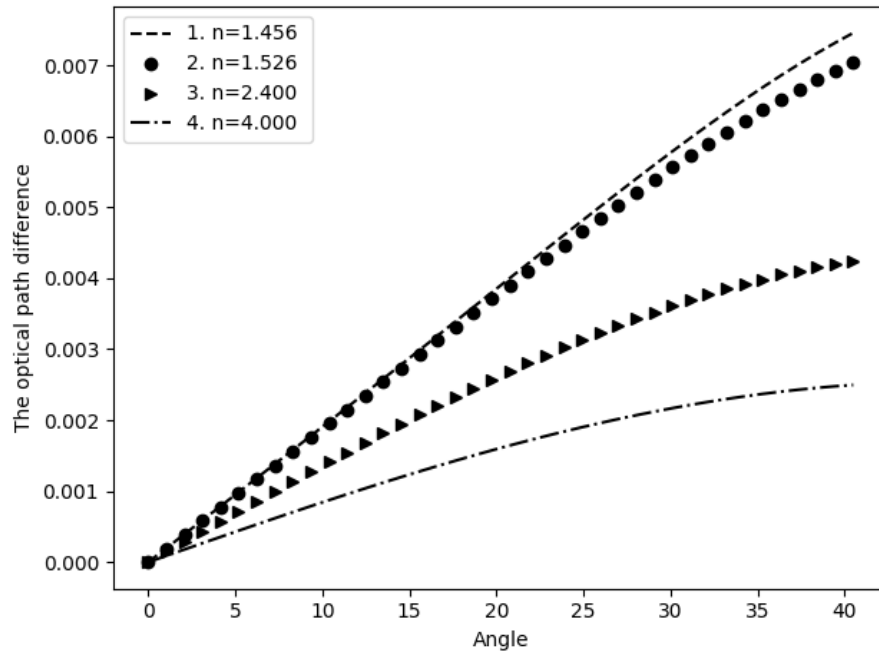


FIGURE 4. Results of calculating the optical path difference for $\lambda = 10$ microns in the interferometer for various optical materials are given as the function of the angle of rotation of the plate: 1. KCl ($n = 1.456$), 2. KBr ($n = 1.526$), 3. ZnSe ($n = 2.401$), 4. Ge ($n = 4.004$).

At large angles, the linearity of the $L(\alpha)$ dependence is violated, which leads to distortion of the desired spectrum. The analysis of the equations showed that distortion occurred when the angle of rotation of the plate exceeded $\pm 15^\circ$.

Spectrum distortion complicates the task of identifying substances using a Fourier spectrometer. Nonlinearity of dependence of optical path from angle of plate rotation occurs to phase shifts in Fourier transforms. Correct spectrum calculation follows to phase correction methods, that is beyond the scope of present paper.

The reported study was funded by RFBR according to the research project No. 19-29-06009.

1. A. Morozov, S. Tabalin, I. Fufurin, I. L. et al, Physical principles of the design of an interferometer with a rotating plate, *Journal of Optical Technology*, 2013, 80(8), pp. 495, doi:10.1364/jot.80.000495.
2. A. N. Morozov and S. I. Svetlichny, *Principles of Fourier Spectroradiometry*, 2-nd ed., 2014, Nauka, Moscow, pp. 456. (in Russian).
3. V. A. Vagin, M. A. Gershun, G. N. Zhizhin, et al., *HighAperture Spectral Devices*, Ed. by K. I. Tarasov, Nauka, Moscow, 1988) (in Russian).
4. W. Wadsworth, J.-P. Dybwad, Rugged high-speed rotary imaging Fourier transform spectrometer for industrial use, *Vibrational Spectroscopy-based Sensor Systems*, SPIE, 2002, doi:10.1117/12.455725.
5. I. Golyak, A. Morozov, S. Svetlichnyi et al, Interferometer with Rotating Plate: Fundamentals, *International Conference on Industrial Informatics, Machinery and Materials (IIMM)*, 2015, pp. 188-192.

SPACE SYSTEM FOR MONITORING COMPLIANCE WITH INTERNATIONAL AGREEMENTS ON THE PROHIBITION OF NUCLEAR WEAPONS TESTS

Vladislav S. Chudnovsky, Leonid S. Chudnovsky, Anatoliy N. Pleshanov,
Sergey A. Perevozchikov, Yuriy P. Vagin

Open Joint-stock Company "Research-and-Production Corporation "Precision System and Instruments", Moscow, Russia

A space monitoring system has been created in the Russian Federation for monitoring compliance with international agreements banning nuclear weapons tests [1].

The on-board equipment is located on the navigation spacecraft of the GLONASS system. On-board equipment registers ionizing, optical and radio emissions from a nuclear explosion. The coordinates of the event are determined using the differential-ranging method. To increase the efficiency of obtaining information, an inter-satellite exchange channel is used.

In the ground-based reception complex, the power of the source is specified, and the coordinates of the event are determined.

In the development of on-board equipment, considerable attention was paid to the physical models of radiation and their comparison with experimental registration data [2]. The trace distortions were also refined [3]. This made it possible to drastically reduce the mass and power consumption of on-board equipment. An increase in the sensitivity of the equipment in the optical range was achieved by special circuitry solutions [4]. A special algorithm has been developed to determine the physical time of arrival of an optical pulse in the presence of additive noise [5]. To suppress false alarms and lightning discharges, special algorithms have been developed. When receiving ionizing radiation, special attention was paid to eliminating false alarms from cosmic showers. When receiving radio

emission, the correction of ionospheric dispersion is carried out [6], as well as the suppression of pulsed and concentrated noise. Developed, emission models, processing algorithms and circuitry solutions allowed to eliminate false alarms of the system during 18 years of operation.

Ground-based information receiving complexes are made in stationary and mobile versions. The complex allows you to receive up to 12 messages from spacecraft of the GLONASS system. A special adaptive filtering of concentrated interference is used at the input.

Periodic functional control of the recording sensors of the on-board equipment allows confirming its operability. The accuracy of determining coordinates in the optical range is checked using laser sensing. To verify the accuracy of registration in the ionizing range, data are compared with other spacecraft, for example, Goes [7]. The correct functioning in the optical range is determined by the density of lightning discharges on the territory of the globe [8]. Functional check in the radio range is carried out after the expiration of electrostatic discharges at the receiving antenna.

The placement of on-board equipment on low-orbit spacecraft can significantly reduce weight and power consumption. To receive radio emission, it is planned to use narrow-band high-efficiency loop antennas [9]. In lower orbits, it is possible to register single lightning discharges. The ionosphere radio noise will also be evaluated to determine the technogenic and anthropogenic places of heating the ionosphere. Additionally, a space microparticle density recording sensor will be included [10].

1. Yu.P.Vagin, A.N.Karkhov, V.S.Chudnovsky, L.S.Chudnovsky, Space system for monitoring agreements for the prohibition of testing nuclear weapons, *Aerospace Courier*, 2012, 6, pp. 64.
2. V.P.Busygin, Yu.P.Vagin, R.G.Kovalenko, I.Yu.Kuzmina, A.P.Mkrtychan, Yu.V.Puzanov, V.E.Fominykh, V.S.Chudnovsky, L.S.Chudnovsky, Optical devices and control systems for nuclear tests, *Physics of a nuclear explosion*, 2017, 5, pp. 690.
3. V.P.Busygin, N.G.Busygina, Yu.P.Vagin, I.Yu.Kuzmina, K.S.Mozgov, Yu.V.Puzanov, L.S.Chudnovsky, Distortion of optical signals on the Earth-Space paths, *Electromagnetic waves and electronic systems*, 2013, 18(1), pp. 60.
4. A.Chudnovsky, The Gauge of Optical Pulse Radiation with an Additive Background Flare, Proceedings of 1st International Conference "Atmosphere, ionosphere, safety" AIS-2008, pp .205.
5. L.S. Chudnovsky, V. M. Ageev, Method for determining the time of arrival of a priori unknown signals with a small base, *Bulletin of the Russian Academy of Natural Sciences*, 2016, 1, pp.38.
6. A.Groznov, S.Panov, A.Chudnovsky, Correction of the Ionosphere Delay in Radio Spectrometer, Proceedings of 2nd International Conference "Atmosphere, ionosphere, safety" AIS-2010, pp .194.
7. Yu.P.Vagin, A.A.Gusev, A.O.Nikitin, V.S.Chudnovsky, Measurement of the spectral characteristics of galactic cosmic rays by spaceborne sensors of spacecraft, *Electromagnetic waves and electronic systems*, 2011, 16(3), pp.58.
8. Y.Vagin, A.Karchov, N.Steel, V.Cudnovsky, Registration of Pulse Optical Sources onboard on the Satellite "Glonass-M", , Proceedings of 1st International Conference "Atmosphere, ionosphere, safety" AIS-2008, pp .166.
9. V.M.Ageev, A.N.Pleshanov, V.T.Polyakov, K.E.Tyupikov, A.L.Chudnovsky, L.S.Chudnovsky, Low-space space lightning registrar, *Electromagnetic waves and electronic systems*, 2018, 23(2), pp.64.
10. V.P.Busigin, L.S.Chudnovsky, V.S.Chudnovsky, Ju.P.Vagin, Micro Particles Streams Registration in Outer Space, Proceedings of V International Conference "Atmosphere, ionosphere, safety" AIS-2016, pp .365.

CONTENTS

ATMOSPHERIC-IONOSPHERIC RELATIONS

<i>Medvedev A.V., Ratovsky K.G., Tolstikov M.V., Vasilyev R.V., Artamonov M.F., Oinats A.V.</i> Method for determining neutral wind velocity full vector by using IGWs propagating parameter statistics.....	3
<i>Wang P. K.</i> Satellite and aircraft evidence of storm mass transport to stratosphere.....	6
<i>Nikolashkin S.V., Ammosova A.M., Koltovskoi I.I.</i> Investigation of wave processes by observing noctilucent clouds.....	8
<i>Kulikov Y.Y., Andriyanov A.F., Demin V.I., Demkin V.M., Kirillov A.S., Ryskin V.G., Shishaev V.A.</i> Influence of sudden stratospheric warming on polar mesospheric ozone.....	11
<i>Bakhmetieva N.V.</i> New results of the research of the Earth's lower ionosphere by the method of creating of artificial periodic irregularities.....	13
<i>Sivtseva V.I., Ammosov P.P., Gavrilieva G.G., Koltovskoi I.I., Ammosova A.M.</i> Comparison of planetary wave activity at Maimaga and Tiksi stations.....	16
<i>Yasyukevich A.S., Chernigovskaya M.A.</i> Relation between variability in total electron content and winter polar stratosphere.....	19
<i>Golubkov G.V., Borchevkina O.P., Manzhelii M.I., Adamson S.O., Bezuglov N.N., Dmitriev A.V., Dyakov Yu.A., Klyucharev A.N., Karpov I.V., Lushnikov A.A., Tsai L.C., Eppelbaum L.V., Golubkov M.G.</i> Vertical remote sensing of the Earth's surface using GPS signals.....	22
<i>Bessarab F.S., Sukhodolov T.V., Klimenko M.V., Klimenko V.V., Korenkov Y.N., Funke B., Rozanov E.V.</i> Effects of the January 2005 solar proton events on the ionosphere in EAGLE model.....	26
<i>Krasnov V.M., Kuleshov Yu.V., Korystin A.A., Drobzheva Ya.V.</i> Influence of oscillatory polarizing current upon ionospheric disturbances during the EISCAT heater operation.....	28
<i>Krivolutsky A.A., Cherepanova L.A., Vyushkova T.Yu., Banin M.V., Repnev A.I.</i> Global structure of electron density in D and E regions simulated with 3D photochemical model CHARM-DE.....	31
<i>Denisenko V.V.</i> 2-D model of the global ionospheric conductor connected with the magnetospheric conductors.....	33

<i>Klimenko M.V., Klimenko V.V., Bessarab F.S., Sukhodolov T.V., Denisenko V.V., Rozanov E.V.</i> EAGLE simulation study of ionospheric electric field: impact of atmosphere-ionosphere coupling and global electric circuit.....	36
<i>Timchenko A.V., Bessarab F.S., Klimenko M.V., Klimenko V.V., Borchevkina O.P., Sukhodolov T.V., Korenkov Yu.N., Rozanov E.V.</i> Analysis of global electron content variations during the major sudden stratospheric warming events.....	38
<i>Tolstikov M.V., Oinats A.V., Medvedeva I.V., Nishitani N.</i> Neutral wind azimuth estimating by statistic of TIDs 2D propagation parameters.....	41
<i>Perevalova N.P., Zherebtsov G.A., Serov M.A., Zhizherin V.S.</i> Impact of atmospheric waves on the high-latitude ionosphere during launches from the Vostochny cosmodrome.....	45
<i>Ryabov A.O.</i> Estimation of the ion composition of the outer ionosphere from the characteristics of ELF–VLF waves.....	47
<i>Nosikov I.A., Klimenko M.V., Kotova D.S., Bessarab P.F.</i> Searching of ionospheric waveguided propagation of radio rays by a direct variational method.....	51
<i>Zorkaltseva O.S., Vasilyev R.V.</i> Fabry-Perot interferometer observations of MLT during sudden stratospheric warming's from 2016 to 2019 over Siberia.....	53
<i>Stupishina O.M., Golovina E.G.</i> On space weather factors which can impact terrestrial atmosphere processes.....	55
<i>Raubo K.V., Zakharov V.E.</i> Non-uniform structure of short waves in the ionosphere and its influence on the polarization characteristics of signals.....	57
<i>Borchevkina O.P., Karpov I.V., Karpov M.I., Korenkova N.A., Vlasov V.I., Leshchenko V.S.</i> Influence of meteorological storms on the lower ionosphere according to vertical sensing data.....	60
<i>Kukoleva A.A., Kononova N.K., Krivolutsky A.A., Pogoreltsev A.I.</i> Sensitivity of the lower atmosphere circulation to the intersection of the sector boundaries of the interplanetary magnetic field.....	62
<i>Kurdyeva Yu.A., Karpov I.V., Borchevkina O.P.</i> Numerical modeling of the solar terminator and solar eclipse using lidar data.....	65
<i>Raubo K.V., Zakharov V.E.</i> Investigation of the wave surface and of the ray trajectories evolution while the ray beam of HF waves propagates in the non-uniform anisotropic absorbing ionosphere.....	68
<i>Rozanov E., Usoskin I., Golubenko K.</i> Impact of natural ionization sources on atmospheric electricity.....	71
<i>Ryabov A.O., Frolov V.L.</i> Artificial precipitation of energetic electrons from the Earth' radiation belt.....	73

<i>Nesterov S.A., Denisenko V.V., Boudjada M.Y., Lammer H.</i> The models of the quasistationary electric field penetration from the ground to the middle latitudes ionosphere.....	76
<i>Kshevenskii S.P., Kurdyeva Yu.A.</i> Numerical study of the propagation of atmospheric waves from the troposphere source.....	79
<i>Leble S.B., Smirnova E.S.</i> Analytical and numerical modeling of the acoustic wave disturbance of the atmosphere by a ground source and the ionospheric effect.....	82

IONOSPHERIC-MAGNETOSPHERIC RELATIONS

<i>Ratovsky K.G., Klimenko M.V., Yasyukevich Yu.V., Vesnin A.M., Klimenko V.V.</i> Statistical analysis of ionospheric total electron contents averaged over different latitudinal zones during geomagnetic storms.....	85
<i>Karpachev A.T.</i> Dynamics of main and ring ionospheric troughs.....	88
<i>Belakhovsky V.B., Jin Y., Miloch W.J., Koustov A.V. Reimer A.</i> Influence of the substorm precipitations and polar cap patches on the GPS signals at polar latitudes.....	91
<i>Mandrikova O.V., Fetisova N.V.</i> Modeling and analysis of ionospheric parameters during magnetic storms (on the example of events in 2017-2019).....	94
<i>Despirak I., Lubchich A., Kleimenova N., Gromova L., Gromov S., Malysheva L.</i> Supersubstorms during two strong magnetic storms.....	97
<i>Syrovatskii S.V., Yasyukevich A.S., Yasyukevich Yu.V.</i> Effect of strong geomagnetic storm on GNSS precise point positioning quality.....	100
<i>Oinats A.V., Edemsky I.K., Rogov D.D.</i> Comparison of the HF ground backscatter simulated using ionosphere model updated by VS and GIM TEC data.....	103
<i>Nikolaeva V.D., Gordeev E.I., Rogov D.D., Nikolaev A.V.</i> Auroral ionosphere stationary model (E-AIM) UV input parameters estimation using satellite data.....	106
<i>Chernyshov A.A., Zakharov V.I., Miloch W., Jin Y.</i> Investigation of influence of the disturbed high-latitude ionosphere on the slips of the main parameters of GPS navigation signals during geomagnetic activity.....	109
<i>Shagimuratov I.I., Efishov I.I., Filstov M.V., Zakharenkova I.E., Despirak I., Tepenitsyna N.Yu.</i> GPS-TEC fluctuations and positioning errors during geomagnetic storm March 17, 2015 over Europe.....	112
<i>Ginzburg E.A., Krivolutsky A.A., Kukoleva A.A., Myagkova I.N.</i> Ionization in the atmosphere in the polar region during solar proton events in September 2017 according to measurements on Russian spacecraft meteor and electro.....	116

<i>Mylnikova A.A., Yasyukevich Yu.V., Vesnin A.M.</i> Mutual comparison of methods for calculating the absolute vertical total electron content.....	119
<i>Deminov M.G., Nepomnyashchaya E.V., Obridko V.N.</i> Features of solar activity indices for the ionosphere in the solar cycle 24.....	122
<i>Shagimuratov I.I., Zakharenkova I.E., Yakimova G.A., Tepenitsyna N.Yu., Efishov I.I.</i> GPS-TEC response to the solar eclipse of August 21, 2017 over America and eclipse impact on GPS positioning performance.....	125
<i>Yasyukevich I.A.S., Yasyukevich Yu.V., Klimenko M.V., Vesnin A.M.</i> Contribution of the plasmasphere to total electron content at middle and high latitudes.....	129
<i>Zakharenkova I.E., Cherniak Iu.V.</i> Multi-instrumental observations of ionospheric plasma density disturbances during geomagnetic storms.....	131
<i>Kotova D.S., Klimenko M.V., Vesnin A.M., Klimenko V.V., Zakharov V.E., Rogov D.D., Blagoveshchensky D.V.</i> Simulation of oblique sounding ionograms during St. Patrick's day 2015 geomagnetic storm: validation and investigation of the influence of the Earth's magnetic field.....	132
<i>Klimenko V.V., Klimenko M.V., Ratovsky K.G., Yasyukevich Yu.V., Zakharenkova I.E., Vasiliev R.V.</i> F2 layer ionospheric response to the geomagnetic storms due to the global thermosphere redistribution.....	135

EFFECTS OF IONIZATION OF THE ATMOSPHERE. NATURAL AND TECHNOGENIC DISASTERS

<i>Klimov P.A., Sharakin S.A., Kaznacheeva M.A.</i> Double elves measured by the TUS space detector.....	137
<i>Titova M.A., Zakharov V.I., Pulinets S.A.</i> Large-scale earthquake of early 2010 on Haiti: the localization and relationship of ionospheric irregularities with certain seismic sources.....	140
<i>Pulinets S.A.</i> Randomness and determinism in earthquake prediction.....	142
<i>Karpov M.I., Karpov I.V., Borchevskina O.P., Yakimova G.A., Korenkova N.A.</i> Ionosphere effects during strong meteorological events in Kaliningrad region in 2010–2018.....	143
<i>Gaivoronskaya T.V., Karpachev A.T.</i> Statistics of earthquakes in relation to solar and geomagnetic activity.....	146
<i>Borchevskina O.P., Kurdyayeva Yu.A., Karpov M.I., Chubarenko B.V., Domnin D.A., Korenkova N.A., Karpov I.V.</i> Effects of storm events on the upper atmosphere on the Baltic sea.....	149

ELEMENTARY PROCESSES IN THE UPPER ATMOSPHERE AND IONOSPHERE

<i>Adamson S.O., Kharlampidi D.D., Golubkov G.V., Dyakov Yu.A., Golubkov M.G.</i> AB Initio calculations of the $1\Sigma_g^+$ and $1\Sigma_u^+$ states of Na_2	152
<i>Bychkov V.L., Maslov T.A., Borchevskina O.P., Adamson S.O., Golubkov G.V., Dyakov Yu.A., Golubkov M.G.</i> To atomic oxygen concentration in the E region of the ionosphere.....	156
<i>Dyakov Yu.A., Adamson S.O., Golubkov G.V., Gubanova D.P., Kazaryan M.A., Golubkov M.G.</i> Photochemical properties of pentalene and its derivatives: aromaticity, antiaromaticity, and changing of chemical activity after the single and double ionization.....	159
<i>Krivolutsky A.A., Vyushkova T.Yu., Banin M.V., Tolstykh M.A.</i> Practical global forecasts of atmosphere parameters based on experimental technology with ozone photochemistry (FOROZ model).....	162
<i>Tomshin O.A., Solovyev V.S.</i> Analysis of the events of large-scale disturbances in aerosol index distribution caused by forest fires in Siberia (2016-2019).....	166
<i>Morozov I.I., Vasiliev E.S., Volkov N.D., Lunin V.V., Savilov S.N.</i> Atmospheric processes involving chlorine-containing particles.....	168
<i>Shirokova E.A., Razuvaev A.G., Mayorov A.V., Aradi B., Frauenheim T., Ignatov S.K.</i> The orientational isomerism in neutral water hexamers in the gas phase.....	171
<i>Bychkov V.L., Gotovtsev V.O., Olkhov O.A.</i> Influence of elementary processes in dry air on parameters of the Coulomb's law.....	174

ELECTROMAGNETIC AND OPTICAL PHENOMENA IN THE ATMOSPHERE INCLUDING LONG-LIVED AND PLASMA OBJECTS

<i>Klimov A.I., Belov N.K., Tolkunov B.N.</i> Measurement of cold neutron flux and soft X-ray radiation in heterogeneous plasmoid.....	178
<i>Nikitin A.I., Nikitin V.A., Velichko A.M., Nikitina T.F.</i> The flickering nature of ball lightning shining.....	180
<i>Chistolinov A.V.</i> Properties of compact long-lived luminous formations in the atmosphere.....	183
<i>Bychkov V.L., Esakov I.I., Shestakov D.V.</i> On electric field distribution the near a charged sphere. high-energy ball lightning and its big charge.....	186
<i>Chepelev V.M., Antipov S.N., Gadzhiev M. Kh.</i> Atmospheric electrode microwave discharge in argon flow: excitation modes and spatio-temporal pattern.....	188

<i>Chistolinov A.V.</i> Hydrodynamic model of compact long-lived luminous formations in the atmosphere.....	191
<i>Chistolinov A.V., Yakushin R.V., Khromov M.A., Sargsyan M.A.</i> Study of non-stationary processes and compact luminous formations in a discharge with a liquid cathode.....	195
<i>Lewis E.</i> Micro ball lightning and states, effects, and directions for research.....	197
<i>Nikitin A.I., Nikitin V.A., Velichko A.M., Nikitina T.F.</i> “Strange” radiation and ball lightning.....	200
<i>Nikitin A.I., Nikitin V.A., Velichko A.M., Nikitina T.F.</i> Effects arising at shooting of bright objects.....	203
<i>Kawano S.</i> Basic study of multiple ball lightnings in line by leader tip models.....	205
<i>Bychkov V.L., Chernikov V.A., Deshko K.I., Goryachkin P.A., Mikhailovskaya T.O., Shvarov A.P., Shapovalov V.L.</i> Electrophysical phenomena in dielectric fluids and clay under influence of corona discharge.....	208
<i>Dijkhuis G.C.</i> On force-free eigenstates for ball lightning.....	210
<i>Nikitin A.I., Velichko A.M., Nikitin V.A., Nikitina T.F.</i> Analysis of forces in the charged cluster.....	214

NOVEL METHODS FOR ENVIRONMENTAL CONTROL AND MONITORING

<i>Kulagina T.P., Smirnov L.P., Andrianova Z.S.</i> Influence of low-frequency sonolysis on the stability of chemical reactions involving associates.....	217
<i>Breslavskaya N.N., Buchachenko A.L.</i> Isotope effects in compressed molecules.....	219
<i>Grigoriev T.E., Antipova Ch.G., Zagoskin Yu.D., Khramtsova E.A., Krashennnikov S.V., Lukanina K.I., Chvalun S.N.</i> Porous biodegradable composites for regenerative medicine.....	221
<i>Zaitseva E.S., Tovbin Yu.K.</i> Simulating rough surfaces of nanoaerosols and its influence on surface energy characteristics and the isotherms and kinetics of adsorption.....	223
<i>Kokorin A.I., Kulak A.I.</i> Photodegradation of chloroorganics catalyzed by nano-TiO ₂ photocatalysts.....	226
<i>Morozova O.S., Firsova A.A., Leipunsky I.A., Vorobjeva G.A., Ostaeva G.Yu., Eliseeva E.A., Bukhtiyarov A.V.</i> Nano-dopants in mechanochemical synthesis of copper-ceria catalysts for H ₂ purification.....	227
<i>Khramtsova E.A., Zak P.P., Petronyuk J.S., Trofimova N.N., Krashennnikov S.V., Titov S.A., Gurieva T.S., Dadasheva O.A., Grigoriev T.E., Levin V.M.</i> Light induced myopia in Japanese quail chicks by acoustic microscopy.....	230

METHODS AND TECHNIQUES FOR REMOTE SENSING AND IDENTIFICATION OF HAZARDOUS CHEMICALS IN THE ATMOSPHERE AND DIFFERENT SURFACES

<i>Anfimov D.R., Fufurin I.L., Golyak Ig.S., Tabalina A.S.</i> Ensemble of harmonic damped oscillators as a model of various types of interaction of radiation with matter.....	233
<i>Vintaykin I.B., Korolev P.A.</i> Static fourier spectrometer.....	235
<i>Balashov A.A., Golyak Il.S., Morozov A.N.</i> The dynamic Fourier-spectrometer for Raman stand-off detection of chemical components.....	236
<i>Golyak Ig.S., Fufurin I.L., Morozov A.N.</i> Mathematical methods for the analysis of multicomponent gas mixtures to study the composition of human breath for the primary diagnosis of diseases.....	239
<i>Fufurin I.L., Morozov A.N., Kareva E.R., Tabalina A.S.</i> Infrared spectroscopic system for human breath analysis.....	242
<i>Demkin P.P., Fufurin I.L.</i> Automatic alignment of the trace Fourier spectrometer.....	244
<i>Korolev P.A., Golyak I.S., Morozov A.N.</i> Determination of the sensitivity of a microbolometer camera as part of a static Fourier spectroradiometer.....	247
<i>Morozov A.N., Nazolin A.L., Fufurin I.L.</i> Optical methods for detecting and tracking unmanned aerial objects against the background of natural objects.....	249
<i>Chudnovsky L.S.</i> Estimation of the level of electromagnetic noise in the ionosphere.....	252
<i>Tabalina A.S., Fufurin I.L., Morozov A.N., Nazolin A.L.</i> Mathematical methods for the detection of unmanned aerial vehicles by signals from optical detection systems.....	254
<i>Berezhansky P.V., Turchaninov S.O.</i> The pollution of the atmospheric air and its connection with the bronchopulmonary diseases in children in the Yaroslavl region.....	257
<i>Fufurin I.L., Tabalina A.S., Morozov A.N., Golyak Ig.S.</i> Application of the causality relations for the identification of substances from reflected infrared radiation.....	259
<i>Scherbakova A.V., Fufurin I.L., Svetlichnyi S.I.</i> Prospects for creating an infrared fourier spectrometer based on a rotating plate interferometer.....	262
<i>Chudnovsky V.S., Chudnovsky L.S., Pleshanov A.N., Perevozchikov S.A., Vagin Yu.P.</i> Space system for monitoring compliance with international agreements on the prohibition of nuclear weapons tests.....	264

